From lakes to lungs

assessing microbial activity in diverse environments

Thesis by

Sebastian Hermann Kopf

In Partial Fulfillment of the Requirements

for the Degree of

Doctor of Philosophy in Geobiology

California Institute of Technology

Pasadena, California

2015

(Defended June 11, 2014)

Abstract

All major geochemical cycles on the Earth's surface are mediated by microorganisms. Our understanding of how these microbes have interacted with their environments (and vice versa) throughout Earth's history, and how they will respond to changes in the future, is primarily based on studying their activity in different environments today. The overarching questions that motivate the research presented in the two parts of this thesis – how do microorganisms shape their environment (and vice versa)? and how can we best study microbial activity *in situ*? – have arisen from the ultimate goal of being able to predict microbial activity in response to changes within their environments both past and future.

Part one focuses on work related to microbial processes in iron-rich Lake Matano and, more broadly, microbial interactions with the biogeochemical cycling of iron. Primarily, we find that the chelation of ferrous iron by organic ligands can affect the role of iron in anoxic environmental systems, enabling photomixotrophic growth of anoxygenic microorganisms with ferrous iron, as well as catalyzing the oxidation of ferrous iron by denitrification intermediates. These results imply that the ability to grow photomixotrophically on ferrous iron might be more widespread than previously assumed, and that the co-occurrence of chemical and biological processes involved in the coupled biogeochemical cycling of iron and nitrogen likely dominate organic-rich environmental systems.

Part two switches focus to *in situ* measurements of growth activity and comprises work related to microbial processes in the Cystic Fibrosis lung, and more broadly, the physiology of slow growth. We introduce stable isotope labeling of microbial membrane fatty acids

and whole cells with heavy water as a new technique to measure microbial activity in a wide range of environments, demonstrate its application in continuous culture in the laboratory at the population and single cell level, and apply the tool to measure the *in situ* activity of the opportunistic pathogen *Staphylococcus aureus* within the environment of expectorated mucus from cystic fibrosis patients. We find that the average *in situ* growth rates of *S. aureus* fall into a range of generation times between $\sim$12 hours and $\sim$4 days, with substantial heterogeneity at the single-cell level. These data illustrate the use of heavy water as a universal environmental tracer for microbial activity, and highlight the crucial importance of studying the physiology of slow growth in representative laboratory systems in order to understand the role of these microorganisms in their native environments.

Acknowledgments

First and foremost, I extend my deepest gratitude to Dianne Newman, Alex Sessions, and Victoria Orphan, and their respective lab groups, for teaching me how to think about science and research, and fostering an environment that inspires curiosity and exchange. I greatly enjoyed and benefitted from the open and collaborative atmosphere in their labs and in the greater geobiology and geochemistry community at Caltech. I am particularly grateful to my thesis advisor Dianne, who has been a pillar of support, and believed in me and my work much earlier than I did, and at times when I needed it the most. I would also like to thank my current and former committee members Shuhei Ono, Tanja Bosak, Dan Rothman and John Eiler. This thesis would not have been possible without their mentorship and support, nor without the generous help of the many people in their labs and beyond, who taught me the skills of my trade.

Special thanks goes to Katja Schmidt and Brian Alexander for first introducing me to research in a geochemistry lab; Alex Poulain, Paula Welander and Arpita Bose for guiding my first steps as a microbiologist; the members of the Newman lab for their continuous help in becoming a better one; Maggie Osburn and Lichun Zhang for showing me the ropes in organic geochemistry; Alex Petroff, Chris Kempes and Josh Silvermann for ever expanding my math horizon; Chia-Hung Wu and Nathan Dalleska for help and creative solutions in analytical chemistry; Shawn McGlynn, Kat Dawson, Grayson Chatwick and Yunbin Guan for introduction into the art of FISH-nano-sims; and Ryan Hunter for teaching me more than I can remember.

I am also particularly grateful to James Morgan for indulging my interests in aquatic chemistry, and to Shuhei Ono for introducing me to stable isotope geochemistry and geobiology at MIT. I would like to thank my undergraduate advisors, Michael Bau, Andrea Koschinsky and Joachim Vogt, for their guidance and support at Jacobs University Bremen and for encouraging me to apply to graduate school. Last but not least, several teachers whom I was fortunate to encounter during primary and secondary education greatly influenced my abilities and interests in science, history and languages. They deserve tremendous credit for shaping my future, and I am deeply grateful for their dedication and efforts in educational systems that rarely give them the credit they deserve. Thank you Herr Jung, Herr Mahlmann, Herr Günther, Frau Bayerlander, Frau Hallermann, Herr Grass, Monsieur Bertholet, Frau Lump, Jim Tucker, Charles Martell and Page-sensei.

None of my "fieldwork" would have been possible without the enthusiasm, generous support and hard work of the Lake Matano research team (Sean Crowe, CarryAyne Jones, Arne Sturm, Cynthia Henny and Sulung Nomosatryo) and the team and directors at the Children's Hospital Los Angeles (Carmen Reyes, Kyle McCallin, Roberta Kato, Fadi Asfour, Douglas Li, Sally Ward and Tom Keens). I owe them a debt of gratitude for enabling my work. I also especially want to thank my summer students Elise Cowley, Yung Hu, and Michael Dieterle, who have been a pleasure to work with and have become fantastic researchers. Elise Cowley still actively contributes to many of my projects, and her hard and excellent work deserves tremendous credit.

Moving with the Newman lab from MIT to Caltech after two years was instrumental in helping me become the scientist that I am today, but leaving Cambridge was not easy. I especially want to thank people in my cohort at MIT and cherished friends in Cambridge for their enduring friendship and positive influence on my early days as a graduate student. My gratitude extends especially to Dan Chavas, Malte Jansen, Nicole Keller, Kate Harris and Creighton Irons. I am equally grateful to my co-transferees and adoptive cohort at Caltech, with special thanks to Suzanne Kern, Lina Bird, Daniel Stolper and Jeff Marlow

for sharing the journey.

The strong support of family and friends was critical to my success, and I would like to thank Florian Clever, Malte Alf, Christian Meroth, Esther Singer and Craig Bergen for their incredible friendship over the years. Lastly, I want to thank my family – both old and new – for their unconditional love and support. I want to especially thank my dad, Manfred Kopf, for nurturing my love of science at an early age and whole-heartedly supporting my scientific interests. While many, many other wonderful individuals make up this group of people stretching from Freiburg to Maiwald, Iceland and the Pacific Northwest, my deepest gratitude goes to three amazing women who are the rocks of my life: my sister Franziska Kopf, who has shown me what it means to grab life by the tail and follow your dreams; my future wife Katie Snell, who kept me sane on the final stretch and inspires me every day to live life to the fullest; and my mom, Gisela Kopf, for whom the life I have chosen is a difficult one to reconcile with. When I first moved away, she gave me a card with a picture of a boy cliff-diving joyfully, and a quote by Johann Wolfang von Goethe that reads "Zwei Dinge sollen Kinder von ihren Eltern bekommen: Wurzeln und Flügel." She has given me both, and it was the greatest gift, and the greatest sacrifice anyone could ask for from a parent. This is for her.

Contents

List of Figures

List of Tables

Chapter 1

Preface

a bit beyond perception's reach
i sometimes believe i see
that life is two locked boxes, each
containing the other's key

Piet Hein

1.1 Why study microbial activity?

When looking around us at the world we live in and are capable of perceiving, unaided, it is difficult to fathom the profound impact that microorganisms, invisible to our naked eyes, exert on our planet. And yet, this vast unseen majority has shaped the chemistry of the Earth's surface for billions of years, and co-evolved with it in turn. Today, we recognize that all major geochemical cycles on the earth's surface – in fact, the chemical transformations in most environments large and small – are mediated by microorganisms. Any predictive understanding of how these microbes, along with their environments, have responded to perturbations and change in the past, and how they will respond in the

future, requires deep insight and understanding of who they are, what they are capable of, and how actively they are growing. The overarching questions that motivate the research presented in this thesis – how do microorganisms shape their environment (and vice versa)? and how can we best study microbial activity *in situ*? – have arisen from a desire to work towards this ultimate goal of being able to predict microbial activity in response to changes within an environment.

1.2 A two-sided approach

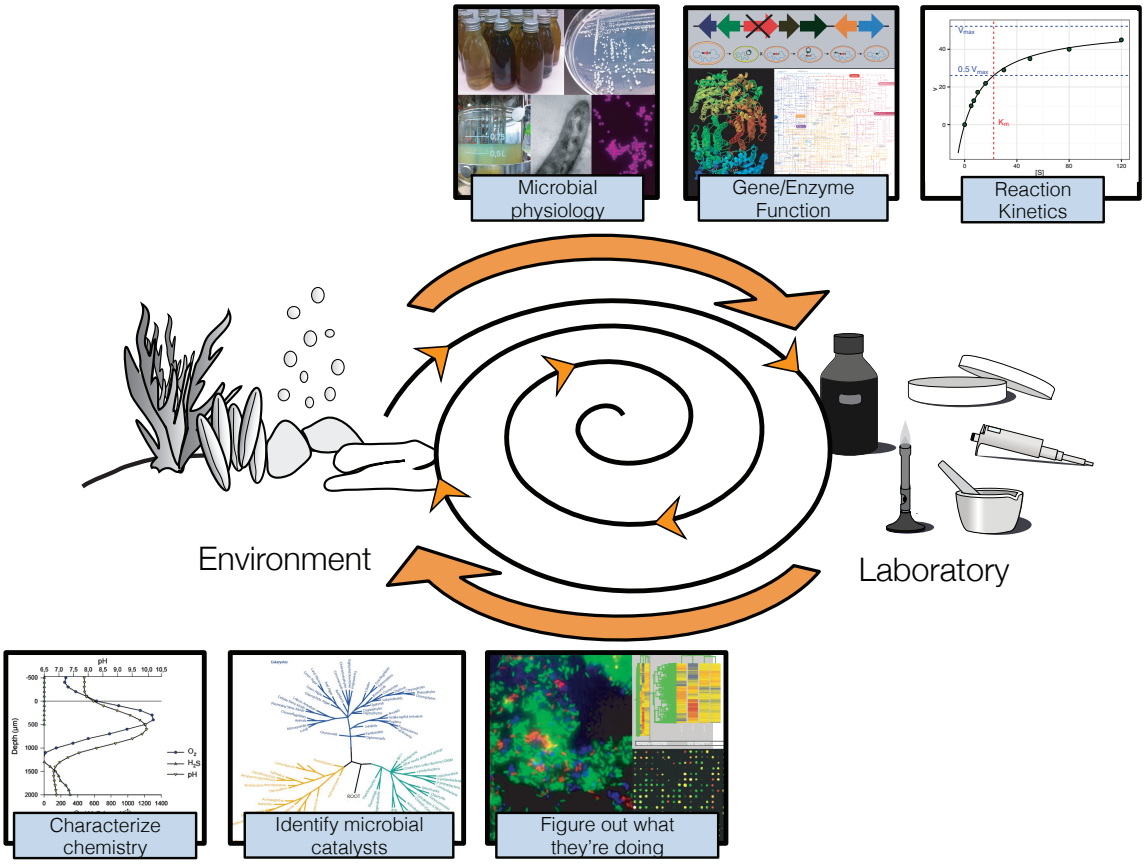

Figure 1.1 – A two-sided approach: iterating between environmental observation and laboratory manipulation.

In order to gain a mechanistic understanding of microbial processes and how they might be affected by environmental change, it is important to combine careful observation of environmental microbial growth conditions with representative laboratory experiments.

Geomicrobiology provides a wide range of analytical tools to characterize an environment increasingly well by measuring its chemistry to understand which geochemical cycles are at play, by identifying the microbial population to figure out which microbes could be involved, and, increasingly, by studying which metabolic parameters best describe their physiological state. At the same time, pure culture isolates of key environmental microorganisms increasingly provide the means to couple environmental observations to laboratory work where growth conditions can be manipulated more easily. This allows for more detailed study of their physiological potential, and the function of specific genes and enzymes, as well as the kinetics at which biologically mediated geochemical transformations can potentially proceed. Information obtained from laboratory studies can be employed to construct a working model of how the microbial community interacts with its environment, which can be used to inform specific hypotheses to test in environmental systems. In practice, this approach constitutes an iterative process (illustrated in a simple cartoon in figure 1.1) where careful observation and hypothesis testing in the environment informs increasingly more accurate laboratory models of environmental processes, and vice versa. In the various chapters that comprise this thesis, I present work representing both sides of this cycle, ranging from research on newly isolated organisms of an environment of particular geochemical interest, to *in situ* studies of the environmental growth parameters of well-understood pure cultures whose native metabolic activity is poorly constrained.

1.3 Outline

All of the papers presented in this thesis were written in collaboration with a number of authors. Although I am deeply grateful to all of my collaborators, several individuals in particular have contributed directly to the ideas and data presented herein.

Part I

Chapter 2 was written together with Arpita Bose and Dianne K. Newman as a book chapter and published in Microbial Metal and Metalloid Metabolism (Bose et al., 2011). In this chapter, we explore various approaches and techniques that a geomicrobiologist might use to study how microbial communities affect their environments and vice-versa. We focus the discussion on iron-rich Lake Matano as an example of an environment that is geochemically fascinating with respect to metal-cycling. This chapter also provides a useful introduction to the biogeochemical cycle of iron, and will be particularly helpful to readers unfamiliar with this topic in familiarizing them with several key concepts revisited in subsequent chapters of part I.

Chapter 3 was written with Dianne K. Newman, and presents our work on the physiology of phototrophic iron oxidation in the purple non-sulfur bacterium *Rhodobacter capsulatus* SB1003. This chapter appears as a paper in the Journal of Geobiology (Kopf and Newman, 2011).

Chapter 4 was written together with Cynthia Henny and Dianne K. Newman, and would not have been possible without the many inspiring conversations I shared with James J. Morgan (for which he generously and stubbornly refuses to take credit). This chapter presents our work on the effects of organic ligands on the chemical oxidation of iron, and appears as a paper in Environmental Science & Technology (Kopf et al., 2013). The research in this chapter was inspired by a desire to understand the physiology of the bacterial isolate *Pseudogulbenkiania* strain MAI-1. MAI-1 is an organism that I was able to isolate from Lake Matano as a result of field work enabled by a collaboration with Sean Crowe, CarriAyne Jones, Arne Sturm, Cynthia Henny, Sulung Nomosatryo, David Fowle and Don Canfield at Lake Matano in the Spring of 2010. Additional information on the physiology of *Pseudogulbenkiania* strain MAI-1 can be found in the supplemental material for this chapter, in Appendix C.

Chapter 5 represents work done in collaboration with Rachel Stanley on primary productivity in Lake Matano, and is based on oxygen samples collected at the lake with Sean Crowe, CarriAyne Jones and Arne Sturm.

Part II

Chapter 6 provides a brief introduction to cystic fibrosis and the approaches taken in subsequent chapters to study microbial activity.

Chapter 7 represents work done in collaboration with Elise Cowley, Yang Hu, Josh Silverman, Alex Sessions and Dianne Newman, and introduces hydrogen isotope labeling as a tool for measuring microbial growth. The work in this chapter focuses on the potential of using heavy water as a metabolic tracer for lipid biosynthesis, and discusses the conceptual approach, laboratory verification, potential impact and limitations of this technique.

Chapter 8 represents work done in collaboration with Shawn McGlynn, Kat Dawson, Victoria Orphan and Dianne Newman, and establishes the framework for using dual hydrogen and nitrogen isotope labeling in secondary ion mass spectrometric analyses of single cells as well as cells embedded and thin sectioned in acryl. The work in this chapter provides the foundation for studying spatial multi-isotope labeling patterns from diverse microbial activity in complex environmental samples that require sectioning approaches for structural resolution.

Chapter 9 represents work done in collaboration with Elise Cowley, Ryan Hunter, Abigail Green, Lindsey VanSambeek, Michael Dieterle, Victoria Orphan, Alex Sessions and Dianne Newman, and applies the techniques developed in chapters 7 and 8 to the study of *in situ* microbial activity rates in the lungs of cystic fibrosis patients.

1.4 References

Bose, A., Kopf, S., Newman, D. K., 2011. From Geocycles to Genomes and Back. In: Microbial Metal and Metalloid Metabolism. ASM Press, Washington, D.C., pp. 13–38.

Kopf, S., Henny, C., Newman, D. K., Mar. 2013. Ligand-enhanced abiotic iron oxidation and the effects of chemical versus biological iron cycling in anoxic environments. Environmental Science & Technology 47 (6), 2602–2611.

Kopf, S., Newman, D. K., Dec. 2011. Photomixotrophic growth of Rhodobacter capsulatus SB1003 on ferrous iron. Geobiology, no–no.

Part I

Lake Matano and the biogeochemical cycling of iron

Chapter 2

From geocycles to genomes and back[1]

2.1 Introduction

A holy grail for environmental microbiologists is being able to predict the effects of any given microbial community on a particular environment. In an era of increasingly-dramatic changes in global climate, this goal is becoming ever-more important. It is now well-accepted that microorganisms have had and continue to have a profound influence on shaping the chemistry of the Earth. It would thus be both intellectually satisfying and practically useful if we could enumerate the microbial players in a specific locale, and, knowing their metabolic potential and how they regulate their various metabolisms, make predictions about how their presence would shape the geochemistry of that locale as it evolves in time.

Despite significant progress that has been made in developing tools that would aid in this effort in the past decade, we are still very far from being able to accomplish this.

[1] Bose et al. (2011) in *Microbial Metal and Metalloid Metabolism: Advances and Applications*. Edited by John F. Stolz and Ronald S. Oremland

This is due to many factors, including our limited understanding of how microorganisms catalyze reactions that have a geochemical impact. While we have gotten good at identifying which organisms inhabit a particular site, we seldom have a complete grasp of their metabolic potential and how their metabolisms are regulated, and have an even poorer understanding of the stability and catalytic rates of their biogeochemically-relevant enzymes. While impressive efforts have been made in describing the metabolic potential of specific microbial communities through large sequencing projects (e.g. metagenomic and metaproteomic reconstruction of microbial communities in acid-mine drainage systems (Wilmes et al., 2009; Allen and Banfield, 2005), large gaps in our understanding remain.

In this chapter, we discuss ways a budding geomicrobiologist might embark on the quest to understand how microbial communities affect their environment and predict how they will respond in the face of environmental change. To this end, we first introduce various methods geomicrobiologists have at their disposal to achieve this goal, including both traditional (non-molecular) and molecular methods. Because this book concerns microbial interactions with metals, we have chosen to focus our discussion on iron—one of the most ubiquitous and biogeochemically relevant metals in the environment. We provide a brief review of the (bio)geochemistry of this element before concluding the final portion of this chapter with a description of Lake Matano, an iron-rich environment that is geochemically fascinating with respect to metal-cycling. We use Lake Matano as a case study to illustrate how the approaches described in the first section might be applied to gain insight into the complex interplay between microorganisms and geochemistry in a specific context.

2.2 Methods available to study microbial communities

Today, geomicrobiologists can take advantage of numerous approaches to ask questions about the roles microorganisms play in any given place. While lately, there has been great enthusiasm for molecular techniques, there is still great value in using traditional methods to characterize the contributions of microorganisms to a system. We begin with a description of the latter, as non-molecular methods provide a foundation upon which to perform molecular studies.

2.2.1 Non-molecular approaches

Non-molecular methods include techniques that involve studying microbial processes in the field (*in situ*) and those that involve studying a microbial process in the laboratory in microcosms or as isolated reactions (*in vitro*). Each approach has its advantages and disadvantages, as we will discuss.

2.2.1.1 *In situ* methods

The success of *in situ* methods depends heavily on having information about a given environment. For most commonly studied environments such as lakes, rivers, wetlands, soils and sediments, this would include geochemical parameters such as pH, redox potential (E_h), solute composition, carbon sources and the availability of terminal electron acceptors in addition to geophysical properties relevant to the respective site (temperature, water depth and stratification, soil horizons, seasonality, wind regime, etc.). This information sets the stage for use of the various *in situ* approaches described hereafter. One has to be aware, however, that *in situ* approaches in general have a few caveats. When studying a natural system, the role of microbes cannot always be based on 'guilt by association'; i.e., the presence of an organism at a site does not necessarily imply that it is mediating

the geomicrobial process under question. In addition, microbes almost never occur in isolation. Either they form stable associations called 'consortia' or they form transient associations where only one or a few members of an association are of interest, and the rest just hitchhike their way into one's data. Also, microbes undergo processes of dispersal, where they might be present in a sample only because they were in transit through the area being sampled.

To simplify *in situ* studies, workers have divided microbes found in a particular sample into: 1) indigenous microbes: part of the normal microflora of the sample site, and most likely are the geomicrobial agents being sought; 2) adventitious microbes: transient passerby organisms that came into the sample site during dispersal; 3) contaminants: organisms introduced during sampling (Ehrlich and Newman, 2008). Using some assumptions we can classify the organisms present in a particular sample. Indigenous microbes will likely represent the numerically dominant species. The adventitious microbes in many cases might be incapable of growth under the prevailing conditions in the sample site while contaminants might be recognized as organisms that are unlikely to be present in the setting where they were found (Ehrlich and Newman, 2008).

In situ microscopy

Use of microscopy to study the role of geomicrobial organisms is a very simple means of studying microbial diversity at a given site. Visual examination followed by light microscopy is a traditional tool for observing microbes when they occur in abundance (Brock, 1978). Samples can either be directly visualized using light microscopy, or after acquiring the microbes of interest such as by the buried-slide method. In this method, a slide buried at a location of interest, such as, for example, in the sediments of a lake or river bed, is retrieved after a few days of incubation, washed and stained appropriately (Lawrence, et al., 1997). Photosynthetic organisms are autofluorescent, and thus can be visualized using fluorescence microscopy (Lawrence, et al., 1997). Capillaries have also been used

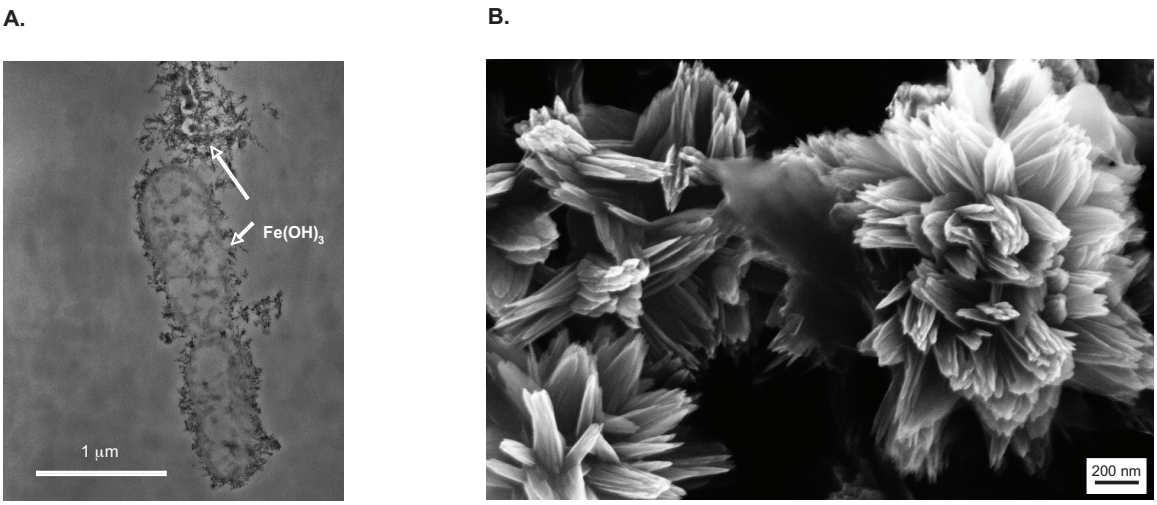

Figure 2.1 – Transmission electron microscopy (TEM) and scanning electron microscopy (SEM) of Rhodobacter strain SW2 grown photoferrotrophically. Panel A. TEM image of Rhodobacter strain SW2 grown photoferrotrophically for 5 days. Arrows indicate Fe(III) precipitates. Image previously published as Figure 4, panel B in (Kappler and Newman, 2004). Panel B. SEM of Rhodobacter strain SW2 grown photoferrotrophically for 4 weeks showing the crystalline regularly shaped Fe(III) precipitates.

to draw up microbes, and then studied under the microscope (Perfil'ev and Gabe, 1969). However, various forms of electron microscopy are also used in the field for less abundant organisms. These include transmission electron microscopy (TEM), scanning electron microscopy (SEM) and environmental SEM (ESEM) (Baker and Banfield, 2003; Ghiorse and Balkwill, 1983; Goebel, 1999; Jannasch and Wirsen, 1981; Sieburth, 1975) (Figure 2.1).

In situ study of geomicrobial activity

Radioisotopes can be used to study the biogeochemistry of certain substances to determine ongoing geomicrobial processes. They are especially useful because of the high sensitivity of their measurement, which allows the experimentalist to add very little radioactivity to a sample even for the detection of slow geomicrobial processes. For example, the globally relevant contribution of microbial communities to the sulfur cycle in the form of sulfate reduction and sulfide oxidation could be studied using either $^{35}SO_4^{2-}$ or $H^{35}S^-$. A small-predetermined amount of these chemicals could be added to a closed vessel at the depth

from which the sample was originally taken (Ivanov and Starkey, 1968). After incubation and the likely action of the geomicrobial organisms present in the sample, $^{35}S^{2-}$ or $^{35}SO_4^{2-}$ could be separated and quantified. This technique is also applicable for the investigation of microbial interactions with metals: in the case of manganese, for example, it can be used to determine the existence and extent of biological manganese oxidation. There are two approaches: the first method assumes that reduced Mn is insoluble and that the change in dissolved $^{54}Mn^{2+}$ after removal of the precipitated form is a measure of microbial $^{54}Mn^{2+}$ oxidation; the second method measures microbially-assimilated ^{54}Mn using a filter based assay (Burdige and Kepkay, 1983). One could envision similar experiments being performed with radioisotopes of iron to quantify the rates of iron transformations, both oxidative and reductive, mediated by microorganisms under various conditions (e.g. in the presence or absence of nitrate; in the presence or absence of light).

On a different scale, voltammetric methods can be used to measure changes in concentrations of metals over short distances. Sensitive voltammetric microelectrodes exist for measuring oxygen, Mn^{2+}, Fe^{2+}, and HS^- (Luther et al., 1998). These techniques are particularly amenable to application in sediment or soil environments as well as microbial biofilms, where the density of microorganisms is higher than in the water column, and geochemical gradients can be expected to change over much smaller scales. However, for environments with slow chemical turnover and/or relatively fast diffusion, we would not expect the changes in concentrations of such chemicals to change substantially, and it would be necessary to utilize *in vitro* methods to better understand the steady-state *in situ* observations.

2.2.1.2 *In vitro* methods

In vitro methods can help support conclusions drawn regarding whether any given microbial process that is observed using *in situ* methods plays a role in a particular environment. However, such methods work best for simple microbial communities, and their success

relies heavily on the accurate reproduction of the environment of the sampling site. In many cases, measurements made in the field represent steady-state concentrations of chemicals. However, microorganisms mediating various geomicrobial processes might require higher concentrations of electron donors and acceptors in non-flow-through systems (e.g. batch culture), so care must be taken in the design of relevant *in vitro* experiments. *In vitro* laboratory reconstruction typically provides more energetically favorable conditions that can enable the selection of organisms that mediate the geobiological process of interest or help maintain a pure culture or consortium stably. In this regard, *in vitro* methods commonly deviate from the actual environment that they strive to reproduce. With this caveat in mind, geomicrobiologists have devised a number of methods to study microbial communities or pure cultures. These are divided into batch cultures and chemostats (White et al., 2000). Though neither of the two methods exactly simulates the natural environment, they permit changes in microbial physiology along with changes in the chemical composition of the culture vessel to be monitored.

Batch cultures and chemostats

The batch culture method is especially popular for studying microbial processes mediated by pure cultures of microbes, and is a closed system approach. It consists of growing cells with a predetermined amount of carbon source, electron donor and electron acceptor (either rich/undefined medium made in a consistent manner or defined medium can be used for such experiments). The growth of the microbial population leads to continuous changes in the medium; substrates deplete, products accumulate and many inhibitory compounds that are products of metabolism result in defined phases of growth (White et al., 2000; Ehrlich and Newman, 2008). These include a lag, exponential, stationary and death phase (for details read Novick, 1955; Ehrlich and Newman, 2008). Batch culture experiments can establish the rates at which particular microorganisms catalyze a given reaction under well-defined conditions.

A chemostat is an open system method where the total volume of medium remains constant. However, unlike a batch culture, the spent medium is replaced by fresh medium at a pre-determined rate called the flow rate (for details read Herbert et al., 1956; White et al., 2000; Ehrlich and Newman, 2008). A steady-state situation allows the microbial population to grow at a maximum rate called the growth rate. However, if the populations were limited for any nutrient the growth rate would change and adjust until a new steady state is reached. Using such concepts, the geomicrobiologist can determine the concentration of a limiting nutrient for a microbial population. Depending on how accurate the lab simulation is to the natural environment, chemostat experiments can be used to assess what nutrient the population might be limited for in its natural setting (Jannasch, 1967; 1969).

Culturing techniques and the enrichment method

In vitro experiments usually rely on the utilization of pure strains or enrichment cultures. The pure culture technique has classical microbiological roots and has served the field of medical microbiology very well (Schlegel, 1993). However, for the environmental microbiologist, this technique has not been as rewarding. This is based on the realization of the 'great plate anomaly'; i.e., that we can culture only 0.1 to 1% of the microbes from any given sample (Staley and Konopka, 2003). Thus, any inference that one makes about a community based on pure culture techniques is always incomplete. Nonetheless, to move from finding the microbe present in an environment to understanding its real role, one has to try to obtain pure cultures. To do so, we must realize that organisms like to grow under conditions where they are found, and that they might prefer growing in stable microbial communities. The role of geochemists in helping microbiologists understand the chemical composition of the environment is becoming apparent. Careful design of medium composition, micro-encapsulation followed by flow cytometry and optical tweezer methods have helped obtain many species in pure culture (Kaeberlein et al., 2002; Zengler

et al., 2002; Rappe et al., 2002; Svensson et al., 2004). However, the ability to sequence partially pure cultures to give rise to whole genome sequences for 'Candidatus' strains helps minimize the anguish caused by the inability to obtain pure cultures (Duan et al., 2009; Tran-Nguyen et al., 2008; Pelletier et al., 2008; Jargeat et al., 2004).

Together, these traditional approaches can be used to begin to describe the microbial contribution to geochemical processes in any environment, by trying to isolate and enrich for some of the strains involved in the geochemical reactions of interest, and by exploring their physiology and metabolic potential in batch cultures and chemostats. To follow up on such studies and better understand the variables that control the microbial community *in situ*, study unculturable organisms, as well as to assess the actual function and importance of isolated strains in a particular environment, work on the molecular level is necessary.

2.2.2 Molecular approaches

In the past few decades, environmental microbiology has been influenced heavily by advances in molecular biology. The ease and affordability of DNA sequencing has aided incorporation of many molecular tools into the geomicrobiologist's tool kit. Molecular methods combined with classical microbial genetics and biochemistry can help us appreciate how microbes perform many geochemical processes. Three simple questions one can answer with molecular tools are: Who is there? What are they doing? How are they doing it? Ultimately, all three questions must be understood in order to predict the influence of a microbial population on a given environment.

2.2.2.1 Who is there?

Culture-independent approaches have taken environmental microbiology to a whole new level. The need for such methods arose with the realization that most microbes from a given environment are recalcitrant to being isolated in pure culture (Eilers et al., 2000). A failure to reproduce the natural conditions in which the organisms reside often contributes

to this problem. In addition, microbes rarely exist in isolation and thus trying to purify them may disrupt important cell-cell interactions that are integral to their survival. One way around this is to extract lipids, DNA, and RNA from natural samples, and use them to infer the identity of the organisms present in that sample. 16S rDNA, i.e., the DNA sequence that encodes the 16S rRNA, has become the molecule of choice for phylogenetic identification (Stahl, 1997; Ward et al., 1990). The reason for this is that ribosomal RNA undergoes only minor sequence changes, because it is part of the ribosome. Translation is an essential information pathway, and extreme changes in the key machinery are rarely tolerated. This realization led Woese and coworkers to show that 16S rRNA sequences from diverse organisms can be used for phylogenetic analysis (Olsen and Woese, 1993).

The 16S rRNA molecule has been tested for its rigor at assigning an unknown microbe a phylogenetic identity for nearly four decades, and proven robust. Many variations have been developed over the years to exploit 16S rRNA. However, it should be noted that while 16S rRNA/DNA-based approaches might help assign an unknown organism an identity, in most cases this does not predict its metabolism (McArthur, 2006). This is because microorganisms are capable of diverse metabolisms, some of which have been moved around through horizontal gene transfer over evolutionary history, giving their genomes a fluidity that restricts the utility of 16S rRNA/DNA to identification and phylogeny (Doolittle, 2000). In addition, other genes that are key players in other information pathways, such as transcription and DNA-replication, can also add robustness to a phylogenetic assignment based on 16S rRNA/DNA (Olsen and Woese, 1993). Some organisms have multiple divergent rrn operons, i.e., ribosomal RNA encoding genes, which complicates identification of an unknown organism (Klappenbach et al., 2001). With these caveats in mind, 16S rRNA/DNA still stands as one of the most commonly used biomolecules for identification and phylogenetic assignment.

In the following sections, we briefly summarize various culture-independent techniques that have become widely used in the past few decades. Such molecular methods can be

applied to any environment of interest.

Polymerase chain reaction (PCR)-based methods

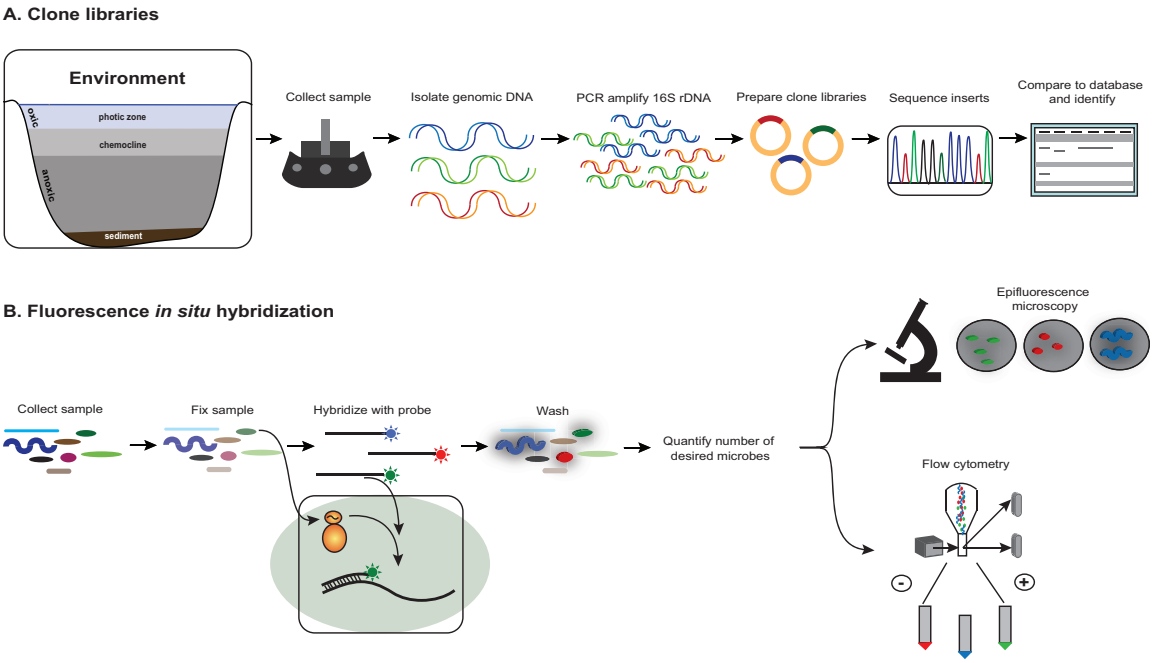

Figure 2.2 – Culture–independent approaches to understand community structure. Panel A. Strategy for construction of clone libraries. Samples are collected from a given environment such as Lake Matano. The total DNA is isolated from the sample using commercial kits. This DNA is used for PCR amplification using degenerate 16S rDNA primers. The PCR products are then cloned into appropriate cloning vectors that are also commercially available. The inserts of each plasmid are then sequenced using primers that are specific for regions of the plasmid. The sequence obtained is then compared to comprehensive databases that have 16S rDNA sequence data to determine the organism with the closest 16S rDNA sequence. Panel B. Genral strategy for performing fluorescence *in situ* hybridization (FISH). A collected sample is fixed to preserve the natural structure and physiological state of the cells and to permeabilize the cells. The samples are then hybridized to a fluorescently labeled probe that targets a desired group of organisms. The excess probe is washed and cells that are now fluorescently labeled can be visualized and quantified using epifluorescence microscopy or sorted and quantified using flow cytometry.

PCR-based methods allow identification of known and unknown organisms exploiting the ability of degenerate primers targeting 16S rDNA to amplify divergent sequences (Guyer and Koshland, 1989). In practice, DNA is purified using commercial kits from any new isolate or complex microbial community. Polymerase chain reaction and degenerate primers are used to amplify the 16S rDNA, and sequenced directly for a pure culture or prepared into a PCR clone library followed by sequencing individual clones. This sequence is

then compared to public databases such as GenBank (http://www.ncbi.nlm.nih.gov/Genbank/) or Ribosome Database Project (http://rdp.cme.msu.edu/). Because the 16S rDNA sequence for any new isolate or microbial community studied is submitted to these public databases, a quick comparison of the unknown sequence to this database allows geomicrobiologists to find the closest phylogenetic relative of the microbe under study (Figure 2.2A). However, the level of sequence identity required to assign a microorganism at the species level is debated. Recent studies show that closely-related 16S rDNA sequences can be binned into clusters that represent bacterial taxa, and called an operational taxonomic unit (OTU). OTUs are defined as clusters with up to 2.5% sequence divergence in 16S rRNA (Hughes et al., 2001). This is based on the observed divergence seen within populations of known species (Stackebrandt and Goebel, 1994). Other workers have considered each 16S rRNA sequence type as a distinct OTU; however, no sequence-based OTU corresponds to the fundamental units of bacterial ecology. As pointed out earlier, 16S rDNA and other single-gene-based approaches, in most cases, are limited to identification (Cohan, 2002; Staley and Konopka, 2003).

An application of the PCR-based approach that gives insight into community composition is denaturing gradient gel electrophoresis (DGGE). This method separates PCR products of similar size but differing sequence (Figure 2.2A). 16S rDNA can be amplified from a community and then hybridized with probes specific for a particular species being sought. Also, individual bands of interest can be cut and eluted for re-amplification, followed by DNA sequencing to identify the associated microbe (Muyzer et al., 1993; Münster and Albrecht, 1994; Ward et al., 1992; 1998). Another technique especially useful for comparing communities is terminal restriction fragment length polymorphism (t-RFLP). One of the PCR primers used has a fluorescent label. DNA is amplified using PCR and digested with restriction enzymes. The DNA bands resulting from this digestion are separated according to size, and each fragment is detected using a laser detector that can detect the fluorescent label. Though a good measure of community structure,

this method does not help in identification of individual organisms or OTUs (Clement et al., 1998; Dunbar et al., 2001; Liu et al., 1997). Finally, the use of DNA microarrays to catalogue microbial diversity is becoming increasingly popular. This method involves hybridization techniques using amplified DNA probed against a library of spotted DNA molecules on a glass-slide that correspond to known organisms (Wu et al., 2006; Gentry et al., 2006).

Fluorescence *in situ* hybridization (FISH) methods

The large diversity of microbial 16S rDNA sequences available allows us to design methods to use these known sequences to identify close relatives in uncharacterized communities. The approach that has exploited growing 16S rDNA sequences the most is FISH, although autoradiography-based approaches have also been used (Giovannoni et al., 1988; Amann et al., 1995). rRNA is an ideal biomolecule for identification of microbes for the following reasons: 1) Ribosomes are essential to survival of all forms of life, including microbes. Under most physiological conditions, microbes have thousands of ribosomal particles, which results in natural amplification of a signal. 2) 16S rDNA is conserved evolutionarily, as discussed above. In addition, RNA molecules do not undergo evolution of the third (Wobble) base of each codon, as happens in protein coding genes. Thus, probes that span much larger regions of RNA can be designed, and allow construction of probes that detect much larger taxonomic units of Bacteria and Archaea. In practice, performing FISH is fairly straightforward (Figure 2.2B); however, the success of FISH depends on many variables, which will be discussed later. First, the microbial cells in a given sample are fixed to stabilize cell morphology and permeabilize cells for later hybridization. Then, the cells are incubated with a labeled probe at which point the probe enters the cell and hybridizes with the rRNA sequence. Excess probe is then washed off to reduce background. The sample can then be visualized by epifluorescence microscopy, or the cells of interest can be sorted using flow cytometry. A database of successful and tested

FISH probes is available on ProbeBase (http://www.microbial-ecology.net/probebase/) (Amann and Fuchs, 2008). One can also design a new FISH probe based on phylogenetic analysis from databases like SILVA (http://www.arb-silva.de/fish-probes/probe-design/) (Amann and Fuchs, 2008). However, success of the new probe entails iterative testing and optimization, making it a tedious, time-consuming process. It also requires a pure culture of the organism being tested, though techniques such as Clone-FISH, which allows probes to be optimized without the need for pure cultures, can circumvent this issue (Amann and Fuchs, 2008). Various modifications of the basic FISH procedure have been developed to counter issues of failure to observe any/weak signal due to low ribosomal content or lack of active transcription. This includes catalyzed reported deposition (CARD) FISH, a method that uses horseradish-peroxidase-labeled oligonucleotide probes. The horseradish peroxidase catalyses the deposition of tyramine molecules, which results in signal amplification (Pernthaler et al., 2002).

Whole genome sequence approaches (i.e. phylogenomics)

The caveats of using single-gene approaches to understand phylogeny ultimately affect our ability to identify organisms with certainty. Whole-genome sequencing is now affordable and routine in microbiology, owing to the relatively small size of microbial genomes. This has led to the development of the concept of phylogenomics that uses all the genes in an organism to determine its phylogeny (for details read Delsuc et al., 2005). Availability of genomic data helps counter the effects due to too-small sample size that phylogenetics faces by expanding the number of characters that can be used in phylogenetic analysis by orders of magnitude. Phylogenomics, unlike phylogenetics, involves the development of tools to analyze large sets of genomic data and make phylogenetic inferences from them. Emerging from these studies are not only more robust phylogenetic trees, but also new species-like characters that are based on genome structure, such as rare genomic changes (RGCs)(Philippe and Laurent, 1998; Rokas and Holland, 2000).

Caveats of using DNA-based methods

All the above-mentioned methods are DNA-based, and therefore, they all suffer from some basic problems. These include: 1) the inability to access microbial cells that adhere to particles; 2) the inability to lyse cells and isolate DNA; 3) co-purification of PCR inhibitors that affect downstream applications; 4) shearing of DNA; 5) PCR bias; and 6) PCR-based errors. Though recognition of these problems leads to development of better technology, another way to circumvent such issues is to use other approaches, like those mentioned below. Information gained from each approach can then converge into a unified and reliable data set.

2.2.2.2 What are they doing?

When analyzing a particular environment for microbial activity, the first step is often to determine which organisms are present in that niche ("Who is there?"). However, due to the concepts of indigenous, adventitious and contaminant organisms introduced earlier, the presence of an organism does not always mean it is playing a direct role in a specific geomicrobial process of interest. The non-molecular *in situ* and *in vitro* methods described earlier can shed light on the specific role of microbes present in a given environment; in addition, a number of molecular methods can help answer the "What are they doing?" question with finer resolution. Such methods can be applied to single cells or microbial communities.

Single-cell approaches

The general principle of single-cell methods combines identification of single cells with separation of the desired population of these cells, and then determining their particular characteristics (Figure 2.3).

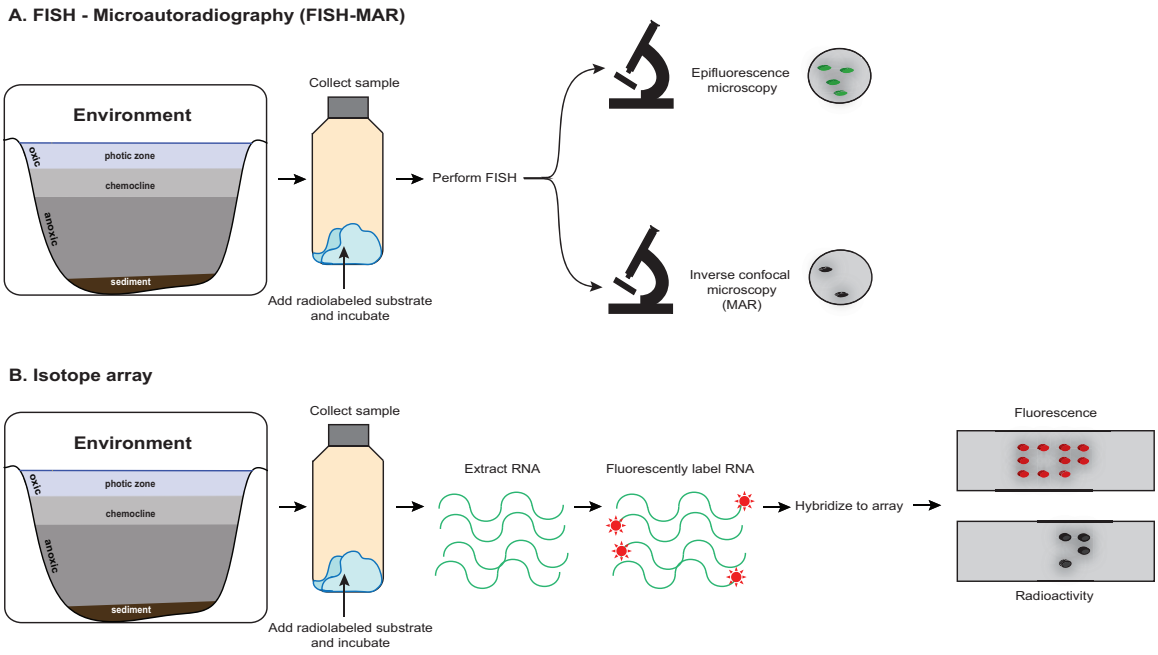

Figure 2.3 – Fluorescent *in situ* hybridization – microaudioradiography (FISH-MAR) and isotope arrays as methods for understanding function of specific organisms in a community. Panel A. FISH-MAR involves collecting a sample, and incubating the sample with a desired radiolabeled substrate. The sample is then used to perform FISH as described in Figure 2.4. The same sample is then treated with a photographic emulsion, and the cells are then visualized by inverse confocal microscopy. Comparison of the FISH image and the photographic image reveal organisms that incorporated the radiolabel into cell material using the substrate provided. Panel B. Isotope array is a modification of the DNA microarray approach that involves the incubation of the sample with a radiolabeled substrate. The RNA from the sample is then isolated and fluorescently labeled. This labeled RNA sample is then hybridized to a DNA microarray that has 16S rDNA oligos for a number of predetermined microbial species spotted onto a glass slide. The fluorescence indicates the organisms that are present in a given sample, and comparison with the radiographic image confirms which of these organisms incorporated the label into their RNA.

FISH-Microautoradiography (FISH-MAR)

This was one of the first single-cell approaches developed to understand microbial communities. It involves the use of radio-labeled substrates and monitoring their incorporation into macromolecules of a desired set of organisms that are identified in parallel using FISH approaches. The use of radio-labeled substrates makes FISH-MAR very sensitive, such that short incubations suffice. However, a disadvantage is that radio-labeled compounds not incorporated into macromolecules are lost during sample preparation for FISH analysis. Thus, the nature of the metabolic products is never obvious (Lee et al., 1999; Ouverney

and Fuhrman, 1999). FISH-MAR also has a number of other limitations: 1) it requires active growth of the microbial population under study; 2) it requires prior knowledge about the kind of organisms that are present in a given sample; 3) only a limited number of populations can be visualized simultaneously using FISH, due to requirement of distinct fluorophores; 4) FISH analysis might not be possible for some microbes; and 5) the unavailability of the desired radio-labeled substrate. The techniques described below help circumvent some of these issues.

FISH-Secondary ion mass spectrometry (FISH-SIMS)

This method combines FISH-based identification of an organism followed by analysis of the stable isotopic composition of the desired cells using an ion microprobe. The advantage of SIMS-based approaches is the ability to analyze the surface of a microbe or microbial assembly to resolve the spatial distribution of small isotopic differences. This powerful technique thus allows spatial tracing of isotopic signals (whether from naturally occurring signatures such as isotopically light methane, or labeled ^{13}C and ^{15}N incubations) as they are assimilated, incorporated and propagated by the different microbial populations fluorescently tagged with FISH. FISH-SIMS has been, for example, very successfully used in the past decade to investigate consortia of methane oxidizing archaea with sulfate-reducing bacteria responsible for anaerobic methane oxidation in numerous natural environments (Orphan et al., 2001; Pernthaler et al., 2008).

Magneto-FISH

Another modification of FISH employs use of magnetic beads attached to antibodies specific for the fluorophore used in the CARD-FISH technique. This allows immunoseparation of a desired phylogenetic group of microbes. The separated cells can then be used to isolate DNA for metagenomic analysis. It is especially useful in isolating microbial consortia (Pernthaler et al., 2008).

Single-cell PCR

Recent advances in single-cell PCR approaches have enhanced our ability to assess single cells of microorganisms while simultaneously linking these capabilities to their phylogeny. Microfluidic digital PCR allows amplification of 16S rDNA sequences along with other genes that serve as markers for a specific metabolic capability. This technique is therefore unbiased with respect to transcriptional levels and protein content, which are major limitations of FISH-based approaches (Ottesen et al., 2006). Single-cell PCR combined with single-cell whole genome sequencing is a powerful tool that paves the road to single-cell phylogenomics.

Community approaches

Although single-cell approaches are useful in understanding the metabolic capabilities of individual cells, figuring out how these metabolisms combine together to give rise to an observed geochemical profile entails studying a whole community. A few of such community-based methods are discussed below. However, newer methods that combine the single-cell approaches with the community-based approaches are becoming increasingly popular.

Stable isotope probing (SIP)

SIP involves tracking stable isotopes from particular substrates into components of microbial cells that provide phylogenetic information (biomarkers). This process has primarily been used to identify microorganisms involved in specific biogeochemical transformations that are important in global elemental cycling. The first instance when SIP was used was to study incorporation of ^{13}C into polar lipid derived fatty acids (PLFA) (Petsch et al., 2003). However, the phylogenetic resolution offered by PLFA is much lower in comparison to 16S rRNA/DNA based methods. Thus, DNA-SIP and RNA-SIP were devised.

DNA labeled with stable isotopes can be isolated from mixed microbial communities, based on the increase in buoyant density associated with isotopic enrichment. Density centrifugation in CsCl gradients can then be used to separate labeled from unlabeled DNA, and 16S rDNA clone libraries constructed from labeled DNA can be sequenced to obtain the identity of organisms assimilating the labeled substrate. Although DNA-SIP offers superior phylogenetic resolution to PLFA-SIP, it requires a high level of isotopic enrichment. For instance, DNA must contain at least 15-20% ^{13}C before it can be isolated on the basis of buoyant density (Radajewski et al., 2000). DNA synthesis is related to replication, but bacterial replication in most environments is slow. Therefore, the incorporation of stable isotopes into DNA may not be efficient for DNA-SIP to be applied. The use of RNA as a biomarker in SIP helps circumvent this drawback of DNA-SIP. Transcription occurs with a much higher turnover rate, and so the incorporation of the stable isotope is much higher in RNA-SIP. Labeled RNA can be isolated by density centrifugation, on caesium trifluoroacetate gradients. Followed by reverse transcription, PCR and sequencing then provide the phylogenetic information desired (Dumont and Murrell, 2005; Whiteley et al., 2006). The advantage of SIP methods is the ability to identify hitherto unknown organisms involved in biogeochemical processes.

Isotope array

Isotope array methods combine the utility of DNA microarrays with the benefits of stable isotope probing. RNA-SIP is performed, and the isolated RNA is then labeled with a fluorescent dye. This labeled RNA is then used to probe a 16S rRNA microarray of predetermined microbes. Isotope arrays are unfortunately limited in application due to the requirement of prior knowledge about the organisms being sought (Hesselsoe et al., 2009; Adamczyk et al., 2003).

Metagenomics, metatranscriptomics and metaproteomics

Metagenomic analysis ensues the direct isolation of genomic DNA from an environment and thus circumvents culturing the organisms under study. Subsequently cloning this DNA into a cultured organism (such as Escherichia coli) confines it for study and preservation (Riesenfeld, et al., 2004). Metagenomics has seen numerous advances such that it is even possible to reconstruct whole genomes of uncultured organisms with some certainty (Woyke et al., 2010). It has also provided new genes that have later been pursued using classical genetic and biochemical tools and shown to encode novel enzymes (Hoff et al., 2008). However, metagenomics alone does not directly tell us the metabolic role a particular organism (or gene) might play in a given environment, as DNA only stores information. The transcription, translation and regulation of the gene products allow organisms to affect their surroundings, resulting in a complex geomicrobial process. In spite of its limitations, metagenomics can offer powerful initial insights into the possible microbes and microbial processes that might occur in a given environment.

Metatranscriptomics helps understand which genes in a community are transcribed at any given time. Thus, unlike metagenomics, direct inferences can be drawn about which genes are important under the condition being assessed. Like metagenomics, metatranscriptomics (or environmental transcriptomics) involves random sequencing, of microbial community mRNA. Because no primers or probes are required for direct sequencing there is no need to anticipate important genes *a priori,* and transcripts from microbial assemblages are sequenced without bias. Further, highly similar sequences, which might crosshybridize on a microarray, can be distinguished by having a unique sequence (Warnecke and Hess, 2009; Shi et al., 2009). Experimental metatranscriptomics involves assessing changes in transcription in a particular environment, and is a powerful tool for understanding the timing and regulation of complex microbial processes within communities and consortia, as well as microbial dexterity in response to changing conditions (Warnecke and Hess, 2009).

Community expression profiling via direct sequencing saves data obtained from individual metatranscriptomic studies and added to community databases. These include CAMERA (http://camera.calit2.net/), MG-RAST (http://metagenomics.nmpdr.org/), or IMG/M (http://img.jgi.doe.gov/cgibin/m/main.cgi).

2.2.2.3 How are they doing it?

Knowledge about which organisms are present in an environment, along with information about the metabolic reactions they perform, can prompt questions such as: How do these organisms do what they do? Which genes are responsible? Do these genes resemble other known genes? If these genes encode enzymes, what is their mechanism and how are their rates of catalytic activity affected by relevant environmental variables? Where are the products of these genes located in the cell? What other molecular factors are required for their assembly? How are these genes or gene products regulated? Only by answering these questions can geomicrobiologists achieve a deeper level of understanding over the variables that control microbial activities. Such depth of knowledge, ultimately, is necessary for being able to predict how microbial communities will respond to, and in turn, modify, an environment as it changes over time. To acquire this information, geomicrobiologists can draw on a wealth of tools from the fields of classical genetics, biochemistry, and cell biology.

Genetics

Classical genetics is extremely powerful, and techniques in microbial genetics have been honed immensely over decades. Genetics has also kept abreast with advances in molecular biology such that molecular genetics is now commonplace. Through tools of both random and directed mutagenesis, scientists can identify genes that are linked a particular metabolic capability (Maloy et al., 1994). The prerequisites for performing random mutagenesis on an organism are: 1) existence of a pure or partially pure culture; 2) ability

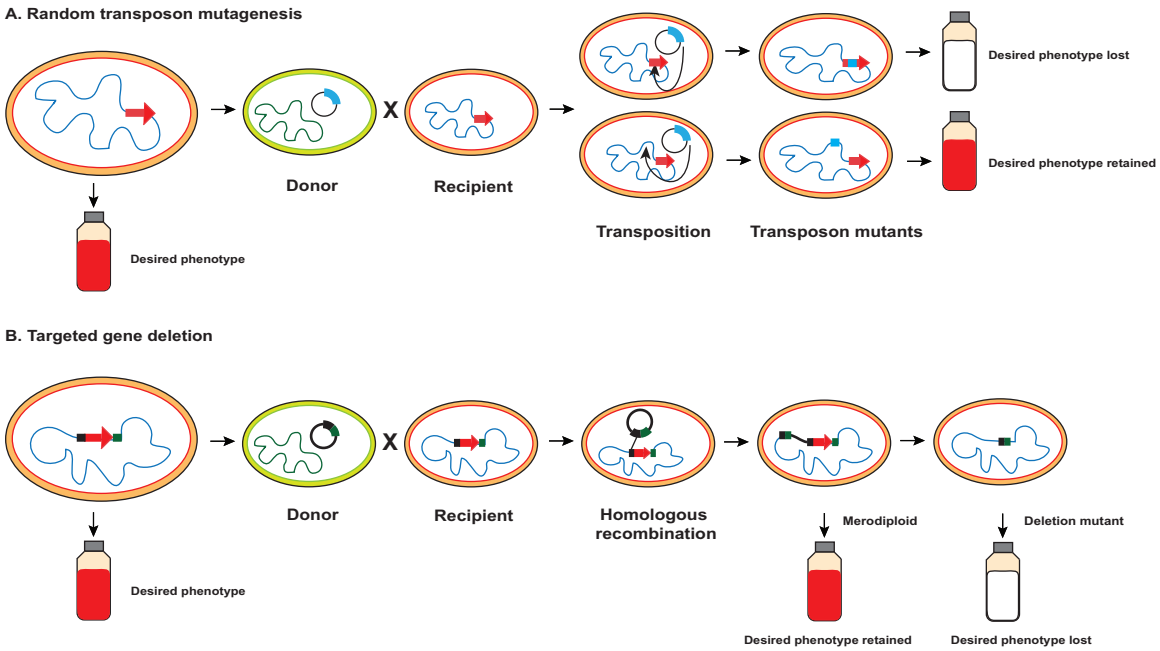

Figure 2.4 – 'Loss of function' genetic strategies to determine which genes are responsible for a particular phenotype in an environmental isolate. Panel A. Random transposon mutagenesis. This approach involves the use of randomly inserting transposons to find a desired genetic locus. A plasmid carrying a transposon and a selectable marker, usually for antibiotic resistance, is introduced into an environmental isolate either via conjugation or other means. The plasmid carrying the transposon cannot replicate in the environmental isolate. However, once the plasmid is transferred to the isolate, a transposition event occurs randomly into the chromosome of the isolate, conferring a selectable phenotype. Subsequent selection and search for the loss of the desired phenotype results in identification of a genetic locus likely responsible for the phenotype. Later complementation experiments confirm that the genetic locus predicted to confer the phenotype is indeed due to the identified locus. Panel B. Targeted gene deletion via homologous recombination. Bioinformatic or other means allow the prediction of a genetic locus that likely confers a desired phenotype. The upstream and downstream region of the desired locus is cloned into a plasmid vector that carries both a selectable marker (usually resistance to an antibiotic) and a counterselectable marker (a gene whose presence cause the cell to die when a certain selection is applied). This vector is then transferred to the isolate and selection is applied. The inability of the carrier plasmid to replicate in the isolate forces the plasmid to integrate into the chromosome via homologous recombination when selected for antibiotic resistance. Subsequent segregation and counterselection leads to deletion of the desired gene.

of the organism to form colonies on solidified media; 3) ability to transfer DNA into the isolated organism; 4) ability to assay the phenotype being sought; 5) the ability of one or more plasmids to stably replicate in the native host for complementation experiments. If all these requirements are met, random mutagenesis can be performed using various established protocols (Figure 2.4A) (Salyers et al., 2000). The use of targeted gene deletion requires, in addition to the requirements for random mutagenesis, the knowledge

of the genome sequence, or at least the region surrounding the locus to be deleted. Two methods are generally used, both based on homologous recombination: 1) Insertional inactivation, and 2) markerless deletion (Figure 2.4B) (Rother and Metcalf, 2005; Guss et al., 2005; Pritchett et al., 2004).

In case an organism does not fulfill the requirements listed above, the method of heterologous complementation can be applied using a closely related genetically tractable organism. DNA isolated from the organism under study is cloned into plasmids that replicate in the host organism. The host organism is then tested for gain of the activity that is being sought (Figure 2.5). Many examples exist where this approach has been successfully applied (Croal et al., 2007; Beja et al., 2000; Martinez et al., 2007).

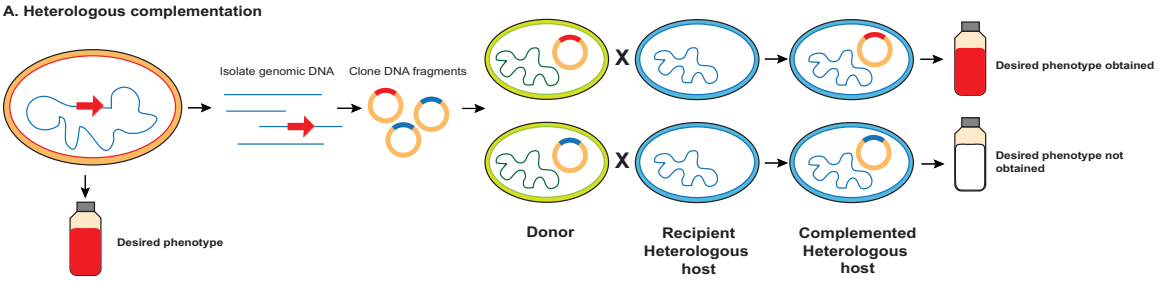

Figure 2.5 – 'Gain of function' genetic strategy to determine the genes responsible for a particular phenotype. Panel A. Heterologous complementation involves isolation of genomic DNA from an environmental isolate. This DNA is then cloned into a plasmid that can replicate in an organism that is closely related to the environmental isolate being studied that lacks the phenotype specific to the environmental isolate (a heterologous host). The plasmid is then transferred to the heterologous host using conjugation. If a genetic locus can confer the phenotype being sought then we determine the sequence of the inserted DNA. The identity of the genetic locus can then be revealed by homology searches to publicly available sequence databases.

Bioinformatics and subsequent studies

The identification of a genetic locus that confers a certain metabolic capability to an organism leads to the question of what these genes encode. Standard bioinformatics tools provided as public online user-interfaces are available on the World Wide Web. NCBI blast (http://blast.ncbi.nlm.nih.gov/Blast.cgi), a basic alignment search tool, helps find the closest homologs of an unknown gene from available sequences submitted to GenBank. Other websites such as **E**xpert **P**rotein **A**nalysis **S**ystem (http://www.expasy.ch/) and

EMBL-EBI servers (http://www.ebi.ac.uk/Tools/) provide numerous tools that allow users to determine the likely protein or RNA domains and motifs present in a DNA sequence. Though bioinformatics points to the putative role a protein or RNA, the actual role of a biomolecule needs to be determined using experimental methods; for instance, biochemical analysis of proteins and the study of function of small RNAs. Localization of proteins can also be studied using methods developed by cell biologists involving use of sophisticated microscopic tools in conjunction with fluorescent reporters (GFP and its derivatives) (Valdivia et al., 2006). Gene regulation studies can also be performed using quantitative reverse transcription – PCR and classical reporter gene fusions (Seeber and Boothroyd, 1996; Miller and Hershberger, 1984).

2.3 The (bio)geochemistry of iron

2.3.1 Iron at the Earth's surface

Iron is the most abundant element on Earth, contributing 32% by weight to the bulk composition of our planet (Morgan and Anders, 1980). A large portion is concentrated in the inner core, but the element still constitutes a remarkable 5% of iron in the Earth's crust on average, exceeded in crustal abundance only by oxygen, silicon and aluminum (Rankama et al., 1950). The chemical reactivity of iron and its role as one of the most important reduction-oxidation (redox) active elements implicate iron in a myriad of highly relevant geochemical as well as biochemical transformations.

Igneous rocks rich in iron bearing mafic minerals, such as olivine and pyroxene, are the primary source of iron to the Earth's crust and surface environment. The (bio) geochemical cycling of iron at the Earth's surface starts with the mobilization of iron during erosion and weathering of exposed igneous rock, as well as during hydrothermal circulation of seawater at oceanic spreading centers (the sources). Subduction of iron-bearing oceanic crust and seafloor sediments ultimately returns iron to the mantle (the

sink) where the rocks can melt, form a magma, and reenter the igneous rock cycle. Once in a mobile phase as a particulate mineral or dissolved ion, many physicochemical processes can occur, altering properties such as solubility and chemical speciation (Ussher et al., 2004). Iron is distributed throughout the hydrosphere by riverine and marine fluxes, transported in the atmosphere in aerosols and dust particles, and spread throughout the lithosphere by sedimentary processes, mineral precipitation and diagenesis, making up a large proportion of soils and sedimentary rocks from where it can be remobilized again. Its complex biogeochemical cycle affects not only its own distribution in the lithosphere, hydrosphere, atmosphere and biosphere, but also the distribution and processes of other important element cycles such as those of carbon, nitrogen and sulfur.

Iron is most commonly observed in its ferrous (oxidation state +2) or ferric (oxidation state +3) form. Reducing conditions in the mantle and deep crust make the ferrous form dominant in magma and fresh igneous rock, but ferric iron is stable at present oxic atmospheric conditions, making +3 the most common oxidation state in surface environments. However, the dynamic and variable chemistry of many surface environments sometimes allows for considerable amounts of ferrous iron and co-occurrence of both oxidation states. The following chemical reactions exemplify two typical redox transformations of iron: (I) the oxidation of Fe^{2+} by molecular oxygen to form a simple, insoluble Fe^{3+} hydroxide and (II) the reduction of Fe^{3+} by excess hydrogen sulfide, partially precipitating as an iron sulfide mineral (pyrite). Both reactions are relevant redox pathways in natural environments.

$$4\,Fe^{2+} + O_2 + 10\,H_2O \rightarrow 4\,Fe(OH)_3(s) + 8\,H+ \tag{2.1}$$

$$2\,Fe^{3+} + 2\,H_2S \rightarrow 2\,FeS_2(s) + Fe^{2+} + 4\,H^+ \tag{2.2}$$

The solubility and chemical behavior of iron in aqueous environments is heavily influenced by its speciation; that is, the actual form in which it is present in solution. Besides the oxidation state of the element, speciation depends largely on acidity/alkalinity of the environment (pH) and the availability of ligands. Ferric iron is generally much less soluble than ferrous iron, especially at circumneutral pH, although strong ligands can improve its stability in solution. Ferric iron in marine environments, for example, has been found to be >99% complexed by strong organic ligands (Ussher et al., 2004). The solubility of the ions is ultimately limited by the stability of various minerals; for example, siderite and pyrite for Fe^{2+}, (oxy)hydroxides and oxides like ferrihydrite, goethite and hematite for Fe^{3+}.

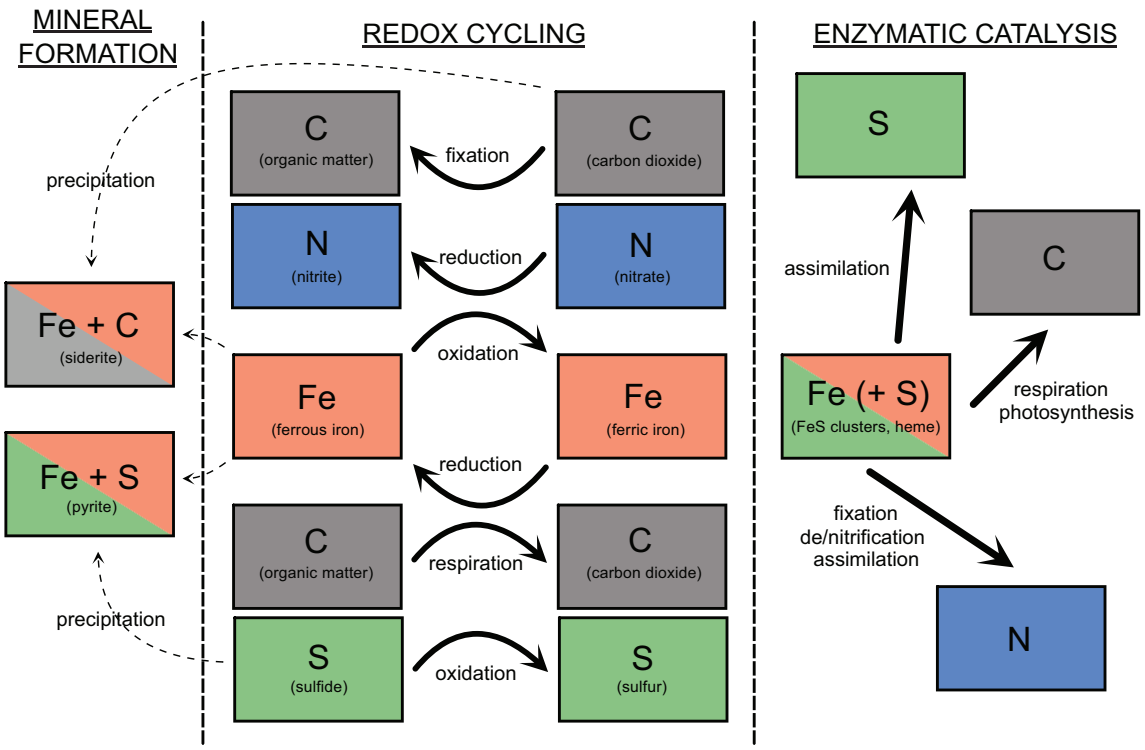

Figure 2.6 – Simplified illustration of the coupling of the biogeochemical cycling of iron (color-coded in red) with the carbon (black), nitrogen (blue) and sulfur (green) cycles. Shown are interactions of the element cycles during mineral formation and dissolution (left column: arrows indicate precipitation, parenthesis provide examples of mineral species), redox cycling (center column: arrows illustrate redox transformations coupled to iron oxidation/reduction, parentheses provide examples of the reduced and oxidized species involved) and enzymatic catalysis (right column: arrows indicate examples of iron-dependent metabolic processes for sulfur, carbon and nitrogen respectively).

The biogeochemical cycling of iron strongly influences other element cycles by means of mineral formation and dissolution, coupling of redox cycles, and enzymatic catalysis. The distribution and transformation of iron in the Earth's surface environment have a particularly noteworthy impact on the previously mentioned, globally important cycling of nitrogen, sulfur and carbon (illustrated schematically in Figure 2.6). While iron and nitrogen redox cycling is coupled directly in the microbial process of anaerobic respiration of ferrous iron with nitrate, iron impacts the nitrogen cycle most pervasively in its role in enzymatic catalysis (Weber et al., 2006b). A wide variety of metalloproteins and cofactors incorporate iron in their active sites, and virtually all processes of the microbially-mediated cycling of nitrogen (nitrogen assimilation, fixation, denitrification, nitrification) require small amounts of iron for this purpose. Many surface environments are rarely limited by iron availability, but the low concentrations of iron in ocean waters can crucially affect the productivity and ecology of the oceans by limiting nitrogen fixation (Falkowski et al., 1998; Morel, 2003).

The sulfur and iron cycle are closely linked through the mutually-controlled formation of iron-sulfur minerals, such as the aforementioned pyrite, and through the reductive interaction of sulfide species with ferric iron (Canfield et al., 1992). The two cycles are, however, most intimately intertwined in their prominent role as iron-sulfur (FeS) clusters in a variety of metalloproteins and cofactors involved in electron transfer reactions that impact a variety of other element cycles.

The biogeochemical cycling of iron is linked to the carbon cycle in various direct and indirect ways. Direct links include the formation of the iron-carbonate mineral siderite as well as the coupling of redox cycling in phototrophic iron oxidation (where ferrous iron is used as a source of electrons to fix carbon) and dissimilatory iron reduction (where organic substrates are respired using ferric iron as the terminal electron acceptor). In its catalytic function in enzymes, iron is central to redox metabolism (Fraústo da Silva and Williams, 2001). It plays an active role, for example, in many enzymes involved in electron transfer

reactions of both respiration and photosynthesis, and furthermore influences the carbon cycle indirectly through its effects on the nitrogen cycle.

Finally, the interaction of iron with the carbon and sulfur cycle has played an important role in the accumulation of atmospheric oxygen throughout Earth's history. The accumulation of oxygen at the Earth's surface is largely controlled by the direct burial of organic carbon and the indirect burial of the reducing power from organic carbon in the form of pyrite. The prior prevents some of the biomass produced during oxygenic photosynthesis to be respired again with the produced oxygen, and thus frees some of the oxygen to accumulate. In the latter case, the organic matter produced by oxygenic photosynthesis drives sulfate reduction and iron reduction, producing pyrite and oxidizing the organic matter to CO_2. Burial of pyrite through the couplings of the carbon, sulfur and iron cycle thus liberates oxygen to the atmosphere (Garrels and Lerman, 1981; Berner and Maasch, 1996; Canfield, 2005).

2.3.2 Iron and the biosphere

The biosphere has a tremendous impact on the distribution of iron at the Earth's surface. Microorganisms, in particular, heavily influence the geochemical cycling of iron in various ways. Most organisms assimilate small amounts of iron to satisfy their nutritional demands for the element. In the process, they heavily influence the mobilization of iron from rocks, soils and sediments, and alter the speciation of iron in aqueous environments. This is a result of both active and passive microbial activities through the deliberate production of molecules for iron acquisition, and by action of common metabolic products such as organic acids, respectively. Many microorganisms can catalyze the oxidation or reduction of iron both actively by metabolizing iron to generate energy for growth, as well as passively, e.g. by influencing the chemistry of their immediate surroundings or providing catalytic surfaces for mineral formation.

2.3.2.1 Iron as a nutrient

Iron is an essential nutrient for the survival, growth and reproduction of almost all forms of life. As a key catalyst in several enzymatic electron transfer reactions, iron is required by most organisms for vital cellular processes ranging from respiration to photosynthesis, nitrogen fixation and the oxidative stress response (Fraústo da Silva and Williams, 2001). Many of the iron-bearing enzymes involved in these processes likely evolved at a time in Earth's history when ferrous iron was abundant in the world's oceans as the Earth's surface environment was still anoxic, and the much less soluble ferric form of iron could not yet stabilize (Anbar and Knoll, 2002; Saito et al., 2003; Glass et al., 2009). With the evolutionary invention of oxygenic photosynthesis and the rise of atmospheric oxygen around 2.4 billion years ago, the eventual oxidation of the Earth's surface and oceans brought about drastic changes in atmospheric and marine chemistry, including a severe limitation in the bioavailability of iron. Despite being the most abundant transition metal in the biosphere, most iron is bound in insoluble oxides and hydroxides at near-neutral pH at present atmospheric oxygen levels. It is thus hardly surprising that the biosphere has evolved many elegant ways to influence the cycling of iron to allow for assimilation. In response to the scarcity of bioavailable iron in many natural environments, many microorganisms have, for example, evolved the ability to synthesize potent chelating agents to aid in iron acquisition. The fascinating and complex process of mobilization and acquisition of iron by these iron-specific chelators, commonly known as siderophores, is discussed in detail by Kraemer (2004) and Kraemer et al. (2005).

2.3.2.2 Iron as an energy source

All non-phototrophic organisms take advantage of concentrations of oxidizable and reducible species that are far from those demanded by thermodynamic redox equilibria and kinetically too slow to proceed on their own. This is what happens in respiration, where organic matter (highly reduced) and molecular oxygen (highly oxidized) are out of

thermodynamic equilibrium, but the kinetics of abiotic combustion at standard conditions are so slow that they do not just recombine spontaneously. Microorganisms gain energy by catalyzing such redox reactions in a controlled manner to restore thermodynamic equilibrium. Microbially-mediated transformations of iron are often much faster than their abiotic equivalents, and are ubiquitous in natural environments. A wide variety of physiologically different prokaryotes can use iron for energy generation, either by using ferric iron in dissimilatory iron reduction as an oxidant to respire more reduced substrates, or by metabolizing ferrous iron in dissimilatory iron oxidation with a stronger oxidant. These microbially-mediated redox transformations often occur in combination, and can contribute to extensive (re-)cycling of iron in the environment. Canfield et al. (1993) estimated repeated oxidation and reduction in costal sediments between 100-300 times before ultimate burial into the sediment. A good review of microbially-mediated iron redox processes is provided by Kappler and Straub (2005).

In order to gain energy from the oxidation of ferrous iron with molecular oxygen in aerobic environments, microorganisms have to compete with abiotic oxidation. At circumneutral pH, the chemical reaction proceeds within minutes, and neutrophilic iron-oxidizers have to catalyze iron oxidation extremely fast (Stumm and J Morgan, 1996). Emerson and Weiss (2004) provide a detailed description of aerobic iron oxidation at neutral pH. At more acidic conditions (pH <5), the stability of ferrous iron increases and chemical oxidation proceeds much more slowly, allowing microorganisms to compete more easily. However, the energy gained from oxidation decreases with pH and much larger quantities of iron need to be oxidized to meet cellular energy requirements. A variety of acidophilic iron-oxidizing bacteria from all across the proteobacteria (most prominently Acidithiobacillus ferrooxidans), nitrospira, firmicutes, and acidobacteria as well as several archaeal strains from lineages from the Thermoplasmatales and Sulfolobales (e.g. Edwards et al., 2000) have been identified, particularly in acid mine drainage environments where acidic conditions prevail and sufficient quantities of ferrous iron, mostly in the form of

pyrite, are available (see Baker and Banfield, 2003; for a review). In addition to aerobic iron oxidizers, several microorganisms have been discovered that can oxidize ferrous iron anaerobically by respiring nitrate at neutral pH (see Weber et al., 2006b). Although considered a possible form of anoxic phototrophic metabolism for a long time, the so called photoferrotrophs – bacteria that grow photosynthetically with ferrous iron as their sole source of reducing power – were only discovered in the early '90s by Widdel et al. (1993). In the past decade, several cultures of iron-oxidizing phototrophic bacteria from all three major phylogenetic lineages of anoxygenic phototrophs (purple sulfur bacteria, purple non-sulfur bacteria, and green sulfur bacteria) have been isolated from such diverse environments as iron-rich springs, freshwater marshes and marine sediments (Kappler and Straub, 2005).

Instead of harnessing energy from existing thermodynamic disequilibra, fixation of solar energy by photosynthesis actually creates new thermodynamic gradients that can be harnessed to support cell growth. As such, photoferrotrophy is fundamentally different from all other microbial interactions with the iron cycle. It is, in fact, the only microbial process that can change the redox state of iron species in natural environments against the thermodynamic resting state. As such, photoferrotrophy holds the power to drive redox cycling on the Earth's surface independent of oxygenic photosynthesis. Although such an isolated occurrence of photoferrotrophy, completely decoupled from oxygenic photosynthesis, is unlikely to occur today due to the ubiquity and evolutionary success of oxygenic photosynthesis, it might still constitute an important contribution to primary productivity and the generation of oxidants in shallow sediments and iron rich microenvironments. Furthermore, assuming an early evolution of anoxygenic photosynthesis preceding the evolution of cyanobacteria and oxygenic photosynthesis, photoferrotrophs could have been the dominant primary producers in a ferrous iron rich Archaean ecosystem.

This last assertion is of particular interest in the context of Earth evolution due to the occurrence of massive iron-rich sedimentary deposits, known as banded iron formations

(BIFs), from a time in Earth's history when dissolved ferrous iron was abundant in the Earth's oceans, but molecular oxygen was still extremely scarce. Photochemical oxidation of ferrous iron by UV radiation was considered a possible mechanism, but recent findings have cast doubt on the efficiency of such a process for the deposition of BIF, and it is generally believed that chemical or microbially-mediated oxidation of ferrous iron by molecular oxygen from early oxygenic photosynthesis played the main role in BIF formation (Konhauser et al., 2005). More recently, however, the possibility of photoferrotrophic iron oxidation has been advanced as an alternative or complementary mechanism for banded iron formation (e.g. Kappler et al., 2005a; 2008). A good review on the extent and significance of several major banded iron formations is provided by Beukes and Gutzmer (2008).

The ability to use the product of ferrous iron oxidation, ferric iron, as a terminal electron acceptor is widespread; numerous bacteria and archaea capable of dissimilatory ferric iron reduction at circumneutral and acidic pH have been isolated in the last decade. The environmentally most important inorganic reductant for ferric iron is hydrogen sulfide, which constitutes a kinetically competitive abiotic pathway and commonly contributes to iron cycling, especially when produced in large quantities during microbial sulfate reduction. A variety of organic and inorganic substrates can be respired and some organic substrates fermented with ferric iron depending on the strain and mineral form of the iron available, although not all iron reducing bacteria can grow with iron as the sole electron sink. It is unclear whether this occurs due to an inability to gain energy from the process, or whether the energy gained is insufficient to support growth but could still be important for survival. The ubiquity of iron minerals in sediments and breadth of substrate flexibility makes dissimilatory iron reduction an important metabolic pathway for the anaerobic mineralization of organic matter, especially in environments where sulfate and nitrate are unavailable terminal electron acceptors. However, a challenge of this metabolism is that organisms have to use an insoluble electron acceptor and cope with the difficulty of either

solubilizing the iron mineral or transferring electrons from the cell to the mineral surface. Three different strategies seems to have evolved in response to this problem, although their distribution in natural environments remains inconclusive: a) physical contact with the mineral surface for direct electron transfer, b) synthesis of iron chelators to solubilize ferric iron, and c) synthesis of redox active molecules to shuttle electrons to the mineral surface. See Lovley et al. (2004) for a comprehensive review.

Because the majority of ferrous iron-oxidizing and ferric iron-reducing prokaryotes were isolated during the last decade, it is hardly surprising that our knowledge of these microorganisms, their metabolism and especially their contribution to the biogeochemical cycling of iron is still in its infancy (Kappler and Straub, 2005). This is particularly true for the most recently discovered group of anoxygenic phototrophic iron oxidizers, whose metabolic potential and place in microbial ecosystems is only recently starting to be investigated and fully appreciated.

2.4 From geocycles to genomes and back: Lake Matano as a case study

A recent study of the iron-rich lake Matano in Indonesia by Crowe et al. (2008a) provides an interesting case study for a joint geochemical and microbiological effort to investigate the roles microorganisms play in shaping the geochemistry of this environment. In this final section, we describe what is known about Lake Matano, and discuss how the traditional and molecular microbiological approaches described above may be used to gain insight into how microorganisms affect the biogeochemical cycling of iron and other elements in this environment.

Lake Matano, a part of the Malili Lakes system of Indonesia, is among the ten deepest lakes on Earth. It is estimated to be between one and four million years old (Brooks, 1950). It has relatively stable physical characteristics, leading to species endemism,

which has been studied in this lake by numerous workers (Sabo et al., 2008; Myers et al., 2000). Its unique iron geochemistry makes the lake a particularly interesting analogue for the chemistry of the oceans on early Earth (Crowe et al., 2008a), which differed markedly from modern environments. As discussed earlier, the lack of oxygen and presence of low concentrations of sulfide along with the abundance of ferrous iron have implicated microbially-mediated Fe(II) oxidation as a possible mechanism for the formation of extensive BIFs in the Archaean ocean (Canfield et al., 2000; Canfield, 2005; Isley and Abbott, 1999). Because Lake Matano's geochemistry may resemble the composition of ancient oceans (Crowe, et al., 2008a), it provides an opportunity to study the closely-linked biogeochemical cycles of iron, carbon and sulfur in an environment that can be characterized both geochemically and microbiologically. As discussed in detail below, numerous interesting observations have emerged from the study of the geochemistry of this lake, and point to the likelihood of novel microbial metabolisms working within it that actively shape the geochemistry of the lake (Crowe et al., 2008b;a).

Lake Matano is a tropical lake, which therefore shows many typical characteristics of lake systems at low latitudes, such as higher annual irradiance, lack of seasonal variation, and high amounts of Fe and Mn hydroxides supplied from extensive weathering of iron-rich country rock in the drainage basin. The lack of large temperature fluctuations can facilitate poor mixing of the different layers of water, often leading to seasonal stratification, i.e., a separation of the water column into stable layers of differing water densities due to temperature and salinity differences. In the case of Lake Matano, the great depth and relatively small surface area of the lake allows this commonly seasonal phenomenon to persist, leading to a permanently stratified water column.

Stratification of lakes can lead to subsequent chemical stratification of redox sensitive elements due to the redox activity of microorganisms. Measurements of physical parameters in Lake Matano reveal that is has a permanent pycnocline at $\sim$100 m depth stably separating the mixolimnion, the upper mixed water layer in contact with the atmosphere,

from the monimolimnion, the deep anoxic waters. The redox- or chemocline, marking the gradual chemical transition from completely oxygenated surface waters to increasingly reducing deep waters, extends from ~100 m to ~220 m depth (Crowe et al., 2008b).

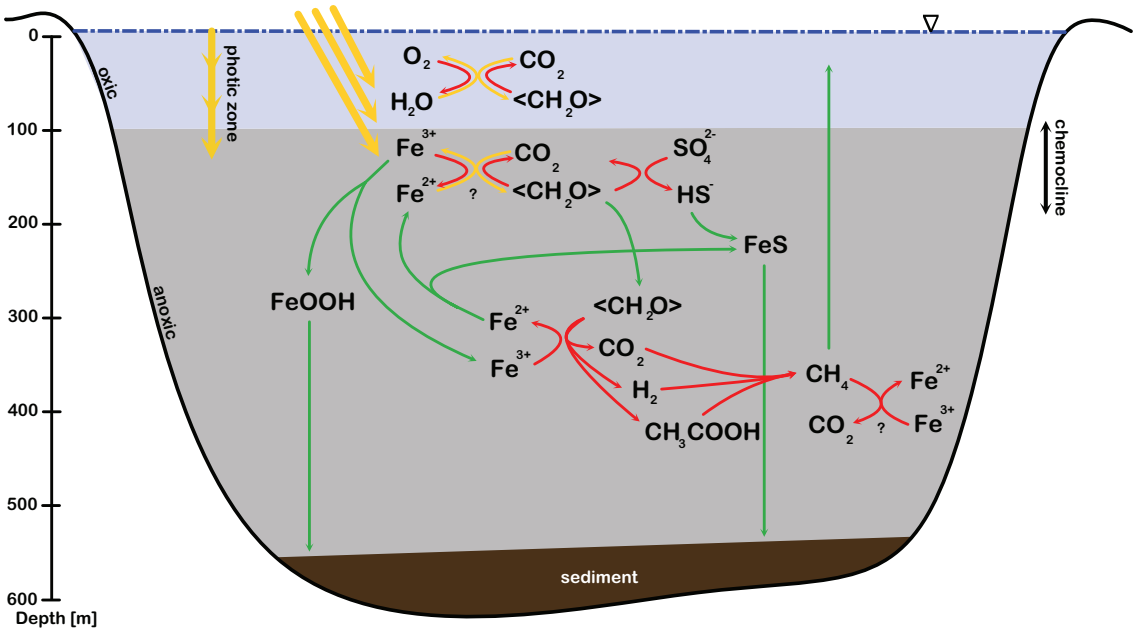

Figure 2.7 – Simplified schematic illustrating element cycling in Lake Matano at various depths. The oxic surface waters are shown in light blue, and the anoxic monimolimion is shown in light grey. Phototrophic transformations are indicated in yellow, non-phototrophic microbial transformations in red, precipitation and diffusion in green. Coupled arrows, such as organic matter oxidizing to carbon dioxide ($<CH_2O>$ to CO_2) while sulfate is being reduced to hydrogen sulfide (SO_4^{2-} to HS^-), illustrate closely-linked redox transformations. Hypothesized, but still insufficiently investigated, potential processes in Lake Matano, such as photoferrotrophy and iron-dependent anaerobic methane oxidation, are highlighted with a question mark.

The unique geochemistry of Lake Matano arises due to the interplay between the geophysical characteristics of the environment and the activity of resident microbes in the lake. Spatio-chemical stratification of electron acceptors is observed in the lake as follows: oxygen concentrations drop until they reach undetectable levels at ~100 m depth. At this depth, the dissolved Mn concentration increases to 10 µM, and Fe(II) to 140 µM. Both Fe(II) and dissolved Mn concentrations do not drop dramatically from this concentration as the depth increases to 300 m (Crowe, et al., 2008b). At the same time, the sulfate concentrations in Lake Matano remain very low (<20 µM). Modeling studies predict that

microbially-mediated sulfate reduction is not expected to occur in the water column, but rather in the sediment, while sulfide accumulation in the water column is limited to below detection by the low solubility of iron sulfide minerals and the high concentration of Fe(II) (Crowe et al., 2008b).

Spatio-chemical stratification of various electron donors is intimately linked to microbial oxidation of organic matter. The autochthonous organic carbon from primary productivity in the lake is very low, and it is the degradation of allochthonous organic matter, accounting for most of the dissolved organic carbon (DOC), that likely leads to spatio-chemical stratification. The DOC is mineralized completely between 100-200 m depth concomitant with the increase in Fe(II) concentrations, suggesting microbial Fe(III) reduction as a possible means of substrate oxidation. It is likely that an iron cycle operates across the chemocline with some flux of iron from the sediment to the water column. Modeling studies suggest that a combination of various phenomena might lead to the steady state concentrations of Fe in this region. These include a) the descent of insoluble Fe(III) hydroxides, b) appearance of Fe(II) due to microbially-mediated Fe(III) reduction, c) diffusion of Fe(II) from the monimolimnion, d) regeneration of Fe(III) by Fe(II) oxidation at the redox boundary, and e) upward flux of soluble Fe(II) from the sediment to monimolimnion (Figure 2.7) (Crowe et al., 2008b).

In the anoxic deep waters, once anaerobic microorganisms have utilized the more favorable electron acceptors, methanogenesis and anaerobic methane oxidation (AOM) can contribute to the carbon cycle. Sulfate reduction is more energetically favorable than methanogenesis, and sulfate reducing bacteria (SRB) outcompete methanogens for acetate as a carbon source (Reeburgh, 2007; Capone and Kiene, 1988). The absence of sulfate in the Lake Matano water column precludes this competition. However, the abundance of Fe and Mn introduces the possibility of microbes that reduce these minerals competing with methanogens for acetate. In addition, the absence of sulfate and nitrate in Lake Matano, the two well-established electron acceptors that are coupled to AOM, raises

the possibility that Fe and Mn are more important players in AOM in this environment (Crowe et al., 2008a; Boetius et al., 2000; Raghoebarsing et al., 2006). The recent demonstration that marine sediments can couple anaerobic methane oxidation to Fe and Mn reduction shows that such reactions are feasible (Beal et al., 2009). Methane production occurs primarily in the sediment in spite of the presence of considerable amounts of Fe and Mn. Disappearance of methane below the pycnocline between 100-200 m suggests likelihood of AOM in this zone (Crowe et al., 2008a).

The concentrations of nitrogen and phosphorus are below detection limits in the mixolimnion. Ammonium is detected in the monimolimnion as the predominant N species, while soluble phosphate is the predominant P species across the chemocline. The appearance of soluble phosphate increases with the Fe(II) concentration, suggesting that the P and Fe cycles are linked in this environment, likely involving sorption and removal of phosphate from the mixolimnion by particulate Fe(III) species. The lack of essential nutrients along with the high concentration of chromium (Cr(VI)) might account for the low primary productivity in the mixolimnion of Lake Matano (Crowe et al., 2008b).

Given the many spatio-chemical gradients of common substrates for microbial metabolisms in Lake Matano, the likelihood of finding organisms that actively contribute to shaping these gradients is high. For example, photosynthetic pigment measurements in the lake have revealed that chlorophyll a (Chl a) is present at low levels in the surface oxic layer where cyanobacteria would be commonly expected to contribute significantly to primary productivity in nutrient richer environments. The low levels of light-absorbing pigments such as Chl a in the surface layer allow light to penetrate to the deeper layers where bacteriochlorophyll e (Bchl e) predominates. This pigment is characteristic of anoxygenic photosynthetic bacteria that belong to the Chlorobiaceae that thrive under lower light conditions. Consistent with this, 16S rDNA studies have indicated the presence of various members of this family in the redoxcline of Lake Matano (Crowe et al., 2008a). The high concentration of Fe(II) in this layer suggests that it might be serving as an electron

donor for anoxygenic photosynthesis for these organisms, and that their activities might influence iron-cycling in the lake. However, whether this is in fact the case, or whether other Fe(II)-oxidizing and Fe(III)-reducing organisms make greater contributions to the iron cycle is not clear. Indeed, it is possible that different groups of microorganisms control the iron biogeochemistry of the lake at different times, and that these microbial communities change altogether from year to year. Such depth of knowledge, ultimately, is necessary for being able to predict how microbial communities will respond to, and in turn, modify, an environment like Lake Matano as it changes over time. How can we resolve this?

As described at the beginning of this chapter, a variety of traditional as well as molecular microbiological methods could be used to provide some insight and inform our understanding of the microbial communities and biogeochemical dynamics in this environment. Fortunately, recent work on Lake Matano has provided us with detailed information on the geochemistry of the lake (Crowe et al., 2008a;b; Crowe, 2008), paving the road for some of the *in situ* techniques. Traditional light microscopy could be used to study microbial populations in the lake sediments and their spatial variability close to the chemocline (e.g. by the buried slide method). Due to low concentrations of microorganisms in the water column itself, however, more powerful techniques such as TEM and SEM could be necessary, which would provide the additional benefit of allowing investigation of the physical association of microorganisms with freshly formed minerals, such as iron (hydro)oxides from microbial iron oxidation. A reliable assessment of *in situ* geomicrobial activity via isotope labeling at the chemocline in the case of phototrophic organisms could be foiled by slow growth in the relatively low light at this depth; however, chemotrophic organisms could be operating on faster time scales if external carbon sources to the lake provided sufficient substrate for growth. While limited by slow growth, advanced isotope techniques such as RNA-SIP are of particular interest for an environment like Lake Matano, where a high degree of species endemism

suggests the possible occurrence and likely importance of novel microorganisms and unique metabolic pathways that could be identified by this technique.

In vitro batch culture as well as chemostat studies of microorganisms from this environment are highly desirable to assess their metabolic potential, but depend on enrichment and isolation of organisms from the water column. Slow growth might be a limiting factor in the ultimate success of this approach. Culture-independent techniques, however, could be employed regardless, and FISH could be used, for example, to study the small-scale spatial distribution, abundance and physical association of various bacterial and archaea groups identified by 16S fingerprinting to be present in the lake sediments. Modern extensions of the approach, such as FISH-SIMS, could be similarly successful in investigating microbial populations in the lake, possibly aiding identification and study of a so-far elusive but suspected syntrophic community that combines anaerobic methane oxidation with metal reduction in this unique environment. While technically and computationally challenging, the combination of meta-genomic, -transcriptomic and -proteomic techniques could significantly advance our understanding of the genetic metabolic potential, actively expressed metabolic pathways and geochemically active enzymes the microbial communities in Lake Matano command. Detailed genetic studies of the organisms, however, would require reasonably fast-growing pure cultures, whose metabolic machinery for iron oxidation or reduction, for example, could then be assessed by random mutagenesis (for genetically tractable organisms) or heterologous complementation (for intractable strains with suitable tractable strains that are closely related). Once whole genomes of novel organisms from this environment become available, bioinformatics provides powerful additional tools to search for metabolic key components that contribute to the biogeochemical cycling of iron and other elements in this environment, and whose identification is crucial for our understanding of the biogeochemical dynamics of this system.

2.5 Conclusions

We began this chapter with the assertion that a holy grail for environmental microbiologists is to understand the biogeochemistry of an environment sufficiently well to predict its behavior. This is a tall order, and requires tremendous effort on the part of many groups to achieve for any given environment. One might reasonably ask whether the complexity of real-world systems is so vast as to make this impossible to achieve? Perhaps, but we can hope that first-order predictions about the behavior of a given biogeochemical system is attainable, provided that the dominant pathways are known and the controlling variables are well-defined.

In the case of the example we discussed in detail in this chapter, Lake Matano, although we know basic aspects about its geochemistry and microbial communities, much remains to be learned. We do not have a good appreciation for how the structure of its microbial community changes over time, nor how changes to this structure affect the geochemical profiles of the lake. We do not understand which environmental variables control the success of particular members of the community, nor how functionally redundant it is (e.g. particular organisms may come and go, but the geochemical reactions they catalyze might be similarly catalyzed by a different group of organisms). The better able we are to characterize these aspects, and point to underlying molecular catalysts (e.g. metabolic enzymes), their rates, and the variables that regulate them, the better able we will be to make predictions about how the lake might respond to environmental perturbations.

Despite these knowledge gaps, the current state of research in microbe-metal interactions provides a fascinating outlook. From years of investigations in geochemistry and microbiology, we can appreciate the tremendous scope of possible pathways. We are working in a historically opportune moment, when enough is known about specific microbial processes to allow us to venture into assessing their relative contributions and importance to the complex cycling of iron and other elements *in situ*. The co-evolution

of microbial life and the environment is much akin to a terrific puzzle where we know enough of the pieces to get a first blurry glimpse of the magnificent full picture, but we don't know yet where each one goes nor how they fit together. It will be satisfying to see the details of this picture emerge and sharpen over the coming years in a variety of systems.

2.6 References

Adamczyk, J., Hesselsoe, M., Iversen, N., Horn, M., Lehner, A., Nielsen, P. H., Schloter, M., Roslev, P., Wagner, M., Nov. 2003. The isotope array, a new tool that employs substrate-mediated labeling of rRNA for determination of microbial community structure and function. Applied and Environmental Microbiology 69 (11), 6875–6887.

Allen, E. E., Banfield, J. F., Jun. 2005. Community genomics in microbial ecology and evolution. Nature Publishing Group 3 (6), 489–498.

Amann, R., Fuchs, B. M., May 2008. Single-cell identification in microbial communities by improved fluorescence in situ hybridization techniques. Nature Publishing Group 6 (5), 339–348.

Amann, R. I., Ludwig, W., Schleifer, K. H., Mar. 1995. Phylogenetic Identification and in-Situ Detection of Individual Microbial-Cells Without Cultivation. Microbiological Reviews 59 (1), 143–169.

Anbar, A., Knoll, A., 2002. Proterozoic ocean chemistry and evolution: A bioinorganic bridge? Science 297 (5584), 1137–1142.

Baker, B., Banfield, J., 2003. Microbial communities in acid mine drainage. Fems Microbiology Ecology 44 (2), 139–152.

Beal, E. J., House, C. H., Orphan, V. J., Jul. 2009. Manganese- and iron-dependent marine methane oxidation. Science 325 (5937), 184–187.

Beja, O., Aravind, L., Koonin, E., Suzuki, M., Hadd, A., Nguyen, L., Jovanovich, S., Gates, C., Feldman, R., Spudich, J., Spudich, E., DeLong, E., 2000. Bacterial rhodopsin: Evidence for a new type of phototrophy in the sea. Science 289 (5486), 1902–1906.

Berner, R., Maasch, K., 1996. Chemical weathering and controls on atmospheric O-2 and CO2: Fundamental principles were enunciated by J. J. Ebelmen in 1845. Geochimica Et Cosmochimica Acta 60 (9), 1633–1637.

Beukes, Gutzmer, Aug. 2008. Origin and Paleoenvironmental Significance of Major Iron Formations at the Archean-Paleoproterozoic Boundary, 43.

Boetius, A., Ravenschlag, K., Schubert, C., Rickert, D., Widdel, F., Gieseke, A., Amann, R., Jorgensen, B., Witte, U., Pfannkuche, O., 2000. A marine microbial consortium apparently mediating anaerobic oxidation of methane. Nature 407 (6804), 623–626.

Bose, A., Kopf, S., Newman, D. K., 2011. From Geocycles to Genomes and Back. In: Microbial Metal and Metalloid Metabolism. ASM Press, Washington, D.C., pp. 13–38.

Brock, T. D., Dec. 1978. Thermophilic Microorganisms and Life at High Temperatures. Springer.

Brooks, J. L., Mar. 1950. Speciation in Ancient Lakes 25 (1), 30–60.

Burdige, D. J., Kepkay, P. E., Nov. 1983. Determination of bacterial manganese oxidation rates in sediments using an *in-situ* dialysis technique I. Laboratory studies. Geochimica Et Cosmochimica Acta 47 (11), 1907–1916.

Canfield, D., 2005. The early history of atmospheric oxygen: Homage to Robert A. Garrels. Annual Review Of Earth And Planetary Sciences 33, 1–36.

Canfield, D., Habicht, K. S., Thamdrup, B., Apr. 2000. The Archean sulfur cycle and the early history of atmospheric oxygen. Science 288 (5466), 658–661.

Canfield, D., Raiswell, R., Bottrell, S., 1992. The reactivity of sedimentary iron minerals toward sulfide. American Journal of Science 292 (9), 659–683.

Canfield, D., Thamdrup, B., Hansen, J., 1993. The anaerobic degradation of organic matter in Danish coastal sediments: Iron reduction, manganese reduction, and sulfate reduction. Geochimica Et Cosmochimica Acta 57 (16), 3867–3883.

Capone, D. G., Kiene, R. P., 1988. Comparison of microbial dynamics in marine and freshwater sediments: Contrasts in anaerobic carbon catabolism. Limnology And Oceanography.

Clement, B. G., Kehl, L. E., DeBord, K. L., Kitts, C. L., Jan. 1998. Terminal restriction fragment patterns (TRFPs), a rapid, PCR-based method for the comparison of complex bacterial communities. Journal of microbiological methods 31 (3), 135–142.

Cohan, F. M., 2002. What are bacterial species? Annual Reviews in Microbiology 56 (1), 457–487.

Croal, L. R., Jiao, Y., Newman, D. K., 2007. The fox operon from Rhodobacter strain SW2 promotes phototrophic fe(II) oxidation in Rhodobacter capsulatus SB1003. Journal of Bacteriology 189 (5), 1774–1782.

Crowe, S., Oct. 2008. Biogeochemical cycling in Iron-rich Lake Matano, Indonesia: An early ocean analogue . Ph.D. thesis.

Crowe, S., Jones, C., Katsev, S., Magen, C., O'Neill, A. H., Sturm, A., Canfield, D., Haffner, G. D., Mucci, A., Sundby, B., Fowle, D. A., Oct. 2008a. Photoferrotrophs thrive in an Archean Ocean analogue. Proceedings of the National Academy of Sciences 105 (41), 15938–15943.

Crowe, S., O'Neill, A. H., Katsev, S., Hehanussa, P., Haffner, G. D., Sundby, B., Mucci, A., Fowle, D. A., 2008b. The biogeochemistry of tropical lakes: A case study from Lake Matano, Indonesia. Limnology And Oceanography 53 (1), 319–331.

Delsuc, F., Brinkmann, H., Philippe, H., May 2005. Phylogenomics and the reconstruction of the tree of life. Nature Reviews Genetics 6 (5), 361–375.

Doolittle, W. F., Feb. 2000. Uprooting the tree of life. Scientific American 282 (2), 90–95.

Duan, Y., Zhou, L., Hall, D. G., Li, W., Doddapaneni, H., Lin, H., Liu, L., Vahling, C. M., Gabriel, D. W., Williams, K. P., Dickerman, A., Sun, Y., Gottwald, T., Aug. 2009. Complete Genome Sequence of Citrus Huanglongbing Bacterium, 'Candidatus Liberibacter asiaticus' Obtained Through Metagenomics. Molecular Plant-Microbe Interactions 22 (8), 1011–1020.

Dumont, M. G., Murrell, J. C., Jun. 2005. Stable isotope probing - linking microbial identity to function. Nature Publishing Group 3 (6), 499–504.

Dunbar, J., Ticknor, L. O., Kuske, C. R., 2001. Phylogenetic specificity and reproducibility and new method for analysis of terminal restriction fragment profiles of 16S rRNA genes from bacterial communities. Appl. Environ. Microbiol.

Edwards, K., Bond, P., Gihring, T., Banfield, J., 2000. An archaeal iron-oxidizing extreme acidophile important in acid mine drainage. Science 287 (5459), 1796–1799.

Ehrlich, H. L., Newman, D. K., Dec. 2008. Geomicrobiology, Fifth Edition. CRC Press.

Eilers, H., Pernthaler, J., Glockner, F. O., Amann, R., Jul. 2000. Culturability and in situ abundance of pelagic bacteria from the North Sea. Applied and Environmental Microbiology 66 (7), 3044–3051.

Emerson, D., Weiss, J., 2004. Bacterial iron oxidation in circumneutral freshwater habitats: Findings from the field and the laboratory. Geomicrobiology Journal 21 (6), 405–414.

Falkowski, P., Barber, R., Smetacek, V., 1998. Biogeochemical controls and feedbacks on ocean primary production. Science 281 (5374), 200–206.

Fraústo da Silva, J. R., Williams, R. J. P., 2001. The biological chemistry of the elements: the inorganic chemistry of life, 2nd Edition. Oxford University Press, Oxford, UK.

Garrels, R., Lerman, A., 1981. Phanerozoic cycles of sedimentary carbon and sulfur. Proceedings Of The National Academy Of Sciences Of The United States Of America-Physical Sciences 78 (8), 4652–4656.

Gentry, T. J., Wickham, G. S., Schadt, C. W., He, Z., Zhou, J., Aug. 2006. Microarray applications in microbial ecology research. Microbial Ecology 52 (2), 159–175.

Ghiorse, W. C., Balkwill, D. L., 1983. Enumeration and morphological characterization of bacteria indigenous to subsurface environments. Developments in Industrial Microbiology.

Giovannoni, S. J., DeLong, E. F., Olsen, G. J., Pace, N. R., Feb. 1988. Phylogenetic group-specific oligodeoxynucleotide probes for identification of single microbial cells. Journal of Bacteriology 170 (2), 720–726.

Glass, J. B., Wolfe-Simon, F., Anbar, A. D., 2009. Coevolution of metal availability and nitrogen assimilation in cyanobacteria and algae. Geobiology 7 (2), 100–123.

Goebel, K. J. E. B. M., May 1999. Geomicrobiology of Pyrite (FeS2) Dissolution: Case Study at Iron Mountain, California. Geomicrobiology Journal 16 (2), 155–179.

Guss, A. M., Mukhopadhyay, B., Zhang, J. K., Metcalf, W. W., Mar. 2005. Genetic analysis of mch mutants in two Methanosarcina species demonstrates multiple roles for the methanopterin-dependent C-1 oxidation/reduction pathway and differences in H-2 metabolism between closely related species. Molecular Microbiology 55 (6), 1671–1680.

Guyer, R. L., Koshland, D. E., 1989. The Molecule of the Year. Science 246 (4937), 1543–1546.

Herbert, D., Elsworth, R., Telling, R. C., Jul. 1956. The Continuous Culture of Bacteria; a Theoretical and Experimental Study. Journal of General MIcrobiology 14 (3), 601–622.

Hesselsoe, M., Fuereder, S., Schloter, M., Bodrossy, L., Iversen, N., Roslev, P., Nielsen, P. H., Wagner, M., Loy, A., Dec. 2009. Isotope array analysis of Rhodocyclales uncovers functional redundancy and versatility in an activated sludge. Isme Journal 3 (12), 1349–1364.

Hoff, K. J., Tech, M., Lingner, T., Daniel, R., Morgenstern, B., Meinicke, P., 2008. Gene prediction in metagenomic fragments: A large scale machine learning approach. Bmc Bioinformatics 9 (1).

Hughes, J. B., Hellmann, J. J., Ricketts, T. H., Bohannan, B., Oct. 2001. Counting the uncountable: Statistical approaches to estimating microbial diversity. Applied and Environmental Microbiology 67 (10), 4399–4406.

Isley, A. E., Abbott, D. H., Jul. 1999. Plume-related mafic volcanism and the deposition of banded iron formation. Journal of Geophysical Research: Solid Earth (1978–2012) 104 (B7), 15461–15477.

Ivanov, M. V., Starkey, R. L., Dec. 1968. Microbiological processes in the formation of sulfur deposits. Soil Science 106 (6), 476.

Jannasch, H. W., 1967. Growth of marine bacteria at limiting concentrations of organic carbon in seawater. Limnology And Oceanography.

Jannasch, H. W., Jul. 1969. Estimations of bacterial growth rates in natural waters. Journal of Bacteriology 99 (1), 156–160.

Jannasch, H. W., Wirsen, C. O., 1981. Morphological survey of microbial mats near deep-sea thermal vents. Applied and Environmental Microbiology.

Jargeat, P., Cosseau, C., Ola'h, B., Jauneau, A., Bonfante, P., Batut, J., Becard, G., Oct. 2004. Isolation, free-living capacities, and genome structure of "Candidatus glomeribacter gigasporarum," the endocellular bacterium of the mycorrhizal fungus Gigaspora margarita. Journal of Bacteriology 186 (20), 6876–6884.

Kaeberlein, T., Lewis, K., Epstein, S. S., May 2002. Isolating "Uncultivable" Microorganisms in Pure Culture in a Simulated Natural Environment. Science 296 (5570), 1127–1129.

Kappler, A., Newman, D. K., Mar. 2004. Formation of Fe(III)-minerals by Fe(II)-oxidizing photoautotrophic bacteria. Geochimica Et Cosmochimica Acta 68 (6), 1217–1226.

Kappler, A., Pasquero, C., Konhauser, K., Newman, D. K., 2005a. Deposition of banded iron formations by anoxygenic phototrophic Fe(II)-oxidizing bacteria. Geology 33 (11), 865–868.

Kappler, A., Posth, N. R., Hegler, F., Konhauser, K. O., Oct. 2008. Alternating Si and Fe deposition caused by temperature fluctuations in Precambrian oceans. Nature Geoscience 1 (10), 703–708.

Kappler, A., Straub, K., 2005. Geomicrobiological cycling of iron. Geochemistry Of Non-Traditional Stable Isotopes 59, 85–108.

Klappenbach, J. A., Saxman, P. R., Cole, J. R., Schmidt, T. M., 2001. rrndb: the Ribosomal RNA Operon Copy Number Database. Nucleic Acids Research 29 (1), 181–184.

Konhauser, K. O., Newman, D. K., Kappler, A., Jul. 2005. The potential significance of microbial Fe(III) reduction during deposition of Precambrian banded iron formations. Geobiology 3 (3), 167–177.

Kraemer, S., 2004. Iron oxide dissolution and solubility in the presence of siderophores. Aquatic Sciences 66 (1), 3–18.

Kraemer, S., Butler, A., Borer, P., Cervini-Silva, J., 2005. Siderophores and the dissolution of iron-bearing minerals in marine systems. Geochemistry Of Non-Traditional Stable Isotopes 59 (1), 53–84.

Lee, N., Nielsen, P. H., Andreasen, K. H., Juretschko, S., Nielsen, J. L., Schleifer, K. H., Wagner, M., Mar. 1999. Combination of fluorescent in situ hybridization and microautoradiography - a new tool for structure-function analyses in microbial ecology. Applied and Environmental Microbiology 65 (3), 1289–1297.

Liu, W. T., Marsh, T. L., Cheng, H., Forney, L. J., Nov. 1997. Characterization of microbial diversity by determining terminal restriction fragment length polymorphisms of genes encoding 16S rRNA. Applied and Environmental Microbiology 63 (11), 4516–4522.

Lovley, D., Holmes, D., Nevin, K., 2004. Dissimilatory Fe(III) and Mn(IV) reduction. Advances In Microbial Physiology, Vol 54 49, 219–286.

Luther, G. W., Brendel, P. J., LEWIS, B. L., Sundby, B., Lefrancois, L., Silverberg, N., Nuzzio, D. B., 1998. Simultaneous measurement of O2, Mn, Fe, I-, and S(-II) in marine pore waters with a solid-state voltammetric microelectrode.

Maloy, S. R., Cronan, J. E., Freifelder, D., 1994. Microbial genetics.

Martinez, A., Bradley, A. S., Waldbauer, J. R., Summons, R. E., DeLong, E. F., 2007. Proteorhodopsin photosystem gene expression enables photophosphorylation in a heterologous host. Proceedings of the National Academy of Sciences of the United States of America 104 (13), 5590–5595.

McArthur, J. V., 2006. Microbial Ecology: An evolutionary approach.

Miller, F. D., Hershberger, C. L., 1984. A Quantitative Beta-Galactosidase Alpha-Complementation Assay for Fusion Proteins Containing Human Insulin B-Chain Peptides. Gene 29 (1-2), 247–250.

Morel, F. M. M., May 2003. The Biogeochemical Cycles of Trace Metals in the Oceans. Science 300 (5621), 944–947.

Morgan, J., Anders, E., 1980. Chemical composition of Earth, Venus, and Mercury. Proceedings Of The National Academy Of Sciences Of The United States Of America-Physical Sciences 77 (12), 6973–6977.

Münster, U., Albrecht, D., 1994. Dissolved Organic Matter: Analysis of Composition and Function by a Molecular-Biochemical Approach. In: Microbial Ecology of Lake Plußsee. Springer New York, New York, NY, pp. 24–62.

Muyzer, G., De Waal, E. C., Uitterlinden, A. G., Mar. 1993. Profiling of complex microbial populations by denaturing gradient gel electrophoresis analysis of polymerase chain reaction-amplified genes coding for 16S rRNA. Applied and Environmental Microbiology 59 (3), 695–700.

Myers, N., Mittermeier, R. A., Mittermeier, C. G., da Fonseca, G., Kent, J., 2000. Biodiversity hotspots for conservation priorities. Nature 403 (6772), 853–858.

Novick, A., Oct. 1955. Growth of Bacteria. Annual Reviews in Microbiology 9 (1), 97–110.

Olsen, G. J., Woese, C. R., Jan. 1993. Ribosomal RNA: a key to phylogeny. Faseb Journal 7 (1), 113–123.

Orphan, V. J., House, C., Hinrichs, K., McKeegan, K., DeLong, E., 2001. Methane-consuming archaea revealed by directly coupled isotopic and phylogenetic analysis. Science 293 (5529), 484–487.

Ottesen, E. A., Hong, J. W., Quake, S. R., Leadbetter, J. R., 2006. Microfluidic digital PCR enables multigene analysis of individual environmental bacteria. Science 314 (5804), 1464–1467.

Ouverney, C. C., Fuhrman, J. A., Apr. 1999. Combined Microautoradiography-16S rRNA probe technique for determination of radioisotope uptake by specific microbial cell types in situ. Applied and Environmental Microbiology 65 (4), 1746–1752.

Pelletier, E., Kreimeyer, A., Bocs, S., Rouy, Z., Gyapay, G., Chouari, R., Riviere, D., Ganesan, A., Daegelen, P., Sghir, A., Cohen, G. N., Médigue, C., Weissenbach, J., Le Paslier, D., Apr. 2008. "Candidatus Cloacamonas acidaminovorans": Genome sequence reconstruction provides a first glimpse of a new bacterial division. Journal of Bacteriology 190 (7), 2572–2579.

Pernthaler, A., Dekas, A. E., Brown, C. T., Goffredi, S. K., Embaye, T., Orphan, V. J., May 2008. Diverse Syntrophic Partnerships from Deep-Sea Methane Vents Revealed by Direct Cell Capture and Metagenomics. Proceedings of the National Academy of Sciences of the United States of America 105 (19), 7052–7057.

Pernthaler, A., Pernthaler, J., Amann, R., Jun. 2002. Fluorescence in situ hybridization and catalyzed reporter deposition for the identification of marine bacteria. Applied and Environmental Microbiology 68 (6), 3094–3101.

Petsch, S. T., Edwards, K. J., Eglinton, T. I., 2003. Abundance, distribution and δ^{13}C analysis of microbial phospholipid-derived fatty acids in a black shale weathering profile. Organic Geochemistry.

Philippe, H., Laurent, J., Dec. 1998. How good are deep phylogenetic trees? Current Opinion in Genetics & Development 8 (6), 616–623.

Pritchett, M. A., Zhang, J. K., Metcalf, W. W., Mar. 2004. Development of a markerless genetic exchange method for Methanosarcina acetivorans C2A and its use in construction of new genetic tools for methanogenic archaea. Applied and Environmental Microbiology 70 (3), 1425–1433.

Radajewski, S., Ineson, P., Parekh, N., Murrell, J., 2000. Stable-isotope probing as a tool in microbial ecology. Nature 403 (6770), 646–649.

Raghoebarsing, A., Pol, A., van de Pas-Schoonen, K., Smolders, A., Ettwig, K., Rijpstra, W., Schouten, S., Damste, J., Op den Camp, H., Jetten, M., Strous, M., 2006. A microbial consortium couples anaerobic methane oxidation to denitrification. Nature 440 (7086), 918–921.

Rankama, K., Georg Sahama, T., Committee on Publications in the Physical Sciences, U., 1950. Geochemistry, 927.

Rappe, M. S., Connon, S. A., Vergin, K. L., Giovannoni, S. J., 2002. Cultivation of the ubiquitous SAR11 marine bacterioplankton clade. Nature 418 (6898), 630–633.

Reeburgh, W. S., Feb. 2007. Oceanic Methane Biogeochemistry. Chemical Reviews 107 (2), 486–513.

Rokas, A., Holland, P., Nov. 2000. Rare genomic changes as a tool for phylogenetics. Trends in Ecology & Evolution 15 (11), 454–459.

Rother, M., Metcalf, W. W., Dec. 2005. Genetic technologies for Archaea. Current Opinion In Microbiology 8 (6), 745–751.

Sabo, E., Roy, D., Hamilton, P. B., Hehanussa, P. E., McNeely, R., Haffner, G. D., Dec. 2008. The plankton community of Lake Matano: factors regulating plankton composition and relative abundance in an ancient, tropical lake of Indonesia. Hydrobiologia 615 (1), 225–235.

Saito, M., Sigman, D. M., Morel, F., 2003. The bioinorganic chemistry of the ancient ocean: the co-evolution of cyanobacterial metal requirements and biogeochemical cycles at the Archean-Proterozoic boundary? Inorganica Chimica Acta 356, 308–318.

Salyers, A. A., Bonheyo, G., Shoemaker, N. B., Jan. 2000. Starting a new genetic system: Lessons from Bacteroides. Methods-a Companion to Methods in Enzymology 20 (1), 35–46.

Schlegel, H. G., 1993. General Microbiology. New York City, NY.

Seeber, F., Boothroyd, J. C., 1996. *Escherichia coli* β-galactosidase as an in vitro and in vivo reporter enzyme and stable transfection marker in the intracellular protozoan parasite *Taxoplasma gondii*. Gene.

Shi, Y., Tyson, G. W., Delong, E. F., 2009. Metatranscriptomics reveals unique microbial small RNAs in the ocean's water column. Nature 459 (7244), 266–U154.

Sieburth, J. M., 1975. Microbial Seascapes.

Stackebrandt, E., Goebel, B. M., Oct. 1994. A Place for Dna-Dna Reassociation and 16s Ribosomal-Rna Sequence-Analysis in the Present Species Definition in Bacteriology. International Journal of Systematic Bacteriology 44 (4), 846–849.

Stahl, D., 1997. Molecular Approaches for the Measurement of Density, Diversity and Phylogeny. In: Manual of environmental microbiology. ASM Press.

Staley, J. T., Konopka, A., Nov. 2003. Measurement of in Situ Activities of Nonphotosynthetic Microorganisms in Aquatic and Terrestrial Habitats. dx.doi.org 39 (1), 321–346.

Stumm, W., J Morgan, J., 1996. Aquatic chemistry: chemical equilibria and rates in natural waters, 3rd Edition. John Wiley & Sons, Inc., New York.

Svensson, E., Skoog, A., Amend, J. P., 2004. Concentration and distribution of dissolved amino acids in a shallow hydrothermal system, Vulcano Island (Italy). Organic Geochemistry.

Tran-Nguyen, L. T. T., Kube, M., Schneider, B., Reinhardt, R., Gibb, K. S., Jun. 2008. Comparative genome analysis of "*Candidatus* Phytoplasma australiense" (subgroup tuf-Australia I; rp-A) and "*Ca*. Phytoplasma asteris" strains OY-M and AY-WB. Journal of Bacteriology 190 (11), 3979–3991.

Ussher, S. J., Achterberg, E. P., Worsfold, P. J., 2004. Marine biogeochemistry of iron. Environmental Chemistry 1 (2), 67–80.

Valdivia, R. H., Cormack, B. P., Falkow, S., 2006. The uses of green fluorescent protein in prokaryotes. Methods of biochemical analysis 47, 163–178.

Ward, D. M., Bateson, M. M., Weller, R., Ruffroberts, A. L., 1992. Ribosomal-RNA analysis of microorganisms as they occur in nature. Advances In Microbial Ecology 12 (Chapter 5), 219–286.

Ward, D. M., Ferris, M. J., Nold, S. C., Bateson, M. M., Dec. 1998. A natural view of microbial biodiversity within hot spring cyanobacterial mat communities. Microbiology and Molecular Biology Reviews 62 (4), 1353–+.

Ward, D. M., Weller, R., Bateson, M. M., May 1990. 16S rRNA sequences reveal numerous uncultured microorganisms in a natural community. Nature 345 (6270), 63–65.

Warnecke, F., Hess, M., 2009. A perspective: Metatranscriptomics as a tool for the discovery of novel biocatalysts. Journal of Biotechnology 142 (1), 91–95.

Weber, K. A., Achenbach, L. A., Coates, J. D., Oct. 2006b. Microorganisms pumping iron: anaerobic microbial iron oxidation and reduction. Nature Reviews Microbiology 4 (10), 752–764.

White, D., Drummond, J. T., Fuqua, C., 2000. The Physiology and Biochemistry of Prokaryotes. Oxford University Press, USA.

Whiteley, A. S., Manefield, M., Lueders, T., Feb. 2006. Unlocking the 'microbial black box' using RNA-based stable isotope probing technologies. Current Opinion In Biotechnology 17 (1), 67–71.

Widdel, F., Schnell, S., Heising, S., Ehrenreich, A., Assmus, B., Schink, B., Apr. 1993. Ferrous iron oxidation by anoxygenic phototrophic bacteria. , Published online: 29 April 1993; | doi:10.1038/362834a0 362 (6423), 834–836.

Wilmes, P., Simmons, S. L., Denef, V. J., Banfield, J. F., Jan. 2009. The dynamic genetic repertoire of microbial communities. Fems Microbiology Reviews 33 (1), 109–132.

Woyke, T., Tighe, D., Mavromatis, K., Clum, A., Copeland, A., Schackwitz, W., Lapidus, A., Wu, D., McCutcheon, J. P., McDonald, B. R., Moran, N. A., Bristow, J., Cheng, J.-F., Apr. 2010. One bacterial cell, one complete genome. PLoS ONE 5 (4), e10314.

Wu, L., Liu, X., Schadt, C. W., Zhou, J., Jul. 2006. Microarray-based analysis of subnanogram quantities of microbial community DNAs by using whole-community genome amplification. Applied and Environmental Microbiology 72 (7), 4931–4941.

Zengler, K., Toledo, G., Rappé, M., Elkins, J., Mathur, E. J., Short, J. M., Keller, M., Nov. 2002. Cultivating the uncultured. Proceedings of the National Academy of Sciences of the United States of America 99 (24), 15681–15686.

Chapter 3

Photomixotrophic growth of *Rhodobacter capsulatus* SB1003 on ferrous iron[1]

Abstract

This study investigates the role iron oxidation plays in the purple non-sulfur bacterium *Rhodobacter capsulatus* SB1003. This organism is unable to grow photoautotrophically on unchelated ferrous iron [Fe(II)] despite its ability to oxidize chelated Fe(II). This apparent paradox was partly resolved by the discovery that SB1003 can grow photoheterotrophically on the photochemical breakdown products of certain ferric iron–ligand complexes, yet whether it could concomitantly benefit from the oxidation of Fe(II) to fix CO_2 was unknown. Here, we examine carbon fixation by stable isotope labeling of the inorganic carbon pool in cultures growing phototrophically on acetate with and without Fe(II). We show that *R. capsulatus* SB1003, an organism formally thought incapable of phototrophic

[1] Kopf and Newman (2011),

growth on Fe(II), can actually harness the reducing power of this substrate and grow photomixotrophically, deriving carbon both from organic sources and from fixation of inorganic carbon. This suggests the possibility of a wider occurrence of photoferrotrophy than previously assumed.

3.1 Introduction

Microbial processes throughout Earth's history have had a profound impact on the biogeochemical cycling of iron (Kappler and Straub, 2005; Ehrlich and Newman, 2008). While much attention has been paid to iron's ability to serve as an electron donor or electron acceptor in catabolic processes, beyond a crude accounting for electrons in the metabolisms of a few model organisms, we have little appreciation for how cells make use of iron's redox chemistry. For example, we would expect multiple elements within a cell to be affected by an imbalance in iron homeostasis, which in turn would be expected to change how a cell might regulate its export or uptake of substrates containing these elements. Similarly, we would expect intracellular redox homeostasis to be influenced by iron in myriad ways. How these and other more subtle effects manifest themselves is poorly understood, yet they may be important drivers of the overall iron biogeochemical cycle.

In recognition of this knowledge gap, we chose to explore how ferrous iron [Fe(II)] is used by the anoxygenic phototroph, *Rhodobacter capsulatus* strain SB1003. We chose this organism as a model system because it exhibited a curious phenotype during phototrophic growth. Unlike other Rhodobacter species (Ehrenreich and Widdel, 1994), *R. capsulatus* SB1003 does not oxidize iron (and grow photolithotrophically) in medium containing Fe(II) chloride as the sole source of reducing power (Croal et al., 2007). However, in the presence of chelating agents such as citrate and NTA, Fe(II) oxidation is enabled, and SB1003 can grow photoheterotrophically on supplementary carbon sources (Croal et al., 2007; Poulain

and Newman, 2009), or, in the case of photoactive ferric [Fe(III)]-ligand complexes such as Fe(III)-citrate, on the photochemical breakdown products of the ligand (Caiazza et al., 2007). This shows that Fe(II) oxidation can benefit the organism indirectly, but does not resolve whether Fe(II) oxidation can benefit *R. capsulatus* directly. Poulain and Newman, 2009 first explored the ambiguous role of Fe(II) oxidation in *R. capsulatus* SB1003 and proposed Fe(II) oxidation as a potential detoxification mechanism. Preliminary data on gene expression furthermore revealed that several Calvin cycle genes are upregulated in the presence of Fe(II) (Poulain and Newman, unpublished data), suggesting a potential link to Fe(II) oxidation. Herein, we expand on these studies and show that *R. capsulatus* SB1003 can grow photomixotrophically using Fe(II) as an electron donor for carbon fixation.

3.2 Materials and Methods

3.2.1 Experimental conditions

Rhodobacter capsulatus SB1003 was grown phototrophically in anoxic, minimal-salts freshwater medium, prepared as previously described (Ehrenreich and Widdel, 1994). The medium was buffered at pH 7.0 with 22mM sodium bicarbonate. All experiments were prepared in an oxygen- and hydrogen-free, anaerobic chamber under an atmosphere of pure N2. All reagents and glassware were stored in the chamber at least three days prior to use to remove traces of oxygen. In addition to standard heat sterilization procedures used for all equipment and medium preparation, glassware was precombusted in a muffle furnace at 550°C to remove all remaining traces of organic materials potentially adhered to the glass. Cells were grown anaerobically at 30°C under constant illumination from two 60W incandescent light sources at 30cm distance, providing a total irradiance of ca. 40 W/m^2 (45.5% visible light, 54.4% IR, ~0.1% UV). Growth was followed by optical density at 675nm (OD675). This wavelength was used to decrease distortion by Fe(III)-NTA,

which absorbs strongly at 600nm. OD675 underestimates optical density as compared to a measurement at 600nm.

3.2.2 Phototrophic growth in the presence of iron

Phototrophic growth was assessed in bicarbonate buffered freshwater medium amended with 4mM ferrous Fe(II) complexed by 10mM nitrilotriacetate (NTA), or 5mM ferric Fe(III) complexed by 10mM NTA. Medium amended with either 5mM NTA only or with Fe(II)-NTA incubated in the dark was tested as controls. No additional carbon or electron sources were provided. NTA was chosen as the complexing agent to avoid fast photolytic breakdown of the Fe(III)-ligand complex. Previous work with citrate revealed a high degradation of the more photoreactive Fe(III)-citrate complex (~0.6 mM / day, Caiazza et al., 2007), which allowed for rapid accumulation of acetoacetate, a substrate that can be readily metabolized by *R. capsulatus* and obscures the effect of Fe(II) oxidation. The chosen concentrations of NTA were previously found not to interfere with growth on other substrates (data not shown) while ensuring that virtually all Fe(II) and Fe(III) remain complexed, preventing precipitation of iron hydroxides (Poulain and Newman, 2009). Experiments were conducted in biological triplicates. Fe(II) concentrations were measured at the start and end of the experiment. Fe(II) was quantified throughout this study using the FerroZine assay (Stookey, 1970).

3.2.3 Isotope labeling

For isotope labeling, freshwater medium was buffered with 22mM labeled sodium bicarbonate ($NaH^{13}CO_3$, CAS# 87081-58-01) purchased from Cambridge Isotope Laboratories, Inc. (catalogue # CLM-441, purification grade: >99% ^{13}C). Freshwater medium was amended with 3mM acetate only [A], ~4mM Fe(II)-10mM NTA only [B], or both [C]. Cultures were harvested upon reaching early stationary phase (20 hours after inoculation for [A], 29 hours for [B,C]), washed thrice in deionized water and lyophilized overnight.

Acetate and Fe(II) concentrations were determined before inoculation and at the time of harvest. Acetate was measured using a Dionex ICS-3000 ion chromatography system with a 4x240mm AS-11 IonPac column and NaOH elution gradient (0.5 to 5.0 mM NaOH in 3.5 min followed by 5.0 to 37mM NaOH in 12 min at a flow rate of 2 ml/min). Isotopic composition of bulk cell carbon was determined by EA-IRMS at the UC Davis Stable Isotope Facility (Davis, CA). Carbon isotopic compositions from labeled experiments are reported in terms of atom percent $\%^{13}C = 100\ [^{13}C\ /\ (^{12}C + {}^{13}C)]$ throughout this study. Isotopic composition of acetate, NTA as well as the inoculum culture used in this study were measured and confirmed to be approximately natural abundance ($\approx 1.1\ \%^{13}C$, $\delta^{13}C > -40‰$, data not shown). The labeled bicarbonate was assumed to comply with the manufacturer's specifications ($\approx 99\ \%^{13}C$). Experiments were conducted in biological triplicates [A] or quadruplicates [B,C]. Abiotic controls indicated no significant oxidation of Fe(II) over the course of the experiment.

3.2.4 Carbon assimilation efficiency

The carbon assimilation efficiency of *R. capsulatus* during phototrophic growth on acetate was determined from the consumption of acetate and concomitant increase in cell dry weight of cultures grown to late exponential phase on acetate as the only carbon source. Cultures were pelleted by centrifugation, filtered onto pre-weighed Spin-X centrifuge tube filters, and dried to constant weight in a 60°C drying oven. Total cell carbon content was derived from dry weights based on the elemental composition of *R. capsulatus* ($CH_{1.83}N_{0.183}O_{0.5}$, Dorffler et al., 1998). Acetate consumption was measured by ion chromatography.

3.3 Results and discussion

3.3.1 Fe(II) oxidation promotes growth

To elucidate whether Fe(II) oxidation itself confers any growth benefit to *R. capsulatus*, we assessed phototrophic growth on Fe(II) complexed by nitrilotriacetate (NTA) in anoxic freshwater medium, completely devoid of additional electron donors (trace organics or hydrogen, see Materials and Methods), with bicarbonate as the sole carbon source (Figure 3.1). The lack of growth in the control experiment (NTA only) shows that *R. capsulatus* cannot use NTA as a carbon source. When provided with Fe(II)-NTA in the light, the organism grew rapidly for 2 days, and appeared to grow slowly for the remainder of the experiment. Optical density likely reflects growth, as iron oxides did not precipitate (all Fe(III) complexed by NTA), although small variations in optical density could also be due to morphological changes as the cells aged. Fe(II) was completely oxidized after 2 days, and remained oxidized for the remainder of the experiment. No growth or Fe(II) oxidation occurred in the dark (Figure 3.1). When provided with Fe(III)-NTA instead, the organism had no direct source of reducing power and showed only very little growth, similar to later stage (2+ days) on Fe(II)-NTA (Figure 3.1). Small quantities of reduced Fe(II) (360±80 μM) accumulated in the medium within 2 days. Since the Fe(III)-NTA complex can be photochemically active at the experimental pH and light regime (Andrianirinaharivelo et al., 1993), the observed accumulation of Fe(II) is likely due to photoreduction of Fe(III) in the Fe(III)-NTA complex. This process is expected to photodegrade the ligand, yielding NTA breakdown products that could serve as a carbon source for photoheterotrophic growth or dissimilatory Fe(III) reduction (Dobbin et al., 1996). The apparent slow growth in the presence of Fe(III)-NTA, both when supplied initially or provided by oxidation of Fe(II), suggests that the organism can benefit from photoreduction of Fe(III), photolytic breakdown of NTA, or both. Because Fe(II)-NTA

does not photolyze, and photolysis of unbound NTA is exceedingly slow (Larson and Stabler, 1978), the rapid initial growth in the presence of Fe(II)-NTA cannot be explained by growth on photochemical breakdown products, and suggests that the oxidation of Fe(II) provides a growth benefit to *R. capsulatus*.

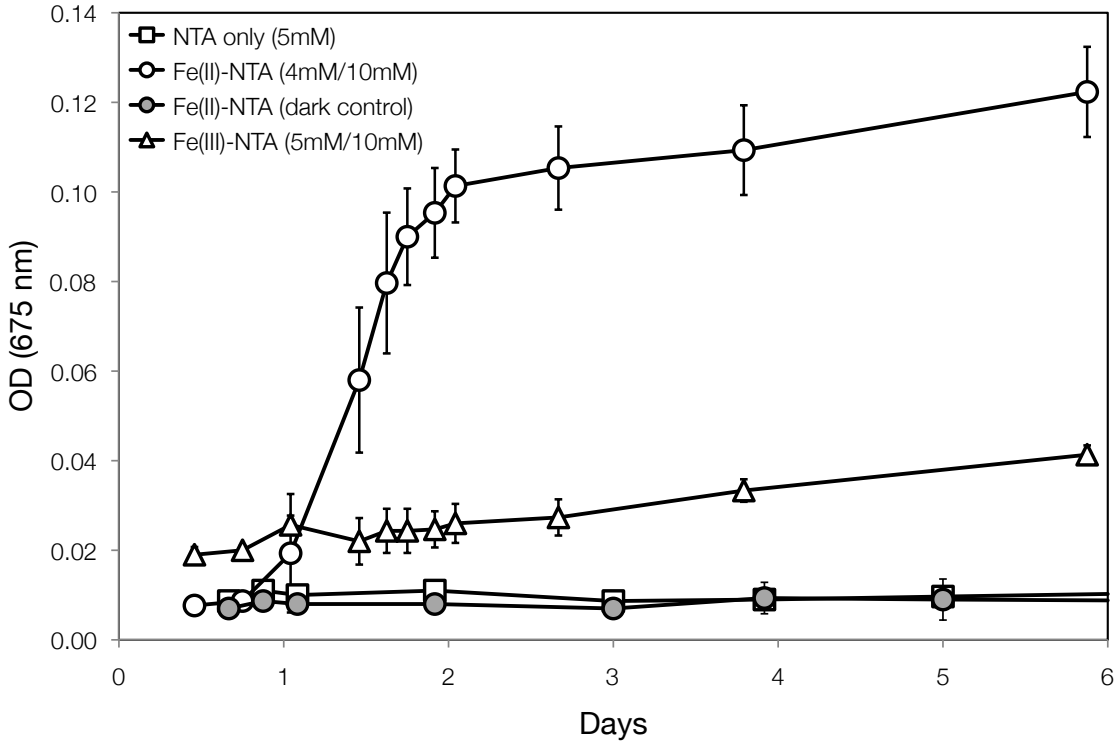

Figure 3.1 – Fe(II) oxidation promotes growth. Phototrophic growth was assessed in freshwater medium amended with NTA only, ferrous Fe(II)-NTA (light and dark), or ferric Fe(III)-NTA. Symbols represent the averages of biological triplicates. Error bars indicate standard deviation, and may be smaller than symbol size. OD (675nm) is optical density at 675nm.

3.3.2 Fe(II) oxidation allows for carbon fixation

To test whether Fe(II) serves as an electron donor for carbon fixation, we conducted isotope labeling experiments with ^{13}C labeled bicarbonate. If CO_2 is fixed during growth on Fe(II)-NTA, inorganic ^{13}C should be strongly incorporated into cell carbon. However, purple non-sulfur bacteria like *R. capsulatus* also use CO_2 as a sink for excess reducing equivalents to

achieve redox homeostasis during photoheterotrophic growth (Tabita, 2004), potentially obscuring this signal. This is further complicated by any potential contribution to growth from photolytic breakdown products of NTA, which would introduce unlabeled carbon into the cell. To allow a quantitative interpretation of the labeling experiments, we thus explored three different growth conditions: phototrophic growth on [A] acetate alone, [B] Fe(II)-NTA alone, and [C] acetate and Fe(II)-NTA together. Table 3.1 documents optical density as well as acetate and Fe(II) concentrations at the onset and conclusion of each experiment, in addition to the ^{13}C content of the harvested cells (see Materials and Methods for experimental details). Because all organic carbon sources were unlabeled (acetate, NTA) and the entire inorganic pool was labeled (bicarbonate), these isotopic data represent the net assimilation of organic vs. inorganic carbon into biomass for each growth condition. The low variability between biological replicates provides confidence in the reproducibility and comparability of the experimental conditions.

Sample	OD (675nm)		Acetate [mM]		Fe(II) [mM]		Bulk ^{13}C [%]
	Inoculation	Harvest	Start	End	Start	End	
Acetate only [A]	0.007±0.001	0.353±0.001	3.02±0.03	<0.1*	none	none	16.8±0.1
Fe(II)-NTA only [B]	0.007±0.001	0.145±0.003	none	none	4.31±0.08	0.21±0.03	62.8±0.5
Acetate & Fe(II)-NTA [C]	0.008±0.003	0.451±0.026	3.02±0.03	<0.1*	4.32±0.13	0.33±0.11	28.1±0.3

Table 3.1 – Fe(II) oxidation allows carbon fixation. Bulk isotopic composition of *R. capsulatus* after phototrophic growth in freshwater medium containing 22mM $H^{13}CO_3^-$ and amended with acetate only [A], Fe(II)-NTA only [B], or both [C]. Optical density (OD at 675nm), acetate and ferrous Fe(II) concentrations were measured at inoculation (t=0) and at the time of harvest (20 hours after inoculation for [A], 29 hours for [B,C]). Values represent averages of biological triplicates [A] and quadruplicates [B,C] respectively. Reported error is one standard deviation.
*Acetate at time of harvest could no longer be detected, and is reported to be below the lower limit of determination.

The isotopic data from growth condition [A] (acetate only) illustrates the role of carbon fixation for redox homeostasis during photoheterotrophic growth. During photoheterotrophic growth, purple non-sulfur bacteria like *R. capsulatus* generate energy from cyclic phosphorylation while building cell carbon directly from organic carbon sources. The use of organic substrates for biosynthesis, however, can lead to a buildup of excess

reducing power, requiring these phototrophs to find an electron sink to maintain redox homeostasis. In organisms limited for nitrogen, nitrogenase can serve this function by sinking excess electrons into N_2 and H^+, producing ammonium and H_2 (Hillmer and Gest, 1977; Mckinlay and Harwood, 2011). Additionally, certain alternative electron acceptors such as dimethylsulfoxide can provide the necessary electron sink (Richardson et al., 1988). More commonly though, redox homeostasis under photoheterotrophic growth of *R. capsulatus* is achieved by using CO_2 as a sink for excess reducing equivalents through the Calvin-Benson-Bassham pathway (the Calvin cycle) (Tichi and Tabita, 2000; 2001; Bauer et al., 2003; Tabita, 2004). During the experimental conditions employed in this study, photoheterotrophic growth of *R. capsulatus* in the presence of excess ammonium and the absence of alternative electron acceptors, CO_2 fixation via the Calvin cycle provides the only available sink for excess reducing power. This introduces cell carbon derived from the inorganic carbon pool into the cell. Our data indicate that close to 17% (Table 3.1) of cellular carbon is derived from the inorganic carbon pool during photoheterotrophic growth of *R. capsulatus* SB1003 on acetate. This result is in agreement with a detailed metabolic flux analysis of another purple phototroph, *Rhodopseudomonas palustris*, growing photoheterotrophically on acetate (Mckinlay and Harwood, 2010): *R. palustris* metabolizes 22% of the provided acetate to CO2 via central metabolic pathways and reincorporates 68% of the released CO2 into cell carbon via the Calvin cycle, ultimately deriving approximately 16% of its cellular carbon from CO2 (Mckinlay and Harwood, 2010). Several pathways of acetate assimilation that can explain the observed exchange of carbon with the inorganic pool have been discovered in the purple phototrophs (Blasco et al., 1989; Willison, 1998; Filatova et al., 2005; Meister et al., 2005). However, why these organisms build up excess reducing power (that is disposed of via the Calvin cycle or other redox sinks) during growth on substrates that are more oxidized than cell carbon is still poorly understood (Mckinlay and Harwood, 2010). Under the experimental conditions employed in this study, the energetic cost of carbon

fixation via the Calvin cycle is unlikely to significantly affect the energy available to *R. capsulatus*. ATP generation via cyclic photophosphorylation provides energy independently of the growth-limiting sources of reducing power (organic carbon and Fe(II)).

The large incorporation of labeled inorganic carbon in cultures grown phototrophically on Fe(II)-NTA alone (close to 63%, growth condition [B], see Table 3.1) confirms that Fe(II) serves as an electron donor for carbon fixation. However, the dilution of the inorganic signal (99% 13C) indicates that *R. capsulatus* must be capable of assimilating some organic carbon from the chelator NTA, the only unlabeled pool of carbon available in the medium. Because the organism is unable to metabolize NTA directly (Figure 3.1), the isotopic data suggest that it can benefit from photolysis of the ligand. Previous studies (Caiazza et al., 2007) have shown that under similar conditions, growth of *R. capsulatus* SB1003 on Fe(II)-citrate occurs as a result of Fe(II) oxidation and Fe(III)-citrate photochemistry, which produces acetoacetic acid as a consequence of ligand breakdown, a carbon source accessible to the organism. A similar model is conceivable for Fe(II)-NTA with the well-studied photochemically active Fe(III)-NTA complex breaking down to iminodiacetic acid (IDA), formaldehyde (HCHO), CO2 and hydroxyl radicals (Trott et al., 1972; Stolzberg and Hume, 1975; Andrianirinaharivelo et al., 1993; Bunescu et al., 2008). IDA can further disintegrate to formaldehyde and glycine, although this second photolytic step proceeds at slower rates (Stolzberg and Hume, 1975). Based on the presence of genes annotated as hydroxymethyl-transferase (*glyA*, RCC00438), serine-glyoxylate aminotransferase (RCC03109) and hydroxypyruvate reductase (*ttuD*, RCC02615) in the sequenced genome of *R. capsulatus* SB1003, formaldehyde assimilation by the serine pathway should be possible in SB1003, making formaldehyde a potential carbon source (Chistoserdova et al., 2003). This pathway is a common functional module in methylotrophs, and well-understood at the biochemical level. An additional pathway of formaldehyde metabolism using the glutathione-dependent formaldehyde dehydrogenase (*adhC*, RCC00869) present in the genome of SB1003 is also possible, as pointed out

previously (Caiazza et al., 2007). This pathway leads to the net generation of reducing equivalents by oxidizing formaldehyde, and could be used for fixing inorganic carbon, but would not lead to direct assimilation of the organic carbon (which is oxidized to CO_2). *R. capsulatus* is unable to grow photoheterotrophically on IDA (no growth observed on 5mM IDA over the course of 3 days, data not shown) but can grow on glycine as the sole carbon source (growth on 5mM glycine up to an optical density of 0.3 at 675nm, data not shown), rendering glycine an additional potential source for carbon. Lastly, the radicals formed during Fe(III)-NTA photolysis can potentially interact with NTA or IDA to provide additional accessible, yet unidentified carbon sources. Our isotopic data provides evidence that *R. capsulatus* can assimilate some of these NTA breakdown products; however, which photolytic product of NTA degradation is metabolized by the organism, and how it is metabolized, remains to be shown.

The intermediate incorporation of labeled inorganic carbon in cultures grown phototrophically on acetate and Fe(II)-NTA (28%, growth condition [C], see Table 1) is consistent with a combination of the effects observed during growth on acetate alone and growth on Fe(II)-NTA alone (conditions [A] and [B]).

These results indicate that *R. capsulatus* SB1003 grows photomixotrophically by fixing CO2 with Fe(II) as the electron donor (photoautotrophic metabolism) while simultaneously assimilating organic carbon sources (photoheterotrophic metabolism). Why the organism can benefit from the oxidation of Fe(II)-NTA but fails to oxidize unchelated Fe^{2+} is unclear, and merits further research. It could reflect a requirement for ligand-bound Fe(II) to be recognized for efficient uptake into the cell, and/or result from a toxic effect of the free metal ion, as suggested by (Poulain and Newman, 2009).

3.3.3 Mass balance model

The isotopic data shows that *R. capsulatus* can incorporate a mixture of carbon sources during phototrophic growth, and provides a basis for quantitative evaluation of their

respective contributions. In the presence of complexed Fe(II), the organism seems capable of exploiting simple, naturally widespread organic acids (such as acetate), photochemically mobilized refractory carbon (such as ligand breakdown products), and the reducing power of the Fe(II) itself (summarized schematically in Figure 3.2). Isotopic mass balance yields the relative contributions of these carbon sources:

$$\%^{13}C_{TCC}[TCC] = \%^{13}C_{Inoc-C}[Inoc] + \%^{13}C_{Ac} - C_{EAc}[Ac] + \%^{13}C_{Fe-C}R_{C/Fe}[Fe(II)] + \%^{13}C_{NTA-C}[NTA]$$

where [Inoc], [Ac] , [Fe(II)] and [NTA] are the concentrations of the different carbon pools (initial inoculum, acetate assimilation, carbon fixation through Fe(II) oxidation, and acquisition of carbon from Fe(III)-NTA breakdown) contributing to total cell carbon [TCC]. E_{Ac} denotes the net efficiency of acetate assimilation, $R_{C/Fe}$ the net ratio of molecules of CO_2 fixed into cell carbon per atoms of Fe(II) oxidized. $\%^{13}C_{Inoc\text{-}C}$, $\%^{13}C_{Ac\text{-}C}$, $\%^{13}C_{Fe\text{-}C}$ and $\%^{13}C_{NTA\text{-}C}$ indicate the isotopic composition of cell carbon derived from these different sources, respectively. $\%^{13}C_{TCC}$ is the isotopic composition of total cell carbon, as measured in the isotope labeling experiments in this study (Table 3.1).

The net efficiency of carbon assimilation from acetate during photoheterotrophic growth of *R. capsulatus* was 1.75±0.14 mol cell C / mol acetate (E_{Ac} =88% carbon conservation efficiency, average from 5 biological replicates ± SD), in agreement with similar measurements for the anoxygenic phototroph *R. palustris* (Mckinlay and Harwood, 2010). The net ratio of CO_2 fixation to Fe(II) oxidation was estimated to be $R_{C/Fe}$ =0.23, since 4.3 electrons from Fe(II) are required to reduce inorganic carbon to the carbon redox state of of *R. capsulatus* biomass (-0.3, see Supporting Information B for details). The contribution from the inoculum to final biomass was estimated to be 1% of the biomass generated from growth on acetate (the 1% inoculum). Assuming that acetate metabolism proceeds by very similar pathways irrespective of the presence or absence of Fe(II)-NTA metabolism and vice-versa, the mass balance equations for the different experimental conditions [A, B and C] provide the estimates for the unknown parameters ($\%^{13}C_{NTA\text{-}C}$

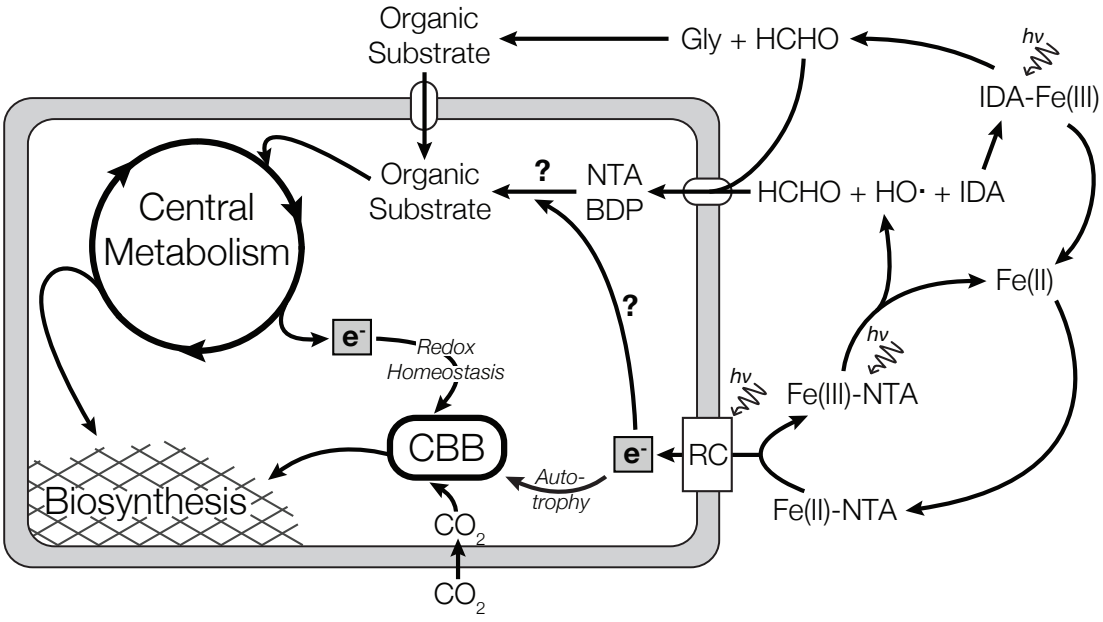

Figure 3.2 – Mixotrophic growth of *R. capsulatus*. Schematic overview of the various pathways that can contribute to photomixotrohpic growth in the presence of Fe(II)-NTA. Question marks (?) indicate hypothesized pathways (discussed in text) that require further investigation. Abbreviations: Calvin-Benson-Bassham pathway (CBB), photosynthetic reaction center (RC), NTA breakdown products (NTA BDP), photochemically/photosynthetically active radiation (*hv*).

and [NTA]) reported in Table 3.2.

NTA breakdown products are metabolized with an exchange of ~18.6% of assimilated carbon with the inorganic pool (either by dearboxylation/recarboxylation reactions or oxidation and refixation via the Calvin cycle), which is similar to our measured value for acetate assimilation (16.9%). The total amount of cell carbon derived from the assimilation of NTA breakdown products (0.70 mM C), corresponds to 0.12mM NTA (a 6C compound) – or 1.2% of the total NTA pool – if all carbon in the photolytic breakdown products can be metabolized by the organism. The precise rate of photolytic breakdown is difficult to estimate because Fe(III)-NTA photolysis is strongly pH- and wavelength-dependent, but would be expected to be slow at circumneutral (or higher) pH with little irradiation in the UV (shorter than ~365nm) (Andrianirinaharivelo et al., 1993).

The estimate for [NTA] also enables calculation of an electron mass balance based on

Carbon sources	Derived cell carbon		Acetate only [A]	Fe-NTA only [B]	Acetate & Fe-NTA [C]
	[mM C]	[% ^{13}C]	Relative contributions [%C-source]		
Inoculum	0.05±0.01	1.1	1.0±0.2%	3.1±0.4%	0.8±0.1%
Acetate assimilation	5.3±0.4	16.9	99.0±0.2%	-	76±2%
Carbon fixation by Fe oxidation	0.95±0.07	99.0	-	56±6%	14±1%
Assimilation of NTA breakdown products	0.7±0.2	18.6	-	41±6%	10±1%
Total biomass C [mM]			5.3±0.4	1.7±0.2	7.0±0.5
Total biomass e- [mM] *			22.9±2.4	7.3±0.9	29.9±2.9
Total e-donor e- [mM] #			24.4±0.3	7.1±0.8	31.2±0.8
e-recovery [%] +			94±10%	103±18%	96±10%

Table 3.2 – Carbon and electron mass balance. Carbon mass balance includes total amounts and isotopic composition of cell carbon derived from the different carbon sources. Electron recovery is based on total e- donor consumption and cellular e^- content. Derived quantities are reported with errors derived by error propagation. Reported error is one standard deviation.
*based on e- content of *R. capsulatus* biomass derived in Supplemental Information B
#assuming substrate from NTA breakdown to be primarily in the oxidation state of formaldehyde (see Table B.1)
+ratio of total e- recovered in biomass / e- available from e-donors

the total electron content of the generated *R. capsulatus* biomass and the total electron content of the consumed substrates (acetate, Fe(II) and NTA breakdown products). For this calculation, we assume that the oxidation state of carbon in the assimilated NTA breakdown product corresponds to the oxidation state of carbon in formaldehyde; making this assumption, we can estimate the total electron recovery for each experimental condition (Table 3.2).

3.3.4 Obligate mixotrophy

Interestingly, the model results and Figure 1 suggest that *R. capsulatus* cannot fully benefit from the assimilation of NTA breakdown products in the absence of Fe(II). In the presence of Fe(II), NTA breakdown products contribute as much as 41% to cell carbon. If provided with Fe(III)-NTA, however, this contribution is not visible in the growth curve. Because all organic carbon sources available to *R. capsulatus* in our experiments are slightly more oxidized than bulk biomass (see Supporting Information for details), the organism requires

some reducing power for net biosynthetic reduction of the substrate. In the case of photoheterotrophic growth on acetate alone, the oxidation of some acetate can provide the necessary reducing power to assimilate the remaining acetate, ultimately contributing to the observed suboptimal efficiency (88%) of acetate assimilation. In the case of NTA breakdown products, however, some of the reducing power available from the oxidation of Fe(II) might be required to fully benefit from these carbon sources (hypothesized pathway, Figure 3.2). If this were the case, the observed phototrophic growth on Fe(II)-NTA would be truly obligate photomixotrophy. This possibility cannot be fully resolved here, but provides a testable hypothesis for further research. Detailed metabolic flux experiments could help elucidate the interdependence of these pathways and explore the role Fe(II) oxidation might play in the assimilation of refractory organic carbon sources. Analogously, the ambiguous function of Fe(II) oxidation in anaerobic chemotrophic Fe(II) oxidizers (Kappler et al., 2005a) might similarly be explained by considering Fe(II) oxidation as an auxiliary mechanism for redox balancing during the assimilation of organic carbon.

3.4 Conclusion

The existence of mixotrophic growth itself is not surprising, and has previously been suggested to occur both in phototrophic (Widdel et al., 1993) and chemotrophic (Hallbeck and Pedersen, 1991) Fe(II) metabolisms. However, its significance is rarely appreciated despite its likely importance in nature. Our results show that an organism not previously considered capable of growing by Fe(II) oxidation, in fact originally thought incapable of oxidizing Fe(II) altogether, can use Fe(II) for growth under certain conditions. The ability to grow photomixotrophically on Fe(II) might be more widespread than previously assumed, even for cultured organisms that have simply not been exposed to conditions that allow this mode of growth to be observed in the laboratory. It will be interesting to learn whether mixotrophic growth accounts for a significant proportion of cellular Fe(II)

oxidation activity by different types of Fe(II) oxidizing organisms. Future research into the different enzymatic pathways of Fe(II) oxidation and a more detailed understanding of their regulation could permit a more accurate assessment of how widespread and environmentally significant microbial Fe(II) oxidation is today and has been throughout Earth's history.

Acknowledgements

We thank Alexandre Poulain for teaching S.K. how to work with *R. capsulatus*, and Alexa Price-Whelan and other members of the Newman Lab for stimulating discussions. Three anonymous reviewers are gratefully acknowledged for constructive criticism. This work was supported by grants to D.K.N. from the National Science Foundation (grant MCB-0616323) and the Howard Hughes Medical Institute. D.K.N. is an Investigator of the Howard Hughes Medical Institute.

3.5 References

Andrianirinaharivelo, S. L., Pilichowski, J. F., Bolte, M., 1993. Nitrilotriacetic acid transformation photo-induced by complexation with iron(III) in aqueous solution. Transition Metal Chemistry 18 (1), 37–41.

Bauer, C., Elsen, S., Swem, L., Swem, D., Masuda, S., 2003. Redox and light regulation of gene expression in photosynthetic prokaryotes. Philosophical Transactions Of The Royal Society Of London Series B-Biological Sciences 358 (1429), 147–153.

Blasco, R., Cardenas, J., Castillo, F., 1989. Acetate metabolism in purple non-sulfur bacteria. FEMS Microbiology Letters 58 (2-3), 129–132.

Bunescu, A., Besse-Hoggan, P., Sancelme, M., Mailhot, G., Delort, A.-M., 2008. Fate of the nitrilotriacetic Acid-Fe(III) complex during photodegradation and biodegradation by Rhodococcus rhodochrous. Applied and Environmental Microbiology 74 (20), 6320–6326.

Caiazza, N. C., Lies, D. P., Newman, D. K., Oct. 2007. Phototrophic Fe(II) oxidation promotes organic carbon acquisition by Rhodobacter capsulatus SB1003. Applied and Environmental Microbiology 73 (19), 6150–6158.

Chistoserdova, L., Chen, S., Lapidus, A., Lidstrom, M., 2003. Methylotrophy in Methylobacterium extorquens AM1 from a genomic point of view. Journal of Bacteriology 185 (10), 2980–2987.

Croal, L. R., Jiao, Y., Newman, D. K., 2007. The fox operon from Rhodobacter strain SW2 promotes phototrophic fe(II) oxidation in Rhodobacter capsulatus SB1003. Journal of Bacteriology 189 (5), 1774–1782.

Dobbin, P., Warren, L., Cook, N., McEwan, A. G., Powell, A., Richardson, D. J., 1996. Dissimilatory iron(III) reduction by Rhodobacter capsulatus. Microbiology-Uk 142, 765–774.

Dorffler, M., Steindorf, A., Oelze, J., 1998. Determination of C/N ratios required for de-repression of nitrogenase in Rhodobacter capsulatus. Zeitschrift Fur Naturforschung C-A Journal Of Biosciences 53 (11-12), 961–967.

Ehrenreich, A., Widdel, F., Nov. 1994. Anaerobic oxidation of ferrous iron by purple bacteria, a new type of phototrophic metabolism. Applied and Environmental Microbiology 60 (12), 4517–4526.

Ehrlich, H. L., Newman, D. K., Dec. 2008. Geomicrobiology, Fifth Edition. CRC Press.

Filatova, L., Berg, I., Krasil'nikova, E., Tsygankov, A., Laurinavichene, T., Ivanovsky, R., 2005. A study of the mechanism of acetate assimilation in purple nonsulfur bacteria lacking the glyoxylate shunt: Acetate assimilation in Rhodobacter sphaeroides. Microbiology 74 (3), 265–269.

Hallbeck, L., Pedersen, K., 1991. Autotrophic and mixotrophic growth of *Gallionella ferruginea*. Journal of General MIcrobiology 137, 2657–2661.

Hillmer, P., Gest, H., 1977. H_2 Metabolism in the Photosynthetic Bacterium *Rhodopseudomonas capsulata:* Production and Utilization of H_2 by Resting Cells. Journal of Bacteriology 129 (2), 724–731.

Kappler, A., Pasquero, C., Konhauser, K., Newman, D. K., 2005a. Deposition of banded iron formations by anoxygenic phototrophic Fe(II)-oxidizing bacteria. Geology 33 (11), 865–868.

Kappler, A., Straub, K., 2005. Geomicrobiological cycling of iron. Geochemistry Of Non-Traditional Stable Isotopes 59, 85–108.

Kopf, S., Newman, D. K., Dec. 2011. Photomixotrophic growth of Rhodobacter capsulatus SB1003 on ferrous iron. Geobiology, no–no.

Larson, R. A., Stabler, P. P., 1978. Sensitized photooxidation of nitrilotriacetic and iminodiacetic acids. Journal Of Environmental Science And Health Part A-Environmental Science And Engineering & Toxic And Hazardous Substance Control 13 (8), 545–552.

Mckinlay, J. B., Harwood, C. S., Jun. 2010. Inaugural Article: Carbon dioxide fixation as a central redox cofactor recycling mechanism in bacteria. Proceedings of the National Academy of Sciences 107 (26), 11669–11675.

Mckinlay, J. B., Harwood, C. S., Mar. 2011. Calvin cycle flux, pathway constraints, and substrate oxidation state together determine the H_2biofuel yield in photoheterotrophic bacteria. mBio 2 (2), e00323–10–e00323–10.

Meister, M., Saum, S., Alber, B., Fuchs, G., 2005. L-malyl-coenzyme A/beta-methylmalyl-coenzyme A lyase is involved in acetate assimilation of the isocitrate lyase-negative bacterium Rhodobacter capsulatus. Journal of Bacteriology 187 (4), 1415–1425.

Poulain, A. J., Newman, D. K., Nov. 2009. Rhodobacter capsulatus catalyzes light-dependent Fe(II) oxidation under anaerobic conditions as a potential detoxification mechanism. Applied and Environmental Microbiology 75 (21), 6639–6646.

Richardson, D. J., King, G. F., Kelly, D. J., McEwan, A. G., Ferguson, S. J., Jackson, J. B., 1988. The role of auxiliary oxidants in maintaining redox balance during phototrophic growth of *Rhodobacter capsulatus* on propionate or butyrate. Archives Of Microbiology 150 (2), 131–137.

Stolzberg, R., Hume, D., 1975. Rapid formation of iminodiacetate from photochemical degradation of Fe(III) nitrilotriacetate solutions. Environmental Science & Technology 9 (7), 654–656.

Stookey, L. L., 1970. Ferrozine - a new spectrophotometric reagent for iron. Analytical Chemistry 42 (7), 779–781.

Tabita, F., 2004. Research on carbon dioxide fixation in photosynthetic microorganisms (1971-present). Photosynthesis Research 80 (1-3), 315–332.

Tichi, M., Tabita, F., 2000. Maintenance and control of redox poise in Rhodobacter capsulatus strains deficient in the Calvin-Benson-Bassham pathway. Archives Of Microbiology 174 (5), 322–333.

Tichi, M., Tabita, F., 2001. Interactive control of Rhodobacter capsulatus redox-balancing systems during phototrophic metabolism. Journal of Bacteriology 183 (21), 6344–6354.

Trott, T., Henwood, R., Langford, C., 1972. Sunlight photochemistry of ferric nitrilotriacetate complexes. Environmental Science & Technology 6 (4), 367–&.

Widdel, F., Schnell, S., Heising, S., Ehrenreich, A., Assmus, B., Schink, B., Apr. 1993. Ferrous iron oxidation by anoxygenic phototrophic bacteria. , Published online: 29 April 1993; | doi:10.1038/362834a0 362 (6423), 834–836.

Willison, J. C., 1998. Pyruvate and acetate metabolism in the photosynthetic bacterium rhodobacter capsulatus. Journal of General MIcrobiology 134, 2429–2439.

Chapter 4

Ligand-enhanced abiotic iron oxidation and the effects of chemical versus biological iron cycling in anoxic environments[1]

Abstract

This study introduces a newly isolated, genetically tractable bacterium (*Pseudogulbenkiania* sp. strain MAI-1) and explores the extent to which its nitrate-dependent iron-oxidation activity is directly biologically catalyzed. Specifically, we focused on the role of iron chelating ligands in promoting chemical oxidation of Fe(II) by nitrite under anoxic conditions. Strong organic ligands such as nitrilotriacetate and citrate can substantially enhance chemical oxidation of Fe(II) by nitrite at circumneutral pH. We show that strain MAI-1 exhibits unambiguous biological Fe(II) oxidation despite a significant contribu-

[1] Kopf et al. (2013), © American Chemical Society

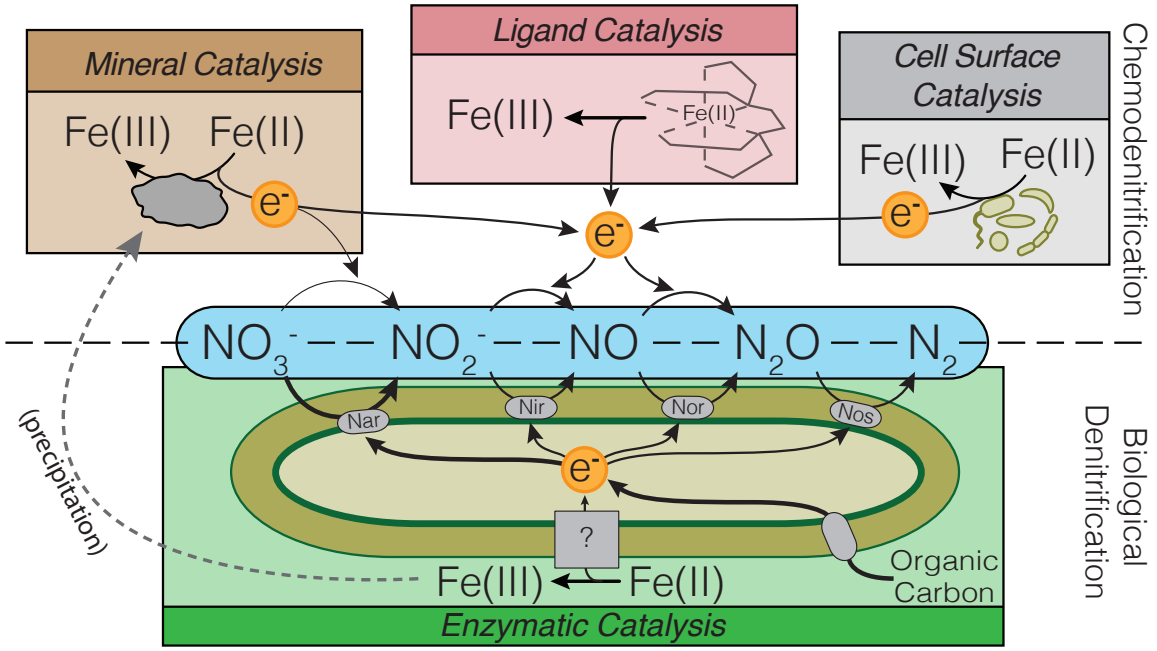

tion (≈30–35%) from ligand-enhanced chemical oxidation. Our work with the model denitrifying strain *Paracoccus denitrificans* further shows that ligand-enhanced chemical oxidation of Fe(II) by microbially produced nitrite can be an important general side effect of biological denitrification. Our assessment of reaction rates derived from literature reports of anaerobic Fe(II) oxidation, both chemical and biological, highlights the potential competition and likely co-occurrence of chemical Fe(II) oxidation (mediated by microbial production of nitrite) and truly biological Fe(II) oxidation.

4.1 Introduction

Fe(II)/Fe(III) is an important redox couple in natural environments (Stumm and J Morgan, 1996). In anoxic systems, iron oxidation can be mediated by several biological agents, such as anoxygenic phototrophs (Ehrenreich and Widdel, 1994; Jiao et al., 2005) and nitrate-dependent chemotrophs (Straub et al., 1996b; Hafenbradl et al., 1996). While the enzymatic machinery for Fe(II) oxidation has been identified and characterized for two anoxygenic phototrophs (Jiao et al., 2005; Croal et al., 2007; Newman et al., 2012)

comparable catalysts have not yet been identified for nitrate-dependent chemotrophs. Towards this end, we isolated a fast growing Fe(II) oxidizing, nitrate-dependent chemotroph from the iron-rich tropical Lake Matano (Crowe et al., 2008b), with the intention of developing it into a model genetic system. However, work with the isolate highlighted a second, often overlooked aspect of Fe(II) oxidation in anoxic environments: direct chemical interaction with nitrite (a form of chemodenitrification (Tiedje, 1988)). Being able to distinguish the mechanisms and turnover rates of direct biological versus abiotic components of anaerobic Fe(II) oxidation is necessary to gain a complete understanding of the biogeochemical coupling of the N and Fe redox cycles. Here, we expand our understanding of chemodenitrification by experimental elucidation of how organic ligands promote abiotic Fe(II) oxidation by nitrite, and discuss its relevance to assessing the potential co-occurrence of chemical and biological Fe(II) oxidation.

The isolation and characterization of an increasing number of microorganisms capable of nitrate-dependent anaerobic Fe(II) oxidation in recent years (Straub et al., 1996b; Hafenbradl et al., 1996; Straub et al., 2004; Coates et al., 2001; Kuenen et al., 2006; Benz et al., 1998; Kappler et al., 2005b; Weber et al., 2006b; Edwards et al., 2003) has revealed the potential for chemotrophic recycling of Fe(II) in anoxic systems. However, deconvolving the chemical and biological aspects of this process remains challenging in many environmental settings (Komatsu et al., 1978; Matocha and Coyne, 2007) and even laboratory studies (Brons et al., 1991; Shelobolina et al., 2003). The complication arises whenever denitrifying organisms reduce nitrate in iron-rich anoxic systems, where the metabolic intermediate nitrite can oxidize Fe(II) (Cooper et al., 2003; Coby and Picardal, 2005; Miot et al., 2009; Chakraborty et al., 2011; Carlson et al., 2012; Pantke et al., 2012). This was recently highlighted in a review by Picardal (Picardal, 2012), which underscored that while biologically induced (through the production of nitrite during biological denitrification), Fe(II) oxidation can be abiotically catalyzed and proceed by chemodenitrification. Because Fe(II) oxidation may also be directly catalyzed by

(potentially the same) denitrifying organisms, two competing pathways exist whose precise mechanisms and relative importance in nature are poorly understood. While the physiology of nitrate-dependent Fe(II)-oxidizing bacteria has been the subject of a growing number of studies (Weber et al., 2006a; Chakraborty et al., 2011; Weber et al., 2009; Blothe and Roden, 2009; Muehe et al., 2009), the chemical aspect of anaerobic Fe(II) oxidation by nitrite has received less attention (Picardal, 2012; Weber et al., 2001), despite its relevance to constraining the extent of its microbial counterpart.

Rapid oxidation of ferrous iron (Fe(II)) by nitrite in strongly acidic conditions was described as early as 1936 (Abel et al., 1936), with high reaction rates linked to the generation and subsequent degradation of nitrous acid (pKa = 3.4). At circumneutral pH, nitrite is stable, and anaerobic Fe(II) oxidation requires a catalyst or suitable Fe(II)-containing mineral to proceed at appreciable rates. Acceleration of this process has been reported with a number of specific Fe(II) mineral phases and catalysts, such as Cu^{2+} (Moraghan and Buresh, 1977), iron oxides and hydroxides (Weber et al., 2001; Van Cleemput and Baert, 1983; Van Cleemput and Samater, 1996a; Sørensen and Thorling, 1991; Tai and Dempsey, 2009), green rust (Pantke et al., 2012; Hansen et al., 1994), as well as siderite (Rakshit et al., 2008) and vivianite (Miot et al., 2009), and even microbial surfaces (Coby and Picardal, 2005), providing possible reaction mechanisms for Fe(II)-oxidizing chemodenitrification. The same is true for nitrate, which is generally less reactive towards Fe(II) than nitrite at circumneutral pH (Moraghan and Buresh, 1977), but can similarly benefit from metal and mineral catalysis (Ottley et al., 1997; Sorensen et al., 1996). However, metals and surfaces are not the only agents for chemical catalysis. While the kinetic effects of ligands (including EDTA, NTA and citrate) on iron redox processes in oxic environments have been explored before (Theis and Singer, 1974; Pham and Waite, 2008; Demmink and Beenackers, 1997; Zang et al., 1988) and often lead to acceleration of Fe(II) oxidation, much less is known about their effects in the absence of molecular oxygen. Several studies have investigated the effect of ligands on iron redox processes

in acidic conditions and solvents (Zang and van Eldik, 1990; Fanning, 1991), but with the notable exception of studies on microbial Fe(II) oxidation in the presence of EDTA (Kuenen et al., 2006; Chakraborty and Picardal, 2013), little is known about the impact of ligands at circumneutral pH.

Here, we investigate the effect of several Fe(II)-chelating ligands on iron-oxidizing chemodenitrification to 1) assess true biological Fe(II) oxidation in the newly isolated β-proteobacterium *Pseudogulbenkiania* sp. strain MAI-1, and 2) elucidate the role ligands could play more generally in abiotic Fe(II) oxidation in laboratory and environmental settings. We use *Paracoccus denitrificans* as a model strain to show how Fe(II) oxidation can appear to be directly biologically catalyzed when, in fact, much of this activity may only be indirectly biologically mediated. We describe the kinetics and potential reaction mechanism of the chemical oxidation of Fe(II) by nitrite observed in these experiments, and discuss their relevance for the interpretation of laboratory and environmental studies. We place our findings in the context of chemical and biological oxidation rates reported in the literature to evaluate their relative importance in anaerobic Fe(II) oxidation.

4.2 Materials and methods

4.2.1 Media

All reagent solutions were autoclaved or filter-sterilized prior to use. The basal medium for all experiments was a freshwater medium containing 500mg/L $MgSO_4 \cdot 7H_2O$, 300mg/L NH_4Cl, 100mg/L $CaCl_2 \cdot 2H_2O$ and 5.4mg/L $KH_2PO_4 \cdot 2H_2O$. For microbial cultures, the medium was amended with a 1000x vitamin mix (final concentrations in the medium: 40µg/L 4-aminobenzoic acid, 10µg/L D-biotin, 100µg/L nicotinic acid, 50µg/L Ca pantothenate, 100µg/L pyridoxamine·2HCl, 100µg/L thiamine·2Cl) and a 1000x trace element solution (final concentrations in the medium: 1.1mg/L $FeSO_4 \cdot 7H_2O$, 42µg/L $ZnCl_2$, 50µg/L $MnCl_2 \cdot 4H_2O$, 190µg/L $CoCl_2 \cdot 6H_2O$, 2µg/L $CuCl_2 \cdot 2H_2O$, 24µg/L $NiCl_2 \cdot 6H_2O$,

18µg/L $Na_2MoO_4{\cdot}2H_2O$, 300µg/L H_3BO_3)(Newman et al., 2004). For aerobic cultures, the medium was buffered to pH 7.2 with 20mM phosphate. For anoxic experiments, the medium was pH buffered with 22mM $NaHCO_3$ and adjusted to pH 7 with 1M HCl under an oxygen-free atmosphere containing 15% CO_2. Phosphate addition was minimal (but not microbially growth inhibiting) to avoid precipitation of vivianite ($Fe_3(PO_4)_2{\cdot}8H_2O$) at high Fe(II) concentrations. The final ionic strength was ~0.04M. Anoxic solutions were prepared using O_2-free deionized water and stored anoxically for at least three days prior to use. Reactant solutions containing nitrite were always prepared fresh from an anoxic stock solution kept at pH 11 to avoid degradation through self-decomposition. All glassware and plastics were autoclaved and stored anoxically for at least three days prior to use.

4.2.2 Bacterial strains

Paracoccus denitrificans strain ATCC 19367 was obtained from the United States Department of Agriculture culture collection, and was grown routinely in anoxic freshwater medium under denitrifying conditions with succinate as the growth substrate. *Pseudogulbenkiania* sp. strain MAI-1 is a newly isolated β-proteobacterium that was routinely grown in anoxic freshwater medium under denitrifying conditions with acetate as the growth substrate.

4.2.3 Isolation

Cultures of anaerobic Fe(II) oxidizing chemotrophs were enriched by inoculating freshwater medium supplemented with 10mM $FeCl_2$, 10mM Na_3NTA, 2mM Na Acetate and 5mM $NaNO_3$ with samples from a microbial mat in the litterol zone of iron-rich tropical Lake Matano, Sulawesi Island, Indonesia. Enrichments were incubated at 30ºC in the dark. After a few days, some enrichments developed the characteristic dark green color of Fe(III)-NTA, indicating Fe(II) oxidation. Cultures exhibiting fast Fe(II) oxidation were transferred successively to fresh Fe(II)-containing medium. After four transfers, serial

dilutions of enrichments were plated on YP agar pates (0.3% yeast extract, 0.3% Difco Bacto Peptone, 1.2% agarose) and incubated aerobically at 30ºC in the dark to identify strains potentially suitable for genetic manipulation. Colonies were picked and subcultured in the Fe(II) enrichment medium. Fast Fe(II) oxidizers were plated again and the purity was assessed by phase-contrast microscopy. The 1497-bp 16S rRNA gene sequence of strain MAI-1 was deposited in the GenBank database under the accession number HQ714499. The pure strain was deposited with the American Type Culture Collection under the ATCC number BAA-2177.

4.2.4 Analytical techniques

The concentration of Fe(II) was determined colorimetrically at 562nm using the ferrozine [3-(2-pyridyl)-5,6 bis(4-phenylsulfonic acid)-1,2,4-triazine, monosodium salt] assay (Stookey, 1970) without prior acidification of analyte. Sample acidification in the presence of nitrite led to underestimation of Fe(II) concentrations(Weber et al., 2001), and was therefore avoided (see supplementary Figure C.4). The assay was calibrated using ferrous ammonium sulfate hexahydrate of known concentration. Nitrite was determined colorimetrically at 520nm using sulfanilamide and N-1-napthylethylenediamine dihydrochloride (Promega, 2009). The chelator EDTA is incompatible with this assay (Colman, 2009), but none of the ligands used in this study interfere with nitrite determination (Figure C.5). The assay was calibrated using a commercial nitrite standard (Fluka Analytical TraceCERT). Samples for Fe(II) and nitrite determination in microbial cultures were obtained with a sterile disposable syringe flushed for 30 seconds with 20%CO_2/80%N_2. The evolution of N_2O in abiotic reactions was assessed qualitatively by gas-chromatography using a Hewlett Packard 5890 Series II Plus Gas Chromatograph equipped with a Thermal Conductivity Detector. Samples were injected onto a HP-MOLSIV column (30m, 0.32mm ID, 12µm film) and eluted with helium at a flow rate of 10mL/min using a temperature gradient from 35ºC to 240ºC (4min at 35ºC, 35ºC/min up to 140ºC, 25ºC/min up to 240ºC).

Formation of the nitrosyliron-NTA complex (Fe(II)-NTA-NO) was assessed qualitatively by monitoring its characteristic absorption peaks (440nm and 600nm) (Lin et al., 1982; Schneppensieper et al., 2002) spectroscopically. Growth of microbial cultures was followed by optical density at 600nm (OD600) in cultures without iron, and at 700nm (OD700) in cultures with iron. This wavelength was used to decrease distortion by Fe(III)-NTA, which absorbs strongly at 600 nm. OD700 underestimates optical density as compared to OD600.

4.2.5 Experimental procedure

Kinetic Fe(II) oxidation experiments were conducted inside an anaerobic chamber (Coy Laboratory Products, Inc.) equipped with palladium catalysts for O2 removal. The chamber contained ~3%H_2/15% CO_2/82% N_2, and experiments were performed at 25ºC using a digital heat block. Samples were taken at varying time points and analyzed immediately for Fe(II) and nitrite concentrations using a BioTek Synergy 4 Microplate Reader housed inside the chamber. Oxidation experiments were conducted in sterile basal freshwater medium containing 2mM Fe(II) and 2mM NO_2^-, and were amended alternatively with 2mM nitrilotriacetate (NTA), 300mg/L Pahokee Peat Humic Acid (PPHA, International Humic Substances Society), 0.1, 0.5 or 2mM citrate, 300mg/L PPHA + 2mM citrate. PPHA was selected as the humic acid of choice due to its high solubility and low capacity for storing redox equivalents that could re-reduce Fe(III) and interfere with the experiment (Bauer and Kappler, 2009). Control experiments included incubations of Fe(II) with or without NTA in the absence of nitrite or in the presence of 2mM nitrate. pH was measured at the beginning and conclusion of each experiment.

Pseudogulbenkiania sp. strain MAI was grown in triplicate at 30ºC in the dark in freshwater medium amended with 0.5mM acetate, 4mM Fe(II) and 8mM NTA, and a headspace of ~3%H_2/15% CO_2/82% N_2. Cultures were sampled regularly for nitrite accumulation and Fe(II) oxidation.

Paracoccus denitrificans was grown in triplicate at 30ºC in the dark in freshwater medium amended with 10mM succinate and 20mM nitrate, and sampled regularly for nitrite accumulation. Upon reaching a nitrite concentration of ~5mM, 5 mL of each culture was withdrawn and processed anaerobically as follows: each withdrawn sample was divided into four aliquots. Two aliquots were left unchanged while the other two were filter sterilized using a 0.2µm syringe filter. All aliquots were spiked with ~5mM Fe(II) and one of each set (one unfiltered *P. denitrificans* and one filter-sterilized aliquot) was further amended with 10mM citrate (all from 1M stock solutions to avoid sample dilution). No citrate was present in cultures prior to spiking. Aliquots were incubated at 25ºC for 4 hours and sampled at regular intervals as described in the kinetic Fe(II) oxidation experiments. The remaining cultures were re-incubated at 30ºC for continued monitoring of growth and nitrite accumulation.

4.2.6 Computation

Nonlinear least-squares model fits and parameter estimates for kinetic data were computed using the statistical model analysis functionality provided by Wolfram Mathematica (v. 8.0). Fe(II) speciation in solution was estimated using the Visual MINTEQ equilibrium speciation model (v. 3.0) with stability constants provided by King (1998) (Fe(II)-carbonate complexes) and the MINTEQ database (Smith and Martell, 1998) (all other Fe(II) species), and precomputed humic substance properties based on the NICA-Donnan model (Kinniburgh et al., 1996). Chemical oxidation of Fe(II) with nitrite produced by MAI-1 was modeled using Euler's method to calculate step-wise solutions of equation 4.7. Nitrite concentrations at each time step were calculated by linear interpolation between closest measurement timepoints. Chemical oxidation with concomitant biological NO consumption was modeled by assuming complete NO removal and subsequent lack of Fe(II)-NTA-NO complex formation.

4.3 Results

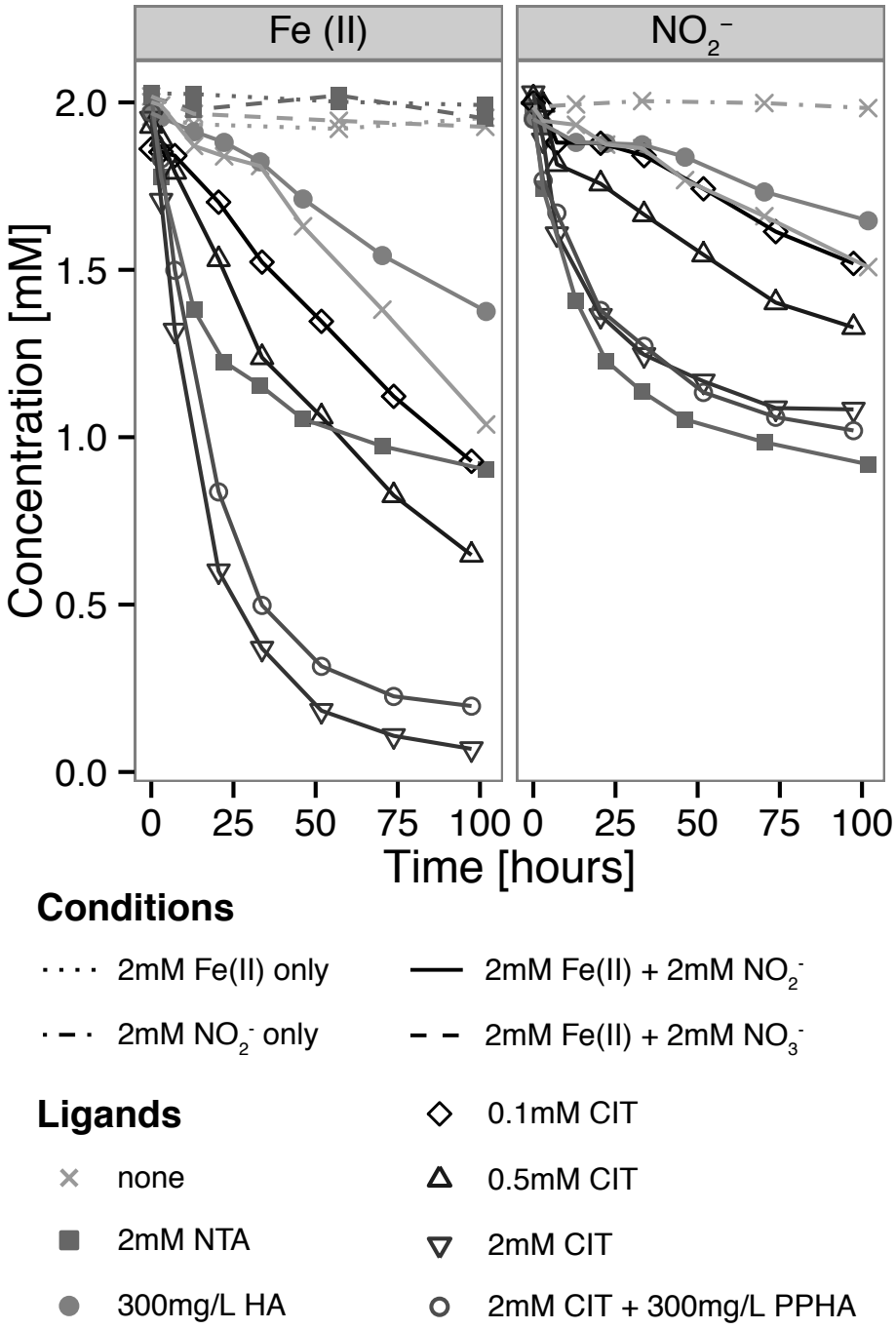

Figure 4.1 – Ligands affect the abiotic oxidation of Fe(II) by NO_2^-. Error bars omitted for clarity (relative standard deviation of Fe(II) and NO_2^- quantitation from all seven experiments estimated at 3% and 2%, respectively).

The enrichment of fast-growing anaerobic Fe(II) oxidizing chemotrophs led to the

successful isolation of *Pseudogulbenkiania* sp. strain MAI-1, a novel β-proteobacterium closely related to the lithoautotrophic Fe(II) oxidizer *Pseudogulbenkiania* sp. 2002 (Weber et al., 2006b; 2009) (96.9% 16S rRNA gene sequence similarity, 97.3% to the type strain *Pseudogulbenkiania* subflava BP-5, Lin et al., 2008). MAI-1 has several key characteristics necessary for routine genetic manipulation: the strain forms colonies on plates (aerobically within 24 hours), grows rapidly both aerobically and anaerobically (overnight at 30ºC), is sensitive to antibiotics, and cryopreserves well. Most importantly, it displays the desired phenotype: rapid nitrate-dependent Fe(II) oxidation (10mM in less than 24 hours, Figure C.1) in the presence of a chelator, nitrilotriacetate - NTA, which prevents the formation of mineral precipitates (that obscure cells in automated assays), but does not serve as a growth substrate for the organism (Figure C.2). When first isolated, MAI-1 appeared to be an ideal candidate for elucidating the genes required for nitrate-dependent Fe(II) oxidation. However, although Fe(II)-NTA is highly stable in abiotic controls in the presence of nitrate (Figure 4.1, Figure C.1), adding Fe(II)-NTA to filter-sterilized spent MAI-1 growth medium that had accumulated substantial amounts of nitrite lead to rapid Fe(II) oxidation with concomitant nitrite reduction (Figure C.3). The strain's ability to use a wide range of chelators as a carbon substrate (e.g. citrate, humic acids, DTPA) and its inability to grow and oxidize free Fe^{2+} (Figure C.1) precluded avoiding NTA. Additionally, MAI-1 cannot use alternate electron acceptors (e.g. DMSO, TMAO, fumarate), requiring the use of nitrate (and consequentially risking the production of nitrite) for anaerobic culturing.

To quantitatively assess the effect of Fe(II) chelation on chemical oxidation by nitrite at circumneutral pH, we conducted kinetic experiments with NTA as well as two environmentally relevant Fe(II)-chelating ligands (citrate - CIT, and Pahokee Peat Humic Acid - PPHA). Attempts to investigate the effect of Fe(II) chelation with the siderophore desferoxamine (DFO) and the organic pollutant ethylenediaminetetraacetate (EDTA) proved unsuccessful because of interference with the ferrozine assay and the nitrite assay, respectively (Figure C.5). They were not pursued further. Figure 4.1 shows the oxidation

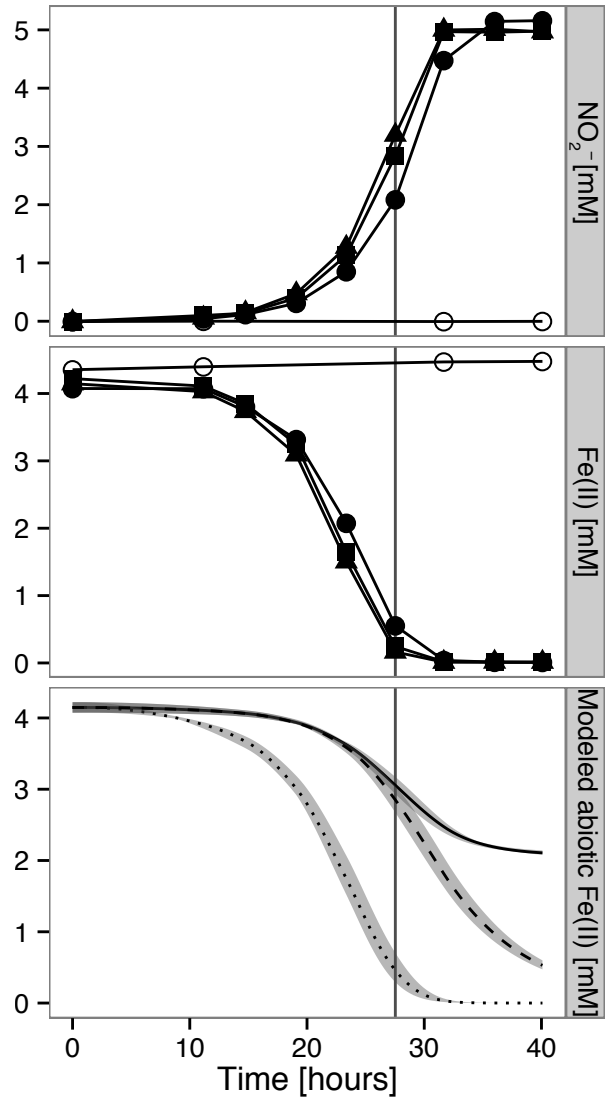

Figure 4.2 – Fe(II) oxidation by *Pseudogulbenkiania* sp. strain MAI-1 during anaerobic growth with nitrate. Nitrite accumulation during growth depicted in top panel, concomitant Fe(II) oxidation in middle panel, modeled abiotic Fe(II) oxidation in bottom panel (see Materials and Methods for details on computation). Solid and dashed lines indicate Fe(II) oxidation without/with biological NO consumption, respectively. Dotted line indicates Fe(II) oxidation with 6x higher rate constant and NO consumption. Model range for three biological replicates shaded in gray. Vertical line indicates timepoint addressed in text. Experiment conducted in biological triplicates (solid markers) and with abiotic control (empty circles - ◯). All data are shown.

of Fe(II) and concomitant reduction of NO_2^- over the course of ~100 hours (4.2 days) for each condition. Nitrite-free controls without any oxidant or amended with nitrate show little Fe(II) oxidation (a maximum of 2% without oxidant, 5% with nitrate, see Table 4.1)

	Reactant changes within ~100 hours			Fe(II) oxidation		NO_2^- reduction	
	ΔFe(II) [μM] (%‡)	**ΔNO_2^-** [μM] (%‡)	**ΔFe(II)/ΔNO_2^-** (± 1σ)#	**Model** R^2	**k_{app} (LCI;UCI*)** [10^{-3} M^{-1} s^{-1}]	**Model** R^2	**k_{app} (LCI;UCI*)** [10^{-3} M^{-1} s^{-1}]
Controls							
2mM NO_2^- only		-3 (0%)					
2mM Fe(II) only	-3 (0%)						
+ 2mM NTA	-35 (2%)						
+ 2mM NO_3^-	-91 (5%)						
+ 2mM NTA + 2mM NO_3^-	-64 (3%)						
Kinetically unresolved							
2mM Fe(II) + 2mM NO_2^-	-963 (48%)	-478 (24%)	2.0±0.3				
+ 0.1mM Citrate	-933 (50%)	-480 (24%)	1.9±0.2				
+ 300mg/L PPHA	-592 (30%)	-303 (16%)	2.0±0.4				
Second-order kinetics							
+ 0.5mM Citrate	-1281 (66%)	-686 (34%)	1.9±0.2	0.9995	0.98 (0.92;1.04)	0.9995	1.04 (0.88;1.19)
+ 2mM Citrate	-1883 (96%)	-945 (47%)	2.0±0.1	0.9979	4.67 (4.18;5.17)	0.9992	4.31 (3.57;5.06)
+ 2mM Citrate + 300mg/L PPHA	-1773 (90%)	-931 (48%)	1.9±0.1	0.9963	3.31 (2.85;3.78)	0.9997	3.59 (3.24;3.93)
+ 2mM NTA	-1119 (55%)	-1065 (54%)	1.1±0.1	0.9987	6.66 (5.19;8.13)	0.9993	6.11 (5.15;7.07)

Table 4.1 – Summary of kinetic Fe(II) oxidation experiments by nitrite. The rate constant k_{app} is reported for reactions that are described well by second-order kinetics. The experiments were conducted at 25ºC, pH 6.9 to 7.1.

The p-values for the model parameter kapp are <0.001 for all conditions. R^2 is the adjusted regression coefficient for the least-squares fit.

‡: percentage change of [Fe(II)] and [NO_2^-] relative to starting concentrations

#: derived by error propagation from measurement errors (relative standard deviation of Fe(II) and NO_2^- quantitation during experiments estimated at 3% and 2% respectively)

*: lower (LCI) and upper (UCI) 95% confidence interval of parameter derived from model fit

over the course of the experiment. This provided confidence that O_2 contamination is not a significant source of error in our experimental setup, and suggested that nitrate is relatively unreactive towards Fe(II) even in the presence of ligands (see abiotic control in Figure C.1). Nitrite in the absence of iron shows high stability, confirming the expected absence of nitrite self-decomposition that occurs at acidic pH (Van Cleemput and Baert, 1976). In the absence of any chelating moieties, less than 9% of Fe(II) is oxidized by nitrite within the first 22 hours. Similar control experiments in previous reports have yielded Fe(II) oxidation rates at ~8% Fe(II) within 10 h (Sørensen and Thorling, 1991), ~9% within 20 h (Rakshit et al., 2008), and ~1% within 24 h (Tai and Dempsey, 2009). Complexation by both citrate and NTA, however, leads to rapid depletion of Fe(II) and nitrite, indicating that these organic ligands can accelerate Fe(II) oxidation by nitrite

(Figure 4.1).

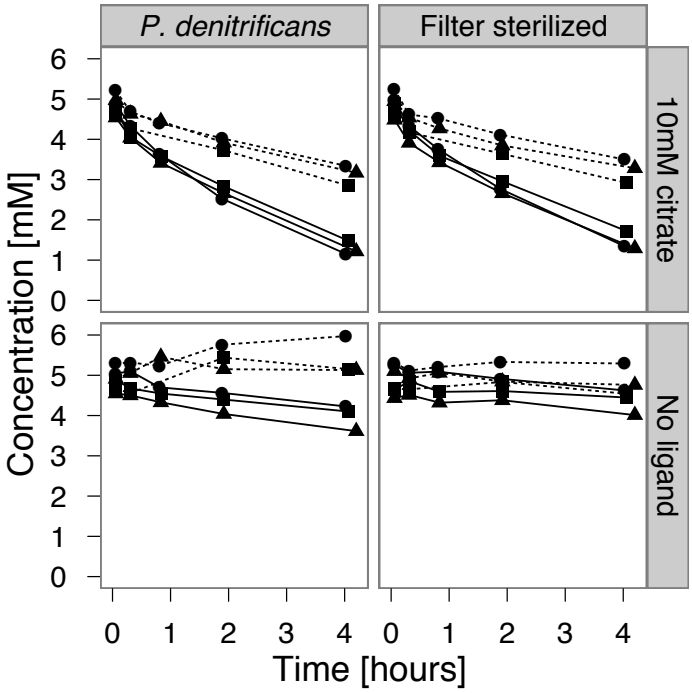

Figure 4.3 – Fe(II) oxidation in *P. denitrificans* cultures and filter-sterilized spent medium. Fe(II) concentrations shown as solid lines, NO2- concentrations as dashed lines. Samples are drawn from triplicate cultures (Figure S6) after accumulation of ~5mM NO_2^- and spiked with Fe(II) +/- citrate at 0 hours. All data are shown.

	Reactant changes within ~4 hours		Fe(II) oxidation		NO_2^- reduction	
	ΔFe(II) [mM] (%‡)	**ΔNO_2^- [mM] (%‡)**	**Model R^2**	**k_{app} (LCI;UCI*) [10^3 M^{-1} s^{-1}]**	**Model R^2**	**k_{app} (LCI;UCI*) [10^3 M^{-1} s^{-1}]**
P.denitrificans						
#1	-3.7 (76%)	-1.9 (36%)	0.9991	12 (11;14)	0.9991	11 (8;15)
#2	-3.3 (73%)	-1.8 (36%)	0.9984	11 (9;13)	0.9996	10 (8;12)
#3	-3.2 (69%)	-1.8 (38%)	0.9977	10 (7;13)	0.9985	11 (6;17)
Filter Sterilized						
#1	-3.6 (73%)	-1.8 (33%)	0.9990	11 (9;12)	0.9981	10 (6;15)
#2	-3.2 (71%)	-1.7 (34%)	0.9985	11 (9;13)	0.9995	10 (8;12)
#3	-3.2 (65%)	-1.7 (37%)	0.9983	9 (7;11)	0.9988	12 (7;17)

Table 4.2 – Summary of kinetic Fe(II) oxidation experiments by nitrite in *P. denitrificans* cultures and spent medium. The experiment was conducted at 25ºC.

P-values for the model parameter k_2 are <0.01. R^2 is the adjusted regression coefficient for the least-squares fit.

‡: percentage change of [Fe(II)] and [NO_2^-] relative to starting concentrations

#: derived by error propagation from measurement errors (relative standard deviation of Fe(II) and NO_2^- quantitation during experiments estimated at 3% and 2% respectively)

*: lower (LCI) and upper (UCI) 95% confidence interval of parameter derived from model fit

Equipped with an estimate for the extent of chemical Fe(II) oxidation by nitrite in the presence of NTA, we grew MAI-1 in the presence of Fe(II)-NTA while closely monitoring the accumulation of nitrite (Figure 4.2) to model the maximal abiotic Fe(II) oxidation resulting from an abiotic reaction with nitrite. Given the strong effect of citrate on the chemical oxidation of Fe(II) by nitrite, we also tested the hypothesis that abiotic Fe(II) oxidation could be mediated by the biological production of nitrite during denitrification in general. For this purpose, *P. denitrificans*, a model denitrifying microorganism, was grown anaerobically on succinate and nitrate, such that substantial quantities of nitrite accumulated during early exponential growth (Figure C.6). After accumulation of ~5 mM nitrite, filter-sterilized culture medium as well as active cultures of *P. denitrificans* were amended with ~5 mM Fe(II) with or without 10 mM citrate. Figure 4.3 illustrates the resulting oxidation of Fe(II) over the course of 4 hours. Moderate oxidation occurred in the absence of chelation both with *P. denitrificans* cultures as well as in spent medium (up to 21% and 12%, respectively). Higher oxidation rates for cultures are likely a consequence of continued denitrification by *P. denitrificans*, increasing the measured pool of nitrite by up to 13%. However, the most striking feature is the rapid depletion of Fe(II) and nitrite (up to 76% Fe(II), 38% NO_2^-) observed with the addition of 10mM citrate, regardless of the presence of *P. denitrificans* (Table 4.2, Figure 4.3).

4.4 Discussion

4.4.1 Reaction mechanisms and kinetics

Understanding the kinetics of Fe(II) oxidation in the presence of ligands provides the tools for predicting the potential effects of ligand-enhanced Fe(II) oxidation in microbial systems. The total consumption of Fe(II) and nitrite (Table 4.1) suggests that Fe(II) oxidation by nitrite proceeds with 2:1 Fe(II):NO2- stoichiometry regardless of complexation (no ligand, PPHA, citrate), with the notable exception of NTA, which appears to deplete Fe(II) and

NO2- in a 1:1 ratio. The 2:1 stoichiometry is in agreement with literature reports that the predominant product of nitrite reduction at pH regimes between 6 and 8 is N_2O (Coby and Picardal, 2005; Moraghan and Buresh, 1977; Sørensen and Thorling, 1991; Tai and Dempsey, 2009; Bonner and Pearsall, 1982), according to the following representative net reaction:

$$4\,Fe^{2+} + 2\,NO_2^- + 6\,H^+ \xrightarrow{k_1} 4\,Fe^{3+} + N_2O + 3\,H_2O \tag{4.1}$$

where Fe^{2+} can be unbound Fe^{2+} or a ligand-bound Fe(II)-L species, and Fe^{3+} can be ligand-bound Fe(III)-L or contained within an (oxy)hydroxide mineral (e.g., FeOOH). This net reaction likely comprises a number of elementary reaction steps; we consider the following three to contextualize our observations:

$$Fe^{2+} + NO_2^- + 2\,H^+ \xrightarrow{k_2(\text{slow})} Fe^{3+} + NO_{aq} + H_2O \tag{4.2}$$

$$Fe^{2+} + NO_{aq} \xrightarrow{k_3(\text{fast})} (Fe(II) - NO)^{2+} \tag{4.3}$$

$$(Fe(II) - NO)^{2+} + H^+ \xrightarrow{k_4(\text{fast})} Fe^{3+} + \frac{1}{2}\,N_2O + \frac{1}{2}\,H_2O \tag{4.4}$$

Reactions 4.3 (Kustin et al., 1966) and 4.4 (Pearsall and Bonner, 1982) proceed rapidly at circumneutral pH, with 4.2 being the rate limiting step ($k_1 \approx k_2$). Accordingly, the reaction consumes 2 Fe(II) for every NO_2^-, except in the case of NTA. Both citrate and NTA complexes with ferrous iron can bind nitric oxide such that the following reactions can occur in competition with reaction 4.3:

$$(Fe(II) - CIT)^- + NO_{aq} \xrightarrow{k_5} (Fe(II) - CIT - NO)^- \tag{4.5}$$

$$(Fe(II)-NTA)^- + NO_{aq} \xrightarrow{k_6} (Fe(II)-NTA-NO)^- \tag{4.6}$$

However, Fe(II)-NTA forms a considerably stronger complex with NO ($k_6 \approx 2.1 \cdot 10^7 M^{-1}s^{-1}$, $K_{eq} = 10^{6.26}$) (Lin et al., 1982; Demmink et al., 1997; Schneppensieper et al., 2001) than Fe(II)-citrate ($k_5 \approx 4.4 \cdot 10^5 M^{-1}s^{-1}$, $K_{eq} = 10^{2.83}$) (Schneppensieper et al., 2001) or Fe^{2+} alone ($k_3 \approx 6.2 \cdot 10^5 M^{-1}s^{-1}$, $K_{eq} = 10^{2.65}$) (Kustin et al., 1966), potentially preventing reaction 4.4 from proceeding. For example, if 100µM Fe(II) reacted with 100µM NO_2^- to form NO in the presence of 2mM NTA, more than 99.98% of the produced NO would form the highly stable Fe(II)-NTA-NO complex. The 1:1 stoichiometry of Fe(II) oxidation by nitrite observed in the presence of NTA is likely a consequence of this stable Fe(II)-NTA-NO complex formation. As expected, we confirmed evolution of N2O during Fe(II) oxidation by nitrite by gas chromatography in the presence of citrate, but no N_2O formed in the presence of NTA (Figure C.8); the formation of the Fe(II)-NTA-NO complex could be observed instead (Figure C.9).

Based on the rate-limiting, Fe(II) and NO_2^- dependent first reaction step (4.2), a plausible scheme for the overall reaction kinetics is a second-order rate expression with overall rate constant k_{app} in analogy with oxidation of Fe(II) and Mn(II) by O_2(King, 1998; Morgan, 2005)

$$\frac{dFe(II)}{dt} = -2\,k_{app} \cdot [Fe(II)][NO_2^-] \tag{4.7}$$

$$\frac{dNO_2^-}{dt} = -k_{app} \cdot [Fe(II)][NO_2^-] \tag{4.8}$$

where Fe(II) comprises the total pool of ferrous iron (free Fe^{2+} as well as all complexed Fe(II)). Given the equimolarity of initial total Fe(II) and NO_2^- in our experimental setup, we integrate equations 4.7 and 4.8 to yield the following decay equations (see Appendix

C for details):

$$Fe(II)(t) = \frac{Fe(II)_0}{-1 + 2 \cdot e^{Fe(II)_0 \cdot k_{app} t}} \tag{4.9}$$

$$NO_2^-(t) = \frac{NO_2^- \cdot e^{NO_2^- \cdot k_{app} t}}{-1 + 2 \cdot e^{NO_2^- \cdot k_{app} t}} \tag{4.10}$$

Least-squares fits of equations 4.9 and 4.10 to our experimental results for Fe(II) and NO_2^- depletion provide two separate estimates of the overall rate constant k_{app} for each condition (Table 4.1 & 4.2). Reactions without a ligand and with low citrate or PPHA are better described by a linear least-squares fit (apparent zero-order kinetics), and are therefore considered kinetically unresolved (no k_{app} determined). Elementary reaction steps and kinetic constraints for these conditions cannot be deduced from our observations, and it remains unclear why the reactions appear to be zero-order. Oxidation in these conditions likely proceeds as a consequence of ferric (oxy)hydroxide precipitation (observed visually) and subsequent heterogeneous autocatalysis as reported by Tai and Dempsey (2009). Apparent zero-order kinetics could reflect the complex balance between the generation of catalytic mineral surfaces and depletion of dissolved Fe(II) and nitrite.

At higher concentrations of citrate and NTA, the reactions remained homogenous, and are in agreement with a second-order kinetic interpretation of our data (Table 4.1 & 4.2 and Figure C.7). Rate constants derived from Fe(II) oxidation and nitrite reduction agree well within their 95% confidence intervals, lending further credence to the model. The pH remained close to 7.0 in all conditions, with an average change of 0.1 by the end of the experiment (Table S1), suggesting that the presence of the ligands, rather than fluctuations in pH, are responsible for the observed differences in reaction kinetics. The reaction progression observed in the presence of PPHA suggests that chelation of Fe(II) by the humic acid moieties (10% of the initial Fe(II) pool is organically complexed) has little to no effect on the kinetics of iron oxidation (see Figure 4.1, PPHA & CIT + PPHA).

Rather than accelerating Fe(II) oxidation, PPHA appears to have a slight retarding effect. In contrast to experiments without a ligand, PPHA is likely to impede iron oxide formation and autocatalysis as a result of its high affinity for Fe(III). In combination with citrate, PPHA leads to diminished formation of the Fe(II)-citrate complex (Table C.2), which appears to reduce the overall reaction rate (Table C.1).

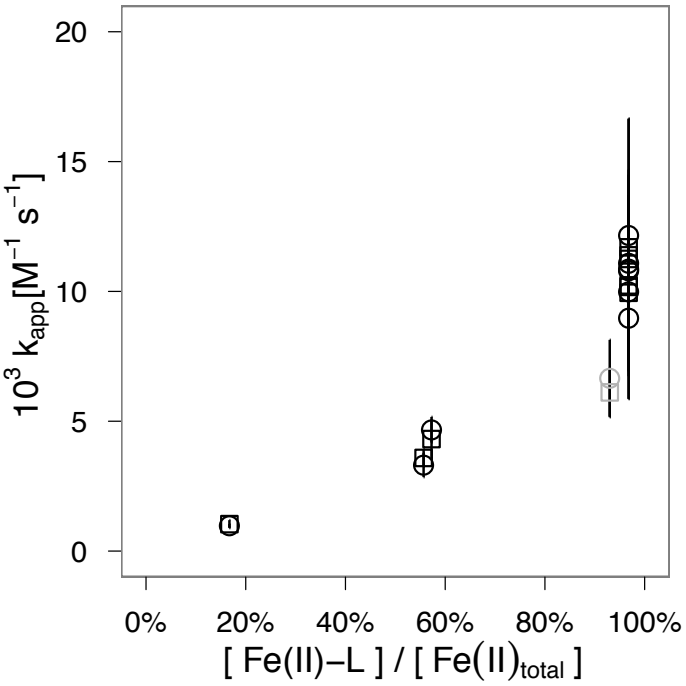

Figure 4.4 – Rate constants increase with increasing degree of Fe(II) complexation. Second-order rate constants for oxidation experiments in the presence of citrate (black symbols) and NTA (grey symbols) are plotted against the degree of Fe(II) complexation by citrate/NTA. Rate constants derived from [Fe(II)] depicted as circles (◯), constants derived from [NO_2^-] as squares (□). Error bars indicate 95% confidence intervals (Table 4.1 & 4.2). Details on speciation can be found in Table S1. Larger confidence intervals for data reported in Table 4.2 are a consequence of reduced temporal resolution and greater deviation from the assumption that initial Fe(II) and NO_2^- concentrations are equimolar.

Additional information for predicting the contribution of chemical Fe(II) oxidation, especially in well-defined laboratory systems, can be gained from identifying the reactive species. In analogy to Fe(II) and Mn(II) oxidation by O_2, the overall rate constant k_{app} observed in our experiments can likely be explained in terms of the weighted sum of the oxidation rates of individual Fe(II) species (King, 1998; Morgan, 2005) $k_{app} = \sum k_i \alpha_i$,

where α_i is the fraction of each Fe(II) species in solution, and k_i the species-specific second-order rate constant for oxidation by nitrite. A comparison of k_{app} with the extent of Fe(II) complexation for each experimental condition (Figure 4.4, Table C.2) suggests that the Fe(II)-L complex is involved in accelerating Fe(II) oxidation, although the effect is ligand-specific (no effect for PPHA, variable magnitude for citrate and NTA). The observed reaction rates at low species fractions of Fe(II)-L (< 20%) suggest the existence of other Fe(II) species with appreciable nitrite-dependent oxidation rates. We speculate that the carbonate species Fe(II)-CO_3-OH- and Fe(II)-$(CO_3)_2^{2-}$ (Table S2) could provide such reactive species in analogy to their role in Fe(II) oxidation by molecular oxygen (King, 1998). However, the precise mechanism and species-specific reaction rates k_i for the observed oxidation of Fe(II) by nitrite are beyond the scope of this report, and await further study. Due to the uncertainty surrounding the reactive species involved, we recommend caution in applying the rate constants derived in Table 4.1 and 4.2 to aqueous environments with widely differing Fe(II) complexation, pH or ionic strength.

4.4.2 Biological Fe(II) oxidation by *Pseudogulbenkiania* sp. strain MAI-1

Using the kinetic rate constants derived for the oxidation of Fe(II) by nitrite in the presence of NTA with the nitrite accumulation measured in culture of MAI-1 (Figure 4.2), we modeled the purely abiotic Fe(II) oxidation that would result from the interaction of Fe(II) with the accumulated nitrite (Figure 4.2, bottom), assuming the presence of cell surfaces (Coby and Picardal, 2005) to have negligible effects on purely chemical oxidation. Even if we conservatively assume the upper 95% confidence interval for the rate constant ($8.13\,M^{-1}\,s^{-1}$), see Table 4.1) and that produced NO is biologically consumed (thus leaving more Fe(II) free to react by preventing formation of the highly stable Fe(II)-NTA-NO complex), abiotic oxidation would maximally account for ~30%/35% (solid vs. dashed curve) of the observed Fe(II) oxidation after 28 hours (timepoint indicated by

vertical line in Figure 4.2). In fact, a six-times-higher rate constant (combined with biological consumption of any produced NO) would be required to attribute observed Fe(II) oxidation to purely chemical processes (Figure 4.2, dotted model). Based on the kinetic quantification of chemical oxidation of Fe(II), it thus becomes evident that *Pseudogulbenkiania* sp. MAI-1 can directly oxidize Fe(II), establishing the organism as a novel neutrophilic nitrate-dependent chemotroph with unambiguous biological Fe(II)-oxidizing activity. The potential to easily genetically manipulate this strain makes it a good candidate for elucidating the machinery involved in biological Fe(II) oxidation. Whether the biological component of Fe(II) oxidation in MAI-1 occurs via a dedicated enzyme system or via non-specific reactions with redox active components of the cell, such as periplasmic thiols or components of the electron transport chain (Pantke et al., 2012; Carlson et al., 2012), is a question that could be addressed in the future.

4.4.3 Chemical vs biological Fe(II) oxidation in laboratory and environmental studies

Given the aforementioned difficulty in discriminating between chemical and biological contributions to anaerobic Fe(II) oxidation in many systems, it can be informative to compare Fe(II) oxidation rates observed in a variety of environmental and laboratory settings. Table 4.3 provides an overview of the maximal Fe(II) oxidation rates reported in a number of publications on chemical and biological Fe(II) oxidation in nitrite/nitrate-rich anoxic environments at circumneutral pH. Several observations are particularly noteworthy:

1. The majority of observed maximal rates of chemical and biological Fe(II) oxidation fall within a similar range of values (~10-100μM/hr), highlighting the likely competition and co-occurrence of chemical and biological processes involved in the coupled biogeochemical cycling of iron and nitrogen. Moreover, because nitrite is produced and often accumulates during the microbial denitrification process, they

	Experimental conditions					Maximal rates	Source
	pH	**buffer**	**Fe(II)**	**Nitrite**	**Nitrate**	**ΔFe(II) [μM/hr]**	**Reference**
Chemical (abiotic)							
+30mg/L lepidocrocite (gamma-FeOOH)	7.5	auto-titration	0.2mM	0.2mM		-7	[1], Fig. 5
+30mg/L lepidocrocite (gamma-FeOOH)	8.5	auto-titration	0.2mM	0.2mM		-40	[1], Fig. 5
Fe(II) as siderite (10g/L ~ 80mM)	6	MES/PIPES/ HEPES	10g/L	4.6mM		-265	[2], Fig. 5
Fe(II) as siderite (10g/L ~ 80mM)	6.5	MES/PIPES/ HEPES	10g/L	4.6mM		-169	[2], Fig. 5
Fe(II) as siderite (10g/L ~ 80mM)	7.9	MES/PIPES/ HEPES	10g/L	4.6mM		-140	[2], Fig. 5
+2.5mM Fe(II) as HFO, 64μM average solid-bound Fe(II)	6.8	PIPES	0.38mM	0.38mM		-158	[3], Table 1, #6
+17.5mM Fe(III) as HFO, 188μM average solid-bound Fe(II)	6.8	PIPES	0.34mM	0.32mM		-301	[3], Table 1, #11
F(II) as green rust	8.25	auto-titration	10.81mM		14.2mM	-139	[4], Table 1
+2mM NTA	7	bicarbonate	2mM	2mM		-192	This study, Table 1
+2mM CIT	7	bicarbonate	2mM	2mM		-134	This study, Table 1
+10mM CIT, *P. denitrificans* spent medium	7	bicarbonate	5mM	5mM		-1695	This study, Table 2
+10mM CIT, *P. denitrificans* culture	7	bicarbonate	5mM	5mM		-1910	This study, Table 2
Mixed (chemical + biological)							
D. frappieri strain G, Fe(II) complexed by 10mM NTA	~7	bicarbonate	4.8mM	1.4mM	2.5mM	-294	[5], Fig. 5
D. frappieri strain G, Fe(II) as smectite	~7	bicarbonate	3mM	1.4mM	5mM	-175	[5], Fig. 6
Pseudogulbenkiania sp. MAI-1, Fe(II)-NTA	7	bicarbonate	4mM	5mM	10mM	-360	This study, Figure 2
Chemotrophic							
Enrichment culture, +1mM acetate	7	bicarbonate	10mM	?	3mM	-106	[6], Fig. 1
Enrichment culture containing *Sideroxydans* species	6.8	bicarbonate	10mM	?	4mM	-156	[7], Fig. 1a
Pseudogulbenkiania strain 2002	6.8	bicarbonate	10mM	?	2.2mM	-74	[8], Fig. 4
Strain HidR2, +1mM acetate	6.7	bicarbonate	6mM	<30μM	5mM	-66	[9], Fig. 2
Ferroglobus placidus, 85C	7	bicarbonate	2mM	up to 550μM	0.64mM	-173	[10], Fig. 4
Cell suspension of *D. suillum*, grown on acetate+nitrate	6.8	bicarbonate	10mM	?	10mM	-4700	[11], Fig. 3a
Paracoccus ferrooxidans, +25mM EDTA, +1mM ethanol	7	bicarbonate	25mM	?	5mM	-1600	[12] , Fig. 3a
Acidovorax sp strain BoFeN1, +2mM acetate	6.8	bicarbonate	2.5mM	<1mM	5mM	-48	[13], Fig. 2
Acidovorax sp strain BoFeN1, +5mM acetate	7	bicarbonate	10mM	0mM	10mM	-240	[14], Fig 1a
Acidovorax sp strain 2AN, + 1.6mM acetate	6.85	bicarbonate	8.3mM	up to 1mM	5mM	-158	[15], Fig. 2a
Acidovorax sp strain 2AN, + 4mM EDTA, +1.2mM ethanol	7	PIPES	4mM	?	5mM	-970	[16], Fig. 3c
Dechloromonas sp UWNR4, + 4mM EDTA, +1.2mM ethanol	7	PIPES	4mM	?	5mM	-950	[16], Fig. 3d
Lake sediment slurry	~7	bicarbonate	1.4mM	0.01mM	1mM	-6	[17], Fig. 3
Phototrophic							
Rhodopseudomonas palustris strain TIE-1, + 0.2mM citrate	7	bicarbonate	4.5mM			-21	[18], Fig. 2
Rhodobacter capsulatus strain SB1003, + 0.2mM citrate	7	bicarbonate	0.1mM			-34	[18], Fig. 4
Rhodobacter capsulatus strain SB1003, + 1mg/L HA	7	bicarbonate	0.1mM			-50	[19], Fig. 4
Rhodobacter capsulatus strain SB1003, + 0.2mM NTA	7	bicarbonate	0.1mM			-112	[19], Fig. 4

Table 4.3 – Maximal rates of Fe(II) oxidation reported for various anaerobic processes at circumneutral pH (25-30ºC, except where otherwise indicated).
[1]Sørensen and Thorling (1991), [2] Rakshit et al. (2008), [3]Tai and Dempsey (2009), [4]Sorensen et al. (1996), [5] Shelobolina et al. (2003), [6]Straub et al. (1996b), [7]Blothe and Roden (2009), [8]Weber et al. (2006b), [9]Benz et al. (1998), [10]Hafenbradl et al. (1996), [11] Coates et al. (2001), [12]Kuenen et al. (2006), [13]Kappler et al. (2005b), [14] Muehe et al. (2009), [15]Chakraborty et al. (2011), [16]Chakraborty and Picardal (2013), [17]Senn (2002), [18]Jiao et al. (2005), [19]Poulain and Newman (2009)

are intrinsically coupled. This biologically-induced chemical oxidation of iron (via the microbial production of nitrite) in organic rich environments such as soils and

wetlands is likely to contribute significantly to the cycling of iron and immobilization of metal contaminants and organic pollutants on iron (oxy)hydroxides. High oxidation rates reported for environmental samples with mixed contributions from biological and chemical catalysis (Shelobolina et al., 2003) illustrate the interplay of this process, and call for caution in interpreting an observed effect to stem from solely one or the other mechanism.

2. In the case of mineral accelerated Fe(II) oxidation, the presence of amorphous hydrous ferric oxide (HFO / ferrihydrite) (Tiedje, 1988; Weber et al., 2001; Tai and Dempsey, 2009) and green rust (Sorensen et al., 1996) appears to cause the most significant acceleration of Fe(II) oxidation (see Table C.3 for additional detail on rate constants derived for mineral catalysis). This effect is likely to be highly relevant in natural settings where poorly crystalline iron oxides are ubiquitous. However, it is also important to consider this effect in laboratory studies where iron oxides precipitate over the course of an experiment and can provide catalytic surfaces for chemodenitrification, as suggested previously (Miot et al., 2009; Chakraborty et al., 2011; Pantke et al., 2012).

3. In the case of ligand-enhanced Fe(II) oxidation by nitrite, the absence of a major effect of the humic acid representative PPHA and low environmental abundance of the anthropogenic ligand NTA (maximal levels of 10-100 nM in aqueous systems) (Stumm and J Morgan, 1996) suggests that citrate (detected in soil solutions in appreciable quantities, ~100 µM range) is likely to be the only ligand investigated in this study that could be relevant in natural systems. In laboratory studies of iron-oxidizing microorganisms in the presence of citrate or NTA, the ligands' effect on oxidation kinetics is a crucial aspect of Fe(II) depletion that cannot be disregarded. This is particularly clear from the experiment reported in Figure 4.3, which confirmed that ligand-enhanced chemical oxidation of Fe(II) by nitrite can be an important side

effect of microbial denitrification in general. Here, chemical Fe(II) oxidation could be mistaken for direct biological catalysis by *P. denitrificans*. Such direct catalysis may indeed be at play; it would simply be challenging to unambiguously identify without appropriate controls. While biologically-induced chemical Fe(II) oxidation is the dominant Fe(II) oxidation pathway in our experiments with *P. denitrificans*, it is likely that the complex interplay and relative importance of chemical and biological Fe(II) oxidation in many denitrifying microorganisms is strongly dependent on the precise culturing conditions, and may even vary from strain to strain.

Acknowledgements

We thank Jim Morgan for many insightful conversations and inspiring S.H.K. to pursue this project; Sean Crowe, CarriAyne Jones, Arne Sturm, Sulung Nomosatryo, David Fowle, and Don Canfield for sample acquisition and fieldwork in Indonesia; Nathan Dalleska and the Caltech Environmental Analysis Center for instrumentation that benefited this project; Andreas Kappler, Nicole Klüglein, and Jay Labinger for helpful discussions; and members of the Newman Lab and the anonymous reviewers for constructive criticism that improved the manuscript. This work was supported by grants to D.K.N. from the Dreyfus Foundation and the Howard Hughes Medical Institute (HHMI). D.K.N. is an HHMI Investigator. S.H.K. is an HHMI International Student Research Fellow.

4.5 References

Abel, E., Schmid, H., Pollak, F., 1936. Kinetik der Oxydation von Ferro-Ion durch salpetrige Säure. Monatshefte für Chemie/Chemical Monthly.

Bauer, I., Kappler, A., Jun. 2009. Rates and Extent of Reduction of Fe(III) Compounds and O_2 by Humic Substances. Environmental Science & Technology, 1–7.

Benz, M., Brune, A., Schink, B., 1998. Anaerobic and aerobic oxidation of ferrous iron at neutral pH by chemoheterotrophic nitrate-reducing bacteria. Archives Of Microbiology 169 (2), 159–165.

Blothe, M., Roden, E. E., Nov. 2009. Composition and activity of an autotrophic Fe(II)-oxidizing, nitrate-reducing enrichment culture. Applied and Environmental Microbiology 75 (21), 6937–6940.

Bonner, F. T., Pearsall, K. A., 1982. Aqueous nitrosyliron (II) chemistry. 1. Reduction of nitrite and nitric oxide by iron (II) and (trioxodinitrato) iron (II) in acetate buffer. Intermediacy of nitrosyl hydride. Inorganic Chemistry 21 (5), 1973–1978.

Brons, H. J., Hagen, W. R., Zehnder, A. J. B., 1991. Ferrous iron dependent nitric oxide production in nitrate reducing cultures of *Escherichia coli*. Archives Of Microbiology 155 (4), 341–347.

Carlson, H. K., Clark, I. C., Melnyk, R. A., Coates, J. D., Jan. 2012. Toward a mechanistic understanding of anaerobic nitrate-dependent iron oxidation: balancing electron uptake and detoxification. Frontiers in Microbiology 3, 57–57.

Chakraborty, A., Picardal, F., Jan. 2013. Induction of nitrate-dependent Fe(II) oxidation by Fe(II) in *Dechloromonas* sp. strain UWNR4 and *Acidovorax* sp. strain 2AN. Applied and Environmental Microbiology 79 (2), 748–752.

Chakraborty, A., Roden, E. E., Schieber, J., Picardal, F., Dec. 2011. Enhanced growth of *Acidovorax* sp. strain 2AN during nitrate-dependent Fe(II) oxidation in batch and continuous-flow systems. Applied and Environmental Microbiology 77 (24), 8548–8556.

Coates, J. D., Chaudhuri, S., Lack, J., 2001. Biogenic magnetite formation through anaerobic biooxidation of Fe(II). Applied and Environmental Microbiology 67 (6), 2844–2848.

Coby, A. J., Picardal, F. W., Sep. 2005. Inhibition of NO_3^- and NO_2^- reduction by microbial Fe(III) reduction: evidence of a reaction between NO_2^- and cell surface-bound Fe^{2+}. Applied and Environmental Microbiology 71 (9), 5267–5274.

Colman, B. P., Jun. 2009. Understanding and eliminating iron interference in colorimetric nitrate and nitrite analysis. Environmental Monitoring and Assessment 165 (1-4), 633–641.

Cooper, D. C. D., Picardal, F. W. F., Coby, A. J. A., 4, Jun. 2003. Chemical and biological interactions during nitrate and goethite reduction by Shewanella putrefaciens 200. Applied and Environmental Microbiology 69 (6), 3517–3525.

Croal, L. R., Jiao, Y., Newman, D. K., 2007. The fox operon from Rhodobacter strain SW2 promotes phototrophic fe(II) oxidation in Rhodobacter capsulatus SB1003. Journal of Bacteriology 189 (5), 1774–1782.

Crowe, S., O'Neill, A. H., Katsev, S., Hehanussa, P., Haffner, G. D., Sundby, B., Mucci, A., Fowle, D. A., 2008b. The biogeochemistry of tropical lakes: A case study from Lake Matano, Indonesia. Limnology And Oceanography 53 (1), 319–331.

Demmink, J., Beenackers, A., 1997. Oxidation of ferrous nitrilotriacetic acid with oxygen: A model for oxygen mass transfer parallel to reaction kinetics. Industrial & Engineering Chemistry Research 36 (6), 1989–2005.

Demmink, J., vanGils, I., Beenackers, A., 1997. Absorption of nitric oxide into aqueous solutions of ferrous chelates accompanied by instantaneous reaction. Industrial & Engineering Chemistry Research 36 (11), 4914–4927.

Edwards, K. J., Rogers, D. R., Wirsen, C. O., McCollom, T. M., May 2003. Isolation and Characterization of Novel Psychrophilic, Neutrophilic, Fe-Oxidizing, Chemolithoautotrophic α- and γ-Proteobacteria from the Deep Sea. Applied and Environmental Microbiology 69 (5), 2906–2913.

Ehrenreich, A., Widdel, F., Nov. 1994. Anaerobic oxidation of ferrous iron by purple bacteria, a new type of phototrophic metabolism. Applied and Environmental Microbiology 60 (12), 4517–4526.

Fanning, J. C., 1991. The interaction of iron complexes with small nitrogen-containing molecules and ions. Coordination Chemistry Reviews 110 (2), 235–273.

Hafenbradl, D., Keller, M., Stetter, K., Nov. 1996. Ferroglobus placidus gen. nov., sp. nov., A novel hyperthermophilic archaeum that oxidizes Fe2+ at neutral pH under anoxic conditions. Archives Of Microbiology 166 (5), 308–314.

Hansen, H. C. B., Kragholm Borggaard, O., Sørensen, J., Jun. 1994. Evaluation of the free energy of formation of Fe(II)-Fe(III) hydroxide-sulphate (green rust) and its reduction of nitrite. Geochimica Et Cosmochimica Acta 58 (1), 2599–2608.

Jiao, Y., Newman, D. K., Kappler, A., Croal, L., 2005. Isolation and characterization of a genetically tractable photo autotrophic Fe(II)-oxidizing bacterium, *Rhodopseudomonas palustris* strain TIE-1. Applied and Environmental Microbiology 71 (8), 4487–4496.

Kappler, A., Schink, B., Newman, D. K., Oct. 2005b. Fe(III) mineral formation and cell encrustation by the nitrate-dependent Fe(II)-oxidizer strain BoFeN1. Geobiology 3 (4), 235–245.

King, D., 1998. Role of carbonate speciation on the oxidation rate of Fe(II) in aquatic systems. Environmental Science & Technology 32 (19), 2997–3003.

Kinniburgh, D., Milne, C., Benedetti, M., Pinheiro, J., Filius, J., Koopal, L., VanRiemsdijk, W., 1996. Metal ion binding by humic acid: Application of the NICA-Donnan model. Environmental Science & Technology 30 (5), 1687–1698.

Komatsu, Y., Takagi, M., Yamaguchi, M., 1978. Participation of Iron in Denitrification in Waterlogged Soil. Soil Biology & Biochemistry 10 (1), 21–26.

Kopf, S., Henny, C., Newman, D. K., Mar. 2013. Ligand-enhanced abiotic iron oxidation and the effects of chemical versus biological iron cycling in anoxic environments. Environmental Science & Technology 47 (6), 2602–2611.

Kuenen, J. G., Kumaraswamy, R. R., Sjollema, K. K., van Loosdrecht, M. M., Muyzer, G. G., Jun. 2006. Nitrate-dependent [Fe(II)EDTA]$^{2-}$ oxidation by *Paracoccus ferrooxidans* sp. nov., isolated from a denitrifying bioreactor. Systematic and Applied Microbiology 29 (4), 11–11.

Kustin, K., Taub, I. A., Weinstoc, E., 1966. A kinetic study of formation of ferrous-nitric oxide complex. Inorganic Chemistry 5 (6), 1079–1082.

Lin, M.-C., Chou, J.-H., Arun, A. B., Young, C.-C., Chen, W.-M., Oct. 2008. *Pseudogulbenkiania subflava* gen. nov., sp. nov., isolated from a cold spring. International Journal Of Systematic And Evolutionary Microbiology 58 (10), 2384–2388.

Lin, N., Littlejohn, D., Chang, S. G., 1982. Thermodynamics and kinetics of the coordination of NO to Fe^{II}NTA in aqueous solutions. Industrial & Engineering Chemistry Process Design And Development 21 (4), 725–728.

Matocha, C. J., Coyne, M. S., 2007. Short-term response of soil iron to nitrate addition. Soil Science Society Of America Journal 71 (1), 108.

Miot, J., Benzerara, K., Morin, G., Bernard, S., Beyssac, O., Larquet, E., Kappler, A., Guyot, F., Jun. 2009. Transformation of vivianite by anaerobic nitrate-reducing iron-oxidizing bacteria. Geobiology 7 (3), 373–384.

Moraghan, J. T., Buresh, R. J., 1977. Chemical reduction of nitrite and nitrous oxide by ferrous iron. Soil Science Society Of America Journal 41 (1), 47–50.

Morgan, J. J., Jan. 2005. Kinetics of reaction between O_2 and Mn(II) species in aqueous solutions. Geochimica Et Cosmochimica Acta 69 (1), 35–48.

Muehe, E. M., Gerhardt, S., Schink, B., Kappler, A., Dec. 2009. Ecophysiology and the energetic benefit of mixotrophic Fe(II) oxidation by various strains of nitrate-reducing bacteria. Fems Microbiology Ecology 70 (3), 335–343.

Newman, D. K., Croal, L., Gralnick, J., Malasarn, D., 2004. The genetics of geochemistry. Annual Review Of Genetics 38, 175–202.

Newman, D. K., Saraiva, I. H. I., Louro, R. O. R., Jul. 2012. Functional characterization of the FoxE iron oxidoreductase from the photoferrotroph Rhodobacter ferrooxidans SW2. Journal of Biological Chemistry 287 (30), 25541–25548.

Ottley, C., Davison, W., Edmunds, W., 1997. Chemical catalysis of nitrate reduction by iron(II). Geochimica Et Cosmochimica Acta 61 (9), 1819–1828.

Pantke, C., Kappler, A., Obst, M., Benzerara, K., Morin, G., Ona-Nguema, G., Dippon, U., Feb. 2012. Green rust formation during Fe(II) oxidation by the nitrate-reducing *Acidovorax* sp. strain BoFeN1. Environmental Science & Technology 46 (3), 1439–1446.

Pearsall, K. A., Bonner, F. T., 1982. Aqueous nitrosyliron(II) chemistry. 2. Kinetics and mechanism of nitric oxide reduction. The dinitrosyl complex. Inorganic Chemistry 21 (5), 1978–1985.

Pham, A. N., Waite, T. D., Jun. 2008. Modeling the kinetics of Fe(II) oxidation in the presence of citrate and salicylate in aqueous solutions at pH 6.0-8.0 and 25 °C. The Journal of Physical Chemistry A 112 (24), 5395–5405.

Picardal, F. F., Jan. 2012. Abiotic and microbial interactions during anaerobic transformations of Fe(II) and N. Frontiers in Microbiology 3, 112–112.

Poulain, A. J., Newman, D. K., Nov. 2009. Rhodobacter capsulatus catalyzes light-dependent Fe(II) oxidation under anaerobic conditions as a potential detoxification mechanism. Applied and Environmental Microbiology 75 (21), 6639–6646.

Promega, May 2009. Griess Reagent System Technical Bulletin, TB229, 1–8.

Rakshit, S., Matocha, C. J., Coyne, M. S., 2008. Nitrite reduction by siderite. Soil Science Society Of America Journal 72 (4), 1070.

Schneppensieper, T., Wanat, A., Stochel, G., Goldstein, S., Meyerstein, D., van Eldik, R., 2001. Ligand effects on the kinetics of the reversible binding of NO to selected aminocarboxylato complexes of iron(II) in aqueous solution. European Journal of Inorganic Chemistry, 2317–2325.

Schneppensieper, T., Wanat, A., Stochel, G., van Eldik, R., May 2002. Mechanistic information on the reversible binding of NO to selected iron(II) chelates from activation parameters. Inorganic Chemistry 41 (9), 2565–2573.

Senn, D. B., Jun. 2002. Nitrate controls on iron and arsenic in an urban lake. Science 296 (5577), 2373–2376.

Shelobolina, E. S., VanPraagh, C. G., Lovley, D. R., Mar. 2003. Use of ferric and ferrous iron containing minerals for respiration by *Desulfitobacterium frappieri*. Geomicrobiology Journal 20 (2), 143–156.

Smith, R., Martell, A., 1998. NIST standard reference database 46. NIST Critically Selected Stability Constants of Metal Complexes.

Sorensen, Hansen, H. C. B., Koch, C., Nancke-Krogh, H., Borggaard, O., 1996. Abiotic nitrate reduction to ammonium: key role of green rust. Environmental Science & Technology 30 (6), 2053–2056.

Sørensen, J., Thorling, L., May 1991. Stimulation by lepidocrocite (gamma-FeOOH) of Fe(II)-dependent nitrite reduction. Geochimica et Cosmochimica Acta; (United States) 55:5 (5), 1289–1294.

Stookey, L. L., 1970. Ferrozine - a new spectrophotometric reagent for iron. Analytical Chemistry 42 (7), 779–781.

Straub, K., Schonhuber, W., Buchholz-Cleven, B., Schink, B., 2004. Diversity of ferrous iron-oxidizing, nitrate-reducing bacteria and their involvement in oxygen-independent iron cycling. Geomicrobiology Journal 21 (6), 371–378.

Straub, K. L., Benz, M., Schink, B., Widdel, F., Apr. 1996b. Anaerobic, nitrate-dependent microbial oxidation of ferrous iron. Applied and Environmental Microbiology 62 (4), 1458–1460.

Stumm, W., J Morgan, J., 1996. Aquatic chemistry: chemical equilibria and rates in natural waters, 3rd Edition. John Wiley & Sons, Inc., New York.

Tai, Y.-L., Dempsey, B. A., Jan. 2009. Nitrite reduction with hydrous ferric oxide and Fe(II): Stoichiometry, rate, and mechanism. Water Research 43 (2), 546–552.

Theis, T. L., Singer, P. C., 1974. Complexation of iron(II) by organic matter and its effect on iron(II) oxygenation. Environmental Science & Technology 8 (6), 569–573.

Tiedje, J. M., 1988. Ecology of denitrification and dissimilatory nitrate reduction to ammonium. Biology of anaerobic microorganisms (717), 179–244.

Van Cleemput, O., Baert, L., 1976. Theoretical considerations on nitrite self-decomposition reactions in soils. Soil Science Society Of America Journal 40 (2), 322–324.

Van Cleemput, O., Baert, L., 1983. Nitrite stability influenced by iron compounds. Soil Biology & Biochemistry 15 (2), 137–140.

Van Cleemput, O., Samater, A., 1996a. Nitrite in soils: Accumulation and role in the formation of gaseous N compounds. Fertilizer Research 45 (1), 81–89.

Weber, K., Coates, J. D., Pollock, J., Cole, K., O'Connor, S., Achenbach, L., 2006a. Anaerobic nitrate-dependent iron(II) bio-oxidation by a novel lithoautotrophic betaproteobacterium, strain 2002. Applied and Environmental Microbiology 72 (1), 686–694.

Weber, K. A., Achenbach, L. A., Coates, J. D., Oct. 2006b. Microorganisms pumping iron: anaerobic microbial iron oxidation and reduction. Nature Reviews Microbiology 4 (10), 752–764.

Weber, K. A., Hedrick, D. B., Peacock, A. D., Thrash, J. C., White, D. C., Achenbach, L. A., Coates, J. D., 2009. Physiological and taxonomic description of the novel autotrophic, metal oxidizing bacterium, Pseudogulbenkiania sp strain 2002. Applied Microbial Biotechnology 83 (3), 555–565.

Weber, K. A., Picardal, F. W., Roden, E. E., Apr. 2001. Microbially catalyzed nitrate-dependent oxidation of biogenic solid-phase Fe(II) compounds. Environmental Science & Technology 35 (8), 1644–1650.

Zang, V., Kotowski, M., van Eldik, R., 1988. Kinetics and mechanism of the formation of Fe^{II}(EDTA)NO in the system Fe^{II}(EDTA)/NO/HONO/NO_2^- in aqueous solutions. Inorganic Chemistry 27 (19), 3279–3283.

Zang, V., van Eldik, R., 1990. Kinetics and mechanism of the autoxidation of iron(II) induced through chelation by ethylenediaminetetraacetate and related ligands. Inorganic Chemistry 29 (9), 1705–1711.

Chapter 5

Primary productivity in Lake Matano from triple oxygen isotopes

5.1 Introduction

The iron-rich tropical Lake Matano provides a unique field site for studying microbial activity at the interface of a permanently stratified large water body with oxic surface waters and ferrugenous bottom waters. Recent work on the geochemical cycles of this Lake have highlighted its potential as an analogue for the anoxic, iron-rich Archean and Early Proterozoic oceans (Crowe et al., 2008b), particularly through the transition from anoxia throughout the water column before the advent of oxygenic photosynthesis, to the gradual oxygenation of the surface waters by early oxygenic phototrophs.

In Lake Matano, one consequence of water column stratification appears to be a low concentration of biomass and chlorophyll in the surface waters (Sabo et al., 2008; Crowe et al., 2008c). This is mainly attributed to either metal toxicity from high levels of iron and chromium in the lake, or to the scavenging and removal of bioavailable phosphate by

sedimenting particles of iron oxyhydroxides[1]. However, with only a single rate estimate of primary productivity from a measurement of $H^{13}CO_3^-$ incorporation by the microbial community at 35m water depth (Crowe et al., 2008c), the oxygen and carbon production rates in the surface waters of Lake Matano are ill-constrained. Here, we present insights gained from triple oxygen isotope measurements of water samples from the oxic surface waters of the lake to constrain gross primary production, reflecting the total amount of oxygenic photosynthesis in the system, as well as net community production, a measure of the net amount of carbon added from the surface waters.

5.2 Materials and methods

5.2.1 Terminology

There is a bit of confusion in the naming of distinct layers in stratified lakes in limnology due to different terminology used for permanently stratified (meromictic) and non-permanently (i.e. mixed at least once a year) stratified (holomictic) lakes. Usually, the layer below the permanent pycnocline/chemocline in a meromictic lake is referred to as the monimolimnion. The layer above the chemocline is either referred to as the mixolimnion or the epilimnion. If referred to as the mixolimnion, this layer is often further subdivided if a seasonal pycnocline exists, in which case the whole mixolimnion is treated as a "pseudo-holomictic lake" with an epilimnion above the seasonal pycnocline (i.e. the mixed surface layer) and a hypolimnion below the seasonal pycnocline (above the permanent pycnocline). To avoid the confusion associated with epilimnion here, this term is not used at all, and the layer above the seasonal pycnocline (here called **thermocline**) is just referred to as the **mixed layer** (0 to ∼35m depth). The permanent pycnocline is referred to as the

[1]Whether surface ocean productivity in a gradually oxygenating Proterozoic ocean would have been limited by the availabililty of phosphate due to absorption and removal by iron hydroxides is a matter of active debate, and depends strongly on the levels of dissolved silica (Canfield and Bjerrum, 2002; Konhauser et al., 2007).

chemocline (∼110m depth). Samples were all taken from above the chemocline (no O_2 below) at different water depths (3, 10, 25, 50, 80, 85m).

5.2.2 Sampling and analysis

Twice 3 samples for gas and oxygen stable isotope analysis were collected at Lake Matano in two different sampling casts, six days apart from each other, using a local fishing boat. All water samples were collected with 5L Go-Flow Niskin bottles attached in series to a stainless steel cable and a hand-operated winch. The bottles were placed at depth to an accuracy of $\pm$1 m with the help of a commercial fish finder. Water samples from the Niskin bottles were collected as described in Hendricks et al. (2007b) and Stanley and Howard (2013). Briefly, custom-made borosilicate glass sample bottles with 9 mm Louwers–Hapert valves (Emerson et al., 1999) were poisoned with 100 µL saturated mercuric chloride solution and dried at 40C. All flasks were evacuated to less than 10^{-3}torr. It is imperative not to get air into the sample bottles while collecting the sample, so samples were collected by gravimetric flow of bubble-free, freshly-recovered lake water from the Niskin bottle into the overflowing valve side arm, and entrained from the side arm into the evacuated flask after thorough rinsing of the side arm. The gases exsolve into the head space of the bottles, and equilibrium is reached before the liquid is drained from the bottle without loss of the gases. The sample O_2 and Ar were quantitatively separated from N_2, CO_2, and H_2O by an automated gas chromatographic system (Blunier et al., 2002) in preparation for mass spectrometric analysis of $\delta^{17}O$, $\delta^{18}O$ and $\frac{[O_2]}{[Ar]}$. The oxygen-argon mixture was measured by dual inlet mass spectrometry (Finnigan MAT 252) against a standard mixture of oxygen and argon.

5.2.3 Calculations

5.2.3.1 Isotope notation

Isotope ratios ($^{x}R = {}^{x}O / {}^{16}O$) and delta notation ($^{x}\delta_{ref} = {}^{x}R_{sample} / {}^{x}R_{ref} - 1$) are used as commonly defined (all ratios are for oxygen so x = 17 or 18). Capital delta notation is defined as

$$^{17}\Delta = ln\left(1 + {}^{17}\,\delta\right) - \lambda \cdot ln\left(1 + {}^{18}\,\delta\right) \tag{5.1}$$

δ values are reported in ‰ (which implies multiplication by a factor of 10^3), and Δ is reported in ppm (implying multiplication by a factor of 10^6). Omission of the reference name (*ref*) implies δ values are relative to atmospheric O_2 except where otherwise indicated. The mass-dependent fractionation slope is assumed to be λ=0.518 (the slope for respiration, as discussed in Luz and Barkan, 2005), except where otherwise indicated. The employed Δ notation is independent of the isotopic reference standard (i.e., for two mass-dependently related materials a and b, Δ works out correctly as: $\Delta_a = \Delta_b$).

5.2.3.2 Equilibrium O_2

There is considerable disagreement about the isotopic composition of water O_2 in equilibrium with air (Luz and Barkan, 2005; Juranek, 2005; Hendricks et al., 2007a; Luz and Barkan, 2009; Stanley et al., 2010; Kaiser, 2011). Principally, values cluster around $^{17}\Delta_{eq} = 8ppm$ and $^{17}\Delta_{eq} = 16ppm$, but the cause of this discrepancy is unclear (Stanley et al., 2010). However, temperature does seem to affect $^{17}\Delta_{eq}$. Given the relatively high water temperatures of Lake Matano (~30C at the surface), we use the equation presented by Luz and Barkan (2009) to obtain a temperature-corrected $^{17}\Delta_{eq} = 0.6 \cdot T + 1.8$ (T in degree Celsius), at 30C, $^{17}\Delta_{eq} = 19.8ppm$. It is important to note that this value is higher than any value actually measured by Luz and Barkan (2009) (3.5 to 25C). $^{17}\delta_{eq} = 0.707‰$

is calculated from ${}^{17}\Delta_{eq} = 19.8ppm$ and ${}^{18}\delta_{eq} = 0.707‰$ (Luz and Barkan, 2011) using Equation 1.

5.2.3.3 Photosynthetic O_2

The isotopic composition of photosynthetic O_2 varies depending on type of primary producer. In the case of oligotrophic Lake Matano, cyanobacteria dominate the mixed surface layer numerically (Sabo et al., 2008), and the isotopic composition of photosynthetically produced O_2 is best approximated by ${}^{18}\delta_{cyano} = -22.868‰$, ${}^{17}\delta_{cyano} = -11.635‰$ (values for *Synechocystis* are the only available measure for cyanobacteria; average phytoplankton would be ${}^{18}\delta_{all} = -20.014‰$, ${}^{17}\delta_{all} = -10.126‰$, ${}^{17}\Delta_{all} = 249ppm$ instead) (Luz and Barkan, 2011). This describes O_2 produced by photosynthesis from VSMOW (${}^{18}\delta_{VSMOW} = -23.324‰$, ${}^{17}\delta_{VSMOW} = -11.883‰$), and for cyanobacteria, the corresponding fractionation factors are ${}^{18}\alpha_{photo-VSMOW} = 1.00047$ and ${}^{17}\alpha_{photo-VSMOW} = 1.00025$ (i.e., hardly any fractionation associated with photosynthetic production of O_2 from water). Adjusting the isotopic composition of photosynthetic O_2 for Lake Matano requires taking the isotopic offset of Lake Matano water from VSMOW into consideration. The surface waters of Lake Matano are depleted in ^{18}O by about ~4.5‰ relative to VSMOW (Katsev et al., 2010). The mass scaling factor for the global meteoric water line is 0.528, and the ^{17}O isotopic offset of meteoric water relative to VSMOW (due to the slight differences in mass scaling in equilibrium and diffusive processes) in Indonesia averages 54ppm (based on 4 measurements of rain in Borneo from Luz and Barkan (2010)). Accordingly, Lake Matano water has an isotopic composition of ${}^{18}\delta = -27.719‰$ and ${}^{17}\delta = -14.180‰$ relative to atmospheric oxygen. The adjusted isotopic composition of photosynthetically produced O_2 in Lake Matano is then ${}^{18}\delta_{photo} = -27.265‰$ and ${}^{17}\delta_{photo} = -13.933‰$ (using the above-mentioned fractionation factors representative of cyanobacteria).

5.2.3.4 Piston velocity (k)

O_2 piston velocities were calculated from the wind speeds using the empirical relationships described in Wanninkhof et al. (1985):

$$k = K \cdot u^2 \cdot \left(\frac{Sc}{660}\right)^{-1/2} \tag{5.2}$$

where k is the gas transfer velocity (in cm/hr), u is wind speed (in m/s), K is a constant that takes a value of 0.31 for steady winds, and Sc is the Schmidt number for O_2 at the relevant temperatures (this relationship was empirically derived for CO_2 at 20C, hence the factor of 660). The Schmidt number for oxygen in freshwater systems is described by the polynomial

$$Sc = A - B \cdot T + C \cdot T^2 - D \cdot T^3 \tag{5.3}$$

where T is the temperature in Celsius, and A=1800.6, B=120.1, C=3.7818, D=0.047608 (Wanninkhof et al., 1985). A word of caution: this empirical fit was derived for the temperature range 0 to 30ºC, and should not be used outside this range. The surface waters of Lake Matano with T=29.8 are very close to the end points and this approximation.

5.2.3.5 Biological O_2 saturation (BOS)

The physical properties of Argon and O_2 are very similar, but Ar has no biological sources or sinks. Consequently, simultaneous measurements of Ar and O_2 allow for the correction of O_2 concentrations for physical effects. Biological saturation of O_2 (that is, O_2 saturation corrected for physical processes) can be calculated directly from MS measurements (Luz and Barkan, 2009):

$$BOS = \left(\frac{[O_2]}{[O_2]_{eq}}\right)_{bio} = \frac{\left(\frac{O_2}{Ar}\right)_{sample}}{\left(\frac{O_2}{Ar}\right)_{equilib}} \tag{5.4}$$

with $(O_2 / Ar)_{sample}$ measured against a reference gas (usually air) and reported in delta notation as $\delta(O2/Ar) = (O2 / Ar) / (O2 / Ar)_{ref} - 1$. Here, it is assumed that the reference gas is air with $(O2 / Ar)_{air} = 20.946/0.9340$. Equilibrium $(O2 / Ar)_{equilib}$ ratios are calculated from temperature and salinity data for each water sample using the solubility relations for O_2 and Ar equilibrium concentrations reported in the literature, most recently for Ar (Hamme and Emerson, 2004) as

$$ln[Ar]_{eq} = A_0 + A_1 \cdot T_s + A_2 \cdot T_s^2 + A_3 \cdot T_s^3 + S \cdot \left(B_0 + B_1 \cdot T_s + B_2 \cdot T_s^2\right) \quad (5.5)$$

and for O_2(Garcia and Gordon, 1992b) as

$$\begin{aligned} ln[O_2]_{eq} =& A_0 + A_1 \cdot T_s + A_2 \cdot T_s^2 + A_3 \cdot T_s^3 + A_4 \cdot T_s^3 + A_5 \cdot T_5^5 + \\ & S \cdot \left(B_0 + B_1 \cdot T_s + B_2 \cdot T_s^2 + B_3 \cdot T_s^3\right) + C_0 \cdot S^2 \end{aligned} \quad (5.6)$$

with scaled temperature

$$T_s = ln\left(\frac{298.15 - t}{273.15 + t}\right) \quad (5.7)$$

with temperature t in ºC and salinity S in ‰/psu. The constants for Ar are A_0=2.79150, A_1=3.17609, A_2=4.13116, A_3=4.90379, B_0=-6.96233 x 10-3, B_1=-7.66670 x 10^{-3}, B_2=-1.16888 x 10^{-2} (Hamme and Emerson, 2004). The constants for O_2 are A_0=5.80871, A_1=3.20291, A_2=4.17887, A_3=5.10006, A_4=-9.86643 x 10^{-2}, A_5=3.80369, B_0=-7.01577 x 10^{-3}, B_1=-7.70028 x 10^{-3}, B_2=-1.13864 x 10^{-2}, B_3=-9.51519 x 10^{-3}, C_0=-2.75915 x 10^{-7}(Garcia and Gordon (1992b) with recommended coefficients derived from data of Benson and Krause Jr, 1984).

5.2.3.6 Gross oxygen production (GOP) and net oxygen production (NOP)

Mixed layer gross oxygen production can be estimated either based on $^{17}\Delta$ or, as more recently discussed by Luz and Barkan (2011); Prokopenko et al. (2011) and Kaiser (2011),

directly based on $^{17}\delta$ and $^{18}\delta$. While the $^{17}\Delta$ notation is very intuitive for qualitative interpretation (see Figure 2) the derivation based directly on $^{17}\delta$ and $^{18}\delta$ is preferable for quantitation, particularly, because the biological endmember is better constrained in δ-space (there is a fair amount of confusion surrounding the value of the biological $^{17}\Delta$ endmember as a consequence of varying scaling factors and $^{17}\Delta$ definitions). Here, I thus use

$$GOP = k \cdot [O_2]_{eq} \cdot \frac{\left(1 - \frac{\delta^{17}O_{eq}+1}{\delta^{17}O_{dis}+1}\right) - 0.518 \cdot \left(1 - \frac{\delta^{18}O_{eq}+1}{\delta^{18}O_{dis}+1}\right)}{\left(\frac{\delta^{17}O_{p}+1}{\delta^{17}O_{dis}+1} - 1\right) - 0.518 \cdot \left(\frac{\delta^{18}O_{p}+1}{\delta^{18}O_{dis}+1} - 1\right)} \tag{5.8}$$

where *k* is the piston velocity, subscripts *dis, eq* and *p* stand for dissolved, equilibrium and photosynthetic O_2, and *GOP* is the gross rate of O_2 production by photosynthesis integrated over the depth of the mixed layer (in mol O_2 area^{-1} time^{-1}), assuming that the mixed layer is at steady state. Similarly, net oxygen production (*NOP*, same units as *GOP*) over the mixed layer can be estimated from the biological oxygen saturation (BOS) (e.g. Hendricks et al., 2007b):

$$NOP = k \cdot [O_2]_{eq} \cdot (BOS - 1) \tag{5.9}$$

Both equations assume a mixed layer at steady state under the simplifying assumption that there is no interaction between the mixed layer and the seasonal thermocline (Luz and Barkan, 2009). There are no strong winds that would be likely to temporarily erode the seasonal thermocline at Lake Matano, so it is assumed that quasi-steady state is a reasonable approximation (this will be discussed in more detail in Section 5.3). For the thermocline, GOP can only be evaluated assuming neither addition nor loss of O_2 from/to the mixed layer. GOP in the thermocline can be assessed by evaluating the production between different time points, as outlined for example in Luz and Barkan (2009) and Kaiser (2011). Thermocline GOP at any single depth (in $mol \cdot volume^{-1} \cdot time^{-1}$) is

derived as (Kaiser, 2011):

$$P = c \cdot \frac{\frac{1}{1+^{17}\delta} \cdot \frac{d^{17}\delta}{dt} - \gamma_R \cdot \frac{1}{1+^{18}\delta} \cdot \frac{d^{18}\delta}{dt}}{\frac{^{17}\delta_P - ^{17}\delta}{1+^{17}\delta} - \gamma_R \cdot \frac{^{18}\delta_P - ^{18}\delta}{1+^{18}\delta}} \tag{5.10}$$

5.2.3.7 Gross carbon production (GCP) and net carbon production (NCP)

The gross oxygen production by photosynthesis is stoichiometrically linked to carbon fixation by the photosynthetic quotient (PQ). The PQ depends on the redox state of the nitrogen source for primary producers. The PQ is 1.1 for ammonia-based production (N recycled) and 1.4 for nitrate-based production (new production) (Laws, 1991). For Lake Matano, it is prudent to assume a mixed contribution and we use a conservative PQ=1.25. Additionally, the Mehler reaction (photosynthetic production of O_2 without carbon fixation) and photorespiration to CO_2 lead to O_2 production without concomitant net carbon fixation. This loss term (L) was previously estimated to be ~15% (Juranek, 2005; Nicholson et al., 2012). This translates into a conversion factor of 1.25 x 0.85 from GOP (mol O_2 Area^{-1} time^{-1}) to GCP (mol C Area^{-1} time^{-1}):

$$GCP = PQ \cdot L \cdot GOP \tag{5.11}$$

Net carbon production can only be estimated from GCP if autotrophic respiration rates are known. Bender et al. (1999) estimated plant respiration to account for ~35% of GCP, such that NCP = 0.65 x GCP (Juranek, 2005).

5.2.4 Error assessment

Hendricks et al. (2007b) discuss errors introduced in samples stored for an extended period of time (627 days in their case), observing that for flasks stored with water in the sidearm, leakage of atmospheric O_2 (and Ar) leads to up to a 7% increase in O_2 content, lowering $^{17}\Delta$ by up to 8ppm and changing O_2/Ar ratio up to 5%. Overall, even the maximal

errors estimated by Hendricks et al. (2007b) are unlikely to make a significant difference in the interpretation of our data. Routine error of the measurement itself is ~7ppm in the Stanley lab. The largest error in all calculated quantities is likely a consequence of uncertainties in the piston velocity k because of approximate wind speeds and likely inaccuracies in the empirical relationships used to derive this quantity. Also, the *in situ* oxygen concentrations measured at Lake Matano might have a systematic error associated with them that is difficult to assess in absence of precise oxygen concentration data from Winkler titrations.

5.3 Results and Discussion

5.3.1 Wind data

O_2piston velocities are calculated from wind speeds using the equations' outlines in section 5.2.3.4. Wind data is available for the sampling days from the airport near the Lake, and for an extended period of time preceding the sampling date from the INCO mining plant nearby. INCO plant measurements are available in half-hour intervals and allow for an estimate of the average daily wind speeds (and range of speeds) as illustrated in Figure 5.1. The wind speeds from the plant are not likely to be perfectly representative of wind at the Lake, but are the best estimate currently available for long-term speeds. Given the relative stability of daily average wind speeds, we use average piston velocities derived from wind data spanning a 60-day period prior to each sampling date for calculations.

5.3.2 Isotopic data and productivity calculations

The primary processes (photosynthesis, respiration and gas exchange) affecting the isotopic composition of O_2 in the surface layer (assuming steady state, no exchange with thermocline) all change the isotopes in very specific ways that are helpful to consider for discussing the data in triple oxygen isotope space. Gas exchange always redirects surface

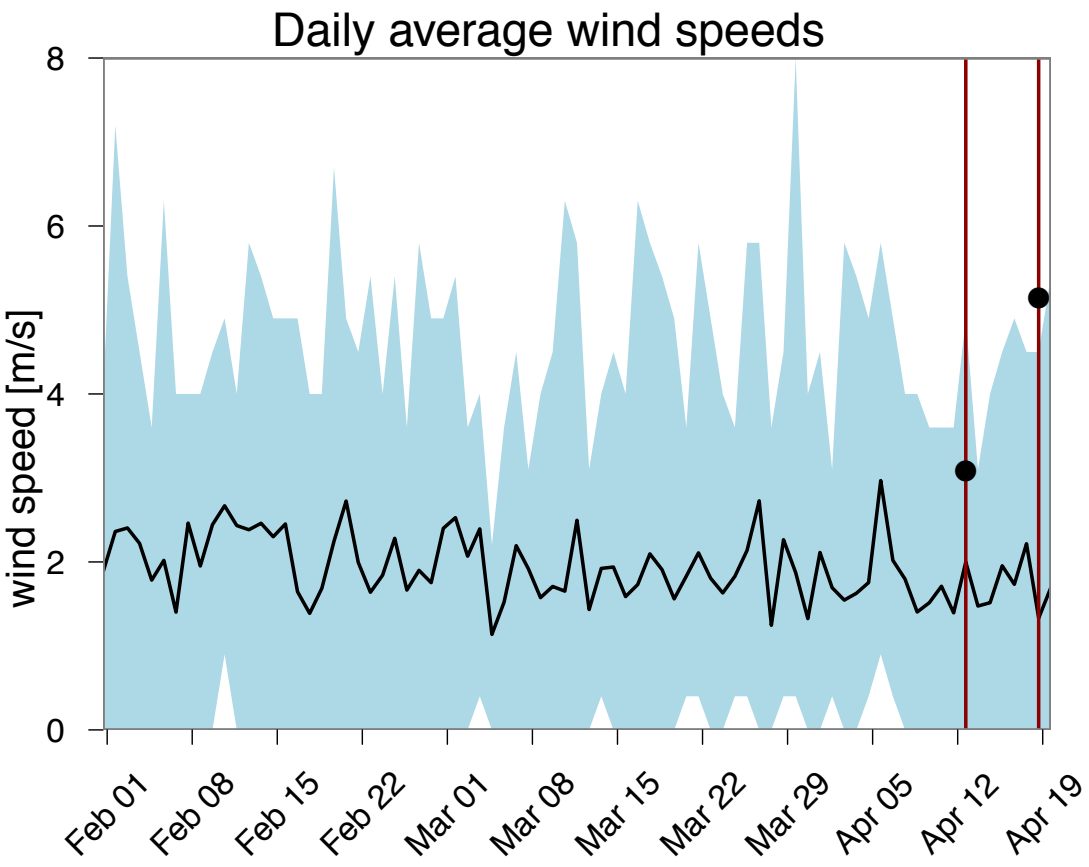

Figure 5.1 – Wind data from INCO plant near Lake Matano. Black line: daily averages from 47 daily measurements (half hourly from 0:30 to 23:30). Blue band: range of daily wind speeds. Sampling days are indicated in red. Wind speeds measured at Soroako airport on sampling dates indicated in black.

$^{18}\delta$ and $^{17}\Delta$ **towards equilibrium** with the atmosphere, i.e. towards the equilibrium values outlined in Section 5.2.3.2. Photosynthesis injects isotopically light O_2 (**decreasing** $^{18}\delta$) from water oxygen with very little fractionation (the O_2 is isotopically light because the water is light compared to atmospheric O_2 to begin with). Additionally, photosynthetic O_2 is heavy in ^{17}O, leading to an **increase** in $^{17}\Delta$. It is important to note that while photosynthesis fractionates mass-dependently, atmospheric O_2 is anomalous in its triple O composition due to mass-independent stratospheric processes (Mauersberger, 1981; Gao, 2001; Luz et al., 1999), and O_2 derived from water consequently has non-zero $^{17}\Delta$ relative

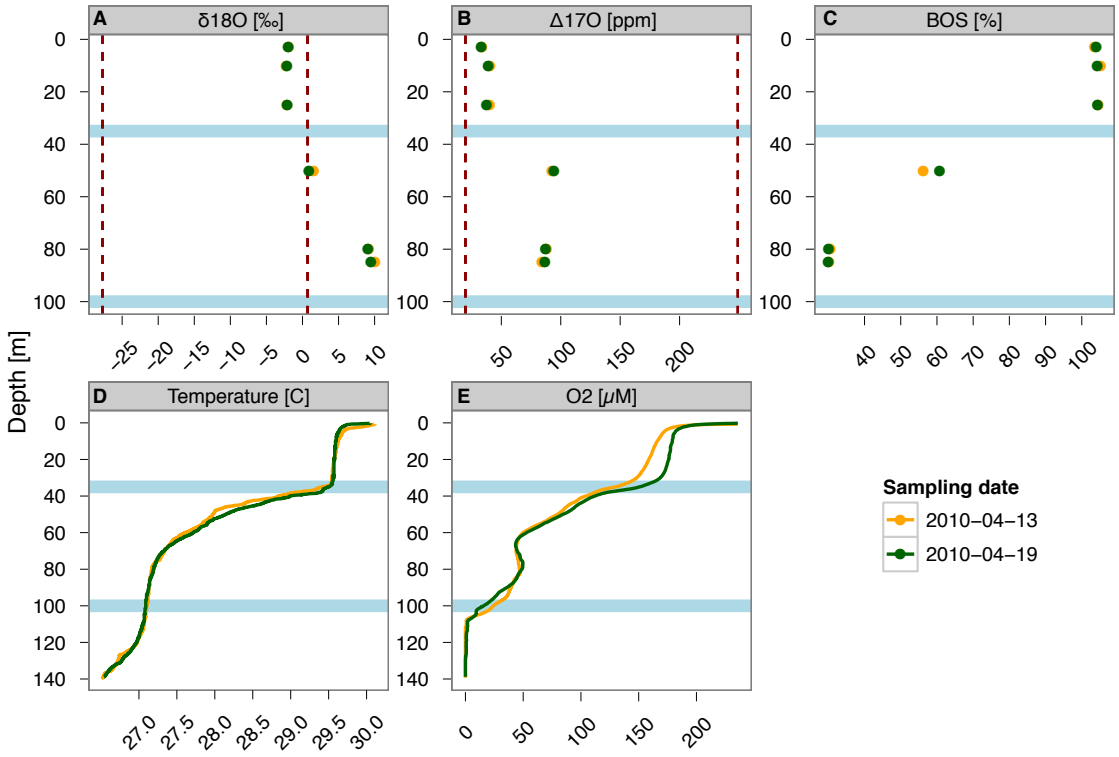

Figure 5.2 – Chemical and oxygen isotope depth profiles of Lake Matano. A) $\delta^{18}O$ of water samples, red lines indicate isotopic endmembers - composition of Lake Matano water (-27.7‰) and O_2 equilibrated with the atmosphere (0.7‰). B) $\Delta^{17}O$ of water sample, red lines indicate isotopic endmembers (exact values are debated) - O_2 equilibrated with the atmosphere (20ppm) and biologically produced O_2 (249ppm). C) Biological oxygen saturation as defined in text. D&E) Temperature and dissolved O_2 profiles from CTD cast.

to atmospheric O_2 as the standard[2]. Respiration consumes O_2 mass-dependently with a preference for light O (∼20‰), leaving residual O_2 enriched (**increasing** $^{18}\delta$) but not changing $^{17}\Delta$ (**constant**). Many papers on the subject illustrate this very well; see, for example, Figure 1 in Hendricks et al. (2004) for an informative schematic.

5.3.2.1 Mixed layer

Consistently similar isotopic composition of the surface layer between the 2 casts suggests that primary productivity is relatively invariant and reaches a rate of gross oxygen production of ∼10mmol m^{-2} d^{-1}. This rate is low even in comparison to other oligotrophic

[2]This is a consequence of the traditional use of atmospheric O_2 instead of VSMOW as the reference standard in isotope measurements of molecular oxygen.

Cast	Depth $[m]$	$^{17}\Delta$ $[ppm]$	$^{17}\delta$ [‰]	$^{18}\delta$ [‰]	Temp $[C]$	O_2 $[\mu M]$	BOS [%]	avg k $[m/d]$	GOP $[mmol\ O_2\ m^{-2}\ d^{-1}]$	NOP $[mmol\ O_2\ m^{-2}\ d^{-1}]$	GCP $[mmol\ C\ m^{-2}\ d^{-1}]$	NCP $[mmol\ C\ m^{-2}\ d^{-1}]$
4/13/10	3	34	-0.972	-1.940	29.8	177	104	0.39	7.9	3.3	8.4	5.5
4/13/10	10	40	-1.135	-2.267	29.6	166	105	0.39	11.7	4.8	12.5	8.1
4/13/10	25	40	-1.074	-2.150	29.6	155	105	0.39	11.8	4.2	12.6	8.2
4/19/10	3	33	-0.977	-1.950	29.7	186	104	0.39	7.7	3.6	8.1	5.3
4/19/10	10	39	-1.070	-2.138	29.6	179	104	0.39	11.0	4.0	11.7	7.6
4/19/10	25	38	-1.044	-2.086	29.6	174	104	0.38	10.1	4.0	10.7	7.0

Table 5.1 – Oxygen isotope composition of mixed layer at Lake Matano.

environments and is consistent with previous estimates of low abundances of primary producers in the surface waters of Lake Matano (Sabo et al., 2008). However, this mixed layer average rate is higher than the single previous estimate of carbon fixation rates of 0.35µg C l^{-1} hr^{-1}(equivalent to a flux of ∼0.7 mmol C m^{-2} d^{-1}) provided by incubation with isotopically labeled bicarbonate ($H^{13}CO_3^-$) at 32 m water depth (Crowe et al., 2008b). This closed-bottle bicarbonate incubation measurement captures only the carbon fixation rate close to the bottom of the mixed layer (at 32 m water depth), suggesting that the measured rate of gross oxygen production reflects a dominant contribution from photosynthesis occuring closer to the surface (above 32 m water depth) at higher light intensities.

5.3.2.2 Thermocline

Cast	Depth $[m]$	$^{17}\Delta$ $[ppm]$	$^{17}\delta$ [‰]	$^{18}\delta$ [‰]	Temp $[C]$	O_2 $[\mu M]$	BOS [%]
4/13/10	50	93	0.888	1.538	28.0	80	56
4/13/10	80	88	4.807	9.154	27.2	47	31
4/13/10	85	84	5.257	10.041	27.1	43	30
4/19/10	50	94	0.558	0.897	28.1	84	61
4/19/10	80	87	4.758	9.061	27.2	49	30
4/19/10	85	87	4.971	9.477	27.1	44	30

Table 5.2 – Oxygen isotope composition of thermocline at Lake Matano.

The small difference in isotopic composition between the two casts (within measurement error of each other) makes GOP (gross oxygen production, Section 5.2.3.6) difficult to assess from the current data. Given the small differences of the measurements combined with the uncertainty in actual sampling depth, GOP below the surface layer cannot be quantified at this point. However, the small difference between the casts (1 week apart)

would suggest that there is very little primary productivity. If the time of establishment of the seasonal pycnocline were known, primary productivity could be evaluated over the much longer time frame (from establishment of the pycnocline until time of the cast) when making the assumption that original thermocline waters have mixed layer isotopic composition and slowly shift to higher $^{17}\Delta$ as photosynthesis below the mixed layer produces additional ^{17}O heavy O_2 (slowly enough for water between 50 and 85m depth to be well-mixed but separated from the surface by the seasonal pycnoline). The increased $^{18}\delta$ values of O_2 below the mixed layer suggest active aerobic respiration in this area (does not affect $^{17}\Delta$). The $^{18}\delta$ gradient from 50m to 85m depth could indicate that respiration rates are higher than the mixing rates of the water in this depth interval, and that respiration is higher at greater depth. However, the low O_2 concentration (<50μM at 80m) likely affects accurate determination of $^{18}\delta$, and the difference might be insignificant within error. Also, exchange between the mixed layer and thermocline, as well as isotopics effects from loss of O_2 to non-respiratory processes (for example, chemical reaction with Fe^{2+} at the chemocline) are currently poorly constrained, and not taken into consideration.

Overall, the data reported here confirm low rates of primary productivity throughout the water column of the oxic surface waters of Lake Matano, and are consistent with previous observations of low concentrations of chlorophyll and biomass (Sabo et al., 2008; Crowe et al., 2008c). However, an integrated seasonal flux model of oxygen and carbon production and exchange between the surface mixed layer, thermocline and bottom waters would require higher temporal resolution oxygen isotope data over the course of the formation and decline of the seasonal pycnocline.

Acknowledgements

I would like to thank Rachel Stanley for her generous and enthusiastic response to my suggestion of measuring primary productivity in Lake Matano, and for collaborating with

me on this project and running all of the samples (unfortunately, I was no longer at MIT by the time the extraction line was ready). I would also like to thank Shuhei Ono for supporting this collaboration and providing equipment for sampling at Lake Matano, and of course Sean Crowe, CarriAyne Jones and Arne Sturm for the joint field season at the Lake and help with collecting the samples.

5.4 References

Bender, M., Orchardo, J., Dickson, M., Barber, R., Lindley, S., 1999. In vitro O2 fluxes compared with 14C production and other rate terms during the JGOFS Equatorial Pacific experiment. Deep-Sea Research Part I-Oceanographic Research Papers 46 (4), 637–654.

Benson, B. B., Krause Jr, D., 1984. The concentration and isotopic fractionation of oxygen dissolved in freshwater and seawater in equilibrium with the atmosphere. Limnology And Oceanography, 620–632.

Blunier, T., Barnett, B., Bender, M. L., Hendricks, M., Sep. 2002. Biological oxygen productivity during the last 60,000 years from triple oxygen isotope measurements. Global Biogeochemical Cycles 16 (3), 3–1–3–13.

Canfield, D., Bjerrum, C., 2002. Ocean productivity before about 1.9 Gyr ago limited by phosphorus adsorption onto iron oxides. Nature 417 (6885), 159–162.

Crowe, S., Jones, C., Katsev, S., Magen, C., O'Neill, A. H., Sturm, A., Canfield, D., Haffner, G. D., Mucci, A., Sundby, B., Fowle, D. A., Oct. 2008b. Photoferrotrophs thrive in an Archean Ocean analogue. Proceedings of the National Academy of Sciences 105 (41), 15938–15943.

Crowe, S., O'Neill, A. H., Katsev, S., Hehanussa, P., Haffner, G. D., Sundby, B., Mucci, A., Fowle, D. A., 2008c. The biogeochemistry of tropical lakes: A case study from Lake Matano, Indonesia. Limnology And Oceanography 53 (1), 319–331.

Emerson, S., Stump, C., Wilbur, D., Quay, P., 1999. Accurate measurement of O_2, N_2, and Ar gases in water and the solubility of N_2. Marine Chemistry 64 (4), 337–347.

Gao, Y. Q., May 2001. Strange and unconventional isotope effects in ozone formation. Science 293 (5528), 259–263.

Garcia, H., Gordon, L., 1992b. Oxygen solubility in seawater: Better fitting equations. Limnology And Oceanography, 1307–1312.

Hamme, R. C., Emerson, S. R., 2004. The solubility of neon, nitrogen and argon in distilled water and seawater. Deep Sea Research Part I: Oceanographic ....

Hendricks, M., Bender, M., Barnett, B., Nov. 2004. Net and gross O2 production in the southern ocean from measurements of biological O2 saturation and its triple isotope composition. Deep-Sea Research Part I-Oceanographic Research Papers 51, 1541–1561.

Hendricks, M., Reuer, M. K., Barnett, B. A., Bender, M. L., Falkowski, P. G., Jun. 2007a. New estimates of Southern Ocean biological production rates from O2/Ar ratios and the triple isotope composition of O2. Deep-Sea Research Part I-Oceanographic Research Papers 54 (6), 951–974.

Hendricks, M., Reuer, M. K., Barnett, B. A., Bender, M. L., Falkowski, P. G., Jun. 2007b. New estimates of Southern Ocean biological production rates from O2/Ar ratios and the triple isotope composition of O2. Deep-Sea Research Part I-Oceanographic Research Papers 54 (6), 951–974.

Juranek, L. W., 2005. In vitro and in situ gross primary and net community production in the North Pacific Subtropical Gyre using labeled and natural abundance isotopes of dissolved O 2. Global Biogeochemical Cycles 19 (3).

Kaiser, J., 2011. Technical note: Consistent calculation of aquatic gross production from oxygen triple isotope measurements. Biogeosciences.

Katsev, S., Crowe, S., Mucci, A., Sundby, B., Nomosatryo, S., Haffner, G. D., Fowle, D. A., 2010. Mixing and its effects on biogeochemistry in the persistently stratified, deep, tropical Lake Matano, Indonesia. Limnology And Oceanography 55 (2), 763–776.

Konhauser, K. O., Lalonde, S. V., Amskold, L., Holland, H. D., 2007. Was there really an Archean phosphate crisis? Science 315 (5816), 1234–1234.

Laws, E. A., 1991. Photosynthetic quotients, new production and net community production in the open ocean. Deep-Sea Research 38 (1), 143–167.

Luz, B., Barkan, E., 2005. The isotopic ratios O-17/O-16 and O-18/O-16 in molecular oxygen and their significance in biogeochemistry. Geochimica Et Cosmochimica Acta 69 (5), 1099–1110.

Luz, B., Barkan, E., Sep. 2009. Net and gross oxygen production from O2/Ar, 17O/16O and 18O/16O ratios. Aquatic Microbial Ecology 56, 133–145.

Luz, B., Barkan, E., Nov. 2010. Variations of 17O/16O and 18O/16O in meteoric waters. Geochimica Et Cosmochimica Acta 74 (22), 6276–6286.

Luz, B., Barkan, E., Oct. 2011. Proper estimation of marine gross O 2production with 17O/ 16O and 18O/ 16O ratios of dissolved O 2. Geophysical Research Letters 38 (19).

Luz, B., Barkan, E., Bender, M., Thiemens, M., Boering, K., 1999. Triple-isotope composition of atmospheric oxygen as a tracer of biosphere productivity. Nature 400 (6744), 547–550.

Mauersberger, K., 1981. Measurement of heavy ozone in the stratosphere. Geophysical Research Letters.

Nicholson, D. P., Luz, B., Stanley, R. H. R., Barkan, E., Karl, D. M., Quay, P. D., Doney, S. C., 2012. Evaluating triple oxygen isotope estimates of gross primary production at the Hawaii Ocean Time-series and Bermuda Atlantic Time-series Study sites. Journal of Geophysical Research-Oceans 117 (C).

Prokopenko, M. G., Pauluis, O. M., Granger, J., Yeung, L. Y., Jul. 2011. Exact evaluation of gross photosynthetic production from the oxygen triple-isotope composition of O 2: Implications for the net-to-gross primary production ratios. Geophysical Research Letters 38 (14).

Sabo, E., Roy, D., Hamilton, P. B., Hehanussa, P. E., McNeely, R., Haffner, G. D., Dec. 2008. The plankton community of Lake Matano: factors regulating plankton composition and relative abundance in an ancient, tropical lake of Indonesia. Hydrobiologia 615 (1), 225–235.

Stanley, R. H. R., Howard, E. M., Jul. 2013. Quantifying photosynthetic rates of microphytobenthos using the triple isotope composition of dissolved oxygen. Limnology and Oceanography-Methods 11, 360–373.

Stanley, R. H. R., Kirkpatrick, J. B., Cassar, N., Barnett, B. A., Bender, M. L., Oct. 2010. Net community production and gross primary production rates in the western equatorial Pacific. Global Biogeochemical Cycles 24 (4).

Wanninkhof, R., Ledwell, J. R., Broecker, W. S., Mar. 1985. Gas exchange-wind speed relation measured with sulfur hexafluoride on a lake. Science 227 (4691), 1224–1226.

Part II

Cystic Fibrosis and the physiology of slow growth

Chapter 6

Introduction

> The study of the growth of bacterial cultures does not constitute a specialized subject or branch of research: it is the basic method of Microbiology.
>
> Jacques Monod (1949)

Cystic fibrosis (CF) is an autosomal recessive genetic disorder arising from two defect copies of the gene encoding the cystic fibrosis transmembrane conductance regulator. The genetic defect interferes with salt homeostasis throughout the body, leading to excessive water uptake into mucosal membranes. This leaves mucus throughout the body of CF patients dehydrated and significantly more viscous than healthy mucus. The effect is particularly detrimental in the lung, where thick mucus collects over time and allows for progressive colonization of the pulmonary system by a polymicrobial community of opportunistic pathogens, which leads to chronic infection of the airways and contributes to most of the morbidity and mortality associated with CF (Goss and Burns, 2007).

While it is well-established that the physiological state of individual pathogens within the lung plays an important role in microbial persistence and drug tolerance (Hirschhausen et al., 2013; Hart and Winstanley, 2002; Davies, 2002; Nguyen et al., 2011; Baek et al.,

2011), very few direct measurements of actual growth-activity rates of these populations exist in the host. While largely unconstrained, the growth rates and metabolisms of opportunistic pathogens *in vivo* are potentially vsery different from conditions commonly studied in the laboratory, and are likely to change dynamically within the host. A better understanding of how populations grow *in vivo* is crucial to developing representative laboratory tests of potential therapies that produce reliable results and lead to safe and effective treatment strategies (Harrison, 2007).

In Geomicrobiology, a number of techniques have been developed to study the growth and metabolism of microbial populations in difficult environments using tools from microbial ecology and stable isotope geochemistry. These techniques can provide unique new insights into the growth rates of microbial communities in cystic fibrosis infections and inform the appropriate conditions to study in laboratory experiments. However, the complex, organic rich mucus environment of CF infections provides an obstacle for the use of traditional carbon- or nitrogen-based isotopic tracers. Chapter 7 thus introduces hydrogen isotope labeling as a new tool for measuring microbial growth, and focuses on the potential of using heavy water as a metabolic tracer for lipid biosynthesis, discussing the conceptual approach, laboratory verification, potential impact and limitations of this technique. Heavy water provides an ideal isotopic tracer for complex environments like infections, which are often saturated with bioavailable carbon and nitrogen. Heavy water minimally alters any aquatic chemical environment (due to D_2O being the label), is an equally universal substrate for all forms of life, and can be used safely within biological systems (Kushner et al., 1999b; Jones and Leatherdale, 1991a; Steinhauser and Lechene, 2013).

^2H incorporation into bacterial fatty acids provides a bulk measure of microbial activity, but cannot provide insight into growth heterogeneity within a target population. While it is likely that the physiological states of individual cells in such complex communities vary, little is known about the extent of this variation within the CF lung. Given the

hypothesized correlation between physiological diversification and antimicrobial resistance, it is highly desirable to know the extent of *in situ* heterogeneity in the metabolic states of individual cells at different stages of infection. Multi-isotope secondary ion Imaging Mass Spectrometry (MIMS or nanoSIMS) provides one of the most sensitive and precise analytical methods available for the study of elemental and isotopic composition at high spatial resolution. While primarily applied in the study of spatiometabolic activity of microbial communities in environmental systems (Pernthaler et al., 2008a; Orphan et al., 2009; Dekas et al., 2009; Dekas and Orphan, 2011; Dekas et al., 2013), as well as symbiotic microbe-animal interactions (Lechene et al., 2007; Kuypers, 2007; Pernice et al., 2012), this technique poses tremendous potential for application in the quantitative study of metabolic processes of infectious communities. Examples of applications in medical research to date include studies of stem cell division and metabolism in mice (Steinhauser et al., 2012; Gormanns et al., 2012), protein renewal in kidney cells (Lechene et al., 2006), and microbial activity studies of oral biofilms (Spormann et al., 2008). As evidenced by this accelerating body of work since the first applications of MIMS/nanoSIMS, this technique could be useful far beyond its original purpose in disciplines as diverse as geobiology, biogeochemistry, host-microbe interactions and biomedical research (Orphan and House, 2009; Steinhauser and Lechene, 2013; Hoppe et al., 2013). However, the application to potentially slow-growing, diverse microbial communities in complex mucus samples likewise limits the use of carbon and nitrogen isotope tracers. Chapter 8 thus establishes the framework for using dual hydrogen and nitrogen isotope labeling in secondary ion mass spectrometric analyses of single cells as well as cells embedded and thin-sectioned in acryl.

Chapter 9 finally presents the application of these new techniques to study microbial activity rates in the lungs of cystic fibrosis patients.

References

Baek, S.-H., Li, A. H., Sassetti, C. M., May 2011. Metabolic regulation of mycobacterial growth and antibiotic sensitivity. Plos Biology 9 (5).

Davies, J. C., 2002. *Pseudomonas aeruginosa* in cystic fibrosis: pathogenesis and persistence. Paediatric respiratory reviews.

Dekas, A. E., Chadwick, G. L., Bowles, M. W., Joye, S. B., Orphan, V. J., Aug. 2013. Spatial distribution of nitrogen fixation in methane seep sediment and the role of the ANME archaea. Environmental Microbiology.

Dekas, A. E., Orphan, V. J., 2011. Identification of diazotrophic microorganisms in marine sediment via fluorescence in situ hybridization coupled to nanoscale secondary ion mass spectrometry (FISH-NanoSIMS). Methods in enzymology 486, 281–305.

Dekas, A. E., Poretsky, R. S., Orphan, V. J., Oct. 2009. Deep-sea archaea fix and share nitrogen in methane-consuming microbial consortia. Science 326 (5951), 422–426.

Gormanns, P., Gormanns, P., Reckow, S., Reckow, S., Poczatek, J. C., Poczatek, J. C., Turck, C. W., Turck, C. W., Lechene, C. P., 2012. Segmentation of multi-isotope imaging mass spectrometry data for semi-automatic detection of regions of interest. PLoS ONE.

Goss, C. H., Burns, J. L., 2007. Exacerbations in cystic fibrosis center. 1: Epidemiology and pathogenesis. Thorax 62 (4), 360–367.

Harrison, F., 2007. Microbial ecology of the cystic fibrosis lung. Microbiology.

Hart, C. A., Winstanley, C., 2002. Persistent and aggressive bacteria in the lungs of cystic fibrosis children. British Medical Bulletin 61 (1), 81–96.

Hirschhausen, N., Block, D., Bianconi, I., Bragonzi, A., Birtel, J., Lee, J. C., Dübbers, A., Küster, P., Kahl, J., Peters, G., Kahl, B. C., Dec. 2013. Extended Staphylococcus aureus persistence in cystic fibrosis is associated with bacterial adaptation. International Journal of Medical Microbiology 303 (8), 685–692.

Hoppe, P., Cohen, S., Meibom, A., May 2013. NanoSIMS: Technical aspects and applications in cosmochemistry and biological geochemistry. Geostandards and Geoanalytical Research 37 (2), 111–154.

Jones, P. J., Leatherdale, S. T., Apr. 1991a. Stable isotopes in clinical research: safety reaffirmed. Clinical science (London, England : 1979) 80 (4), 277–280.

Kushner, D. J., Baker, A., Dunstall, T. G., Feb. 1999b. Pharmacological uses and perspectives of heavy water and deuterated compounds. Canadian Journal Of Physiology And Pharmacology 77 (2), 79–88.

Kuypers, M. M. M., Sep. 2007. Microbiology. Sizing up the uncultivated majority. Science 317 (5844), 1510–1511.

Lechene, C. P., Hillion, F., McMahon, G., Benson, D., Kleinfeld, A. M., Kampf, J. P., Distel, D., Luyten, Y., Bonventre, J., Hentschel, D., Park, K. M., Ito, S., Schwartz, M., Benichou, G., Slodzian, G., 2006. High-resolution quantitative imaging of mammalian and bacterial cells using stable isotope mass spectrometry. Journal of Biology 5 (6), 20.

Lechene, C. P., Luyten, Y., McMahon, G., Distel, D. L., Sep. 2007. Quantitative imaging of nitrogen fixation by individual bacteria within animal cells. Science 317 (5844), 1563–1566.

Monod, J., 1949. The growth of bacterial cultures. Annual Reviews in Microbiology 3 (1), 371–394.

Nguyen, D., Joshi-Datar, A., Lepine, F., Bauerle, E., Olakanmi, O., Beer, K., McKay, G., Siehnel, R., Schafhauser, J., Wang, Y., Britigan, B. E., Singh, P. K., Nov. 2011. Active starvation responses mediate antibiotic tolerance in biofilms and nutrient-limited bacteria. Science 334 (6058), 982–986.

Orphan, V. J., House, C. H., Jun. 2009. Geobiological investigations using secondary ion mass spectrometry: microanalysis of extant and paleo-microbial processes. Geobiology 7 (3), 360–372.

Orphan, V. J., Turk, K. A., Green, A. M., House, C. H., Jul. 2009. Patterns of 15N assimilation and growth of methanotrophic ANME-2 archaea and sulfate-reducing bacteria within structured syntrophic consortia revealed by FISH-SIMS. Environmental Microbiology 11 (7), 1777–1791.

Pernice, M., Meibom, A., Van Den Heuvel, A., Kopp, C., Domart-Coulon, I., Hoegh-Guldberg, O., Dove, S., Jan. 2012. A single-cell view of ammonium assimilation in coral–dinoflagellate symbiosis. The ISME Journal 6 (7), 1314–1324.

Pernthaler, A., Dekas, A. E., Brown, C. T., Goffredi, S. K., Embaye, T., Orphan, V. J., 2008a. Diverse syntrophic partnerships from-deep-sea methane vents revealed by direct cell capture and metagenomics. Proceedings of the National Academy of Sciences of the United States of America 105 (19), 7052–7057.

Spormann, A. M., Behrens, S., Losekann, T., Pett-Ridge, J., Weber, P. K., Ng, W.-O., Stevenson, B. S., Hutcheon, I. D., Relman, D. A., May 2008. Linking microbial phylogeny to metabolic activity at the single-cell level by using enhanced Element Labeling-catalyzed reporter deposition Fluorescence *In Situ* Hybridization (EL-FISH) and NanoSIMS. Applied and Environmental Microbiology 74 (10), 3143–3150.

Steinhauser, M. L., Bailey, A. P., Senyo, S. E., Guillermier, C., Perlstein, T. S., Gould, A. P., Lee, R. T., Lechene, C. P., 2012. Multi-isotope imaging mass spectrometry quantifies stem cell division and metabolism. Nature 481 (7382), 516–U131.

Steinhauser, M. L., Lechene, C. P., Aug. 2013. Quantitative imaging of subcellular metabolism with stable isotopes and multi-isotope imaging mass spectrometry. Seminars in Cell and Developmental Biology 24 (8-9), 661–667.

Chapter 7

Hydrogen isotope labeling as a novel tracer for growth in microbial ecology

7.1 Introduction

Stable isotope labeling is a key tool in microbial ecology that provides insights into the flux of carbon, nitrogen and sulfur through microbial communities and entire ecosystems. In an era where molecular techniques provide powerful tools for studying microbial activity in well-understood microbial systems, stable isotope techniques are the key to pushing the frontiers of what we understand about microbial activity in complex, dynamically changing, poorly-explored environments. In these systems, quantiative insights into basic physiological constraints (such as growth rates and nutrient fluxes) are the first step towards making these environments accessible to representative study in the lab and developing well-informed molecular tools that, in turn, can provide higher-resolution (at the species, or even gene level) insights into specific environmental processes.

For example, ribosomal RNA (rRNA) provides a powerful tool for measuring species-specific abundances of ribosomes, which can be linked to microbial activity patterns for well-understood organisms in relatively static systems. However, rRNA concentrations don't scale linearly with growth rates across taxa and are limited as a reliable indicator of metabolic state in microbial communities, slow-growing/dormant cells or dynamically changing environments (Blazewicz et al., 2013; Ecker and Schaechter, 1963), mostly because our understanding of how these conditions affect this molecular proxy are limited.

Isotope labeling techniques provide an approach for measuring biosynthesis directly, due to the nature of a chemically-identical but isotopically-enriched tracer whose incorporation into biomass is dictated directly by biological activity. Additionally, analytical techniques developed for the study of minute differences in naturally occurring isotopic variations provide exceedingly high sensitivity for the incorporation of minute amounts of an isotopically-enriched tracer. However, traditional isotopic labels face two major drawbacks for the study of metabolic activity in microbial communities. First, labeled substrates can change the nutrient availability in an environment, which biases measures of activity towards organisms that can quickly respond to changes in the added substrate. For example, the quantitative use of nitrogen and carbon as tracers is often limited by a) their differential use in communities with mixed metabolisms (preference by certain members of the community for a specific organic or inorganic carbon or nitrogen source), and b) the alteration of nutrient availability by the isotopic tracer (adding for example bioavailable nitrogen to a nitrogen starved community). Second, isotopic tracers do not easily provide phylogenetic information to tease apart the differential contribution of the various members of a microbial community, unless enrichment is high enough to make biomolecules amenable to preparatory separation techniques (as successfully employed in stable isotope probing; e.g., Kreuzer-Martin (2007); Whiteley et al. (2006); Dumont and Murrell (2005); Radajewski et al. (2000)), which negates their potential in the analysis of slow-growing or low-spike communities.

Here, we discuss the use of hydrogen isotope labeling with deuterated water as an important new addition to the isotopic toolkit available to microbial ecologists. This tool provides a labeling technique that minimally alters any aquatic chemical environment (due to D_2O being the label), can be administered with strong labels even in minimal addition (natural background is very low), is an equally universal substrate for all forms of life even in complex, carbon and nitrogen saturated systems, and can be combined with other isotopic tracers (e.g. Wegener et al., 2012; Kellermann et al., 2012). Additionally, while hydrogen exchanges rapidly in reactive groups and most O-^{2}H, N-^{2}H and S-^{2}H bonds (especially all acidic or basic functional groups) (Thomas, 1971; Katz, 1960), it is stably incorporated in many, virtually non-exchangable C-^{2}H bonds (Sessions et al., 2004) that can be used in compound specific isotope analyses of organic molecules to provide coarse phylogenetic resolution of microbial activity over a tremendous dynamic range.

Most importantly, ^{2}H in the form of heavy water (D_2O) can be administered easily and safely in environmental as well as within biological systems (Kushner et al., 1999a; Jones and Leatherdale, 1991a; Steinhauser and Lechene, 2013). It mixes well, and diffuses rapidly in aquatic environments. Additionally, cell water equilibrates within minutes or less in response to an osmotic gradient, as water exchanges readily across the lipid bilayer and through specific water transport proteins (aquaporins) (Verkman, 2013).

Lastly, deuterated compounds (especially water) have been produced in large quantities because of the nuclear industry since the discovery of deuterium by Harold Urey in 1931 (published in Urey et al., 1932b[1]). This makes the purchase and application of heavy water (and other deuterated compounds) easily affordable and has already established deuterium as an important tool in biochemical research (Kushner et al., 1999a).

Here, we present an overview of the conceptual approach to stable isotope labeling in the study of microbial activity in general, and with D_2O in particular. We provide a detailed discussion of the theoretical basis, experimental approach, analytical challenges,

[1]A feat that earned Harold Urey the Nobel Prize in Chemistry only three years later, and is largely to credit with inspiring his broader interest in many aspects of isotope geochemistry.

scientific opportunity and quantitative caveats posed by D_2O as an isotopic tracer, and present data on its experimental verification in continuous culture systems.

7.2 Theoretical model for the incorporation of isotope tracers

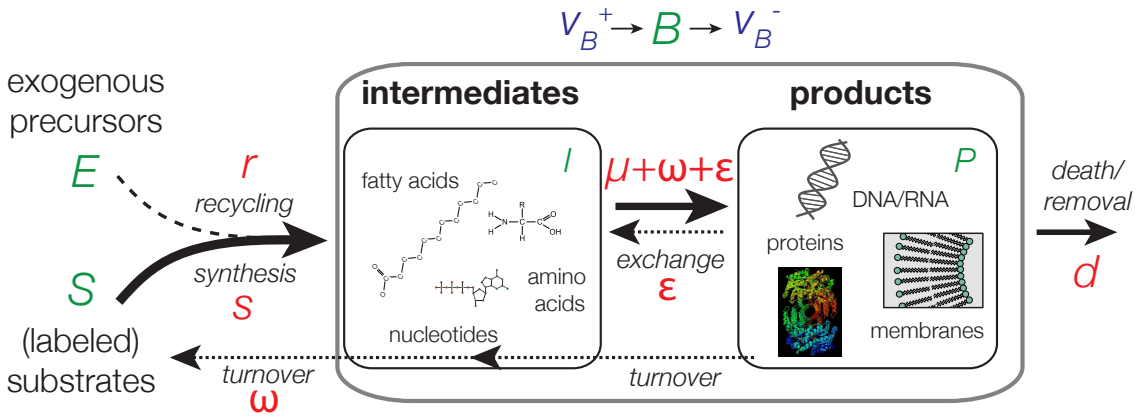

Figure 7.1 – Flow of isotopically-labeled nutrients through a biological system. Most isotopic tracers employed in environmental studies of microbial activity are simple substrates (**S**: $^{15}NH_4^+$, HCO_3^-, D_2O, etc.) that enter the biological system by *de novo* synthesis of cellular intermediates (**I**: simple organic acids, amino acids, nucleotides, fatty acids, etc.) that are turned into cellular components for replication (**P**: proteins, membranes, DNA). Biomass (**B** = **P** + **I**, i.e. the bulk cells) is produced with rate constant **μ** (often called the specific growth rate) and removed with death/removal rate **d** (cells removed for example by predation, death or direct physical removal). This simple model can be further expanded by taking into account the recycling of exogenous precursors (**E**, rate **r**) as well as the turnover of biomolecules (rate **ω**), both pictured in this overview cartoon and discussed in more detail in section 7.4.6. The presence, branching pattern, and exchange flux (**ε**) between specific pools of biosynthetic intermediates represents another layer of complexity that is addressed in section 7.4.5. Legend: the different pools are highlighted in green (**E, S, I, P, B**), rate constants are highlighted in red (**s**, **μ**, **d**, **r**, **ω**) and fluxes in and out of reservoirs are highlighted in blue ($\mathbf{v_B}^{+/-}$).

Figure 7.1 illustrates a simplified view of the flow of isotopically-labeled substrates through a biological system, such as, for example, a population of microorganisms. An isotope label administered as a pulse of isotopically-enriched substrate will propagate through this system as a function of the kinetic rates (all in units of reciprocal time) that govern biosynthesis, degradation and death. Typically, microbial activity is assessed by

measuring the incorporation of the stable isotope label into the bulk biomass B over time. The flux into this overall cellular pool can be considered in terms of the rate of biosynthesis s from (labeled) substrates and the rate of recycling r of exogenous precursors. s and r combine to form the overall biosynthetic rate, or specific growth rate μ (which signifies cellular replication), plus excess biosynthesis (which compensates for degradation due to turnover of proteins or lipids, etc. and can be viewed as part of maintenance). The flux out of B comprises both losses due to turnover degradation/maintenance ω as well as any type of physical removal or straight-out death d of individual cells in the population. The following equations summarize the flux in (+) and out (-) of the total biomass B.

$$\begin{aligned} v_B^+ &= (s+r)\cdot B = (\mu+\omega)\cdot B \\ v_B^- &= (d+\omega)\cdot B \end{aligned} \tag{7.1}$$

Based on the fluxes outlined in equation 7.1, the set of differential equations describing the rate of change in total biomass B and the rate of change in new biomass B_{new} is the difference between the synthesis and degradation fluxes, in the case of B_{new} weighed appropriately by the fraction of new biomass in their source pools:

$$\begin{aligned} \frac{dB}{dt} &= v_B^+ - v_B^- = (\mu - d)\cdot B \\ \frac{dB_{new}}{dt} &= f_S \cdot v_B^+ - f_{B_{new}} \cdot v_B^- = \left[f_S\,(\mu+\omega) - f_{B_{new}}\,(d+\omega)\right]\cdot B \end{aligned} \tag{7.2}$$

with the fraction $f_{B_{new}}$ of new vs. total biomass in B $\left(f_{B_{new}} = \frac{B_{new}}{B}\right)$ weighing the flux v_B^- of new biomass out of B, and the fraction f_S of substrate-derived (new) vs. substrate-derived + recycled (total) weighing the flux v_B^+ into B $\left(f_S = \frac{s}{r+s}\right)$. These expressions can be used to obtain a differential equation for the time-dependent fraction of new biomass

using the quotient rule and substituting Eqs. 7.2 to arrive at:

$$\begin{aligned}\frac{df_{B_{new}}}{dt} &= \frac{\partial}{\partial t}\left(\frac{B_{new}}{B}\right) = \frac{1}{B}\frac{dB_{new}}{dt} - \frac{B_{new}}{B^2}\frac{dB}{dt} = \frac{1}{B}\left(\frac{dB_{new}}{dt} - f_{B_{new}}\frac{dB}{dt}\right) \\ &= f_S\,(\mu+\omega) - f_{B_{new}}\,(d+\omega) - f_{B_{new}}(\mu-d) \\ &= (f_S - f_{B_{new}})\cdot(\mu+\omega)\end{aligned} \tag{7.3}$$

Integration of these differential equations readily leads to a solution for the biomass $B(t)$ and the accumulated fraction of new biomass $f_{B_{new}}(t)$ in the system as a function of time since t_0 :

$$\begin{aligned}B\,(t) &= B_0 \cdot e^{(\mu-d)\cdot t} \\ f_{B_{new}}(t) &= f_S \cdot \left(1 - e^{-(\mu+\omega)\cdot t}\right)\end{aligned} \tag{7.4}$$

When an isotopic label is added to the nutrient pool at t_0, we can use this relation for the fraction of new biomass $f_{B_{new}}$ to derive the isotopic mass balance[2] between the original and new material to get to the temporal evolution of the isotopic composition of the bulk biomass:

$$\begin{aligned}{}^{x}F_B(t) &= \frac{B_{new}\cdot {}^{x}F_{new} + B_{old}\cdot {}^{x}F_{old}}{B} \\ &= f_{B_{new}}(t)\cdot\alpha_{B/S}\cdot {}^{x}F_L + (1 - f_{B_{new}}(t))\cdot {}^{x}F_B(t_0) \\ &= f_S\cdot\left(1 - e^{-(\mu+\omega)\cdot t}\right)\cdot\left(\alpha_{B/S}\cdot {}^{x}F_L - {}^{x}F_B(t_0)\right) + {}^{x}F_B(t_0)\end{aligned} \tag{7.5}$$

where ${}^{x}F_B$ is the fractional abundance of the isotope label (e.g. x = 2 (^{2}H), 13 (^{13}C), 15 (^{15}N)) in the biomass at time t_0 (isotopic composition of the population prior to pulse labeling) and at time t after the spike, ${}^{x}F_L$ is the fractional abundance of the

[2]Here in terms of fractional abundances. The use of mass balance approximation with isotopic values in δ-notation is discouraged for calculations involving strong isotope labels. See section D.5.1 in Appendix D for details.

isotope label in the spiked substrate pool, and $\alpha_{B/S}$ [3]is the fractionation factor associated with biosynthetic incorporation of the substrate into biomass. The inverse expression for calculating the specific growth rate μ from isotopic measurements is readily derived as

$$\mu = -\ln\left(1 - f_S^{-1} \cdot \frac{{}^{x}F_B(t) - {}^{x}F_B(t_0)}{\alpha_{B/S} \cdot {}^{x}F_L - {}^{x}F_B(t_0)}\right) \cdot t^{-1} - \omega \tag{7.6}$$

We can use Equations 7.5 and 7.6 to evaluate the incorporation of an isotopic tracer due to microbial activity, but before applying these formulae, it is important to discuss their assumptions, and useful to highlight some of their implications.

7.2.1 Assumptions

- *All flux rates (μ, d, ω, $s + r$) are time-invariant over the labeling interval.* For this model to apply, the rates have to be constant (however, the fluxes and pool size are not fixed, as discussed shortly). This implies, for example, that over the labeling interval, the growth rate – whatever it may be for the population at the time (set by the metabolic constraints imposed on the population) – is assumed to remain essentially constant. This also assumes by extension that since the rates are constant, the isotopic effects expressed during overall biosynthesis ($\alpha_{B/S}$) can be assumed to remain constant.

- *The proportion of recycling rate vs. de novo synthesis rate is time-invariant ($f_s = const$).* This assumption implies that it must be possible to consider the dietary habits of the population between recycling exogenous materials and *de-novo* biosynthesis constant over the labeling interval. In practice, this requires that any change in nutrient availability in the environment does not significantly alter metabolism over the course of a labeling experiment. However, it is possible to integrate the

[3] $\alpha_{B/S}$ is usually reported/known in terms of $\alpha_{B/S} = \frac{R_B}{R_S}$; see section D.5.2 in Appendix D for details on how to calculate this effect exactly, and information about the error introduced if using the approximation $\alpha_{B/S} \cdot F_S$

differential equations in 7.2 with a time-dependent parametrization of f_s if it is known to change in time-dependent manner during the labeling interval, in similar manner as derived for the isotopic label strength ${}^{x}F_L$.

- *The isotopic labeling strength (${}^{x}F_L$) is time-invariant.* This model assumes that the isotopic spike is instantaneously distributed into the bioavailable substrate pool (that is, the material the cells actually take up and use is spiked without time-delay), the isotope label is not diluted out of the substrate pool over time by any process including the potential influx of unlabeled material from turnover ω, and the consumption of the substrate does not significantly alter its isotopic composition. This is a reasonable assumption during relatively long labeling times with highly diffusible labels in a closed system where turnover ω can be expected to release relatively little material to dilute the labeled pool. However, it is also possible to include a time-dependent parametrization of ${}^{x}F_L$ if it is known to change in time-dependent manner during the labeling interval. The derivation follows from Equations 7.3, 7.4 and 7.5, and is illustrated with a dilution model for the isotopic label strength (${}^{x}F_L(t) = {}^{x}F_{L0} \cdot e^{-kt}$):

$$\begin{aligned}\frac{B_{new} \cdot {}^{x}F_{new}}{B} &= \int \mathrm{d}f_{B_{new}} \cdot \alpha_{B/S} \cdot {}^{x}F_L(t)\,\mathrm{d}t \\ &= \int f_S \cdot (\mu+\omega) \cdot e^{-(\mu+\omega)\cdot t} \cdot \alpha_{B/S} \cdot {}^{x}F_{L0} \cdot e^{-k\cdot t}\,\mathrm{d}t \\ &= \alpha_{B/S} \cdot {}^{x}F_{L0} \cdot f_S \cdot \frac{\mu+\omega}{\mu+\omega+k} \cdot \left(1 - e^{-(\mu+\omega+k)\cdot t}\right)\end{aligned} \tag{7.7}$$

with dilution rate constant k, rare isotope fractional abundance of the initial spike ${}^{x}F_{L0}$, and all other variables as previously named. Substituting back into Eq. 7.5

yields

$$
\begin{aligned}
{}^{x}F_{B}^{\#}(t) &= \frac{B_{new} \cdot {}^{x}F_{new} + B_{old} \cdot {}^{x}F_{old}}{B} \\
&= \alpha_{B/S} \cdot {}^{x}F_{L0} \cdot f_S \cdot \frac{\mu + \omega}{\mu + \omega + k} \cdot \left(1 - e^{-(\mu+\omega+k)\cdot t}\right) \\
&\quad + \left(1 - f_S \cdot \left(1 - e^{-(\mu+\omega)\cdot t}\right)\right) \cdot {}^{x}F_{B}(t_0)
\end{aligned}
\tag{7.8}
$$

which provides the basis for modeling the impact of tracer dilution and can be fitted to experimental data numerically but does not have an analytical solution like Equation 7.6 for μ.

- *The biomass removal flux d is unbiased.* It is implicitly assumed that the biomass removal flux d is unbiased; i.e., cells are removed randomly without a preference for older or newer material. Removal thereby reduces the entire bulk pool (and all its components proportionally to their size) without affecting the relative proportions of old and new biomass. As a consequence of this assumption, the removal term d drops out in Equation 7.3.

- *All isotopically analyzed cellular materials are representative of the bulk biomass B.* This assumption needs to be considered carefully when only specific components of a cell are analyzed, or during bulk analysis after significant portions are lost. Intracellular exchange kinetics (ϵ in figure 7.1) and branching patterns of cellular intermediates can cause significant deviations from expected isotope incorporation into individual compounds, and have to be taken into consideration when inferring microbial activity from isotopic enrichments of specific cellular components (such as pools I or P in Figure 7.1, or their components) instead of bulk biomass (see Chen et al. (2012) for a recent discussion of this aspect). Section 7.4.5 provides additional detail on this issue. However, the recycling and exchange ϵ of biosynthetic intermediates within the whole system does not affect the labeling dynamics of the bulk biomass (only exogenous input does), and it is safe to ignore this aspect if it is reasonable to assume that this is captured analytically.

7.2.2 Implications

- *The population itself does not have to be in steady state*. The isotope tracer will be incorporated as a function of growth and turnover ($\mu + \omega$) *regardless* of any temporal changes in the total biomass $B(t)$ (Eq. 7.4). Total biomass can remain the same ($\mu = d$), accumulate ($\mu > d$) or decline ($\mu < d$) over the course of a labeling experiment without affecting this measurement. This also implies that a single pulse labeling experiment *cannot* provide a constraint for the removal/death rate d, which drops out in Eq. 7.3 without any additional constraints. Section D.4 in Appendix D illustrates this point in detail.

- *A labeling experiment usually measures the biosynthetic activity rate (apparent growth rate)*. Without knowing either the turnover/maintenance rate ω or the specific growth rate μ of the population *a priori*, the only quantity that can be measured from isotopic enrichment is the biosynthetic activity or apparent growth rate $\mu_{act} = \mu + \omega$, which *always* overestimates the true growth rate $(\omega > 0)$. If it is reasonable to assume that turnover/maintenance is negligible ($\omega \ll \mu$), then $\mu \approx \mu_{act}$. This measure also allows an estimate of the apparent generation time of the population $g_{act} = \frac{ln(2)}{\mu_{act}}$. μ and μ_{act} are not to be confused with population net growth/decline $\mu_{net} = \mu - d$, which results from the balance of biomass production and removal processes ($B(t)$ in Eq. 7.4) and cannot be determined without an independent constraint for d. μ_{net} relates to the true generation/doubling time of the population (the time the total biomass would double in size) as $g_{true} = \frac{ln(2)}{\mu_{net}}$.

- *Approximations:* The equations for the isotopic composition of the population over time (7.5 and 7.8) can be approximated by Taylor expansion around $t = 0$ (and

simplifying with $\mu_{act} = \mu + \omega$):

$$
\begin{aligned}
{}^{x}F_B(t) &= \sum_{n=0}^{\infty} \frac{{}^{x}F_B^{(n)}(t_0)}{n!} (t - t_0)^n \\
&= {}^{x}F_B(t_0) + f_S \cdot \left(\alpha_{B/S} \cdot {}^{x}F_L - {}^{x}F_B(t_0)\right) \cdot \mu_{act} \cdot t \\
&\quad - \frac{1}{2} \cdot f_S \left(\alpha_{B/S} \cdot {}^{x}F_L - {}^{x}F_B(t_0)\right) \cdot \mu_{act}^2 \cdot t^2 + ... \\
{}^{x}F_B^{\#}(t) &= {}^{x}F_B(t_0) + f_S \cdot \left(\alpha_{B/S} \cdot {}^{x}F_L - {}^{x}F_B(t_0)\right) \cdot \mu_{act} \cdot t \\
&\quad - \frac{1}{2} \cdot f_S \left(\alpha_{B/S} \cdot {}^{x}F_L \cdot (\mu_{act} + k) - {}^{x}F_B(t_0) \cdot \mu_{act}\right) \cdot \mu_{act} \cdot t^2 + ...
\end{aligned}
\tag{7.9}
$$

As long as incubation times t are relatively small compared to the generation time of the population, second- and higher-order terms are relatively insignificant, and both equations simplify to

$$
\begin{aligned}
{}^{x}F_B(t) &\approx {}^{x}F_B(t_0) + f_S \cdot \left(\alpha_{B/S} \cdot {}^{x}F_L - {}^{x}F_B(t_0)\right) \cdot \mu_{act} \cdot t \\
\mu_{act} &\approx \frac{{}^{x}F_B(t) - {}^{x}F_B(t_0)}{f_S \cdot \left(\alpha_{B/S} \cdot {}^{x}F_L - {}^{x}F_B(t_0)\right)} \cdot t^{-1}
\end{aligned}
\tag{7.10}
$$

This linear approximation always *overestimates* isotope labeling as a function of growth, and consequently *underestimates* biosynthetic activity and *overestimates* apparent generation times as a function of label incorporation (i.e., at a given label incorporation, this approximation projects a lower growth / longer generation time than is actually the case). Section D.5.3 in Appendix D illustrates the errors introduced when using this approximation in greater detail.

7.2.3 The use of D_2O as an isotopic tracer

The use of heavy water as an isotopic tracer provides a unique tool for measuring microbial activity in a diverse range of environments. The label is easy to administer both in environmental and medical contexts, does not distort substrate availability to the benefit of some organisms over others, and is stably incorporated into fatty acids and other

hydrocarbon membrane components with stable C-H bonds during active metabolism. Additionally, its low natural abundance ($^2F_{nat} = 156ppm$, de Laeter et al., 2003) enables relatively minor isotopic spikes to capture a wide range of microbial activity in a short time span. Figure 7.2 shows the incubation times required to capture an enrichment signal of $\delta_D = 500‰$ with two different isotopic spikes, labeling new biomass with deuterium at $^2F_L = 1\%$ and 15%, for a wide range of microbial populations doubling anywhere from once an hour to once in a hundred years. The model illustrates that a 1% label can easily capture microbial activity rates on a day to year time scale with only a few hours to days of exposure to the label; a 15% label can capture rates on the 100-year time scale within less than a month.

7.3 Materials and methods

All media and reagent solutions used for culturing were autoclaved or filter-sterilized prior to use. All non-consumable glassware used for lipid extraction and derivatization was pre-combusted in a muffle furnace at 550 °C to remove all remaining traces of organic materials potentially adhered to the glass. All heavy water used for labeling experiments was purchased as sterile 70% D_2O solution from Cambridge Isotope Laboratories (#DLM-2259-70-1L).

7.3.1 Bacterial strains and growth media

Culturing experiments were conducted with a well-studied, prototrophic K-12 derivative of *Escherichia coli* (NCM 3722, Soupene et al., 2003), a well studied wild-type clinical isolate of the gram-negative opportunistic pathogen *Pseudomonas aeruginosa* (PA14, RAHME et al., 1995), a clinical isolate of the gram-negative opportunistic pathogen *Stenotrophomonas maltophilia* (Hugh and Leifson, 1963), and a well-studied wild-type

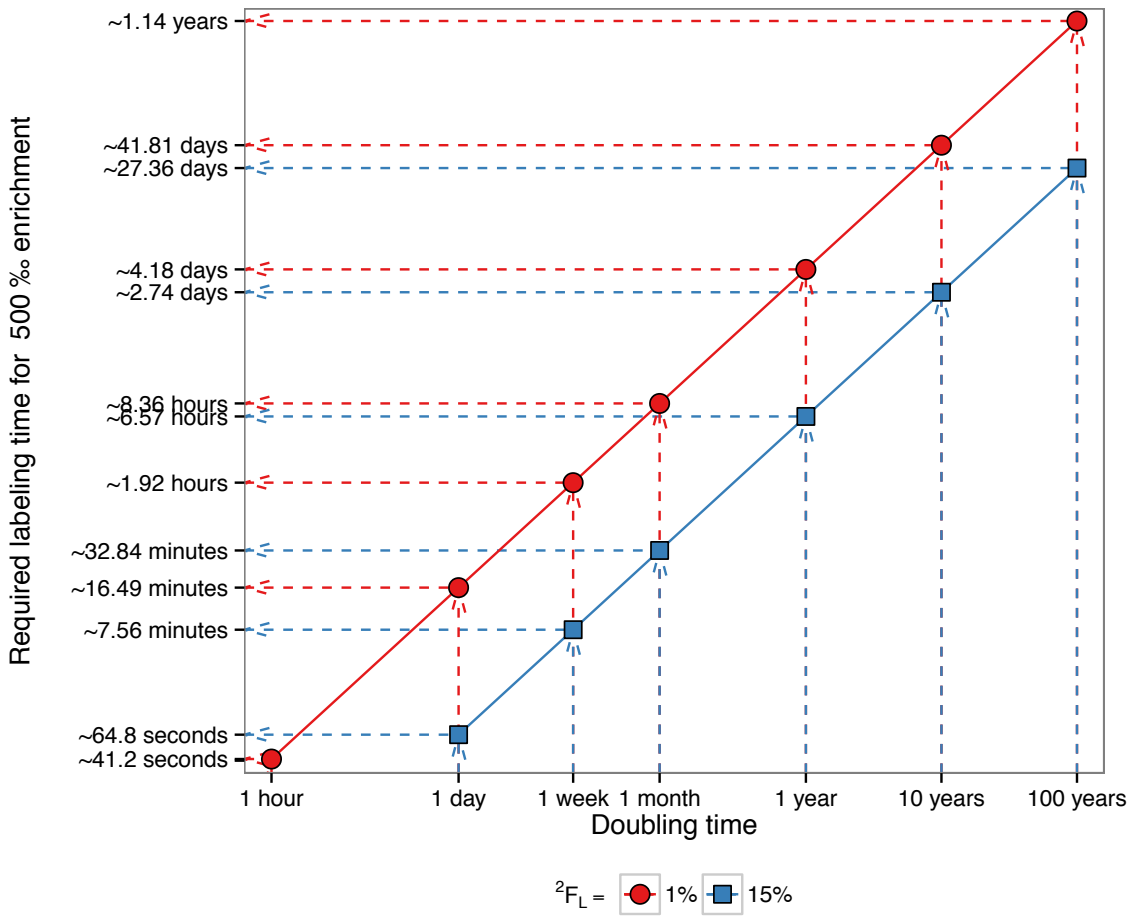

Figure 7.2 – Incubation time requirements. This figure illustrates the incubation times required to reach an isotopic enrichment in deuterium of $\delta_D = 500‰$, depending on the strength of the isotopic label in new biomass and the average generation/doubling time of a microbial population. Details on an interactive version of this plot can be found in Appendix D, section D.6.2

clinical isolate of the gram-positive opportunistic pathogen *Staphylococcus aureus* (MN8, KREISWIRTH et al., 1983).

For routine growth, all strains were grown in a phosphate-buffered minimal medium (hereafter referred to as "minimal") at pH 7.2 containing 2.5 g/L NaCl, 13.5 g/L K_2HPO_4, 4.7 g/L KH_2PO_4, 1 g/L K_2SO_4 and 0.1 g/L $MgSO_4 \cdot 7H_2O$ with 5 mM / 1.35 g/L succinate hexahydrate (*E. coli* and *P. aeruginosa*) or 6.5 mM / 470µL/L glycerol (*S. aureus*) as the carbon source and 10 mM NH_4Cl as the only source of nitrogen. Additionally, the medium

was amended with iron (3.6μM / 1mg/L $FeSO_4 \cdot 7\ H_2O$) complexed by EDTA (8 μM) for *S. aureus* and *P. aeruginosa*. *S. aureus* further exhibits auxotrophy for several amino acids and vitamins (some phenotypic, some genotypic; Aldeen and Hiramatsu (2004); LINCOLN et al. (1995); Mah et al. (1967)). For routine growth of this organism, the medium was further amended with 11.5 mg/L proline, 10mL/L 50x MEM Amino Acid solution (Sigma-Aldrich, #M5550, final amino acid concentrations: 63.2 mg/L arginine, 15.6 mg/L cysteine, 21 mg/L histidine, 26.35 mg/L isoleucine, 26.2 mg/L leucine, 36.3 mg/L lysine, 7.6 mg/L methionine, 16.5 mg/L phenylalanine, 23.8 mg/L threonine, 5.1 mg/L tryptophan, 18.0 mg/L tyrosine, 23.4 mg/L valine) as well as 100μg/L thiamine (B1), 100 μg/L nicotinic acid (B3) and 10 μg/L biotin (B7).

For growth in a simulated "complex" medium, *P. aeruginosa* and *S. aureus* were grown in defined synthetic cystic fibrosis sputum medium (hereafter referred to as "SCFM"). This medium is designed to mimic the average nutritional environment of the cystic fibrosis lung, and was chosen as a representative model medium that simulates a clinical context more closely. The medium was prepared as described in (Palmer et al., 2007); briefly, it is a MOPS buffered medium (adjusted to pH 6.8) that contains basic salts, a mixture of amino acids (about ∼19mM equivalents in total), glucose (3.2mM) and lactate (9.3 m). Due to the high concentration of amino acids, microbial growth in this medium tends to raise the pH significantly (>pH 8), and this medium was buffered with 50mM instead of 10mM MOPS in this study. Like in minimal medium, SCFM was amended with the essential vitamins for growth experiments with *S. aureus*.

All culturing experiments were conducted aerobically at 37ºC with agitation, and were inoculated from fresh (exponential or early stationary phase) cultures grown on the same medium and verified microscopically to be axenic. Growth was monitored by measuring optical density at 600nm. Cells intended for isotopic analysis were generally harvested by centrifugation at 5000rpm for 10min (at 4ºC), washed by resuspension in 1x phosphate buffered saline solution, repelleted and frozen immediately at -80ºC until lipid extraction

and analysis.

7.3.2 Experimental Setup

7.3.2.1 Water fraction factor

To determine the isotopic composition of new biomass synthesized by *E. coli, P. aeruginosa* and *S. aureus* in medium with source water of a given isotopic composition, the organisms were grown aerobically in 10mL replicate batch cultures in source water of different isotopic compositions. Cells were harvested in exponential or early stationary phase, pelleted by centrifugation and frozen at -80°C until lipid extraction and analysis. *P. aeruginosa* was additionally grown in separate chemostats with identical dilution rates but source waters of different isotopic compositions. Cells were harvested in steady-state, pelleted and frozen until lipid extraction and analysis.

7.3.2.2 Continuous culture

For growth experiments in continuous culture, all medium was amended with 100µL/L Antifoam 204 (Sigma Aldrich, #A6426) for growth of *E. coli,* and with 500µL/L for *P. aeruginosa* and *S. aureus*. A Sartorius Biostat QPlus autoclavable chemostat system was set up for continuous culture, with medium supplied at different flow rates (depending on the desired dilution rate) by high-precision Watson Marlow peristaltic pumps. Overflow from a reactor vessel was continuously removed to maintain the vessel at a fixed volume (measured precisely after termination of each experiment, usually between 500 and 600mL). A reactor vessel was equipped with heating jacket, exhaust gas condenser, temperature, pH, redox and pO_2 sensors, and was autoclaved fully assembled and kept as a closed, sterile system after autoclaving (with supply medium, overflow waste, gas inlet and exhaust also protected by sterile air filters). During operation, a reactor vessel was kept at 37°C, stirred at 500rpm and continuously sparged with filtered air at a flow rate of 1 L/min. Reactor vessel medium supply lines were maintained at ∼90°C for 5cm tubing length right

before the vessel inlet via a custom-made aluminum heating block and heating tape to prevent any potential growth in the medium supply lines. pH probes were calibrated prior to autoclaving, and pO_2 probes were calibrated after autoclaving and at least 2 hours after connection to the amplifier. Uninoculated reactor vessels were first sparged with pure N_2 to calibrate 0% oxygen saturation, and then with air until signal equilibration for 100% oxygen saturation. Reactor vessels were run at least 24 hours prior to inoculation to confirm sterility and then inoculated from a single colony pre-grown in the same medium (via a septum port sterilized with 70% ethanol). Slow continuous flow of medium was started with inoculation, and set to and maintained at the experimental dilution rate once cultures reached exponential growth. Redox potential, pH and dissolved oxygen were monitored continuously and optical density was measured periodically in aliquots withdrawn aseptically from vessel overflow. Experiments (for example isotope spiking) were conducted only once cultures reached steady state as gauged from the monitored physiological parameters, usually after 4-6 generation times ($\sim$3-4 complete medium turnovers). Purity of the culture was checked periodically by light and epifluorescence microscopy. The dilution rate of each vessel was calculated from the gravimetric medium flow rate and the weight of the total volume in the vessel (measured immediately after conclusion of an experiment).

7.3.2.3 Isotope tracer incorporation

For isotope labeling experiments, chemostat reactor vessels were spiked with small aliquots of 70% D_2O (1 or 2mL depending on the experiment) once at steady-state, and 5-10 mL samples were withdrawn from the reactor vessel at regular time intervals afterwards using a sterile sampling device (generating suction with a sterile filter and 30mL syringe). Cell growth was arrested immediately after sample withdrawal by adding the sample directly into an equal volume of ice. Cells were harvested, washed once and frozen immediately. Sampling intervals were never as small and sample sizes as large as to exceed the rate of

medium replenishment by continuous flow.

7.3.2.4 Fatty acid recycling

Experiments aimed at assessing the recycling of exogenous fatty acids by *S. aureus* were carried out in 250 mL flasks with 100 mL of the minimal medium. The glycerol concentration in the medium was increased to 10mM and the medium was amended with no exogenous fatty acids (control), 100µg perdeuterated pentadecanoic acid (C15:0 FA), or 100µg perdeuterated octadecanoic acid (C18:0) from 10 mg/mL stock solutions in DMSO (addition of 100µL the solvent alone did not have affect growth). The perdeuterated fatty acids were purchased from CDN Isotopes and are completely deuterated ($CD_3(CD_2)_{13}COOH$ and $CD_3(CD_2)_{16}COOH$, respectively) with the sole exception of the carboxylic acid hydrogen (which exchanges too quickly in solution to retain a label). Cells were harvested in early stationary phase ($OD_{600} \approx 0.8$), washed twice, and frozen immediately.

7.3.3 Analytical Procedures

7.3.3.1 Isotopic composition of water

The isotopic composition of water in all culture media was measured from 1mL aliquots using a Los Gatos Research DLT-100 liquid water isotope analyzer. Samples were analyzed in 4+ replicate analyses with 10 injections each. Samples close to natural abundance isotopic composition were calibrated against four working standards (δ^2H values: $-117‰$, $-11‰$, $+290‰$, $1270‰$) that in turn were calibrated against the VSMOW, GISP, and SLAP international standards (Coplen, 1988). Average precision was $3.2‰$ / $0.5ppm$ (1σ). Samples that were more heavily enriched from isotope tracer work ($\delta^2H > 1270‰$ / ${}^2F > 350ppm$) were calibrated against enriched working standards (${}^2F$ values: $500ppm$, $1000ppm$, $1250ppm$, $1500ppm$). Average precision was $2.5ppm$ (1σ). The presence of doubly-substituted species (DOD) was not taken into consideration due to fast equi-

libration of water molecules by protonation/deprotonation and consequently negligible abundance of DOD at these levels (${}^2F_{max} = 1500ppm$). Samples beyond this scale were no longer in the linear response range of the instrument, and were analyzed by isotope dilution with natural abundance water of known isotopic composition.

7.3.3.2 Extraction and derivatization of fatty acids

Frozen cell pellets were lyophilized, weighed out into ~1mg aliquots of dry cell mass, and spiked with 10µg of 21:0 phosphatidyl choline as a phospholipid extraction standard. All samples from experiments on water fraction factors and isotope tracer incorporation were transesterified in the presence of an acid catalyst (acetyl chloride in anhydrous methanol, 1:20 v/v) at 100°C for 10 min (Rodríguez-Ruiz et al., 1998; Lepage and Roy, 1986). Samples from experiments on the recycling of exogenous fatty acids were transesterified in the presence of a base catalyst (0.5M NaOH in anhydrous methanol) at room temperature for 10 min (Christie, 1997; Metcalffe and Wang, 1981; Griffiths et al., 2010). Free fatty acids are not transesterified under these basic conditions, which prevented the derivatization of any remaining exogenous perdeuterated free fatty acids not consumed by the microorganisms or removed during washing steps. The resulting fatty acid methyl esters (FAMEs) from all samples were extracted into hexane after addition of a quantification standard (10µg C25:0 FAME), and concentrated under a stream of N_2 at room temperature prior to analysis. All preparation, processing and analysis of samples containing perdeuterated materials was performed in a separate laboratory to avoid any risk for cross-contamination of natural-abundance or isotope-tracer experiments.

7.3.3.3 Identification and analysis

Fatty acid methyl esters (FAMEs) from water-fraction-factor and isotope-tracer experiments were analyzed by gas chromatography/mass spectrometry (GC/MS) on a Thermo-Scientific Trace DSQ equipped with a ZB-5ms column (30m x 0.25mm i.d., film thickness

0.25µm) and PTV injector operated in splitless mode, using He as a carrier gas at 0.8 ml/min. The GC oven was held at 80ºC for 1 minute, ramped at 20ºC/min to 130ºC, and ramped at 5ºC/min to a final temperature of 320ºC (held for 20min). Peaks were identified by comparison of mass spectra and retention times to authentic standards and library data. Fatty acids are reported using the nomenclature z-$C_{x:y}$, where x is the total number of carbons in the fatty acid skeleton (regardless of structure), y is the number of double bonds, and z is a prefix describing additional structural features of the compound. z="cyclo-" identifies fatty acids with cyclopropyl rings, z="i-" (iso-methyl branched) identifies fatty acids that have a methyl branch on the penultimate carbon (second carbon from the tail end), z="a-" (*ante*iso-methyl branched) identifies fatty acids that have a methyl branch on the *ante*-penultimate carbon (third carbon from the tail end). The position and stereochemistry of the double bonds or cyclopropyl rings was not determined (Christie, 2006).

The isotopic composition of the most abundant FAMEs was measured by GC/pyrolysis/isotope-ratio mass spectrometry (GC-ir-MS) on a Thermo-Scientific Delta$^+$ XP with methane of known isotopic composition as the calibration standard and squalene of known isotopic composition as an external standard. Additionally, a multi-compound FAME standard was run every 4-6 samples to verify instrument accuracy and precision. Chromatographic conditions were identical to those from GC/MS analysis except for a thick-film column (ZB-5ms, 30m x 0.25mm i.d., film thickness 1.00µm) and slight modifications to the temperature program to optimize chromatographic separation of key FAMEs for the characteristic lipid profiles of the different species. Peaks were identified based on retention order and relative height based on the GC/MS analysis. Samples that were abundant enough for replicate analyses were analyzed at least in triplicate. All data were corrected for the addition of methyl hydrogen during derivatization. The root-mean-square (RMS) error of the squalene standard was 2.5‰. Relative proportions of fatty acids for isotope mass balance calculations were determined from peak areas corrected for

derivatization and isotopic composition of each analyte.

Samples from recycling experiments were analyzed on a Waters Micromass GCT Premier 6890N equipped with a Zebron-ZB-Wax column (29.5m x 0.25mm i.d., film thickness 0.25µm) and PTV injector operated at a 10:1 split ratio, using He as a carrier gas at 15 ml/min. The GC oven was ramped at 2ºC/min to 200ºC, held for 1min, and ramped at 18ºC/min to a final temperature of 250ºC (held for 7min). Heavily deuterated fatty acids were detected as distinct peaks that eluted earlier than their respective natural abundance counterparts (see section Appendix D.1 for details), and the degree of deuteration was determined from the mass shift of their molecular ions.

7.3.4 Computation / Modeling

Symbolic computations including analytical solutions to differential equations were determined using equation-solving in Wolfram *Mathematica* (v. 9.0). Data processing, analysis, model simulations and plotting were performed in R (R Core Team, 2014) using functionality provided by various analytical and graphical packages (Soetaert et al., 2013; Wickham, 2014a; Wickham and Chang, 2013; Xie, 2013b; Neuwirth, 2011; Dragulescu, 2013).

Hydrogen isotope measurements were recorded in the conventional δ-notation (measuring isotope ratios of analytes against isotope ratios of laboratory reference standards with known isotopic composition relative to VSMOW), but are also converted to fractional abundances using the known isotopic composition of VSMOW ($\frac{^2H}{^1H} = 155.7643ppm$, de Laeter et al. (2003)) to allow consistent reporting and exact mass balance calculations in all isotope tracer experiments[4]. In tables and plots, the fractional abundance of deuterium ^2F is reported in parts per million ($ppm = 10^6 \cdot x$). All conversions were performed using an isotopes R module described in Section A.2 of Appendix A.

[4]See Section D.5.1 in the appendix on the topic of exact mass balance calculations.

7.4 Results and Discussion

7.4.1 Limitations of D_2O as an isotopic tracer

The use of high-strength heavy water labels as tracers for microbial activity is a very desirable option, especially when either short incubation times are of interest (e.g. in high temporal resolution studies of microbial activity response to environmental stimuli, toxins or other effectors), or when very slow microbial activity is the subject matter, such as for example in extreme environments like the deep biosphere (D'hondt, 2002; Morono et al., 2011b; Jørgensen and Boetius, 2007; Hoehler and Jørgensen, 2013). The first concern for the use of such a strong label is biological compatibility. ^2H / deuterium is unique amongst the stable isotopes in its chemical effects on biological systems due to its extreme relative increase in mass from^1H. At high concentrations of ^2H, the heavy isotope starts to significantly affect the solvent properties of water, affecting biological macromolecules in the process. At the same time, there are significant isotopic effects as a consequence of ^2H substituting for ^1H in functional groups, catalytic sites and key substrates. However, these effects don't usually come to bear until D_2O exposure reaches levels that are typically well beyond those relevant for isotope tracer work. Most organisms, including mammals and insects, are usually unaffected by relatively low doses of D_2O ($\sim$10%). Most microorganisms are able to handle much higher concentrations (20-30%), with some groups, including certain phototrophs, capable of adapting to extreme doses of heavy water (>50%) without significant adverse effects (Kushner et al., 1999a). We have found similar capability for tolerating D_2O in experiments with *P. aeruginosa* and *S. aureus,* whose growth rates were not adversely affected by $\sim$20% and $\sim$15% D_2O, and only showed substantial retardation from exposure to 50% D_2O (see Section D.2 of Appendix D for details). We thus consider isotopic spikes as high as 15-20% to be safe for use without any adverse effects, and high label (up to $\sim$35%) to be of reasonable potential

for use if the application necessitates such a strong spike and the potential effects on all relevant organisms is reasonably well-understood.

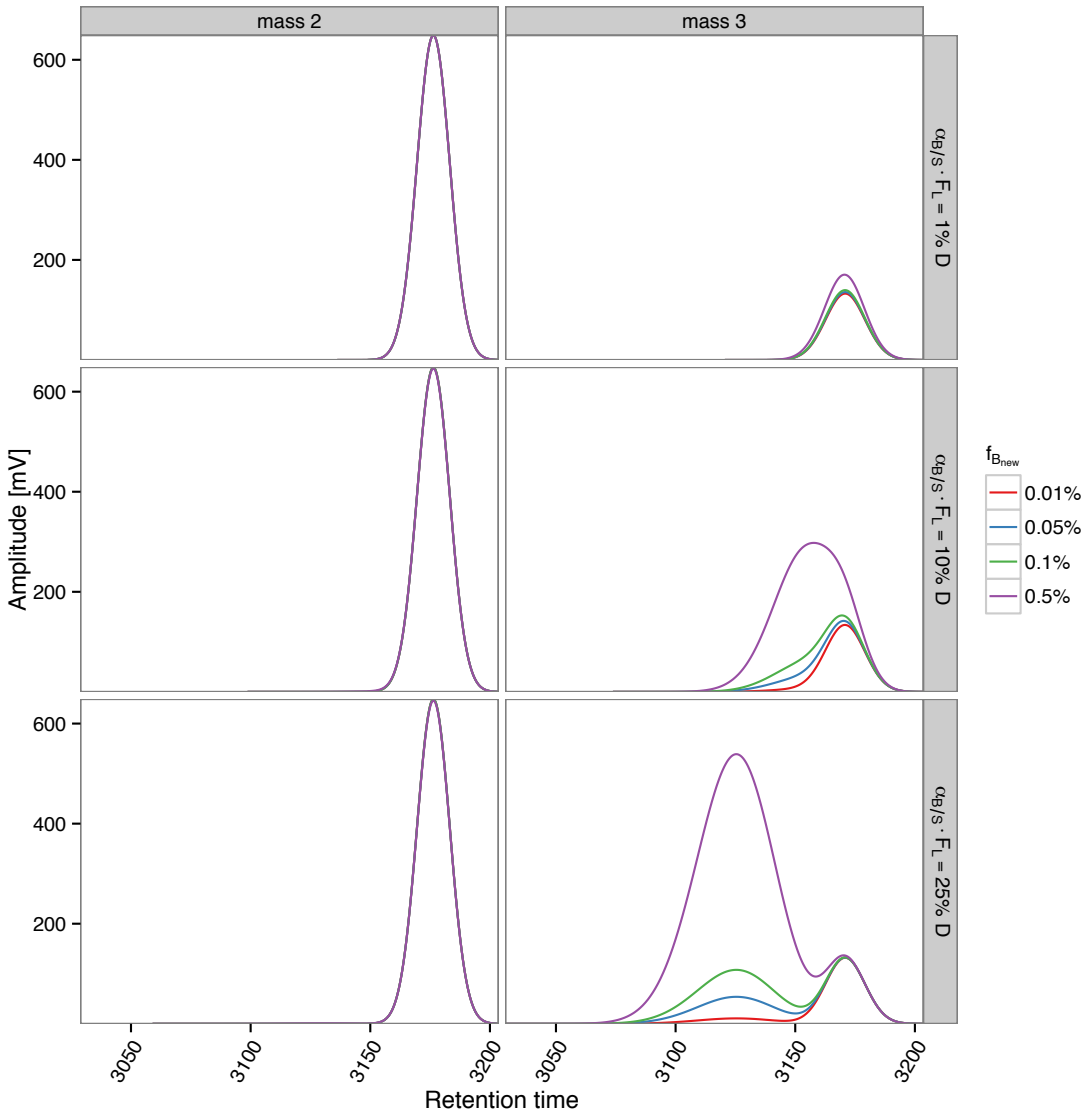

Figure 7.3 – Chromatographic overlap during heavy ^{2}H labeling. This plot models the peak broadening and formation of a double peak in isotope labeling experiments with strong deuterium isotope tracers.

The second concern is analytical in nature, and pertains to measuring growth activity by incorporation of ^{2}H into biological membranes. Typically, compound-specific isotope ratio analysis of hydrogen in organic molecules requires chromatographic separation of

different analytes of interest. However, it is well-established that deuterium substitution has a non-trivial effect on the chromatographic behavior of organic molecules. This effect has been studied in numerous publications, e.g. McCloskey et al. (1967); Rohrer and Olechno (1992); Turowski et al. (2003); Iyer et al. (2004), and is well-appreciated for its potential in separating deuterated isotopologues. In fact, in this study, we take advantage of this effect to resolve exogenous perdeuterated fatty acid compounds of microbial membranes by chromatographic separation (see Section 7.4.6 for details).

In the case of compound-specific hydrogen isotope analysis of relatively "low" enrichment (on the order of hundreds or thousands of ‰, but far from perdeuteration), this phenomenon can have very undesirable side effects. It is important to note that what we tend to think of as a change in overall isotopic composition during isotope enrichment, is actually the mixing of two isotopically distinct pools. These pools (the old biomass and newly synthesized, isotopically-labeled biomass) more or less maintain their distinct isotopic signatures, but the change in their relative proportions leads to overall isotopic enrichment. While tremendous overall isotopic enrichment can be achieved in a short amount of time, it is absolutely crucial to consider the chromatographic effects of deuterium substitution in the new pool on the broadening of the mass 3 signal in the isotopic analysis, in order to capture this microbial activity accurately.

Figure 7.3 illustrates the limitations of strong D_2O spikes. Here, we show a a simulated analysis of a C18:0 fatty acid methyl ester peak affected by different isotopic spikes (chromatographic attributes and signal strengths of the peak taken from an actual analysis of a natural abundance sample analyzed with a slow temperature ramp aimed at increasing resolution). Enrichment is simulated with isotopic spikes that lead to an isotope composition of new biomass of 1%, 10% and 25% ^2H, and relative proportions of the new to total biomass (the actual growth of the microbial population) ranging from 0.01% to 0.5%. It is clear from the simulation that labeling with excessive D_2O requires very careful integration of chromatographic peaks in order to capture the full signal. While this

is technically feasible with due diligence in the case of isolated peaks, most environmental samples have messy chromatograms where such peak broadening might make it impossible to still resolve the isotopic composition of individual analytes. Additional details on the calculations and modeling are presented in Appendix D, Section D.1.

7.4.2 Biological parameters: water fraction factors

For the application of D_2O as a quantitative isotopic tracer for microbial activity, it is important to be able to estimate the isotopic composition of newly synthesized biomass ${}^2F_{B_{new}}$ at a given source water isotopic composition ${}^2F_{water}$. Here, we are interested in determining this relation specifically between microbial lipids ${}^2F_{lipid}$ and source water, with the goal of spiking the source water with D_2O to affect the isotopic composition of lipids in actively synthesizing populations. To first order, ${}^2F_{lipid}$ follows ${}^2F_{water}$ - offset by isotopic fractionation associated with biosynthesis (Hayes, 2001; Sachse et al., 2012). Extensive work on environmental systems and laboratory cultures of microbial phototrophs (Sauer et al., 2001; Schouten et al., 2006; Zhang et al., 2009b; Sachse and Sachs, 2008; Romero-Viana et al., 2013) revealed substantial variability in this isotopic effect. Additional work in other metabolic systems (Campbell et al., 2009; Sessions et al., 2002; Valentine et al., 2004; Kreuzer-Martin et al., 2006) matched this observation, and hinted at a more complex role of metabolism in the isotopic offset between source water and microbial lipids. Although fatty acid biosynthesis is conserved throughout the bacterial domain, a number of different metabolic levers can affect this process. During central metabolism, $NADP^+$ is reduced to NADPH by hydride ion (H^-) transfer from a metabolically derived reductant and can subsequently be used in anabolic reactions[5]. During lipid biosynthesis, the nascent fatty acid chain is elongated progressively by the addition of acetyl-CoA (via malonyl-CoA) (KANEDA, 1991), with a number of hydrogen additions occurring during reductive steps.

[5]Sometimes, the redox carrier NADH, typically used for catabolic reactions, is used as a reductant in fatty acid biosynthesis in addition to NADPH (White et al., 2005). The two can also be interconverted by transhydrogenases (HOEK and RYDSTROM, 1988), which can carry additional strong isotopic effects (Zhang et al., 2009a; Jackson et al., 1999).

The hydrogen composition of the resulting fatty acid depends on the exact structure (saturation state, branching), but to first order, this highly-conserved pathway includes 50% hydrogen derived from NAD(P)**H**, 25% from water (as a proton) and 25% from the precursor acetyl-CoA (Zhang et al., 2009a; Valentine, 2009) in all bacterial fatty acids. The isotopic composition and source of hydrogen in NADPH and acetyl-CoA, however, depend strongly on the metabolic program of the organism with hydrogen in both pools ultimately sourced from either of the two end-member reservoirs: water (as is the case in autotrophic organisms), or organic substrates. Enzymatic differences in the biosynthetic and reductive steps themselves, although existent in some organisms, are likely to be of secondary importance for the hydrogen isotopic composition of the resulting fatty acid, and as shown and discussed before (Sessions and Hayes, 2005; Zhang et al., 2009a), the isotopic composition of lipids can thus be considered in terms of the combination of the mole fraction of ultimately water-derived hydrogen x_w with water isotopic composition ${}^2F_w$ and associated net hydrogen isotope fraction ${}^2\alpha_{l/w}$, and substrate-derived hydrogen $(x_w - 1)$ with substrate isotopic composition ${}^2F_s$ and associated net isotope fractionation ${}^2\alpha_{l/s}$[6]:

$$ {}^2F_{lipid_{new}} = x_w \cdot \quad \alpha_{l/w} \cdot {}^2F_w + (1 - x_w) \cdot \alpha_{l/s} \cdot {}^2F_s \tag{7.11} $$

Unfortunately, the exact values of x_w, $\alpha_{l/w}$ and $\alpha_{l/s}$ cannot be determined from culturing experiments (they can only be constrained some). However, for the purposes of isotope labeling experiments where the overall effects of different substrates can be assessed in culture, it is sufficient to determine the combined effects of the water hydrogen mole fraction and biosynthetic fractionation $x_w \cdot \alpha_{l/w}$ (here termed the *water fraction factor* – a concatenation of "water fraction" x_w and "fractionation factor" $\alpha_{l/w}$) and the combined substrate offset $(1 - x_w) \cdot \alpha_{l/s} \cdot {}^2F_S$ (here termed the *substrate offset*). These

[6] See D.5.2 in Appendix D for details on how to calculate isotopic fractionation of a fractional abundance ${}^xF$ with a fractionation factor ${}^x\alpha$ exactly, and information about the error introduced if using the approximation ${}^x\alpha \cdot F_x$.

can be readily obtained from the slope and intercept of culturing experiments with different water isotopic compositions F_w, and are reported here for the heterotrophic *E. coli*, *P. aeruginosa*, *S. aureus* and *S. maltophilia*. Previous data on these parameters of hydrogen metabolism only exist for *E. coli* grown on LB and glucose (Zhang et al., 2009a).

Medium	Condition	Microbe	Compound	% Membrane	water fraction factor $(x_w \cdot \alpha_{l/w})$	substrate offset $(1-x_w)\cdot\alpha_{l/s}\cdot {}^2F_S$ [ppm]	R^2
Minimal	Batch (Stationary)	EC	C16:1 FA	20.2	0.81 ± 0.07	38 ± 12	1.0
Minimal	Batch (Stationary)	EC	C16:0 FA	44.4	0.85 ± 0.07	32 ± 12	1.0
Minimal	Batch (Stationary)	EC	cyclo-C17:0 FA	12.7	0.82 ± 0.07	39 ± 13	1.0
Minimal	Batch (Stationary)	EC	C18:1 FA	22.7	0.81 ± 0.07	40 ± 12	1.0
Minimal	Batch (Stationary)	PA	C16:1 FA	7.6	0.72 ± 0.05	78 ± 8	1.0
Minimal	Batch (Stationary)	PA	C16:0 FA	39.2	0.83 ± 0.03	69 ± 5	1.0
Minimal	Batch (Stationary)	PA	C18:1 FA	43.7	0.77 ± 0.03	77 ± 5	1.0
Minimal	Batch (Stationary)	PA	cyclo-C19:0 FA	7.7	0.75 ± 0.05	81 ± 9	1.0
Minimal	Batch (Stationary)	SA	a-C15:0 FA	46.7	0.47 ± 0.04	66 ± 7	1.0
Minimal	Batch (Stationary)	SA	a-C17:0 FA	20.2	0.46 ± 0.08	73 ± 14	1.0
Minimal	Batch (Stationary)	SA	C18:0 FA	6.7	0.52 ± 0.29	76 ± 50	0.9
Minimal	Batch (Stationary)	SA	i/a-C19:0 FA	10.7	0.49 ± 0.05	75 ± 9	1.0
Minimal	Batch (Stationary)	SA	C20:0 FA	10.1	0.58 ± 0.20	70 ± 35	1.0
SCFM	Batch (Exponential)	PA	C16:1 FA	7.6	0.74 ± 0.06	61 ± 10	1.0
SCFM	Batch (Exponential)	PA	C16:0 FA	37.4	0.80 ± 0.04	50 ± 7	1.0
SCFM	Batch (Exponential)	PA	C18:1 FA	47.4	0.78 ± 0.04	54 ± 7	1.0
SCFM	Batch (Stationary)	PA	C16:1 FA	12.0	0.65 ± 0.07	82 ± 12	1.0
SCFM	Batch (Stationary)	PA	C16:0 FA	37.1	0.72 ± 0.08	76 ± 13	1.0
SCFM	Batch (Stationary)	PA	C18:1 FA	48.9	0.67 ± 0.08	84 ± 13	1.0
SCFM	Batch (Stationary)	SA	a-C15:0 FA	51.2	0.42 ± 0.11	82 ± 18	0.9
SCFM	Batch (Stationary)	SA	a-C17:0 FA	29.6	0.41 ± 0.11	87 ± 18	0.9
SCFM	Batch (Stationary)	SA	i/a-C19:0 FA	8.5	0.36 ± 0.12	94 ± 19	0.9
SCFM	Batch (Stationary)	SM	C14:0 FA	4.9	0.65 ± 0.01	61 ± 2	1.0
SCFM	Batch (Stationary)	SM	i-C15:0 FA	59.7	0.52 ± 0.02	75 ± 3	1.0
SCFM	Batch (Stationary)	SM	a-C15:0 FA	17.1	0.53 ± 0.01	72 ± 2	1.0
SCFM	Batch (Stationary)	SM	C16:0 FA	11.2	0.73 ± 0.03	51 ± 4	1.0
SCFM	Continuous ($\tilde{1}$9hrs)	PA	C16:1 FA	5.7	0.74 ± 0.06	41 ± 10	1.0
SCFM	Continuous ($\tilde{1}$9hrs)	PA	C16:0 FA	45.9	0.86 ± 0.24	24 ± 41	0.9
SCFM	Continuous ($\tilde{1}$9hrs)	PA	C18:1 FA	33.8	0.89 ± 0.06	21 ± 10	1.0
SCFM	Continuous ($\tilde{1}$9hrs)	PA	cyclo-C19:0 FA	9.0	0.84 ± 0.06	32 ± 10	1.0
SCFM	Continuous ($\tilde{2}$hrs)	PA	C16:1 FA	6.9	0.64 ± 0.05	60 ± 8	1.0
SCFM	Continuous ($\tilde{2}$hrs)	PA	C16:0 FA	40.9	0.61 ± 0.19	60 ± 32	0.9
SCFM	Continuous ($\tilde{2}$hrs)	PA	C18:1 FA	42.4	0.65 ± 0.03	60 ± 5	1.0

Table 7.1 – Water fraction factors. Summary of the water fraction factors and substrate offsets of major fatty acids (>5% relative abundance) derived from water fraction factor experiments with *E. coli* (EC), *P. aeruginosa* (PA), *S. aureus* (SA) and *S. maltophilia* (SM). Errors are 95% confidence intervals of the coefficients from the linear regression fit.

Table 7.1 summarizes the water fraction factors and substrate offsets for the major fatty acids (comprising more than 5% of the membrane of the respective organisms) from experiments in a variety of growth conditions. Figure 7.4 and 7.5 illustrate these visually for ease of discussion. Additional details on the experiment and derivation of these biological parameters are available in section D.3 of Appendix D. Here, we describe and discuss the three main sources of variability observed in the data: variation between

different membrane components, variation between organisms, and variation between growth conditions.

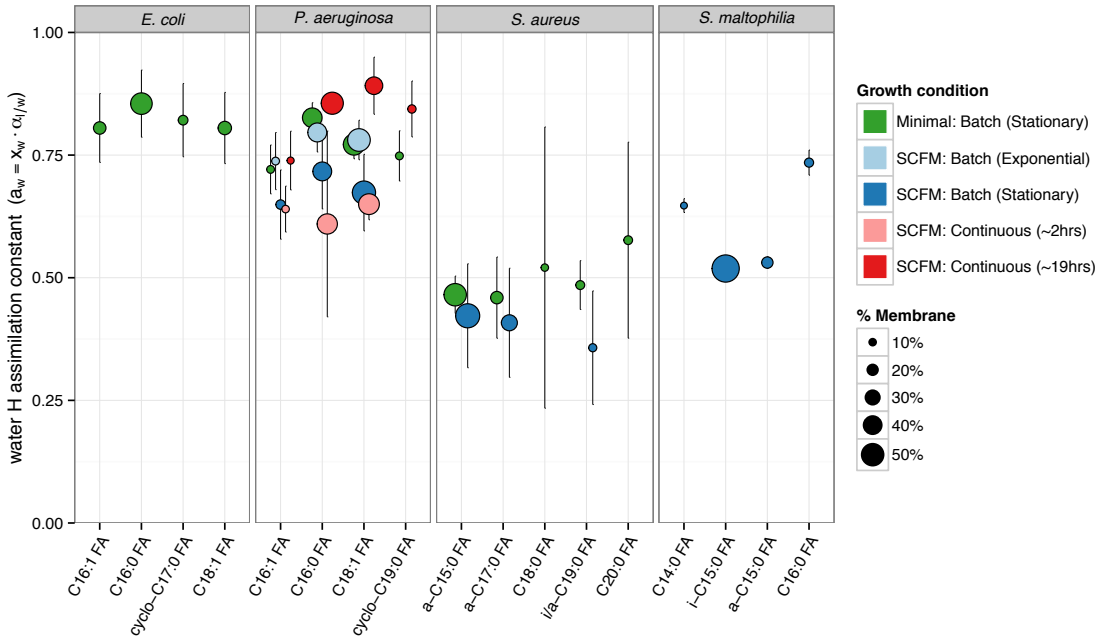

Figure 7.4 – Water fraction factors. Summary of the water fraction factors. Different colors indicate tested growth conditions. Size of symbols indicates the relative membrane abundance of the compound. Symbols from different experiments are slightly offset from the central axis for each compound to increase clarity. Error bars are 95% confidence intervals of the coefficients from the linear regression fit.

7.4.2.1 Same organism, same medium, different membrane components

Different membrane fatty acids produced by the same culture generally show similar water fraction factors and substrate offsets. This is consistent with the level of biosynthetic overlap between different fatty acids, which are all extended by the same fatty acid synthase, one 2-carbon unit (from acetyl-CoA) at a time. However, some of the variation observed here hints at the subtle differences in the biosynthetic pathways for different fatty acid classes. This is most notable in the strikingly higher water fraction factor of straight chain fatty acids ($C_{14:0}$ and $C_{16:0}$) in *S. maltophilia* compared to the rest of the membrane, which is primarily composed of methyl branched (i-$C_{15:0}$and a-$C_{15:0}$) fatty acids. The difference in this case lies with the initiation of fatty acid biosynthesis.

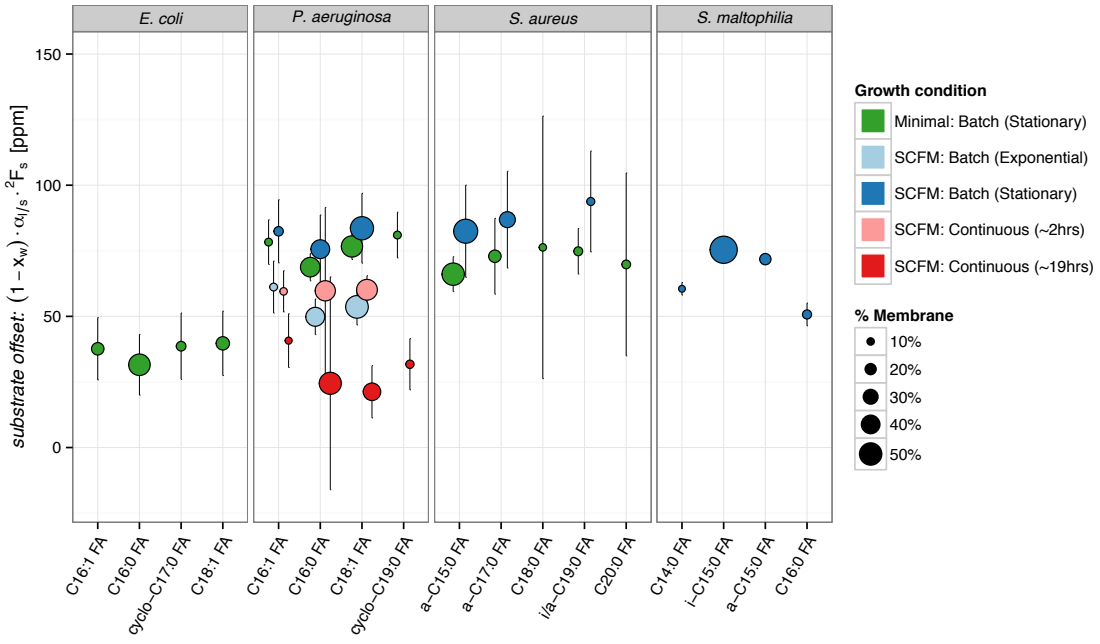

Figure 7.5 – Substrate offsets. Summary of the substrate offsets. Different colors indicate tested growth conditions. Size of symbols indicates the relative membrane abundance of the compound. Symbols from different experiments are slightly offset from the central axis for each compound to increase clarity. Error bars are 95% confidence intervals of the coefficients from the linear regression fit.

In addition to its role in chain elongation during the biosynthesis of all fatty acids, acetyl-CoA is also the primer for the initiation of straight chain fatty acid biosynthesis. Methyl-branched fatty acids are elongated by the same enzyme using acetyl-CoA just like their straight chain counterparts, but biosynthesis is initiated differently. Instead of acetyl-CoA, several α-keto acids act as primers via transamination and decarboxylation by branched chain α-keto acid decarboxylase. Specifically, in the case of odd-chain iso- and anteiso- methyl branched fatty acids, which constitute a major portion of the membranes of *S. aureus* and *S. maltophilia*, leucine and isoleucine act as the respective primers (KANEDA, 1991; Kaneda, 1971; Oku and KANEDA, 1988; Christie and Han, 2010). Given the presence of leucine and isoleucine in both SCFM and *S. aureus* minimal medium, it is reasonable to assume that hydrogen incorporated into mature methyl-branched fatty acids via these primers is not affected by the hydrogen isotope composition of the source water.

Compared to the acetyl-CoA primer of straight chain fatty acids, which contributes only the 3 hydrogens on the terminal carbon directly to the mature fatty acid, both leucine- and isoleucine-derived primers contribute a total of 9 hydrogens to the fatty acid tail. This implies, for example, that i-$C_{15:0}$ only contains 20 (29 - 9) hydrogens that could be affected by water hydrogen vs. 28 (31 - 3) in straight chain $C_{16:0}$, and suggests that x_w for i-$C_{15:0}$ should be ~25% lower than x_w for $C_{16:0}$. The resulting water fraction factor is expected to be reduced similarly, assuming that isotopic fractionation of the overall biosynthetic process $\alpha_{l/s}$ does not change substantially. For *S. maltophilia*, we observe a reduction in the water fraction factor of ~27% from $C_{16:0}$to i-$C_{15:0}$, consistent with this interpretation (~22% from $C_{14:0}$ to i-$C_{15:0}$, with the expected reduction at ~20%). Similar trends are observed for the respective fatty acids classes in *S. aureus,* and are mirrored in the substrate offsets for both organisms (which are affected as $1 - x_w$).

Additional trends expected between different fatty acid classes include a similar reduction of water-derived hydrogen x_w from saturated to unsaturated fatty acids (for example $C_{16:0}$ to $C_{16:1}$in *E. coli* and *P. aeruginosa*) due to two hydrogens that could be affected by water missing in the double bond (the missing reductive step introduces a proton and an NADPH hydrogen). This prediction can be observed as a general trend in our data, but is difficult to ascertain within the projected error ranges.

Cyclo-propyl fatty acids (for example, cyclo-$C_{17:0}$ and cyclo-$C_{19:0}$) are derived from their unsaturated precursors (e.g. $C_{16:1}$ and $C_{18:1}$) by addition of a methylene group derived from S-adenosylmethionine across the double bond (Grogan and Cronan, 1997). This introduces hydrogen from the methionine methyl (which, in turn, is derived from 5-methyl-tetrahydrofolate in *de-novo* synthesis of methionine, Guest et al. (1964)) but the hydrogen isotopic composition and ultimate source of this hydrogen (water vs. substrate) likely depends on the nutritional environment, and its effect on water fractionation factors is difficult to predict. In *E. coli* growing on minimal medium, there is no statistically significant difference between the water fraction factors and substrate offsets of $C_{16:1}$ and

its derivative cyclo-$C_{17:0}$. In *P. aeruginosa,* there appears to be a slight decrease in the water fraction factor (increase in the substrate offsets) from $C_{18:1}$ to its derivative cyclo-$C_{19:0}$ both in Minimal and SCFM medium, but the statistical support for this difference is also weak.

7.4.2.2 Same medium, different organisms

Within error, *E. coli* and *P. aeruginosa* show similar water fraction factors for their shared fatty acids at comparable conditions (growth in minimal medium on succinate). These are also consistent with observations made by Zhang et al. (2009a) for the facultative freshwater bacterium *Cupriavidus oxalaticus* in minimal succinate medium (0.83 for $C_{16:1}$, 0.80 for $C_{16:0}$ and 0.89 for $C_{18:1}$, compared to 0.81, 0.85 and 0.81 for *E. coli* and 0.72, 0.83 and 0.77 for *P. aeruginosa* on succinate in our study).

However, there is a significant difference in the substrate offset of *P. aeruginosa* and *E. coli* in minimal medium. This is surprising because both show similar water fraction factors, and are grown on exactly the same carbon source. Assuming that the isotopic fractionation between lipid and water $\alpha_{l/w}$ is similar for this metabolism, it implies that x_w must also be similar, and suggests that the hydrogen isotope fractionation factor between substrate (i.e. succinate) and lipid $\alpha_{l/s}$ in *P. aeruginosa* is significantly higher than in *E. coli*. Zhang et al. (2009a) hypothesized high $\alpha_{l/s}$ in succinate metabolism to be a consequence of two complementary effects:

- The first is removal of one of two methylene H from succinate by succinate dehydrogenase prior to abstraction of the second H by isocitrate dehydrogenase to generate the NADP**H** used in lipid biosynthesis. The H removal by succinate dehydrogenase likely carries a very strong kinetic isotope effect that has been measured at 4,400‰ *in vitro* (Zhang et al., 2009a; Rétey et al., 1970), which leaves the remaining hydrogen that is used for fatty acid biosynthesis via NADPH strongly enriched in ^{2}H and lead to a high net $\alpha_{l/s}$. This effect depends primarily on the property of these TCA

cycle enzymes. While it is likely a strong contributor to a high $\alpha_{l/s}$ in both *E. coli* and *P. aeruginosa*, it is unlikely to lead to significant differences between the two organisms.

- The second effect relates to the anabolic need for NADPH vs. the catabolic need for NADH. During high flux through the TCA cycle, high production of NAPDH likely exceeds anabolic needs for the reductant, and is balanced by interconversion to NADH via transhydrogenase (HOEK and RYDSTROM, 1988), which can carry strong kinetic isotope effects (Jackson et al., 1999) that leave residual NADPH enriched in ^{2}H as suggested by Zhang et al. (2009a). This effect depends primarily on the balance between energy generation and biosynthesis, and could indeed vary between *E. coli* and *P. aeruginosa* growing on the same substrate. The observed difference in the substrate offset (figure 7.5) would then suggest that *P. aeruginosa* ultimately converts more substrate to energy and less substrate to biomass than *E. coli* (i.e., it is less efficient at building up biomass).

The same observation applies not only in minimal medium but also in comparison of *P. aeruginosa* and *S. aureus* in SCFM medium, where the substrate offset of *P. aeruginosa* is relatively enriched, although this is more difficult to interpret due to the complex nature of the SCFM medium.

Most of the variability between *P. aeruginosa* and *S. maltophilia* (comparable in SCFM medium) is likely due to the differences between straight-chain and methyl-branched fatty acids discussed before, as supported by the similar water fraction factors of $C_{16:0}$ (the only fatty acids that constitute a significant component of the membranes of both organisms and can be compared directly). However, *S. aureus* water fraction factors are lower than their *P. aeruginosa* or *S. maltophilia* counterparts in SCFM medium (marked in blue in Figure 7.4). Assuming isotopic fractionation between water and lipid $\alpha_{l/w}$ to be similar for all these heterotrophs when grown in the same medium (Zhang et al., 2009a), this suggests

that *S. aureus* incorporates less hydrogen from water (~11% lower x_w in the direct comparison of a-$C_{15:0}$ produced both by *S. aureus* and *S. maltophilia*). This difference is mirrored accordingly in the substrate offset, as expected from its dependence on $1 - x_w$. Although there is not enough information to draw conclusions as to the mechanisms underlying this difference, it is worthwhile to point out that the gram-positive *S. aureus* is the most phylogenetically different organism among the four strains. It is the one most adapted to (and dependent on) growth in the presence of multiple carbon substrates, and might be using a different combination of substrates than the other organisms in the multi-substrate SCFM medium.

7.4.2.3 Same organisms, different growth conditions

Comparisons of the water fraction factors and substrate offsets for the same organism grown under different conditions further highlights the potential range of the parameters controlling the isotopic composition of hydrogen in lipids (x_w, $\alpha_{l/w}$, $\alpha_{l/s}$) as a function of metabolism, and were explored in some detail with *P. aeruginosa*.

The first difference arises from growth in simple (Minimal) vs. more complex (SCFM) medium. In *P. aeruginosa*, this implies a transition from growth on succinate to growth on a mixture of lactate, glucose and various amino acids, and is accompanied by a significant drop in the water fraction factor (substrate offsets are not directly comparable, because the isotopic composition of all the organic hydrogen sources is not known). As discussed before (Zhang et al., 2009a), this is likely a consequence of both reducing $\alpha_{l/w}$ and x_w in switching from succinate (a relatively high $\alpha_{l/w}$) to a more complex medium (smaller x_w due to increased assimilation of preformed cell constituents). The same pattern is observed in comparing growth of *E. coli* on minimal succinate medium in our study (high water fraction factors: $\alpha_{l/w} \cdot x_w$ = 0.81 for $C_{16:1}$, 0.85 for $C_{16:0}$ and 0.81 $C_{18:1}$) to growth of *E. coli* in complex medium (LB broth: $\alpha_{l/w} \cdot x_w$ = 0.44 for $C_{16:1}$, 0.52 for $C_{16:0}$ and 0.48 for $C_{18:1}$, Zhang et al. (2009a)).

Additionally, the same pattern can be observed in water fraction factors from *P. aeruginosa* cultures harvested in stationary phase (dark blue, Figure 7.4) vs. exponential phase (light blue) in SCFM medium. *P. aeruginosa* metabolizes certain substrates (aspartate, alanine, arginine) in SCFM preferentially, and others (glucose, leucine, lysine) only once it depletes the prior sources (Behrends et al., 2009). Stationary-phase cultures carry the integrated signal of hydrogen metabolism during exponential phase where preferred substrates are consumed, and hydrogen metabolism during the transition to stationary phase where the remaining substrates are consumed. Although little is known about the individual effects of these substrates, the observed pattern suggests that hydrogen metabolism of early substrates (aspartate, alanine, arginine) occurs with a higher $\alpha_{l/w}$ (not offset by changes in x_w), higher x_w (not offset by changes in $\alpha_{l/w}$), or both. The mirrored shift in substrate offsets suggests that changes in x_w play a substantial role in altering the water fraction factors (lower x_w for the consumption of refractory materials are then consistently reflected in the $1 - x_w$ dependence of the substrate offset), and/or that refractory substrates are isotopically heavier or less fractionated (or more strongly reversely fractionated if $\alpha_{l/s} > 1$).

Comparing *P. aeruginosa* grown in batch culture to stationary phase vs. growth in continuous culture at an intermediate doubling time of ~2 hours (dark blue and pink in figure 7.4) shows similar water fraction factors ($x_w \cdot \alpha_{l/w}$) within error, consistent with both representing the cumulative hydrogen isotope effects from consumption of all substrates. However, the substrate offset ($(1 - x_w) \cdot \alpha_{l/s} \cdot F_s$) in continuous culture is significantly reduced, without a clear physiological explanation in light of the conserved water fraction factors. Given the complexity of the medium and its use of a range of common laboratory substrates (amino acids, lactate, glucose, etc.), it is conceivable, however, that one or multiple substrates came from different vendors/batches with different isotopic composition F_s in the two experiments.

The most interesting comparison lies with the continuous culture experiments at

different growth rates. Cultures of *P. aeruginosa* grown in continuous culture with a long doubling time (∼19hrs) vs. intermediate doubling time (∼2hrs) show a significant shift in water fraction factors to higher values, and a mirrored shift in substrate offsets to lower values (red and pink in Figure 7.4). Both experiments were conducted in close succession, and care was taken to include the same batch of chemicals to ensure no changes in the chemical environment or substrate isotopic composition between these cultures. This suggests that isotopic effects in individual steps of the biosynthetic pathways likely remained unchanged, though, the relative rate of biosynthesis (doubling only once in 19 hours) provides a much longer time scale for isotopic exchange and equilibration of precursors and reagents with water hydrogen (effectively raising x_w towards 1). The most important site of potential exchange would be hydrogen carried on NAD(P)H. As pointed out by Zhang et al. (2009a), experiments with NADP^{2}H and purified fatty acid synthesis enzymes incubated *in vitro* over 5 hours resulted in ^{2}H-incorporation into fatty acids without loss of the label (suggesting no exchange with water during fatty acid synthesis itself), while experiments with crude cell extracts showed substantial loss of the label to exchange reactions (Saito et al., 1980). This H-exchange is likely mediated by a wide range range of enzymes in the cell that perform NAD(P)H chemistry. The enzymes and kinetics involved are difficult to estimate *in vivo* with the limited information available at present. However, if the time scale of *in vitro* experiments (∼5 hours) provides a reasonable timescale for exchange, the rate of metabolic turnover of NADPH in fast-growing cultures likely exceeds the rates of the various potential exchange reactions (preserving most if not all of the primary metabolic hydrogen isotope signal), while slow-growing cultures are affected much more significantly. This hypothesis would explain our observations in continuous culture with *P. aeruginosa* at a ∼19hr doubling time, and merits further research into the rates and mechanisms of NAD(P)H hydrogen exchange.

The implications of the various observations for the use of D^{2}O in isotope tracer experiments to measure microbial activity can be summarized as follows: (i) to first

order, the heterotrophs studied here and elsewhere (Zhang et al., 2009a) display a similar range of water fraction factors from ~0.4 to ~0.9; (ii) different growth substrates and metabolic programs as well as membrane fatty acid composition modulate where individual organisms' water fraction factors fall within this range; (iii) slow growth increases water fraction factors, likely due to hydrogen exchange of metabolic intermediates with water hydrogen (ultimately increasing x_w); (iv) substrate offsets do not readily translate to other media without detailed knowledge of the hydrogen isotope composition of the growth substrates.

7.4.3 Isotope labeling in continuous culture

We applied hydrogen isotope labeling in continuous culture experiments to estimate microbial activity as a proof of concept, and to assess various parameters that could affect the interpretation of data from environmental applications. Continuous culture, or chemically static (chemostat) experiments provide the ideal setting for testing any tracer of microbial activity. The chemostat was developed independently around 1950 by Jacques Monod at the Pasteur Institute (MONOD, 1950), who coined the term continuous culture (and called the device a *bactogène*), and by Aaron Novick and Leo Szilard at the University of Chicago (Novick and SZILARD, 1950), who gave it its modern name. The theory and application of chemostats was refined in subsequent years, and led to fascinating new insights into fundamental aspect of microbial physiology (e.g. Novick (1955); Herbert et al. (1956)). The molecular revolution saw its use diminish for several decades, but the importance of continuous culture to physiological research remains as important today as it was 60 years ago, which is increasingly re-recognized for a wide range of research applications (Hoskisson, 2005). Briefly, a chemostat provides a chemically constant environment for microbial culture by continuously feeding fresh medium at a constant rate into a reactor vessel that is kept at a constant volume by removing the overflow. Assuming that cells are either not actively degraded, or if they are, their (partly

labeled) cellular constituents are recycled by the remainder of the population (i.e. cells are not completely lost to the dissolved organic matter pool), the only form of actual removal of biomass is the dilution rate imposed by the continuous culture setup. This sets a fixed dilution rate of the microbial culture (equivalent conceptually to removal rate d discussed in Section 7.2), which the population needs to counteract by doubling at the same rate ($\mu = d$) once at steady-state[7]. Here, we take advantage of a culturing environment with an independently controlled growth rate to test incorporation of an isotopic spike of D_2O administered at steady-state as a function of growth. Towards this end, we expand on the equations and concepts derived in Sections 7.2 and 7.4.2.

In the case of an isotope labeling experiment in an environmental setting, the overall metabolic mode (heterotrophy vs. autotrophy, chemotrophy vs. phototrophy) can likely be constrained, and laboratory values for the water fraction factor $x_w \cdot \alpha_{l/w}$ (Eq. 7.11, Table 7.1 and Figure 7.4) provide reasonable estimates for the corresponding environmental values. The exact nature and hydrogen isotope composition of the environmental growth substrate(s) F_s is rarely known, providing limited information on how to apply the substrate offset or substrate fraction factor (if known). However, with an estimate of the *water fraction factor* and knowledge of the natural isotopic composition of the source water $F_{w_{nat}}$, the medium/environment specific *substrate offset* can be estimated simply from observing the natural isotopic composition of the lipids ${}^2F_{lipid}(t_0)$ before application of an isotopic spike:

$$(1 - x_w) \cdot \alpha_{l/s} \cdot {}^2F_s = {}^2F_{lipid}(t_o) - x_w \cdot \alpha_{l/w} \cdot {}^2F_{w_{nat}} \tag{7.12}$$

[7] A tremendous amount of literature exists on the theory and application of chemostats; please see e.g. Smith (1995) for details.

which, substituted back into Eq. 7.11 to provide an expression for the isotopic composition of newly synthesized lipids, yields:

$$^2F_{lipid_{new}} = x_w \cdot \quad \alpha_{l/w} \cdot \left(^2F_w - {}^2F_{w_{nat}}\right) + {}^2F_{lipid}(t_0) \tag{7.13}$$

Using Eq. 7.13 to describe the isotopic composition of newly-formed lipids, with a dilution model for the isotopically spiked water $^2F_w(t) = {}^2F_{w_{spiked}} \cdot e^{-kt}$ (with initial isotopic composition of the spiked medium water $^2F_{w_{spiked}}$ and dilution rate constant k) and substituting back into Equation 7.8 finally yields:

$$\begin{aligned}
^2F_{lipid}(t) &= \frac{B_{new} \cdot {}^2F_{new}}{B} + \frac{B_{old} \cdot {}^2F_{old}}{B} \\
&= \Bigg[x_w \cdot \alpha_{l/w} \cdot {}^2F_{w_{spiked}} \cdot f_S \cdot \frac{\mu+\omega}{\mu+\omega+k} \cdot \left(1 - e^{-(\mu+\omega+k)\cdot t}\right) \\
&\quad + \left(^2F_{lipid}(t_0) - x_w \cdot \alpha_{l/w} \cdot {}^2F_{w_{nat}}\right) \cdot f_S \cdot \left(1 - e^{-(\mu+\omega)\cdot t}\right)\Bigg] \\
&\quad + \left[^2F_{lipid}(t_0) \cdot \left(1 - f_S \cdot \left(1 - e^{-(\mu+\omega)\cdot t}\right)\right)\right] \\
&= x_w \cdot \alpha_{l/w} \cdot f_S \cdot \left[^2F_{w_{spiked}} \cdot \frac{\mu+\omega}{\mu+\omega+k} \cdot \left(1 - e^{-(\mu+\omega+k)\cdot t}\right) - {}^2F_{w_{nat}} \cdot \left(1 - e^{-(\mu+\omega)\cdot t}\right)\right] \\
&\quad + {}^2F_{lipid}(t_0)
\end{aligned} \tag{7.14}$$

which in the case of a constant isotopic label (no dilution or other variation of the water isotopic composition over the course of the isotope labeling experiment), would simplify to:

$$^2F_{lipid}(t) = x_w \cdot \alpha_{l/w} \cdot f_S \cdot \left(^2F_{w_{spiked}} - {}^2F_{w_{nat}}\right) \cdot \left(1 - e^{-(\mu+\omega)\cdot t}\right) + {}^2F_{lipid}(t_0) \tag{7.15}$$

where $x_w \cdot \alpha_{l/w}$ is the *water fraction factor*, f_S the fraction of *de novo* biosynthesis (vs. recycling of exogenous lipids), $^2F_{w_{spiked}}$ the isotopic composition of the spiked

medium/environmental source water, ${}^2F_{w_{nat}}$ the natural isotopic composition of the source water, μ the growth rate of the population, ω the turnover rate and ${}^2F_{lipid}$ the isotopic composition of the microbial lipids at time t (all parameters as described previously).

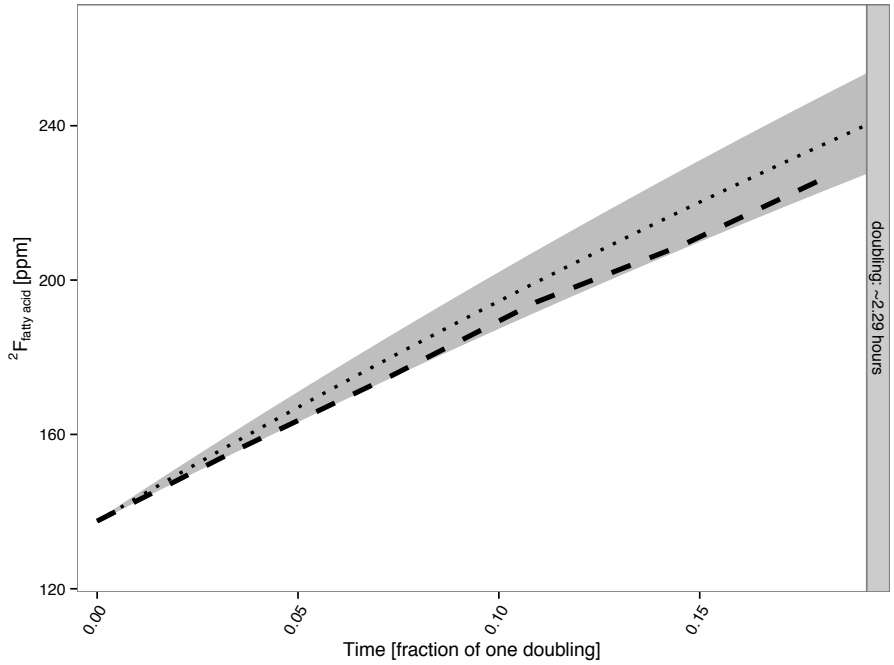

Figure 7.6 – Isotope labeling of *E. coli*. This figure illustrates the isotopic enrichment of major membrane components (>5%) of *E. coli* after an isotopic D_2O spike into a culture grown continuously at a fixed dilution rate equivalent to doubling every ~2.3 hours. Time is shown as the fraction of a doubling for ease of comparison to other experiments. Colors indicate the different fatty acids, symbol sizes represent the relative pool sizes (% of all fatty acids in the membrane). The thick dashed line indicates the average isotopic composition of the whole membrane. The dotted thin line indicates the predicted enrichment from theoretical considerations, and is based on the weighted average water fraction factor determined for this medium (Table 7.1). The gray shaded band indicates the maximal range of predicated labeling considering the maximal range of measured water fraction factors (of any fatty acid of this organism) in combination with the 95% confidence interval on the measurement of the initial water isotopic composition of the D_2O spiked reactor.

Figure 7.6 shows the incorporation of ^2H into the major fatty acid components of *E. coli* over the course of ~1/5 of a doubling after an isotopic spike with D_2O ($^2F_{W_{spiked}}$= 1208ppm) during growth in continuous culture at a constant growth rate of ~7.3 day^{-1}(a doubling time of ~2.3 hours) in Minimal medium (see Table D.14 for the data). These data show immediate incorporation of the water tracer into all membrane components, consistent with rapid osmotic equilibration predicted to occur in microorganisms due to

their high surface-to-volume ratio (Verkman, 2013). Additionally, the different fatty acids show substantial divergence in their labeling patterns, with C16:1 getting over-labeled with respect to the major membrane component C16:0, and C18:1 and cyclo-C17:0 getting under-labeled (significantly so in the case of cyclo-C17:0). This divergence pattern provides potential insight into dynamics within this microbial population, and is discussed in some detail in Section 7.4.5. Here, we focus on the overall isotopic labeling of the membrane as a whole (the weighted isotopic average, or mass balance, of all membrane components), as shown in Figure 7.6 by the thick dashed line. Since the growth rate μ is controlled by the chemostat setup, we can model the expected isotopic enrichment using Equation 8.2 with the following measured parameters: ${}^2F_{w_{spiked}}$ is the isotopic composition of the medium water after the spike (diluted with dilution rate k set by the chemostat), ${}^2F_{w_{nat}}$ is the natural isotopic composition of the medium water, $x_w \cdot \alpha_{l/w}$ is the weighted average water fraction factor for *E. coli* in this medium (see Section 7.4.2 for details on individual fatty acids), ${}^2F_{lipid}(t_0)$ the weighted average isotopic composition of the membrane measured at the onset of the labeling experiment, and $f_S = 1$ (the medium is well-defined, and contains no exogenous fatty acid sources). The dotted line in Figure 7.6 represents the resulting theoretical level of enrichment, which closely matches the actual labeling pattern of the major fatty acid (C16:0), but slightly overestimates the observed labeling of the membrane as a whole. The single largest source of error in the prediction stems from uncertainty in the water fraction factor (see Figure 7.4). This is illustrated in Figure 7.6 by the gray band, which represents the maximal and minimal labeling prediction based on the entire range of water fraction factors of all membrane components observed for *E. coli* combined with uncertainty in the water isotope measurement (the latter is a minor component). The observed isotope labeling of the membrane matches the theoretical prediction well within this uncertainty, indicating that this method could be used in reverse for its original purpose (predicting growth rates from isotopic enrichment).

It is important to note that the slight under-labeling of the membrane as a whole with respect to the model prediction could also hint at a role of metabolically produced water in diluting the water label within the cells (Kreuzer-Martin et al., 2006). This effect could explain the observed enrichment if the heavy water label is effectively diluted by 5-10% within the cells due to water produced from metabolic activity. However, given the uncertainty in the water fraction factor, the current data does not reveal whether this effect occurs in this experiment or what its exact magnitude might be. If present, it is reasonable to assume that its importance would increase at faster growth rates and decrease at slower growth rates due to its direct dependence on metabolic water production. This merits careful evaluation when applying this technique to even faster-growing cultures.

7.4.4 The role of turnover / maintenance

For any technique to quantitatively capture microbial activity, it is important that it scales well to lower, environmentally-relevant growth rates. This is particularly important in the case of isotopic tracers, because the premise of high sensitivity and low detection limits of small isotopic enrichments partly motivates their use in studying microbial activity in the first place. Here, we report on several experiments with *P. aeruginosa* and *S. aureus* in continuous culture at different growth rates (from doubling times of ∼2 hours to ∼13 days) and discuss the role of turnover/maintenance activity in slower-growing microorganisms.

Figure 7.7 illustrates the results from three separate labeling experiments with *P. aeruginosa* at growth rates that correspond to doubling times of ∼2.2 hours, ∼16.2 hours and ∼5.4 days (details listed in Table 7.2, data in Table D.12). The figure shows the isotopic enrichment of all major fatty acid membrane components after administration of an isotopically-labeled water spike in combination with the weighted average enrichment of the membrane as a whole (dashed thick line) and the theoretically predicted enrichment (dotted thin black line with gray confidence bands). As discussed in Section 7.4.3 for *E. coli*, substantial divergence in the labeling pattern of individual fatty acids can be observed

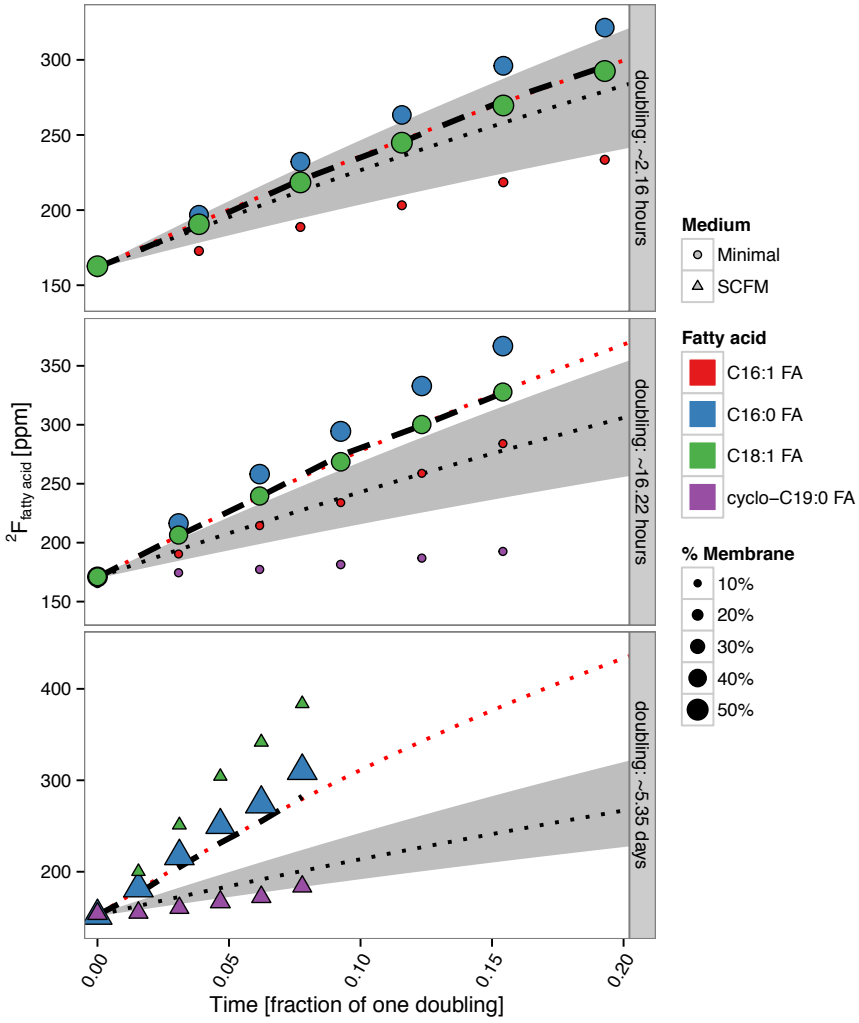

Figure 7.7 – Growth-rate-dependent isotope labeling of *P. aeruginosa*. This figure illustrates the isotopic enrichment of major membrane components (>5%) of *P. aeruginosa* after an isotopic D_2O spike into cultures grown continuously at fixed dilution rates. Time is shown as the fraction of a doubling for ease of comparison. Colors indicate the different fatty acids, symbol sizes represent the relative pool sizes (% of all fatty acids in the membrane). The thick dashed line indicates the average isotopic composition of the whole membrane. The dotted thin line indicates the predicted enrichment from theoretical considerations, and is based on the weighted average water fraction factor determined for this medium (Table 7.1). The gray shaded band indicates the maximal range of predicated labeling considering the maximal range of measured water fraction factors (of any fatty acid of this organism) in combination with the 95% confidence interval on the measurement of the initial water isotopic composition of the D_2O spiked reactor. The dotted red line indicates the best fit of the theoretical model with a variable turnover rate ω.

as well in *P. aeruginosa*. Additionally, growth at slower rates is shown to affect the overall membrane composition of the organism, and alters the isotopic enrichment divergence pattern.

This is most striking in terms of the switch in divergence between C16:0 and C18:1 at the slowest growth rate and the growth-rate-dependent increase of cyclo-C19:0. Specifically, cyclo-C19:0 production increases with a decrease in growth rate, and comes at the expense of the unsaturated precursor C18:1 to the point where in the slow-growth condition of doubling every ∼5 days, the majority of C18:1 has been converted to cyclo C19:0. This is consistent with known patterns of cyclo-propyl fatty acid (CFA) formation. CFAs have been observed for a long time to be a side effect of batch cultures transitioning from exponential to stationary phase, which – physiologically – is similar to a radical reduction in growth rate. However, the effect is particularly striking in continuous culture, which implies that CFAs are an inherent feature of slow metabolism, rather than a unique aspect of the sudden, radical metabolic transition experienced from exponential to stationary phase growth in batch culture. Historically, the timing of CFA production (right before growth arrest) and the accompanying reduction of unsaturated fatty acids (which are amenable to damage by lipid peroxidation), have been interpreted as evidence for cells preparing for adverse conditions. However, given the substantial energetic cost and absence of conclusive evidence for a protective effect, the role and regulation of CFA formation remains unresolved (Grogan and Cronan, 1997).

The second, and key observation, however, lies with the the observed enrichment relative to the theoretical prediction (dashed thick line vs. dotted think black line). During relatively fast growth conditions (∼2 hours in the top panel), the theoretical prediction closely matches the observed isotope labeling of the membrane as a whole, and lies well within the projected error from uncertainty in the water fraction factors. As growth slows, the isotopic enrichment increasingly *exceeds* theoretical predictions (beyond even the extremes of the entire range of water fraction factors), which implies that the cellular membranes of these microbial populations are produced *faster* than necessary for replication, suggesting that membrane turnover in excess of growth plays a substantial role. The exact same observation applies to our data from four separate labeling experiments

with *S. aureus* at growth rates that correspond to doubling times from ∼6.4 hours to ∼13.3 days as illustrated in Figure 7.8 (details listed in Table 7.2, data in Table D.13).

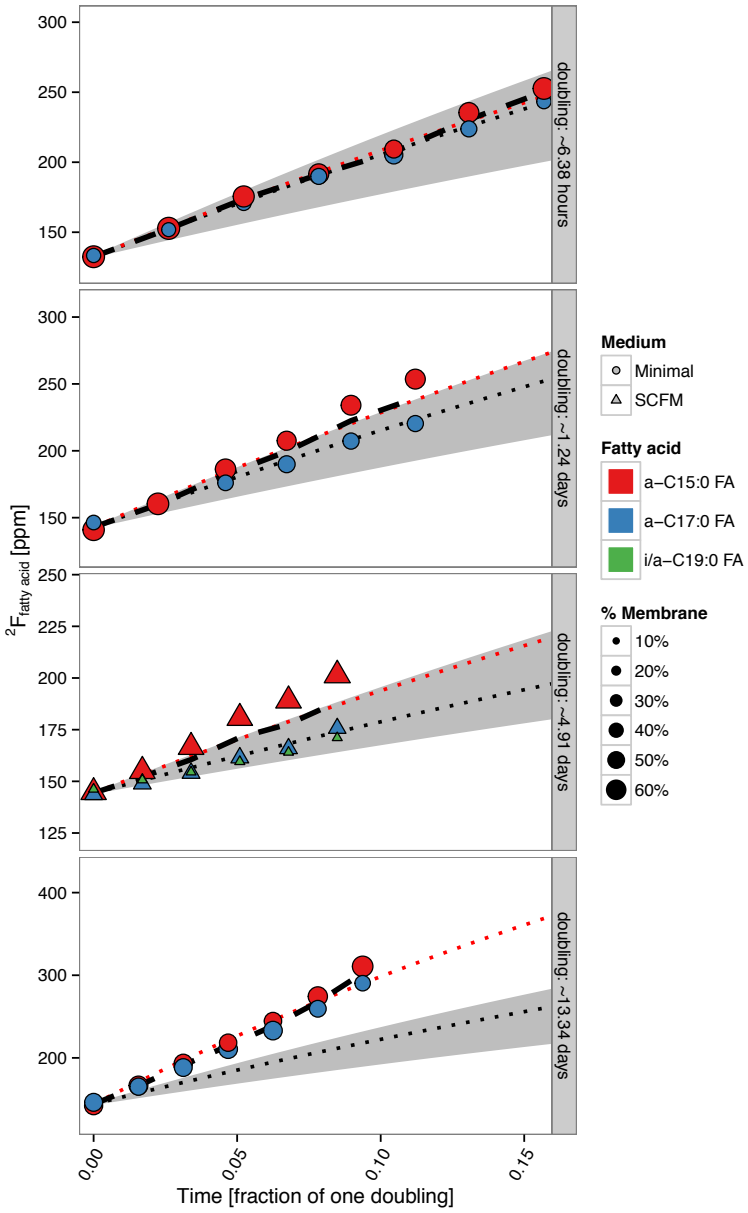

Figure 7.8 – Growth-rate-dependent isotope labeling of *S. aureus*. This figure illustrates the isotopic enrichment of major membrane components (>5%) of *S. aureus* after an isotopic D_2O spike into cultures grown continuously at fixed dilution rates.

Such turnover is a theoretically unnecessary sink for energy that might only be required in order to "repair" the membrane or, in terms of a broader concept in cell biology, *maintain* cellular functionality – even if growth were entirely absent. The concept of a

fundamental *maintenance energy* is well-established in cell biology, and comprises a rich body of literature from over half a century of work (Marr et al., 1963a; Harder, 1997; van Bodegom, 2007; Arbige and Chesbro, 1982; Tempest and Neijssel, 1984; Anderson and Domsch, 1985; Tijhuis et al., 1993; Pirt, 1965). Here, the turnover rate ω is closely related conceptually to *maintenance energy,* and directly corresponds to the specific maintenance rate a defined originally by Marr et al. (1963a). Often, this rate is considered a constant (akin to a minimum quantum of energy necessary to stay alive), and derived by extrapolation from substrate specific biomass yields at various (relatively fast) growth rates. In reality, this maintenance rate is likely variable, and depends on the growth rate as discussed by van Bodegom (2007).

Microbe	Medium	Weighted avg. $x_w \cdot \alpha_{l/w}$	Isotope spike ${}^2F_{w_{spiked}}[ppm]$	Doubling time	Growth rate $\mu[day^{-1}]$	Turnover rate $\omega[day^{-1}]$
EC	Minimal	0.829	1208.100	2.29 hours	7.267	
PA	SCFM	0.740	1421.914	5.35 days	0.130	0.23 ± 0.01
PA	Minimal	0.788	1566.207	16.22 hours	1.026	0.52 ± 0.03
PA	Minimal	0.788	1415.049	2.16 hours	7.700	1.15 ± 0.14
SA	Minimal	0.482	2747.675	13.34 days	0.052	0.05 ± 0.01
SA	SCFM	0.411	1440.456	4.91 days	0.141	0.06 ± 0.01
SA	Minimal	0.482	2464.333	1.24 days	0.559	0.11 ± 0.03
SA	Minimal	0.482	2477.390	6.38 hours	2.609	0.12 ± 0.09

Table 7.2 – Modeling parameters and turnover rate estimates. This table shows the parameters of the continuous culture growth experiments together with the estimated values of ω from non-linear least squares fitting. Errors are 95% confidence intervals for the turnover/maintenance rate ω from the fit of the data to Equation 8.2 with the parameters listed in this table. The water fraction factor $x_w \cdot \alpha_{l/w}$ is the weighted average from lipid-specific water fraction factors derived in Section 7.4.2 for the appropriate medium. Potential variations in water fraction factor were not taken into consideration when solving for ω, but the range of values is illustrated in Figures 7.7 and 7.8.

The isotope labeling approach taken here allows a uniquely different approach to estimating maintenance rates directly from lipid turnover, with the caveat that it describes membrane maintenance, rather than whole-cell (protein, DNA, etc.) maintenance. Taking the turnover rate ω to be the only unconstrained parameter in Equation 8.2, we can derive an estimate of ω directly from fitting Equation 8.2 to the isotope enrichment data at each growth rate. Figures 7.7 and 7.8 illustrate this fit with a dotted red line, Table 7.2 includes the derived turnover rates, and Figure 7.9 illustrates them visually.

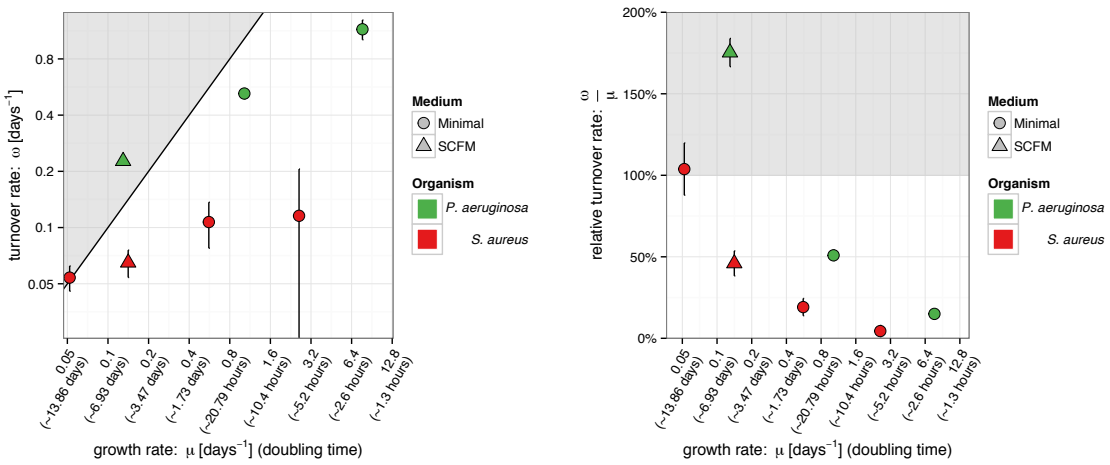

Figure 7.9 – Turnover/maintenance rate estimates. This figure shows the absolute and relative turnover/maintenance rates observed for *P. aeruginosa* and *S. aureus* in continuous culture as a function of growth rate. The area shaded in gray indicates the regime were turnover *exceeds* growth.

This figure shows an interesting trend (left panel) with turnover/maintenance rates decreasing as a function of growth rate, rather than staying constant. This trend implies that at slower growth, the cells adapt to some degree to the low nutrient-flux conditions and expend *less* total energy on maintenance, which is consistent with data compiled in van Bodegom (2007). As the growth rate decreases, maintenance (although decreasing in absolute terms) constitutes a *larger* portion of overall activity, to the extreme where maintenance rates exceed growth rates (area shaded in grey in Figure 7.9) and become negligible at fast growth (right panel). To our knowledge, some of these maintenance rates are measured at the lowest growth rate to date in a controlled laboratory setting, and uniquely reach all the way into the regime were maintenance exceeds growth (gray zone in Figure 7.9) as compared to the literature compilation and discussion of microbial maintenance by van Bodegom (2007). It is important to keep in mind that these estimates are based on a constant water fraction factor (the mean weighted average of all growth conditions for the same organism in the same medium). However, significantly higher water fraction factors at lower growth rates would only lead to an amplification of this trend (even stronger gradient from higher turnover rates at fast growth to lower turnover rates at slow growth).

The data further suggest that *P. aeruginosa* has fundamentally higher maintenance rates than *S. aureus,* which is consistent with *P. aeruginosa* turning organic substrate into biomass with a lower efficiency, potentially due to high energy expenditure for the operation of its wide array of export pumps and the synthesis of various secondary metabolites.

7.4.5 Divergence of different fatty acids in isotope labeling

Figures 7.6, 7.7 and 7.8 show substantial divergence in the incorporation of the isotopic label into different fatty acids. While the divergence itself does not affect the isotope labeling of the membrane as a whole, it reflects the underlying dynamics of the biological system and could inform our understanding of how it operates mechanistically. Here, we suggest two separate and fundamentally different hypotheses that could explain this phenomenon.

7.4.5.1 Kinetics of label propagation

One hypothesis predicts differential label propagation through different components of the biological system as a consequence of the inherent kinetics and turnover times for individual precursor and end-member pools. The simplest case to model is that of label divergence in the production of cyclopropyl fatty acids (CFA), which are formed directly from their unsaturated precursors attached to a phospholipid head-group in the membrane (Grogan and Cronan, 1997). This constitutes a pathway where both pools of interest (unsaturated precursor and derived CFA) are actually measured. A more complicated pathway needs to be invoked for the interesting case where different fatty acids are derived from one another during *de novo* biosynthesis but cannot be converted once membrane bound. Examples of this are straight chain fatty acids that are two carbon units apart (e.g. C16:0 and C18:0 or a-C15:0 and a-C17:0), but chain elongation requires the free fatty acid rather than its polar intact polar lipid form. Any significant labeling divergence due to the kinetics of isotope label propagation requires either this precursor pool of free fatty acids to be

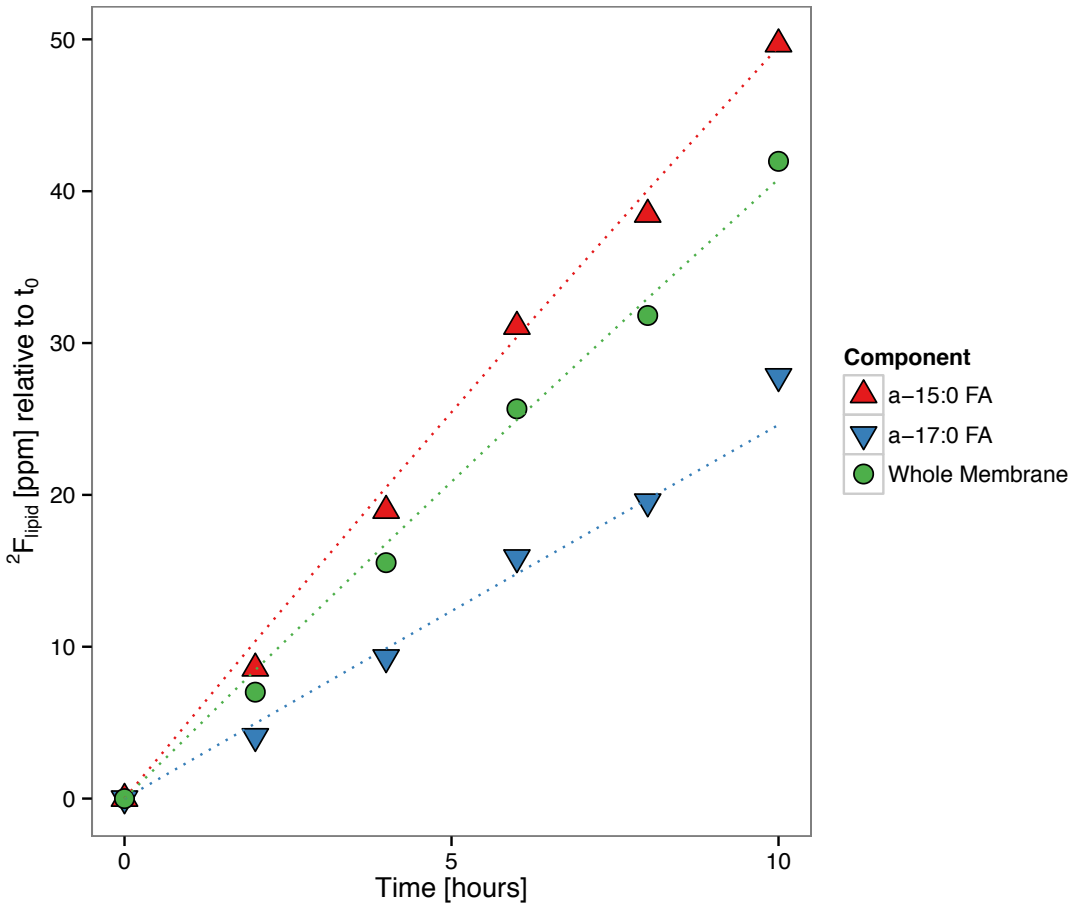

Figure 7.10 – Kinetically-driven divergence in fatty acid labeling. Fit of a model of a-C17:0 fatty acid formation from free a-C15:0 fatty acid, and its effects on the kinetics of isotope label propagation. Shown is the data from continuous culture of *S. aureus* in SCFM medium with the observed divergence pattern of the a-C15:0 and a-C17:0 fatty acids. Dashed lines represent a numerical solution to the system of differential equations governing the biosynthetic model.

relatively large, or an active exchange between the intact polar lipid bound and free forms of the precursor. The prior (large free fatty acid pool) is inconsistent with what we know about fatty acid and membrane biology, so we focus here primarily on the latter (active exchange with rate ϵ, as indicated in Figure 7.1).

The system of differential equations describing this biosynthetic model with a free fatty acid pool of the shorter chain fatty acid that exchanges with its membrane bound version and can be elongated to form the longer fatty acid does not have an analytical solution, but can be fitted numerically. Here, we show the results of this approach for the

data of *S. aureus* growing in continuous culture in SCFM medium at a growth rate of ∼4.9 days (Figure 7.8), where the two major fatty acids produced by *S. aureus* (a-C15:0 and a-C17:0) diverged significantly in their isotope incorporation. A numerical fit of the differential equations to these data by optimization with the exchange rate ϵ and free a-C15:0 pool size as free parameters illustrates how this model could indeed explain the data (see Figure 7.10). The best-fit parameters suggest a relatively small free fatty acid pool of a-C15:0 (<0.005% of the total membrane bound a-C15:0), but requires a relatively large exchange rate $\epsilon = 1.1\mu$ on the order of the overall growth rate of this culture (and about twice the turnover rate ω as shown in Table 7.2). Unlike the turnover (ω), this exchange (ϵ) between the free and membrane bound forms of a-C15:0 cannot explain overall isotopic enrichment of the whole membrane beyond the incorporation rate from active growth (μ), but it amplifies kinetic effects that cause the divergence of different fatty acid components. The exchange rate is large relative to the growth rate (which represents a ∼4.9 day doubling time in this experiment) but loses significance at faster growth rates. This can be observed in the data where *S. aureus* growing at slower rates (∼1.2 days and ∼6.4 hours doubling time, see Figure 7.8) shows significantly less divergence in the isotope incorporation into a-C15:0 and a-C17:0. However, a return to lower divergence at even slower growth rates than ∼4.9 days (13.3 days in the last panel of Figure 7.8) is not explained by this model, and requires further research into the dynamics of lipid turnover and exchange in this context.

7.4.5.2 Population heterogeneity

An alternative hypothesis predicts divergence in the isotope labeling pattern as a consequence of population heterogeneity. Data on the relative abundances of different fatty acids during different growth conditions (see tables in Section D.7 and Figures 7.6, 7.7 and 7.8 for a visual representation) suggests that growth rate has an effect on overall lipid composition. Additionally, observations in long-term experiments of

stationary phase cultures suggest that at any point in time, the population actually consists of distinct subpopulations that are dynamically increasing and declining over time (Finkel, 2006). While this growth advantage in stationary phase (GASP) phenotype of different subpopulations is mostly reported in the context of batch cultures where chemical conditions are not constant, it is likely that a slow-growing chemostat provides an environment that also supports substantial heterogeneity within the culture, although this diversity may only be phenotypic and not genotypic given the time scales of the experiment. If chemostat populations actually represent individual cells with a diverse range of growth rates (that average out to the turnover rate), and growth rates affect the fatty acid profiles of individual cells, it is conceivable that an isotopic spike will show divergent incorporation into different fatty acids. Specifically, any fatty acid component that has a higher abundance in the membranes of the more active part of the population, relative to its abundance in the membrane of the less active part of the population, would turn out net over-labeled, while relatively less-abundant fatty acids would be under-labeled.

For example, the relative abundance of a-C15:0 and a-C17:0 in cultures of *S. aureus* changes as a result of growth (see Figure 7.8), with a-C17:0 increasing in its relative importance in slower-growing cultures. At the same time, a-C15:0 (relatively more abundant in fast-growing cultures) is over-labeled in isotope labeling experiments, while a-C17:0 turns out under-labeled. Figure 7.11 simulates the effect of population heterogeneity in terms of the growth rates and fatty acid compositions on the divergence of isotopic enrichment in the a-C15:0 and a-C17:0 pools after administration of an isotopic spike. The figure illustrates that neither heterogeneity in growth rates alone, nor heterogeneity in membrane composition alone can lead to a divergence pattern (no over- / under-representation of any one more strongly / less strongly enriched membrane component is possible without heterogeneity in both). The black trace in Figure 7.11 further illustrates the level of divergence consistent with data from the same growth experiment evaluated in the previous hypothesis. This suggests that the divergence could be explained by this

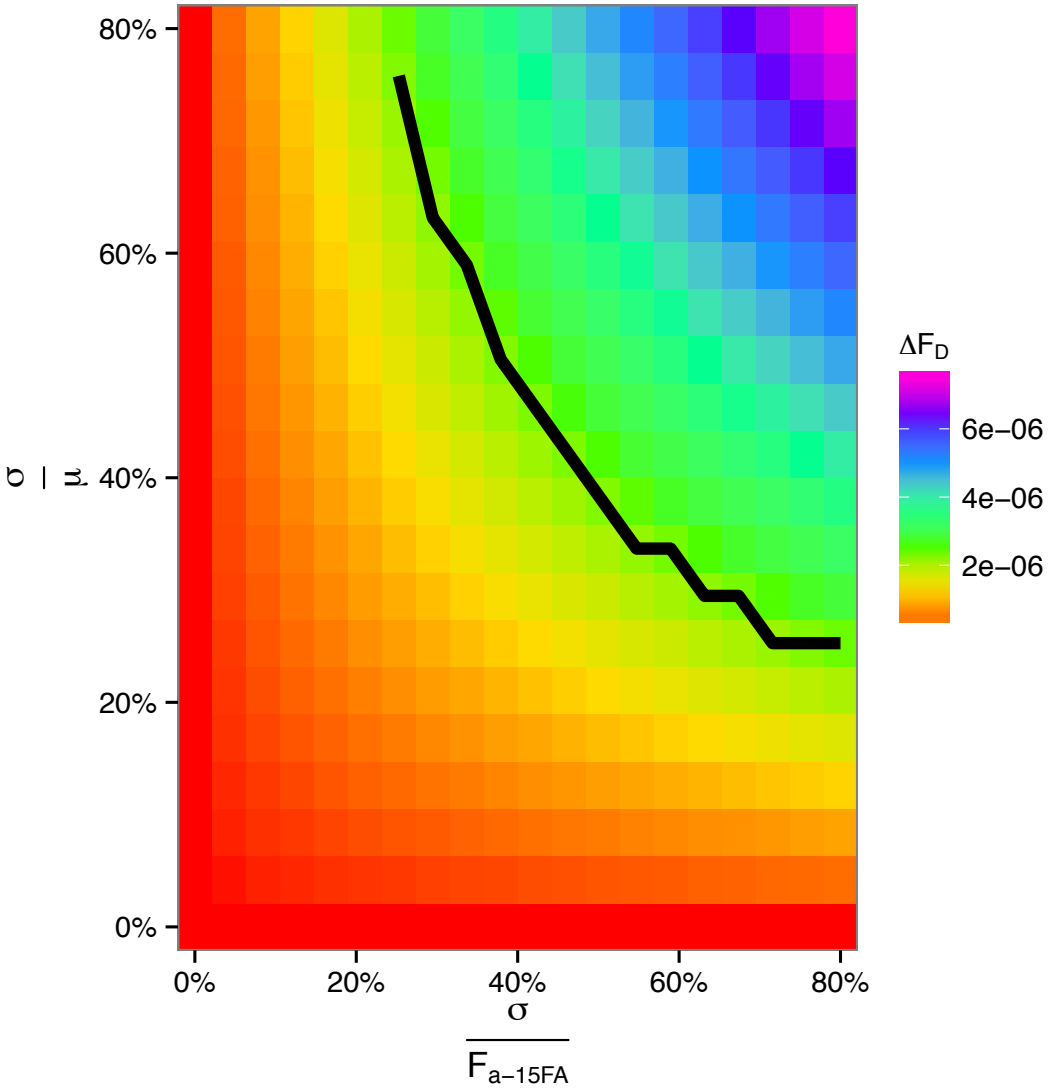

Figure 7.11 – The effect of population heterogeneity on fatty acid divergence. Model simulation of divergence in isotopic composition ΔF_D between a-C15:0 and a-C17:0 as a consequence of population heterogeneity in terms of fatty acid composition (F_{a-15FA} signifies the fraction of a-C15:0 in the membrane) and growth rate (μ). Heterogeneity is modelled as a gaussian distribution, and expressed on both axes in terms of the standard deviation relative to the mean (for example, $\frac{\sigma}{\mu} = 0\%$ implies a uniform population with growth rate μ and no spread, whereas $\frac{\sigma}{\mu} = 50\%$ implies a diverse population with growth rates normally distributed around μ with variance $\sigma^2 = 0.25 \cdot \mu$). Shown in black is the contour of labeling divergence that is consistent with the divergene data from continuous culture of *S. aureus* in SCFM medium (panel 3 in figure 7.8).

model of heterogeneity, but it requires a substantial range in growth rate and/or fatty acid composition. The relative abundance data on fatty acids of *S. aureus* suggests that while the composition varies, the variation in the abundance of a-C15:0 in favor of a-

C17:0 does not exceed ~30%, even at the slowest growth rate investigated (13.3 days doubling), although this of course represents an average of the whole populations. If 30% variation is considered a reasonable estimate for the maximal relative deviation in fatty acid abundance, this implies that the relative deviation in growth rate reaches as high as 80%. This suggests that growth rates can vary on the order of ~2-fold within the population, which is not at all unreasonable if compared to relative variations in the GASP phenotype. Additionally, a return to lower divergence in isotope labeling patterns at the slowest growth rates investigated (13.3 days in the last panel of Figure 7.8) could be simply a consequence of reaching a limiting uniform fatty acid composition (even if divergence in growth rates should further increase).

7.4.6 Recycling of exogenous fatty acids

Recycling exogenous sources is an important caveat to isotope labeling experiments in substrate-rich environments. If organisms can build their membranes from pre-existing fatty acids, or fatty acid fragments, that are available in their environment, they no longer need to synthesis all fatty acids *de novo*. Consequentially, an isotopic tracer in the form of ^{2}H-rich water would be incorporated into the total membrane at a much slower rate. Without knowledge of the rate of recycling, isotopic enrichment alone could *underestimate* true growth of the population, because growth with recycled fatty acids does not incorporate the tracer. This concept is represented in Figure 7.1 by the relative fractional rate of *de novo* synthesis f_S (relative to total incorporation from *de novo* synthesis and recycling).

Two examples for this process are provided by recent work on this topic in *P. aeruginosa* (Yuan et al., 2012a;b). First, the organism appears capable of recycling exogenous free fatty acids, such as C16:0, by direct incorporation *en bloc* during phospholipid biosynthesis. Any fatty acid recycled by this mechanism would carry its original isotopic signature from when it was first synthesized, rather than incorporate any water isotope signal present at

the time of *en bloc* incorporation. Second, the initiating step of fatty acid synthesis from acetyl-CoA as the primer is catalyzed by a ß-acetoacetyl-ACP synthase (*fabH* in *E.coli*). In *P. aeruginosa*, a closely-related, but distinct new class of synthases (now called *fabY*) catalyze this step instead (Yuan et al., 2012b). Additionally, a wide range of genetically very similar enzymes exist in these organisms, and even with a deletion mutant of *fabY*, *P. aeruginosa* is capable of growing. Yuan et al. (2012a) discovered that in the absence of *fabY*, the preferred fatty acid synthesis pathway initiated from acetyl-CoA (which is no longer possible without the gene) can be replaced in the presence of exogenous fatty acids (C_8, C_{12}, C_{16}, undefined mixtures like LB, etc.). *P. aeruginosa* can shunt C_8-CoA from ß-oxidation degradation of fatty acid metabolism back into fatty acid biosynthesis via the enzyme encoded by open reading frame PA3286, thereby skipping the *de novo* synthesis of the C_8 precursor carbon skeleton. From the scavenged intermediate, the organism can produce all longer chain cellular fatty acids, including both saturated and unsaturated fatty acids. Any fatty acid recycled by this mechanism would carry a mixed isotopic signature with the C_8 tail maintaining its original isotopic composition, while the *de novo* elongated remainder of the molecule would reflect the water isotope signal present at the time of re-elongation.

Here, we investigated the capability of *S. aureus* to recycle fatty acids by a similar approach to that employed by Yuan et al. (2012b). Perdeuterated precursor fatty acids (entirely ^{2}H-substituted in the hydrocarbon tail) were provided as an exogenous source of free fatty acids in batch cultures of *S. aureus*. Unfortunately, methyl-branched precursors are not commercially available in their perdeuterated form, so only straight chain fatty acids (perdeuterated C15:0 and C18:0) were tested. Figure 7.12 illustrates the resulting fatty acid profiles of *S. aureus*. The complete data is listed in Table D.15 of Appendix D.

The data indicate that *S. aureus* is indeed capable of incorporating exogenous fatty acids *en bloc,* as can be seen from the presence of significant amounts of completely perdeuterated C15:0 and C18:0 in the intact polar lipids of the organism. Additionally, it

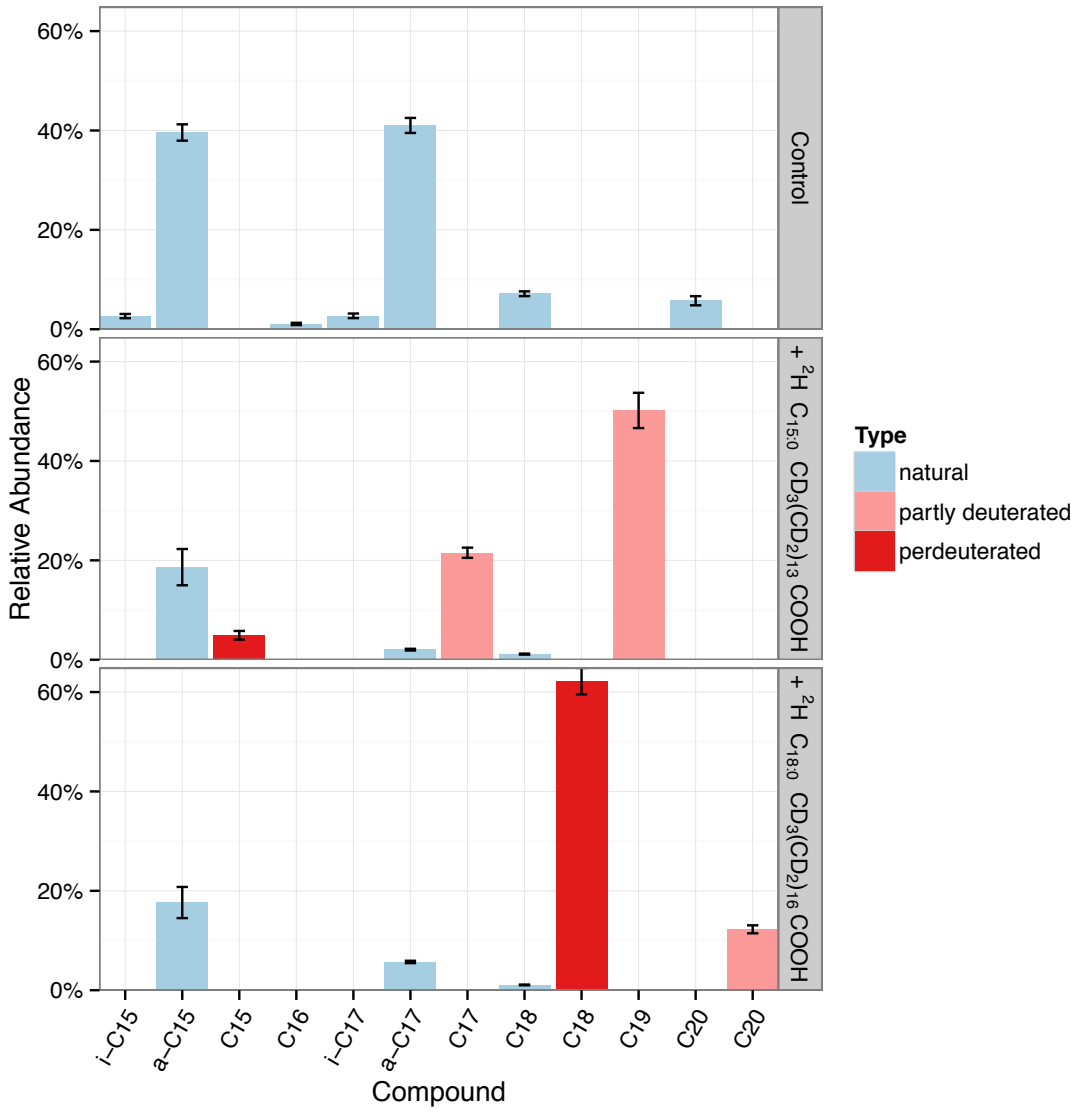

Figure 7.12 – Recycling of exogenous fatty acids by *S. aureus*. Summary of the *en bloc* incorporation and recycling of exogenous fatty acids by *S. aureus* growing in minimal medium amended with perdeuterated C_{15} and C_{18} fatty acid. Error bars are 95% confidence intervals from analytical replicates.

appears to be capable of elongating the exogenously-provided free fatty acids by extension with 2 carbon units (acetyl-CoA), as witnessed by the presence of partly deuterated C17:0 and C19:0 when grown with perdeuterated C15:0 (the mass spectrum reveals a completely deuterated C15 skeleton extended with undeuterated C2 / C4), and partly deuterated C20:0 when grown with perdeuterated C18:0 (again, a completely deuterated C18 skeleton extended with undeuterated C2). Curiously, none of these fatty acids are membrane

components that *S. aureus* naturally produces in significant quantities (except some minor amounts of C18:0), yet they constitute a significant portion of the intact polar lipid membrane fraction when provided exogenously. It is striking that the major, naturally occurring component that is altered the most in its abundance, is the longer chain a-C17:0 fatty acid, which is produced naturally by elongation of a-C17:0. This suggests that either chain elongation of the exogenous fatty acids directly competes for substrate (acetyl-CoA) with elongation of a-C15:0 to make a-C17:0 FA, or a regulatory response of the organism compensates for the presence and effect of the longer chain fatty acids on the physical properties of the membrane by reducing a-C17:0 production.

The second key observation, however, is that, unlike *P. aeruginosa*, *S. aureus* does not appear to partly break down the exogenous fatty acids and build them back up during fatty acid degradation (no partly deuterated fatty acids shorter than C17/C20 could be detected in any analysis). For the regular dominant components of its membrane (a-C15:0 and a-C17:0 fatty acids), this is consistent with the known biosynthetic pathway of anteiso methyl branched fatty acids, which are built from an isoleucine primer in *de novo* fatty acid synthesis (KANEDA, 1991; Kaneda, 1971; Oku and KANEDA, 1988; Christie and Han, 2010), and could not possibly be initiated from any partially degraded straight chain fatty acid by known biosynthetic mechanisms.

This suggests that during isotope labeling experiments to measure microbial activity of *P.* aeruginosa in an environment that experiences a heavy continuous influx of exogenous fatty acids from breakdown of organic matter, the potential rate of fatty acid recycling must be considered carefully. In studies with *S. aureus* in the presence of exogenous fatty acids, any fatty acid potentially elongated directly from an exogenous precursor is equally problematic; however, *unless* external sources provide significant quantities of iso/anteiso methyl branched fatty acids (direct precursors to a-C15:0 and a-C17:0 FA) or the fatty acids themselves, the methyl-branched fatty acids are likely pure products of *de novo* synthesis. If the contribution is solely from other members of the same population, any

isotopic spike still captures the activity of the population as a whole, although the sizes of the individual reservoirs and fluxes through the biosynthetic and recycling pathway affect the labeling efficiency. See Section 7.4.5 for a discussion of this aspect.

7.5 Conclusions

Here, we present stable isotope labeling of microbial membrane fatty acids with heavy water as a promising new technique to measure microbial activity in a wide range of environments, especially including slow-growth settings. An overview of the conceptual approach to isotope labeling, results from modeling isotopic enrichment with D_2O as a tracer, and results from culturing work in batch and continuous culture are presented and discussed in light of the capabilities and potential caveats of this approach: analytical limits, uncertainty in biological parameters, biological activity decoupled from growth (i.e. maintenance), recycling of exogenous fatty acids, and differential labeling patterns between different fatty acids.

Specifically, analytical limits are outlined by considering the chromatographic behavior of heavily deuterated organic molecules. The range and diversity of water fraction factors is discussed as the primary source of uncertainty in the biological uptake of a heavy water isotope tracer. The main source of **overestimating** "true growth" (potentially by orders of magnitude) is the difference between microbial activity (growth + maintenance) vs. the true generation time of a population, although this aspect only becomes significant at slow growth rates and can be mediated by reasonable estimates of turnover rates from laboratory experiments. The main sources for **underestimating** growth are microbial recycling mechanisms of exogenous fatty acid sources in organic rich environments, as well as interpreting a low component terminal lipid biomarker that is likely to under-label, although more research into the kinetic fluxes of the isotope label through the system is required for establishing a predictive model of fatty-acid dependent incorporation.

To first order, with some knowledge of the likely overall membrane composition of an organism, it is reasonable to assume that a single measurement of a major straight chain or methyl branched fatty acid will overestimate growth rates for the shortest fatty acid chain, and underestimate growth for the longer chains. Unsaturated fatty acids are more difficult to interpret in the absence of a representative laboratory labeling experiment (we observe over-labeling in *E. coli* and under-labeling in *P. aeruginosa* with respect to the equivalent straight chain fatty acids). Cyclopropyl fatty acids appear to always underestimate growth, likely due to their derivation from unsaturated fatty acids in intact polar lipids. Larger membrane components are always safer to interpret than minor fatty acids.

All of these present important constraints that we need to carefully consider when interpreting environmental growth data derived from D_2O stable isotope labeling. However, they also also present great scientific opportunities for novel insights into the various mechanisms at play in the growth dynamics of microbial populations, and this work barely scratches the surface.

Acknowledgements

I would like to thank Dianne Newman and Alex Sessions for agreeing to this project and supporting me throughout, Magdalena Osburn and Lichun Zhang for showing me the ropes on the extraction and analysis of fatty acids from microbial cultures, Elise Cowley and Yang Hu for all their hard work helping me run the chemostats and various water fraction factor experiments and for helping to extract the many, many samples during their summer internships and beyond, Nathan Dalleska for letting us run perdeuterated samples on his GC-MS, and the whole Newman lab for teaching me how to work with microorganisms and providing critical feedback at various points. I'd also like to especially acknowledge the various conversations with Maggie Osburn and Josh Silverman on water fraction factors and labeling dynamics, respectively, which were crucial to the theoretical

framework presented herein. None of this work would have been possible without the generous support of the Howard Hughes Medical Institute in the form of a predoctoral fellowship.

7.6 Glossary

μ The specific growth rate is a rate constant that has units of reciprocal time and represents the frequency by which an exponentially growing population (for example clonally replicating microorganisms) grows by a factor of e. This is sometimes also called relative growth rate, exponential growth rate or continuous growth rate, and abbreviated either as μ or k.

d The specific death or removal rate is a rate constant that has units of reciprocal time and represents the frequency by which a population diminishes by a factor of e (cells completely removed/degraded rather than just recycled within the population, for example by predation, death and degradation, or direct physical removal).

ω The turnover rate is rate constant that represents the rate of excess biosynthesis and degradation that is not part of cellular replication. This process has no net effect on biomass accumulation or removal, but contributes to its turnover. It can be viewed as a process that is part of maintaining the cell even in situations where there is no net growth.

μ_{act} The apparent or activity growth rate is a rate constant that represents overall **biosynthetic activity** from the combination of growth(μ) and turnover(ω).

μ_{net} The net growth rate is a rate constant that represents the overall **accumulation/decline of biomass** due to growth(μ) and death/removal(d).

g_{true} The true generation or doubling time of a population is the time it takes to net double in biomass, taking into consideration all counteracting processes that contribute to increase and decline of the population. It relates to the net growth rate as $g_{true} = \frac{ln(2)}{\mu_{net}}$.

g_{act} The apparent generation time or doubling activity of a population is the time it takes until half the biomass consists of new material (by a combination of replacement and new growth). It represents the time that a population appears to be doubling and would be equal to the true generation/doubling time without the effects of death/removal and turnover/maintenance processes. It relates to the apparent growth or activity rate as $g_{act} = \frac{ln(2)}{\mu_{act}}$.

7.7 References

Aldeen, D. A., Hiramatsu, K., May 2004. Staphylococcus Aureus. Molecular and Clinical Aspects. Elsevier.

Anderson, T. H., Domsch, K. H., 1985. Maintenance carbon requirements of actively-metabolizing microbial populations under *in situ* conditions. Soil Biology & Biochemistry.

Arbige, M., Chesbro, W. R., Oct. 1982. Very slow growth of Bacillus polymyxa: Stringent response and maintenance energy. Archives Of Microbiology 132 (4), 338–344.

Behrends, V., Ebbels, T. M. D., Williams, H. D., Bundy, J. G., Apr. 2009. Time-Resolved Metabolic Footprinting for Nonlinear Modeling of Bacterial Substrate Utilization. Applied and Environmental Microbiology 75 (8), 2453–2463.

Blazewicz, S. J., Barnard, R. L., Daly, R. A., Firestone, M. K., Jul. 2013. Evaluating rRNA as an indicator of microbial activity in environmental communities: limitations and uses. The ISME Journal, 1–8.

Campbell, B. J., Li, C., Sessions, A., 2009. Hydrogen isotopic fractionation in lipid biosynthesis by H_2-consuming *Desulfobacterium autotrophicum*. ... et Cosmochimica Acta 73, 2744–2757.

Chen, S. S., Sperling, E., Silverman, J. M., Davis, J. H., Williamson, J. R., 2012. Measuring the dynamics of E. coli ribosome biogenesis using pulse-labeling and quantitative mass spectrometry. Molecular BioSystems 8 (12), 3325.

Christie, W., Jul. 2006. Gas chromatography and Lipids book, 1–191.

Christie, W. W., May 1997. Preparation of ester derivatives of fatty acids for chromatographic analysis. In: Advances in Lipid Methodology. Elsevier, Dundee, pp. 69–111.

Christie, W. W., Han, X., 2010. Lipid analysis - isolation, separation, identification and lipidomic analysis. Bridgwater, UK.

Coplen, T. B., 1988. Normalization of oxygen and hydrogen isotope data. Chemical Geology: Isotope Geoscience section 72 (4), 293–297.

de Laeter, J. R., Böhlke, J. K., De Bièvre, P., Hidaka, H., Peiser, H. S., Rosman, K. J. R., Taylor, P. D. P., 2003. Atomic weights of the elements. Review 2000 (IUPAC Technical Report). Pure and applied chemistry 75 (6), 683–800.

D'hondt, S., Mar. 2002. Metabolic activity of subsurface life in deep-sea sediments. Science 295 (5562), 2067–2070.

Dragulescu, A. A., 2013. xlsx: Read, write, format Excel 2007 and Excel 97/2000/XP/2003 files. R package version 0.5.5.
URL http://CRAN.R-project.org/package=xlsx

Dumont, M. G., Murrell, J. C., Jun. 2005. Stable isotope probing - linking microbial identity to function. Nature Publishing Group 3 (6), 499–504.

Ecker, R. E., Schaechter, M., Oct. 1963. Ribosome content and the rate of growth of *Salmonella typhimurium*. Biochimica et biophysica acta 76 (2), 275–279.

Finkel, S. E., Feb. 2006. Long-term survival during stationary phase: evolution and the GASP phenotype. Nature Publishing Group 4 (2), 113–120.

Griffiths, M. J., Hille, R. P., Harrison, S. T. L., Sep. 2010. Selection of direct transesterification as the preferred method for assay of fatty acid content of microalgae. Lipids 45 (11), 1053–1060.

Grogan, D. W., Cronan, J. E., Dec. 1997. Cyclopropane ring formation in membrane lipids of bacteria. Microbiology and Molecular Biology Reviews 61 (4), 429–441.

Guest, J. R., Friedman, S., Foster, M. A., Tejerina, G., Woods, D. D., Sep. 1964. Transfer of the methyl group from N5-methyltetrahydrofolates to homocysteine in Escherichia coli. Biochemical Journal 92 (3), 497–504.

Harder, J., May 1997. Species-independent maintenance energy and natural population sizes. Fems Microbiology Ecology 23 (1), 39–44.

Hayes, J. M., 2001. Fractionation of carbon and hydrogen isotopes in biosynthetic processes. Geochemistry Of Non-Traditional Stable Isotopes 43, 225–277.

Herbert, D., Elsworth, R., Telling, R. C., Jul. 1956. The Continuous Culture of Bacteria; a Theoretical and Experimental Study. Journal of General MIcrobiology 14 (3), 601–622.

Hoehler, T. M., Jørgensen, B. B., 2013. Microbial life under extreme energy limitation. Nature Reviews Microbiology.

HOEK, J. B., RYDSTROM, J., 1988. Physiological Roles of Nicotinamide Nucleotide Transhydrogenase. Biochemical Journal 254 (1), 1–10.

Hoskisson, P. A., Oct. 2005. Continuous culture - making a comeback? Microbiology 151 (10), 3153–3159.

Hugh, R., Leifson, E., Jul. 1963. A description of the type strain of Pseudomonas maltophilia. International Bulletin of Bacteriological Nomenclature and Taxonomy 13 (3), 133–138.

Iyer, S. S., Zhang, Z.-P., Kellogg, G. E., Karnes, H. T., Aug. 2004. Evaluation of deuterium isotope effects in normal-phase LC-MS-MS separations using a molecular modeling approach. Journal of chromatographic science 42 (7), 383–387.

Jackson, J. B., Peake, S. J., White, S. A., 1999. Structure and mechanism of proton-translocating transhydrogenase. Febs Letters 464 (1-2), 1–8.

Jones, P. J., Leatherdale, S. T., Apr. 1991a. Stable isotopes in clinical research: safety reaffirmed. Clinical science (London, England : 1979) 80 (4), 277–280.

Jørgensen, B. B., Boetius, A., Oct. 2007. Feast and famine — microbial life in the deep-sea bed. Nature Reviews Microbiology 5 (10), 770–781.

Kaneda, T., Jan. 1971. Incorporation of branched-chain C6-fatty acid isomers into the related long-chain fatty acids by growing cells of Bacillus subtilis. Biochemistry 10 (2), 340–347.

KANEDA, T., Jun. 1991. Iso-Fatty and Anteiso-Fatty Acids in Bacteria - Biosynthesis, Function, and Taxonomic Significance. Microbiological Reviews 55 (2), 288–302.

Katz, J. J., Dec. 1960. Chemical and biological studies with deuterium. Am. Scientist Vol: 48.

Kellermann, M. Y., Wegener, G., Elvert, M., Yoshinaga, M. Y., Lin, Y.-S., Holler, T., Mollar, X. P., Knittel, K., Hinrichs, K.-U., Nov. 2012. Autotrophy as a predominant mode of carbon fixation in anaerobic methane-oxidizing microbial communities. Proceedings of the National Academy of Sciences 109 (47), 19321–19326.

KREISWIRTH, B. N., LOFDAHL, S., BETLEY, M. J., OREILLY, M., SCHLIEVERT, P. M., BERGDOLL, M. S., NOVICK, R. P., 1983. The Toxic Shock Syndrome Exotoxin Structural Gene Is Not Detectably Transmitted by a Prophage. Nature 305 (5936), 709–712.

Kreuzer-Martin, H. W., 2007. Stable Isotope Probing: Linking Functional Activity to Specific Members of Microbial Communities. Soil Science Society Of America Journal 71 (2), 611.

Kreuzer-Martin, H. W., Lott, M. J., Ehleringer, J. R., Hegg, E. L., 2006. Metabolic processes account for the majority of the intracellular water in log-phase Escherichia coli cells as revealed by hydrogen isotopes. Biochemistry 45 (45), 13622–13630.

Kushner, D., Baker, A., Dunstall, T., 1999a. Pharmacological uses and perspectives of heavy water and deuterated compounds. Canadian Journal Of Physiology And Pharmacology 77 (2), 79–88.

Lepage, G., Roy, C. C., Jan. 1986. Direct transesterification of all classes of lipids in a one-step reaction. Journal of lipid research 27 (1), 114–120.

LINCOLN, R. A., LEIGH, J. A., JONES, N. C., Jul. 1995. The amino acid requirements of *Staphylococcus aureus* isolated from cases of bovine mastitis. Veterinary Microbiology 45 (2-3), 275–279.

Mah, R. A., Fung, D. Y., Morse, S. A., Jul. 1967. Nutritional requirements of Staphylococcus aureus S-6. Applied microbiology 15 (4), 866–870.

Marr, A. G., Nilson, E. H., Clark, D. J., 1963a. The maintenance requirement of Escherichia coli. Annals of the New York Academy of Sciences.

McCloskey, J. A., Lawson, A. M., Leemans, F., 1967. Gas-chromatographic and mass-spectrometric properties of perdeuterated fatty acid methyl esters. Chemical Communications (London) (6), 285–287.

Metcalffe, L. D., Wang, C. N., 1981. Rapid Preparation of Fatty Acid Methyl Esters Using Organic Base-Catalyzed Transesterification. Journal of chromatographic science 19 (10), 530–535.

MONOD, J., 1950. La Technique De Culture Continue Theorie Et Applications. Annales De L Institut Pasteur 79 (4), 390–410.

Morono, Y., Terada, T., Nishizawa, M., Ito, M., Hillion, F., Takahata, N., Sano, Y., Inagaki, F., Nov. 2011b. Carbon and nitrogen assimilation in deep subseafloor microbial cells. Proceedings of the National Academy of Sciences 108 (45), 18295–18300.

Neuwirth, E., 2011. RColorBrewer: ColorBrewer palettes. R package version 1.0-5.
URL http://CRAN.R-project.org/package=RColorBrewer

Novick, A., Oct. 1955. Growth of Bacteria. Annual Reviews in Microbiology 9 (1), 97–110.

Novick, A., SZILARD, L., 1950. Description of the Chemostat. Science 112 (2920), 715–716.

Oku, H., KANEDA, T., Dec. 1988. Biosynthesis of branched-chain fatty acids in Bacillus subtilis. A decarboxylase is essential for branched-chain fatty acid synthetase. Journal of Biological Chemistry 263 (34), 18386–18396.

Palmer, K. L., Aye, L. M., Whiteley, M., Nov. 2007. Nutritional cues control *Pseudomonas aeruginosa* multicellular behavior in cystic fibrosis sputum. Journal of Bacteriology 189 (22), 8079–8087.

Pirt, S. J., Oct. 1965. The maintenance energy of bacteria in growing cultures. Proceedings of the Royal Society of London. Series B, Biological Sciences 163 (991), 224–231.

R Core Team, 2014. R: A Language and Environment for Statistical Computing. R Foundation for Statistical Computing, Vienna, Austria.
URL http://www.R-project.org/

Radajewski, S., Ineson, P., Parekh, N., Murrell, J., 2000. Stable-isotope probing as a tool in microbial ecology. Nature 403 (6770), 646–649.

RAHME, L. G., STEVENS, E. J., WOLFORT, S. F., SHAO, J., TOMPKINS, R. G., AUSUBEL, F. M., 1995. Common Virulence Factors for Bacterial Pathogenicity in Plants and Animals. Science 268 (5219), 1899–1902.

Rétey, J., Seibl, J., Arigoni, D., Cornforth, J. W., Ryback, G., Zeylemaker, W. P., Veeger, C., Jun. 1970. Stereochemical studies of the exchange and abstraction of succinate hydrogen on succinate dehydrogenase. European journal of biochemistry / FEBS 14 (2), 232–242.

Rodríguez-Ruiz, J., Belarbi, E. H., Sánchez, J. L. G., Alonso, D. L., 1998. Rapid simultaneous lipid extraction and transesterification for fatty acid analyses. Biotechnology techniques 12 (9), 689–691.

Rohrer, J. S., Olechno, J. D., 1992. Secondary isotope effect: the resolution of deuterated glucoses by anion-exchange chromatography. Analytical Chemistry.

Romero-Viana, L., Kienel, U., Wilkes, H., Sachse, D., Apr. 2013. Growth-dependent hydrogen isotopic fractionation of algal lipid biomarkers in hypersaline Isabel Lake (Mexico). Geochimica Et Cosmochimica Acta 106 (C), 490–500.

Sachse, D., Billault, I., Bowen, G. J., Chikaraishi, Y., Dawson, T. E., Feakins, S. J., Freeman, K. H., Magill, C. R., McInerney, F. A., van der Meer, M. T. J., Polissar, P., Robins, R. J., Sachs, J. P., Schmidt, H.-L., Sessions, A., White, J. W. C., West, J. B., Kahmen, A., May 2012. Molecular paleohydrology: interpreting the hydrogen-isotopic composition of lipid biomarkers from photosynthesizing organisms. Annual Review Of Earth And Planetary Sciences 40 (1), 221–249.

Sachse, D., Sachs, J. P., 2008. Inverse relationship between D/H fractionation in cyanobacterial lipids and salinity in Christmas Island saline ponds. Geochimica Et Cosmochimica Acta 72 (3), 793–806.

Saito, K., Kawaguchi, A., Okuda, S., Seyama, Y., Yamakawa, T., May 1980. Incorporation of hydrogen atoms from deuterated water and stereospecifically deuterium-labeled nicotin amide nucleotides into fatty acids with the Escherichia coli fatty acid synthetase system. Biochimica et biophysica acta 618 (2), 202–213.

Sauer, P. E., Eglinton, T. I., Hayes, J. M., Schimmelmann, A., Sessions, A., Jan. 2001. Compound-specific D/H ratios of lipid biomarkers from sediments as a proxy for environmental and climatic conditions. Geochimica Et Cosmochimica Acta 65 (2), 213–222.

Schouten, S., Ossebaar, J., Schreiber, K., Kienhuis, M., Langer, G., Benthien, A., Bijma, J., 2006. The effect of temperature, salinity and growth rate on the stable hydrogen isotopic composition of long chain alkenones produced by Emiliania huxleyi and Gephyrocapsa oceanica. Biogeosciences 3 (1), 113–119.

Sessions, A., Hayes, J. M., Feb. 2005. Calculation of hydrogen isotopic fractionations in biogeochemical systems. Geochimica Et Cosmochimica Acta 69 (3), 593–597.

Sessions, A., Hayes, J. M., Sylva, S., Summons, R., 2004. Isotopic exchange of carbon-bound hydrogen over geologic timescales. Geochimica Et Cosmochimica Acta 68 (7), 1545–1559.

Sessions, A., Jahnke, L. L., Schimmelmann, A., 2002. Hydrogen isotope fractionation in lipids of the methane-oxidizing bacterium< i> Methylococcus capsulatus</i>. ... et Cosmochimica Acta.

Smith, H. L., 1995. The theory of the chemostat: dynamics of microbial competition 13.

Soetaert, K., Petzoldt, T., Setzer, W., 2013. deSolve: General Solvers for Initial Value Problems of Ordinary Differential Equations (ODE), Partial Differential Equations (PDE), Differential Algebraic Equations (DAE), and Delay Differential Equations (DDE). R package version 1.10-8.
URL http://CRAN.R-project.org/package=deSolve

Soupene, E., van Heeswijk, W. C., Plumbridge, J., Stewart, V., Bertenthal, D., Lee, H., Prasad, G., Paliy, O., Charernnoppakul, P., Kustu, S., Sep. 2003. Physiological studies of Escherichia coli strain MG1655: Growth defects and apparent cross-regulation of gene expression. Journal of Bacteriology 185 (18), 5611–5626.

Steinhauser, M. L., Lechene, C. P., Aug. 2013. Quantitative imaging of subcellular metabolism with stable isotopes and multi-isotope imaging mass spectrometry. Seminars in Cell and Developmental Biology 24 (8-9), 661–667.

Tempest, D. W., Neijssel, O. M., 1984. The status of YATP and maintenance energy as biologically interpretable phenomena. Annual Reviews in Microbiology.

Thomas, A. F., 1971. Deuterium Labeling in Organic Chemistry.

Tijhuis, L., Van Loosdrecht, M. C. M., Heijnen, J. J., Aug. 1993. A thermodynamically based correlation for maintenance gibbs energy requirements in aerobic and anaerobic chemotrophic growth. Biotechnology and Bioengineering 42 (4), 509–519.

Turowski, M., Yamakawa, N., Meller, J., Kimata, K., Ikegami, T., Hosoya, K., Tanaka, N., Thornton, E. R., Nov. 2003. Deuterium isotope effects on hydrophobic interactions: the importance of dispersion interactions in the hydrophobic phase. Journal of the American Chemical Society 125 (45), 13836–13849.

Urey, H. C., Brickwedde, F. G., Murphy, G. M., 1932b. A hydrogen isotope of mass 2 and its concentration. Physical review 40 (1), 1–15.

Valentine, D. L., 2009. Isotopic remembrance of metabolism past. Proceedings of the National Academy of Sciences of the United States of America 106 (31), 12565–12566.

Valentine, D. L., Sessions, A., Tyler, S. C., CHIDTHAISONG, A., Jul. 2004. Hydrogen isotope fractionation during H_2/CO_2 acetogenesis: hydrogen utilization efficiency and the origin of lipid-bound hydrogen. Geobiology 2 (3), 179–188.

van Bodegom, P., May 2007. Microbial maintenance: a critical review on Its quantification. Microbial Ecology 53 (4), 513–523.

Verkman, A. S., Jan. 2013. Aquaporins. Current biology : CB 23 (2), R52–5.

Wegener, G., Bausch, M., Holler, T., Thang, N. M., Prieto Mollar, X., Kellermann, M. Y., Hinrichs, K.-U., Boetius, A., Apr. 2012. Assessing sub-seafloor microbial activity by combined stable isotope probing with deuterated water and 13C-bicarbonate. Environmental Microbiology 14 (6), 1517–1527.

White, S. W., Zheng, J., Zhang, Y.-M., Rock, 2005. The structural biology of type II fatty acid biosynthesis. Annual Review of Biochemistry 74, 791–831.

Whiteley, A. S., Manefield, M., Lueders, T., Feb. 2006. Unlocking the 'microbial black box' using RNA-based stable isotope probing technologies. Current Opinion In Biotechnology 17 (1), 67–71.

Wickham, H., 2014a. plyr: Tools for splitting, applying and combining data. R package version 1.8.1.
URL http://CRAN.R-project.org/package=plyr

Wickham, H., Chang, W., 2013. ggplot2: An implementation of the Grammar of Graphics. R package version 0.9.3.1.
URL http://CRAN.R-project.org/package=ggplot2

Xie, Y., 2013b. knitr: A general-purpose package for dynamic report generation in R. R package version 1.5.
URL http://CRAN.R-project.org/package=knitr

Yuan, Y., Leeds, J. A., Meredith, T. C., Oct. 2012a. Pseudomonas aeruginosa directly shunts β-oxidation degradation intermediates into de novo fatty acid biosynthesis. Journal of Bacteriology 194 (19), 5185–5196.

Yuan, Y., Sachdeva, M., Leeds, J. A., Meredith, T. C., Oct. 2012b. Fatty acid biosynthesis in Pseudomonas aeruginosa is initiated by the FabY class of β-ketoacyl acyl carrier protein synthases. Journal of Bacteriology 194 (19), 5171–5184.

Zhang, X., Gillespie, A. L., Sessions, A., Aug. 2009a. Large D/H variations in bacterial lipids reflect central metabolic pathways. Proceedings of the National Academy of Sciences of the United States of America 106 (31), 12580–12586.

Zhang, Z., Sachs, J. P., Marchetti, A., Mar. 2009b. Hydrogen isotope fractionation in freshwater and marine algae: II. Temperature and nitrogen limited growth rate effects. Organic Geochemistry 40 (3), 428–439.

Chapter 8

Spatiometabolic activity of complex microbial communities by multi-isotope imaging mass spectrometry with H, C and N

8.1 Introduction

Multi-isotope secondary ion Imaging Mass Spectrometry (MIMS or nanoSIMS) provides one of the most sensitive and precise analytical methods available for the study of elemental and isotopic composition at high spatial resolution. Increasingly, this powerful technique is applied to answer questions in biological systems that greatly benefit from the high spatial resolution and the vast possibilities conferred by the use of stable isotope tracers. This is especially the case in microbial ecology, where linking the identity of microorganisms to their activity in the environment remains a crucial gap in our understanding of microbial communities. In addition to using the technique to measure the natural isotopic

composition of individual cells in environmental systems (Orphan et al., 2001a; 2002; Fike et al., 2008), this has been very successfully employed in studying the spatiometabolic activity of deep sea methane oxidizing consortia (Pernthaler et al., 2008a; Orphan et al., 2009; Dekas et al., 2009; Dekas and Orphan, 2011; Dekas et al., 2013), soil microbe-mineral co-localization (Herrmann et al., 2006), and symbiotic microbe-animal interactions (Lechene et al., 2007; Kuypers, 2007; Pernice et al., 2012) using various ^{15}N labeled isotope tracers. Additionally, the non-toxic nature of stable isotope labels combined with the high sensitivity and spatial resolution of this technique poses tremendous potential for application in the quantitative study of metabolic processes within any model organism ranging from microbes to humans[1]. Examples include the application of isotopically labeled ^{15}N-thymidine to trace stem cell division and metabolism in mice (Steinhauser et al., 2012; Gormanns et al., 2012),^{13}C-oleic acid to study fatty acid transport in lipid droplets, ^{15}N-leucine to trace protein renewal in kidney cells (Lechene et al., 2006), various ^{15}N labeled amino acid for the study of protein turnover in hair-cell sterocilia (Zhang et al., 2012), ^{18}O-trehalose penetration into the nucleus of mouse sperm (Lechene et al., 2012) and dual ^{13}C and ^{15}N-labeld substrated in microbial activity studies of oral biofilms (Spormann et al., 2008). As evidenced by this accelerating body of work since the first applications of MIMS/nanoSIMS, this technique could be useful far beyond its original purpose in disciplines as diverse as geobiology, biogeochemistry, host-microbe interactions and biomedical research. For additional inspiration on this topic, we refere the reader to three excellent reviews: Orphan and House (2009), Steinhauser and Lechene (2013), and Hoppe et al. (2013).

The predominant traditional isotopic tracers (^{13}C and ^{15}N) face two major drawbacks for the study of metabolic activity in complex host systems and microbial communities. ^{13}C and ^{15}N labeled substrates frequently change the nutrient availability in an envi-

[1] Steinhauser and Lechene (2013) recently highlighted the extensive record of the safe application of stable isotopic studies in human subjects including infants, pregnant women, elderly and severely ill patients with diverese isotope tracers including the stable isotopes of hydrogen, carbon, nitrogen, oxygen, magnesium, calcium, iron, copper, zinc and selenium.

ronment, which biases measures of activity towards organisms that can quickly respond to changes in the added substrate. For example, the quantitative use of nitrogen and carbon as tracers is often limited by a) their differential use in communities with mixed metabolisms (preference by certain members of the community for a specific organic or inorganic carbon or nitrogen source), and b) the alteration of nutrient availability by the isotopic tracer (adding for example bioavailable nitrogen to a nitrogen-starved community). Here, we introduce the use of hydrogen isotope labeling with deuterated water as an important new addition to the isotopic toolkit available for use in mult-isotope imaging mass spectrometry. This tool provides a labeling technique that minimally alters any aquatic chemical environment (due to $^{2}H_2O$ being the label), can be administered with strong labels even in minimal addition (natural background is very low), and is an equally universal substrate for all forms of life even in complex, carbon- and nitrogen-saturated systems. Additionally - although analytically challenging - it can be combined with carbon and nitrogen tracers by simultaneous detection of all three isotopic systems in nanoSIMS imaging, as demonstrated for the first time in this study.

In this manuscript, we present the proof-of-concept application of truly simultaneous detection of all three isotope systems (hydrogen, carbon and nitrogen) in the isotopic analysis of single cells, establish the necessary calibration for the use of $^{2}H_2O$ in stable isotope tracer work with single cells at environmentally relevant levels of ^{13}C, ^{15}N and ^{2}H enrichment, and demonstrate its application in a study of microbial activity and population heterogeneity of *Staphylococcus aureus* during slow growth in continuous culture. Additionally, we expand the single cell calibration for isotopic tracer work with ^{2}H, ^{13}C and ^{15}N to applications in plastic embedded thin-sectioned samples, which we expect to further expand the range of applicability of this technique in complex systems.

8.2 Materials and Methods

8.2.1 Experimental setup

All media and reagent solutions used for culturing were autoclaved or filter-sterilized prior to use.

8.2.1.1 Bacterial isotope standards

Bacterial hydrogen, carbon and nitrogen isotopic standards for single cell analysis were created by growing the well-studied gram-positive organism *Staphylococcus aureus* (MN8 (KREISWIRTH et al., 1983)) and the well-studied gram-negative organism *Pseudomonas aeruginosa* (PA14 (RAHME et al., 1995)) in minimal medium with nutrients of different isotopic composition. A phosphate buffered minimal medium at pH 7.2 containing 2.5 g/L NaCl, 13.5 g/L K_2HPO_4, 4.7 g/L KH_2PO_4, 1 g/L K_2SO_4 and 0.1 g/L $MgSO_4 \cdot 7H_2O$ served as the basis for all experiments. *P. aeruginosa* was grown in this medium with different amounts of D_2O (up to 1%, from 70% stock, Cambridge Isotope Laboratories, #DLM-2259-70-1L), 10 mM ammonium chloride (spiked up to 10% ^{15}N with 98% enriched$^{15}NH_4Cl$, Sigma-Aldrich, #299251) and 10mM sodium succinate (spiked up to 10% with 99% enriched succinic-1,2-$^{13}C_2$ acid, Sigma-Aldrich, #491977). *S. aureus* was grown in this medium with different amounts of D_2O, 10 mM amonium chloride (both spiked identically to *P. aeruginosa* cultures) and 10mM glycerol (no isotopic label available at the time). *S. aureus* further exhibits auxotrophy for several amino acids and vitamins (Aldeen and Hiramatsu, 2004; LINCOLN et al., 1995; Mah et al., 1967) and the medium was further amended with 11.5 mg/L proline, 10mL/L 50x MEM Amino Acid solution (Sigma-Aldrich, #M5550, final amino acid concentrations: 63.2 mg/L arginine, 15.6 mg/L cysteine, 21 mg/L histidine, 26.35 mg/L isoleucine, 26.2 mg/L leucine, 36.3 mg/L lysine, 7.6 mg/L methionine, 16.5 mg/L phenylalanine, 23.8 mg/L threonine, 5.1 mg/L

tryptophan, 18.0 mg/L tyrosine, 23.4 mg/L valine) and 100µg/L thiamine (B1), 100 µg/L nicotinic acid (B3) and 10 µg/L biotin (B7).

All cells were grown in 50mL batch cultures aerobically at 37ºC, and were inoculated from fresh (exponential) cultures grown on the same medium and verified microscopically to be axenic. Cultures were harvested in mid-exponential phase to ensure as homogenous a population as possible for consistent isotopic composition. Cells were harvested by centrifugation at 4000rpm for 10min at 4ºC, and washed 5 times by resuspension in 1x phosphate buffered saline (PBS) solution to remove all traces of the isotopic labels. Before the last washing step, samples were split into separate aliquots for bulk isotopic analysis and single cell analysis. Aliquots for bulk analysis were pelleted, frozen and stored at -80C until further processing. Aliquots for single cell analysis were fixed in 1% freshly prepared formaldehyde in PBS (Paraformaldehyde, Electron Microscopy Sciences, #15713) for 2 hours at room temperature, then washed once in 1% PBS and dehydrated in 50% ethanol. A small aliquot was stored at 4C for whole single cell analysis, and the remainder was embedded for thin-sectioning.

Additional aliquots from samples grown without an isotopic label (i.e. natural abundance samples) were washed, fixed, dehydrated and embedded in identical manner to all other samples, except that the strongest employed mixture of isotope labels (~1% D_2O, ~10% $^{15}NH_4$, ~10% ^{13}C succinate) was spiked into the aliquots just prior to addition of the formaldehyde fixative in order to test the effects of fixation in the presence of unwashed isotope tracers.

8.2.1.2 Continuous culture

Continuous culture experiments were carried out with *S. aureus* growing in the same medium (+500µL/L Antifoam 204) at three different growth rates (corresponding to doubling times of ~6 hours, ~1 day and ~2 weeks) as described in detail in Section 7.3.2.2 of chapter 7. Briefly, once at steady state, culture vessels (usually ~500-600mL working

volume) were spiked with 1mL D_2O and 10mM $^{15}NH_4$ isotope tracers, and samples were withdrawn at regular intervals depending on the growth rate. Samples for single cell analysis were collected before adding the isotopic spike, at the last data point used for bulk analysis (see *S. aureus* cultures in minimal medium in Chapter 7), and twice more at equal intervals afterwards for a total of 4 samples (t0 + 60min, 120min and 180min for the fastest chemostat, 200min, 400min and 600min for the intermediate chemostat, 30hours, 60hours and 90hours for the slowest chemostat). Cell growth was arrested immediately after sample withdrawal by adding the sample directly into an equal volume of ice. Samples were washed, fixed and dehydrated in identical manner to bacterial isotope standards prepared for whole single cell analysis.

8.2.2 Bulk analysis

All bulk analyses were carried out on homogenized dry biomass from lyophilized cell pellets.

8.2.2.1 Bulk C and N analysis

For nitrogen isotope analysis, lyophilized cell pellets were additionally incubated at 80C for 24 hours to drive off any residual ammonium. For each sample, 300 to 800 µg of cell powder were weighed out into tin capsules in duplicate, and the bulk carbon and nitrogen isotopic composition was determined by EA-ir-MS at the UC Davis Stable Isotope Facility (Davis, CA).

8.2.2.2 Bulk H isotope analysis

Hydrogen exchanges rapidly in reactive groups and most O-H, N-H and S-H bonds (especially all acidic or basic functional groups) (Thomas, 1971; Katz, 1960), but is stably incorporated in many, virtually non-exchangable C-H bonds (Sessions et al., 2004) that can be used in compound specific isotope analyses of membrane fatty acids. Here, we thus use the average membrane fatty acid hydrogen isotopic composition as a measure of

bulk ^2H incorporation. This enables comparison with other compound-specific membrane component analysis of bulk biomass, as described, for example, in Chapter 7.

For hydrogen isotope analysis, lyophilized cell pellets were weighed out into ~1mg aliquots of dry cell mass and spiked with 10µg of 21:0 phosphatidyl choline as a phospholipid extraction standard. Samples were transesterified in the presence of an acid catalyst (acetyl chloride in anhydrous methanol, 1:20 v/v) at 100°C for 10 min (Rodríguez-Ruiz et al., 1998; Lepage and Roy, 1986), extracted into hexane, and concentrated under a stream of N_2 at room temperature prior to analysis. All non-consumable glassware used for lipid extraction and derivatization was pre-combusted in a muffle furnace at 550 °C to remove all remaining traces of organic materials potentially adhered to the glass. Fatty acid methyl esters (FAMEs) were identified by gas chromatography/mass spectrometry on a Thermo-Scientific Trace DSQ, and analyzed in triplicate for their isotopic composition by GC/pyrolysis/isotope-ratio mass spectrometry on a Thermo-Scientific Delta Plus XP (described in detail in Section 7.3.3.3 of Chapter 7). All data were corrected for the addition of methyl hydrogen during derivatization. Reported bulk hydrogen isotope compositions represent the mass balance weighted average isotopic composition of the whole membrane from all major fatty acid components for each organism (a-C15:0 and a-C17:0 fatty acid for *S. aureus* and C16:1, C16:0 and C18:1 fatty acid for *P. aeruginosa*).

8.2.3 Single cell analysis

8.2.3.1 Sample preparation

1µL aliquots of fixed whole cells suspended in 50% EtOH (both isotopic standards and continuous culture samples) were spotted onto custom-cut indium tin oxide (ITO) coated glass (TEC15, Pilkington Building Products, Greensboro, NC, USA) and air-dried at room temperature.

Lightly pelleted concentrates of the isotopic standards were suspended in a few drops of molten noble agar (2% Difco Agar Noble in 50mM HEPES buffered filter-sterilized water), solidified by cooling at room temperature, cut into ~2mm^{3}cubes, resuspended in 50% EtOH in PBS, and dehydrated in 100% Ethanol over the course of 3 exchanges, with final resuspension in 100% for at least 1 hour. Ethanol was then replaced twice with 100% Technovit 8100 infiltration solution (Heraeus Kulzer GmbH, #64709012) to infiltrate the agar plugs over night. Agar plugs were finally suspended in airtight 0.6mL microcentrifuge tubes in Technovit 8100 infiltration solution amended with hardener II reagent and stored at 4C over night to complete polymerization. Technovit is a cold-polymerising nitrogen-free acryl plastic composed of methyl methacrylate and glycol methacrylate.

Thin sections (1-2 µm thick) were cut using a rotary microtome. Each section was stretched on the surface of a 1.5µL drop of 0.2µm filtered deionized water on a 1" diameter round microprobe slide (Lakeside city, IL) and air-dried at room temperature. All ITOs and glass rounds were fully mapped microscopically with a 40x air objective for later orientation and sample identification during secondary ion mass spectrometry. ITO-coated glass is conductive, and spotted cells are too small to interfere with substrate conductivity. To prepare samples in plastic sections on glass rounds for analysis, the rounds were made conductive by sputter-coating with a 50nm layer of gold (Dekas et al., 2009; Dekas and Orphan, 2011).

8.2.3.2 NanoSIMS analysis

All samples were analyzed with a CAMECA NanoSIMS 50L (CAMECA, Gennevilliers, France) housed in the Division of Geological and Planetary Sciences at Caltech, with a mass resolving power of approximately 5000. Whole cells on ITO were analyzed using a ~3.6pA primary Cs^+ beam and were presputtered with ~20pC/µm^2. Cells embedded in plastic were analyzed using a ~1.9pA primary Cs^+ beam with a nominal spot size of ~300nm, and were presputtered with ~340pC/µm^2. Details on presputtering and

ionization efficiency are discussed in Section 8.3.1.1 of the Appendix. Seven masses were collected in parallel ($^{1}H^{-}$, $^{2}H^{-}$, $^{12}C^{-}$, $^{13}C^{-}$, $^{14}N^{12}C^{-}$, $^{15}N^{12}C^{-}$, $^{28}Si^{-}$) using electron multipliers. Individual samples were located using the NanoSIMS CCD camera, and random analytical spots were chosen within a sample area. For all analyses, the beam was rastered over a square region of 10µm by 10µm for 15min per analytical plane/frame, and images were collected in 256x256 pixel resolution. Presputtering was typically carried out on a larger region of 15µm by 15µm to make sure that the analytical frame was fully within. Analytical parameters including primary beam focus, secondary beam centering and mass resolution for all ions were verified and tuned every ~30 minutes (i.e. after every 2 frame analysis).

8.2.4 Quantification

Bulk carbon, nitrogen and hydrogen isotope measurements were recorded in the conventional δ-notation ($\delta^{13}C$ vs VPDB, $\delta^{15}N$ vs air, $\delta^{2}H$ vs VSMOW), but are converted to fractional abundances using the known isotopic composition of the reference standards (VPDB $\frac{^{13}C}{^{12}C} = 1.1180\%$, Air $\frac{^{15}N}{^{14}N} = 0.3676\%$, VSMOW $\frac{^{2}H}{^{1}H} = 155.7643ppm$, de Laeter et al. (2003)) to allow consistent reporting and exact mass balance calculations[2]. Fractional abundances of single cell analyses were calculated directly from raw ion counts and calibrated against bulk measurements (Section 8.3.2). In this study, the fractional abundance values of most isotopically enriched standards and samples fall into the percent (10^{-2}) range, and are thus reported in %. All conversions and mass balance calculations were performed using an isotopes R module described in the Appendix. All data processing, analysis, model simulations and plotting were performed in R (R Core Team, 2014) using functionality provided by various analytical and graphical packages (Soetaert et al., 2013; Wickham, 2014a; Wickham and Chang, 2013; Xie, 2013b; Neuwirth, 2011; Dragulescu, 2013).

[2]See Section D.5.1 in the Appendix of Chapter 7 on the topic of exact mass balance calculations.

8.2.4.1 Ion image processing

Raw data from all acquired ion images was processed using the open-source MATLAB plugin Look@NanoSIMS (Polerecky et al., 2012). Ion images from multiple frames were corrected and aligned, and discrete regions of interest (ROIs) were hand-drawn to identify the cellular outlines. Here, ROIs refer to the spatial demarkation of individual cells (the isotopic composition of an ion map inside the cell outline). The terms *ROI* and *single cell* represent the same concept in this manuscript, and are used interchangeably. The raw ion counts for all collected ions from individual and aggregated frames in the individual ROIs were exported from Look@NanoSIMS, and further processed in R.

8.2.4.2 Error in single cell isotope measurements

Even if detection, amplification and signal conversion in isotope ratio measurements were completely free of noise, there would still be a theoretical limit to the maximum attainable precision of isotopic data. This limit is posed by shot noise, a consequence of the discrete nature of electronic charge (whether it is carried by electrons or ions). The statistical error from shot noise is rarely a concern in standard bulk isotope measurements, but due to the low number of ions detected from measuring individual cells in secondary ion mass spectrometry, this error can become significant. This is particularly relevant in measurements of ions from low abundance elements, ions with low ionization efficiency or with rare minor isotopes (hydrogen qualifies for the last two). The error from shot noise is often considered in terms of the resulting isotope ratio or δ-value (Hayes, 2002), but rarely in terms of fractional abundances. The relevant equation is derived in detail in the Appendix (E.1), and yields

$$\left(\frac{\sigma_F}{F}\right)^2 = (1-F)^2\left(\frac{1}{N_m}+\frac{1}{N_M}\right) = \frac{(1-F)^2}{N_M F} \tag{8.1}$$

where N_m is the ion count of the minor isotope, N_M the ion count of the major isotope, and F/σ_F is the resulting fractional abundance and standard deviation.

8.2.4.3 Quality control

Due to the low ionization efficiency of hydrogen and the rare abundance of ^{2}H, primary ion beam currents employed in this study have to be relatively high. This is less problematic in plastic sections where the acryl support matrix provides higher resistance to ablation by the primary ion beam, but causes relatively fast destruction of unsupported whole single cells. Typically, this allows for a maximum of three sequential frames during analysis of single cells. Two frames were collected routinely, and individual ROIs[3] were screened for consistency between the isotopic values of two subsequent frames to control for higher quality data not distorted by sample destruction. ROIs with isotopic value F_i in any frame deviating by more than $2 \cdot \sigma_F$ (eq. 8.1) and more than 1% from the frames' accumulated average F were discarded. For details, see Sections 8.3.1.1 and E.2.1 of the Appendix.

8.3 Results and Discussion

8.3.1 Simultaneous analysis of H, C and N isotopes

The CAMECA NanoSIMS 50L is a multicollector secondary ion mass spectrometer equipped with 7 electron multiplier detectors on movable trolleys that provide simultaneous detection of up to 7 secondary ions at a fixed magnetic field strength. The large dynamic range of the instrument typically allows parallel detection of ions with vastly different masses up to a ~22:1 ratio (i.e. $m_{max} = 22 \cdot m_{min}$). This allows, for example, routine parallel detection of several of the most important biological ions with $^{12}C^-$ at 12 Da, $^{14}N^{12}C^-$ (the ionized form of nitrogen) at 26 Da, $^{31}P^-$ at 31Da and $^{32}S^-$ at 32 Da as well as their

[3]Here, **R**egions **O**f **I**nterest (ROIs) refer to the spatial demarkation of individual cells (the isotopic composition of an ion map inside the cell outline). The term *ROI* and *single cell* represent the same concept in this manuscript, and are used interchangeably.

minor isotopes, $^{13}C^-$ at 13 Da, $^{15}N^{12}C^-$ at 27 Da and $^{34}S^-$ at 34 Da. However, due to the low mass of hydrogen, simultaneous measurement of $^{1}H^-$ at 1 Da ($m_{min} = 1$) and $^{2}H^-$ at 2 Da can only be combined with other ions up to a mass of 22 Da ($m_{max} = 2$), which allows multi-isotope imaging for H and C in parallel, but not H and N in parallel. This restriction provides a serious impediment to the use of hydrogen labeled isotopic tracers in combination with nitrogen (both an important isotopic tracer and identifying ion for biomass). One approach to this problem is to use the instrument in magnetic field switching mode, which requires alternating magnetic field strengths to capture the various ions in subsequent frames of the same analysis. However, cycling the magnetic field is time consuming, does not allow for true simultaneous detection, and retaining the mass resolving power required for resolving all isotopologues (especially isobaric interference at 27 Da for $^{15}N^{12}C^-$) is often unreliable.

An alternative approach was proposed in recent work (Lozano et al., 2013; Kraft and Klitzing, 2014) by measuring the $^{12}C^{2}H^-$ vs. $^{12}C^{1}H^-$ ions with a NanoSIMS 50L in experiments with highly ^{2}H enriched sphingomeylin lipids as tracers, and correcting the measured ratio for isobaric interferences from $^{13}C^{1}H^-$ and $^{12}C^{2}H^-$. However, the mass resolving power achievable by the CAMECA NanoSIMS 50L is insufficient to resolve these interferences at any level that makes the method applicable to environmental tracer experiments without highly enriched ^{2}H (Doughty et al., 2014). Yet another method is currently under development at the National Resource for Imaging Mass Spectrometry operated by the Harvard Medical School. This method takes advantage of the deflection plates located in front of the electron multipliers to use electrostatic peak switching for quasi-simultaneous detection of $^{12}C_2{}^{2}H^-$ and $^{12}C^{14}N^-$ (both nominally at 26 Da). However, significant isobaric interferences include $^{13}C_2{}^-$, $^{12}C^{13}C^{1}H^-$ and $^{12}C_2{}^{1}H_2{}^-$, which makes it questionable whether this method will be suitable for environmental tracer experiments.

Here, we demonstrate the feasibility of measuring the actual $^{1}H^-$, $^{2}H^-$, $^{12}C^-$, $^{13}C^-$, $^{14}N^{12}C^-$ ions all in parallel by extending the positions of the detector trolleys at the high

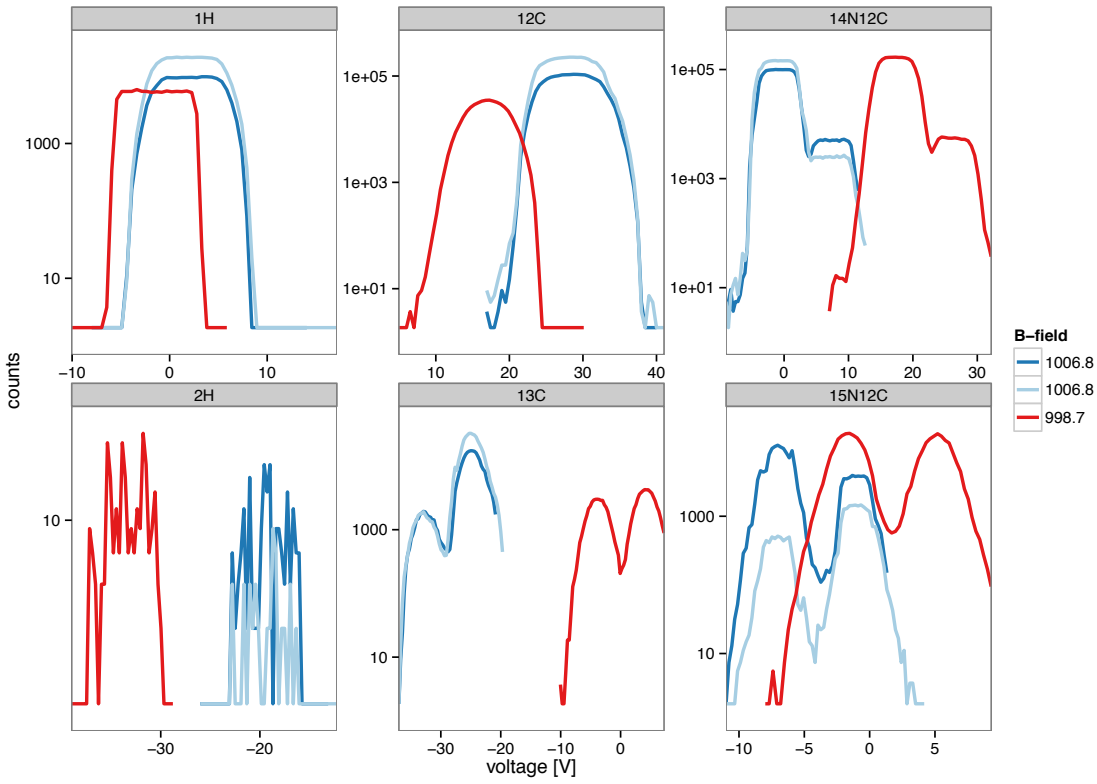

Figure 8.1 – HMR curves for H, C, N isotope analysis on a CAMECA NanoSIMS 50L. The dynamic range and mass resolving power of the multicollector NanoSIMS 50L at the Center for Microanalysis at Caltech permits multi-isotope imaging mass spectrometry with fully resolved H, C and N for the first time. Intensities are plotted on a logarithmic scale.

and low end to their maximally possible configuration in a CAMECA NanoSIMS 50L to gain an effective dynamic mass range of 28:1. Figure 8.1 shows the mass resolution curves at a magnetic field strength of 1006.8 T for two different samples (dark blue is enriched in ^{15}N, ^{13}C and ^{2}H, light blue is natural abundance), and at a magnetic field strength of 998.7 T (red curve). Both magnetic field strengths and trolley setups performed well, and allowed simultaneous detection of all ions with key isobaric interferences well-resolved. All curves plotted on a log scale to emphasize overlap:$^{13}C^-$ is resolved from the slightly higher mass $^{12}C^1H^-$, $^{14}N^{12}C^-$ is resolved from the slightly higher mass $^{12}C^{13}C^1H^-$and $^{15}N^{12}C^-$ is resolved from the slightly higher mass $^{14}N^{13}C^-$. The configuration with the higher magnetic field strength additionally allowed detection of $^{28}Si^-$ with the 7th detector, while the configuration with the slightly weaker magnetic field showed slightly higher peak

stability. The key here for parallel analysis even of natural abundance hydrogen isotopes is the detection at 1 Da and 2 Da, where the lack of isobaric interferences allows for complete resolution and high sensitivity to minor enrichments.

8.3.1.1 Optimizing presputtering conditions

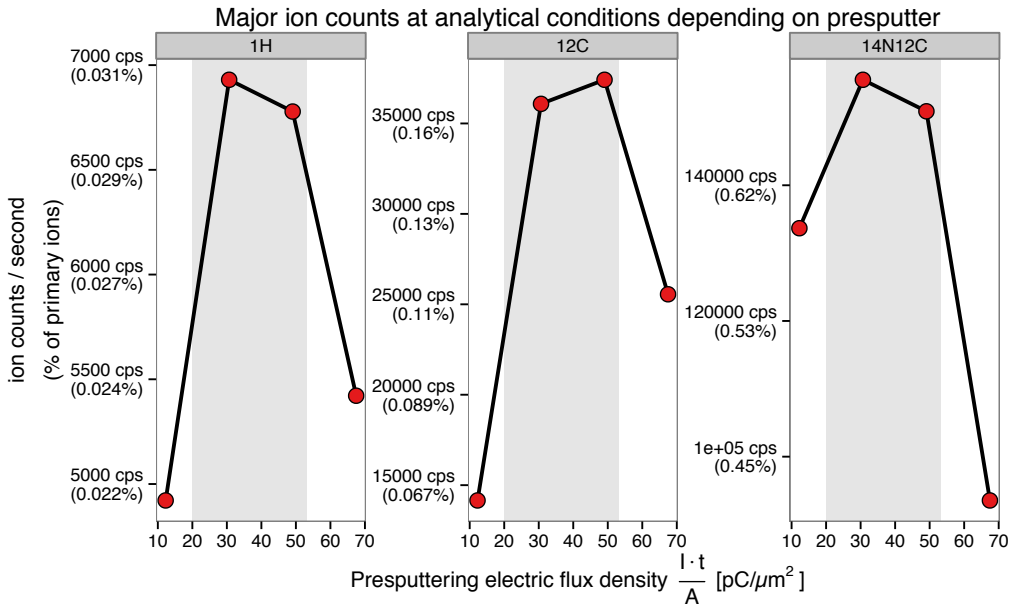

Figure 8.2 – Ionization efficiency and sample ablation in free cells.

One challenge of the simultaneous measurement of hydrogen, carbon and cyanide ions is their different ionization efficiencies. Hydrogen ionizes least efficiently, but requires high ion counts due to exceptionally low natural abundance of ^{2}H (~150ppm). To detect a sufficiently high number of ions without excessively long analysis times, a relatively strong primary beam current is required, which limits the maximal spatial resolution. In balancing primary beam current, aperture, presputtering and analysis time, additional complications arise from the destructive nature of the technique and the faster ionization of nitrogen. Presputtering is a process where the sample is bombarded with a higher primary beam current for a short amount of time prior to analysis in order to "embed" primary ions in the sample matrix (Hoppe et al., 2013). This greatly improves ionization efficiency,

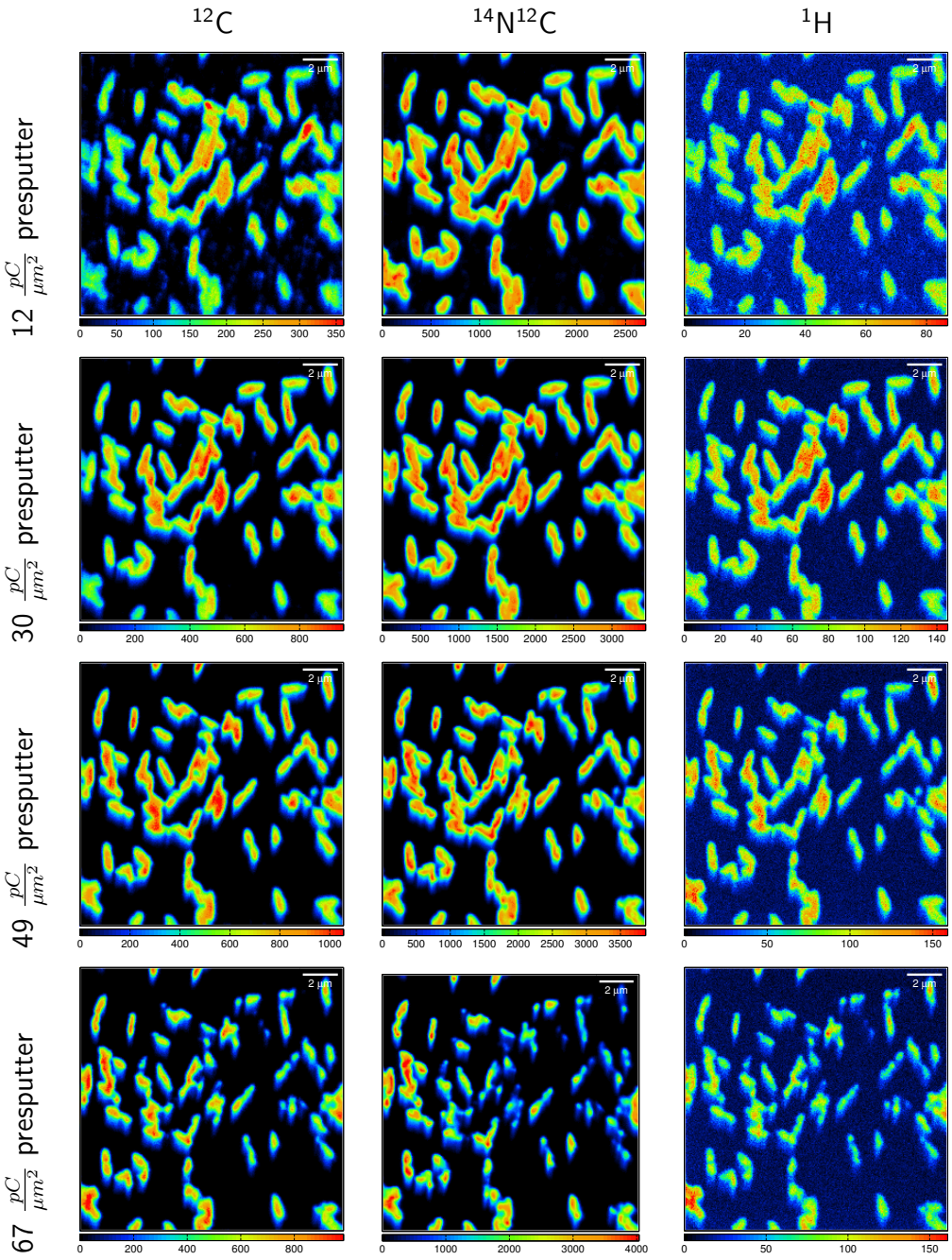

Figure 8.3 – Depth degradation test with whole cells. Ionization/degradation test with a 15µm x 15µm raster after various times of presputtering. Ion maps collected in a 4min analysis with a primary beam current of ~3.6pA. See Figure 8.2 for details.

and consequently provides higher secondary ion counts during analysis, but also degrades the sample and changes ionization efficiency differentially depending on the ion. Figure 8.2 illustrates the change in ion counts per second for the major isotopes' ions (^{1}H, ^{12}C,

$^{14}N^{12}C$) as a function of pre-exposing the sample surface (here, a cluster of single whole cells of *P. aeruginosa* on ITO coated glass) to increasing amounts of charge (from the primary ion beam) per unit area. The figure shows how presputtering increases ionization efficiency up to a maximum, at which point the sample is increasingly degraded, and ion counts drop as the organic material disappears. This can also be observed visually, as illustrated in the ion maps in Figure 8.3, which correspond to images acquired during short analyses at each data point in Figure 8.2 (ion counts for the minor isotopes from these quick analyses would not be sufficient for determining cells' isotopic composition). Additionally, the faster increase in the ionization efficiency of nitrogen, and subsequent quicker depletion of the element in response to presputtering, is clearly visible. This requires adapting analytical conditions to capture ion images ideally during peak ionization before cellular degradation. The corresponding analytical window targeted in this study for all analyses of intact single cells is indicated by the gray band in Figure 8.2. Lastly, the figure also indicates the ion counts as a percentage of the primary beam current. This measure depends on both the total abundance of each element and their respective ionization efficiencies, and as such is *not* an indication of absolute ionization efficiencies. However, it provides some information about relative differences between elements, and illustrates the relatively high ionization efficiency of nitrogen: $^{14}N^{12}C^-$ ions reach ~0.7% of the primary beam current compared to ~0.2% for $^{12}C^-$, although the abundance of carbon in organic material exceeds that of nitrogen (*P. aeruginosa* cells were measured to have a C:N mole ratio of ~4.5). Likewise, the low ionization efficiency of hydrogen becomes apparent: $^1H^-$ions reach only ~0.03%, although hydrogen is by far the most abundant element in organic material.

Figure 8.4 illustrates the change in ion counts per second for the major isotopes' ions as a function of pre-exposing plastic-embedded cells to increasing amounts of charge from the primary ion beam. Compared to whole single cells, the plastic matrix provides a material that is much more resilient to ion bombardment, as evidenced by the significantly

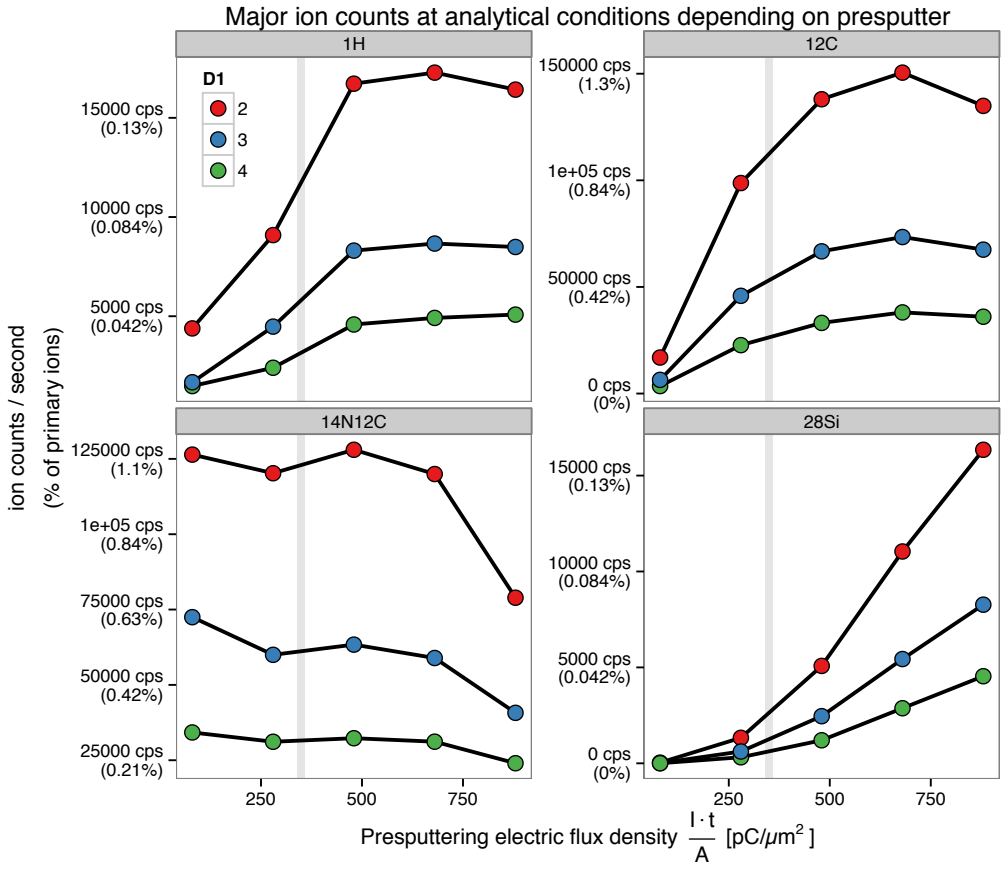

Figure 8.4 – Ionization efficiency and sample ablation in embedded cells.

higher presputtering flux (>10x higher) required for an increase in ionization efficiency and sample degradation. This is partly due to the gold coating, but the primary ion beam vaporizes the thin gold layer relatively quickly (the gold is already removed by the time of the first data point in Figure 8.4), and is mostly a consequence of the plastic matrix. This figure also shows the same trends observed for whole cell analysis, namely the faster increase in ionization efficiency and subsequent quicker depletion of nitrogen. Additionally, $^{28}Si^-$ ions were collected in addition to H, C and N ions, and illustrate the gradual degradation of the plastic to the point where the underlying glass starts to contribute to the secondary ion beam. Figure 8.4 also illustrates the effects of altering the analytical beam current by changing the aperture from ~1.9pA (aperture D1-2) to ~0.9pA (D1-3) to ~0.45pA (D1-4). Figure 8.5 finally shows the ion maps, which correspond

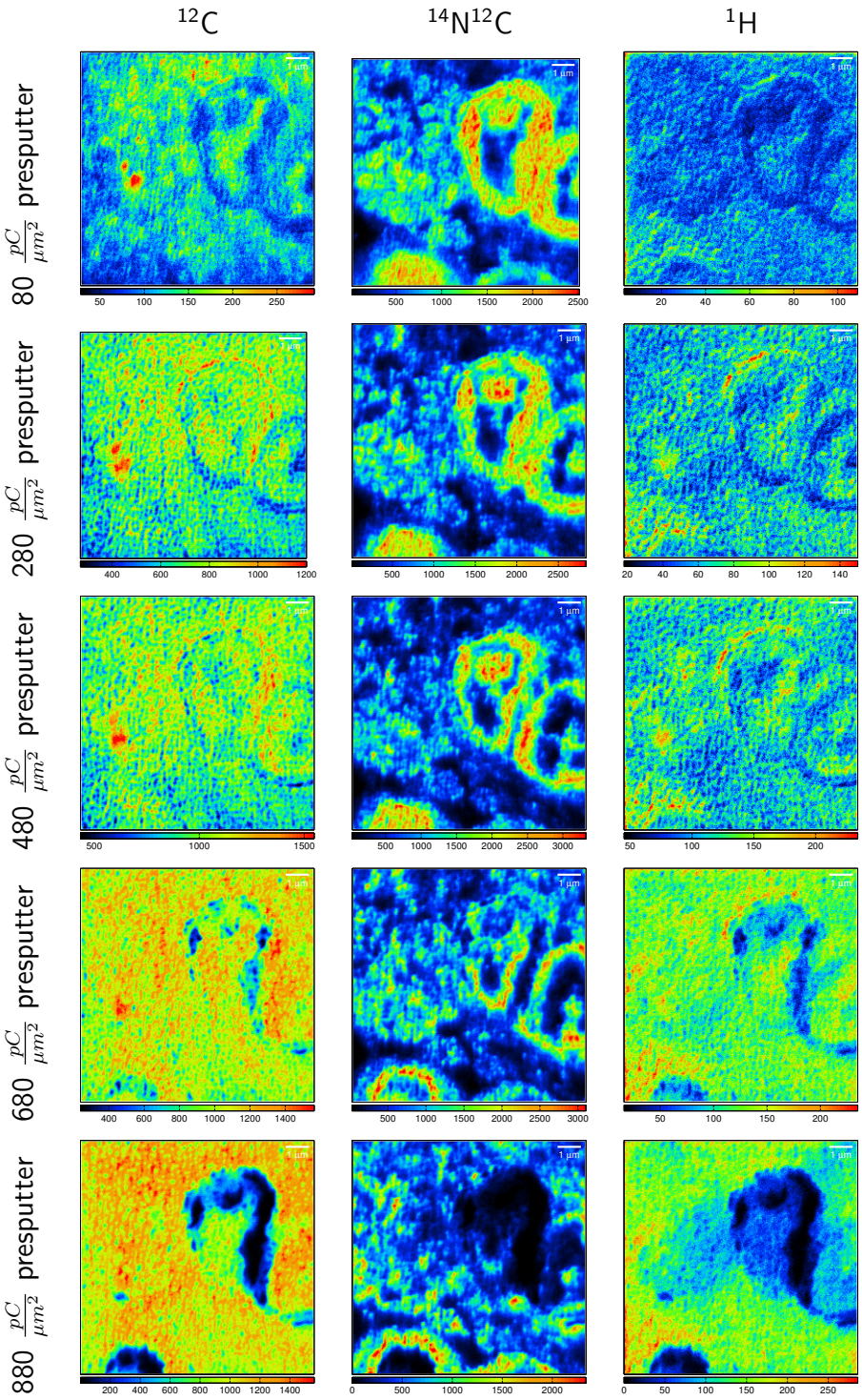

Figure 8.5 – Depth degradation test in plastic. Ionization/degradation test with a 10µm x 10µm raster after various times of presputtering. Ion maps collected in an 8min analysis with a primary beam current of ~1.9pA. See Figure 8.4 for details.

to images acquired with the highest beam current (~1.9pA) during short analyses at each data point in Figure 8.4. While the plastic embedded samples degrade at a much slower rate, thus extending the window for analysis, this figure clearly illustrates the accelerated degradation of nitrogen containing cellular material (here, the nuclei of two eukaryotic cells), highlighting the importance of timing analysis with presputtering such that ionization efficiencies are relatively high, but all cellular components are still intact. In this study, analysis was targeted roughly to the analytical window starting at the gray band in Figure 8.4. Despite the relatively high primary beam current, we maintained high spatial resolution that allowed distinct detection of individual cells of *S. aureus* at sizes below ~300nm^2 (see ion maps for isotopic standards in Figure E.6).

8.3.2 Single cell vs. bulk analysis

To calibrate the simultaneously acquired measurements of hydrogen, carbon and nitrogen isotopic composition of single cells by NanoSIMS, we measured single cells of isotopically labeled homogenous cultures of *S. aureus* and *P. aeruginosa* with independently measured bulk isotopic composition. This calibration step is particularly important for hydrogen due to the high capacity for H exchange in organic material, and is prudent in light of the first application of multi-isotope imaging mass spectrometry with H, C and N simultaneously. Although natural abundance cells of *Escherichia coli* and spores of *Clostridia* (Davission et al., 2008; Orphan et al., 2009; Dekas and Orphan, 2011) as well as highly ^{15}N enriched (~50% ^{15}N) cells of *P. fluorescences* (Herrmann et al., 2006) have been used as reference materials for isotopic analysis of whole single cells, to our knowledge, an actual calibration with enriched isotopic standards does also not exist for carbon or nitrogen analysis of free whole cells. Additionally, in the case of isotope analysis of cells embedded within a plastic polymer (which introduces large quantities of carbon and hydrogen), it is crucial to calibrate for matrix effects.

Calibration parameters were calculated from 1/x weighted linear regression of the

Type	Organism	Isotope	${}^{x}F_{cells}$ vs. ${}^{x}F_{bulk}$ slope	${}^{x}F_{cells}$ vs. ${}^{x}F_{bulk}$ intercept ${}^{x}F[\%]$	R^2
free	*P. aeruginosa*	${}^{2}H$	0.67 ± 0.05	0.0 ± 0.0	0.998
free	*S. aureus*	${}^{2}H$	0.59 ± 0.05	0.0 ± 0.0	0.997
free	*P. aeruginosa*	${}^{13}C$	0.73 ± 0.07	0.1 ± 0.2	0.997
free	*P. aeruginosa*	${}^{15}N$	0.94 ± 0.06	-0.0 ± 0.1	0.998
free	*S. aureus*	${}^{15}N$	0.91 ± 0.03	0.0 ± 0.0	1.000
plastic	*P. aeruginosa*	${}^{2}H$	0.30 ± 0.06	0.0 ± 0.0	0.985
plastic	*S. aureus*	${}^{2}H$	0.34 ± 0.07	0.0 ± 0.0	0.981
plastic	*P. aeruginosa*	${}^{13}C$	0.17 ± 0.02	0.6 ± 0.0	0.994
plastic	*P. aeruginosa*	${}^{15}N$	0.95 ± 0.04	0.0 ± 0.1	0.999
plastic	*S. aureus*	${}^{15}N$	1.31 ± 0.29	-0.2 ± 0.3	0.981

Table 8.1 – Summary of single cell vs. bulk analysis. Calibration parameters for all isotopic standards tested in this study. PA = *Pseudomonas aeruginosa*, SA = *Staphylococcus aureus*.

average isotopic composition of all single cells for a given standard vs. the measured bulk isotopic composition. Table 8.1 summarizes the calibration parameters for all isotopic standards tested in this study, and is discussed in detail hereafter. Calibration curves are illustrated visually in Figures 8.6, 8.7, E.8 and E.10. In calculations of the average single cell composition, individual cells were weighted inversely by the Poisson error in their isotopic measurement to offset the influence of highly imprecise measurements (from small ROIs and low ion counts).

8.3.2.1 Whole cells

Figures 8.6 and 8.7 show the calibration curves for single whole cell analyses of *P. aeruginosa* (172 ROIs) and *S. aureus* (222 ROIs), respectively. Additional detail on all ROIs is presented in the Appendix, Figures E.2, E.4, E.7 and E.9, with ion maps in Figure E.6. As expected, the nitrogen isotope compositions of single cells for both organisms mirror the bulk isotopic composition, with near perfect linear correlation and slope close to 1. However, it is important to note that both slopes fall slightly short of 1.0 (0.94±0.06 and 0.91±0.03), suggesting either systematic dilution of the cellular isotopic signal from trace nitrogen on ITO coated glass, systematic isotope fractionation in the analytical process, or both. Background analysis of nitrogen ion counts on ITO coated glass indicates that this component, while present, contributes maximally ~1% of cellular

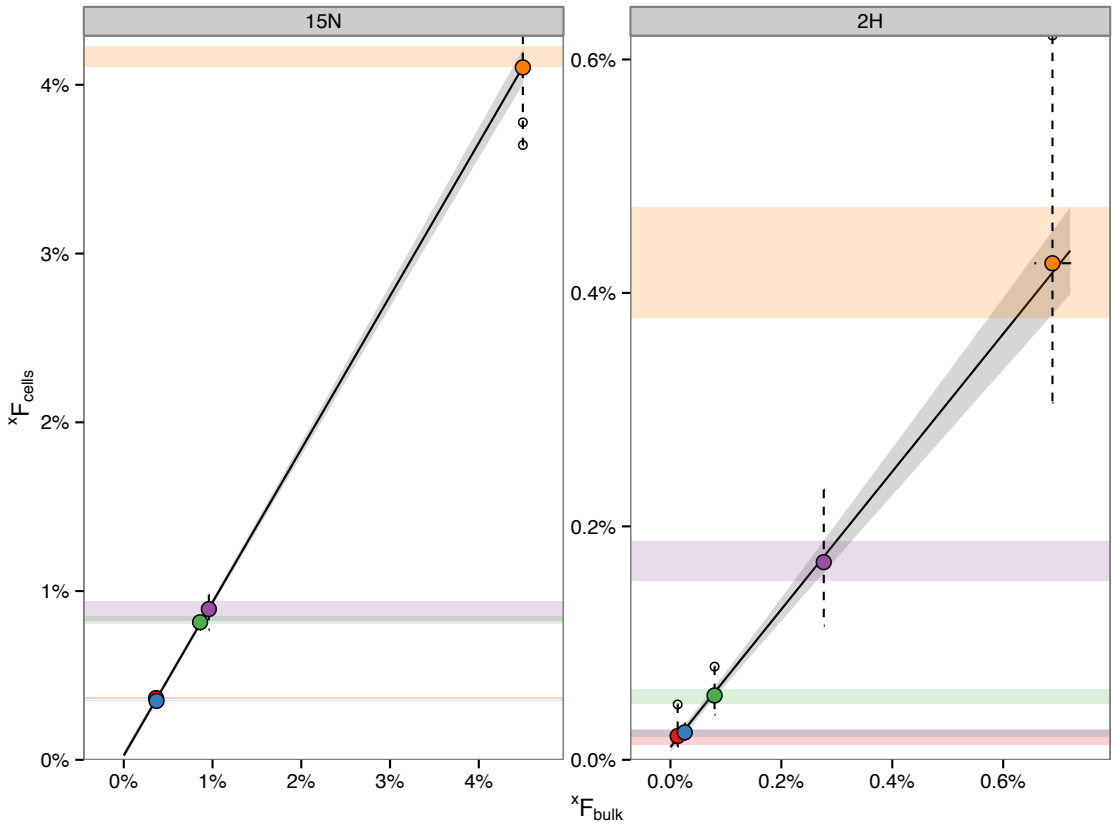

Figure 8.6 – Calibration curve for whole single cells of *S. aureus*. Calibration curve for isotopic composition of single cells measured by NanoSIMS vs. bulk isotopic composition of the population (measured by EA-ir-MS / GC-pyrolysis-ir-MS). Data points represent the mean isotopic composition of all measured single cells. The colored bands for each data point represent the range that comprises 50% of the single cell data. The dashed whiskers represent the entire range of all single cells. The empty white circles represent statistical outliers. Horizontal error bars represent the maximum interval of the measured bulk isotopic composition (smaller than symbol sizes in most cases).

nitrogen (data not shown). Since isotope ratios and fractional abundances of single cells are derived here directly from NanoSIMS ion count measurements without comparison to an authentic reference standard, fractionating effects during ionization and analysis likely contribute to the observed discrepancy.

Similar effects are observed for the carbon isotope composition of single *P. aeruginosa* cells (no ^{13}C standards were prepared for *S. aureus*), which closely follow the bulk isotopic composition but also fall short, with a slope of 0.73 ± 0.07. This also suggests a combination of systematic dilution and isotopic fractionation during analysis. Background

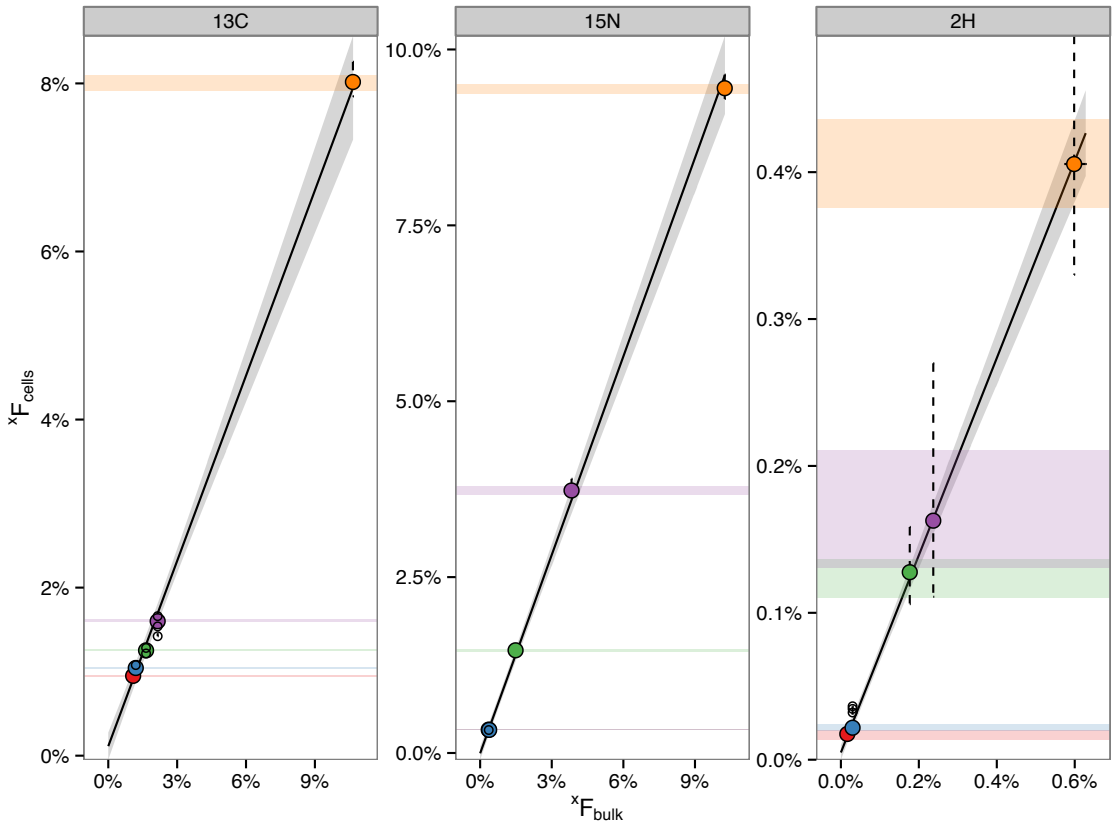

Figure 8.7 – Calibration curve for whole single cells of *P. aeruginosa*. Calibration curve for isotopic composition of single cells measured by NanoSIMS vs. bulk isotopic composition of the population (measured by EA-ir-MS / GC-pyrolysis-ir-MS). Data points represent the mean isotopic composition of all measured single cells. The colored bands for each data point represent the range that comprises 50% of the single cell data. The dashed whiskers represent the entire range of all single cells. The empty white circles represent statistical outliers. Horizontal error bars represent the maximum interval of the measured bulk isotopic composition (smaller than symbol sizes in most cases).

analysis also indicates a maximal contribution of organic carbon adhered to the ITO coated glass of ~3%. However, in the case of carbon, fixed single cells are expected to be slightly offset isotopically from the unfixed bulk population due to the introduction of near natural abundance carbon in formaldehyde. Musat et al. (2014) recently reported this effect to account for a ~4% dilution of cellular carbon in experiments with *Pseudomonas putida*, which could explain part of the observed offset in the calibration. Lastly, it is important to note that the nitrogen isotopic composition of highly enriched *S. aureus* cells shows a significant amount of spread with a predominant cluster of cells at the expected value, but

several outliers (see Figure 8.6) deviating by more than 10%. This is likely a consequence of slight heterogeneities even in the exponentially growing cultures modulating the isotopic composition of individual cells due to differential incorporation of the diverse sources of nitrogen available to *S. aureus* (several amino acids present in addition to the isotopically labeled ammonium; see Section 8.2.1.1 for detail).

Finally, the hydrogen isotope composition of single cells for both organisms show a robust linear dependence on the bulk (whole membrane) isotopic composition. The slope is substantially lower than unity (0.67±0.05 for *P. aeruginosa* and 0.59±0.05 for *S. aureus*). This is consistent with the expected effects of hydrogen exchange. While the measured bulk isotopic composition is based on non-exchangeable hydrogen incorporated into membrane fatty acids, the ^{2}H content of individual cells measured by NanoSIMS is necessarily based on the integrated signal from all cellular hydrogen. Here, we employed a strict multi-step washing protocol for all cultures, with the goal of exchanging all readily exchangeable hydrogen with natural abundance H ($\delta^2 H \approx -60‰$) from the washing solutions. This should allow for applying the calibration between single cell ^{2}H content measured by NanoSIMS and bulk membrane incorporated ^{2}H measured by GC-pyrolysis-ir-MS for cells treated identically. The calibration parameters inferred for *P. aeruginosa* and *S. aureus* suggest, however, that there can be a substantial degree of variability between individual organisms. The observed pattern indicates that *S. aureus* cells contain a higher proportion of hydrogen that exchanges during these washing steps (lower slope) than *P. aeruginosa* (higher slope), which is consistent with the gram-positive (one lipid membrane instead of two), spherical (lower surface to volume ratio) *S. aureus* containing a lower proportion of lipid bound hydrogen than the gram-negative (two lipid membranes), rod-shaped *P. aeruginosa.* In the absence of any isotope fractionation in the detection of hydrogen during NanoSIMS analysis, the observed slopes would indicate that about ~40% of the hydrogen was lost to exchange with water during the washing steps for *S. aureus*, and ~30% for *P. aeruginosa*. Lastly, single cell isotopic measurements of

hydrogen show substantial variability around the mean for both *S. aureus* and *P. aeruginosa* (Figures 8.6 and 8.7), which likely reflects both the high statistical uncertainty in the measurements for each single cell from low ion counts of ^{2}H (see Section E.1 , Figure E.7 and Figure E.9 in the Appendix), as well as random variation in the exact cellular components (highly exchangeable vs. non-exchangeable parts of the cell) sampled by the ion beam. This aspect of hydrogen isotope measurements of single cells by secondary ion mass spectrometry is a fundamental constraint that limits the ability to resolve small isotopic differences between individual cells, and requires the analysis of many cells (10s to 100s) within a microbial population if isotopically similar communities need to be distinguished.

This calibration provides the empirical parameters for inferring the bulk (whole membrane) hydrogen isotopic composition from the analysis of single whole cells of *S. aureus* and *P. aeruginosa*, with the statistical caveats outlined above. The technique is applied and cross-validated in a case study of growth and population heterogeneity in continuous culture of *S. aureus* (see Section 8.3.3 below). While this calibration is likely applicable to other gram-negative and gram-positive cells of similar morphology that are prepared identically for NanoSIMS analysis, this extrapolation to other microorganisms has to be interpreted with care.

8.3.2.2 Thin sectioned cells

Multi-isotope imaging mass spectrometry in thin-section vastly expands the range of applicability of this technique in complex systems. However, many thin sectioning techniques with a relatively soft, removable matrix (e.g. embedding in OCT for cryosectioning, or embedding in paraffin) do not permit cutting sections thinner than ~5µm. While less problematic for large eukaryotic cells, this limits the potential applicability for microbial cells within larger communities or host systems where accurate targeting and identification of individual microbial cells in an ion image require even thinner sections. Hard polymerizing

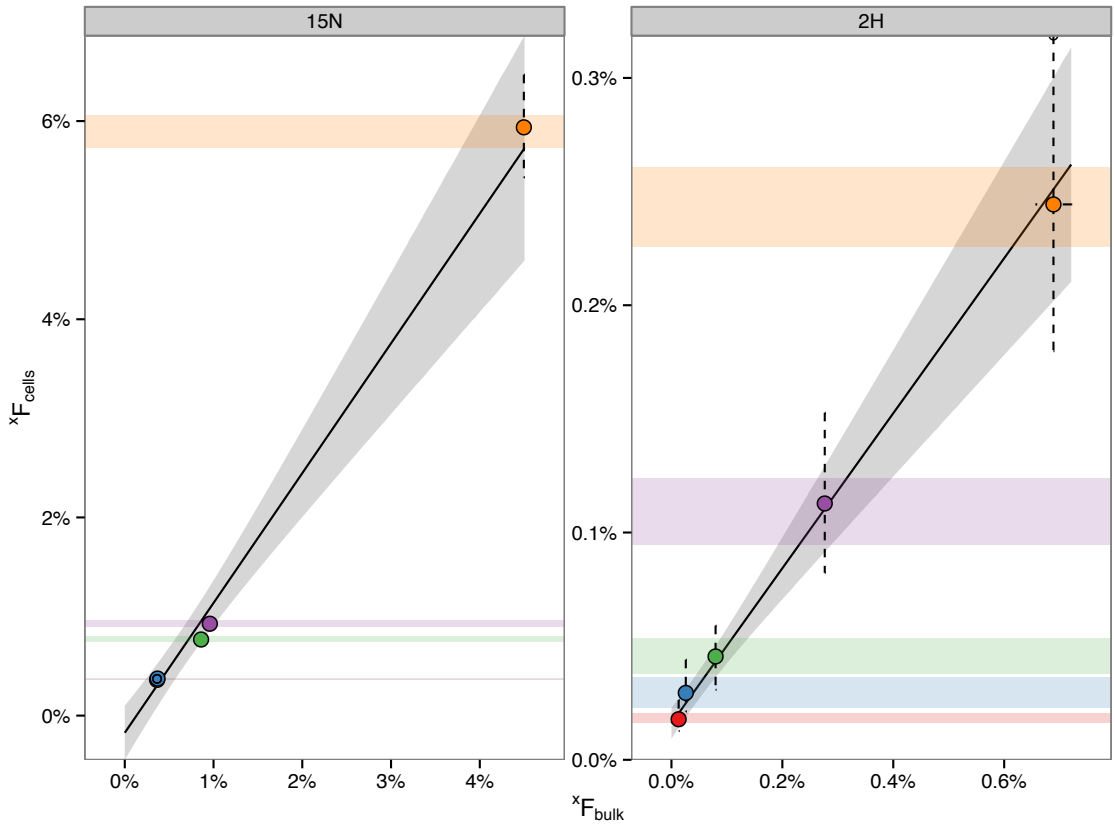

Figure 8.8 – Calibration curve for embedded single cells of *S. aureus*. Calibration curve for isotopic composition of single cells measured by NanoSIMS vs. bulk isotopic composition of the population (measured by EA-ir-MS / GC-pyrolysis-ir-MS). Data points represent the mean isotopic composition of all measured single cells. The colored bands for each data point represent the range that comprises 50% of the single cell data. The dashed whiskers represent the entire range of all single cells. The empty white circles represent statistical outliers. Horizontal error bars represent the maximum interval of the measured bulk isotopic composition (smaller than symbol sizes in most cases).

plastic resins developed for electron microscopy, such as LR White, provide the matrix support required for ultra-thin sections, however, they are often too dense to permit the use of fluorescent staining techniques important for microbial identification, such as fluorescent *in-situ* hybridization. Here, we thus use the plastic polymer Technovit, which is of intermediate hardness, and allows both routine sectioning to ~1µm thickness as well as application of most fluorescent staining techniques (Takechi et al., 1999). Technovit works well for preserving the structure of a sample and, unlike most resins, polymerizes at cold temperatures (~4C), precluding the need for extended exposure to relatively high heat

(and the associated risk for structural changes). The structural support lent by the plastic matrix provides thin-sections with a smooth surface that enables high spatial resolution in imaging mass-spectrometry due to the lack of strong topological features. It also retards sample destruction by the ion beam, as discussed in Section 8.3.1.1. However, as an acryl plastic (a combination of methyl methacrylate and glycol methacrylate), the Technovit resin contributes significant amounts of isotopically circumnatural carbon and hydrogen that dilute the isotopic signal from enriched cells. It is thus imperative to calibrate and correct any isotopic measurements of single cells embedded in plastic.

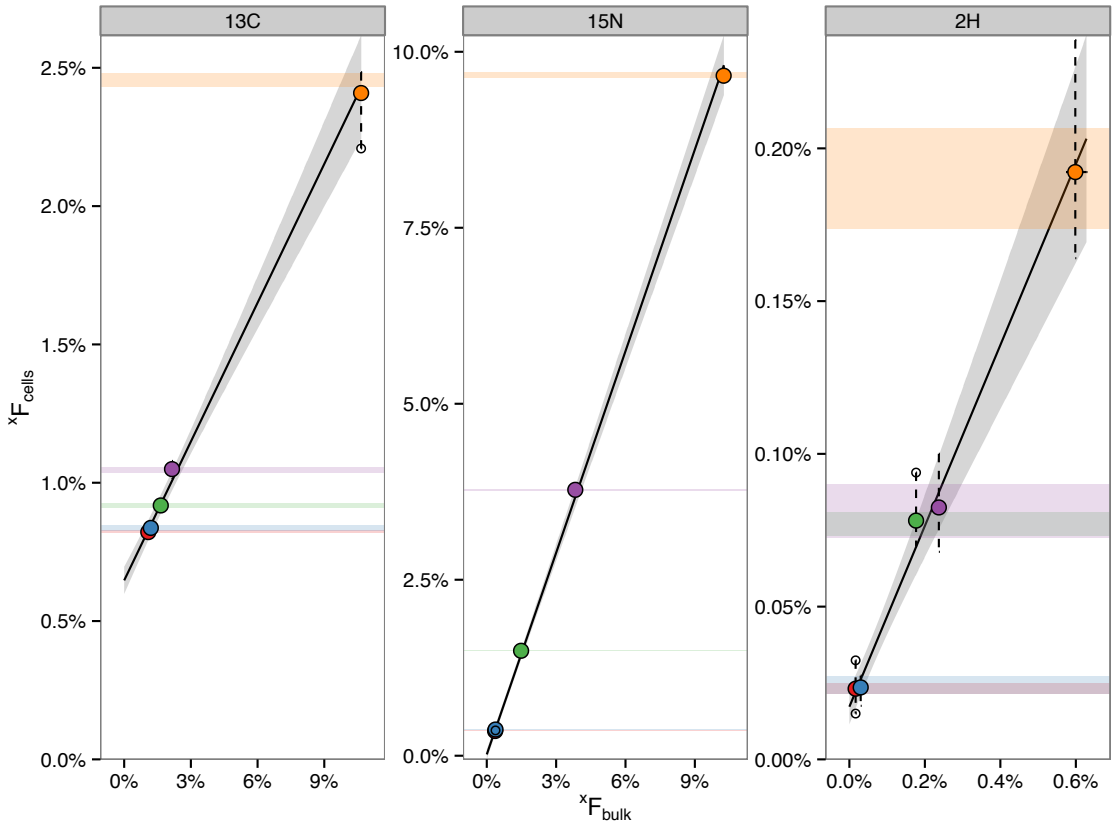

Figure 8.9 – Calibration curve for embedded single cells of *P. aeruginosa*. Calibration curve for isotopic composition of single cells measured by NanoSIMS vs. bulk isotopic composition of the population (measured by EA-ir-MS / GC-pyrolysis-ir-MS). Data points represent the mean isotopic composition of all measured single cells. The colored bands for each data point represent the range that comprises 50% of the single cell data. The dashed whiskers represent the entire range of all single cells. The empty white circles represent statistical outliers. Horizontal error bars represent the maximum interval of the measured bulk isotopic composition (smaller than symbol sizes in most cases).

Here, we present the necessary calibration curves for cells of *S. aureus* (Figure 8.8, based on 104 ROIs) and *P. aeruginosa* (Figure 8.9, based on 100 ROIs) embedded in Technovit as described in Materials and Methods. Additional detail on all ROIs is presented in the Appendix, Figures E.3, E.5, E.8 and E.10, with ion maps in Figure E.6). Calibration parameters are listed in the Summary Table 8.1.

As expected, the nitrogen isotope compositions of embedded single cells for both organisms are not diluted by the plastic polymer (which contains no nitrogen). In *P. aeruginosa*, the calibration slope for embedded cells closely matches the slope for free whole cells (0.94 ± 0.06 and 0.95 ± 0.04), with near perfect linear correlation and slope close to 1. In the case of *S. aureus,* the substantial variability in the nitrogen isotopic composition of individual cells, as discussed above, likely effects the large uncertainty observed in the calibration slope for embedded cells (which increases to 1.31 ± 0.29), and should be applied with caution.

The key observation, however, is the effect of the plastic on the carbon and hydrogen isotopic composition of the microbial isotope standards. As expected, the calibration parameters for both carbon (*P. aeruginosa* only) and hydrogen suggest substantial dilution of the isotopic signal by the plastic polymer, with the slope for carbon dropping from 0.73 ± 0.07 to 0.17 ± 0.02, and for hydrogen from 0.67 ± 0.05 to 0.30 ± 0.06 (*P. aeruginosa)* and from 0.59 ± 0.05 to 0.31 ± 0.10 (*S. aureus*). To first order, these parameters suggest a dilution of the cellular carbon by ~75% and the cellular hydrogen by ~50%. Although the calibration curve for carbon in embedded cells vs. bulk isotopic composition provides a robust linear correlation, the hydrogen calibration curves for both organisms suffer from elevated scatter, likely due to the same effects observed in whole cells, that reduce their predictive value.

These empirical relationships show that the isotopic enrichment of embedded single cells in both hydrogen and carbon (and of course nitrogen) can be quantified and used to estimate bulk isotopic compositions of individual cells in addition to measuring diversity

(which can be assessed in relative terms without calibration). However, our results indicate that the high dilution of C and H by the plastic polymer restrict the accuracy of single cell isotopic measurements at relatively low levels of enrichment, and should not be used for values below ~$1000‰$ (i.e. 2x natural abundance). Additionally, the same caveats as for the analysis of single whole cells (extrapolation to other organisms and morphologies, statistical significance for distinguishing isotopically similar populations, etc.) equally apply. Lastly, given the relatively high scatter for these calibration curves, it is important to apply caution when using them in relating single cell isotopic compositions in plastic back to bulk equivalents, and carefully take the uncertainty into consideration.

8.3.2.3 Effect of isotopic spike present during fixation

Microbe	Isotope	natural abundance cells $avg^x F_{cells}$ [%]	natural abundance cells $\sigma_{x\,F}$ [%]	spiked during fixation $avg^x F_{cells}$ [%]	spiked during fixation $\sigma_{x\,F}$ [%]
PA	13C	0.90	0.06	0.81	0.01
PA	15N	0.35	0.01	2.2	0.2
PA	2H	0.021	0.005	0.026	0.005
SA	15N	0.361	0.005	2.2	0.1
SA	2H	0.021	0.007	0.026	0.005

Table 8.2 – Effect of isotopic spike during fixation.

In environmental applications of isotope labeling techniques combined with microscopy and imaging mass spectrometry, cells are typically fixed with formaldehyde (or other fixatives) prior to analysis to arrest metabolism and preserve cellular structure. Frequently, fixatives are added to samples still in the presence of (some of) the isotopic label, because extensive washing procedures are either impractical (for very complex samples) or deemed a risk to the structure and integrity of the target cells. However, fixation can both chemically and/or physically trap unincorporated isotope label that is not actually part of the cell. Such trapped isotope label is retained in excess of true cellular label incorporation, and can lead to an overestimate of microbial activity upon analysis. To estimate the potential extent of this effect, we fixed cells grown with natural abundance substrates in the presence of a strong isotopic label, as described in Materials and Methods. Table 8.2 summarizes the potential effects of the presence of a strong isotopic label during the microbial fixation

with formaldehyde prior to embedding in plastic. The presence of carbon (^{13}C succinate) and hydrogen ($^{2}H_2O$) does not have a significant enrichment effect within the analytical error, but the presence of $^{15}NH_4$ leads to strong apparent enrichment of the microbial population ($^{15}F \approx 2.2\%$, i.e. ~5000‰ above natural abundance). This is likely a consequence of cross-linking reactions of proteins with the isotope label and subsequent trapping of the label. The effect is considerably exaggerated here due to the nature of the experiment of mixing finely suspended single cells rapidly with both an isotope tracer and a fixating agent. Previous work on environmental samples reported less severe, but still significant abiotic ^{15}N retention of $^{15}F \approx 0.6\%$ (Orphan et al., 2009). Due to importance of sample conservation, this is often an unavoidable risk when working with a $^{15}NH_4$label. Ideally, samples are washed to remove the label prior to fixation, but whenever this is not a viable option, it is important to determine the potential extent of this effect in control experiments representative of experimental conditions.

8.3.3 Growth diversity in continuous culture

Here, we present an example of employing hydrogen isotope labeling and secondary ion mass spectrometry to study both the activity and heterogeneity of microbial populations. *S. aureus* was grown in continuous culture at three different growth rates as described in detail in Materials and Methods and Chapter 7, and spiked at steady state simultaneously with both a $^{2}H_2O$ isotope label as well as a $^{15}NH_4^+$ label for comparison. Samples were withdrawn at regular intervals, and the hydrogen and nitrogen isotopic composition of individual cells was measured by multi-isotope NanoSIMS as described in 8.3.1. Single cell values from 1135 ROIs were converted to equivalent bulk cell compositions using the calibration for whole *S. aureus* cells described in Section 8.3.2.1, and are presented here for both ^{15}N and ^{2}H.

Figure 8.10 shows the aggregated data for ^{15}N enrichment from continuous culture experiments at three different growth rates (generation times of ~6.4 hours, ~1.2 days

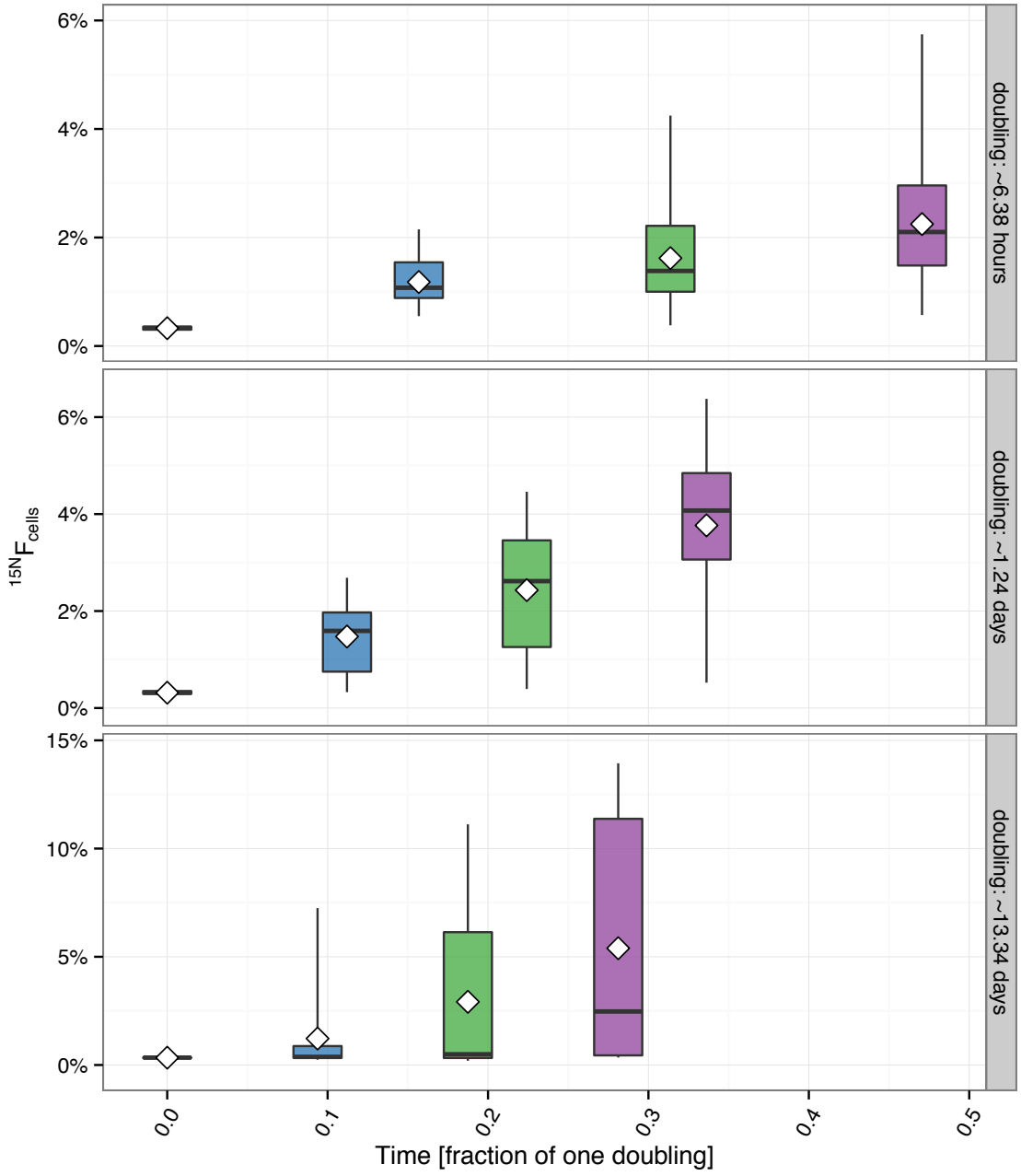

Figure 8.10 – Growth-rate-dependent single cell labeling of *S. aureus* with ^{15}N ammonium. The three panels show data from continuous culture experiments at different growth rates. The colored bands for each time point represent the range that comprises 50% of the single cell data. The whiskers represent the entire range of all single cells (upper and lower quartile). White diamonds represent the average isotopic composition of all measured cells at a time point, the black lines represent the median. Differences between the mean and the median reflect a skewed distribution in the isotopic composition of individual cells that is discussed in detail in the text. All single cell data is corrected to reflect the corresponding bulk cell composition.

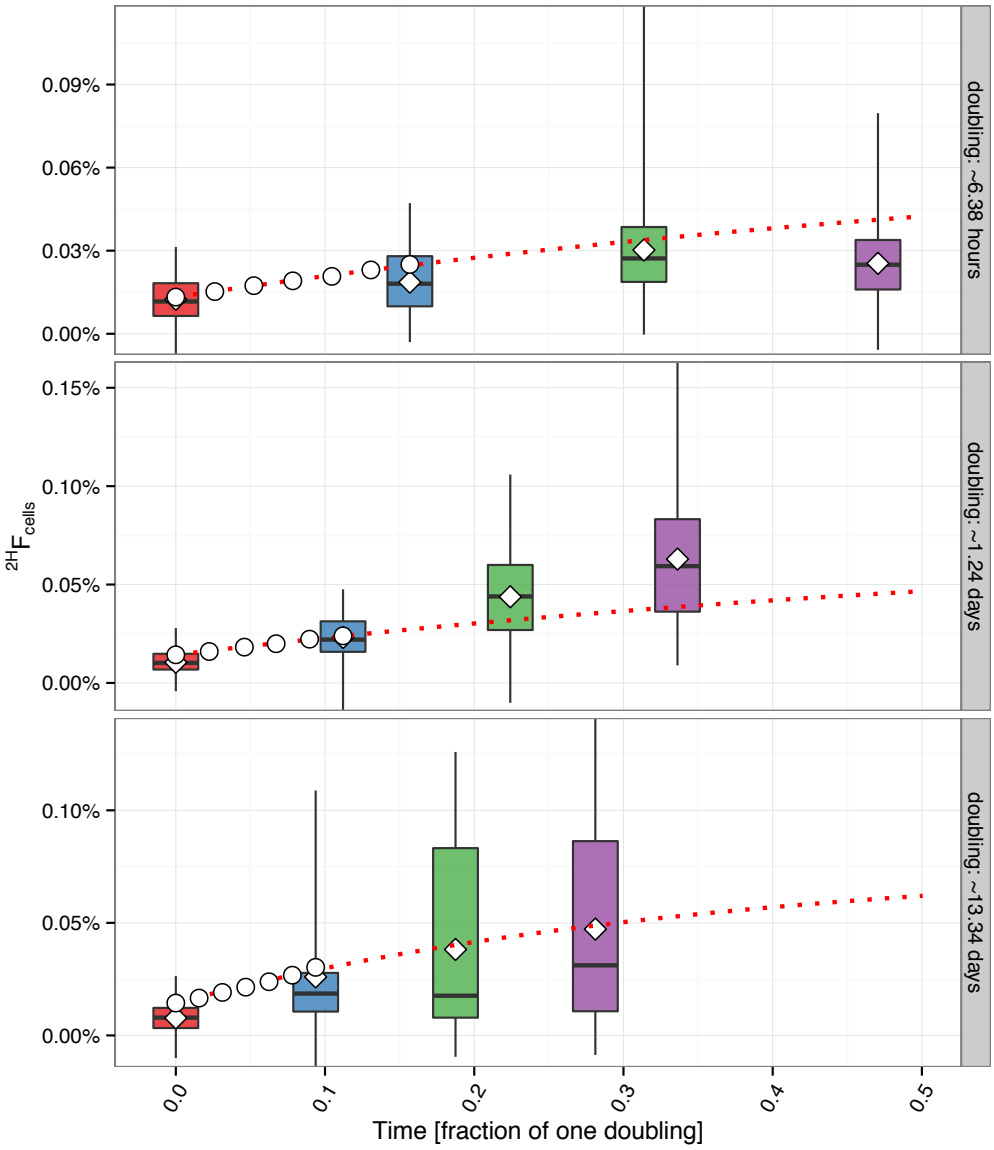

Figure 8.11 – Growth-rate-dependent single cell labeling of *S. aureus* with ^2H_2O. The three panels show data from continuous culture experiments at different growth rates. The white circles show data from bulk isotopic composition (whole membrane) measurements. The dashed red line indicates the projected whole cell isotopic composition based on continuous culture growth rates and bulk-data-derived turnover rates. The colored bands for each time point represent the range that comprises 50% of the single cell data. The whiskers represent the entire range of all single cells (upper and lower quartile). White diamonds represent the average isotopic composition of all measured cells at a time point, and the black lines represent the median. Differences between the mean and the median reflect a skewed distribution in the isotopic composition of individual cells that is discussed in detail in the text. All single cell data is corrected to reflect the corresponding bulk cell composition.

and ~13.3 days), illustrating both the average isotopic composition of all measured cells as well as the range of single cell enrichments. Additional detail on all ROIs is presented

in the appendix, figures E.11, E.12, E.13 and E.14). As expected, the data show overall isotopic enrichment over time as the population increasingly assimilates ^{15}N from the ammonium spike. Additionally, the spread in single cell enrichments (bars and whiskers) provides insight into the range of heterogeneity within each population. The data reveals substantial diversity in cellular activity rates even for the fastest growing culture, which is further amplified at slower growth. In the slowest-growing culture, it becomes evident that this diversity is significantly spread asymmetrically, with the majority of cells hardly active and some cells highly active, as shown visually by the medians (black bar) falling out substantially lower than the mass balance population averages (white diamonds).

Figure 8.11 shows the data from the same cells for ^{2}H enrichment, which matches the pattern observed in ^{15}N. However, it is worthwhile to point out that this is achieved here in hydrogen isotope labeling with a much smaller isotopic spike (1mL 70% D_2O into a ~500mL reactor) despite the relatively low ($^{2}F_{max} \approx 0.1\%$) and analytically challenging signal. The much stronger ^{15}N spike (~10mM of 99% $^{15}NH_4^+$) provides enrichment up to $^{15}F_{max} \approx 10\%$, but cannot be interpreted quantitatively because of the presence of amino acids, which provide an alternative source of nitrogen for *S. aureus*. This illustrates the exact scenario that inspired the development of hydrogen isotope labeling with heavy water presented in this manuscript, as a tool for measuring microbial activity in nutritionally complex environments.

The hydrogen enrichment presented in Figure 8.11 can be interpreted quantitatively based on measuring the isotopic composition of the source water after the spike, and the water fraction factors measured experimentally for *S. aureus* in Chapter 7. Additionally, the bulk hydrogen isotopic data from whole membrane measurements discussed in Chapter 7 can serve as a point of comparison for the single cell data. Figure 8.11 thus shows an overlay of the enrichment data from bulk measurements (white circles) as well as the predicted isotope enrichment based on the apparent/activity growth rate μ_{act} of each population (derived from the growth rate μ of the continuous culture setups and the

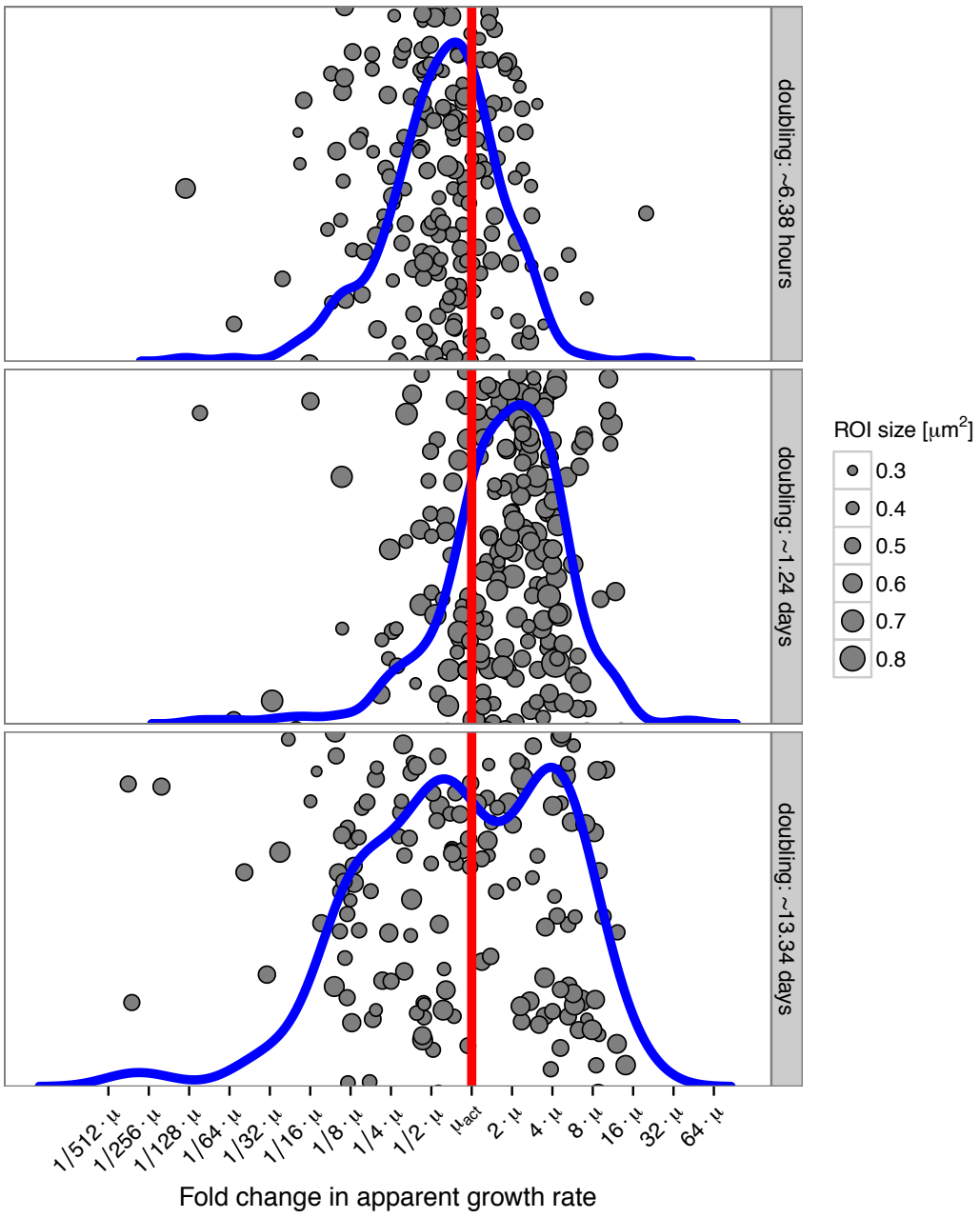

Figure 8.12 – Growth-rate-dependent single cell diversity of *S. aureus* from isotope labeling experiments with ^2H_2O. The three panels show data from continuous culture experiments at different growth rates. The individual data points indicates the apparent growth rates of individual cells/ROIs (scattered for clarity, vertical position has not meaning for the data points). The blue line indicates the kernel density estimation of the probability density function that represents the data. The vertical red line indicates the independent apparent growth rate (μ_{act}) estimates of the different populations, derived from the continuous culture setups and the bulk isotope labeling patterns. All data are plotted relative to the respective bulk apparent growth rate (μ_{act}) of the culture on a logarithmic scale. For reference, the corresponding generation times change with the inverse of the growth rate ($2 \cdot \mu \propto \frac{g}{2}$).

turnover/maintenance rates ω inferred from bulk isotope labeling patterns; see Chapter 7 for details). Although overall population enrichment is slightly underestimated by single cell data at the fastest growth rate (panel 1), and slightly overestimated at the intermediate growth rate (panel 2), the single cell hydrogen isotope data matches the projected isotopic composition within error for the majority of the cells.

Finally, the apparent growth rate $\mu_{act} = \mu + \omega$ for each individual cell can be estimated from the relation derived in Chapter 7:

$$ {}^2F_{cell}(t) = x_w \cdot \alpha_{l/w} \cdot \left[{}^2F_{w_{spiked}} \cdot \frac{\mu_{act}}{\mu_{act} + k} \cdot \left(1 - e^{-(\mu_{act}+k)\cdot t}\right) - {}^2F_{w_{nat}} \cdot \left(1 - e^{-\mu_{act}\cdot t}\right) \right] + {}^2F_{cell}(t_0) \tag{8.2} $$

with water fraction factor $x_w \cdot \alpha_{l/w}$ (measured for *S. aureus* in Chapter 7), isotopic composition of the spiked medium source water ${}^2F_{w_{spiked}}$ (measured after application of the isotopic spike), natural isotopic composition of the source water ${}^2F_{w_{nat}}$ (measured before application of the isotopic spike), the spike dilution rate k (set by the dilution rate of the continuous culture setup) and the cellular hydrogen isotope composition ${}^2F_{cell}$ at time t (measured by NanoSIMS and converted using the calibration derived in Section 8.3.2.1). The resulting growth rates of all measured cells are shown in Figure 8.12 relative to the expected growth rate of the whole population for each growth condition.

The observed pattern confirms that substantial heterogeneity exists for all growth conditions, with some cells growing faster than the average, and some cells growing slower than the average. However, it is particularly striking how diversity in growth activity *increases* at slower average growth rates. This reaches an extreme at the slowest growth condition tested in this study (generation times of ~13.3 days) where the population of *S. aureus* clearly falls into a bimodal activity pattern with two distinct populations. No clear pattern as to a dependence of growth activity on cell size (represented to first order

by ROI size) could be distinguished.

8.4 Conclusions

Here, we present stable isotope labeling of microbial populations with heavy water in combination with multi-isotope imaging mass spectrometry by NanoSIMS, as a novel technique to measure single cell microbial activity in a wide range of environments. A discussion of the analytical challenges, calibration of single cell measurements against bulk isotopic composition, and example application in continuous culture is presented in light of the capabilities and potential caveats of this approach.

The main analytical challenges are posed by a) the large dynamic mass range required to analyze both hydrogen isotopes and nitrogen isotopes simultaneously in a multicollector secondary ion mass spectrometer, b) the low ionization efficiency of hydrogen and vanishingly small natural abundance of the ^{2}H isotope, and c) the fast degradation of small individual microbial cells at high primary beam currents. We demonstrate, for the first time, that simultaneous multi-isotope analysis of hydrogen, carbon and nitrogen at high-mass resolution can be achieved on a CAMECA NanoSIMS 50L by extending the positions of the detector trolleys at the high and low end to their maximally possible configuration, and show its successful application to microbial samples.

We also report calibration data on linking measured single cell isotopic compositions of free whole cells as well as cells embedded in plastic back to bulk isotopic compositions. While this calibration provides the necessary parameters for inferring the bulk (whole membrane) hydrogen isotopic composition from the hydrogen isotope analysis of single whole cells of *S. aureus* and *P. aeruginosa*, it is important to recognize its likely limitations in translating to vastly different cell types (phylogenetically or morphologically different, or prepared very differently), as well as in resolving small isotopic differences between individual cells.

Lastly, we apply this technique to the study of microbial activity and population heterogeneity of slow-growing *S. aureus* cells in continuous culture. Our data reveal both accurate detection of population growth even by relatively low isotope labeling ($^2F_{max} \approx 0.1\%$) and quantitative insight into the range and diversity of heterogenous population activity rates.

The analytical challenge, measurement uncertainty and need for calibration all present important constraints that need to be considered carefully when planning or interpreting single cell environmental growth data from D_2O stable isotope labeling (or any stable isotope labeling for that matter). However, the technique also represents incredible scientific opportunity for studying spatiometabolic microbial diversity with a non-disruptive isotope tracer that can be employed even in the most complex environments.

Acknowledgements

Yunbin Guan. No dice without him. He's the man. Also, Shawn McGlynn for teaching me how to use the NanoSIMS, and he, Abbie Green and Michael Dieterle for their immense help and moral support during long analytical runs. Victoria Orphan for giving me full access to her lab, and providing guidance and continuous support and excitement about this project. Ryan Hunter for first teaching me how to thin-section embedded samples, and Lindsey VanSambeek for helping me to hone my skills. Lastly, I'd also like to especially acknowledge the many conversations with Grayson Chadwick, Kat Dawson and Shawn McGlynn on the topic of NanoSIMS in microbial ecology.

8.5 References

Aldeen, D. A., Hiramatsu, K., May 2004. Staphylococcus Aureus. Molecular and Clinical Aspects. Elsevier.

Davission, M. L., Weber, P. K., Pett-Ridge, J., Singer, S., 2008. Development of standards for NanoSIMS analyses of biological materials. Laurence Livermore National Laboratory.

de Laeter, J. R., Böhlke, J. K., De Bièvre, P., Hidaka, H., Peiser, H. S., Rosman, K. J. R., Taylor, P. D. P., 2003. Atomic weights of the elements. Review 2000 (IUPAC Technical Report). Pure and applied chemistry 75 (6), 683–800.

Dekas, A. E., Chadwick, G. L., Bowles, M. W., Joye, S. B., Orphan, V. J., Aug. 2013. Spatial distribution of nitrogen fixation in methane seep sediment and the role of the ANME archaea. Environmental Microbiology.

Dekas, A. E., Orphan, V. J., 2011. Identification of diazotrophic microorganisms in marine sediment via fluorescence in situ hybridization coupled to nanoscale secondary ion mass spectrometry (FISH-NanoSIMS). Methods in enzymology 486, 281–305.

Dekas, A. E., Poretsky, R. S., Orphan, V. J., Oct. 2009. Deep-sea archaea fix and share nitrogen in methane-consuming microbial consortia. Science 326 (5951), 422–426.

Doughty, D. M., Dieterle, M., Sessions, A., Fischer, W. W., Newman, D. K., 2014. Probing the subcellular localization of hopanoid lipids in bacteria using nanoSIMS. PLoS ONE.

Dragulescu, A. A., 2013. xlsx: Read, write, format Excel 2007 and Excel 97/2000/XP/2003 files. R package version 0.5.5.
URL http://CRAN.R-project.org/package=xlsx

Fike, D. A., Gammon, C. L., Ziebis, W., Orphan, V. J., Jul. 2008. Micron-scale mapping of sulfur cycling across the oxycline of a cyanobacterial mat: a paired nanoSIMS and CARD-FISH approach. Isme Journal 2 (7), 749–759.

Gormanns, P., Gormanns, P., Reckow, S., Reckow, S., Poczatek, J. C., Poczatek, J. C., Turck, C. W., Turck, C. W., Lechene, C. P., 2012. Segmentation of multi-isotope imaging mass spectrometry data for semi-automatic detection of regions of interest. PLoS ONE.

Hayes, J. M., Aug. 2002. Practice and Principles of Isotopic Measurements in Organic Geochemistry, 25.

Herrmann, A. M., Clode, P. L., Fletcher, I. R., Nunan, N., Stockdale, E. A., O'Donnell, A. G., Murphy, D. V., 2006. A novel method for the study of the biophysical interface in soils using nano-scale secondary ion mass spectrometry. Rapid Communications in Mass Spectrometry 21 (1), 29–34.

Hoppe, P., Cohen, S., Meibom, A., May 2013. NanoSIMS: Technical aspects and applications in cosmochemistry and biological geochemistry. Geostandards and Geoanalytical Research 37 (2), 111–154.

Katz, J. J., Dec. 1960. Chemical and biological studies with deuterium. Am. Scientist Vol: 48.

Kraft, M. L., Klitzing, H. A., Mar. 2014. Imaging lipids with secondary ion mass spectrometry. Biochimica et biophysica acta.

KREISWIRTH, B. N., LOFDAHL, S., BETLEY, M. J., OREILLY, M., SCHLIEVERT, P. M., BERGDOLL, M. S., NOVICK, R. P., 1983. The Toxic Shock Syndrome Exotoxin Structural Gene Is Not Detectably Transmitted by a Prophage. Nature 305 (5936), 709–712.

Kuypers, M. M. M., Sep. 2007. Microbiology. Sizing up the uncultivated majority. Science 317 (5844), 1510–1511.

Lechene, C. P., Hillion, F., McMahon, G., Benson, D., Kleinfeld, A. M., Kampf, J. P., Distel, D., Luyten, Y., Bonventre, J., Hentschel, D., Park, K. M., Ito, S., Schwartz, M., Benichou, G., Slodzian, G., 2006. High-resolution quantitative imaging of mammalian and bacterial cells using stable isotope mass spectrometry. Journal of Biology 5 (6), 20.

Lechene, C. P., Lee, G. Y., Poczatek, J. C., Toner, M., Biggers, J. D., 2012. 3D multi-isotope imaging mass spectrometry reveals penetration of 18O-trehalose in mouse sperm nucleus. PLoS ONE 7 (8), e42267.

Lechene, C. P., Luyten, Y., McMahon, G., Distel, D. L., Sep. 2007. Quantitative imaging of nitrogen fixation by individual bacteria within animal cells. Science 317 (5844), 1563–1566.

Lepage, G., Roy, C. C., Jan. 1986. Direct transesterification of all classes of lipids in a one-step reaction. Journal of lipid research 27 (1), 114–120.

LINCOLN, R. A., LEIGH, J. A., JONES, N. C., Jul. 1995. The amino acid requirements of *Staphylococcus aureus* isolated from cases of bovine mastitis. Veterinary Microbiology 45 (2-3), 275–279.

Lozano, M. M., Liu, Z., Sunnick, E., Janshoff, A., Kumar, K., Boxer, S. G., Apr. 2013. Colocalization of the ganglioside G(M1) and cholesterol detected by secondary ion mass spectrometry. Journal of the American Chemical Society 135 (15), 5620–5630.

Mah, R. A., Fung, D. Y., Morse, S. A., Jul. 1967. Nutritional requirements of Staphylococcus aureus S-6. Applied microbiology 15 (4), 866–870.

Musat, N., Stryhanyuk, H., Bombach, P., Adrian, L., Audinot, J.-N., Richnow, H. H., Apr. 2014. The effect of FISH and CARD-FISH on the isotopic composition of 13C- and 15N-labeled Pseudomonas putida cells measured by nanoSIMS. Systematic and Applied Microbiology, 1–10.

Neuwirth, E., 2011. RColorBrewer: ColorBrewer palettes. R package version 1.0-5. URL http://CRAN.R-project.org/package=RColorBrewer

Orphan, V. J., House, C., Hinrichs, K., McKeegan, K., DeLong, E., 2001a. Methane-consuming archaea revealed by directly coupled isotopic and phylogenetic analysis. Science 293 (5529), 484–487.

Orphan, V. J., House, C. H., Jun. 2009. Geobiological investigations using secondary ion mass spectrometry: microanalysis of extant and paleo-microbial processes. Geobiology 7 (3), 360–372.

Orphan, V. J., House, C. H., Hinrichs, K.-U., McKeegan, K. D., Delong, E. F., May 2002. Multiple archaeal groups mediate methane oxidation in anoxic cold seep sediments. Proceedings of the National Academy of Sciences of the United States of America 99 (11), 7663–7668.

Orphan, V. J., Turk, K. A., Green, A. M., House, C. H., Jul. 2009. Patterns of 15N assimilation and growth of methanotrophic ANME-2 archaea and sulfate-reducing bacteria within structured syntrophic consortia revealed by FISH-SIMS. Environmental Microbiology 11 (7), 1777–1791.

Pernice, M., Meibom, A., Van Den Heuvel, A., Kopp, C., Domart-Coulon, I., Hoegh-Guldberg, O., Dove, S., Jan. 2012. A single-cell view of ammonium assimilation in coral–dinoflagellate symbiosis. The ISME Journal 6 (7), 1314–1324.

Pernthaler, A., Dekas, A. E., Brown, C. T., Goffredi, S. K., Embaye, T., Orphan, V. J., 2008a. Diverse syntrophic partnerships from-deep-sea methane vents revealed by direct cell capture and metagenomics. Proceedings of the National Academy of Sciences of the United States of America 105 (19), 7052–7057.

Polerecky, L., Adam, B., Milucka, J., Musat, N., Vagner, T., Kuypers, M. M. M., Jan. 2012. Look@NanoSIMS - a tool for the analysis of nanoSIMS data in environmental microbiology. Environmental Microbiology 14 (4), 1009–1023.

R Core Team, 2014. R: A Language and Environment for Statistical Computing. R Foundation for Statistical Computing, Vienna, Austria. URL http://www.R-project.org/

RAHME, L. G., STEVENS, E. J., WOLFORT, S. F., SHAO, J., TOMPKINS, R. G., AUSUBEL, F. M., 1995. Common Virulence Factors for Bacterial Pathogenicity in Plants and Animals. Science 268 (5219), 1899–1902.

Rodríguez-Ruiz, J., Belarbi, E. H., Sánchez, J. L. G., Alonso, D. L., 1998. Rapid simultaneous lipid extraction and transesterification for fatty acid analyses. Biotechnology techniques 12 (9), 689–691.

Sessions, A., Hayes, J. M., Sylva, S., Summons, R., 2004. Isotopic exchange of carbon-bound hydrogen over geologic timescales. Geochimica Et Cosmochimica Acta 68 (7), 1545–1559.

Soetaert, K., Petzoldt, T., Setzer, W., 2013. deSolve: General Solvers for Initial Value Problems of Ordinary Differential Equations (ODE), Partial Differential Equations (PDE), Differential Algebraic Equations (DAE), and Delay Differential Equations (DDE). R package version 1.10-8.
URL http://CRAN.R-project.org/package=deSolve

Spormann, A. M., Behrens, S., Losekann, T., Pett-Ridge, J., Weber, P. K., Ng, W.-O., Stevenson, B. S., Hutcheon, I. D., Relman, D. A., May 2008. Linking microbial phylogeny to metabolic activity at the single-cell level by using enhanced Element Labeling-catalyzed reporter deposition Fluorescence *In Situ* Hybridization (EL-FISH) and NanoSIMS. Applied and Environmental Microbiology 74 (10), 3143–3150.

Steinhauser, M. L., Bailey, A. P., Senyo, S. E., Guillermier, C., Perlstein, T. S., Gould, A. P., Lee, R. T., Lechene, C. P., 2012. Multi-isotope imaging mass spectrometry quantifies stem cell division and metabolism. Nature 481 (7382), 516–U131.

Steinhauser, M. L., Lechene, C. P., Aug. 2013. Quantitative imaging of subcellular metabolism with stable isotopes and multi-isotope imaging mass spectrometry. Seminars in Cell and Developmental Biology 24 (8-9), 661–667.

Takechi, K., Sakamoto, W., Katsuhara, M., Murata, M., Motoyoshi, F., 1999. In situ RNA hybridization using Technovit resin in Arabidopsis thaliana. Plant Molecular Biology Reporter 17 (1), 43–51.

Thomas, A. F., 1971. Deuterium Labeling in Organic Chemistry.

Wickham, H., 2014a. plyr: Tools for splitting, applying and combining data. R package version 1.8.1.
URL http://CRAN.R-project.org/package=plyr

Wickham, H., Chang, W., 2013. ggplot2: An implementation of the Grammar of Graphics. R package version 0.9.3.1.
URL http://CRAN.R-project.org/package=ggplot2

Xie, Y., 2013b. knitr: A general-purpose package for dynamic report generation in R. R package version 1.5.
URL http://CRAN.R-project.org/package=knitr

Zhang, D.-S., Piazza, V., Perrin, B. J., Rzadzinska, A. K., Poczatek, J. C., Wang, M., Prosser, H. M., Ervasti, J. M., Corey, D. P., Lechene, C. P., Jan. 2012. Multi-isotope imaging mass spectrometry reveals slow protein turnover in hair-cell stereocilia. Nature 481 (7382), 520–524.

Chapter 9

Microbial activity in cystic fibrosis

9.1 Introduction

Cystic fibrosis (CF) is an autosomal recessive genetic disorder arising from two defective copies of the gene encoding the cystic fibrosis transmembrane conductance regulator. The genetic defect affects the production of mucus in a variety of organs, and is particularly detrimental in the lung, where thick mucus collects over time and allows for progressive colonization of the pulmonary system by a polymicrobial community of opportunistic pathogens. This leads to chronic infection of the airways, and contributes to most of the morbidity and mortality associated with CF (Goss and Burns, 2007).

While it is well-established that the physiological state of individual pathogens within the lung plays an important role in microbial persistence and drug tolerance (Hirschhausen et al., 2013; Hart and Winstanley, 2002; Davies, 2002; Nguyen et al., 2011; Baek et al., 2011), very few direct measurements of actual growth-activity rates of these populations exist in the host. However, a better understanding of how populations grow *in vivo* is crucial to developing representative *in vitro* tests of potential therapies that produce reliable results and lead to safe and effective treatment strategies (Harrison, 2007).

The sole currently available quantitative estimate of the range of growth activities in cystic fibrosis stems from an assessment of ribosome content of fast-growing *Pseudomonas aeruginosa* cells in sputum measured by fluorescent *in situ* hybridization (FISH) calibrated against liquid batch culture growth rates (Yang et al., 2008). However, this indirect proxy for metabolism is ambiguous for the complex conditions encountered in most clinical samples, as rRNA concentrations don't scale linearly with growth rates across taxa, and provide an unreliable indicator of metabolic state in microbial communities, slow-growing/dormant cells and dynamically changing environments (Blazewicz et al., 2013; Ecker and Schaechter, 1963).

Here, we use the incorporation of a stable isotope tracer into biosynthetically active cells as an alternative direct measure of metabolic activity in sputum samples from cystic fibrosis patients. Specifically, we use the method presented in Chapter 7 based on hydrogen isotope enrichment of microbial fatty acids from ^2H_2O incorporation. Heavy water (^2H_2O) provides an ideal isotopic tracer for complex environments like infections, which are often saturated with bioavailable carbon and nitrogen such that ^{13}C and ^{15}N labeled substrates would change the nutrient availability and only capture microbial activity of organisms consuming the particular labeled substance. ^2H_2O can be administered with strong labels even in minimal addition (natural background is very low), is an equally-universal substrate for all forms of life even in complex, carbon- and nitrogen-saturated systems, can be combined with other isotopic tracers (e.g. specific carbon or nitrogen sources), and can be used safely within biological systems (Kushner et al., 1999b; Jones and Leatherdale, 1991a; Steinhauser and Lechene, 2013).

In this study, we focus on the growth rates of the opportunistic pathogen *Staphylococcus aureus* for its importance in lung infections of pediatric cystic fibrosis patients and its unique fatty acid profile. *S. aureus* is one of the earliest bacteria detected in infants and children with CF, is the most prevalent organism among U. S. children with CF, and has gained a tremendous amount of attention in the last decade due to the rise of beta-

lactam-resistant strains (methicillin-resistant *S. aureus*, or MRSA) (Goss and Muhlebach, 2011; Kahl, 2010).

Lastly, ^{2}H incorporation into bacterial fatty acids provides a bulk measure of microbial activity, but cannot provide insight into growth heterogeneity within a target population. While it is likely that the physiological states of individual cells in such complex communities vary, little is known about the extent of this variation within the CF lung. Given the hypothesized correlation between physiological diversification and antimicrobial resistance, it is highly desirable to know the extent of *in situ* heterogeneity in the metabolic states of individual cells at different stages of infection. This is particularly important in persistent infections in which slow- or non-growing bacteria play a major role (Helaine et al., 2010; Stewart et al., 2011; Helaine et al., 2014).

Here, we build on the tools presented in Chapter 8 to combine thin-sectioning of sputum samples with fluorescent *in situ* hybridization (FISH) and nano-scale secondary ion mass spectrometry (nanoSIMS) to measure microbial activity in clinical samples at the single cell level, and gain quantitative insights into the heterogeneity in microbial activity rates.

9.2 Material and Methods

All reagent solutions were filter-sterilized prior to use. All non-consumable glassware used for lipid extraction and derivatization was pre-combusted in a muffle furnace at 550 °C to remove all remaining traces of organic materials potentially adhered to the glass.

9.2.1 Sample collection

9.2.1.1 Study design

Fifteen participants (aged 11 to 20 years) were recruited from Children's Hospital Los Angeles (CHLA). Inclusion criteria were: a positive diagnosis of cystic fibrosis, ability to

expectorate sputum, informed consent, and recent detection of an infection by *S. aureus* from clinical data. The study was approved by the ethical commissions of the California Institute of Technology and the Children's Hospital Los Angeles.

9.2.1.2 Sample collection

Immediately upon expectoration (usually within 5-10min), sputum samples were suspended at the hospital in a pre-warmed phosphate buffered saline (PBS) isotope labeling solution (with 1 to 30% D_2O), and incubated at 37C for up to 60 minutes. Microbial growth activity in samples for lipid analysis was arrested by flash-freezing in liquid nitrogen at the end of sample incubation, and samples were preserved at -20C until transfer to and processing at the California Institute of Technology. Microbial growth in samples for single cell analysis was arrested by transfer to a freshly thawed 1% formaldehyde solution in PBS (Paraformaldehyde, Electron Microscopy Sciences, #15713). Just prior to sample preservation, the residual labeling solution was collected and filter-sterilized for water isotope analysis.

Typically, most pediatric patients could not expectorate more than 0.5 - 1g of sputum, but when sufficiently large sputum samples (>0.6g) were expectorated, the sample was divided into multiple aliquots prior to isotope labeling by division with a scalpel or transfer with a large syringe, and sub-samples were incubated for different amounts of time from 0 to 60 minutes. The full sampling procedure, is illustrated in the flow chart in Figure 9.1, which served to standardize sample collection.

9.2.1.3 Isotopic composition of water

The water hydrogen isotopic composition ${}^2F_w$ of all samples was measured using a Los Gatos Research DLT-100 liquid water isotope analyzer. Samples were analyzed in 3 replicate analyses with 10 injections each. Samples close to natural abundance isotopic composition were calibrated against four working standards (δ^2H values: $-117‰$, $-11‰$,

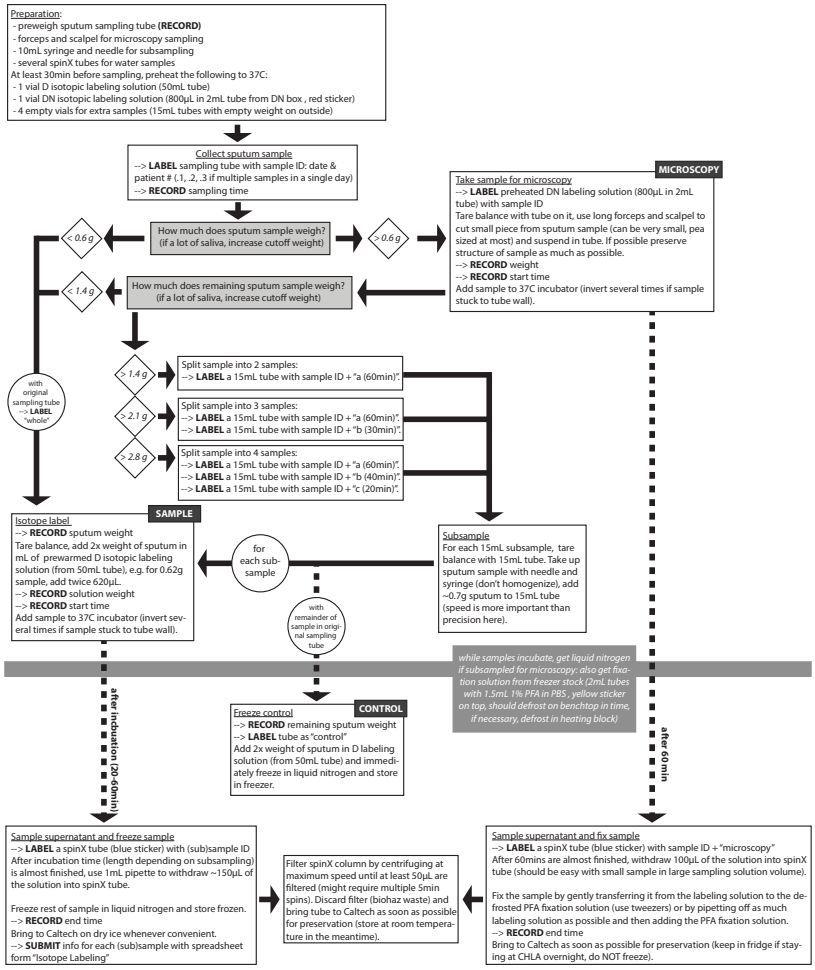

Figure 9.1 – Sampling procedure for clinical samples. This flowchart portrays the sampling protocol used for collection of clinical samples.

$+290‰$, $1270‰$) that in turn were calibrated against the VSMOW, GISP, and SLAP international standards (Coplen, 1988). Heavily-enriched samples from isotope tracer solutions were beyond the linear response range of the instrument, and were analyzed by isotope dilution with natural abundance water of known isotopic composition.

9.2.2 Fatty acid analysis

9.2.2.1 Extraction and derivatization

Frozen sputum samples were lyophilized for at least 48 hours. Homogenized dry powder was weighed out in up to ~40mg aliquots (or the maximum available amount), and spiked with 10µg of 21:0 phosphatidyl choline as a phospholipid extraction standard. Samples were transesterified in the presence of a base catalyst (0.5M NaOH in anhydrous methanol) at room temperature for 10 min (Christie, 1997; Metcalffe and Wang, 1981; Griffiths et al., 2010). Free fatty acids and aldehydes are not transesterified under basic conditions, which prevents the derivatization of fatty acids from degraded materials in the sputum sample, as well as the derivatization of abundant aldehydes, which interfere chromatographically with target analytes. Derivatized fatty acid methyl esters (FAMEs) were extracted into hexane after addition of a quantification standard (10µg C25:0 FAME), and concentrated under a stream of N_2 at room temperature.

Primary target analytes (a-C15:0 FA and a-C17:0 FA produced by *S. aureus*) typically constituted less than 1% of host-derived fatty acids (see Figure F.2 in the Appendix for a visual example). The high abundance of host material (primarily C18:1 FA, C18:2 FA, and longer chain (poly)-unsaturated fatty acids) interfered with compound-specific isotope ratio analysis of less-abundant compounds due to column overload. The low total amount of target analytes available from most sample sizes precluded the use of elaborate purification steps with low yields or risk of contamination. To remove several major host compounds and increase relative abundance of the analytes sufficiently for isotope ratio analysis, saturated FAMEs were separated from unsaturated FAMEs using Discovery® Ag-Ion solid phase extraction columns in combusted glass cartridges (Supelco, custom preparation[1]). Extracted samples were dried to 1 ml and applied to preconditioned columns, followed by elution of saturated FAMEs in 0.125% acetone in hexane, and mono-

[1]Standard columns are only available in plastic cartridges with contaminant bleed high enough to interfere chromatographically with the low-abundance analytes.

and disaturated FAMEs in acetone. Separation of unsaturated and saturated fatty acids was quantitative using this procedure with lipid extracts from up to ~40mg of dry sputum (see Figure F.3 in the Appendix). Fractions were evaporated to dryness and resuspended in hexane prior to analysis.

9.2.2.2 Analysis

Fatty acid methyl esters (FAMEs) were analyzed by gas chromatography/mass spectrometry (GC/MS) on a Thermo-Scientific Trace DSQ equipped with a ZB-5ms column (30m x 0.25mm i.d., film thickness 0.25µm) and PTV injector operated in splitless mode, using He as a carrier gas at 0.8 ml/min. The GC oven was held at 80ºC for 1 minute, ramped at 20ºC/min to 130ºC, and ramped at 5ºC/min to a final temperature of 320ºC (held for 20min). Peaks were identified by comparison of mass spectra and retention times to authentic standards and library data.

The isotopic composition of the primary target analytes (a-C15:0, a-C17:0, and other microbially produced fatty acids) was measured in the saturate fraction by GC/pyrolysis/isotope-ratio mass spectrometry (GC-ir-MS) on a Thermo-Scientific Delta^{+}XP with methane of known isotopic composition as the calibration standard. A multi-compound FAME standard was run every 4-6 samples to verify instrument accuracy and precision. Chromatographic conditions were identical to those from GC/MS analysis except for a thick-film column (ZB-5ms, 30m x 0.25mm i.d., film thickness 1.00µm) and slight modifications to the temperature program to optimize chromatographic separation of key analytes (i-C15:0 and a-C15:0 / i-C17:0 and a-C17:0) despite peak broadening from heavy isotope labeling (see Section 7.4.1 in Chapter 7 for a discussion). Samples were injected in highly-concentrated aliquots to obtain maximum signal for target analytes. Peaks were identified based on retention order and relative height based on the GC/MS analysis. High-abundance components in the saturate fraction (C16:0, C18:0, C20:0) that were too concentrated relative to target analytes were prevented from entering the source

by appropriately-timed backflush of the column effluent. Relative proportions of fatty acids for isotope mass balance calculations were determined from peak areas corrected for derivatization and isotopic composition of each analyte.

9.2.3 Single cell analysis

9.2.3.1 Sample preparation

Immediately upon receipt of samples from the hospital, on the same day as sputum expectoration and incubation with isotope label, formaldehyde-fixed sputum samples were transferred to excess PBS solution (10mL) in a column above an 8µm sterile filer. The sample was washed by slowly rinsing it with a total of 50mL PBS solution that was added to the column in 10mL aliquots and drained by gravimetric or slight vacuum flow through the filter.

Samples for cryosectioning were suspended in O.C.T. Compound (a poly ethylene glycol and polyvinyl alcohol based embedding solution, Tissue-Tek), which was allowed to infiltrate the sample for 48 hours at 4C. Samples in O.C.T. were slowly frozen by contact with dry-ice cooled ethanol and stored at -80C. Thin sections (down to ∼5µm) were cut using a rotary microtome in a cryostat and transferred to 1-inch-diameter round microprobe slide. The water soluble O.C.T. was removed by slowly dipping the round into 1x PBS solution, followed by dehydration in 50%, 75% and 100% ethanol.

Samples for plastic thin-sectioning were suspended in a few drops of molten noble agar (2% Difco Agar Noble in 50mM HEPES buffered filter-sterilized water), solidified by cooling at room temperature, and cut into ∼2mm^{3}cubes. Fixed and washed agar cubes were incubated for at least 1 hour at 30C in freshly prepared 1mg/ml lysozyme and 50µg/mL lysostaphin (Sigma-Aldrich, #L2898) in 10mM tris buffered water to digest *S. aureus* cell wall, washed once in PBS, resuspended in 50% EtOH in PBS, and dehydrated in 100% Ethanol over the course of 3 exchanges, with final resuspension in 100% for at least 1 hour. Ethanol was then replaced twice with 100% Technovit 8100 infiltration

solution (Heraeus Kulzer GmbH, #64709012) to infiltrate the agar cubes overnight. Agar cubes were finally suspended in airtight 0.6mL microcentrifuge tubes in Technovit 8100 infiltration solution amended with hardener II reagent and stored at 4C for overnight polymerization. Thin sections (1 µm thick) were cut using a rotary microtome. Each section was stretched on the surface of a water drop on polylysine-coated microscope slides and air-dried at room temperature.

9.2.3.2 Fluorescent in situ hybridization (FISH)

Fluorescent *in situ* hybridization (FISH) was conducted on the cryo-sections and plastic thin-sections using the universal bacterial probe EUB338 (5' to 3': GCTGCCTCCCG-TAGGAGT, Amann et al., 1990), which hybridizes to bacterial 16S ribosomal RNA, probe Sau (5' to 3': GAAGCAAGCTTCTCGTCCG, Kempf et al., 2000), which hybridizes to *S. aureus* 16S ribosomal RNA, and probe Psae (5' to 3': TCTCGGCCTTGAAACCCC, Hogardt et al. 2000; Trebesius et al. 2000), which hybridizes to *P. aeruginosa* 23S ribosomal RNA. Both probes were specifically designed and tested for use in microbial identification in cystic fibrosis sputum (Hogardt et al., 2000; Tajbakhsh et al., 2008b;a). Additionally, probe Non338 (5' to 3': ACTCCTACGGGAGGCAGC, Wallner et al., 1993), an oligonucleotide complementary to the probe EUB338, served as a negative control for nonspecific binding. Probes EUB338 and Non338 were labeled with the cyanine dye Cy3, probe Sau with the cyanine dye Cy5, and probe Psae with fluorescein. All probes were labeled on both the 5' and 3' end to increase fluorescence intensity (Stoecker et al., 2010).

For hybridization, each section was covered with 20µl of hybridization buffer (0.9 M NaCl, 20mM Tris-HCl at pH 8, 0.01% sodium dodecyl sulfate, 20% formamide, Kempf et al. 2000; Tajbakhsh et al. 2008b) containing 50 ng of unlabeled oligonucleotide probe BET42a (5' to 3': GCCTTCCCACTTCGTTT, Manz et al., 1992) and preincubated for 10min at 46C to reduce nonspecific binding of labeled oligonucleotide probes (Hogardt et al., 2000). Probes EUB338 (or Non338), Sau and Psae were added (5ng/µL), and

samples were incubated in a moisture chamber at 46C for 3 hours. Stringent washing was performed by incubating the samples in washing buffer at decreased NaCl concentration (Lathe, 1985) (225mM NaCl with 5mM EDTA, 20 mM Tris-HCl at pH 8, 0.01% sodium dodecyl sulfate) at 48°C for 12 min. Finally, samples were dipped into ice-cold deionized water to rinse off the salt, air-dried and mounted in the glycerol-based soft mount Vectashield (®Vector Laboratories, Florijn et al., 1995) with 1.5 µg/ml 4',6-diamidino-2-phenylindole (DAPI) as a DNA counterstain.

The proper functioning of the FISH probes in technovit plastic sections was tested extensively using embedded pure culture standards. This revealed problems with the targeting of *S. aureus* by FISH probes (universal EUB338 or specific Sau) in plastic thin sections, despite digestion with lysozyme/lysostaphin to permeabilize the gram-positive *S. aureus* cells. While the same procedure (cell wall digestion + FISH) yielded excellent results in whole cells (see Figure F.6 in the Appendix), only a small portion of the cells were labeled successfully in plastic thin section. The problem was solved by including the cell wall digestion step prior to embedding in plastic (Figure F.7 in the Appendix), suggesting reduced efficiency / failure of lysozyme to hydrolyze glyocosidic bonds within the plastic polymer matrix. It was also confirmed that the employed procedure did not disrupt *P. aeruginosa* cells, suggesting that gram-negative cells were not adversely affected (Figure F.7). Accordingly, all clinical samples were processed with cell wall digestion prior to embedding.

Samples were routinely imaged using a Zeiss Axio Imager microscope, and mapped extensively for sample identification and target localization for FISH-NanoSIMS (Dekas and Orphan, 2011; Dekas et al., 2013) using a Keyence BZ-9000 microscope equipped with a mercury lamp and filter cubes for DAPI, GFP, Cy3 and Cy5). For secondary ion mass spectrometry, samples were made conductive by sputter-coating with a 50nm layer of gold (Dekas et al., 2009).

All samples were analyzed with a CAMECA NanoSIMS 50L (CAMECA, Gennevilliers,

France) housed in the Division of Geological and Planetary Sciences at Caltech. Free samples in cryo-sections were analyzed using a ~3.6pA primary Cs^+ beam, and were presputtered with ~20pC/μm^2. Cells embedded in plastic were analyzed using a 1.9pA - 3.6pA primary Cs^+ beam, and were presputtered with ~340pC/μm^2. Seven masses were collected in parallel ($^1H^-$, $^2H^-$, $^{12}C^-$, $^{13}C^-$, $^{14}N^{12}C^-$, $^{15}N^{12}C^-$, $^{28}Si^-$) using electron multipliers. Target locations in individual samples were located using the NanoSIMS CCD camera, secondary electron image and $^{14}N^{12}C^-$ ion maps. For all analyses, the beam was rastered over a square region ranging from 5x5 to 20x20μm^2 for 5-30min per analytical plane/frame, and images were collected in 256x256 pixel resolution up to 12x12μm^2 and 512x512 pixel resolution for larger areas. Presputtering was carried out on a region larger than the analytical frame by at least 2μm on each side. Analytical parameters including primary beam focus, secondary beam centering and mass resolution for all ions were verified and tuned every ~30minutes.

9.2.4 Quantification

Raw data from all acquired ion images was processed using the open-source MATLAB plugin Look@NanoSIMS (Polerecky et al., 2012). Ion images from multiple frames were corrected and aligned, and the corresponding microscopy images were warped onto the $^{14}N^{12}C^-$ ion image using functionality provided by Look@NanoSIMS. Discrete regions of interest (ROIs) were hand-drawn around individual microbes based on the $^{14}N^{12}C^-$ ion image and the FISH+DAPI images. The raw ion counts for all collected ions from individual and aggregated frames in the individual ROIs/cells were exported from Look@NanoSIMS and further processed in R using a custom module. Isotopic values are reported in fractional abundances to allow for exact mass balance calculations. Fractional abundances of single cell analyses were calculated directly from raw ion counts and calibrated against bulk measurements (Section 8.3.2 in Chapter 8). All conversions and mass balance calculations were performed using an isotopes R module described in Section A.2 of

Appendix A. All data processing, analysis, model simulations and plotting were performed in R (R Core Team, 2014) using functionality provided by various analytical and graphical packages (Wickham, 2014a; Wickham and Chang, 2013; Xie, 2013b; Neuwirth, 2011; Dragulescu, 2013).

9.3 Results and discussion

9.3.1 Lipid profiles

The stable incorporation of isotopically heavy hydrogen from ^2H_2O into membrane fatty acids during microbial growth can be combined with compound-specific isotope analyses to provide coarse phylogenetic resolution of microbial activity. Figure 9.2 illustrates the average fatty acid profiles of *Burkholderia cenocepacia, Haemophilus influenzae, Pseudomonas aeruginosa, Staphylococcus aureus, Stenotrophomonas maltophilia* and *Streptococcus pneumoniae*[2], several major opportunistic pathogens involved in lung infections of cystic fibrosis patients (Goss and Burns, 2007; Harrison, 2007; Goss and Muhlebach, 2011). The fatty acid profiles show differences between the various organisms that can be used to track microbial activity of one population vs. another in polymicrobial infections. However, in the complex environment present by the human lung, both the mucus as well as host cells within the mucus (mostly immune system cells) provide a substantial source of host-derived fatty acids, highlighted in red in Figure 9.2. While some of these (e.g. C16:1, 3-OH-C16:0,

[2]Data on *Streptococcus pneumoniae* from Lu and Rock (2005) grown in Todd–Hewitt broth supplement with 0.5% yeast extract at pH 7.0 (TY medium), cultures harvested in mid-log phase. Data on *Stenotrophomans maltophilia* represents the average lipid profile from batch culture growth experiments with a clinical isolate of *S. maltophilia* in Chapter 7 and data from batch culture growth experiments by Norman et al. (1997), with several plant isolates of *S. maltophilia* grown on Trypticase Soy brooth amended with 5% sucrose and harvested in late exponential phase. Data on *Burkholderia cenocepacia* is from a study by Krejci and Kroppenstedt (2006) with 15 clinical isolates grown as colonies on tryptic soy brooth agar plates. Data on *Haemophilus influenzae* is from a study by Jantzen et al. (1980) with 35 different strains from both type culture collections and personal isolates, grown as colonies on chocolate blood agar. Data on *P. aeruginosa* is largely from batch and continuous culture experiments discussed in Chapter 7, combined with data from biofilm experiments by Chao et al. (2010). Data on *S. aureus* is from batch and continuous culture experiments discussed in Chapter 7.

C18:1) make attractive targets to trace the activity of important pathogens, such as *B. cenocepacia* and *P. aeruginosa*, isotopic enrichment of a component also produced by the host can only be interpreted if the relative contributions from pathogens vs. host can be well-constrained, or if pathogens can be separated physically from host material prior to analysis. Several fatty acids that are produced exclusively by the microbial population in the lung (highlighted in green in Figure 9.2), such as cyclo-C17:0 and cyclo-C19:0, provide excellent targets from an analytical perspective, but must be considered in the context of their physiological role. Both of these lipid components tend to be produced during slow growth and stationary-phase-like growth conditions, as discussed in detail in Chapter 7. This implies that any signal of microbial activity from these fatty acids is biased towards recording growth of the less active members of the microbial community, potentially underestimating average growth of the entire population. The relative contribution of cyclo-C19:0 to the total membrane fatty acid pool of *P. aeruginosa,* for example, can vary from virtually absent to almost 30% as a function of growth conditions (see Figure F.1 in the Appendix for details).

Here, we thus focus first on the microbial activity of the important early-stage gram-positive CF pathogen *Staphylococcus aureus* (Goss and Muhlebach, 2011), which produces anteiso C15 (a-C15:0) and anteiso C17 (a-C17:0) fatty acids as the two major components of its membrane. Both of these methyl branched odd-carbon number fatty acids are microbial in nature, and can be distinguished from host material in bulk fatty acid extracts of cystic fibrosis sputum samples. Additionally, amongst the major pathogens typically considered to play a dominant role in CF infections, only *S. maltophilia* can potentially contribute to the pool of a-C15:0, allowing a-C15:0 and a-C17:0 to be reasonably used as *S. aureus*-specific targets for measuring microbial activity. Given the high incidence of *S. aureus* infections in pediatric CF patient populations, and the crucial role of this pathogen in establishing polymicrobial chronic infections (Goerke and Wolz, 2010; Kahl, 2010; Stone and Saiman, 2007), we investigated the microbial activity of *S. aureus* in a

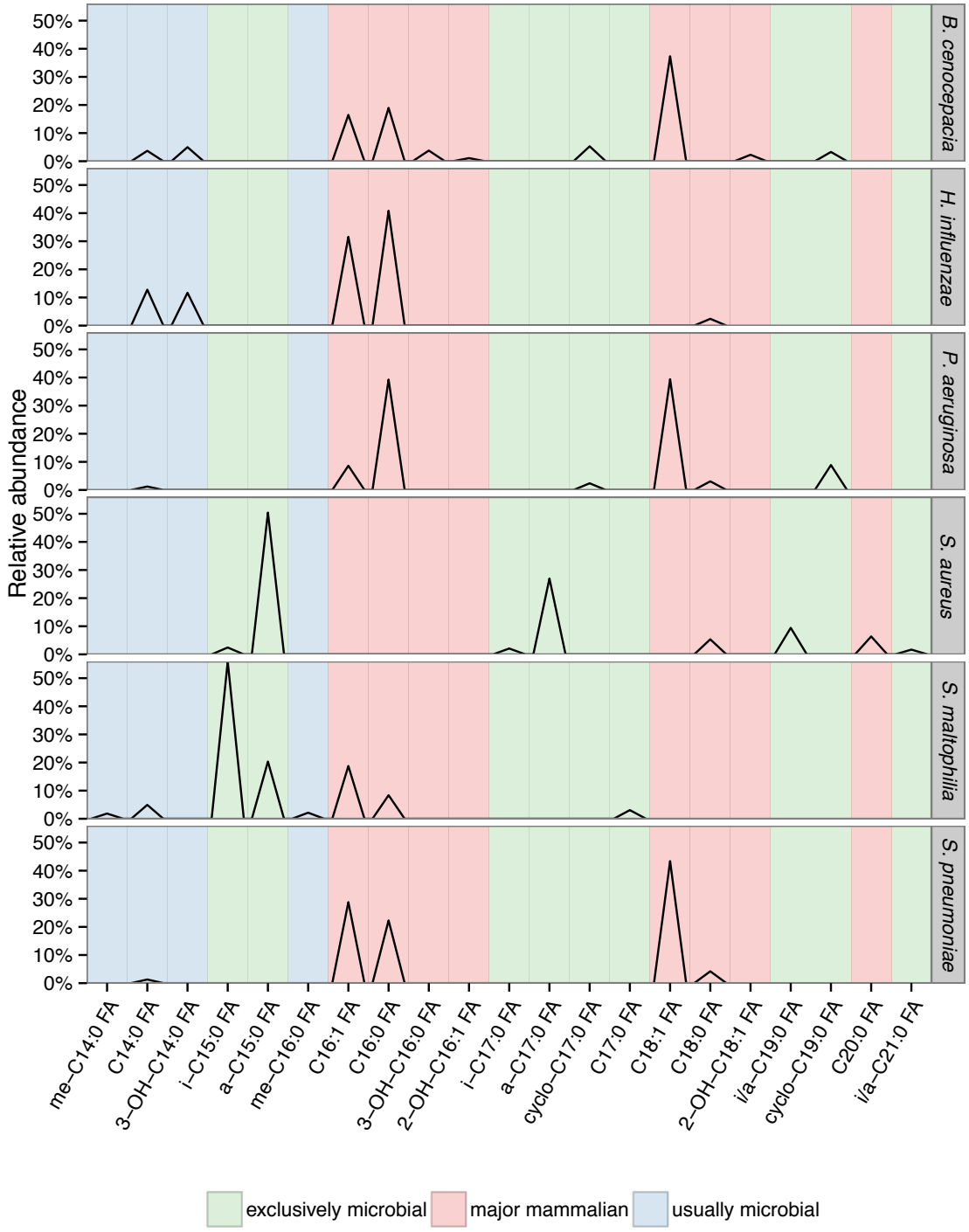

Figure 9.2 – Fatty acid profiles of key CF pathogens.

cohort of patients at the Children's Hospital Los Angeles with a clinical record of recent *S. aureus* infection.

9.3.2 Growth rates of *S. aureus* in clinical samples

As part of this study, we collected 38 samples from 15 different patients with sufficient quantities of a-C15:0, a-C17:0 or both, for compound-specific isotope ratio analysis to determine the biosynthetic activity of *S. aureus* during the incubation interval. The experimental conditions were chosen such that minimal time expired between sputum expectoration and conclusion of the experiment (typically a little over 1 hour), as to ensure as close to *in situ* conditions as possible without requiring any invasive procedures. The interpretation of the isotopic enrichment in the context of microbial activity is based on equations derived in detail in Chapter 7 (see, e.g., Equation 8.2). However, instead of the isotopic tracer being diluted *out* of the system (as in Chapters 7 and 8), it mixes *into* system in the clinical experiments studied here.

9.3.2.1 Label mixing

Water provides an excellent isotope tracer due to its rapid self-diffusivity, which is well-understood in aqueous solutions ($\approx 2.9 \cdot 10^{-5} cm^2 s^{-1}$ for H_2O at 35C, almost identical for $H_2{}^{18}O$, lower for fully tritiated water ^3H_2O at $0.81 \,\text{to}\, 1.02 \cdot 10^{-5} cm^2 s^{-1}$) (Dibdin, 1981; Easteal et al., 1984; Holz et al., 2000), but more difficult to assess in the context of the highly viscous, biofilm-like sputum samples. Although biofilm-like organic structures have a water content typically around ~90%, high cell densities and the presence of extracellular polymeric substances arrest convective flow and slow down diffusion of all molecules (Stewart, 2003; 1998), including water.

On long time scales, water diffusion would be negligible, but due to the short incubation time scales required for quasi *in situ* experiments with expectorated sputum samples, this effect becomes significant. The lack of data and complexity of sputum poses difficulty in

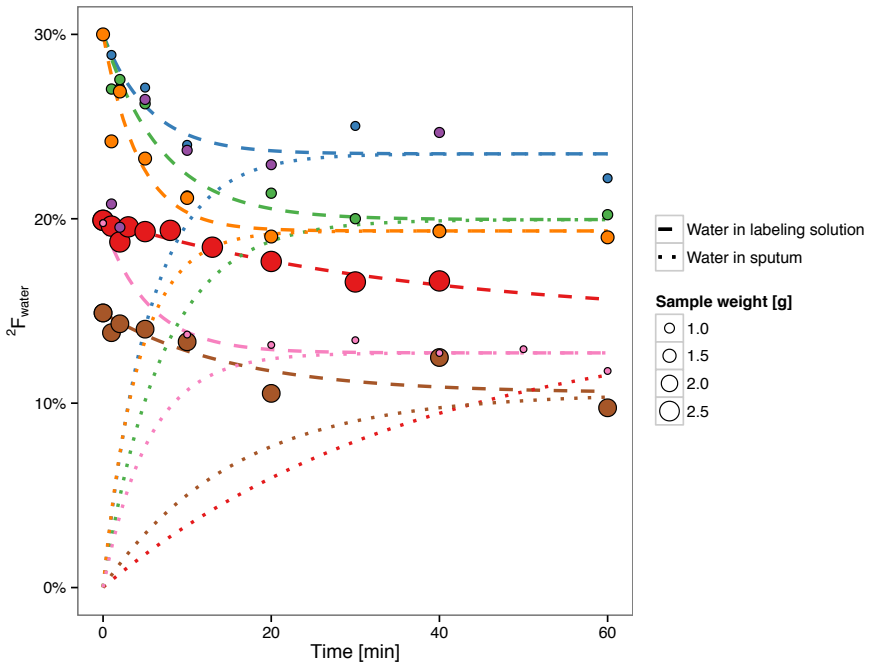

Figure 9.3 – Heavy water tracer mixing in sputum samples.

calculating the mixing of the isotopic labeling solution with water in the sputum sample *ab initio*. Here, we instead conducted several mixing experiments with sputum samples to derive a simple empirical mixing relationship of the form $1 - e^{-kt}$ that allows a functional parametrization of the isotope label mixing. In several experiments with sputum samples of different weights ranging from ~0.5 to 2.5g, the equilibration of the hydrogen isotopic composition of water in the isotope labeling solution ${}^2F_{w_{sln}}(t)$ from exchange with water contained within the suspended sputum sample ${}^2F_{w_{sputum}}(t)$ (about 2:1 w/w) was tracked over time, as illustrated in Figure 9.3. The hydrogen isotope composition of both end-member pools was described as mixing towards the equilibrium isotope composition ${}^2F_{w_{eq}}$ of the fully exchanged combined water pool with mixing rate constant k:

$$ {}^2F_{w_{sln}}(t) = {}^2F_{w_{eq}} + \left({}^2F_{w_{spike}} - {}^2F_{w_{eq}}\right) \cdot e^{-k \cdot t} \tag{9.1} $$

$$^2F_{w_{sputum}}(t) = {}^2F_{w_{eq}} + \left({}^2F_{w_{nat}} - {}^2F_{w_{eq}}\right) \cdot e^{-k \cdot t} \tag{9.2}$$

where $^2F_{w_{spike}}$ is the hydrogen isotope composition of the spiked isotope labeling solution (i.e. $^2F_{w_{sln}}$ at t_0), and $^2F_{w_{nat}}$ is the natural isotope composition of water contained within the sputum sample (i.e. $^2F_{w_{sputum}}$ at t_0). The data in Figure 9.3 is fitted to Equation 9.1 (fit of both equations illustrated in dashed and dotted lines, respectively), to derive a measure of k for each sample.

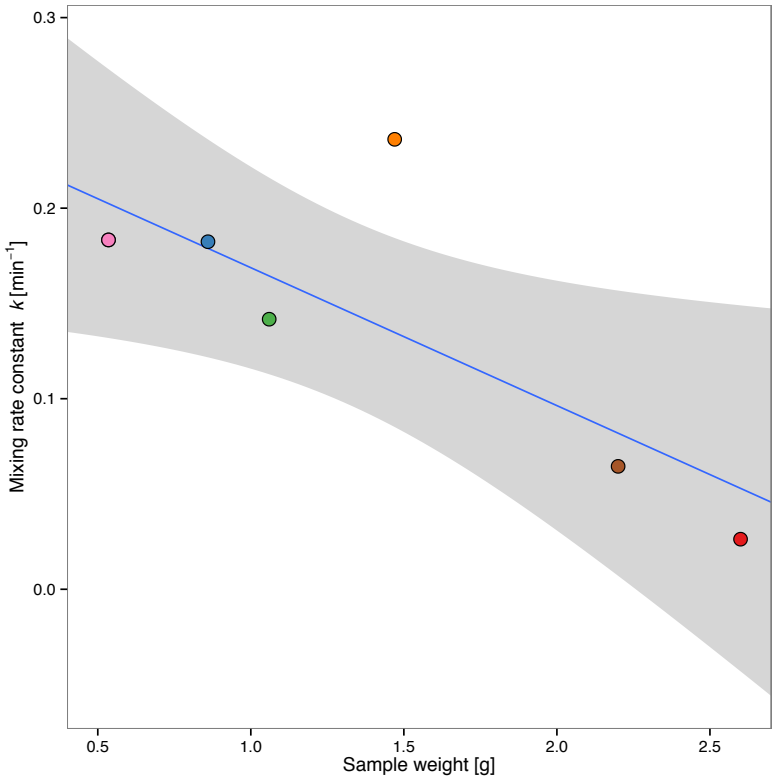

Figure 9.4 – Weight dependence of tracer mixing rate.

Figure 9.4 illustrates the derived values of k, which show a relationship with the sample weight as expected, and provides a model to estimate k for samples of differing weights. As samples become larger, it takes water from the isotopic labeling solution longer to mix with water in the sputum sample (lower k) than in small samples (higher k). In order

to substantially reduce the effect of water mixing (and effects of errors in estimating the exact value of k), we aimed for an ideal clinical sample size of ~0.5 g, which was rarely higher than actual samples from the pediatric cohort. An example of the water mixing with samples of differing weights is illustrated in Figure F.4 in the Appendix.

For each isotopically-labeled clinical sample, the hydrogen isotope composition of water in the labeling solution ${}^2F_{w_{sln}}(t_{inc})$ was measured in the residual solution at the conclusion of the experiment (at time t_{inc}), and the corresponding equilibrium isotopic composition between labeling solution and sample water ${}^2F_{w_{eq}}$ was calculated using the estimated value of k for the given sample weight:

$$ {}^2F_{w_{eq}} = \frac{{}^2F_{w_{sln}}(t_{inc}) - {}^2F_{w_{spike}} \cdot e^{-k \cdot t_{inc}}}{1 - e^{-k \cdot t_{inc}}} \tag{9.3} $$

Based on these parameters, we can use Equation 9.2 to model the time-course of the sputum water isotopic composition that the microbial population experiences over the entire incubation time interval (assuming sputum water is a reasonable representation of bioavailable water – see the discussion on water exchange and labeling in continuous culture in Chapter 7 for reference). The isotopic composition of newly-synthesized lipids is then described by

$$ \begin{aligned} {}^2F_{lipid_{new}}(t) &= x_w \cdot \alpha_{l/w} \cdot \left({}^2F_{w_{sputum}}(t) - {}^2F_{w_{nat}}\right) + {}^2F_{lipid}(t_0) \\ &= x_w \cdot \alpha_{l/w} \cdot \left({}^2F_{w_{eq}} - {}^2F_{w_{nat}}\right) \cdot \left(1 - e^{-k \cdot t}\right) + {}^2F_{lipid}(t_0) \end{aligned} \tag{9.4} $$

with water fraction factor $x_w \cdot \alpha_{l/w}$ (measured for *S. aureus* in Chapter 7), equilibrium isotopic composition ${}^2F_{w_{eq}}$ of sputum water mixed with the isotope labeling solution (Equation 9.3), original isotopic composition of the sputum water ${}^2F_{w_{nat}}$ (estimated to be circumnatural), the mixing rate k and the natural lipid hydrogen isotope composition ${}^2F_{lipid}(t_0)$. Substituting back into Equation 7.8 in Chapter 7 and integrating finally yields

an equation for the overall isotopic composition:

$$
\begin{aligned}
{}^2F_{lipid}(t) &= \frac{B_{new} \cdot {}^2F_{new}}{B} + \frac{B_{old} \cdot {}^2F_{old}}{B} \\
&= \Big[-x_w \cdot \alpha_{l/w} \cdot \left({}^2F_{w_{eq}} - {}^2F_{w_{nat}}\right) \cdot f_S \cdot \frac{\mu_{act}}{\mu_{act}+k} \cdot \left(1 - e^{-(\mu_{act}+k)\cdot t}\right) \\
&\quad + \left({}^2F_{lipid}(t_0) + x_w \cdot \alpha_{l/w} \cdot \left({}^2F_{w_{eq}} - {}^2F_{w_{nat}}\right)\right) \cdot f_S \cdot \left(1 - e^{-\mu_{act}\cdot t}\right) \Big] \\
&\quad + \left[{}^2F_{lipid}(t_0) \cdot \left(1 - f_S \cdot \left(1 - e^{-\mu_{act}\cdot t}\right)\right) \right] \\
&= x_w \cdot \alpha_{l/w} \cdot f_S \cdot \left({}^2F_{w_{eq}} - {}^2F_{w_{nat}}\right) \cdot \left[1 - e^{-\mu_{act}\cdot t} - \frac{\mu_{act}}{\mu_{act}+k} \cdot \left(1 - e^{-(\mu_{act}+k)\cdot t}\right) \right] \\
&\quad + {}^2F_{lipid}(t_0)
\end{aligned}
\tag{9.5}
$$

where μ_{act} is the apparent microbial activity (comprising both actual growth μ as well as maintenance activity ω, see Section 7.2 in Chapter 7 for details), f_S is the fraction of lipids derived from *de novo* synthesis vs. recycling (here assumed to be $f_S = 1$ because *S. aureus* was shown be unable to recycle any major host fatty acids for partial synthesis of the target analytes a-C15:0 and a-C17:0; see Section 7.4.6), and all other variables are as described before[3]. If mixing-in of the label were practically instantaneous relative to the incubation and growth time scales ($k \to \infty$) , this would simplify to (and would always *overestimate* true label incorporation):

$$
{}^2F_{lipid}(t) = x_w \cdot \alpha_{l/w} \cdot f_S \cdot \left({}^2F_{w_{eq}} - {}^2F_{w_{nat}}\right) \cdot \left(1 - e^{-\mu_{act}\cdot t}\right) + {}^2F_{lipid}(t_0) \tag{9.6}
$$

9.3.2.2 Growth rate estimates

Figure 9.5 shows all growth rate estimates for *S. aureus* in sputum, derived separately for a-C15:0 and a-C17:0 (whenever it could be quantified) as well as from the combined weighted average isotopic composition of both components. Several observations are particularly striking. First, the majority of all samples fall into an activity range equivalent

[3]For single samples with not enough material for subsampling, ${}^2F_{lipid}(t_0)$ was estimated from the average isotopic composition of all measured control samples (Figure F.5 in the Appendix).

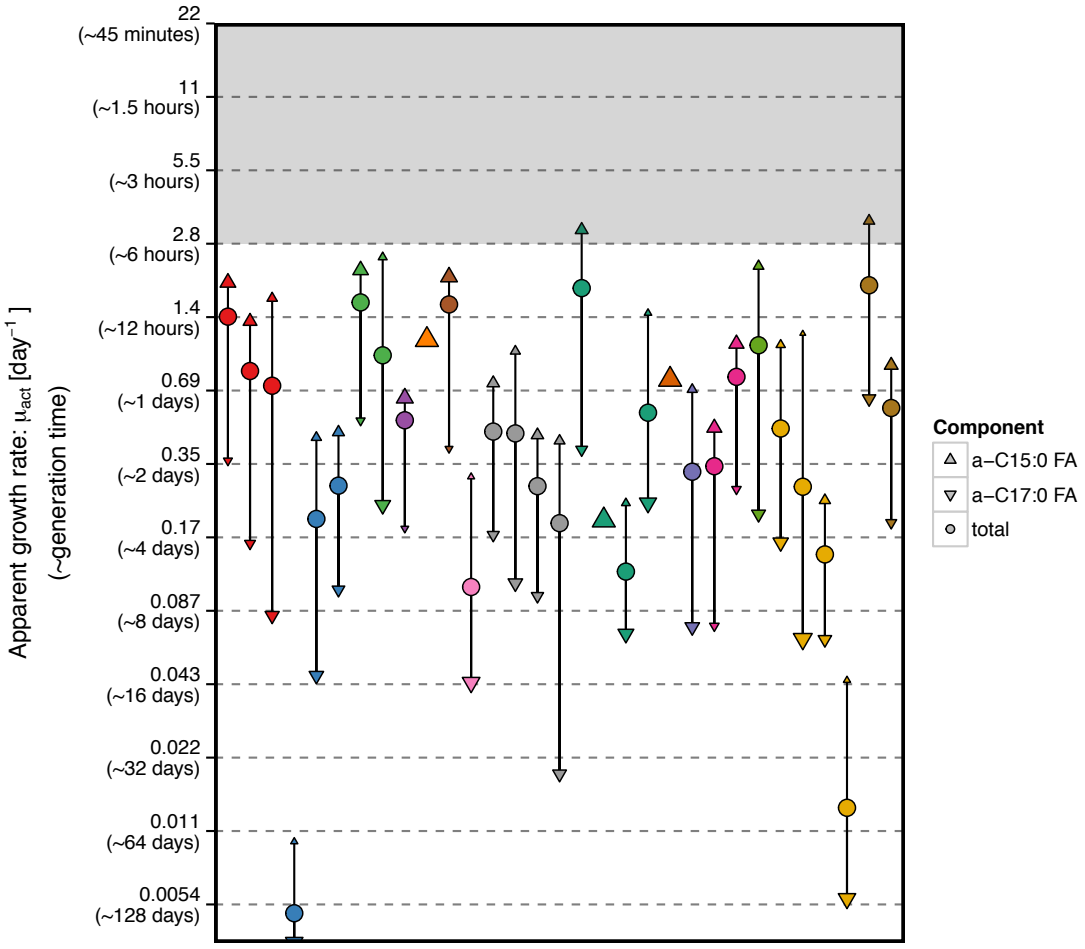

Figure 9.5 – Growth rate estimates from ^{2}H lipid labeling. Circles show weighted average isotopic composition for each data point from both major *S. aureus* membrane components (a-C15:0 and a-C17:0). Size of each symbol illustrates the relative abundance of the component within each sample. Colors represent samples from different patients. Area highlighted in gray represents the typical range of growth rates studies in laboratory experiments with *S. aureus*.

to generation times of ∼12 hours to ∼4 days. This is significantly different from growth rates typically employed in laboratory studies with *S. aureus* (roughly equivalent to the area highlighted in gray in Figure 9.5). Second, there appears to be significant divergence between the individual fatty acid components (a-C15:0 a-C17:0) associated with the entire *S. aureus* population present in each sputum sample. The pattern consistently shows an over-labeling of a-C15:0, and under-labeling of a-C17:0 relative to the weighted average,

which is consistent with, but more extreme than, the divergence pattern observed for *S. aureus* grown in continuous culture in synthetic cystic fibrosis medium at slow growth rates (see discussion in Chapter 7). The exact cause of this pattern in some laboratory experiments is yet undetermined, but could be a reflection of underlying heterogeneity in the microbial population with slower-growing cells producing a-C17:0 preferentially and faster-growing cells producing a-C15:0 (Section 7.4.5.2 in Chapter 7). In this case, the divergence would highlight that measures of microbial activity in *S. aureus* based on isotopic labeling of a-C15:0 would always provide an **upper limit** on growth rates, whereas measures based on isotope labeling of a-C17:0 would provide a **lower limit** on growth. However, the observed divergence pattern could also reflect a mixed contribution from multiple organisms (for example, *S. aureus* and *S. maltophilia*) with different activity rates.

Figure 9.6 shows a closer focus on several samples that provide additional information on sample variability. Samples 1.1, 1.2 and 1.3 (red, blue and green symbols) represent a unique case of multiple samples expectorated separately by the same patient within a 30-minute window. Samples 2 and 3 represent two samples from different patients that were large enough for subsampling and a time-course incubation of the aliquots. If the microbial population within the whole lung (1.1, 1.2, 1.3) or within individual sputum samples (2 & 3) were perfectly homogenous, microbial activity would be expected to be identical across each sample group. And indeed, the replicate measures are relatively similar within the larger scheme of fast- vs. slow-growth, and given the wide range of growth-rate estimates derived from different *S. aureus* fatty acids (a-C15:0 vs. a-C17:0). However, substantial variation exists on an absolute scale, with each group spanning approximately a 2x range in apparent growth rates for each component. While there is uncertainty in growth-rate estimates (error in the analytical measurements of water and lipid isotopic composition, and error in the estimated water-mixing-rate constants), this variation suggests heterogeneity in the microbial population on the scale of a single

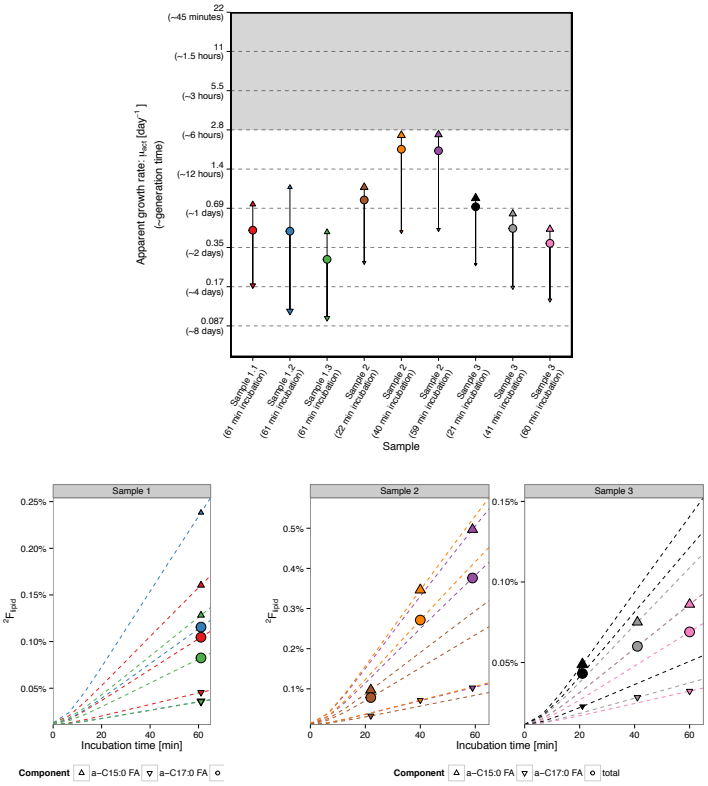

Figure 9.6 – Sample variability. Circles in upper panel show weighted average isotopic composition for each data point from both major *S. aureus* membrane components (a-C15:0 and a-C17:0). Size of each symbol illustrates the relative abundance of the component within each sample. Colors represent different (sub)samples. Area highlighted in gray represents the typical range of growth-rate studies in laboratory experiments with *S. aureus*. Dashed lines in lower panel represent the isotope labeling contours from the estimated growth rates derived separately for each data point (and each component).

sputum sample (subsamples of 2 & 3) and within the larger community (1.1, 1.2 and 1.3) at any point in time. The potential range of variation was investigated on the single-cell level, and is discussed in section 9.3.3.

9.3.2.3 Correlations with clinical parameters

Clinical information was collected for all samples whenever available. While limited in its statistical significance by the total number of samples and the nature of a cross-sectional study, several parameters with relatively high coverage across the sample set were investigated for correlation with the microbial activity data for *S. aureus* derived from weighted average isotopic enrichment of combined a-C15:0 and a-C17:0 FA. Sample

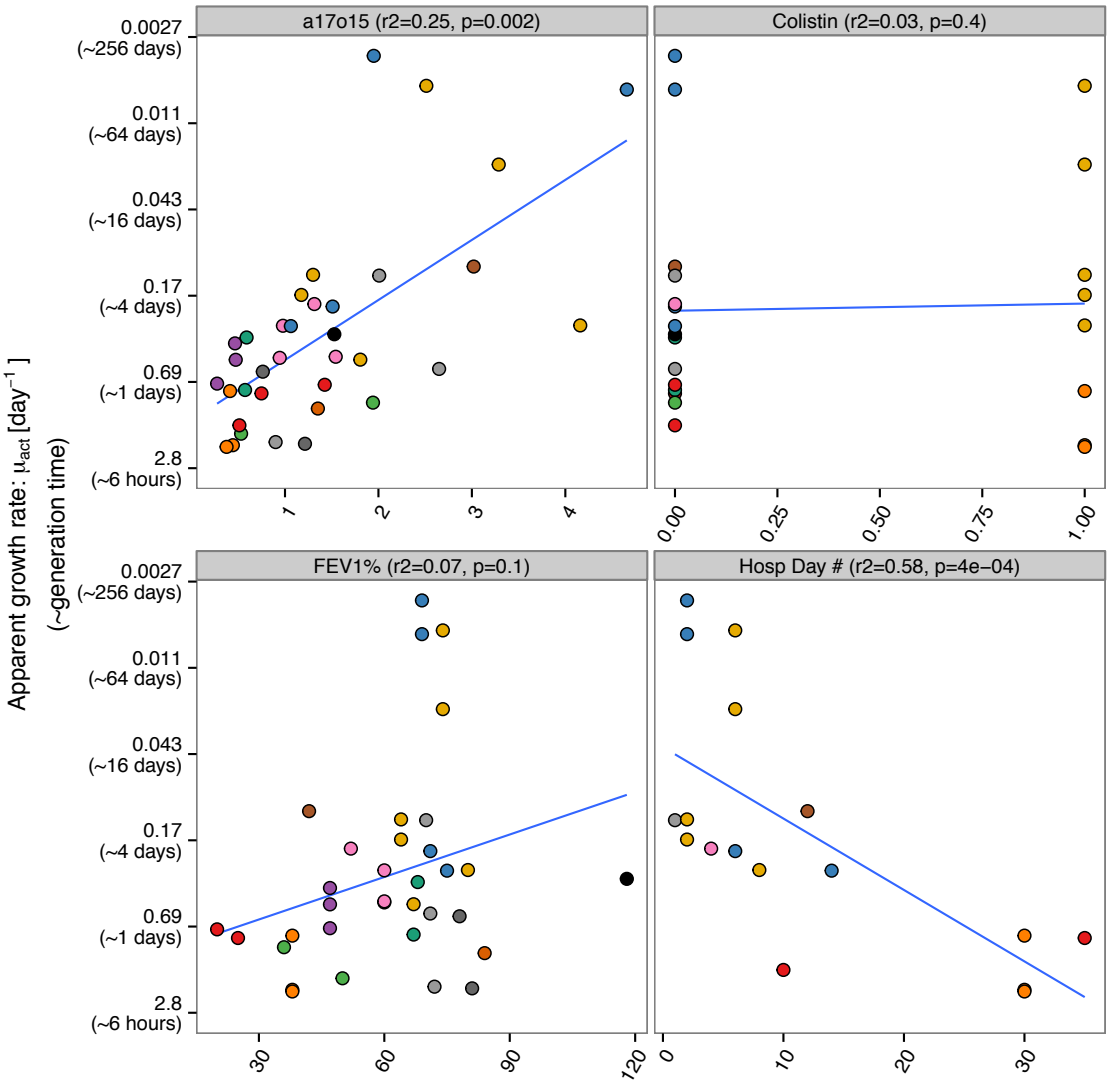

Figure 9.7 – Correlation between microbial activity and clinical parameters. The left panel shows the correlation between FEV1 values and the growth rates of *S. aureus* measured in all clinical samples (from weighted average isotopic composition of combined a-15:0 and a-17:0). The right panel shows the correlation for the day of the hospital visit. Panel headers denote the respective $R^2$and p-values for the linear correlation (but growth rates are plotted on a logarithmic scale for clarity). The different colors indicate samples from different patients in the study. Not all clinical information was available for all data points.

parameters that should be unrelated to microbial growth rates, such as the isotopic labeling strength or the weight of a subsample, were confirmed to be uncorrelated (both have an R^2value smaller than 0.01). Figure 9.7 illustrates a subset of four clinical parameters that

we discuss in more detail. All other correlation plots are presented in Figure F.8 of the appendix.

The most commonly-used indicator of disease severity and declining lung function is the forced expiratory volume in one second FEV_1 (lower left panel in Figure 9.7), with values below 40% indicating severe impairment of lung function, values from 40% to 69% indicating moderate lung function, and values from 70% to 89% indicating mildly impaired lung function (Flume et al., 2007; Miller et al., 2005). The FEV_1 value shows a positive correlation (faster microbial growth correlates with worse lung function), suggesting a more active microbial community in more severe disease states, although the correlation is not statistically robust enough (p-value=0.1) to be interpreted fully.

The Hospital Day # (lower right panel) indicates the day of an in-patient's stay at the hospital at the time of sample collection, with day 0 representing the day of admission. Microbial activity shows a statistically significant correlation with this parameter (p-value < 0.0005) with higher microbial activity in samples from patients who have been at the hospital for a longer duration. This correlation is likely a consequence of sicker patients staying longer at the hospital.

The ratio of a-C17:0 over a-C15:0 (upper left panel) indicates the measured relative abundance of the two *S. aureus* membrane components in the sample, and shows a positive correlation with growth rates ($p < 0.002$). This could reflect slower-growing populations of *S. aureus* that are producing membranes composed of a higher proportion of a-C17:0, in accordance with similar membrane composition patterns observed for *S. aureus* grown in continuous culture in minimal medium at slow growth rates (see discussion in Chapter 7).

Lastly, the colistin parameter indicates whether the patient was taking the polymyxin antibiotic colistin (binary yes=1/no=0, upper right panel) at the time of sample collection, and shows no correlation with growth rates. Colistin is mostly used as an antibiotic to treat and prevent chronic infections of *P. aeruginosa,* and is not known to have a strong

effect on *S. aureus*. However, like any antibiotic administered as part of a multi-drug treatment (most of the patients receive at least 2 antibiotics while hospitalized), these data are difficult to interpret quantitatively, and require more targeted studies of microbial activity at different antibiotic regimes for the same patient.

9.3.3 Heterogeneity of microbial activity

Hydrogen isotope enrichment of microbial fatty acids from ^2H_2O incorporation provide a first quantitative measure of average microbial activity. Here we combine thin-sectioning of sputum samples with fluorescent *in situ* hybridization (FISH) and nano-scale secondary ion mass spectrometry (NanoSIMS) to measure microbial activity in clinical samples at the single-cell level, with the goal of estimating the range of microbial activities encountered in cystic fibrosis lung infections.

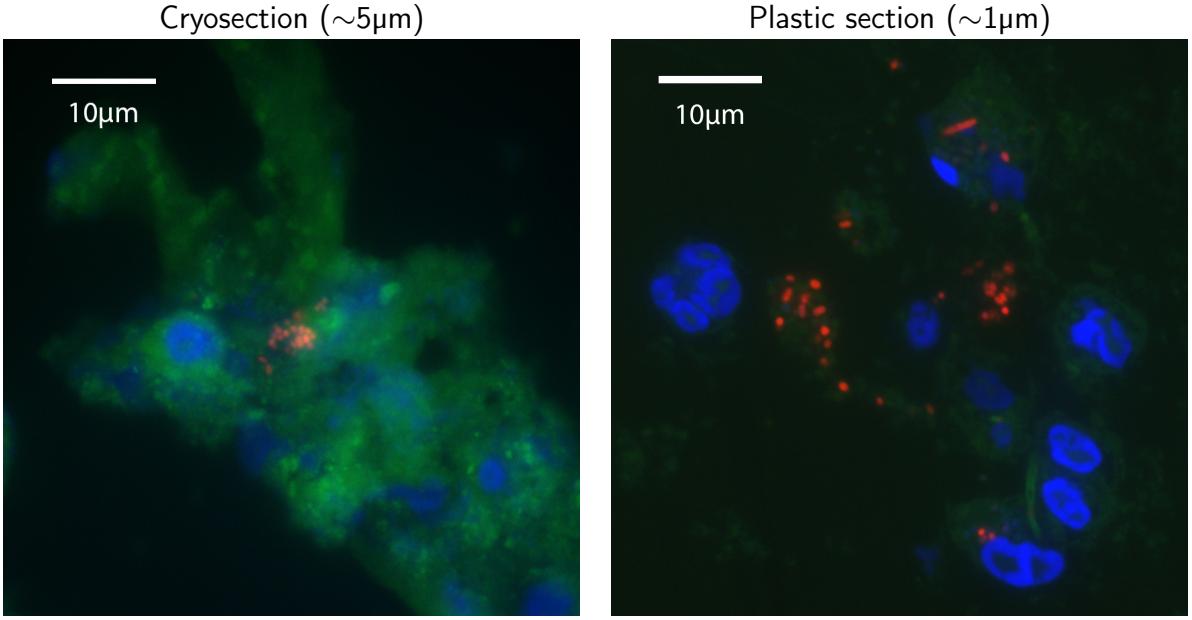

Figure 9.8 – Cryo vs. plastic thin section. DNA stained with DAPI and shown in blue (host cell nuclei predominate the signal). Bacterial cells identified by FISH with universal bacterial probe EUB338 and shown in red. Autofluorescence of the mucus matrix recorded in the GFP channel and shown in green. Scale bars are 10µm.

9.3.3.1 Cryo- vs. plastic sections

Sections with a soft, removable matrix, such as those produced by embedding and cryosectioning in O.C.T., provide an attractive strategy for investigating structurally complex samples by FISH-NanoSIMS. The embedding and sectioning procedure is relatively straightforward and, most importantly, the matrix is easy to remove, which allows single-cell isotopic measurements without the complicating contribution of matrix material. However, this technique does not not permit cutting sections thinner than ∼5µm, which can be a limiting factor in imaging mass spectrometry of microbial targets. ∼1µm plastic sections are more difficult to produce, less established in combination with fluorescent *in situ* hybridization, and require careful calibration of any isotopic measurement to account for matrix effects (discussed in detail in Chapter 8). For the application of FISH-NanoSIMS on microbial targets in the complex sputum matrix of clinical samples from cystic fibrosis patients, we found the spatial resolution and ion-image correlations in cryo-sections to be insufficient for single cell quantitation, and developed hydrogen isotope measurements of single cells embedded in Technovit plastic as an alternative with the desired spatial resolution. Figure 9.8 illustrates the difference in clarity between a 5µm cryo- and 1µm plastic section from sputum samples with microbial targets ∼500nm to 1µm in size. While optical clarity in the fluorescent mapping of sample sections is a welcome benefit of the thinner sections, the major difficulty of the cryosections lies with the identification of microbial cells within the ion images captured by secondary ion mass spectrometry.

Figure 9.9 illustrates the difficulty of locating targets in cryosection, and the approach taken in the thinner plastic sections. In cryosection, the sample's thickness and lack of a support matrix causes the ion beam to hit and ionize organic material in the sample at different depths on the topographically irregular surface exposed to the beam. As a consequence, nitrogen (in the form of the $^{14}N^{12}C^-$) is detected in similar amounts everywhere on the exposed surface of the highly complex sputum sample (rich in extracellular DNA

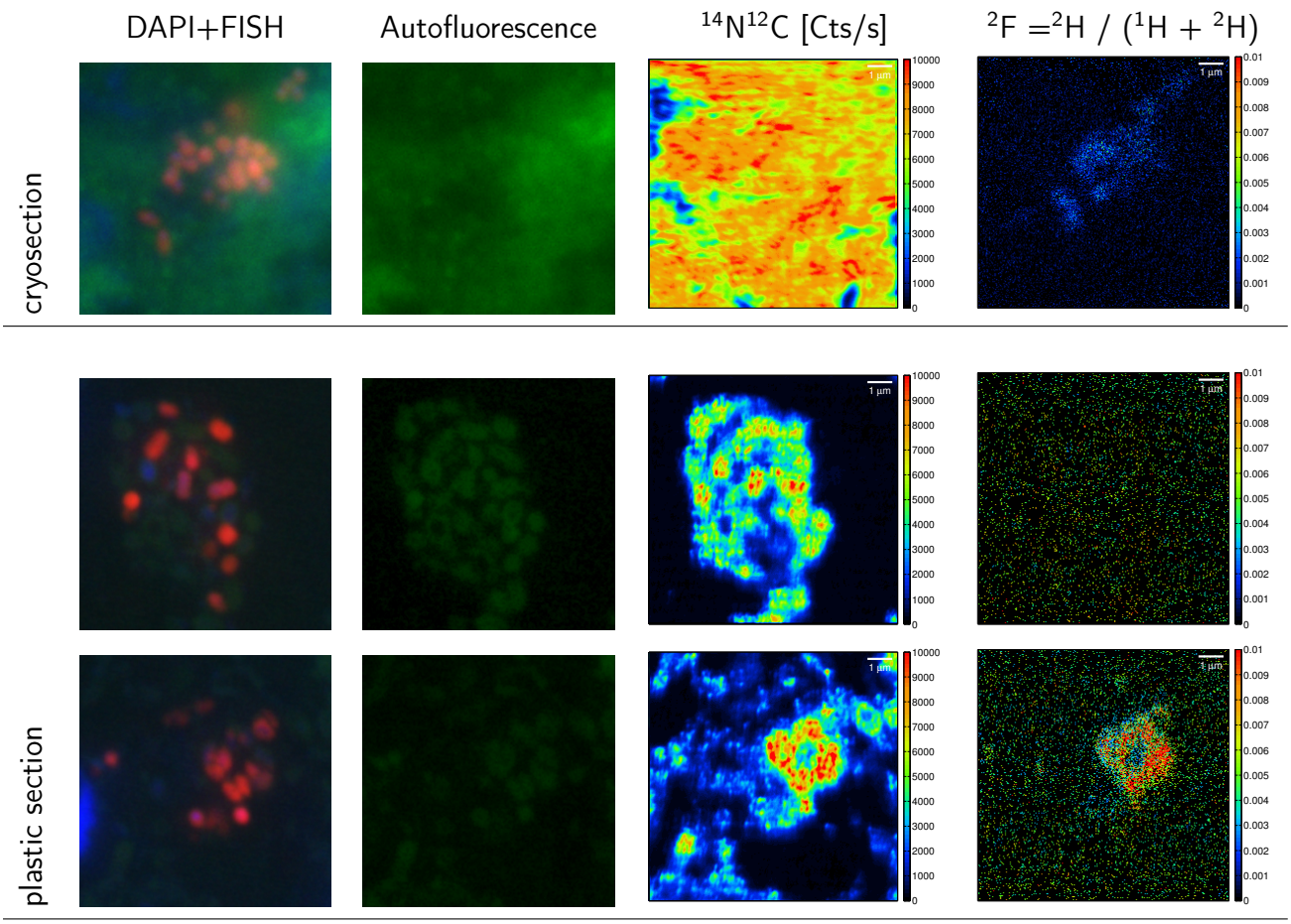

Figure 9.9 – Target identification and ^{2}H enrichment in cryo- and plastic sections. Frames shown are 10µm by 10µm, and the scale bar in ion maps is 1µm. First column shows microscopy pictures with overlaid DAPI (blue), bacterial EUB338 FISH (red) and sample autofluorescence in the GFP channel (green); second column shows the autofluorescence alone (slightly enhanced for contrast), third column the $^{14}N^{12}C^{-}$ ion image, and the last column the fractional abundance image of ^{2}H.

and glycoproteins), and does not provide any information as to the precise location of the target pathogens. The same is true for ion maps of carbon, phosphorus and sulfur, and the only means of localizing the target microorganisms is provided by the isotopic enrichment maps (here showing evidence of ^{2}H incorporation in several microbes). However, this approach implies that only highly active microbial targets can be identified, and are preferentially recorded. In the plastic section, on the other hand, the ion beam samples a relatively smooth surface with organic sample material embedded in the Technovit plastic polymer, which does not contain any nitrogen. This allows for direct mapping of the

auto-fluorescent image onto the $^{14}N^{12}C^-$ ion image, enabling identification of individual cells in the ion image from fluorescent microscopy – independent of isotopic enrichment, or lack thereof, in individual cells.

It is notable that all microbial clusters displayed in Figure 9.9 are targets from the larger microscopy images displayed in Figure 9.8. The two clusters analyzed in the shown plastic section illustrate visually how different organisms within the same microscopy frame can exhibit vastly different single-cell growth activities, as recorded here in ^2H incorporation. The first cluster (second row) did not incorporate any ^2H above background, suggesting that the cells were not (or not significantly) active during the incubation time, whereas the cluster on the right (third row) was highly active, incorporating hydrogen as a consequence of biosynthesis. Lastly, the microorganisms shown here are all examples of targets that were identified as microbial with the EUB338 FISH probe, but were neither *Pseudomonas aeruginosa* nor *Staphylococcus aureus* cells.

9.3.3.2 Heterogeneity in clinical samples

Single cells of *S. aureus* were located, mapped and analyzed in plastic thin sections from sputum samples of four different patients. One sample contained both a significant population of *S. aureus* cells and bacterial cells of an unidentified species (verified to be bacterial with the EUB338 probe, and confirmed to be neither *S. aureus* nor *P. aeruginosa*). The isotopic composition of all ROIs/cells is pictured in Figure F.9 in the Appendix. NanoSIMS measurements of single-cell hydrogen isotope compositions were converted to equivalent bulk (whole membrane) ^2F abundances using the calibration established in Chapter 8, and apparent growth rates for each individual cell were estimated from the relation derived in Equation 9.5. Figure 9.10 illustrates the distribution of single-cell growth rates for the different samples. The observed pattern confirms that substantial heterogeneity exists within the *S. aureus* population in all measured samples, with a particularly wide, apparently bimodal distribution observed in the sample depicted in panel

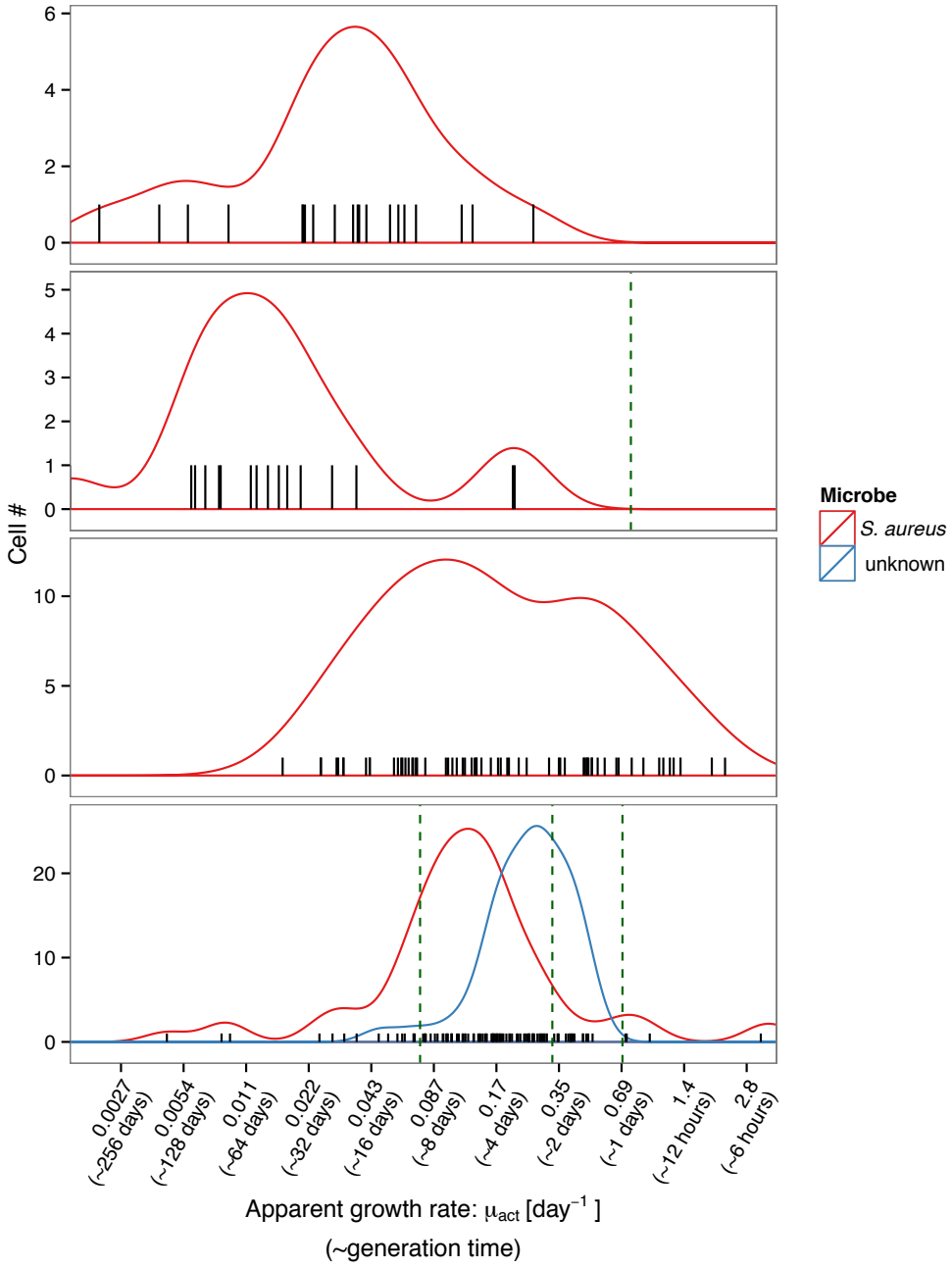

Figure 9.10 – Single-cell microbial activity in cystic fibrosis samples. The four panels show data of single-cell growth rates of *S. aureus* cells as well as an unidentified group of bacteria from different clinical samples. The bean bars indicate the measured growth rates of individual cells/ROIs. The curves illustrate the smoothed density distribution function of the data for each sample. The vertical dashed green lines indicate growth rate estimates from bulk fatty acid hydrogen isotope enrichments of samples collected on different days from the same patient. All growth-rates are plotted on a logarithmic scale for clarity.

3. The large number of unidentified bacteria measured in addition to *S. aureus* cells in the sample depicted in panel 4 appears to form a separate group of pathogens that is on average more active than the co-occurring *S. aureus* population. Several growth-rate estimates from bulk isotopic enrichment of the *S. aureus* membrane components a-C15:0 and a-C17:0 are available from other samples from the same patients (collected on different days), which are shown in vertical dashed lines in Figure 9.10. The comparison highlights the variation that can exist from day to day in the same patient, as illustrated already in the aggregated bulk measurements shown in Figure 9.5.

9.4 Conclusions

Here, we present the first application of hydrogen isotope labeling to measure average population growth rates and single-cell microbial activity in a complex environmental context.

For this study, sputum samples from a cohort of cystic fibrosis patients were collected at the Children's Hospital Los Angeles, and were isotopically labeled with heavy water for up to 60 minutes immediately upon expectoration. We focus on the opportunistic pathogen *S. aureus* for its importance in lung infections of pediatric cystic fibrosis patients and its unique fatty acid profile and, for the first time, estimate quasi *in situ* microbial activity rates both on the population and single-cell level applying the tools and calibrations developed in chapters 7 and 8.

Our cross-sectional study indicates that the average growth rates of *S. aureus* in sputum fall into a range of generation times between $\sim$12 hours and $\sim$4 days, suggesting that the organism most likely experiences much more pronounced slow-growth conditions than typically considered in laboratory studies. Additionally, our results from single-cells analysis of *S. aureus* indicate substantial population heterogeneity in sputum. Neither the slow average growth rates nor the heterogeneity are a surprising feature of this microbial

population given its role and persistence in chronic infections of the CF airways, but this is the first time that these physiological parameters are demonstrated to occur directly in the sputum environment. This highlights the crucial importance of studying the physiology of slow growth in representative laboratory systems in order to understand the role and response of different pathogens, as well as their potential resistance and susceptibility to antimicrobial therapies in the infection context.

While this cross-sectional study provides limited context for clinical interpretation of *S. aureus* growth rates due to the obscuring effects of patient-to-patient variability, it lays the groundwork for more targeted investigations into the efficacy of different treatment regimes and their effects on pathogen growth and metabolic heterogeneity in longitudinal studies with cystic fibrosis patients.

Acknowledgements

This project would not have been possible without the support of many, many people. I would like to first, and foremost, acknowledge the tremendous hard work of Elise Cowley, Abigail Green and Lindsey VanSambeek in the processing and preparation of various samples that greatly benefited this project. I want to especially thank Magdalena Osburn, Lichun Zhang, Shawn McGlynn, Yunbin Guan, Kat Dawson, Roland Hatzenpichler, Megan Bergkessel and Ryan Hunter for their patience, help and support in learning and applying the various techniques used in this study. I also owe a debt of gratitude to the team and directors at CHLA for their enthusiasm and support, especially Carmen Reyes, Kyle McCallin, Roberta Kato, Fadi Asfour, Douglas Li, Sally Ward and Thomas Keens. Lastly, many members of the Newman, Sessions and Orphan labs provided important feedback and advice. None of this work would have been possible without the generous support of the Howard Hughes Medical Institute in the form of a predoctoral fellowship, as well as support from an NIH grant to D.K.N.

9.5 References

Amann, R. I., Krumholz, L., Stahl, D. A., Feb. 1990. Fluorescent-oligonucleotide probing of whole cells for determinative, phylogenetic, and environmental studies in microbiology. Journal of Bacteriology 172 (2), 762–770.

Baek, S.-H., Li, A. H., Sassetti, C. M., May 2011. Metabolic regulation of mycobacterial growth and antibiotic sensitivity. Plos Biology 9 (5).

Blazewicz, S. J., Barnard, R. L., Daly, R. A., Firestone, M. K., Jul. 2013. Evaluating rRNA as an indicator of microbial activity in environmental communities: limitations and uses. The ISME Journal, 1–8.

Chao, J., Wolfaardt, G. M., Arts, M. T., Dec. 2010. Characterization of Pseudomonas aeruginosa fatty acid profiles in biofilms and batch planktonic cultures. Canadian Journal of Microbiology 56 (12), 1028–1039.

Christie, W. W., May 1997. Preparation of ester derivatives of fatty acids for chromatographic analysis. In: Advances in Lipid Methodology. Elsevier, Dundee, pp. 69–111.

Coplen, T. B., 1988. Normalization of oxygen and hydrogen isotope data. Chemical Geology: Isotope Geoscience section 72 (4), 293–297.

Davies, J. C., 2002. *Pseudomonas aeruginosa* in cystic fibrosis: pathogenesis and persistence. Paediatric respiratory reviews.

Dekas, A. E., Chadwick, G. L., Bowles, M. W., Joye, S. B., Orphan, V. J., Aug. 2013. Spatial distribution of nitrogen fixation in methane seep sediment and the role of the ANME archaea. Environmental Microbiology.

Dekas, A. E., Orphan, V. J., 2011. Identification of diazotrophic microorganisms in marine sediment via fluorescence in situ hybridization coupled to nanoscale secondary ion mass spectrometry (FISH-NanoSIMS). Methods in enzymology 486, 281–305.

Dekas, A. E., Poretsky, R. S., Orphan, V. J., Oct. 2009. Deep-sea archaea fix and share nitrogen in methane-consuming microbial consortia. Science 326 (5951), 422–426.

Dibdin, G. H., Jan. 1981. Diffusion of sugars and carboxylic acids through human dental plaque in vitro. Archives of Oral Biology 26 (6), 515–523.

Dragulescu, A. A., 2013. xlsx: Read, write, format Excel 2007 and Excel 97/2000/XP/2003 files. R package version 0.5.5.
URL http://CRAN.R-project.org/package=xlsx

Easteal, A. J., Edge, A., Woolf, L. A., 1984. Isotope effects in water. Tracer diffusion coefficients for H/sub 2//sup 18/O in ordinary water. J. Phys. Chem.;(United States).

Ecker, R. E., Schaechter, M., Oct. 1963. Ribosome content and the rate of growth of *Salmonella typhimurium*. Biochimica et biophysica acta 76 (2), 275–279.

Florijn, R. J., Slats, J., Tanke, H. J., Raap, A. K., Feb. 1995. Analysis of antifading reagents for fluorescence microscopy. Cytometry 19 (2), 177–182.

Flume, P. A., O'Sullivan, B. P., Robinson, K. A., Goss, C. H., Mogayzel, P. J., Willey-Courand, D. B., Bujan, J., Finder, J., Lester, M., Quittell, L., Rosenblatt, R., Vender, R. L., Hazle, L., Sabadosa, K., Marshall, B., Cystic Fibrosis Foundation, Pulmonary Therapies Committee, Nov. 2007. Cystic fibrosis pulmonary guidelines: chronic medications for maintenance of lung health.

Goerke, C., Wolz, C., 2010. Adaptation of Staphylococcus aureus to the cystic fibrosis lung. International Journal of Medical Microbiology.

Goss, C. H., Burns, J. L., 2007. Exacerbations in cystic fibrosis center. 1: Epidemiology and pathogenesis. Thorax 62 (4), 360–367.

Goss, C. H., Muhlebach, M. S., Sep. 2011. Review: Staphylococcus aureus and MRSA in cystic fibrosis. Journal of Cystic Fibrosis 10 (5), 298–306.

Griffiths, M. J., Hille, R. P., Harrison, S. T. L., Sep. 2010. Selection of direct transesterification as the preferred method for assay of fatty acid content of microalgae. Lipids 45 (11), 1053–1060.

Harrison, F., 2007. Microbial ecology of the cystic fibrosis lung. Microbiology.

Hart, C. A., Winstanley, C., 2002. Persistent and aggressive bacteria in the lungs of cystic fibrosis children. British Medical Bulletin 61 (1), 81–96.

Helaine, S., Cheverton, A. M., Watson, K. G., Faure, L. M., Matthews, S. A., Holden, D. W., Jan. 2014. Internalization of *Salmonella* by macrophages induces formation of nonreplicating persisters. Science 343 (6167), 204–208.

Helaine, S., Thompson, J. A., Watson, K. G., Liu, M., Boyle, C., Holden, D. W., Feb. 2010. Dynamics of intracellular bacterial replication at the single cell level. Proceedings of the National Academy of Sciences of the United States of America 107 (8), 3746–3751.

Hirschhausen, N., Block, D., Bianconi, I., Bragonzi, A., Birtel, J., Lee, J. C., Dübbers, A., Küster, P., Kahl, J., Peters, G., Kahl, B. C., Dec. 2013. Extended Staphylococcus aureus persistence in cystic fibrosis is associated with bacterial adaptation. International Journal of Medical Microbiology 303 (8), 685–692.

Hogardt, M., Trebesius, K., Geiger, A., Hornef, M., Rosenecker, J., Heesemann, J., 2000. Specific and rapid detection by fluorescent in situ hybridization of bacteria in clinical samples obtained from cystic fibrosis patients. Journal of clinical microbiology 38 (2), 818.

Holz, M., Heil, S. R., Sacco, A., 2000. Temperature-dependent self-diffusion coefficients of water and six selected molecular liquids for calibration in accurate 1H NMR PFG measurements. Physical Chemistry Chemical Physics 2 (20), 4740–4742.

Jantzen, E. E., Berdal, B. P. B., Omland, T. T., Mar. 1980. Cellular fatty acid composition of Haemophilus species, Pasteurella multocida, Actinobacillus Actinomycetemcomitans and Haemophilus vaginalis (Corynebacterium vaginale). Acta pathologica et microbiologica Scandinavica. Section B, Microbiology 88 (2), 89–93.

Jones, P. J., Leatherdale, S. T., Apr. 1991a. Stable isotopes in clinical research: safety reaffirmed. Clinical science (London, England : 1979) 80 (4), 277–280.

Kahl, B. C., 2010. Impact of Staphylococcus aureus on the pathogenesis of chronic cystic fibrosis lung disease. International Journal of Medical Microbiology.

Kempf, V. A., Trebesius, K., Autenrieth, I. B., Feb. 2000. Fluorescent In situ hybridization allows rapid identification of microorganisms in blood cultures. Journal of clinical microbiology 38 (2), 830–838.

Krejci, E., Kroppenstedt, R. M., Mar. 2006. Differentiation of species combined into the *Burkholderia cepacia* complex and related taxa on the basis of their fatty acid patterns. Journal of clinical microbiology 44 (3), 1159–1164.

Kushner, D. J., Baker, A., Dunstall, T. G., Feb. 1999b. Pharmacological uses and perspectives of heavy water and deuterated compounds. Canadian Journal Of Physiology And Pharmacology 77 (2), 79–88.

Lathe, R., 1985. Synthetic oligonucleotide probes deduced from amino acid sequence data: theoretical and practical considerations. Journal Of Molecular Biology 183 (1), 1–12.

Lu, Y.-J., Rock, C. O., Nov. 2005. Transcriptional regulation of fatty acid biosynthesis in Streptococcus pneumoniae. Molecular Microbiology 59 (2), 551–566.

Manz, W., Amann, R., Ludwig, W., Wagner, M., Schleifer, K.-H., Dec. 1992. Phylogenetic oligodeoxynucleotide probes for the major subclasses of proteobacteria: problems and solutions. Systematic and Applied Microbiology 15 (4), 593–600.

Metcalffe, L. D., Wang, C. N., 1981. Rapid Preparation of Fatty Acid Methyl Esters Using Organic Base-Catalyzed Transesterification. Journal of chromatographic science 19 (10), 530–535.

Miller, M. R., Crapo, R., Hankinson, J., Brusasco, V., Burgos, F., Casaburi, R., Coates, A., Enright, P., van der Grinten, C. P. M., Gustafsson, P., Jensen, R., Johnson, D. C., MacIntyre, N., McKay, R., Navajas, D., Pedersen, O. F., Pellegrino, R., Viegi, G., Wanger, J., ATS/ERS Task Force, Jul. 2005. General considerations for lung function testing. The European respiratory journal 26 (1), 153–161.

Neuwirth, E., 2011. RColorBrewer: ColorBrewer palettes. R package version 1.0-5. URL http://CRAN.R-project.org/package=RColorBrewer

Nguyen, D., Joshi-Datar, A., Lepine, F., Bauerle, E., Olakanmi, O., Beer, K., McKay, G., Siehnel, R., Schafhauser, J., Wang, Y., Britigan, B. E., Singh, P. K., Nov. 2011. Active starvation responses mediate antibiotic tolerance in biofilms and nutrient-limited bacteria. Science 334 (6058), 982–986.

Norman, D. J., Chase, A. R., Hodge, N. C., Stall, R. E., Nov. 1997. Differentiation of three species of Xanthomonas and Stenotrophomonas maltophilia using cellular fatty acid analyses. European Journal of Plant Pathology 103 (8), 687–693.

Polerecky, L., Adam, B., Milucka, J., Musat, N., Vagner, T., Kuypers, M. M. M., Jan. 2012. Look@NanoSIMS - a tool for the analysis of nanoSIMS data in environmental microbiology. Environmental Microbiology 14 (4), 1009–1023.

R Core Team, 2014. R: A Language and Environment for Statistical Computing. R Foundation for Statistical Computing, Vienna, Austria.
URL http://www.R-project.org/

Steinhauser, M. L., Lechene, C. P., Aug. 2013. Quantitative imaging of subcellular metabolism with stable isotopes and multi-isotope imaging mass spectrometry. Seminars in Cell and Developmental Biology 24 (8-9), 661–667.

Stewart, M. K., Cummings, L. A., Johnson, M. L., Berezow, A. B., Cookson, B. T., Dec. 2011. Regulation of phenotypic heterogeneity permits Salmonella evasion of the host caspase-1 inflammatory response. Proceedings of the National Academy of Sciences 108 (51), 20742–20747.

Stewart, P., Aug. 1998. A review of experimental measurements of effective diffusive permeabilities and effective diffusion coefficients in biofilms. Biotechnology and Bioengineering 59 (3), 261–272.

Stewart, P., 2003. Diffusion in biofilms. Journal of Bacteriology 185 (5), 1485–1491.

Stoecker, K., Wagner, M., Dorninger, C., Daims, H., Jan. 2010. Double labeling of Oligonucleotide Probes for Fluorescence *In Situ* Hybridization (DOPE-FISH) improves signal intensity and increases rRNA accessibility. Applied and Environmental Microbiology 76 (3), 922–926.

Stone, A., Saiman, L., 2007. Update on the epidemiology and management of Staphylococcus aureus, including methicillin-resistant Staphylococcus aureus, in patients with cystic fibrosis. Current opinion in pulmonary medicine.

Tajbakhsh, S., Hogardt, M., Heesemann, J., Grzonka, C., 2008a. Detection of Pseudomonas aeruginosa in sputum samples by modified fluorescent in situ hybridization. African Journal of . . . 7 (5), 553–556.

Tajbakhsh, S., Hogardt, M., Heesemann, J., Grzonka, C., Adler, K., Tajbakhsh, S., 2008b. Detection of Pseudomonas aeruginosa in sputum samples by modified fluorescent in situ hybridization. African Journal of Biotechnology 7 (5).

Trebesius, K., Panthel, K., Strobel, S., Vogt, K., Faller, G., May 2000. Rapid and specific detection of Helicobacter pylori macrolide resistance in gastric tissue by fluorescent in situ hybridisation. Gut 46 (5), 608–614.

Wallner, G., Amann, R., Beisker, W., 1993. Optimizing fluorescent in situ hybridization with rRNA-targeted oligonucleotide probes for flow cytometric identification of microorganisms. Cytometry 14 (2), 136–143.

Wickham, H., 2014a. plyr: Tools for splitting, applying and combining data. R package version 1.8.1.
URL http://CRAN.R-project.org/package=plyr

Wickham, H., Chang, W., 2013. ggplot2: An implementation of the Grammar of Graphics. R package version 0.9.3.1.
URL http://CRAN.R-project.org/package=ggplot2

Xie, Y., 2013b. knitr: A general-purpose package for dynamic report generation in R. R package version 1.5.
URL http://CRAN.R-project.org/package=knitr

Yang, L., Haagensen, J. A. J., Jelsbak, L., Johansen, H. K., Sternberg, C., Hoiby, N., Molin, S., Apr. 2008. *In situ* growth rates and biofilm development of *Pseudomonas aeruginosa* populations in chronic lung infections. Journal of Bacteriology 190 (8), 2767–2776.

Chapter 10

What have we learned?

Where do we go from here?

Part I of this thesis presented research related to microbial processes in iron-rich Lake Matano and, more broadly, in the biogeochemical cycling of iron. The results illustrated that the chelation of Fe(II) by organic ligands can fundamentally alter the role of Fe(II) in anoxic environmental systems. Specifically, chelation can both enable biological processes through mixotrophic growth of phototrophic microorganisms with Fe(II), as well as affect abiotic processes through enhancing chemical reaction rates of Fe(II) with denitrification intermediates. On the biological side, this implies that the ability to grow photomixotrophically on Fe(II) might be more widespread than previously assumed, even for cultured organisms that have simply not been exposed to accessible species of Fe(II). Future research could, for example, target the hitherto un-identified enzymatic pathways involved in photomixotrophic Fe(II) oxidation to enable assessment of how widespread and environmentally significant this type of microbial Fe(II) oxidation might be. On the abiotic side, our work highlights the likely competition and co-occurrence of chemical and biological processes involved in the coupled biogeochemical cycling of iron and nitrogen.

The biologically-induced chemical oxidation of Fe(II) – via the microbial production of nitrite in chelator-rich environments such as soils and wetlands – is likely to contribute significantly to the cycling of iron and immobilization of metal contaminants and organic pollutants on iron (oxy)hydroxides. Future research should focus on gaining a quantitative understanding of the interplay between biological processes and chemical catalysis in environmental settings, by targeting, for example, the nitrogen isotope signatures of different biological and abiotic pathways, as well as the *in situ* activity of the microbial mediators of this process.

Part II of this thesis presented research related to microbial processes in the Cystic Fibrosis lung, and more broadly, the physiology of slow growth, and the tools available to study slow growth *in situ*. The results highlighted stable isotope labeling of microbial membrane fatty acids and whole cells with heavy water as a promising new technique to measure microbial activity in a wide range of environments, and showed that slow growth plays an important role in infections of the Cystic Fibrosis airways. Specifically, we outlined the conceptual approach to quantitative isotope labeling with heavy water as a measure for growth, demonstrated its application in continuous culture in the laboratory at the population and single cell level, and applied the tool to measure the *in situ* activity of *Staphylococcus aureus* in clinical sputum samples from cystic fibrosis patients. Our laboratory studies highlighted several features of microbial metabolism at slow growth that present ample opportunity for follow-up work. For example, our continuous culture work with *S. aureus* and *Pseudomonas aeruginosa* revealed both substantial differences in membrane turnover between these species, and an apparent growth-rate dependence of the maintenance rate. Membrane turnover is a poorly understood phenomenon and future work using this isotope labeling approach should investigate the role of Gm-positive (*S. aureus*) vs. Gm-negative (*P. aeruginosa*) cell envelopes in the loss and repair of lipid membranes. Maintenance, on the other hand, is a well-studied concept in cell biology that is often considered a constant. At slow environmental growth rates, however,

maintenance rates are likely variable and future work should follow up on our observation of this phenomenon to study how maintenance is affected by growth. Our clinical work presented the first application of hydrogen isotope labeling to measure average population growth rates and single-cell microbial activity in a complex environmental context. Our data revealed that the average growth rates of *S. aureus* in sputum fall into a range of generation times between ∼12 hours and ∼4 days, suggesting that the organism most likely experiences much more pronounced slow-growth conditions than typically considered in laboratory studies. Undoubtedly, extension of this research presents one of the most exciting avenues for follow-up work. Particularly, it would be important to understand what features of the chemical environment limit microbial growth *in situ* by supplying exogenous supplements (such as oxygen) during growth rate measurements. Likewise, the *in situ* efficacy of therapeutic agents could be tested in similar manor to inform microbial susceptibility. Furthermore, the experimental setup in our work to date with freshly expectorated sputum was chosen such that sputum samples for isotope labeling experiments were as similar as possible to *in situ* conditions. While this quasi *in situ* state provides a close approximation of the infection environment, stable isotope labeling approaches could be applied directly within the host in future work, as ^{2}H in the form of heavy water can be administered to patients easily and safely. Lastly, the isotopic labeling methods introduced here, provide a tool that enables the study of microbial activity and spatiometabolic diversity in a much broader range of environmental and medical systems, with a non-disruptive isotope tracer that can be employed even in the most nutritionally-complex habitats, and can trace slow and fast growth over several orders of magnitude (for example, in the study of intracellular pathogens, or slow-growth infectious diseases such as tuberculosis). It is exciting to ponder the potential of this method in combination with other emerging tools for the *in situ* study of microbial activity, in advancing not only our understanding of the *"who's there?"* of environmental microbial systems, but also the next step of *"what are they doing?"* and *"how do they respond to environmental change?"*.

Part III

Appendices

Appendix A

R packages for isotopic data processing

A.1 Introduction

The key to reproducible data reduction and data processing in scientific research is the ability to faithfully record every step of the process in a reproducible format that is transparent and easy to communicate. This is not an easy task. Most of the time in experimental research that is not primarily computational in nature, it falls victim to the enormous effort required to design experiments well, generate the data and interpret the results, with little time left to invest in documenting and constructing a reproducible data reduction workflow. While this is understandable, it introduces a high risk for error, makes it extremely difficult to share and discuss one's approach or review others', reproduce the calculations at a later point or even just revisit what was done conceptually. Part of the problem lies inherently with most data processing being difficult to document or entirely divorced from the narrative of the scientific work it represents. This issue has been recognized for a long time in computer science where good and effective documentation

is absolutely crucial to collaborative work and usefulness of indivduals' contributions. One concept that was developed in response is the idea of literate programming, where a single document contains both source code and associated documentation, where both can be automatically extracted for their respective purposes, but are written and maintained together (Knuth, 1992). In recent years, a similar concept of literate data analysis has increasingly gained traction in some scientific communities (still primarily computational ones) with tools available for this purpose exanding steadily. Today, interactive scientific computing that is enabling the combination of narrative with data processing, and accomplishes a highly transparent and completely reproducible data reduction, is available through Wolfram Mathematica as one of the pioneers of this approach, but also in open-source software such as, for example, IPython(Pérez and Granger, 2007) in python and Sweave (Leisch, 2002) as well as knitr (Xie, 2013a;b) in R. At the same time, open-source projects like python and R are expanding rapidly from contributions of modules (called packages in R) developed by the scientific community itself that are publicly available and provide an enormous wealth of preexisting functionality, often custom-taylor to and hugely enabling for a specific discipline. Two prominent examples are the Bioconductor network in R (Gentleman et al., 2006) and QIIME in python (Caporaso et al., 2010). While any of these tools require some initial time investment to get started, they are becoming increasingly more accessible and easier to use, and are likely to become a core part of any future curriculum even in traditionally less-computational disciplines.

What I perceive to be largely missing in the geochemical community are basic modules that enable the kinds of calculations and data processing we need to do on a day to day basis. Here, I present two prototype R packages, one that could be useful to the larger geochemical community (the **isotopia** package for working with isotope values and notation), and one that could be useful to a more specialized subdiscipline (the **isoread** package for processing isodat files). As an example of literate programming, all the code in this chapter is *stored and executed* inside the document itself. This provides

both transparency and reproducibility and makes it easy to communicate to readers and reviewers what is being done in such a way that they can follow, reproduce, and adapt the calculations if they chose to do so.

Acknowledgements

This work is dedicated to Shuhei Ono and Alex Sessions who are largely to credit with my interest in isotope geochemistry, and Florian Clever, who first taught me how to program and is to credit for instilling in me the importance and beauty of elegance, readibility and good documentation in software design.

A.2 isotopia R package

In geochemical calculations, we use a number of different representations of isotopic information and processes (ratios, abundances, delta values, alpha values, epsilon values, fractionation factors, refereence frame shifts, mass balance calculations, mass-indepentent effects, etc., etc.) that are constantly being converted back and forth and used for different kinds of isotope arithmetic. Very frequently, the tangle of keeping track of this information and how all the calculations are done properly makes code very hard to read, difficult to communicate - or even understand oneself later on, and as anyone knows who's ever dropped a -1 or $\cdot 1000$ at the wrong place, prone to small mistakes that can make a huge difference.

The **isotopia** package uses the S4 object system of R to *define* elemental isotopic data classes so that it can automatically keep track of what is a ratio, what is a delta value (and is it in $‰$ notation or in ppm), etc., and perform isotope arithmetic accordingly [1]. This allows the user to focus on the actual calculations and communicate to the reader exactly

[1] the multiple dispatch system of S4 allows any generic function to be dispached to a method based on the class of the argument, i.e. a fractionation function can be implemented *differently* whether it is supposed to fractionate an isotope ratio or a delta value

what each value represents. Most importantly, the isotope value object structure allows **isotopia** to put safeguards in place against non-sense calculations and makes it easy to implement rigorous, automatically executed tests (Wickham, 2011) for every single formula and computation (currently there are over 350 tests implemented, see section A.2.6 for a few examples). This means that any time *any* of the **isotopia** source code is modified, it has to pass all the tests that ensure it is functioning exactly as expected. This kind of test-driven implementation provides high confidence in the calculations and protects from small code changes leading to incorrect results and interpretation.

The **isotopia** module thus provides several isotopic data types that can be initialized by calling the respective *ratio*, *abundance*, *delta*, *fractionation_factor* and *intensity* functions. Each data type has additional attributes (such as name of the minor and major isotopes, and what compound it represents, what the reference ratio is for delta values, and what notation is used), which are all described in great detail in the help functions of **isotopia** that are accessible directly from R. Each data type can be initialized as a single vector of isotopic data or an entire system of isotope values for the same element (e.g. all oxygen or all sulfur isotopes). As all isotope data objects are implemented as extensions of primitive data types in R, they can be structured and aggregated in all the ways familiar to people with prior R experience, but should be intuitive enough to be useful "out of the box" for users new to this language. Isotope data types can then be converted from one type to another using *to_ratio*, *to_abundance*, *to_delta*, *to_fractionation_factor* methods, can be used in operations (*mass_balance*, *fractionation*, etc.) or transferred from one notation to another using *switch_notation*. Here, I provide a few examples how **isotopia** works and how it can be used, with the complete documentation available in the reference manual in section A.2.8.

A.2.1 Installation

The isotopia R module can be installed directly from the source code, which is hosted on the open-source version control and code sharing platform GitHub, by using the R development tools module (Wickham and Chang, 2014). The version of isotopia that is installed here and used throughout this document is v0.4. I recommend installing this version for the purpose of running any of these code examples locally because isotopia is still under active development and future versions will likely include additional functionality with syntax that might not be backwards compatible. If interested in the newest version of isotopia, visit isotopia on GitHub.

```
install.packages('devtools', depen=T)
library(devtools)
install_github('isotopia', 'sebkopf', ref = "v0.4")
```

A.2.2 Data types

After **isotopia** is installed, it can be loaded at any time like any other R module using *library(isotopia)*. The basic data types are initialized simply by calling the respective *ratio*, *abundance*, *delta* and *fractionation_factor* functions with single or multiple values.

```
library(isotopia)
show(ratio(0.1))

## An isotope value object of type 'Ratio value': R
## [1] 0.1

show(abundance(c(0.1, 0.2)))

## An isotope value object of type 'Abundance value': F
## [1] 0.1 0.2

show(delta(100, notation = "permil"))
```

```
## An isotope value object of type 'Delta value': d [permil]
## [1] 100

show(fractionation_factor(seq(0.97, 1.03, by=0.01), notation = "alpha"))

## An isotope value object of type 'FractionationFactor value': alpha
## [1] 0.97 0.98 0.99 1.00 1.01 1.02 1.03

show(intensity(100, unit = "mV"))

## An isotope value object of type 'Intensity value':  [mV]
## [1] 100
```

A.2.2.1 Attributes

All data types have certain attributes that are stored with the data values. For example, an isotope ratio can specify what minor and major isotope it represents and what compound it belongs to.

```
show(ratio(`13C` = 0.011, major = "12C", compound = "CO2"))

## An isotope value object of type 'Ratio value': CO2 R 13C/12C
## [1] 0.011
```

And a fractionation factor, for example, can additionally describe what the two reservoirs are between which it fractionates (introducing the shortcut *ff* instead of the identical long version *fractionation_factor* in the following).

```
show(ff(`13C` = 0.995,  major = "12C", ctop = "CO2", cbot = "DIC"))

## An isotope value object of type 'FractionationFactor value': 13C alpha_CO2/DIC
## [1] 0.995
```

All attributes can also be changed on an already initialized object using the *set_attrib()* function. However, changing previously defined attributes will always trigger a warning to alert the user to the fact that they are overwriting an attribute.

```
r <- ratio(`18O` = 0.002, major = "16O", compound = "CO2")
r <- set_attrib(r, minor = "17O")

## Warning:  changing the isotope name ('Ratio value' object) from '18O'
to '17O'

show(r)

## An isotope value object of type 'Ratio value': CO2 R 17O/16O
## [1] 0.002
```

There are also a large number of safeguards in place that trigger errors if non-sensical isotope values are initialized (for example a negative isotope ratio or alpha fractionation factor).

A.2.2.2 Isotope systems

Entire isotope systems can be initialized in identical ways, by simply passing several separate values (or entire sequences of values) to the initialization functions (introducing the shortcut *ab* instead of the identical long version *abundance* in the following).

```
show(ab(`33S` = 0.0075, `34S` = 0.0421, `36S` = 0.0002, major = "32S"))

## An isotope system object of type 'Abundances' with F 33S, F 34S, F 36S
##      33S    34S   36S
## 1 0.0075 0.0421 2e-04
```

A.2.3 Notation

Closely related to the attributes system is the notation system implemented in **isotopia**. Notation is special because it is an attribute that, when changed, also changes the numerical value of an isotope object with it. All isotope value objects keep track internally what notation they are in, which allows them to be used correctly in any operations and conversions completely independent of what notation the user prefers to work in. Notation is first specified when an isotope value object is initialized and several different notations

are implemented for the different isotope value objects. If not specified during intialization, **isotopia** assumes tha an object is created with its default notation. A number of default settings can be specified and retrieved using *set_iso_opts()* and *get_iso_opts()*. Here an example of checking and setting the default notation for fractionation factors (which can be either α values, raw $\epsilon = \alpha - 1$ or ϵ values in ‰ notation), initializing a new object with default notation (i.e. without specifying *notation="x"* during initialization) and converting it back and forth.

```
show(get_iso_opts("default_ff_notation"))

## [1] "alpha"

show(ff(1.02)) # alpha notation

## An isotope value object of type 'FractionationFactor value': alpha
## [1] 1.02

set_iso_opts(default_ff_notation = "permil")
show(p <- ff(20))  # permil notation

## An isotope value object of type 'FractionationFactor value': eps [permil]
## [1] 20

show(switch_notation(p, "eps"))

## An isotope value object of type 'FractionationFactor value': eps
## [1] 0.02

show(switch_notation(p, "alpha"))

## An isotope value object of type 'FractionationFactor value': alpha
## [1] 1.02
```

It is important to note that of course all of these values are equivalent, they are just representions of the same fractionation factor in different notation. Accordingly, they behave *exactly* the same in all calculations implemented by **isotopia** regardless what notation they are in.

A.2.4 Conversions

One of the core features of **isotopia** is the implementation of all standard conversions between different types of isotope values. Conversions are done by simply calling *to_ratio*, *to_abundance*, *to_delta*, etc. on the object that needs to be converted to the specified type and **isotopia** automatically recognizes from the object's class what the proper calculation entails. These conversions work both on single objects as well as entire isotope systems (which is of course important for example when going from ratios in a multi-isotope system to the equivalent fractional abundances). As with all functionality in **isotopia**, non-sensical conversions or conversions with not enough information (e.g. from a delta value to a ratio without knowing the reference) are rigourosly checked for and trigger errors whenever attempted. All conversions also take into consideration the notation of the isotope value that is to be converted and adjust the calculations accordingly. Attributes that are shared between the ingoing and outcoming value types are transferred (for example the minor and major isotope names) and the notation of the new object is always switched to the default setting for its data type (which can be changed as desired, for example, *set_iso_opts(default_ab_notation = "percent", default_delta_notation = "raw", default_ff_notation = "permil")*).

```
i <- intensity(`32S` = 9502, `33S` = 75, `34S` = 421, `36S` = 2,
               major = "32S", unit = "#")
show(i)

## An isotope system object of type 'Intensities' with 32S [#], 33S [#], 34S [#],
##    32S 33S 34S 36S
## 1 9502  75 421   2

r <- to_ratio(i)
show(r)

## An isotope system object of type 'Ratios' with R 33S/32S, R 34S/32S, R 36S/32S
##        33S     34S       36S
## 1 0.007893 0.04431 0.0002105
```

```
ab <- to_abundance(r)
show(ab)

## An isotope system object of type 'Abundances' with F 33S, F 34S, F 36S
##      33S    34S   36S
## 1 0.0075 0.0421 2e-04
```

Because the system of intensities (here as ion counts #) had the major isotope attribute specified, the conversion *to_ratio* could automatically figure out what ratios to form. Without specifying which one is the major isotope, the intensities would have still initialized just fine but **isotopia** would have thrown an error when trying to convert to isotope ratios. There's much more functionality in the conversions, which are all listed in the reference manual available for **isotopia** (section A.2.8) or directly within R by calling *?isotopia* or *?to_ratio* or any other function defined in the module.

A.2.4.1 Delta values and reference standards

In the case of delta values, conversions often require the specification or use of a reference ratio. This can simply be done by specifying the reference ratio when converting *to_delta* and since **isotopia** stores the reference ratio with the delta value object, it can be used automatically in the reverse calculation.

```
r <- ratio(`13C` = 0.0115, major = "12C")
ref_r <- ratio(`13C` = 0.011237, major = "12C", compound = "VPDB")
d <- to_delta(r, ref_ratio = ref_r)
show(d)

## An isotope value object of type 'Delta value': d13C [permil] vs. VPDB
## [1] 23.4

show(to_ratio(d))

## An isotope value object of type 'Ratio value': R 13C/12C
## [1] 0.0115
```

Additionally, **isotopia** keeps a register of known reference materials with several default values already entered and the possibility for the user to add additional ones they want to use (with the *register_standard()* function). Standards can be retrieved as *ratio* objects by calling *get_standard()* and specifying which standard to retrieve for which isotope (see the manual in section A.2.8 for details). The list of all registered ratios can be retrieved as any other option with a call to *get_iso_opts* (here turned into a table with the k-table or *kable* command provided by the knitr module (Xie, 2013b)):

```
library(knitr)
kable(get_iso_opts("standards"), format = "latex")
```

minor	major	name	ratio
2H	1H	VSMOW	0.0002
13C	12C	VPDB	0.0112
15N	14N	Air	0.0037
18O	16O	VSMOW	0.0020
34S	32S	CDT	0.0045

Table A.1 – Default reference ratios available in isotopia.

Registered standards provide **isotopia** with the means to automatically select the correct reference ratio during conversions with delta objects that have sufficiently specific attributes (a message informs the user what was selected, if not enough information is provided to match exactly to one correct standard, this will fail with an error unless the user specifically provides a reference ratio for the conversion).

```
d <- delta(`2H` = 100, major = "1H", ref = "VSMOW")
show(d)

## An isotope value object of type 'Delta value': d2H [permil] vs. VSMOW
## [1] 100

r <- to_ratio(d)

## Successfully found a registered standard to convert delta value:  VSMOW
R 2H/1H: 0.0001558
```

```
show(r)

## An isotope value object of type 'Ratio value': R 2H/1H
## [1] 0.0001713
```

A.2.5 Operations

With the conversions and data types all in place, **isotopia** can easily expand its functionality by building on top of the data types. Currently, operations are limited to a number of key features, such as *mass_balance()* calculations for fractional abundances and delta values, as well as fractionating (*fractionate()*) isotope data objects with fractionation_factors and shifting the reference frame on delta values (*shift_reference()*). As always, attributes are carried through these operations in the most sensible way for what they actuallly represent.

A.2.5.1 Mass balance

Mass balance makes use of an additional attribute not mentioned before, the *weight* attribute. This allows one to weight values according to their reservoir sizes such that during mass balance calculations, isotopically different pools are mixed according to their relative proportions. Weight can be specified either during initialization or by using the *weight()* function later on. Imagine a reservoir of CO2 that receives a tiny spike of heavily labeled additional carbon. For convenience, we're introducing here the **isotopia** options to set the default minor and major isotope names - this is nice for working on a problem in a specific isotope system. Also, we're going to do the mass balance exact by converting to fractional abundances (although **isotopia** provides the approximate *mass_balance()* directly with delta value objects as well).

```
set_iso_opts(
     default_minor = "13C",
```

```
     default_major="12C",
    default_ab_notation = "percent")
res <- delta(-10, compound = "CO2", ref = "VPDB", weight = 100)
show(res)

## A weighted isotope value object of type 'Delta value': CO2 d13C [permil] vs. VP
##   value weight
## 1   -10    100

spike <- ab(seq(5, 25, by = 5), compound = "Cspike")
show(spike)

## An isotope value object of type 'Abundance value': Cspike F 13C [%]
## [1]  5 10 15 20 25

mb <- mass_balance(
    to_ab(res), # convert reservoir to abundance
    weight(spike, 0.1) #weight spike
)
show(mb)

## A weighted isotope value object of type 'Abundance value': CO2+Cspike F 13C [%]
##   value weight
## 1 1.104  100.1
## 2 1.109  100.1
## 3 1.114  100.1
## 4 1.119  100.1
## 5 1.124  100.1
```

Notice that the result of the mass balance again is a weighted isotope value object itself. It can be converted to other data types or you can keep adding additional components to it with mass balance calculations. In fact, since **isotopia** keeps track of the weight, you can keep tagging multiple mass balances together (the *mass_balance()* function takes as many parameters as desired). Additionally, since R implements basic arithmetic operators as functions, **isotopia** redefines adding (+) and subtracting (-) for *abundance* and *delta* objects to be interpreted as mass balance calculations. This means *mass_balance(x, y)* is the same as $x + y$ for these isotope value objects. This allows short-hand calculations like the following (although *mass_balance()* is recommended in more complex situations

for clarity of recording what is happening). Here, we are adding a heavy relatively small but heavy pool (40permil, weight=2) to a circumneutral reservoir (5permil, weight=10) and then *remove* an isotopically light fraction from the pool (-10permil, weight=4).

```
mb <-
        delta(5, weight = 10) +
        delta(40, weight = 2) -
        delta(-10, weight = 4)
show(mb)

## A weighted isotope value object of type 'Delta value': d13C [permil]
##   value weight
## 1 21.25      8
```

A.2.5.2 Fractionate

During fractionation, a fractionation factor modifies an isotope value object (for example an isotope ratio or a delta value).

```
a <- ff(0.95, ctop = "DIC", cbot = "CO2")
r <- ratio(0.0114, compound = "CO2")
r <- fractionate(a, r)
show(r)

## An isotope value object of type 'Ratio value': DIC R 13C/12C
## [1] 0.01141
```

Notice that **isotopia** automatically keeps track of what compound is represented. After fractionation, the ratio represents no longer CO_2 but *DIC* according to the fractionation factors attributes. If these attributes do not "cancel" correctly, this command fails with an error and the relevant error message. Same as with *mass_balance()*, **isotopia** implements arithmetic shorthand for this, isotope value objects can be simply fractionationed by multiplying with a fractionation factor. I.e., *fractionate(a, b)* is the same as *a*b* (this also means fractionation factors can be easily chained with *a1*a2*a3*b* but only if the "numerators" and "denominators" cancel properly).

```
ff(-25, notation = "permil", ctop = "Corg", cbot = "DIC") *
    ff(-5, notation = "permil", ctop = "DIC", cbot = "CO2") *
    delta(100, compound = "CO2")

## An isotope value object of type 'Delta value': Corg d13C [permil]
## [1] 67.14
```

A.2.5.3 Shift reference

The last operation to introduce for now is shifting a reference frame. This is only defined for *delta* values and requires the denominator and numerator to cancel (otherwise fails with an error). It is also implemente with the *delta * delta* arithmetic shorthand. This is a typical scenario useful for processing laboratory data which is measured against a standard of known isotopic composition relative to an international reference.

```
sample <- delta(-5, compound = "sample", ref = "my_std")
standard <- delta(-2.5, compound = "my_std", ref = "VPDB")
show(shift_reference(sample, standard))

## An isotope value object of type 'Delta value': sample d13C [permil] vs. VPDB
## [1] -7.487

show(sample * standard)

## An isotope value object of type 'Delta value': sample d13C [permil] vs. VPDB
## [1] -7.487
```

A.2.5.4 Arithmetic

Several of the arithmetic shorthands were introduced already, but there are several more (for all, see the manual). For all of these, it is always recommend to use the actual real functions in more complex scenarios for clarity. Here's just an example of what **isotopia** can automatically keep track of in terms of isotope data objects. Here are two ways of turning isotope ratios into a fractionation factor in permil notation - it works booth by explicit mention of each functional step, or by the arithmetic equivalent.

```
r1 <- ratio(0.011)
r2 <- ratio(0.0113)
p <- switch_notation(to_ff(r1, r2), "permil")
show(p)

## An isotope value object of type 'FractionationFactor value': 13C eps [permil]
## [1] -26.55

p <- (r1/r2 - 1) * 1000
show(p)

## An isotope value object of type 'FractionationFactor value': 13C eps [permil]
## [1] -26.55
```

A.2.6 Testing

Testing of all functionality in **isotopia** is implemented using the **testthat** module (Wickham, 2011), which provides a simple and uniform way of writing tests that can be run automatically to report any incorrect behaviour immediately. This enables multiple developers to contribute to the core functionality of the project without the risk of breaking prior implementations, but also allows users to easily write a few tests of their own to be confident that the module is doing what it is supposed to be doing, or just to test their own code and formulas on a regular basis. Here are few examples from the many tests already implemented for **isotopia** to give an idea of the range of functionality tests:

```
library(testthat)

set_iso_opts(default_ab_notation = "raw", default_delta_notation = "permil", defau

expect_error(ratio(-0.2), "cannot be negative")

expect_false(is.ratio(abundance(0.1)))

expect_equal(to_ff(delta(200), delta(-200)), ff(1.2 / 0.8))

expect_is({

   amix <-

        abundance(`13C` = 0.2, weight = 2, compound = "a") +
```

```
        abundance(`13C` = 0.5, compound = "b") +
        abundance(`13C` = 0.3, weight = 3, compound = "c")
}, "Abundance")
expect_equal(get_label(amix), "a+b+c F 13C")
expect_equal(get_value(amix), (0.2*2 + 0.5 + 0.3*3) / (2+1+3))
expect_equal(get_value(ff(0.8) * delta(200) + delta(100), "permil"),
                          1000*(0.8*1.2 - 1 + 0.1)/2)
```

And this is what happens as soon as a test fails (here have to catch the error, otherwise this document would not compile):

```
tryCatch(
expect_equal(fractionate(ff(0.995), delta(42)), delta(42)),
error = function(e) print(e))

## <simpleError: fractionate(ff(0.995), delta(42)) not equal to delta(42)
## Mean relative difference: 0.124>
```

A.2.7 Future extensions

The **isotopia** package currently implements a lot of the core functionality for isotope arithmetic. However, there is much that could built on top of it, including support for mass-scaling and mass-independent data objects and multiply subsituted isotopologues. The goal with all of these would be to provide an interface that can implement rigorous unit tests to ensure calculations are always performed the exact same way, tools to convert between reference frames and make it easier to compare and visualize data in different isotopic spaces, and, above all, to make it fun, intuitive and reproducible to work with isotopic data.

A.2.8 Manual

Package 'isotopia'

May 29, 2014

Type Package

Title Work with isotopic data in R

Version 0.4

Date 2014-05-28

Author Sebastian Kopf

Maintainer Sebastian Kopf <seb.kopf@gmail.com>

Description R interface for working with isotopic data (abundances, ratios,fractionation factors, delta values, etc.).

License GPL-3

LazyLoad yes

Roxygen list(wrap = FALSE)

VignetteBuilder knitr

URL https://github.com/sebkopf/isotopia

BugReports https://github.com/sebkopf/isotopia/issues

Suggests testthat,knitr

Collate 'utils.R' 'classes.R' 'validation.R' 'conversion.R' 'operations.R' 'arithmetic.R' 'attribs.R' 'show.R' 'initialization.R' 'options.R' 'isotopia.R' 'notation.R' 'zzz.R'

R topics documented:

`isotopia-package` *isotopia package*

Description

R interface for working with isotopic data (abundances, ratios, delta values, etc.).

Details

This package provides several isotopic data types that can be initialized by calling the respective `ratio`, `abundance`, `delta`, `fractionation_factor` and `intensity` functions. Each data type has additional attributes (such as name of the major isotope for all data types, reference ratio for `delta` values, notation for `delta` and `fractionation_factor`, unit for `intensity`) and these are described in detail in the help for each function. The attributes of any existing isotope data object can be modified easily by calling `set_attrib`

Each data type can be initialized as a single vector of isotopic data or an entire system of isotope values for the same element (e.g. all oxygen or all sulfur isotopes). To intialize an isotope system, simply pass multiple named data vectors with the same number of data points to the initialization functions (please see examples for details). Isotope systems are returned as a `data.frame` with all the different components of the system as separate columns. This object can be treated and manipulated just like a regular R data.frame. The column headers are named after the individual named data vectors (e.g. `ratio(34S = 0.1, 33S = 0.2)` will produce a data.frame with columns `34S` and `33S`) - careful if using names like '12C' that start with a number, they are not syntactically valid variable names in R and must be back quoted as `34S`. Isotope data objects in an isotope system that are not named generate columns named `iso, iso.1, iso.2, ...`.

Isotope data objects (both single vectors and isotope systems) can then be converted to different data types using the respective `to_ratio`, `to_abundance`, `to_delta` functions. Notations can also be changed using `switch_notation`

Global options for isotopia can be set using `set_iso_opts` and standard reference ratios can be registered using `register_standard`

Author(s)

Sebastian Kopf

See Also

`ratio`, `is.ratio`, `to_ratio`, etc.

Examples

```
# these examples are for initializing isotope ratio objects but apply equally to other data types
ratio(0.1) # single value
ratio(c(0.1, 0.2, 0.3)) # multiple values
ratio(13C = c(0.1, 0.2, 0.3)) # named ratio
ratio(33S = c(0.1, 0.2, 0.3), 34S = c(0.2, 0.4, 0.6), major = "32S") # isotope system
```

---

abundance *Fractional abundance*

Description

Generate an isotope abundance object. See isotopia for general information on initializing and converting isotope data objects.

Usage

```
abundance(..., major = get_iso_opts("default_major"), compound = "",
  notation = get_iso_opts("default_ab_notation"), weight = numeric(),
  single_as_df = FALSE)

ab(..., major = get_iso_opts("default_major"), compound = "",
  notation = get_iso_opts("default_ab_notation"), weight = numeric(),
  single_as_df = FALSE)
```

Arguments

`...`	- numeric vectors (can be named) to turn into isotope abundance objects
`major`	- name of the major isotope in the isotope system [optional], only of importance if converting from abundance to ratio or delta value, and want automatic name propagation
`compound`	- name of the compound the isotopic values belong to [optional]
`notation`	- what notation the abundance is in ('raw' values or 'percent'), see `switch_notation` for details

Details

The ab function is a shorthand for abundance but otherwise identical.

See Also

Other isotope data types: delta; ff, fractionation_factor; intensity; ratio

---

arithmetic *Isotope arithmetic*

Description

Several arithmetic operators (+, -, *, /) are implemented to work with specific isotope value object to allow shorthand data type conversions and calculations. Operations are generally only permitted if the two isotope objects being combined have matching attributes (isotope name, major isotope, etc.).

Usage

```
intensity +- intensity

abundance +- abundance

delta +- delta

alpha - 1

delta * 1000

ff * ratio

delta * delta

intensity / intensity

ratio / ratio

ff / ff

delta / delta
```

Details

`intensity+-intensity` allows the addition of intensity values, the result is a another intensity object

`abundance+-abundance` is a shorthand for calculating the isotopic mass balance of two abundance objects, see mass_balance for details

`delta+-delta` is a shorthand for calculating the isotopic mass balance of two delta objects, see mass_balance for details

`alpha - 1` is a shorthand for converting a fractionation factor from alpha to epsilon notation. The ff object has to be in alpha notation, otherwise this is just interpreted as a regular arithmetic operation and the result will no longer be an isotope object. `eps + 1` is the reverse operation.

`delta * 1000` is a shorthand for converting a raw delta value to permil notation or permil to ppm. The same works for fractionation factors in epsilon notation. `delta / 1000` is the reverse

`ff*ratio`, `ff*ff`, `ff*delta` are a shorthand for fractionating an isotope object with a factionation factor, see `fractionate` for details

`delta*delta`, is a shorthand for shifting the reference frame of the first delta value to that of the second (requires the compound measured in the second to be the reference of the first!), see `shift_reference` for details

`intensity/intensity` allows the creation of an isotope `ratio` object

`ratio/ratio` allows the creation of an isotope `fractionation_factor` This is a shorthand for the to_ff function.

`ff/ff` allows the creation of another isotope `fractionation_factor` object but requires that either the denominator names or numerator names of the two objects are identical (i.e. they "cancel"). This is a shorthand for the to_ff function.

`delta/delta` creates an `fractionation_factor` object that describes the fractionation factor between the two compounds, requires the reference name of the two delta values to be identical. This is a shorthand for the to_ff function.

`as.data.frame` *Convert isotope system to a data frame.*

Description

This function returns the underlying data frame of an isotope system. The individual columns that hold isotope values keep their status as isotope value objects.

Usage

```
## S3 method for class Isosys
as.data.frame(x, ...,
  stringsAsFactors = default.stringsAsFactors())
```

See Also

`as.data.frame`

`convert_isosys` *generic function to convert an isotope system that is part of a data frame and stitch it back together with the columns in the proper positions. uses a callback function that has to do the conversion of the isotope values*

Description

generic function to convert an isotope system that is part of a data frame and stitch it back together with the columns in the proper positions. uses a callback function that has to do the conversion of the isotope values

Usage

```
convert_isosys(iso, class_isosys, conv_fun)
```

Arguments

`iso`	- the isotope system object
`class_isosys`	- the class of the isotope system to convert to
`conv_fun`	- the function which converts the isotope value objects of the data frame, has to accept one parameter that is a data.frame of only the isotope value objects

---

`delta` *Delta value*

Description

Generate an isotope delta value object. See isotopia for general information on initializing and converting isotope data objects. Delta values can be easily converted from values in one notation to values in another notation by using `switch_notation`.

Usage

```
delta(..., major = get_iso_opts("default_major"), compound = "", ref = "",
  ref_ratio = numeric(), notation = get_iso_opts("default_delta_notation"),
  weight = numeric(), single_as_df = FALSE)
```

Arguments

`...`	- numeric vectors (can be named) to turn into delta values
`major`	- name of the major isotope in the isotope system [optional]
`compound`	- name of the compound the isotopic values belong to [optional]
`ref`	- name of the reference material
`ref_ratio`	- value of the reference material
`notation`	- which notation the value is in, `"permil"` (1000x multiplicaiton), `"raw"` (raw value, i.e. no multiplication) and `"ppm"` (10^6 multiplicaiton) are currently implemented for `delta` values. See `switch_notation` on details how to convert between notations.
`weight`	- weight the isotope value (with a mass, concentration, etc.) for easy mass balance calculations. The default value is 1, i.e. an unweighted isotope value. If specified, `weight` must be a single value or a numeric vector of the same size as the data values. The weight of an isotope value obejct can be retrieved and (re)set with the `weight` function.

Details

For mass balance calculations with delta values, simply add the appropriate weights (if different from the default) and use `delta(...) + delta(...)`.

See Also

Other isotope data types: `ab`, `abundance`; `ff`, `fractionation_factor`; `intensity`; `ratio`

Examples

```
delta(50, notation = "permil") # enter as permil value
delta(0.05, notation = "raw") # enter as non-permil value
```

`fractionate` *Fractionate an isotopic value*

Description

This function calculates the outcome of isotopic fractionation by a `fractionation_factor` and can be applied to `ratio` data, `delta` values or other `fractionation_factor` objects.

Usage

```
fractionate(frac, iso)
```

Arguments

`frac`	the fractionation factor `ff` used to fractionate the isotope value
`iso`	the isotope object to fractionate

Value

an object of the same type as `iso`

Note

Several of these calculations are also implemented with an `arithmetic` shorthand. All calculatinos are only permissible if the fractionation factors and isotope values have matching attributes.

See Also

Other operations: `mass_balance`; `shift_reference`

`fractionation_factor` *Fractionation factor*

Description

Generate a fractionation factor object. Can be initialized in `alpha` and `epsilon` notation. Fractionation factors can be easily converted from values in one notation to values in another notation by using `switch_notation`.

Usage

```
fractionation_factor(..., major = get_iso_opts("default_major"),
  notation = get_iso_opts("default_ff_notation"), ctop = "", cbot = "",
  single_as_df = FALSE)

ff(..., major = get_iso_opts("default_major"),
  notation = get_iso_opts("default_ff_notation"), ctop = "", cbot = "",
  single_as_df = FALSE)
```

Arguments

`...`	- numeric vectors (can be named) to turn into fractionation factors
`major`	- name of the major isotope in the isotope system [optional]
`notation`	- which notation the value is in, `"alpha"` (alpha value), `"eps"` (epsilon value), `"permil"` (epsilon * 1000) are currently implemented for `fractionation_factor` values. See `switch_notation` on details how to convert between notations.
`ctop`	- name of the compound representing the top isotope ratio [optional]
`cbot`	- name of the compound representing the bottom isotope ratio [optional]

Details

See isotopia for general information on initializing and converting to other isotope data objects. The `ff` function is a shorthand for `fractionation_factor` but otherwise identical.

See Also

Other isotope data types: `ab`, `abundance`; `delta`; `intensity`; `ratio`

`get_name` *Information about an isotopic data object*

Description

Get information about the name, label and units of an isotopic data object.

Usage

```
get_name(object)

get_units(object)

get_label(object)
```

Details

`get_name()` returns the name of an isotopic data object

`get_units()` provides the units of an isotope data object depending on the object type and notation

`get_label()` provides the full label of an isotope data object

See Also

Other data type attributes: `get_value`; `get_weighted_value`; `get_weight`; `set_attrib`; `switch_notation`; `weight`

Examples

```
## Not run:
get_label(ratio(...))
get_label(abundance(...))
get_label(isosys(ratio(...), ratio(...))

## End(Not run)
```

`get_value` *Retrieve isotope object's primitive values*

Description

This function returns an isotope object's (single value or isotope system) primitive data value(s).

Usage

```
get_value(iso, notation = iso@notation)
```

Arguments

`notation`	specifiy which notation to return the value in (default is the notation that the object is in)

Value

In the case of a single isotope object (Isoval), returns the numeric vector of raw values stored in the object (same as `as.numeric`). In the case of an isotope system (Isosys), returns the data frame underlying the object with all its isotope value objects also replaced with their numeric raw values. To just get the data frame but keep the isotope values intact, use `as.data.frame` instead.

See Also

`as.numeric`, `as.data.frame`, `as.data.frame` (base method)

Other data type attributes: `get_label`, `get_name`, `get_units`; `get_weighted_value`; `get_weight`; `set_attrib`; `switch_notation`; `weight`

`get_weight` *Retrieve isotope object's weights*

Description

This function returns an isotope object's weight values.

Usage

```
get_weight(iso)
```

Value

In the case of a single isotope object (Isoval), returns the numeric vector of weights stored in the object. In the case of an isotope system (Isosys), returns the data frame underlying the object with all its isotope value objects replaced with their weight values.

See Also

`as.data.frame`, `as.data.frame` (base method)

Other data type attributes: `get_label`, `get_name`, `get_units`; `get_value`; `get_weighted_value`; `set_attrib`; `switch_notation`; `weight`

get_weighted_value *Retrieve isotope object's weighted values*

Description

This function returns an isotope object's weighted values.

Usage

```
get_weighted_value(iso)
```

Value

In the case of a single isotope object (Isoval), returns a numeric vector of the object's values weighted by the object's weights. In the case of an isotope system (Isosys), returns the data frame underlying the object with all its isotope value objects replaced with their weighted values.

See Also

as.data.frame, as.data.frame (base method)

Other data type attributes: get_label, get_name, get_units; get_value; get_weight; set_attrib; switch_notation; weight

intensity *Ion intensity*

Description

Generate an ion intensity object (e.g. ion counts or signal intensity). See isotopia for general information on initializing and converting isotope data objects.

Usage

```
intensity(..., major = get_iso_opts("default_major"), compound = "",
  unit = "", single_as_df = FALSE)
```

Arguments

...	- numeric vectors (can be named) to turn into ion intensity objects
major	- name of the major isotope in the isotope system [optional],
compound	- name of the compound the isotopic values belong to [optional]
unit	- units of the measurement (e.g. #, V, mV)

See Also

Other isotope data types: ab, abundance; delta; ff, fractionation_factor; ratio

`is.iso` *Checks for isotope value objects*

Description

Checks for different kinds of isotope value objects. All checks recognize both the vector (single isotope value) and the data.frame (isotope system) version of an isotope value object. `is.isosys(obj)` can be used to make the distinction between the two.

Usage

```
is.iso(obj)

is.isoval(obj)

is.isosys(obj)

is.ratio(obj)

is.abundance(obj)

is.delta(obj)

is.intensity(obj)

is.ff(obj)

\code{is.weighted(iso)}
```

Arguments

`obj`	- object to test

Details

`is.iso` checks whether the object is an isotope value object of any kind. Returns TRUE if it is (e.g. ratio, abundance, delta, etc. - single or system of values), FALSE otherwise.

`is.isoval` checks whether the object is a single isotope value. Returns TRUE if it's a single isotope value object (of any kind, ratio, abundance, delta, etc.) and FALSE otherwise.

`is.isosys` checks whether the object is a an isotope system. Returns TRUE if it's an isotope system (of any kind, ratios, abundances, deltas, etc.) and FALSE otherwise.

`is.ratio` checks whether the object is an isotope ratio object. Returns TRUE if it's a single isotope ratio object or an isotope system of ratios, FALSE otherwise.

`is.abundance` checks whether the object is an isotope abundance object. Returns TRUE if it's a single isotope abundance object or an isotope system of abundances, FALSE otherwise.

`is.delta` checks whether the object is a delta value object. Returns TRUE if it's a single delta value object or an isotope system of delta values, FALSE otherwise.

`is.intensity` checks whether the object is an ion intensity object. Returns TRUE if it's a single ion intensity object or an isotope system of ion intensities, FALSE otherwise.

`is.ff` checks whether the object is an fractionation factor value object. Returns TRUE if it's a single fractionation factor value object or an isotope system of fractionation factor values, FALSE otherwise.

`is.weighted` checks if an isotope object is weighted. An object counts as weighted if any of the weights associated with the data values is != 1, that means only objects whose weights are ALL 1 is considered unweighted.

Examples

```
is.weighted(ratio(0.2)) # returns FALSE
is.weighted(ratio(0.2, weight = 1)) # returns FALSE
is.weighted(ratio(c(0.1, 0.2), weight = c(1,2))) # returns TRUE
```

`iso` *create an isotope value object (this function is not exported and should be access via the appropriate wrapper functions, e.g.* `ratio`*,* abundance*, etc.)*

Description

create an isotope value object (this function is not exported and should be access via the appropriate wrapper functions, e.g. `ratio`, abundance, etc.)

Usage

```
iso(class_isosys, ..., attribs = list(), single_as_df = FALSE)
```

Arguments

`class_isosys`	name of the class for an isotope system (which holds the info on which isoval class belongs to the system as well)
`attribs`	named list of attributes to pass to the isotope data object constructors
`...`	values (can be single data frame or list)
`single_as_df`	whether to return a single value as a data frame

Note

the setup for this function also means that you can modify e.g. an existing ratio with the paramters passed in (say to set the name later on)

`mass_balance` *Calculate isotope mass balance*

Description

This function calculates the isotope mass balance from combining multiple weighted isotope abundance or delta value objects. This calculation is also implemented with an arithmetic shorthand.

Usage

```
mass_balance(iso, iso2, ..., exact = get_iso_opts("exact_mass_balance"))
```

Arguments

`...`	- any number of weighted isotope value objects (have to be all either abundance or delta)
`exact`	- whether to calculate mass balance of delta values exactly (default FALSE), not fully implemented yet

Value

weighted abundance or delta value object that represents the combination of the parameters

See Also

Other operations: `fractionate`; `shift_reference`

`quietly` *Run a calculation quietly.*

Description

This small utility function is just a convenient wrapper for running isotope calculations silently without outputting any of the warnings or messages (it uses suppressMessages and suppressWarnings internally) that might occur. Use with care to suppress warnings, you might end up hiding important information.

Usage

```
quietly(expr)
```

ratio *Isotope ratio*

Description

Generate isotope ratio objects. See isotopia for general information on initializing and converting isotope data objects.

Usage

```
ratio(..., major = get_iso_opts("default_major"), compound = "",
  weight = numeric(), single_as_df = FALSE)
```

Arguments

...	- numeric vectors (can be named) to turn into isotope ratio objects
major	- name of the major isotope in the single ratio or isotope system [optional]
compound	- name of the compound the isotopic values belong to [optional]
weight	- weight the isotope value (with a mass, concentration, etc.) for easy mass balance calculations. The default value is 1, i.e. an unweighted isotope value. If specified, weight must be a single value or a numeric vector of the same size as the data values. The weight of an isotope value obejct can be retrieved and (re)set with the weight function.

See Also

Other isotope data types: ab, abundance; delta; ff, fractionation_factor; intensity

Examples

```
ratio(0.1) # single value
ratio(c(0.1, 0.2, 0.3)) # multiple values
ratio(13C = c(0.1, 0.2, 0.3)) # named ratio
ratio(33S = c(0.1, 0.2, 0.3), 34S = c(0.2, 0.4, 0.6), major = "32S") # isotope system
```

recast_isoval *generic function to recast an isotopic value object during conversions*

Description

generic function to recast an isotopic value object during conversions

Usage

```
recast_isoval(iso, to_class, mods = list(), validate = TRUE)
```

Arguments

`iso`	object
`to_class`	- which class to cast to
`mods`	- list of modifications to existing attributes (can be list(x = NULL) for removing attribute x)
`validate`	- whether to validate after the recast, default TRUE

`register_standard` *Isotope standards*

Description

Isotopia provides functionality to register and retrieve isotope standards. Registered standards can be used for automatic conversions of, for example, delta values which have attributes that match a standard.

Usage

```
register_standard(ratio)

get_standards(minor = NULL, major = NULL, name = NULL)

get_standard(minor = NULL, major = NULL, name = NULL)
```

Arguments

`ratio`	- a `ratio` object with 'minor', and 'major' isotope as well as 'compound' (the name of the standard) attributes all defined
`minor`	- character vector of minor isotope names to search for
`major`	- character vector of major isotope names to search for
`name`	- character vector of standards names to search for

Details

Use `register_standard()` to register an isotope standard. This can be useful for keeping track of standards you use internally and will also allow conversions from `delta` to e.g. `ratio` to automatically try to find the approriate standard for the conversion from the registered values.

Use `get_stanards` to retrieve any number of registered isotope standards that can be identified with the provided search terms. For an overview table of all standards (rather than the actual ratio objects), use `get_iso_opts("standards")` instead.

`get_standard` is the same as `get_standards` except that it returns a single object from the found standards and throws an error if the search criteria did not yield exactly one.

Value

list of ratio objects

See Also

Other options: `get_iso_opts`, `set_iso_opts`

set_attrib *Set attributes of isotope objects*

Description

Set an attribute of an existing isotope value object.

Usage

```
set_attrib(iso, minor = NULL, major = NULL, compound = NULL,
  compound2 = NULL, ref = NULL, ref_ratio = NULL, ctop = NULL,
  cbot = NULL, unit = NULL)
```

Arguments

iso	the isotope value object to update
minor	the name of the minor isotope
major	the name of the major isotope
compound	name of the compound the isotopic values belong to [optional]
ref	name of the reference material (delta values only)
ref_ratio	- value of the reference material (delta values only)
ctop	name of the compound representing the top isotope ratio in a fractionation_factor
cbot	name of the compound representing the bottom isotope ratio in a fractionation_factor
unit	unit for intensity value objects

See Also

Other data type attributes: get_label, get_name, get_units; get_value; get_weighted_value; get_weight; switch_notation; weight

set_iso_opts *Isotopia options*

Description

This allows specifying and retrieving default values for newly created isotopia objects.

Usage

```
set_iso_opts(default_ab_notation = c("raw", "percent"),
  default_ff_notation = c("alpha", "eps", "permil", "ppm"),
  default_delta_notation = c("raw", "permil", "ppm"),
  default_intensity_unit = "", default_major = "", default_minor = "",
  exact_mass_balance = FALSE, standards = c())

get_iso_opts(opts)
```

Arguments

`default_ab_notation`	default notation of abundance objects, see `switch_notation` for details
`default_ff_notation`	default notation of fractionation factors
`default_delta_notation`	default notation of delta values
`default_intensity_unit`	default unit for intensity values
`default_major`	default major isotope on all isotope objects
`default`	minor default minor isotope on all isotope objects
`standards`	isotope ratio objects to register as standards
`exact_mass_balance`	NOT IMPLEMENTED YET! If enabled, mass balance calculations with delta values (i.e. `mass_balance(delta, delta, delta...` or `delta() + delta()`) will always be performed exact by converting to natural abundances first and making the addition in abundance space (will be converted back to delta value afterwards). This is only possible if the `ref_ratio` in the delta values is set and will lead to an error if attempted without the reference ratios set. If disabled, mass balance calculations with delta values (`delta() + delta()`) will be performed in delta space (which is not exact but the discrepancy is negligible unless the minor isotopes in an isotope system make up a significant portion) see `register_standard` for details

Details

`get_iso_opts` allows retrieval of all or individual isotopia options. Returns a single value if only one option is requested, a named list if multiple

Note

Default options are the following and are set during package loading together with the default standards

```
set_iso_opts(
default_ab_notation = "raw",
default_ff_notation = "alpha",
default_delta_notation = "permil",
default_intensity_unit = "",
default_major = "",
default_minor = "",
exact_mass_balance = FALSE
)
```

See Also

Other options: `get_standard`, `get_standards`, `register_standard`

Examples

```
get_iso_opts("standards") # get a table of all standards
get_iso_opts(c("default_major", "default_minor")) # get a named list with the
default major and minor isotopes
```

---

shift_reference *Shift reference frame*

Description

This function shifts the reference frame of an isotopic data object that has a reference associated (currently only delta values.

Usage

```
shift_reference(iso, ref)
```

Arguments

iso	the isotope object whose reference frame to shift (delta)
ref	the isotope object which is relative to the new reference frame (delta)

Value

a delta value with the shifted reference

Note

The function requires the reference of the first delta value to the compound measured in the second delta value. This calculations is also implemented with an arithmetic shorthand. All calculatinos are only permissible if the fractionation factors and isotope values have matching attributes.

See Also

Other operations: fractionate; mass_balance

---

switch_notation *Switch notation*

Description

Convert from one notation to another for an isotope data object.

Usage

```
switch_notation(iso, to)
```

Arguments

iso	isotopic data object (ff, abundance, delta)
to	which notation to convert to

Details

Valid notations depend on the data type:

- abundance: 'raw', 'percent'
- delta: 'raw', 'permil', 'ppm'
- fractionation_factor: 'alpha', 'eps', 'permil', 'ppm'

Value

isotope object with converted notation, an error if it is not a valid conversion

See Also

Other data type attributes: get_label, get_name, get_units; get_value; get_weighted_value; get_weight; set_attrib; weight

---

to_abundance *Convert to isotope abundance*

Description

to_abundance converts another isotopic data type to an abundance. The to_ab function is a shorthand for to_abundance but otherwise identical.

Usage

```
to_abundance(iso)

to_ab(iso)
```

Arguments

iso	isotopic data object (ratio, abundance, delta, etc.)

Value

isotope abundance object if iso can be converted to a abundance, an error otherwise

See Also

Other data type conversions: to_d, to_delta; to_ff; to_r, to_ratio

to_delta *Convert to delta value*

Description

to_delta converts another isotopic data type to a delta value. The to_d function is a shorthand for to_delta but otherwise identical.

Usage

```
to_delta(iso, ref_ratio)

to_d(iso, ref_ratio)
```

Arguments

iso	isotopic data object (ratio, abundance, delta, etc.)
ref_ratio	the refernce ratio associated with the delta value. This is optional but required if planning later conversions back to ratios or abundane values. Can be supplied as a raw numeric numer or a Ratio object (in the case of the latter, the compound name of the Ratio object will be registered as the name of the reference).

Value

isotope delta object if iso can be converted to a delta, an error otherwise

See Also

Other data type conversions: to_ab, to_abundance; to_ff; to_r, to_ratio

to_ff *Fractionation factor*

Description

Calculate/convert to an isotope fractionation_factor

Usage

```
to_ff(iso1, iso2)
```

Arguments

iso1	the top compound in the fractionation factor
iso2	the bottom compound in the fractionation factor

Details

The `to_ff(...)` function calculates the fractionation factor between two isotope data objects (for example two `delta` values, two `ratio`, or two `ff`). All calculatinos are only permissible if the isotope values have matching attributes and fractionation factors will be returend in the default notation (see `set_iso_opts` for details)

Value

isotope `fraction_factor` object if parameters can be converted, an error otherwise

Note

Some of the conversions are also implemented in arithmetic shorthand, for example to generate an fractionation factor in alpha notation from two ratios `to_ff(ratio(), ratio())` is the same as `ratio() / ratio()`. See arithmetic for details.

See Also

Other data type conversions: `to_ab`, `to_abundance`; `to_d`, `to_delta`; `to_r`, `to_ratio`

`to_ratio` *Convert to isotope ratio*

Description

`to_ratio` converts another isotopic data type to a ratio. The `to_r` function is a shorthand for `to_ratio` but otherwise identical.

Usage

```
to_ratio(iso)

to_r(iso)
```

Arguments

`iso`	isotopic data object (`ratio`, `abundance`, `delta`, etc.)

Value

isotope `ratio` object if iso can be converted to a `ratio`, an error otherwise

See Also

Other data type conversions: `to_ab`, `to_abundance`; `to_d`, `to_delta`; `to_ff`

update_iso — *update_iso the attributes of an isotope value object internal function that is called by set_attrib wrapper*

Description

update_iso the attributes of an isotope value object internal function that is called by set_attrib wrapper

Usage

```
update_iso(obj, attribs)
```

weight — *Weight an isotope value object*

Description

`weight(iso, weight)` adds a weight (can be thought of as mass or concentration) to an isotopic value which will be used to weigh the isotope value when adding together multiple isotope values. `get_weight(iso)` returns the weight of an isotope value object.

Usage

```
weight(iso, weight)
```

Arguments

`iso`	- object to get weight or add weight
`weight`	- vector of weight values, has to be a single value or the same length as the data stored in the isotope value object.

Note

This can also be achieved when first initializing (or updating) an object via calls to `ratio`, `abundance`, `delta`, etc.

See Also

Other data type attributes: `get_label`, `get_name`, `get_units`; `get_value`; `get_weighted_value`; `get_weight`; `set_attrib`; `switch_notation`

Examples

```
r <- ratio(0.2)
r <- weight(r, 10)
print(get_weight(r)) # returns 10
```

Index

A.3 isoread R package

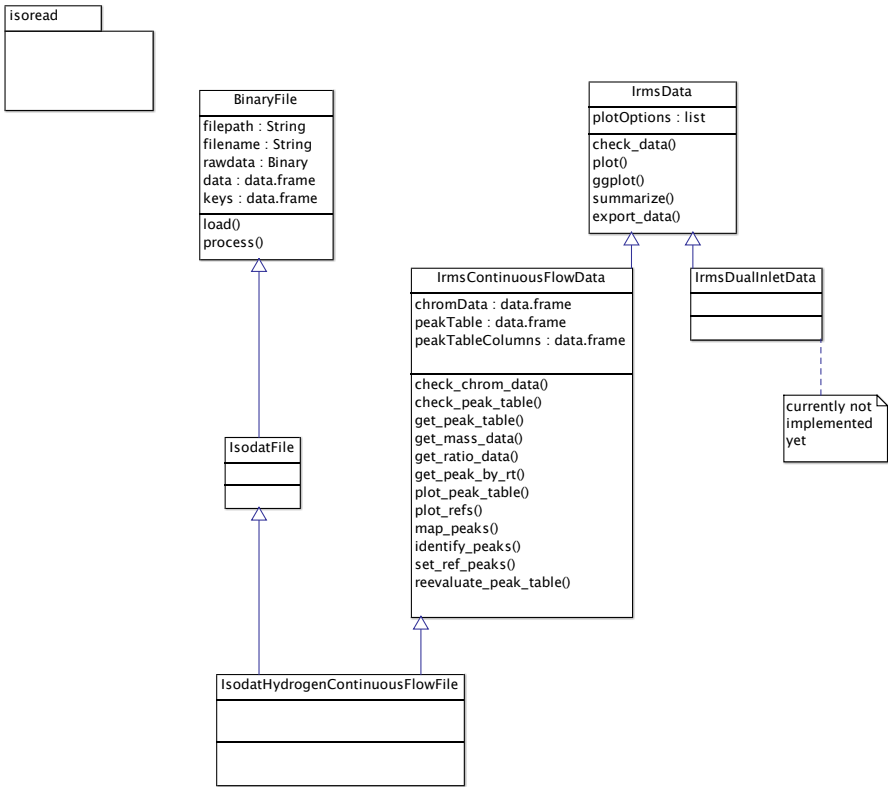

Figure A.1 – Class diagram of isoread. The diagram sketch of the class structure of **isoread** with most basic functionality for reading binary isodat files implemented in *BinaryFile*, and most functionality for interacting with the data implemented dynamically in *IrmsData* and *IrmsContinuousFlowData*. *IsodatHydrogenContinousFlowFile* only contains functionality and structural elements that are highly specific to this data file type.

The **isoread** R module is intended to provide an interface to IRMS file formats typically used in stable isotope geochemistry and is implemented using the R5 reference class object system of R, which allows in place (i.e. traditional object oriented) modification of the data objects. **isoread** is currently only fully implemented for reading compound specific hydrogen isotope data recorded by Isodat 2.0, but the class structure is designed to be easily expandable to other file and data types. An overview sketch is provided in figure A.1.

A.3.1 Installation

The **isoread** R module can also be installed directly from the source code on GitHub. The version of isoread that is installed here and used throughout this document is v0.2. I recommend installing this version for the purpose of running any of these code examples locally because isoread is also still under active development and future versions will likely include additional functionality with syntax that might not be backwards compatible. If interested in the newest version of **isorad**, visit isoread on GitHub.

```
library(devtools)
install_github('isoread', 'sebkopf', ref = "v0.2")
```

A.3.2 Reading an isodat file

Here, we read a simple isodat file that is provided as an example in the module. **isoread** takes all the information directly from the binary, which makes it easy to record each step of what you are doing with the data. **isoread** can also use functionality provided by **isotopia** to interact with this data so we are loading both modules.

```
library(isotopia)
set_iso_opts(default_minor = NULL, default_major = NULL, default_delta_notation =

library(isoread)
file <- isoread(system.file("extdata",
  "6520__F8-5_5uL_isodat2.cf", package="isoread"),
  type = "H_CSIA")

## Reading file /Library/Frameworks/R.framework/Versions/3.1/Resources/library/iso
```

A.3.2.1 Chromatographic data

The *file* variable now contains an isoread object with all the information from the binary file and we can take a look at the chromatographic data in the object, here we look at

the first 5 lines (using the *k-table* or *kable* command from the knitr package (Xie, 2013b) for latex output):

```
kable(file$get_mass_data()[1:5,], format = "latex")
```

time	mass2	mass3	time.s	time.min	mass2.offset	mass3.offset
0.209	194.6	60.02	0.209	0.0035	394.6	60.02
0.418	194.5	60.05	0.418	0.0070	394.5	60.05
0.627	194.5	60.21	0.627	0.0104	394.5	60.21
0.836	194.6	59.92	0.836	0.0139	394.6	59.92
1.045	194.6	59.72	1.045	0.0174	394.6	59.72

Table A.2 – Chromatographic data read by isoread

For convenience, **isoread** also implements several plotting functions based on standard plot as well as the ggplot module (Wickham and Chang, 2013) so we can have a look at the whole chromatograms in figure A.2:

```
library(ggplot2)

file$ggplot()
```

Notice that **isoread** plots all masses and ratios by default and labels the peaks with their peak numbers (reference peaks are marked with *). The plotting functions are of course a lot more flexible and we can use **isoread** functionality to plot just a specific time window of the mass trace chromatogram, and switch the time units to minutes instead of seconds as illustrated in figure A.3:

```
file$plot_masses(tlim = c(12.3, 12.6), tunits = "min")
```

A.3.2.2 File information

Since **isoread** has access to the original raw binary data file, it can extract other parameters stored with the data, here shown with the example of the H3factor registered as the most current during the analysis:

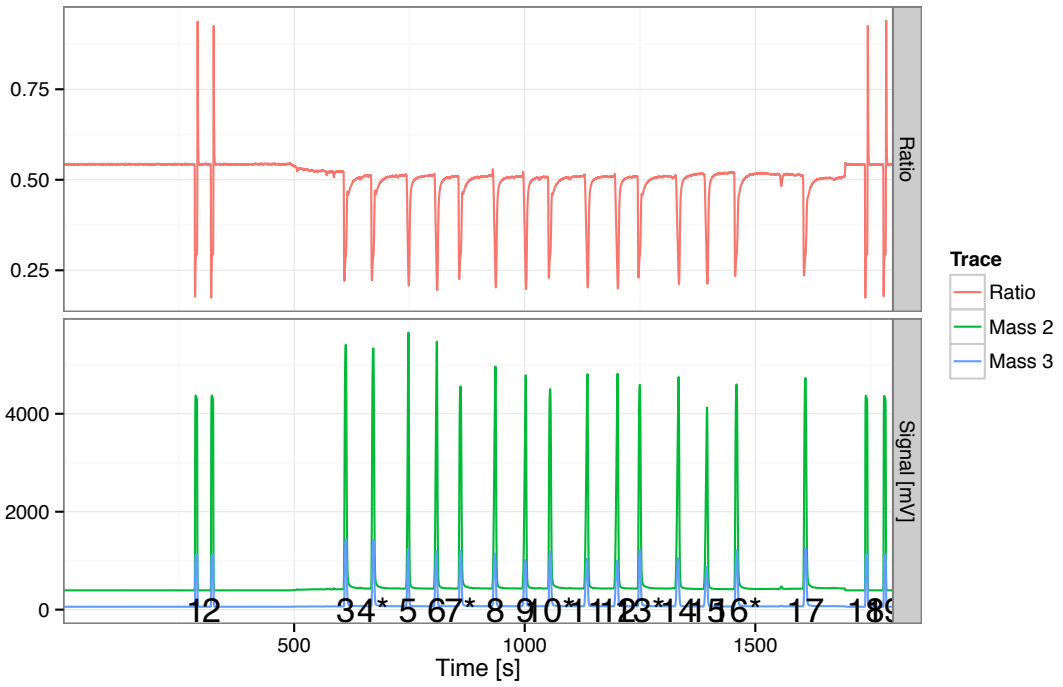

Figure A.2 – A chromatogram of an isodat file read by **isoread**

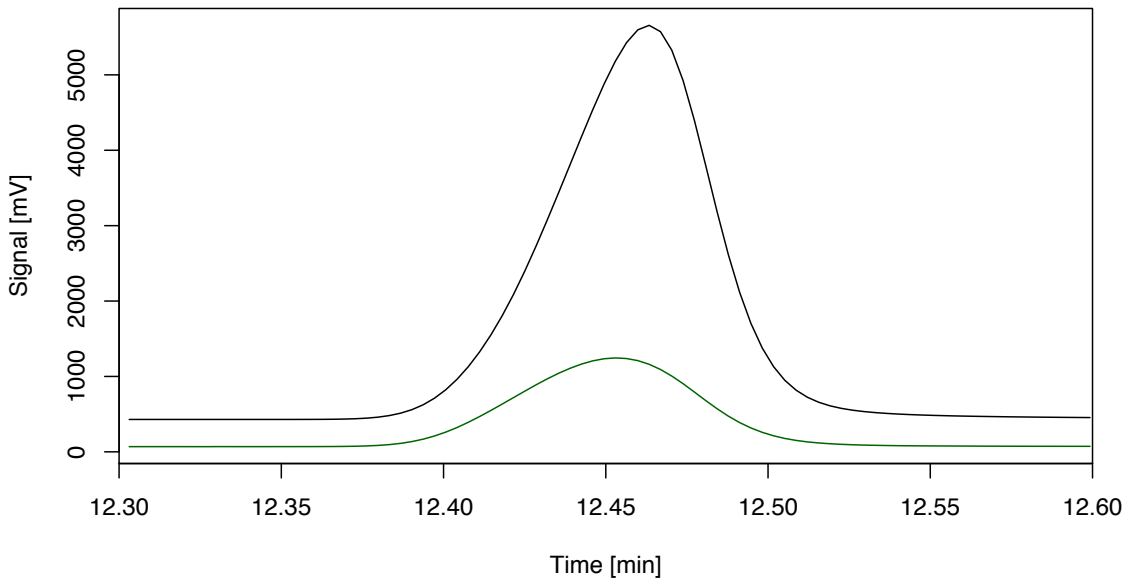

Figure A.3 – A zoomed mass chromatogram of an isodat file read by **isoread**

```
kable(file$get_info("H3factor"), format="latex")
```

	Property	Value
11	H3factor	2.79431047797221

A.3.2.3 Peak table

The table of peaks detected by isodat during the analysis or added by the user later on are also directly accessible. The complete set of 29 columns is available through **isoread**, here a small subset of key components:

```
kable(
  subset(file$get_peak_table(),
     select = c("Peak Nr.", "Status", "Ref. Peak", "Component",
                "Rt", "Start", "End", "Ampl. 2", "d 2H/1H")),
  format = "latex")
```

Peak Nr.	Status	Ref. Peak	Component	Rt	Start	End	Ampl. 2	d 2H/1H
1	Auto	FALSE	-	286.3	283.4	293.0	3978	-160.9
2	Auto	FALSE	-	321.2	318.3	327.9	3979	-160.4
3	Auto	FALSE	-	612.0	606.3	634.9	4993	-154.2
4	Auto	TRUE	-	671.5	666.1	699.3	4906	-151.9
5	Auto	FALSE	-	747.8	740.7	768.1	5227	-218.1
6	Auto	FALSE	-	809.5	801.5	829.3	5044	-210.4
7	Auto	TRUE	-	860.7	855.4	889.5	4129	-151.9
8	Auto	FALSE	-	936.5	927.8	961.6	4534	-155.5
9	Auto	FALSE	-	1002.2	993.4	1023.1	4354	-198.1
10	Auto	TRUE	-	1055.0	1049.0	1086.0	4070	-151.9
11	Auto	FALSE	-	1135.9	1126.7	1154.3	4377	-189.5
12	Auto	FALSE	-	1201.3	1191.9	1223.1	4384	-207.9
13	Auto	TRUE	-	1249.4	1244.2	1283.1	4160	-151.9
14	Auto	FALSE	-	1333.6	1324.4	1356.2	4316	-168.1
15	Auto	FALSE	-	1395.3	1386.3	1416.8	3706	-193.3
16	Auto	TRUE	-	1459.4	1453.6	1490.2	4183	-151.9
17	Auto	FALSE	-	1608.7	1600.9	1636.5	4303	-154.3
18	Auto	FALSE	-	1739.7	1736.4	1746.2	3974	-160.1
19	Auto	FALSE	-	1779.4	1776.7	1786.1	3972	-160.6

Table A.3 – Peak table from an isoread object.

Currently, none of the Components in this peak table are identified, but we can generate a mapping file that identifies which component comes out approximately at which retention time. A simple mapping table, which identifies peaks by retention time, could look like this (here only for 2 components):

```
map <- data.frame(
  Rt = c(940, 1135),
  Component = c("C16:0 FAME", "C18:0 FAME"),
  stringsAsFactors = F)
kable(map, format = "latex")
```

Rt	Component
940	C16:0 FAME
1135	C18:0 FAME

Table A.4 – Mapping table.

Typically, one would maintain this information for example in an excel file and load it directly from there. The map can then be applied to the peak table by **isoread,** which makes the identified peaks accessible by name:

```
file$map_peaks(map)
kable(file$get_peak_by_name(c("C16:0 FAME", "C18:0 FAME"),
    select = c("Peak Nr.", "Component", "Rt", "Ampl. 2", "d 2H/1H")),
  format = "latex")
```

	Peak Nr.	Component	Rt	Ampl. 2	d 2H/1H
8	8	C16:0 FAME	936.5	4534	-155.5
11	11	C18:0 FAME	1135.9	4377	-189.5

Table A.5 – Peak table of select peaks.

Lastly, the delta value reported in column *d 2H/1H* is automatically loaded as a *delta* value object using **isotopia** and can be used accordingly with all the functionality from isotopia. For a simple example, conversion to a fractional abundance (and switch to percent notation):

```
file$map_peaks(map)
d <- file$get_peak_by_name(c("C16:0 FAME", "C18:0 FAME"))[["d 2H/1H"]]
print(d) # delta value

## An isotope value object of type 'Delta value': d2H [permil] vs. VSMOW
## [1] -155.5 -189.5

print(switch_notation(to_abundance(d), "percent")) # abundance in percent

## An isotope value object of type 'Abundance value': F 2H [%]
## [1] 0.01315 0.01262
```

A.3.2.4 Extensions

Having this information available of course opens various possibilities for the implementation of useful features that are specific to the data. For example, an overview of how consistent the reference peaks in a run were is helpful for determining if one of them might be offset by an overlapping analyte or contaminant. This is implement in **isoread** by the *plot_refs()* functionality (output in figure A.4):

```
file$plot_refs()
```

Other extensions that are already provided include streamlined functionality to generate a two-page summary pdf for an **isoread** object which includes the chromatogram, references plot, analytes plot and complete peak table, as well as export of the data to comma-separated-value files. All functionality can be applied across several **isoread** objects at once so it is easy to load and process many analyses together (*isoread_folder()* makes it particularly easy for loading all isodat files in a folder). Planned future extensions include functionality for reintegrating detected peaks after reassigned reference peaks or values, automatic peak detection, adding, editing and deleting as well as well integrated derivatization corrections. For a more detailed overview of existing functionality, see the reference manual below.

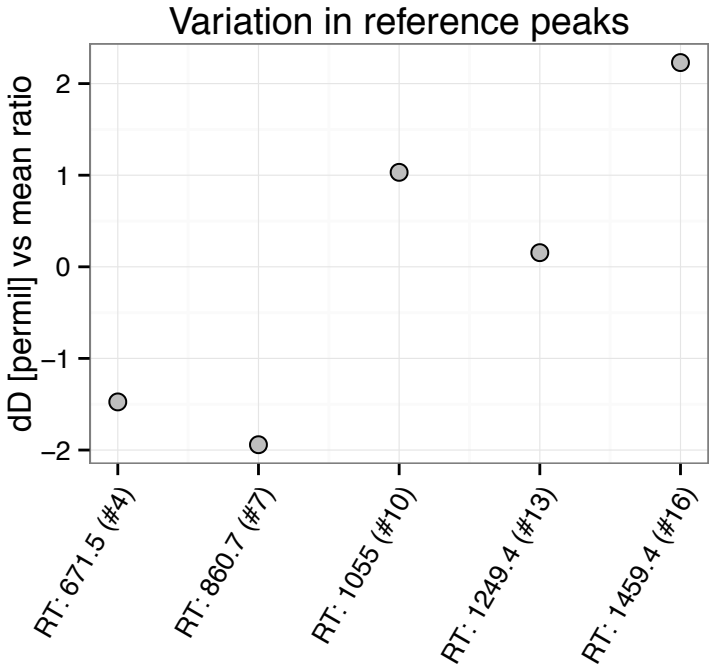

Figure A.4 – Relative deviation of all reference peaks in an isoread object.

Package 'isoread'

May 28, 2014

Type Package

Title Read IRMS data from isodat files.

Version 0.2

Date 2014-05-28

Author Sebastian Kopf

Maintainer Sebastian Kopf <seb.kopf@gmail.com>

Description R interface for accessing isotope ratio mass spectrometry data stored in isodat files.

License GPL-3

LazyLoad yes

Depends plyr,reshape2

Suggests testthat,isotopia,ggplot2,gridExtra

Roxygen list(wrap = FALSE)

VignetteBuilder knitr

URL https://github.com/sebkopf/isoread

BugReports https://github.com/sebkopf/isoread/issues

Collate 'BinaryFileClass.R' 'IrmsDataClass.R' 'IrmsContinuousFlowDataClass.R' 'IrmsDualInletDataClass.R' 'IsodatFileClass.R' 'IsodatHydrogenContinuousFlowFileClass.R' 'export.R' 'isoread.R' 'utilities.R' 'zzz.R'

R topics documented:

`isoread-package` *isoread package*

Description

R interface to IRMS (isotope ratio mass spectrometry) file formats typically used in stable isotope geochemistry.

Details

See `isoread` for details on how to use.

Author(s)

Sebastian Kopf

`BinaryFile` *Binary File reference class*

Description

Binary File reference class

Fields

`filepath` stores the path to the binart file

`filename` stores the filename

`creation_date` stores the date the file was created (if it could be retrieved, which is not always the case when running on linux but no problem on OS X and windows)

`rawdata` this is the binary raw data from the file (typically removed during cleanup unless clean_raw = FALSE)

`keys` these are the Unicode and ASCII text fragments found in the binary file, they are used for navigating in the file when pulling out the relevant data (typically removed during cleanup unless clean_keys = FALSE)

`data` a list that contains all the actual data pulled from the file

Methods

`clean_keys(removeText = NULL, removePattern = NULL, unlessByteLength = 0, unlessText = NULL)` clean up keys by removing randomly found strings that are clearly not proper targets

`cleanup(clean_raw = TRUE, clean_keys = TRUE, ...)` clean up the object by removing the raw data and keys (and other large but only transiently important information) from memory

`find_key(pattern, occurence = 1)` find a key by a regexp pattern

`find_keys(asciiL = 10, unicodeL = 5)` finds all unicode and ascii strings and stores them for navigation around the file

`get_info(show = c())` Get basic information about the object

`initialize(file, ...)` initialize BinaryFile object, requires a file path

`load(...)` load the data from the file and generate key lookup

`move_to_key(key, occurence = 1)` moves position to the end of a specific occurence of a key (use -1 for last occurence)

`parse(type, length = 1, id = NA, skip_first = 0)` parse binary data at current position in the data stream advances pointer by the size of the read data

#' @param type see `map_binary_data_type` #' @param length see `parse_binary_data` #' @param id if provided, will store the parsed data with this key in the `$data` field #' @param skip_first how many bytes to skip before reading this

`parse_array(types, n, id = NA, skip_first = 0)` repeatedly read the same set of information into a data frame

#' @param types a named vector of data types (for data types see `parse_binary_data`), #' the names are used for the columns of the resulting data frame #' @param id if provided, will store the parsed data with this key in the $data field #' @param n length of array #' @param skip_first how many bytes to skip before reading this

`process(...)` process the raw data to fill the data list

`read_file()` read the binary file

#' @note this does not work for very large files probably because of the 2^31-1 #' limit on vector size! think about ways to fix this... #' –> might have to acually read directly from the conection instead of the raw data buffer!

`skip(nbyte)` skip nbyte number of bytes in the raw data stream

`export_data` *Convenience function to export data from multiple IrmsData objects of the same class into a comma-separated value file.*

Description

Convenience function to export data from multiple IrmsData objects of the same class into a comma-separated value file.

Usage

```
export_data(data, file = "irms_data_export.csv", ...)
```

IrmsContinuousFlowData *IrmsContinuousFlowData reference class*

Description

IrmsContinuousFlowData reference class

Fields

`chromData` stores the chromatographic data (the actual mass and ratio data traces),

`peakTable` stores the peak table (detected peaks and all their information)

`peakTableColumns` stores the definition of which columns exist in the peak table and what their proper data types are

`peakTableKeys` stores information about which columns correspond to key elements of the peakTable (e.g. the peak number, retention time and compound name)

Methods

`check_chrom_data(masses = names(.self$plotOptions$masses), ratios = names(.self$plotOptions$rati` checks the consistency of the chromatographic data, by default checks for all masses and ratios

`check_data(...)` check the data consistency, calls `check_crom_data` and `check_peak_table`

`check_peak_table(..., warn = TRUE)` checks the consistency of the peak table and converts data types if necessary

`export_data(file, ...)` export the data stored in this object to file

`get_mass_data(masses = names(.self$plotOptions$masses), melt = FALSE)` get the mass trace data for specific masses, can be provided in `melt = TRUE` format for easy use in ggplot style plotting

`get_peak(peak_nr, select = names(peakTable))` retrieve information for a peak in the peak table (identified by peak_nr), can specify which columns to retrieve with `selec`, retrieves all columns by default

`get_peak_by_name(names, select = names(peakTable))` retrieve information for peak(s) in the peak table (identified by names)

`get_peak_by_rt(rts, select = names(peakTable))` retrieve information for peak(s) in the peak table (identified by retention times)

`get_peak_nr_by_name(names)` find peak numbers (i.e. ids) by name(s), returns a vector of found peak numbers (integer(0) if none found)

`get_peak_nr_by_rt(rts)` find peak numbers (i.e. ids) by retention time(s), returns a vector of found peak numbers (integer(0) if none found)

`get_peak_table(type = c("ref", "data", "both"))` retrieve the peak table

`get_ratio_data(ratios = names(.self$plotOptions$ratios), melt = FALSE)` get the ratio trace data for specific ratios, can be provided in `melt = TRUE` format for easy use in ggplot style plotting

`ggplot(tlim = NULL, tunits = .self$plotOptions$tunits$labels[[.self$plotOptions$tunits$value]],` ggplot the data

#' @param tlim time range (in tunits units)

#' @param tunits units (currently 's' or 'min')

#' @param masses vector of the masses to plot (if NULL, panel excluded)

#' @param ratios vector of the ratios to plot (if NULL, panel excluded)

`ggplot(...)` generate a ggplot object for the data in this IrmsData object

`identify_peaks(rts, compounds)` Identify peaks by mapping compound names to retention times

`init_irms_data()` initialize irms data container

`map_peaks(map)` Add information to peaks by mapping properties from a data frame that contains at least the defined peak number (e.g. 'Peak Nr.') or retention time (Rt) as a column. Additional columns (other than peak nr and retention time) are mapped to the relevant peaks if they correspond to existing columns, otherwise they are disregarded with a warning.

Note: make sure to have the data.frame that is passed in set with `stringsAsFactors = F` (usually the desired setting for the mapping)

`plot(tlim = NULL, mass_ylim = NULL, ratio_ylim = NULL, masses = names(.self$plotOptions$masses),` Plot the data (both masses and ratios) - much faster than ggplot but not as versatile

#' @param tlim time range, should be in the same tunits

#' @param masses which masses to plot (all defined in plot optinos by default)

#' @param ratios which ratios to plot (all defined in plot options by default)

#' @param tunits time units, as defined in tunits (currently either 's' or 'min'), takes the one set in plotOptions as default

`plot_data(y, ylab = "", title = "data peaks")` plot the data of the actual sample peaks, see `plot_peak_table` for details on syntax

`plot_masses(tlim = NULL, ylim = NULL, masses = names(.self$plotOptions$masses), tunits = .self$p` Plot the masses (this if much faster than ggplot but not as versatile)

`plot_peak_table(y = NULL, ylab = "", title = "", data = get_peak_table())` Plot the data points in the peak table

#' @param y = expression which data to plot (will be evaluated in context of the data frame)

#' @param ylab = y axis label

#' @param title = title of the plot

#' @param data = peak table data (by default the whole peak table)

`plot_ratios(tlim = NULL, ylim = NULL, ratios = names(.self$plotOptions$ratios), tunits = .self$p` Plot the ratios (this if much faster than ggplot but not as versatile)

`plot_refs(y, ylab = "", title = "references")` plot the data of the reference peaks, see `plot_peak_table` for details on syntax

`reevaluate_peak_table()` reevalutes the peak table (not currently implemented)

`set_plot_options(...)` set plot options

`set_ref_peaks(rts, set = TRUE, reevaluate = FALSE)` Identify peaks (by their retention times) as reference peaks (or remove their status as a reference peak)

`summarize(file, ....)` summarize the data stored in this object and save it to file

See Also

IrmsData, IrmsDualInletData

IrmsData *IrmsData reference class*

Description

IrmsData reference class

Fields

`plotOptions` holds information about default plotting options

Methods

`export_data(file, ...)` export the data stored in this object to file

`ggplot(...)` generate a ggplot object for the data in this IrmsData object

`init_irms_data()` initialize irms data container

`set_plot_options(...)` set plot options

`summarize(file, ....)` summarize the data stored in this object and save it to file

IrmsDualInletData *IrmsDualInletData reference class*

Description

IrmsDualInletData reference class

Methods

`export_data(file, ...)` export the data stored in this object to file

`ggplot(...)` generate a ggplot object for the data in this IrmsData object

`init_irms_data()` initialize irms data container

`set_plot_options(...)` set plot options

`summarize(file, ....)` summarize the data stored in this object and save it to file

Note

not implemented yet for any actual data reading

See Also

IrmsData, IrmsContinuousFlowData

`IsodatFile` *Isodat file class*

Description

Class representing an isodat binary file.

Methods

`cleanup(clean_raw = TRUE, clean_keys = TRUE, ...)` clean up the object by removing the raw data and keys (and other large but only transiently important information) from memory

`find_key(pattern, occurence = 1)` find a key by a regexp pattern

`get_info(show = c())` Get basic information about the object

See Also

BinaryFile

`IsodatHydrogenContinuousFlowFile`
H-CSIA DataClass

Description

Objects of this class hold the isotopic data from compound specific hydrogen isotope analysis recorded in Isodat file formats (currently supported isodat version is 2.0 for chromatographic and peak table data and isodat version 2.5 and 3.0 for chromatographic data only).

Details

This class is derived from IrmsContinuousFlowData which defines a number of useful plotting, export and data access methods. This class also derived BinaryFile which provides functionality for interacting with the underlying IsodatFile.

Methods

`cleanup(clean_raw = TRUE, clean_keys = TRUE, ...)` clean up the object by removing the raw data and keys (and other large but only transiently important information) from memory

`find_key(pattern, occurence = 1)` find a key by a regexp pattern

`get_info(show = c())` Get basic information about the object

`initialize(file, ...)` initialize BinaryFile object, requires a file path

`plot_data(y, ylab = "", title = "data peaks")` plot the data of the actual sample peaks, see `plot_peak_table` for details on syntax

`plot_refs(y, ylab = "", title = "references")` plot the data of the reference peaks, see `plot_peak_table` for details on syntax

`process(...)` process the raw data to fill the data list

`reevaluate_peak_table()` reevalutes the peak table (not currently implemented)

See Also

BinaryFile, IsodatFile, IrmsContinuousFlowData, IrmsData

`isoread` *Read isotope data files*

Description

Reads isodat file(s) and returns the contents as file type specific instances of `BinaryFile` / `IrmsDataClass` (extends both).

Usage

```
isoread(files, type, load_chroms = T, ...)
```

Arguments

`file`	path to the file(s) to read
`type`	type of the files to be read • 'H_CSIA' = compound specific IRMS data for hydrogen isotopes
`load_chroms`	whether to keep the chromatograms in the objects (otherwise only peak tables are kept)
`...`	parameters passed to the `load` and `process` functions of the IsodatFile objects

Value

List of file `type` specific objects.

- 'H_CSIA' = instance(s) of `IsodatHydrogenContinuousFlowFile` which implements `IrmsContinuousFlowData`.

If file names start with a number, then the number is used as key in the list, otherwise the whole filename is the key. If there is only one file, the object is returned directly.

`isoread_folder` *Reads all isodat files in a folder.*

Description

See `isoread` for paramter and return value details.

Usage

```
isoread_folder(folder, type, extension = ".cf", ...)
```

map_binary_data_type *Binary data type mapping*

Description

Maps binary C data types to proper R data types and byte lengths

Usage

```
map_binary_data_type(type = c("binary", "UTF8", "UTF16", "UTF32", "short",
  "long", "long long", "float", "double"))
```

Arguments

type	• 'binary' = raw with 1 byte (raw data) • 'UTF8' = character with 1 byte (ascii) • 'UTF16' = character with 2 bytes (unicode) • 'UTF32' = character with 4 bytes (unicode) • 'short' = integer with 2 bytes (16bit) • 'long' = integer with 4 bytes (32bit) • 'longlong' = integer with 8 bytes (64bit) • 'float' = numeric with 4 bytes (32bit) • 'double' = numeric with 8 bytes (64bit)

Note

implemented signed int and complex if needed

map_peaks *Map peak table*

Description

Map peak table data of IrmsContinuousFlowData object(s) based on a data frame or input excel file.

Usage

```
map_peaks(iso, map, startRow = 3, libfile = NULL,
  colClasses = c("numeric", "character", "character"), ...)
```

Arguments

iso	IrmsContinuousFlowData object(s)
map	either a data frame with a map (containing column Rt and Component) or the file path to a mapping file, extension determines how it will be processed currently only xlsx and xls are supported. Excel file must include column headers on the indicated row (default startRow = 3) with columns Rt and Component Component

`libfile`	name of the library file, also only xlsx and xls currently supported if provided, will attempt to merge the components in the mapping file with the library information for additional details on Formula and other compound properties

---

`parse_binary_data` *Wrapper for parsing binary data.*

Description

Convenience wrapper for parsing binary data. For more details on reading binary data, check ?readBin

Usage

```
parse_binary_data(data, type, length = 1)
```

Arguments

`type`	data type see `map_binary_data_type` for details
`length`	how many instances of this object (for characters and raw this means length of string, all others a vector)

Value

read data

`quickview` *File quickview*

Description

This functions serves to gain a quick view of a loaded isodat file. It shows the masses plot and prints a minimal subset of the peak table. Optionally reloads the file (tries to keep the peak definitions).

Usage

```
quickview(iso, reload = FALSE, show = c("Peak Nr.", "Status", "Ref. Peak",
  "Component", "Rt", "Start", "End", "Ampl. 2", "d 2H/1H"))
```

Arguments

`iso`	a single isodat file obj
`reload`	whether to reload the file (this is forced if there is no chromatographic data)
`show`	list of peak table columns to show

`reload` *Reload an isodat file object.*

Description

Reload an existing isodat object with all the chromatographic data and resets the peak table if keep_peaks = FALSE. Good for interrogation of an individual file. Requires the original file to still be in the same location.

Usage

```
reload(iso, remap_peaks = TRUE, load_chroms = TRUE)
```

Arguments

`iso`	the object to reload (can be a list)
`remap_peaks`	whether to keep the peak identification or not
`load_chroms`	whether to load the chroms (much smaller object without)

Value

the reloaded obj (or list of objs)

Note

currently only for type = "H_CSIA"

`summarize_all` *Summarize a collection of IrmsData objects*

Description

Summarize a collection of IrmsData objects

Usage

```
summarize_all(iso, ...)
```

Arguments

`iso`	IrmsData object(s)
`...`	all passed to summarize

Index

References

Caporaso, J. G., Kuczynski, J., Stombaugh, J., Bittinger, K., Bushman, F. D., Costello, E. K., Fierer, N., Peña, A. G., Goodrich, J. K., Gordon, J. I., Huttley, G. A., Kelley, S. T., Knights, D., Koenig, J. E., Ley, R. E., Lozupone, C. A., McDonald, D., Muegge, B. D., Pirrung, M., Reeder, J., Sevinsky, J. R., Turnbaugh, P. J., Walters, W. A., Widmann, J., Yatsunenko, T., Zaneveld, J., Knight, R., May 2010. QIIME allows analysis of high-throughput community sequencing data. Nature Methods 7 (5), 335–336.

Gentleman, R., Carey, V., Huber, W., Irizarry, R., Dudoit, S., Jan. 2006. Bioinformatics and Computational Biology Solutions Using R and Bioconductor. Springer.

Knuth, D. E., Jan. 1992. Literate Programming. Stanford Univ Center for the Study.

Leisch, F., Jan. 2002. Sweave: Dynamic Generation of Statistical Reports Using Literate Data Analysis. In: Compstat. Physica-Verlag HD, Heidelberg, pp. 575–580.

Pérez, F., Granger, B. E., May 2007. IPython: a system for interactive scientific computing. Computing in Science and Engineering 9 (3), 21–29.
URL http://ipython.org

Wickham, H., 2011. testthat: Get started with testing. The R Journal 3, 5–10.
URL http://journal.r-project.org/archive/2011-1/RJournal_2011-1_Wickham.pdf

Wickham, H., Chang, W., 2013. ggplot2: An implementation of the Grammar of Graphics. R package version 0.9.3.1.
URL http://CRAN.R-project.org/package=ggplot2

Wickham, H., Chang, W., 2014. devtools: Tools to make developing R code easier. R package version 1.5.
URL http://CRAN.R-project.org/package=devtools

Xie, Y., Jul. 2013a. Dynamic Documents with R and knitr. CRC Press.

Xie, Y., 2013b. knitr: A general-purpose package for dynamic report generation in R. R package version 1.5.
URL http://CRAN.R-project.org/package=knitr

Appendix B

Supplementary material for Chapter 3

B.1 Determination of carbon redox state

The redox state (RS) of carbon atoms in a molecule describes their average oxidation number, and is calculated assuming hydrogen in organic molecules to have an oxidation number of +1, oxygen -2 and nitrogen -3. The latter assumption is based on N in all compounds in this study to be in the form of NH_3 as acquired from NH_4^+ in the medium (for biomass) and released as NH_3 upon complete breakdown (e.g., photolytic degradation of NTA via glycine). The average redox state of each carbon atom in an uncharged organic molecule $C_aH_bN_cO_d$ is thus calculated as:

$$RS_C = (-1b + 2d + 3c)/a$$

For biomass of *R. capsulatus* ($CH_{1.83}N_{0.183}O_{0.5}$), for example, $RS_C = (-1 * 1.83 + 2 * 0.5 + 3 * 0.183)/1 = -0.28$. Table B.1 lists the RS_C values for all organic compounds relevant to this study.

The redox state corresponds conceptually to the notion of electron content in an organic molecule (e.g., Mckinlay and Harwood, 2010). How many electrons become available from the oxidation of an organic compound depends on the redox state of C, N, P and S, and whether they are completely oxidized to CO_2, HNO_3, H_2PO_4 and H_2SO_4 respectively. In compounds containing only C, N, H and O with N acquired/released as NH_3, complete oxidation proceeds as follows:

$$C_aH_bN_cO_d + x * H_2O \rightarrow a * CO2 + c * NH_3 + y * H^+ + y * e^-$$

Balancing this equation for biomass of *R. capsulatus* ($CH_{1.83}N_{0.183}O_{0.5}$) yields:

$$CH_{1.83}N_{0.183}O_{0.5} + 1.5 * H_2O \rightarrow CO_2 + 0.183 * NH_3 + 4.28 * H^+ + 4.28 * e^-$$

suggesting that the carbon in *R. capsulatus* biomass harbors a total 4.28 electrons as compared to its fully oxidized form (CO_2). A more general solution, on a per mol of C basis, yields $H_2O = (2a–d)/a$ and $e^- = (b + 2x–3c)/a = 4 + (b–2d–3c)/a$, a formula familiar from the redox state RS_c. The scaling factor of 4 describes how the redox state scale is anchored at 0 (with positive values denoting electron scarcity and negative values electron richness), as opposed to describing electron richness relative to the completely oxidized CO_2. The two relate as $RS_c = 4–e^-/a$.

Compound	Formula	Carbon redox state (RC_S)
Inorganic carbon	CO_2/HCO_3	+4
Nitrilotriacetate (NTA)	$C_6H_6NO_6$	+1
Glycine	$C_2H_5NO_2$	+1
Acetate	$C_2H_3O_2$	0
Formaldehyde	CH_2O	0
*R. capsulatus**	$CH_{1.83}N_{0.183}O_{0.5}$	-0.3

Table B.1 – Carbon redox states. Average redox state of molecular carbon in inorganic carbon, growth substrates and biomass.
*based on elemental composition of *R. capsulatus* as reported by Dorffler et al., 1998

B.2 References

Dorffler, M., Steindorf, A., Oelze, J., 1998. Determination of C/N ratios required for de-repression of nitrogenase in Rhodobacter capsulatus. Zeitschrift Fur Naturforschung C-A Journal Of Biosciences 53 (11-12), 961–967.

Mckinlay, J. B., Harwood, C. S., Jun. 2010. Inaugural Article: Carbon dioxide fixation as a central redox cofactor recycling mechanism in bacteria. Proceedings of the National Academy of Sciences 107 (26), 11669–11675.

Appendix C

Supplementary material for Chapter 4

C.1 Derivations

Derivation of Fe(II) and NO_2^- reaction equations:

$$\begin{aligned}
\frac{d[Fe(II)]}{dt} &= -2k_{app}[Fe(II)][NO_2^-] \\
[Fe(II)] &= [Fe(II)]_0 + \Delta[Fe(II)] \\
[NO_2^-] &= [Fe(II)]_0 + \frac{1}{2}\Delta[Fe(II)] \\
\frac{d([Fe(II)]_0 + \Delta[Fe(II)])}{dt} &= -2k_{app}([Fe(II)]_0 + \Delta[Fe(II)])([Fe(II)]_0 + \frac{1}{2}\Delta[Fe(II)]) \\
\frac{d\Delta[Fe(II)]}{dt} &= -2k_{app}([Fe(II)]_0 + \Delta[Fe(II)])([Fe(II)]_0 + \frac{1}{2}\Delta[Fe(II)])
\end{aligned} \tag{C.1}$$

$$\begin{aligned}
\frac{d[NO_2^-]}{dt} &= -k_{app}[Fe(II)][NO_2^-] \\
[Fe(II)] &= [NO_2^-]_0 + 2 \cdot \Delta[NO_2^-] \\
[NO_2^-] &= [NO_2^-]_0 + \Delta[NO_2^-] \\
\frac{d([NO_2^-]_0 + \Delta[NO_2^-])}{dt} &= -k_{app}([NO_2^-]_0 + 2\Delta[NO_2^-])([NO_2^-]_0 + \Delta[NO_2^-]) \\
\frac{d\Delta[NO_2^-]}{dt} &= -k_{app}([NO_2^-]_0 + 2\Delta[NO_2^-])([NO_2^-]_0 + \Delta[NO_2^-])
\end{aligned} \tag{C.2}$$

For 1:1 stoichiometry observed in the presence of NTA: The Fe-NTA-NO complex does not appear to be reactive towards NO_2^- such that Eq. C.1 describes Fe(II) oxidation even in the presence of NTA, with the caveat that measured concentrations of Fe(II) (which include the Fe(II)-NTA-NO- complex) require a correction for Fe-NTA-NO. Assuming all NO that is generated complexes with Fe(II)-NTA such that it no longer participates in a redox reaction with nitrite, but is still measured as Fe(II) by the ferrozine assay and assuming the reactions are coupled such that $[Fe(II)]_{ox} = [Fe(II) - NTA - NO]$, then $\Delta[Fe(II)] = -([Fe(II)]_{ox} + [Fe(II) - NTA - NO]) =$ -2 $\cdot [Fe(II)]_{ox} =$ -2 $\cdot$ $([Fe(II)]_0 - [Fe(II)]_{obs})$ and $\Delta[NO_2^-] =$ -$[NO_2^-]_{red} =$ -$([NO_2^-]_0 - [NO_2^-]_{obs})$. This leads eq. C.1 to integrate to:

$$Fe(II)_{obs}(t) = \frac{Fe(II)_0 \cdot e^{Fe(II)_0 \cdot k_{app} t}}{-1 + 2 \cdot e^{Fe(II)_0 \cdot k_{app} t}} \tag{C.3}$$

C.2 Supporting tables

C.3 Supporting figures

C.4 References

Abel, E., Schmid, H., Pollak, F., 1936. Kinetik der Oxydation von Ferro-Ion durch salpetrige Säure. Monatshefte für Chemie/Chemical Monthly.

Colman, B. P., Jun. 2009. Understanding and eliminating iron interference in colorimetric nitrate and nitrite analysis. Environmental Monitoring and Assessment 165 (1-4), 633–641.

Epstein, J., Kustin, K., Warshaw, L., 1980. A kinetics study of the oxidation of iron(II) by nitric-acid. Journal of the American Chemical Society 102 (11), 3751–3758.

Lin, N., Littlejohn, D., Chang, S. G., 1982. Thermodynamics and kinetics of the coordination of NO to Fe^{II}NTA in aqueous solutions. Industrial & Engineering Chemistry Process Design And Development 21 (4), 725–728.

Rakshit, S., Matocha, C. J., Coyne, M. S., 2008. Nitrite reduction by siderite. Soil Science Society Of America Journal 72 (4), 1070.

Sorensen, Hansen, H. C. B., Koch, C., Nancke-Krogh, H., Borggaard, O., 1996. Abiotic nitrate reduction to ammonium: key role of green rust. Environmental Science & Technology 30 (6), 2053–2056.

Stookey, L. L., 1970. Ferrozine - a new spectrophotometric reagent for iron. Analytical Chemistry 42 (7), 779–781.

Tai, Y.-L., Dempsey, B. A., Jan. 2009. Nitrite reduction with hydrous ferric oxide and Fe(II): Stoichiometry, rate, and mechanism. Water Research 43 (2), 546–552.

Van Cleemput, O., Baert, L., 1976. Theoretical considerations on nitrite self-decomposition reactions in soils. Soil Science Society Of America Journal 40 (2), 322–324.

Weber, K. A., Picardal, F. W., Roden, E. E., Apr. 2001. Microbially catalyzed nitrate-dependent oxidation of biogenic solid-phase Fe(II) compounds. Environmental Science & Technology 35 (8), 1644–1650.

Condition	Start	End	Change
2mM Fe(II) + 2mM NO_2^-	7.03	6.88	-0.15
+ 2mM NTA	7.00	7.12	0.12
+ 300mg/L PPHA	6.99	7.03	0.04
+ 100µM Citrate	6.95	7.02	0.07
+ 500µM Citrate	6.97	7.07	0.10
+ 2mM Citrate	6.96	7.06	0.10
+ 2mM Citrate + 300mg/L PPHA	6.94	7.13	0.19

Table C.1 – pH of reactant solutions at the beginning and end of kinetic Fe(II) oxidation experiments.

		2mM Fe(II)							5mM Fe(II)
	Ligand	none	PPHA (300mg/L)	Citrate (0.1mM)	Citrate (0.5mM)	Citrate (2mM)	Citrate + PPHA (2mM+300mg/L)	NTA (2mM)	Citrate (10mM)
$[Fe(II)_{species}] / [Fe(II)_{total}]$	Fe^{2+}	26.66%	23.80%	25.75%	22.26%	11.49%	9.64%	1.89%	0.91%
	$Fe\text{-}OH^+$	0.06%	0.05%	0.06%	0.05%	0.03%	0.02%	< 0.01%	< 0.01%
	$Fe\text{-}HCO_3^+$	4.37%	3.91%	4.22%	3.64%	1.86%	1.57%	0.31%	0.13%
	$Fe\text{-}CO_{3\ (aq)}$	65.68%	58.82%	63.39%	54.60%	27.86%	23.44%	4.57%	1.93%
	$Fe\text{-}CO_3\text{-}OH^-$	0.15%	0.14%	0.15%	0.13%	0.07%	0.06%	0.01%	< 0.01%
	$Fe\text{-}(CO_3)_2^{2-}$	0.09%	0.08%	0.08%	0.07%	0.04%	0.03%	0.01%	< 0.01%
	$Fe\text{-}Cl^+$	0.09%	0.08%	0.08%	0.07%	0.04%	0.03%	0.01%	< 0.01%
	$Fe\text{-}NH_3^{2+}$	0.02%	0.02%	0.02%	0.01%	0.01%	0.01%	< 0.01%	< 0.01%
	$Fe\text{-}HPO_{4\ (aq)}$	0.32%	0.30%	0.32%	0.28%	0.16%	0.14%	0.03%	0.01%
	$Fe\text{-}H_2PO_4^+$	0.08%	0.07%	0.08%	0.07%	0.04%	0.03%	0.01%	< 0.01%
	$Fe\text{-}SO_{4\ (aq)}$	2.48%	2.24%	2.39%	2.06%	1.06%	0.90%	0.17%	0.07%
	$^{\#}Fe\text{-}L^-$			3.46%	16.73%	57.26%	55.67%	93.00%	96.79%
	$^{\#}Fe\text{-}HL$			0.01%	0.03%	0.09%	0.09%	< 0.01%	0.15%
	Fe-HA (complexed)		8.26%				7.04%		
	Fe::HA (weakly bound)		2.23%				1.33%		

Table C.2 – Theoretical Fe(II) inorganic and organic speciation in bicarbonate-buffered freshwater medium at pH 7. Species with relative abundance < 0.01% for all experimental conditions are not shown. Species suggested to be relevant for Fe(II) oxidation by nitrite are highlighted in gray.
#: $Fe\text{-}L^-$ = $Fe\text{-}NTA^-$ or $Fe\text{-}Citrate^-$, Fe-HL = Fe-HNTA or Fe-HCitrate

	Experimental conditions			Kinetic parameters				Source
	pH	Temp	buffer	Order	Rate constant (k)		d[Fe(II)]/dt =	Reference
Oxidation by nitrite								
Fe(II) as siderite (10g/L ~ 80mM)	6	25C	MES/PIPES/HEPES	2nd	1.00E-04	$M^{-1} s^{-1}$	- 2 k [$FeCO_{3(s)}$] [NO_2^-]	Rakshit et al. (2008), Fig. 5
Fe(II) as siderite (10g/L ~ 80mM)	6.5	25C	MES/PIPES/HEPES	2nd	6.39E-05	$M^{-1} s^{-1}$	- 2 k [$FeCO_{3(s)}$] [NO_2^-]	Rakshit et al. (2008), Fig. 5
Fe(II) as siderite (10g/L ~ 80mM)	7.9	25C	MES/PIPES/HEPES	2nd	5.28E-05	$M^{-1} s^{-1}$	- 2 k [$FeCO_{3(s)}$] [NO_2^-]	Rakshit et al. (2008), Fig. 5
Fe(II) as goethite	6.8	30C	carbonate	1st	3.18E-06	s^{-1}	- k [Fe(II)]	Weber et al. (2001), Table 3
Fe(II) as biogenic magnetite	6.8	30C	carbonate	1st	3.38E-05	s^{-1}	- k [Fe(II)]	Weber et al. (2001), Table 3
Fe(II) as HFO	6.8	26-28	PIPES	3rd	3.83E+03	$M^{-2} s^{-1}$	- k [$Fe(II)_{diss}$] [$Fe(II)_{bound}$] [NO_2^-]	Tai et al. (2009)
+2mM NTA	7	25C	carbonate	2nd	6.67E-03	$M^{-1} s^{-1}$	- 2 k [Fe(II)] [NO_2^-]	This study, Table 1
+2mM CIT	7	25C	carbonate	2nd	4.67E-03	$M^{-1} s^{-1}$	- 2 k [Fe(II)] [NO_2^-]	This study, Table 1
+10mM CIT, *P. denitrificans* spent medium	7	25C	carbonate	2nd	9.42E-03	$M^{-1} s^{-1}$	- 2 k [Fe(II)] [NO_2^-]	This study, Table 2
+10mM CIT, *P. denitrificans* culture	7	25C	carbonate	2nd	1.06E-02	$M^{-1} s^{-1}$	- 2 k [Fe(II)] [NO_2^-]	This study, Table 2
Oxidation by nitrate								
Fe(II) as green rust	8.25	25C	auto-titration	2nd	4.93E-05	$M^{-1} s^{-1}$	- 8 k [$Fe(II)_{GR}$] [NO_3^-]	Hansen et al. (1996), Table 1

Table C.3 – Overview of rate constants reported for chemical oxidation of Fe(II) by NO_2^-.

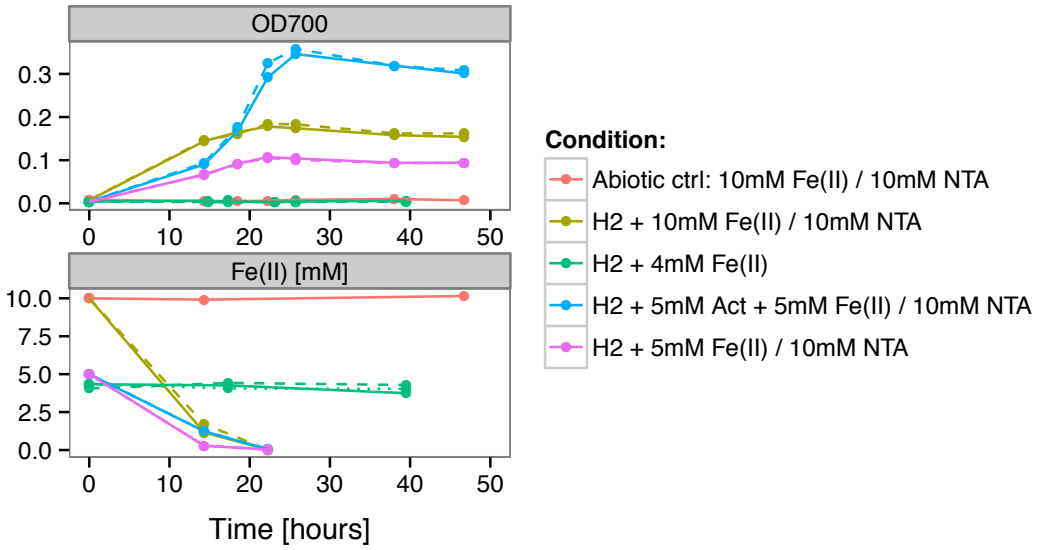

Figure C.1 – Anaerobic growth and concomitant Fe(II) oxidation of *Pseudogulbenkiania* sp. strain MAI-1 in freshwater medium amended with 10mM nitrate and different concentrations of Fe(II), NTA and acetate, and a headspace containing ~3% hydrogen. In the presence of NTA, up to 10mM Fe(II) is oxidized within 24 hours (in yellow), however, in the absence of NTA, neither growth nor Fe(II) oxidation is observed (in green). Replicate culture (duplicates or triplicates) indicated with solid, dashed and dotted lines, respectively.

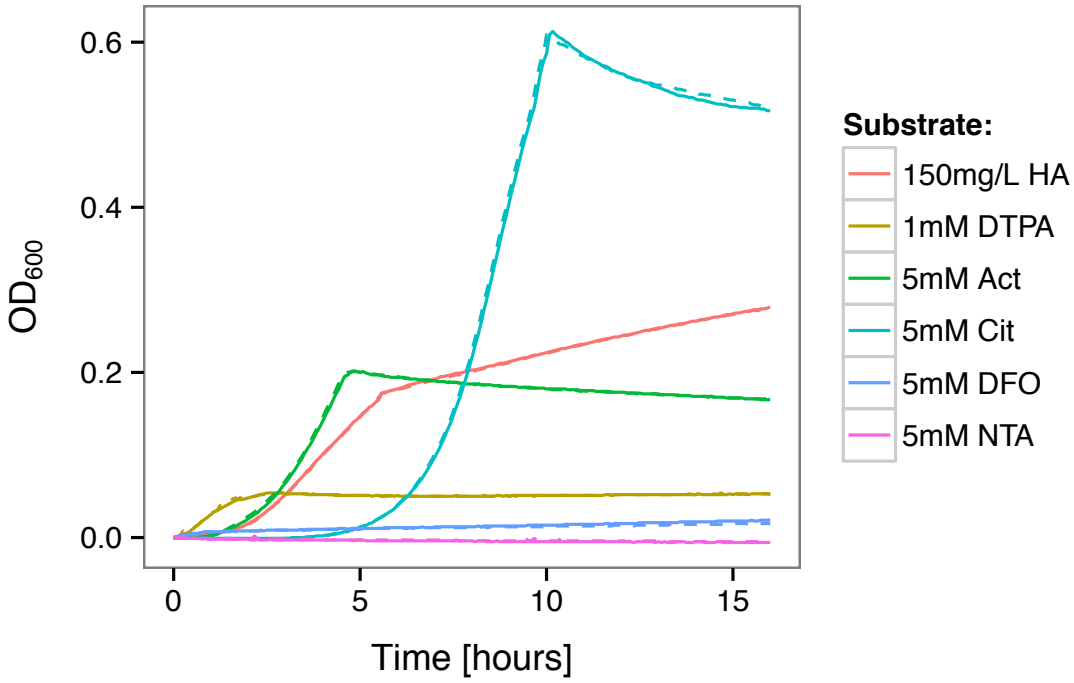

Figure C.2 – Growth of MAI-1 on various Fe(II) chelating ligands. The organism is grown aerobically in freshwater medium in a 96 well plate (OD600 is measured every 5 minutes) with different ligands as the sole carbon source. Citrate (Cit), humic acids (HA), acetate (Act) and diethylene triamine pentaacetic acid (DTPA) can all serve as growth substrates for MAI-1. The strain's ability to use siderophore desferioxamine (DFO) as a carbon source is ambiguous. No growth could be observed in the presence of nitrilotriacetate (NTA) as the sole carbon source. This makes NTA a suitable choice for anaerobic growth experiments, with MAI-1 as a chelator for Fe(II) that does not supply extra carbon. Replicate cultures indicated with dashed and solid lines, respectively.

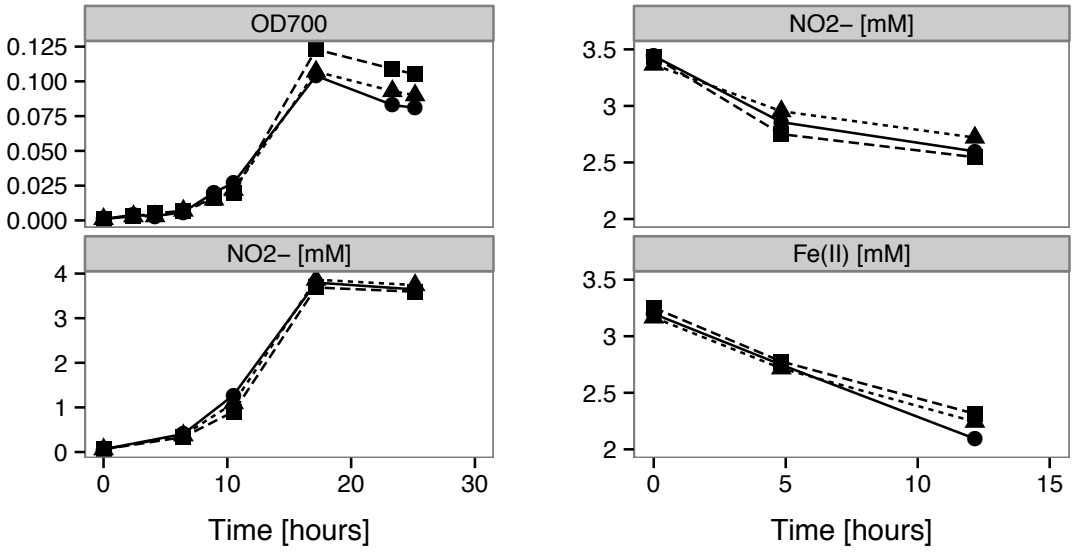

Figure C.3 – Oxidation of Fe(II)-NTA in spent MAI-1 growth medium. Triplicate cultures of Pseudogulbenkiania sp. strain MAI-1 (solid, dashed and dotted line) were grown in freshwater medium amended with 10mM nitrate and 1.25mM acetate, with ~3% H2 present in the headspace. During growth of MAI-1 (upper left panel), significant amounts of nitrite accumulated in the medium (lower left panel). Accumulated nitrite was stable at the end of growth, but upon addition of ~3mM Fe(II)-NTA to filer sterilized spent medium, Fe(II) oxidation and concomitant nitrite reduction could be observed (right panels).

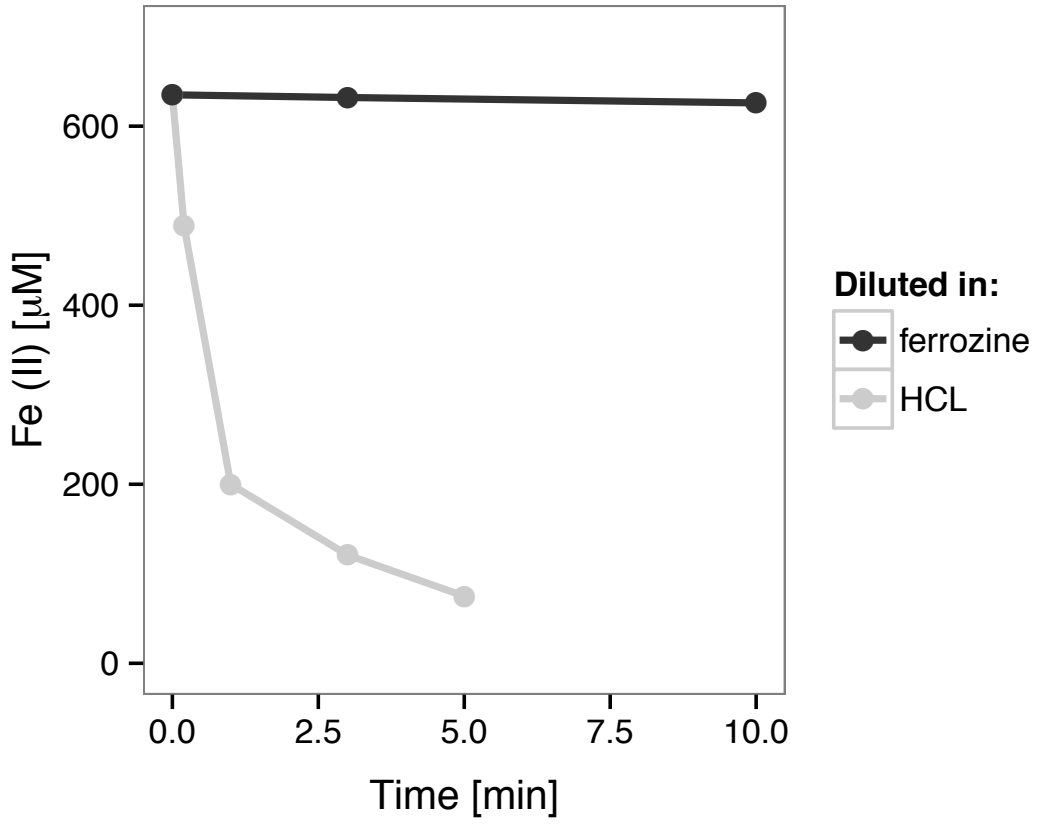

Figure C.4 – Oxidation test of Fe(II) in the presence of nitrite during sample dilution for the ferrozine (Stookey, 1970) assay. The ferrozine assay often includes an acid dilution step prior to spectrophotometric determination of Fe(II) with the ferrozine reagent. Acidification aids in the desorption of strongly coordinated Fe(II) from mineral surfaces and other strong sorption sites, and is an important preparative step for environmental samples. However, at acidic pH, nitrite is protonated (pKa=3.4) to nitrous acid, which can self- decompose to form reactive N-oxides (Van Cleemput and Baert, 1976) as well as oxidize Fe(II) directly (Abel et al., 1936; Epstein et al., 1980). To assess the effect of acidification in the presence of nitrite for our experimental setup, an anoxic freshwater solution containing ~650µM Fe(II) and ~1mM NO2- was diluted 1:10 with 1M HCl, and Fe(II) concentrations were measured after varying time intervals using the ferrozine assay (depicted in grey). Within 10 seconds of acidification, >20% of Fe(II) was oxidized and could no longer be detected by the ferrozine assay. After 1 minute, >60% of Fe(II) was lost. Without the acidification step (e.g. by direct dilution of the sample with the ferrozine reagent), Fe(II) concentrations did not significantly decrease within several minutes (black line). Since our experimental conditions included relatively high concentrations of nitrite, but little to no risk of sorptive loss of Fe(II), all ferrozine measurements were conducted without acidification.

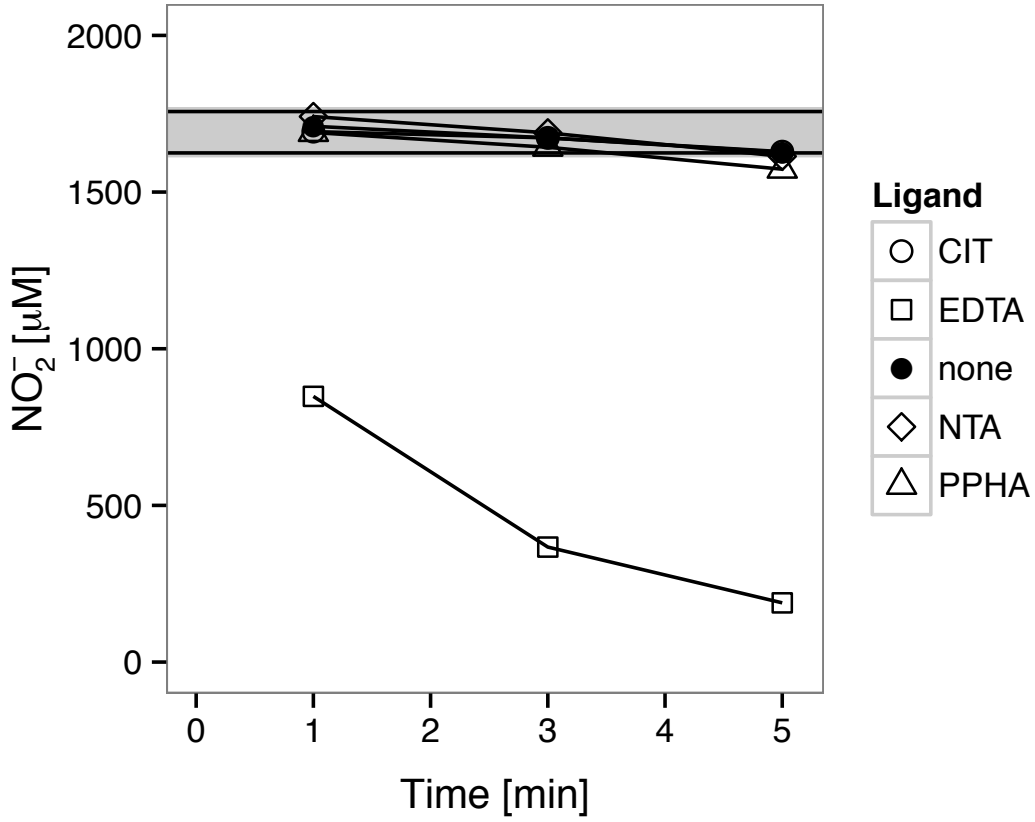

Figure C.5 – Reduction test of nitrite in the presence of Fe(II) during incubation with sulfanilamide in phosphoric acid for the nitrite assay used in this study. To assess the effect of free and chelated Fe(II) on the assay, an anoxic freshwater solution containing ~1.7mM nitrite was amended with 2mM Fe(II) and no ligand / 2mM citrate / 2mM EDTA / 2mM NTA / 300mg/L PPHA, and immediately diluted 1:10 with 1% sulfanilamide in 5% phosphoric acid for diazodization. Nitrite concentrations were determined colorimetrically after varying time intervals by addition of 0.1% N-1-napthylethylenediamine. The true concentration of nitrite measured in the absence of Fe(II) is indicated as a grey band with 95% confidence intervals. As previously observed (Colman, 2009), the presence of Fe(II)-EDTA leads to rapid disappearance of nitrite and significant underestimation of nitrite concentrations by this assay. The addition of Fe(II) without a ligand, as well as with the ligands used in this study, did not significantly affect the determination of nitrite by this assay (all measurements were conducted within 3 minutes of sulfanilamide addition, to prevent nitrite loss).

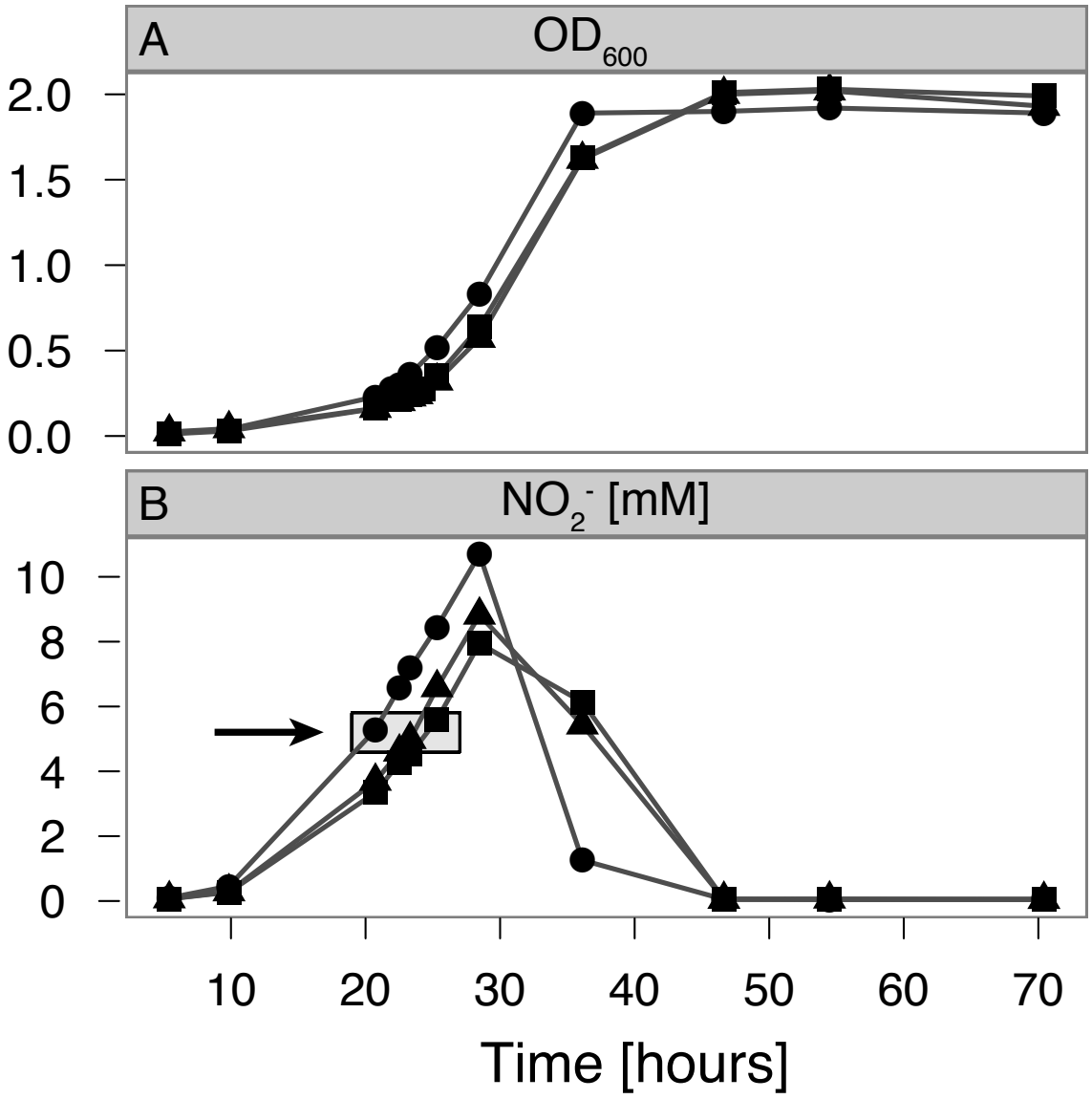

Figure C.6 – NO_2^- production by *P. denitrificans* (B) during anaerobic growth on succinate (A). Samples for Fe(II) oxidation assays were taken after accumulation of ~5mM NO_2^- for each biological replicate, respectively (grey shaded area indicated by arrow in panel B). Experiment conducted in biological triplicates. All data are shown.

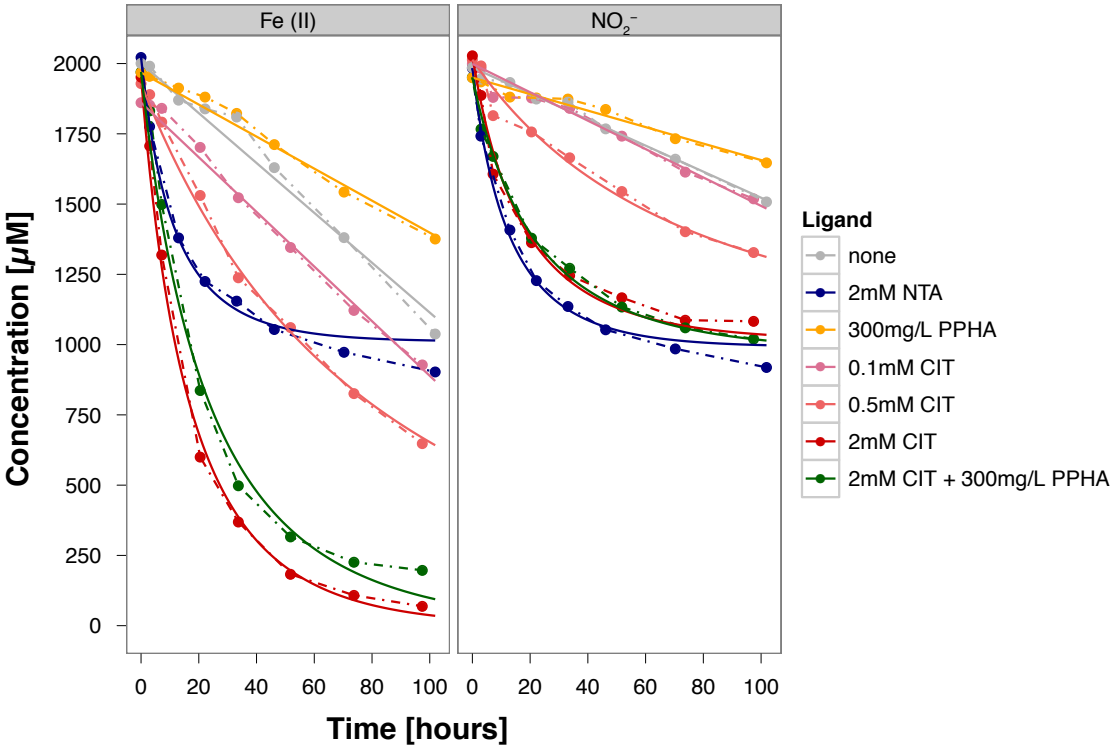

Figure C.7 – Model fits for abiotic Fe(II) oxidation by nitrite. Low citrate, no ligand, PPHA are best described by a zero-order (i.e. linear) reaction model (linear least squares fit illustrated for these conditions instead of 2nd order decay).

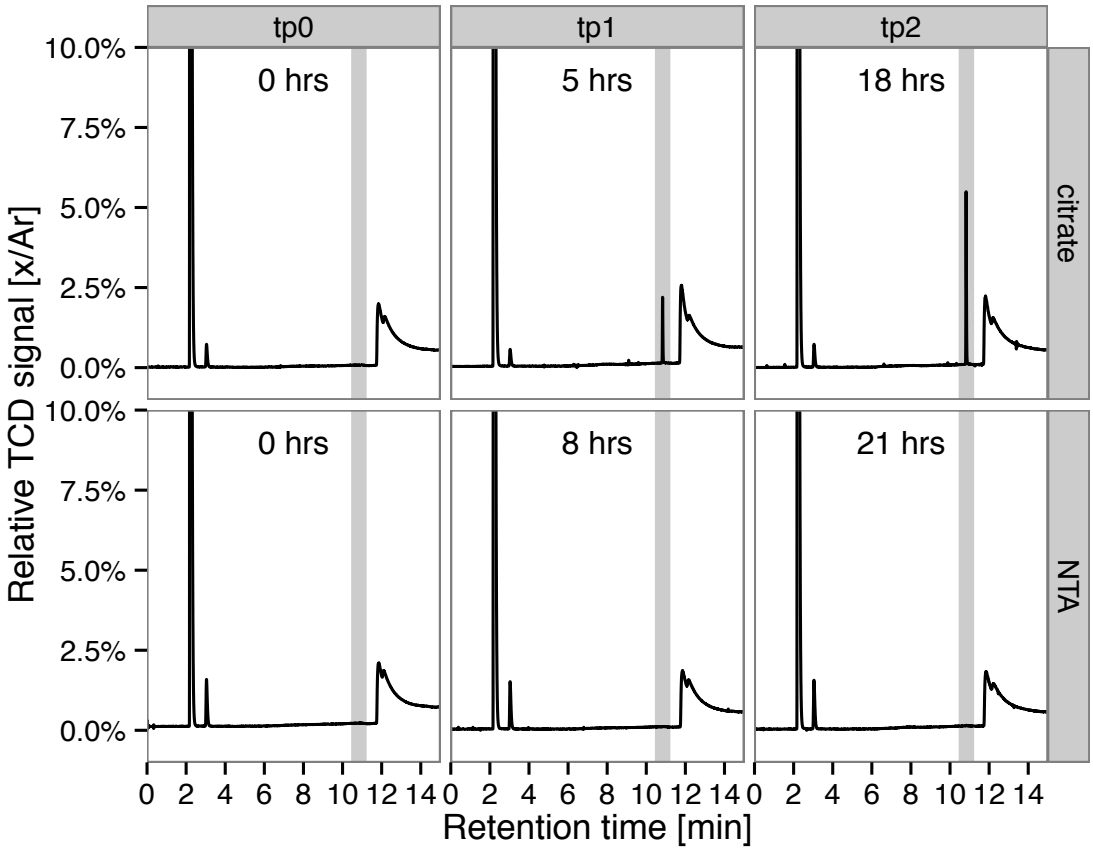

Figure C.8 – Evolution of N_2O in the headspace of sealed septum bottles during the reaction of 5mM nitrite with ~3mM Fe(II) complexed by citrate vs. NTA (peaks normalized to Ar). Retention times of the gases in the headspace were 2.2min (Ar), 3.0min (N2), 10.8min (N_2O) and 12-13min (CO_2, poorly resolved). The accumulation of N_2O (gray band) as a reaction product could only be observed in the presence of citrate, but not in the presence of NTA. Varying trace amounts of N_2 were present in the Ar/CO_2 headspace of the reaction vessels at the start of the experiment, but did not change significantly with reaction progress.

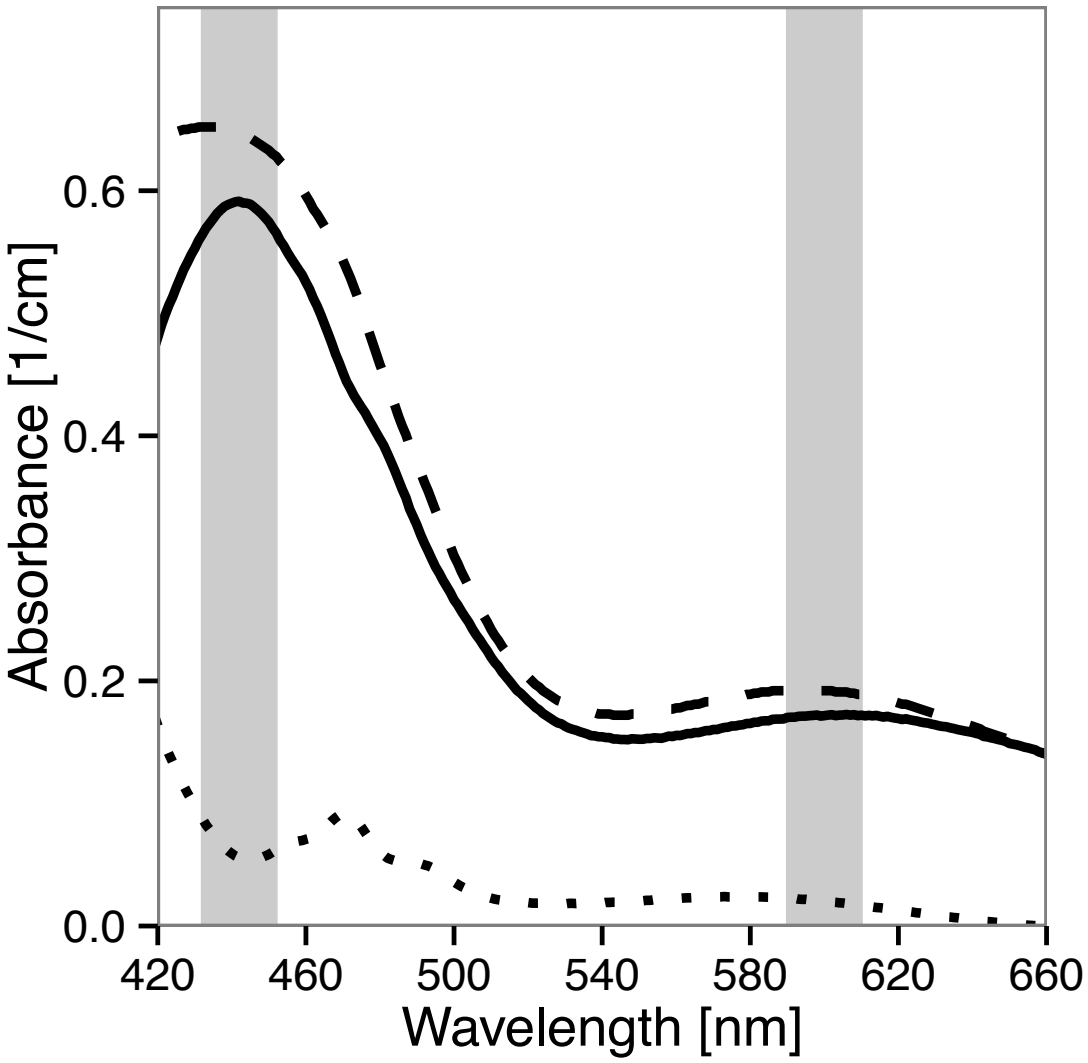

Figure C.9 – Absorption spectrum of a ∼3mM Fe(II)-NTA solution (dashed line) after 950µM NO_2^- was lost by abiotic oxidation of 1086µM Fe(II) (21 hrs data point in Figure C.3). Fe(II)-NTA by itself does not absorb in this wavelength range. The oxidized Fe forms a complex with NTA that absorbs light weakly with a characteristic peak at 470nm (dotted line). Residual light absorption (solid line) after accounting for the effect of Fe(III)-NTA in solution is indicative of Fe(II)-NTA-NO- complex formation. Characteristic absorption peaks of the Fe(II)-NTA-NO- complex (440nm and 600nm) (Lin et al., 1982) are indicated in gray.

Appendix D

Supplementary material for Chapter 7

D.1 Chromatographic effects of ^{2}H substitution

The number of average deuterium substitutions in a lipid molecule, such as a fatty acid methyl ester, depends on the strength of the label. It is important to note that what we tend to think of as a change in overall isotopic composition during isotope enrichment, is actually the mixing of two isotopically distinct pools. These pools (the old and new pool) more or less maintain their distinct isotopic signatures, but the change in their relative proportions leads to overall isotopic enrichment. However, in the context of measuring this overall enrichment in compound-specific analyses of lipid components, it is crucial to consider the effect that deuterium substitution has on the chromatographic behavior of molecules.

The change in chromatographic retention as a function of deuteration has been explored as early as McCloskey et al. (1967), and is well-established (although a mechanistic understanding of the effect is still an area of active research). Our own findings in

$\alpha_{B/S} \cdot F_L$	15:0 FAME	16:0 FAME	18:0 FAME
0.016%	0.0	0.0	0.0
1%	0.3	0.3	0.4
5%	1.5	1.6	1.8
10%	2.9	3.1	3.5
50%	14.5	15.5	17.5
100%	29.0	31.0	35.0

Table D.1 – Number of average deuterium substitutions in fatty acid methyl esters.

this context (measuring the retention times of perdeuterated compounds as part of our experiments on the recycling of exogenous fatty acids by *S. aureus*) corroborate the prior observations. Figure D.1 shows the relative increase in elution rate (the deuterated compounds always elute faster). Despite the normalization to deuteration sites, there is some spread in the change in relation time that is likely a combination of column- and compound-specific effects (for example, difference in saturation).

Compound	Mean d / nD	data points	Min d / nD	Max d / nD	Mean dRT / nD
C14:0 FAME	-0.29%	2	-0.32%	-0.27%	-3.435
C15:0 FAME	-0.33%	1	-0.33%	-0.33%	-3.849
C16:0 FAME	-0.4%	3	-0.42%	-0.39%	-4.724
C16:1 FAME	-0.35%	2	-0.37%	-0.33%	-4.118
C18:0 FAME	-0.47%	3	-0.61%	-0.35%	-5.480
C18:1 FAME	-0.4%	2	-0.41%	-0.39%	-4.700
C18:2 FAME	-0.37%	2	-0.42%	-0.33%	-4.372

Table D.2 – Overview of retention time shifts due to deuterium substitution.

The average change in retention time for C18:0 FAME was scaled by the observed elution times of C16:0 FAME and C18:0 FAME in an actual compound-specific isotope ratio analysis of a fatty acid methyl standard mix (reported in Table D.2). The chromatographic program employed in this experiment was designed to increase peak resolution with a slow temperature gradient. The resulting change in retention time was applied to the exact observed C18:0 FAME peak of the same run to model the impact of multiple deuterium substitutions (as expected from exposure to high levels of D_2O labeling) on peak shape and retention times. Figure D.2 shows the simulation. For simplicity, all hydrogen

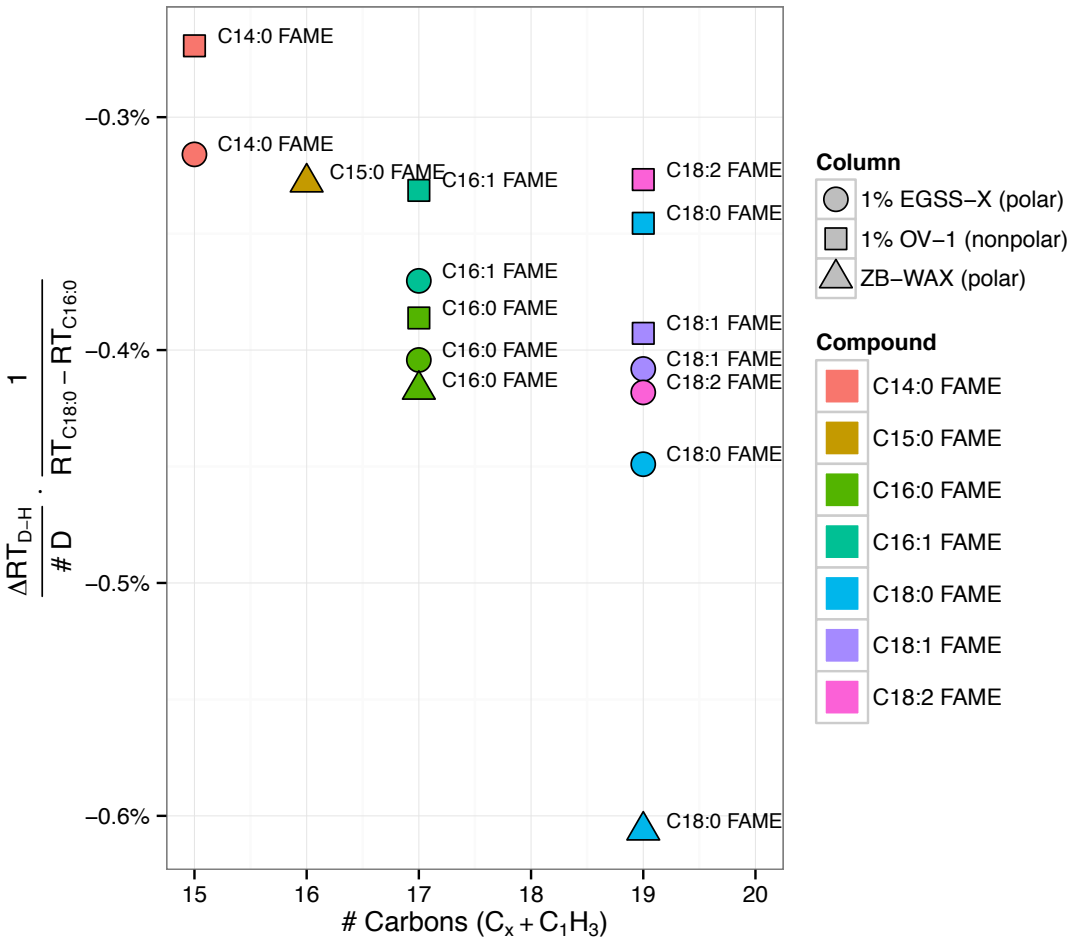

Figure D.1 – Change in retention time as a consequence of deuterium substitution. These data are a synthesis from our own studies with a column and the values reported in McCloskey et al. (1967). The change in retention time as a consequence of deuterium substitution is reported relative to the retention difference of the commonly-encountered C16:0 and C18:0 fatty acid methyl esters.

sites on the molecule are considered to have equal probability of deuterium substitution, and the modeled deuterium concentrations (1%, 10% and 25%) are assumed to be the isotopic abundances of the average biosynthetically incorporated hydrogen (i.e., these values are assumed to be after fractionation and other metabolic factors). The mass 2 and mass 3 tracers are scaled to be the same total amount as the natural abundance sample, albeit with the respective changes in isotopic composition reflected in the signal strengths (scaling data taken from the original data traces, and representative of the

relative differences in amplification of mass 2 and mass 3 ions). The mass 3 signal is simulated to capture the deuterated hydrogen signal fully; i.e., the formation of mass 4 DD molecules (although probabilistically occurring at high D concentrations) is not taken into consideration.

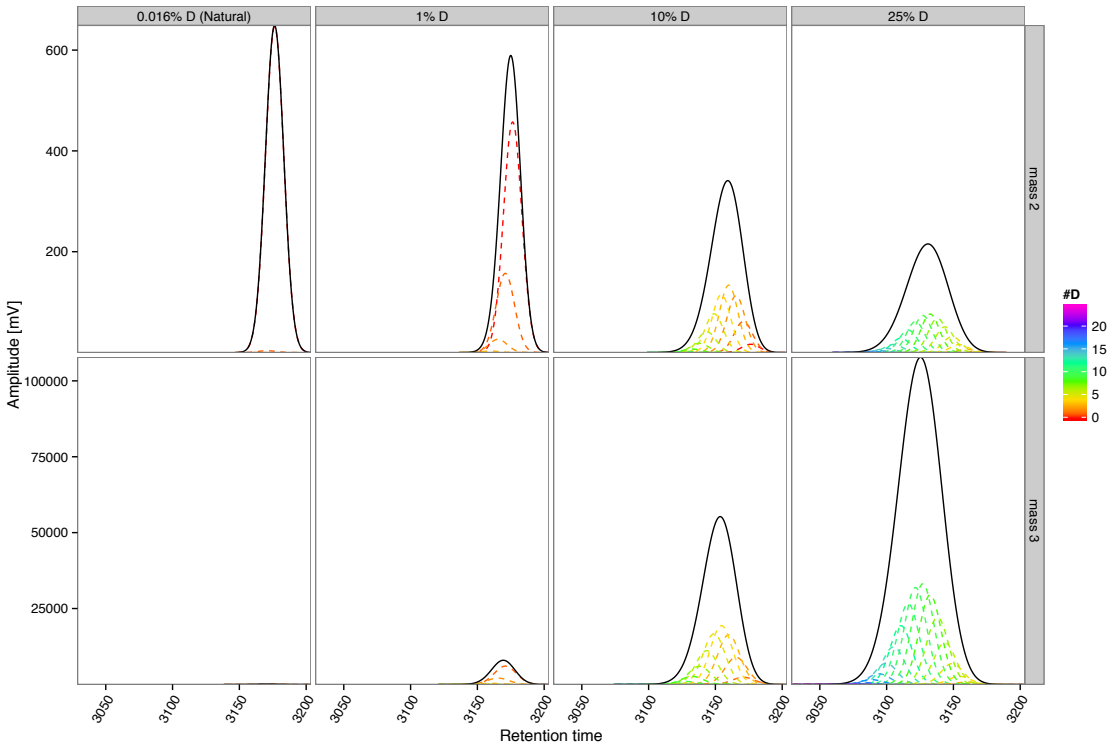

Figure D.2 – Simulation of the effect of deuterium substitution on peak broadening and retention shifts. The simulation illustrates the resulting peaks (in black) of changing isotopic composition with C18:0 derived from natural abundance, 1%, 10% and 25% deuterium. The peaks belonging to the different individual isotopologues that make up the combined peak are illustrated in color depending on their number of deuterium substitutions. Peaks are scaled for both mass traces (measured as hydrogen mass two H2 and mass three HD) to the same amount as the original (natural abundance) peaks on the left, illustrating how the same amount of material, but with different isotopic composition, would change the signal.

D.2 D_2O toxicity

Deuterated water (or heavy water) is known to be toxic to organisms at high concentrations (Kushner et al., 1999b). Here, we report growth experiments with *S. aureus* and *P.*

aeruginosa grown in standard NC medium with varying concentrations of D_2O. Growth experiments were performed at 37ºC in 96 well plates with at least 4 replicates per culture condition. Plates were gently shaken continuously, and optical density (OD_{600nm}) was recorded every 10 minutes. All culture wells were inoculated from overnight cultures that had not previously experienced any elevated level of D_2O. The effect of varying concentrations of D_2O was tested in one experiment for *P. aeruginosa*, and in two separate experiments for *S. aureus*.

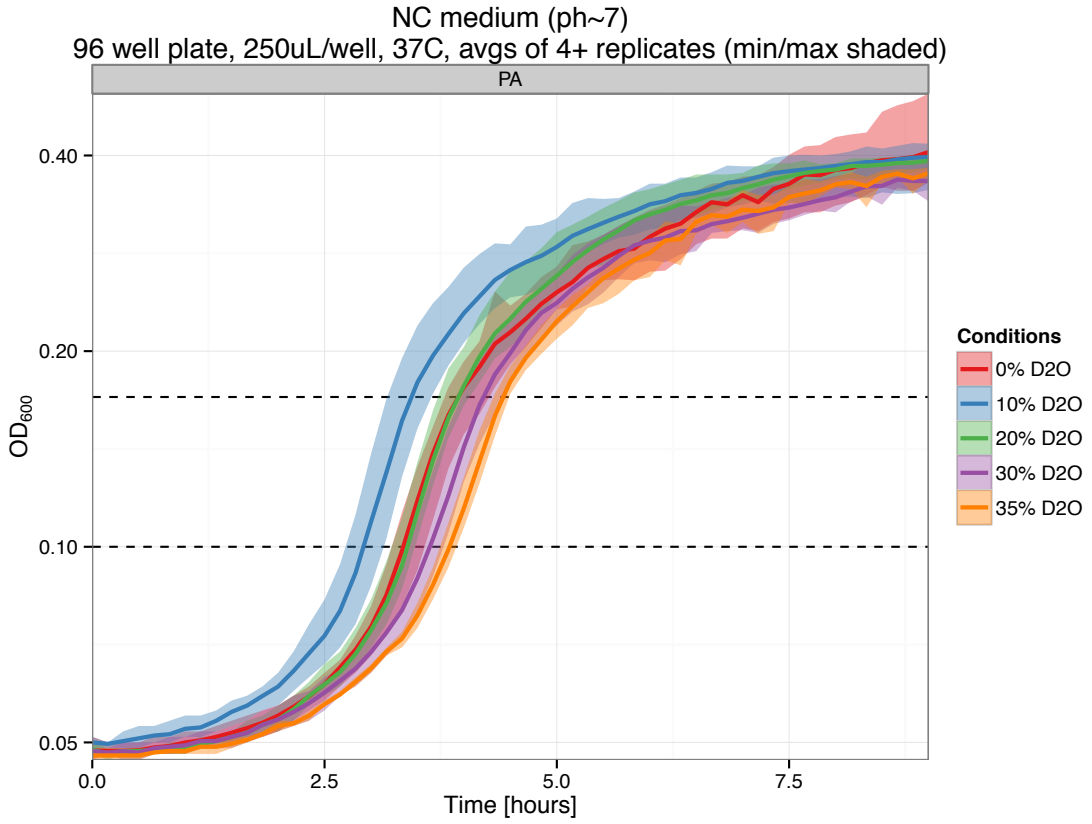

Figure D.3 – Toxicity effects of increasing concentrations of D_2O on *P. aeruginosa*.

The results show that levels of D_2O exposure up to ~20% for *P. aeruginosa* and ~15% for *S. aureus* have no discernible effect on growth rates, but higher levels (>30% and especially 50%) cause a significant decrease for both organisms. Growth rates were

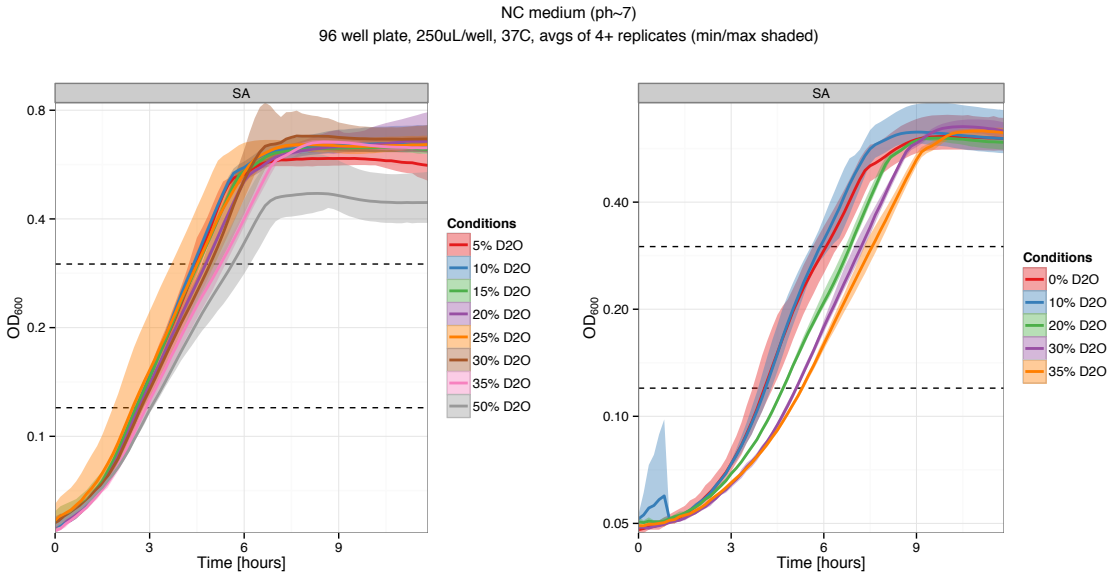

Figure D.4 – Toxicity effects of increasing concentrations of D_2O on *S. aureus* from two experiments.

Experiment	condition	Growth rate [1/hr]	Std. Error
P. aeruginosa	0% D2O	0.989	0.044
P. aeruginosa	10% D2O	1.208	0.035
P. aeruginosa	20% D2O	1.017	0.052
P. aeruginosa	30% D2O	1.003	0.044
P. aeruginosa	35% D2O	0.992	0.024
S. aureus #1	5% D2O	0.477	0.012
S. aureus #1	10% D2O	0.504	0.006
S. aureus #1	15% D2O	0.470	0.005
S. aureus #1	20% D2O	0.436	0.005
S. aureus #1	25% D2O	0.461	0.025
S. aureus #1	30% D2O	0.415	0.015
S. aureus #1	35% D2O	0.397	0.009
S. aureus #1	50% D2O	0.361	0.031
S. aureus #2	0% D2O	0.507	0.030
S. aureus #2	10% D2O	0.544	0.018
S. aureus #2	20% D2O	0.421	0.013
S. aureus #2	30% D2O	0.439	0.024
S. aureus #2	35% D2O	0.406	0.021

Table D.3 – Changes in growth rates from toxicity effects of increasing concentrations of D_2O.

evaluated during mid-exponential phase (during the optical density interval indicated by the dashed lines in Figures D.3 and D.4). Growth rates varied between different experiments (see Table D.3, *S. aureus* Experiment 1 and 2), likely due to slight differences in the inoculums. However, the toxicity patterns between the different experiments are well-conserved, and provide a estimate for the potential toxicity effects of isotope labeling with D_2O in these organisms.

D.3 Water fraction factor data

Medium	Microbe	# Analyses	δD [‰]	$\sigma_{\delta D}$ [‰]	${}^2F$ [ppm]	$\sigma_{{}^2F}$ [ppm]
SCFM	all	6	-80.5	1.1	143.2	0.2
SCFM	all	6	1.0	1.6	155.9	0.3
SCFM	all	6	80.7	1.7	168.3	0.3
SCFM	all	6	162.6	1.9	181.1	0.3
SCFM	all	6	243.1	1.8	193.6	0.3
Minimal	SA	8	-86.4	1.6	142.3	0.3
Minimal	SA	8	23.7	3.3	159.4	0.5
Minimal	SA	8	128.9	4.5	175.8	0.7
Minimal	SA	8	249.4	3.7	194.6	0.6
Minimal	PA	4	-87.6	0.5	142.1	0.1
Minimal	PA	4	19.4	5.1	158.8	0.8
Minimal	PA	4	158.4	6.4	180.4	1.0
Minimal	PA	4	258.0	3.7	195.9	0.6
Minimal	EC	4	-88.3	1.8	142.0	0.3
Minimal	EC	4	20.5	2.6	158.9	0.4
Minimal	EC	4	128.1	3.5	175.7	0.5
Minimal	EC	4	254.0	3.8	195.3	0.6
Chemostat	PA	3	-75.4	0.7	144.0	0.1
Chemostat	PA	3	90.0	0.5	169.8	0.1
Chemostat	PA	3	261.9	0.6	196.5	0.1

Table D.4 – Isotopic composition of source waters in water fraction factor experiments. Reported error is the standard deviation of the replicate analyses of medium water.
SA = *S. aureus*, PA = *P. aeruginosa*, EC = *E. coli*

Table D.4 summarizes the isotopic composition of the source waters used in water fraction factor experiments. Tables D.6, D.7, D.8, D.9, D.10, and D.11 summarize the isotopic composition of the major lipid components (components that constitute >5% of

the total membrane) resulting from growth in media with source waters of different isotopic compositions. Figures D.5, D.6 and D.7 show the membrane fatty acid composition profiles of each culture in minimal medium as an example of the degree of variability. The figures illustrate the high precision of the analytical replicates (error bars indicate 95% confidence intervals), but also highlight the substantial range of membrane compositions between biological replicates. This is not surprising, because individual cultures were likely at slightly different growth phases (near the transition from exponential to stationary phase, for example) at the time of harvest. This is particularly noticeable in the lipid profiles of *E. coli* (Figure D.5). *E. coli* converts substantial amounts of C16:1 to cyclo-C17:0 during stationary phase, which is reflected in the mirrored abundance profiles of C16:1 and cyclo-C17:0. The diversity in membrane make-up is not an issue for determining the water fraction factors in cultures with a single carbon substrate, because additional growth does not mix an isotopically different carbon source into the membrane. This is the case for growth of *E. coli* and *P. aeruginosa* in minimal medium where succinate provides the only source of carbon. In the case of the SCFM medium as well as growth of *S. aureus* on minimal medium (amended with a range of amino acids), the water fraction factors can only be derived from cultures harvested close to the same point during their growth phase. Accordingly, in the case of *S. aureus* growing on minimal medium (with amino acids) or SCFM, for each growth condition, only samples with less than 3% variability from the median a-C15:0 fatty acid relative abundance were considered to be at similar points during growth. For example, three of the cultures from experiment in minimal medium were harvested at a slightly different point during growth (which turned out to make a significant difference) and deviated by more than 3% from the median a-C15:0FA relative abundance (samples ${}^2F_{H_2O}$ = 142ppm [#2], 159 [#2] and 176 [#2]). The data suggest that the first two cultures under-incorporated, and the third culture over-incorporated an additional, isotopically light carbon source relative to all other cultures (reflected also in the shift in fatty acid profiles). They are excluded for the purpose of determining the

water fraction factors of *S. aureus* in this medium.

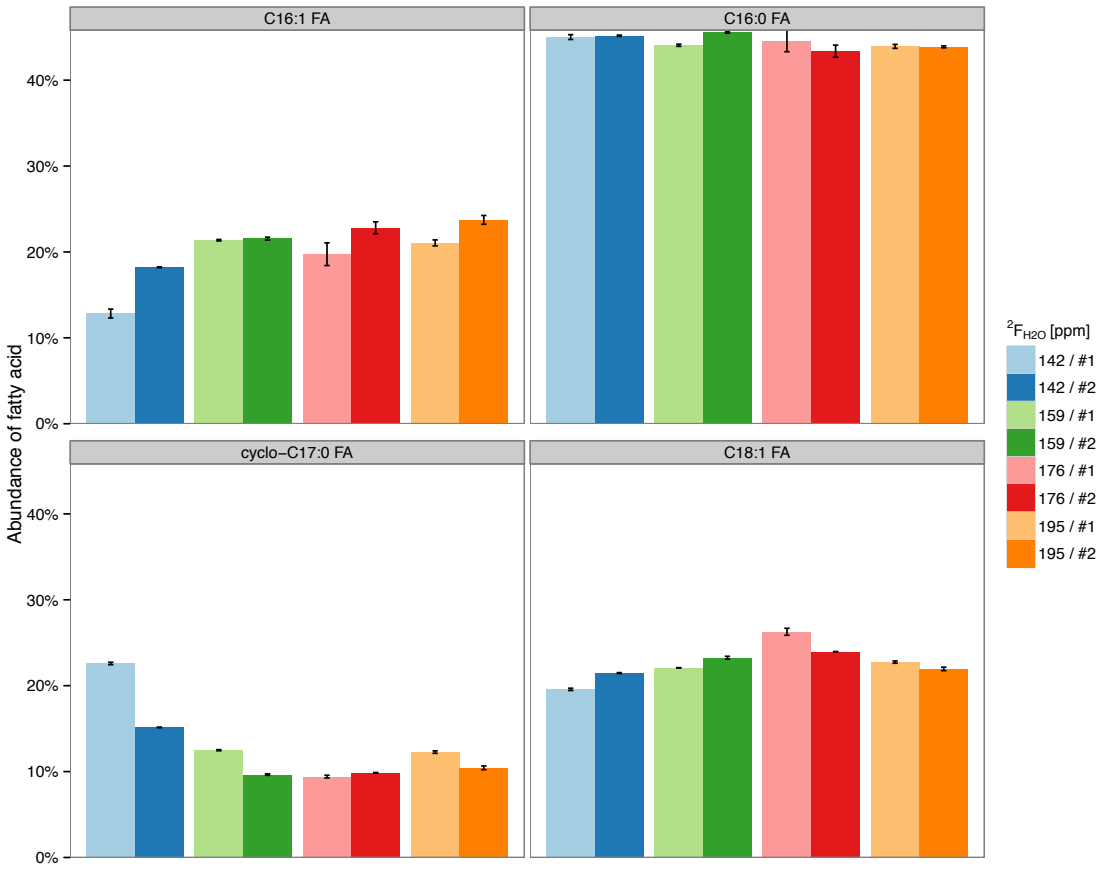

Figure D.5 – Major fatty acid profiles of *E. coli* cultures grown in minimal medium. Indicated error bars are 95% confidence intervals.

Figure D.8 shows the regression lines of $^2F_{lipid}$ vs $^2F_{water}$ to determine the water fraction factors and substrate offset for the different fatty acids that make up the different organisms' membranes. The resulting regression parameters are reported in Table 7.1.

D.4 Patterns of isotope tracer incorporation

Figure D.9 illustrates the evolution of total biomass, new biomass and old biomass over the course of two generation times (the biomass is not necessarily doubling, so these are only the apparent generation times) for varying death/removal rates. The isotopic enrichment during this time interval is illustrated in the lower panel, and is based on an

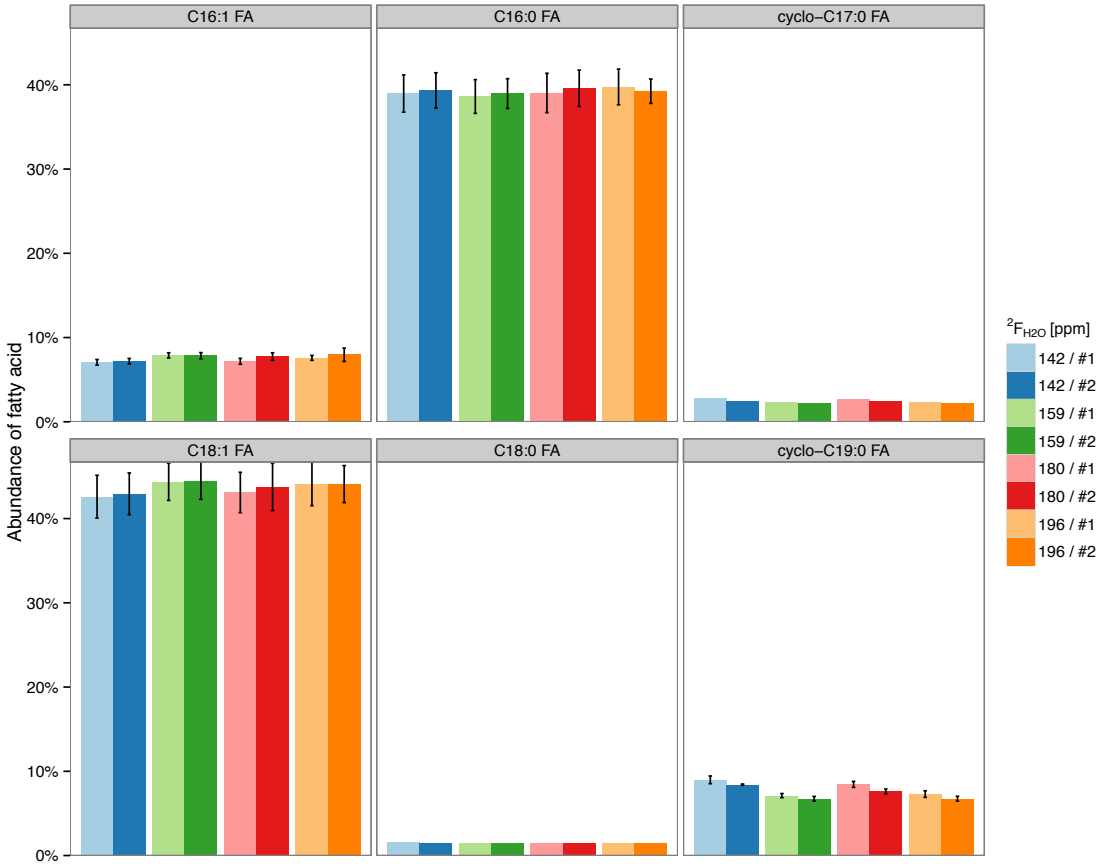

Figure D.6 – Major fatty acid profiles of *P. aeruginosa* cultures grown in minimal medium. Indicated error bars are 95% confidence intervals.

isotopic spike with rare isotope fractional abundance $F_L = 10\%$ and an initial isotopic composition of $F_B(t_0) = 0\%$ (i.e. assuming negligible natural abundance). For clarity, this illustration does not take recycling vs. *de novo* synthesis $(f_S = 1)$, turnover $(\omega = 0)$ or biosynthetic isotope fractionation $(\alpha = 1)$ into consideration.

D.5 Error estimation

D.5.1 Error from using δ-values in mass balance calculations

Isotopic mass balance can be approximated with isotopic values in δ-notation $(\delta_{mix} \sum m_i \approx \sum \delta_i m_i)$ when the isotopic composition of all pools is relatively close to

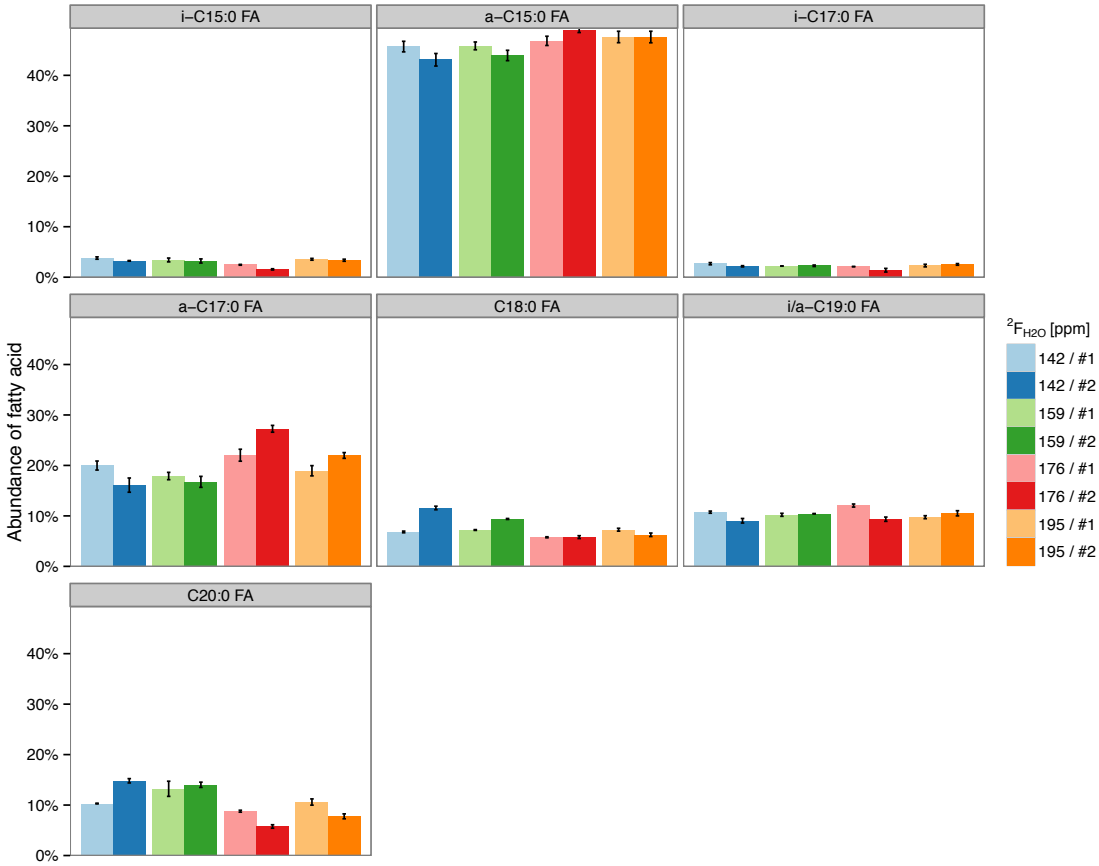

Figure D.7 – Major fatty acid profiles of *S. aureus* cultures grown in minimal medium. Indicated error bars are 95% confidence intervals.

natural abundance. However, this approximation introduces significant error when one or multiple pools of heavily enriched materials are part of the mass balance. This is routinely the case when working with isotopic labels, and it is important to use exact mass balance calculations with fractional abundance values F instead, i.e. $F_{mix} \sum m_i = \sum F_i m_i$. Figure D.10 illustrates the absolute and relative error introduces in the estimate of F_{mix} if mass balance between isotopically-labeled new biomass and natural abundance old biomass is calculated using δ-values (and then converted to F_{mix} for comparison) vs. the exact calculation in abundance space. Mass balance using δ-values systematically overestimates the true value. The error scales with the strength of the isotope label (here pictured up to a composition of $F_{new} = 50\%$ rare isotope in new biomass), and is slightly more

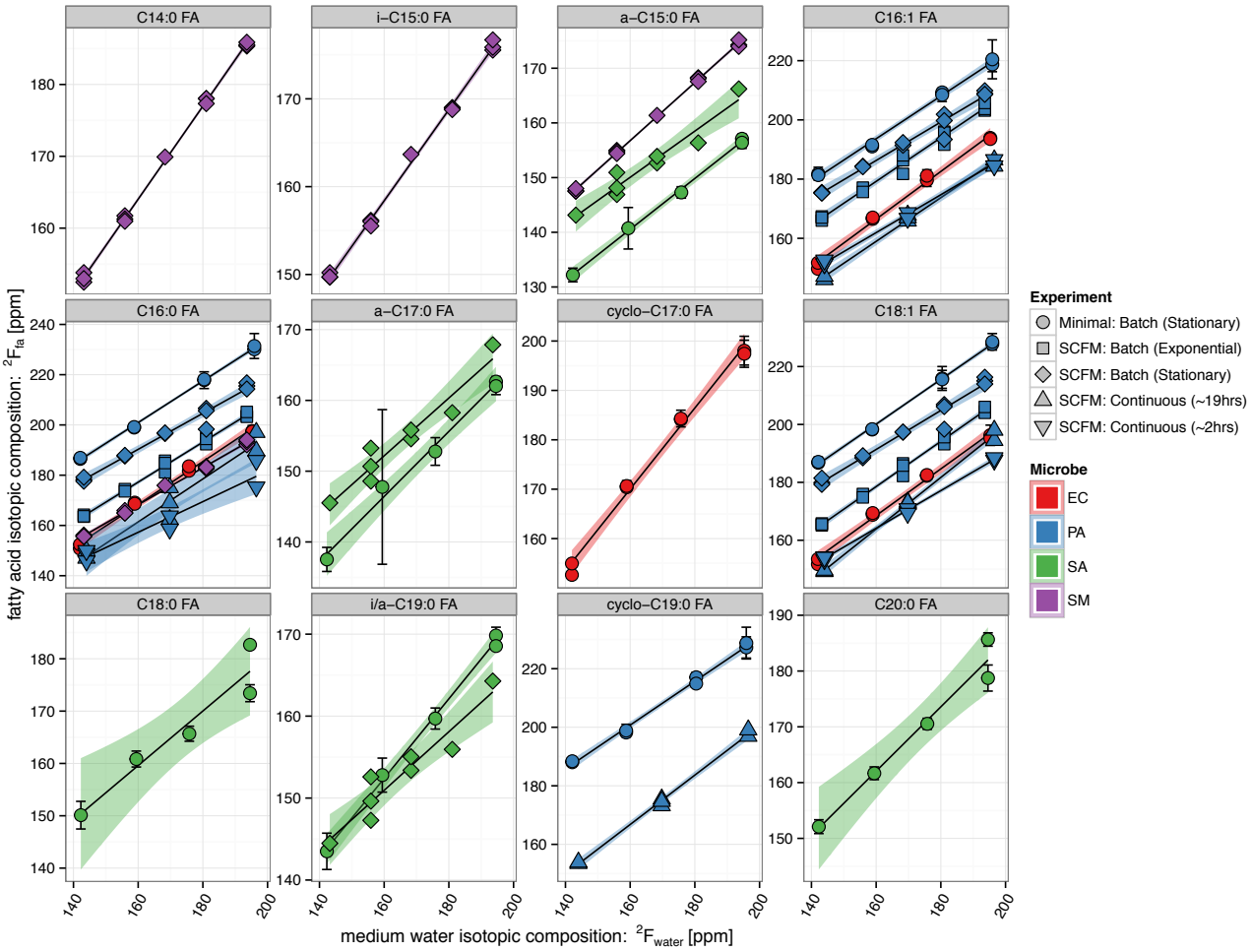

Figure D.8 – Water fraction factor regression lines. Regression lines of $^2F_{lipid}$ vs $^2F_{water}$ to determine the water fraction factors and substrate offset. Error bars shown are 95% analytical confidence intervals from 1-3 separate analyses and confidence band on linear regression is statistical confidence on the regression. Some rare fatty acids could not be quantified in all runs, and some samples were only analyzed once. Data points without any error bars are derived from a single analysis. See Tables D.6, D.7, D.8, D.9, D.10, D.11 for details.

pronounced for isotopic systems with lower natural abundance isotope ratios (error for H > N > C). It is important to note that while the absolute error introduced from calculations with δ-values is most pronounced at a ~1:1 mixing ratio (slightly offset from 50% because natural abundances are not 0), relative errors in the estimate for F_{mix} reach significant levels (> 10%) already with very little production of new biomass (fraction of new biomass plotted on a logarithmic scale for clarity). This aspect of δ-value mass balance limits the ability to accurately infer microbial activity in isotope labeling experiments. The use of

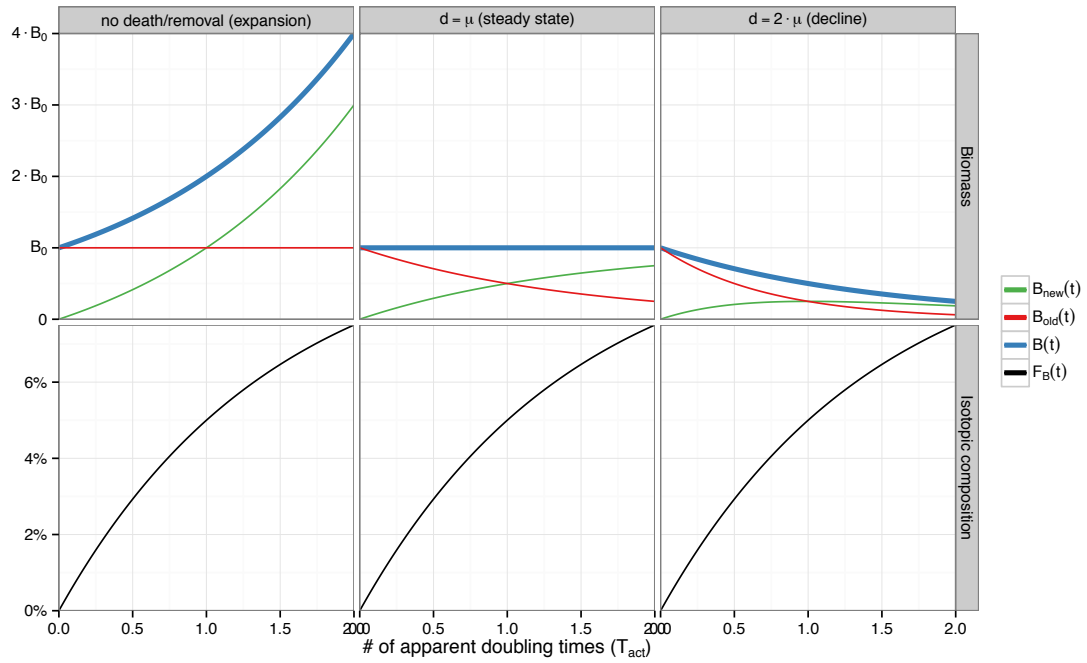

Figure D.9 – Change in biomass and isotopic composition over time. This figure illustrates the change in biomass (total biomass, new biomass and old biomass) and the corresponding isotopic enrichment from a 10% isotope label over the course of two generations.

fractional abundances for all mass balance calculations is strongly recommended.

D.5.2 Error from using fractionation factors in F-value mass balance calculations

Exact mass balance calculations that employ fractional abundances F instead of $\delta-$values are highly recommended in isotope labeling experiments due to the significant deviations discussed above. However, for biosynthetic processes that can introduce significant isotope fractionation, it is important to take known fractionation factors into consideration even for heavily labeled pools. An isotope fractionation factor between two pools a and b is usually reported/known in terms of the ratio of isotope ratios between the two pools $\alpha_{b/a} = \frac{R_b}{R_a}$, and is appropriate only to apply to an isotope ratio. To apply it to a natural

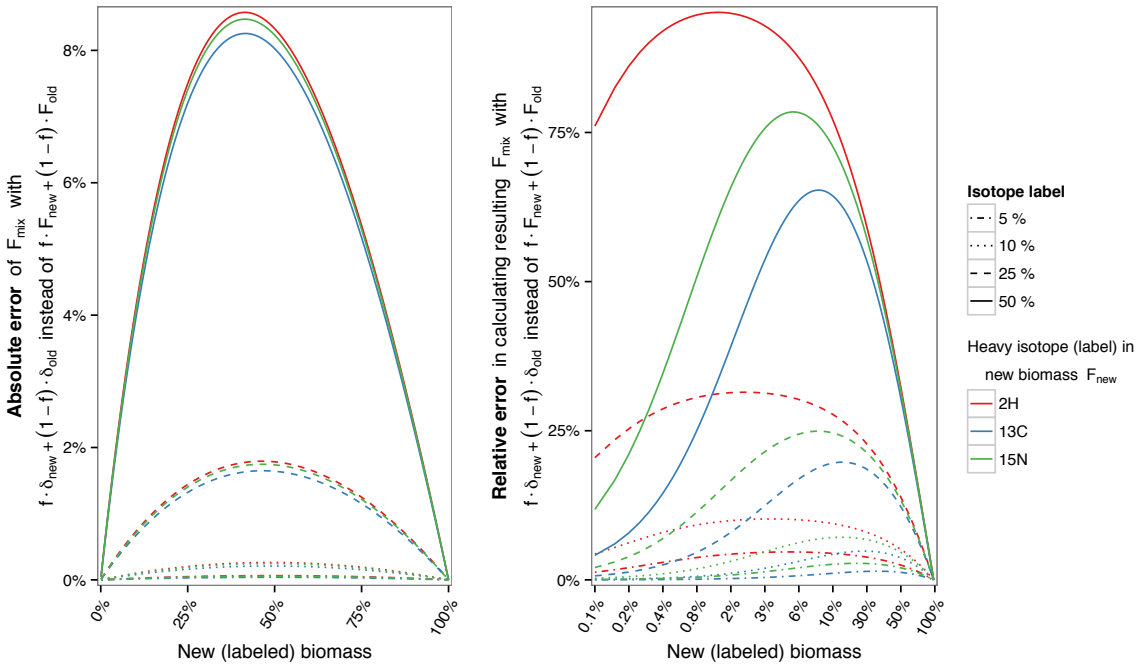

Figure D.10 – Errors in mass balance calculations with δ-values.

abundance value F, the natural abundance must be converted to a ratio $\left(R = \frac{F}{1-F}\right)$[1] to calculate the effect of the fractionating process, and then converted back to an abundance value $\left(F = \frac{R}{1+R}\right)$[1] for mass balance calculations:

$$\begin{aligned} R_b &= \alpha_{b/a} R_a \\ F_b &= \frac{\frac{\alpha_{b/a} \cdot F_a}{1-F_a}}{1 + \left(\frac{\alpha_{b/a} \cdot F_a}{1-F_a}\right)} \end{aligned} \tag{D.1}$$

However, the simplified formula $F_b = \alpha_{b/a} F_a$ provides a reasonable approximation. The relative error introduced by this approximation is illustrated in Figure D.11, and can be

[1] This is only exact for isotope systems with one minor isotope (H, C, N), but a reasonable approximation for others (e.g. O, S) with trace abundances of other minor isotopes. The exact formulae would be ${}^iR = \frac{{}^iF}{1-\sum {}^iF}$ and ${}^iF = \frac{{}^iR}{1+\sum {}^iR}$.

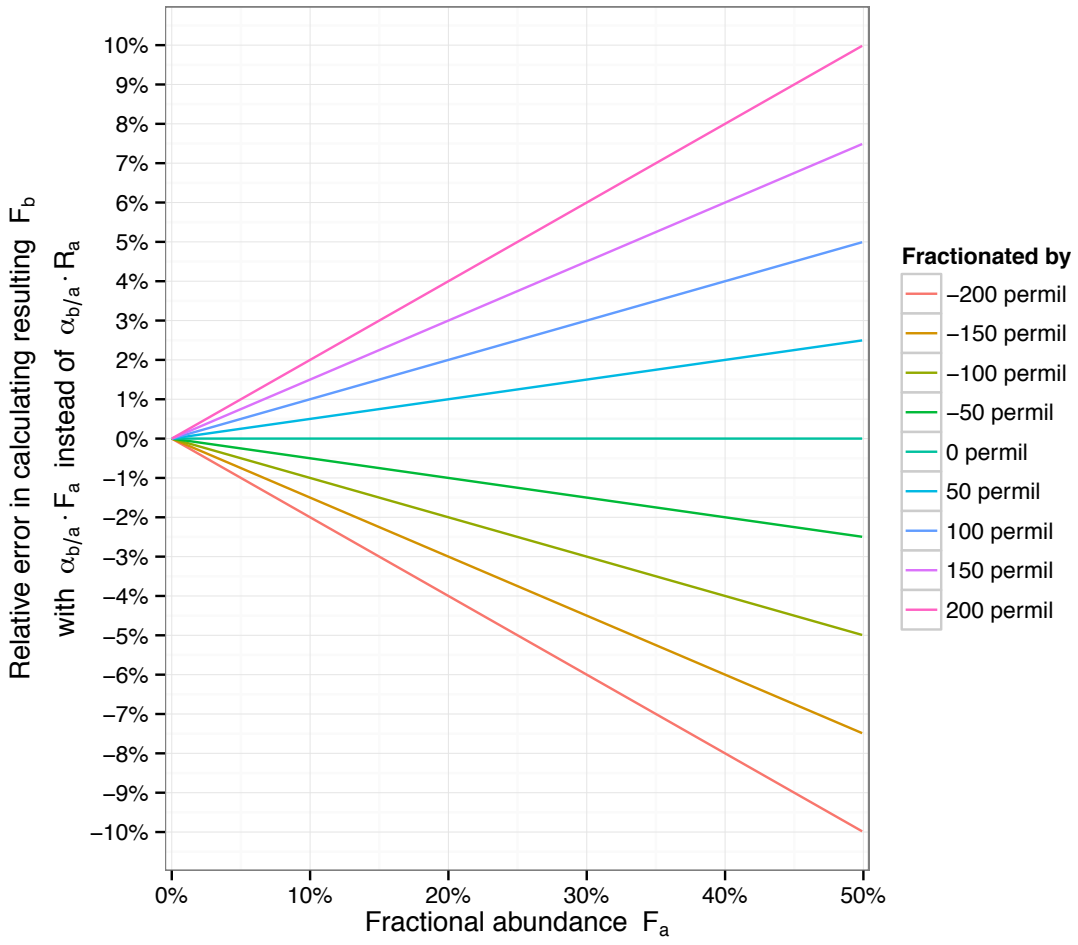

Figure D.11 – Errors in mass balance calculations with δ-values.

calculated as follows.

$$\frac{F_b - F_{b-exact}}{F_b} = \alpha_{b/a} \cdot F_a \cdot \left[\frac{\frac{\alpha_{b/a} \cdot F_a}{1-F_a}}{1 + \left(\frac{\alpha_{b/a} \cdot F_a}{1-F_a} \right)} \right]^{-1} - 1 = (\alpha_{b/a} - 1) \cdot F_a \qquad \text{(D.2)}$$

This implies that this approximation ($F_b = \alpha_{b/a} F_a$) only introduces significant errors in combination with strong fractionation and/or a very high isotope label (both a strong fractionation of $\pm 200‰$ combined with a moderate label of 10% rare isotope, and a

moderate fractionation of $\pm 50‰$ with a strong label of 40% rare isotope introduce a 2% error in the calculated F_b).

D.5.3 Error when using isotope labeling approximations

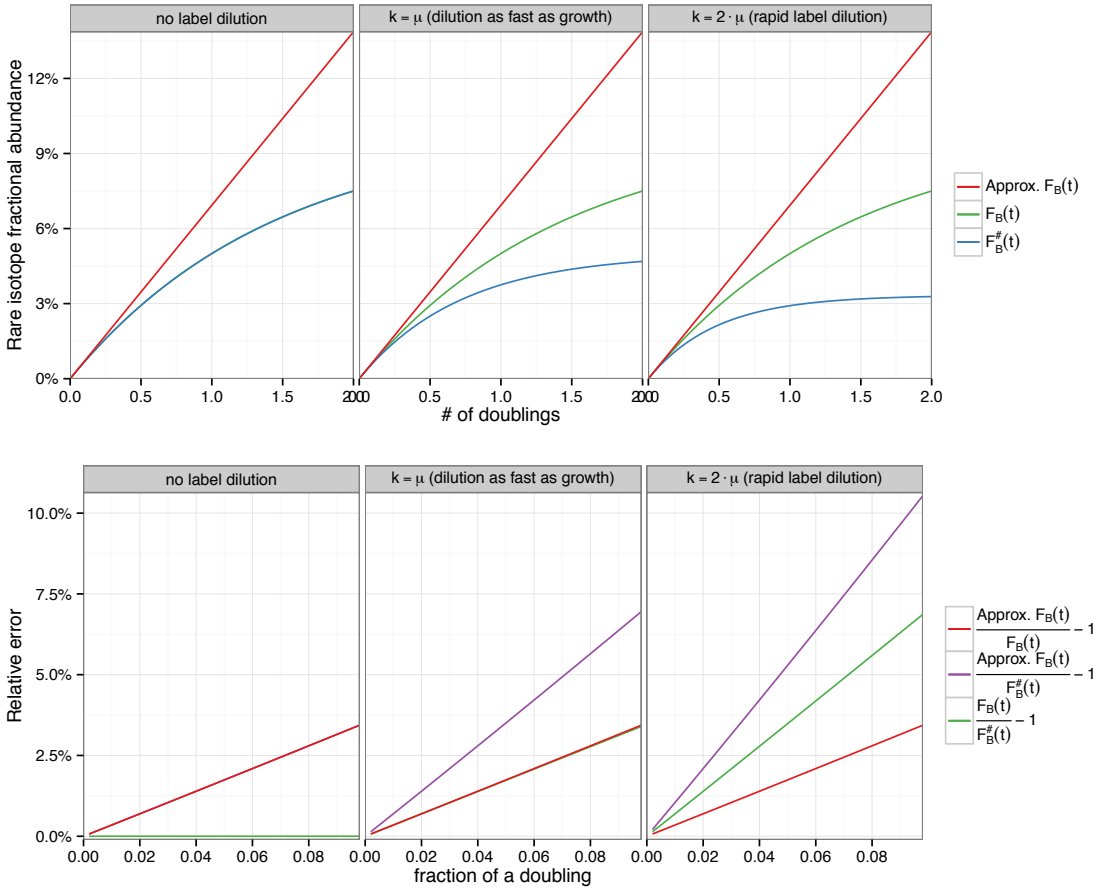

Figure D.12 – Errors in approximating isotope labeling with Taylor expansion.

Figure D.12 illustrates the approximations discussed in Equations 7.9 and 7.10 (upper panel) and shows how the relative error of using these evolves over time (lower panel). The isotopic enrichment is illustrated as a function of multiples of a population doubling, and is based on an initial isotopic spike with rare isotope fractional abundance $F_L = 10\%$ and an initial isotopic composition of $F_B(t_0) = 0\%$ (i.e., assuming negligible natural abundance). Various isotope tracer dilution rates k are considered ($k = 0$, $k = \mu$, $k = 2 \cdot \mu$). For

clarity, this illustration does not take recycling vs. *de novo* synthesis $(f_S = 1)$, turnover $(\omega = 0)$ or biosynthetic isotope fractionation $(\alpha = 1)$ into consideration, which all affect the total isotope enrichment (upper panel), but do not have a significant effect on the relative errors (lower panel). Table D.5 reports the relative error from using different approximations after $\frac{1}{10}$ of a doubling for reference.

Approximating isotope incorporation by using the first term of the Taylor expansion $Approx.F_B(t)$ systematically *overestimates* the actual isotope labeling $F_B(t)$ (so when used in reverse to infer growth rate from a given isotopic signal, it will *underestimate* actual growth / project a slower apparent generation time than is actually the case) and leads to a $\approx 3.5\%$ error relative to $F_B(t)$ (no label dilution) after $\frac{1}{10}$ of a doubling. When label dilution plays a role, the missing higher-order terms from the approximation introduce significantly larger errors, exceeding 10% after $\frac{1}{10}$ of a doubling for scenarios where the label is diluted out of the system twice as fast as the population grows ($k \geqq 2 \cdot \mu$).

The figure also illustrates the effect of considering dilution of the initial isotopic spike on isotope enrichment $\left(F_B^{\#}(t)\right)$. The upper panel shows how there is naturally no effect without any dilution ($k = 0, \rightarrow F_B(t) = F_B^{\#}(t)$), and how isotope enrichment is systematically overestimated when dilution of the label plays a significant role $\left(k > 0 \rightarrow F_B(t) > F_B^{\#}(t)\right)$. Table D.5 shows the relative error introduced when $k > 0$ by approximating isotopic enrichment as if there was no dilution. The error reaches $\approx 3.5\%$ after $\frac{1}{10}$ of a doubling if the dilution rate is comparable to the population growth rate ($k \approx \mu$).

Error	$k = 0$	$k = \mu$	$k = 2 \cdot \mu$
$\frac{F_B(t)}{F_B^{\#}(t)} - 1$	0%	3.46%	7.01%
$\frac{Approx.F_B(t)}{F_B(t)} - 1$	3.51%	3.51%	3.51%
$\frac{Approx.F_B(t)}{F_B^{\#}(t)} - 1$	3.51%	7.09%	10.76%

Table D.5 – Relative error at $\frac{1}{10}$ doubling from approximating isotope labeling with Taylor expansion.

D.6 Isotope labeling calculator

D.6.1 How to choose the strength of an isotopic label?

Estimating the appropriate incubation times for capturing microbial activity in stable isotope spiking experiments is a task that I encounter frequently in my research. For biological relevance (as discussed in some detail in Chapter 7), it is important to consider factors such as chemical changes, excessive sample dilution and potential toxicity that could result from the introduction of the labeled substrate. Additionally, for optimal sensitivity and analytical precision, it is important to choose the strength of the isotopic label and exposure time to the label such that they can capture all relevant processes (i.e. sufficient enrichment to quantify activity), but also that the resulting enrichments stay within a range suitable for isotope ratio mass spectrometry. This latter consideration is often overlooked in isotope labeling experiments where the notion that "bigger is better" frequently prevails and excessive isotope labels are applied. This approach is misguided in *most* environmental applications not only because small enrichments above natural abundance are already more than sufficient to measure activity, but also because large enrichments are problematic analytically (in typical ir-MS applications, in soft ionization and mass spectrometric analyses of larger molecules on the other hand, only strong enrichments stand a chance of quantification). Two major concerns are at the heart of this issue:

D.6.1.1 ir-MS amplifier gain

Most standard isotope ratio mass spectrometers for light stable isotopes are not suitable for measuring isotope ratios of materials vastly more enriched in a rare stable isotope than natural abundance samples. This is because the gain resistors of the standard set of faraday amplifiers are chosen such that they can provide higher amplification for some masses (tuned to measure the ion current of a rare isotope) than for others (tuned to measure

the ion current of abundant isotopes). This feature provides the necessary sensitivity for measuring the ions from the naturally rare isotopes in an ion beam dominated by ions from the abundant isotope, and allows quantification of both with $\approx$ comparable signal strengths. This is important to reduce the effects of non-linearities, and samples are usually analyzed in quantities that provide appropriate ion beams 10x below amplifier saturation. The problem for isotopically labeled materials is that most systems are equipped with only one resistor per amplifier (rather than multiple resistors and an amplifier gain switch), so the amplifier gain is fixed and signals from samples with unnaturally enriched rare isotopes are amplified so strongly that the resulting signal is no longer comparable to the signal of the naturally abundant isotope (which is amplified to a much lesser extent), significantly reducing accuracy and risking saturation of the amplifiers.

D.6.1.2 Reference materials

Isotope ratio mass spectrometers can achieve high accuracy and precision in measuring minute difference in the isotopic composition of different samples by virtue of measuring them relative to the isotope ratios observed in known reference materials. For this purpose, it is important to compare samples to reference standards of similar isotopic composition, to avoid extrapolation errors from unaccounted non-linearities (or ideally, determine and correct for non-linearities by using a range of standards that bracket the sample material). Understandably, but most unfortunate for isotope labeling purposes, commercially available, well-characterized reference materials tend to be similar in isotopic composition to the average abundance encountered in natural samples. The characterization and distribution of enriched standards is a very important contribution to the improvement of isotope labeling techniques, and has fortunately seen some progress in recent years.

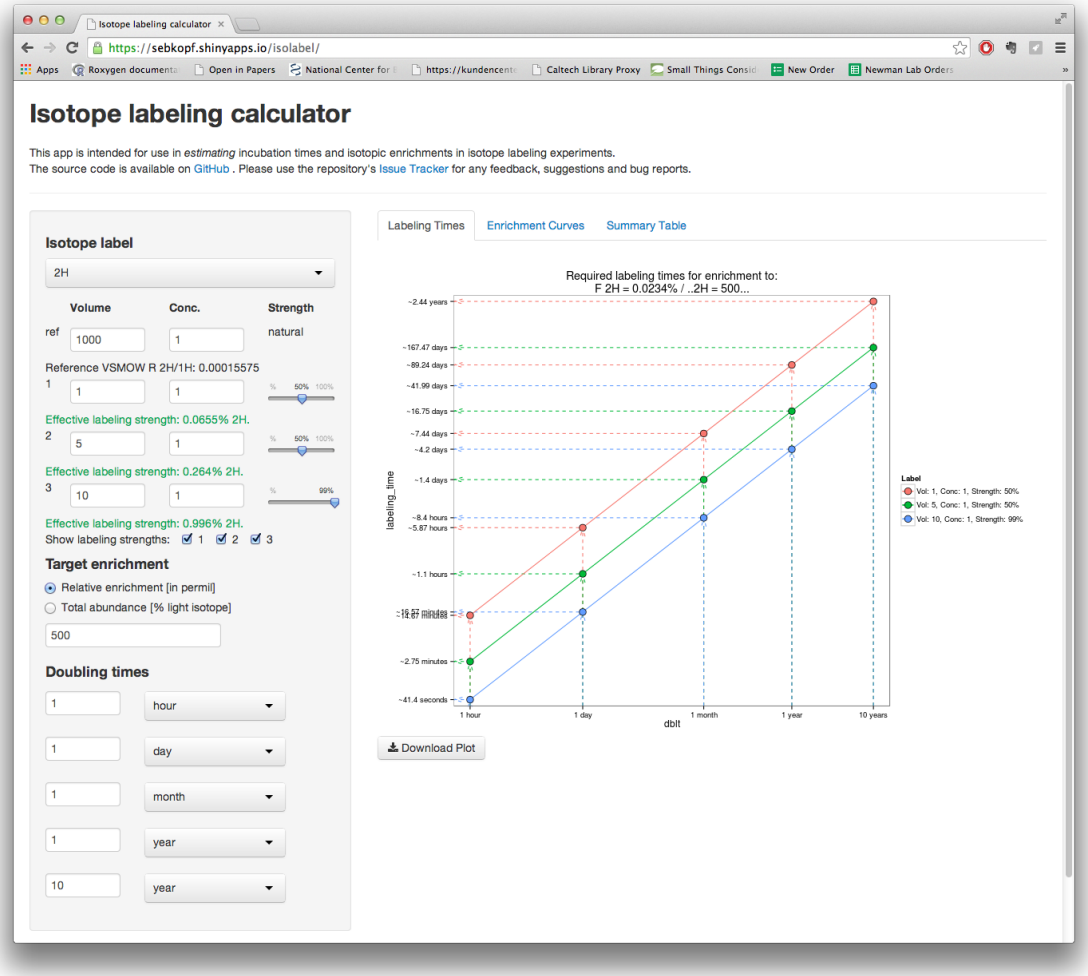

Figure D.13 – **Isotope labeling calculator.** This app is intended for use in estimating incubation times and isotopic enrichments in isotope labeling experiments. The source code is available on GitHub. Please use the repository's IssueTracker for any feedback, suggestions and bug reports.

D.6.2 A tool for label calculation

Figure 7.2 of Chapter 7 provides a plot that illustrates the required incubation times for a desired isotopic enrichment in the context of different microbial generation times. While useful to illustrate the power of hydrogen isotope labeling, this static figure is of limited use for getting a sense of how different labeling strengths, isotopic systems and microbial populations would respond. For this purpose, I implemented an interactive version of this

plot (illustrated in Figure D.13) as an open-source web application (powered by R Core Team, 2014; RStudio, 2014; frameworks), that allows visualization of incubation times, enrichment curves and label summaries for different isotopic systems, label strengths and generation times.

References

Kushner, D. J., Baker, A., Dunstall, T. G., Feb. 1999b. Pharmacological uses and perspectives of heavy water and deuterated compounds. Canadian Journal Of Physiology And Pharmacology 77 (2), 79–88.

McCloskey, J. A., Lawson, A. M., Leemans, F., 1967. Gas-chromatographic and mass-spectrometric properties of perdeuterated fatty acid methyl esters. Chemical Communications (London) (6), 285–287.

R Core Team, 2014. R: A Language and Environment for Statistical Computing. R Foundation for Statistical Computing, Vienna, Austria.
URL http://www.R-project.org/

RStudio, 2014. shiny: Web Application Framework for R. R package version 0.9.1.
URL http://CRAN.R-project.org/package=shiny

D.7 Data tables

Medium	Condition	δD_{H_2O} [‰]	${}^2F_{H_2O}$ [ppm]	Compound	n	Peak [$\%_{total}$]	σ [%]	δD_{FA} [‰]	$\sigma_{\delta D}$ [‰]	${}^2F_{FA}$ [ppm]	$\sigma_{^2F}$ [ppm]
Minimal	Batch (Stationary)	-88.3	142.0	C16:1 FA	3	12.8	0.2	-38.9	1.4	149.7	0.2
Minimal	Batch (Stationary)	-88.3	142.0	C16:1 FA	3	18.2	0.0	-25.7	1.3	151.7	0.2
Minimal	Batch (Stationary)	20.5	158.9	C16:1 FA	3	21.4	0.0	69.5	1.8	166.6	0.3
Minimal	Batch (Stationary)	20.5	158.9	C16:1 FA	3	21.6	0.1	72.5	1.5	167.0	0.2
Minimal	Batch (Stationary)	128.1	175.7	C16:1 FA	3	19.7	0.5	153.3	5.4	179.6	0.8
Minimal	Batch (Stationary)	128.1	175.7	C16:1 FA	3	22.8	0.3	163.2	5.2	181.1	0.8
Minimal	Batch (Stationary)	254.0	195.3	C16:1 FA	3	21.1	0.1	245.2	1.6	193.9	0.3
Minimal	Batch (Stationary)	254.0	195.3	C16:1 FA	3	23.7	0.2	242.7	3.3	193.5	0.5
Minimal	Batch (Stationary)	-88.3	142.0	C16:0 FA	3	45.0	0.1	-31.8	0.7	150.8	0.1
Minimal	Batch (Stationary)	-88.3	142.0	C16:0 FA	3	45.2	0.0	-21.2	1.5	152.4	0.2
Minimal	Batch (Stationary)	20.5	158.9	C16:0 FA	3	44.1	0.0	85.8	1.7	169.1	0.3
Minimal	Batch (Stationary)	20.5	158.9	C16:0 FA	3	45.5	0.0	82.8	2.1	168.6	0.3
Minimal	Batch (Stationary)	128.1	175.7	C16:0 FA	3	44.6	0.5	167.1	2.1	181.8	0.3
Minimal	Batch (Stationary)	128.1	175.7	C16:0 FA	3	43.4	0.3	178.6	1.5	183.5	0.2
Minimal	Batch (Stationary)	254.0	195.3	C16:0 FA	3	43.9	0.1	268.6	5.7	197.6	0.9
Minimal	Batch (Stationary)	254.0	195.3	C16:0 FA	3	43.9	0.0	267.2	2.4	197.4	0.4
Minimal	Batch (Stationary)	-88.3	142.0	cyclo-C17:0 FA	3	22.6	0.1	-19.9	0.5	152.6	0.1
Minimal	Batch (Stationary)	-88.3	142.0	cyclo-C17:0 FA	3	15.1	0.0	-5.0	1.3	155.0	0.2
Minimal	Batch (Stationary)	20.5	158.9	cyclo-C17:0 FA	3	12.5	0.0	94.1	1.1	170.4	0.2
Minimal	Batch (Stationary)	20.5	158.9	cyclo-C17:0 FA	3	9.6	0.0	95.8	2.8	170.7	0.4
Minimal	Batch (Stationary)	128.1	175.7	cyclo-C17:0 FA	3	9.4	0.1	182.1	1.7	184.1	0.3
Minimal	Batch (Stationary)	128.1	175.7	cyclo-C17:0 FA	3	9.9	0.0	183.5	4.4	184.3	0.7
Minimal	Batch (Stationary)	254.0	195.3	cyclo-C17:0 FA	3	12.3	0.1	271.7	7.5	198.0	1.2
Minimal	Batch (Stationary)	254.0	195.3	cyclo-C17:0 FA	3	10.4	0.1	267.7	7.1	197.4	1.1
Minimal	Batch (Stationary)	-88.3	142.0	C18:1 FA	3	19.6	0.1	-25.7	2.5	151.7	0.4
Minimal	Batch (Stationary)	-88.3	142.0	C18:1 FA	3	21.5	0.0	-14.3	1.2	153.5	0.2
Minimal	Batch (Stationary)	20.5	158.9	C18:1 FA	3	22.1	0.0	83.9	2.6	168.8	0.4
Minimal	Batch (Stationary)	20.5	158.9	C18:1 FA	3	23.3	0.1	87.7	1.7	169.4	0.3
Minimal	Batch (Stationary)	128.1	175.7	C18:1 FA	3	26.3	0.2	170.4	1.7	182.3	0.3
Minimal	Batch (Stationary)	128.1	175.7	C18:1 FA	3	24.0	0.0	172.1	3.9	182.5	0.6
Minimal	Batch (Stationary)	254.0	195.3	C18:1 FA	3	22.7	0.1	260.2	9.0	196.3	1.4
Minimal	Batch (Stationary)	254.0	195.3	C18:1 FA	3	22.0	0.1	253.4	3.4	195.2	0.5

Table D.6 – Isotopic composition of major (>5%) *E. coli* lipid components in water fraction factor experiments. Data is corrected for the effects of derivatization on isotopic composition. Reported error is the standard deviation of the replicate analyses (n) for identical samples. Biological replicates are listed separately.

Medium	Condition	δD_{H_2O} [‰]	${}^2F_{H_2O}$ [ppm]	Compound	n	Peak [$\%_{total}$]	σ [%]	δD_{FA} [‰]	$\sigma_{\delta D}$ [‰]	${}^2F_{FA}$ [ppm]	$\sigma_{^2F}$ [ppm]
Minimal	Batch (Stationary)	-87.6	142.1	C16:1 FA	3	7.1	0.1	167.6	5.6	181.8	0.9
Minimal	Batch (Stationary)	-87.6	142.1	C16:1 FA	3	7.2	0.1	164.4	2.7	181.3	0.4
Minimal	Batch (Stationary)	19.4	158.8	C16:1 FA	3	7.9	0.1	226.6	3.8	191.0	0.6
Minimal	Batch (Stationary)	19.4	158.8	C16:1 FA	3	7.8	0.1	230.0	2.1	191.6	0.3
Minimal	Batch (Stationary)	158.4	180.4	C16:1 FA	3	7.2	0.1	343.9	2.6	209.3	0.4
Minimal	Batch (Stationary)	158.4	180.4	C16:1 FA	3	7.7	0.2	338.6	5.9	208.5	0.9
Minimal	Batch (Stationary)	258.0	195.9	C16:1 FA	3	7.6	0.1	404.5	6.3	218.7	1.0
Minimal	Batch (Stationary)	258.0	195.9	C16:1 FA	3	8.0	0.3	415.6	17.0	220.5	2.6
Minimal	Batch (Stationary)	-87.6	142.1	C16:0 FA	3	39.0	0.9	197.5	2.2	186.5	0.3
Minimal	Batch (Stationary)	-87.6	142.1	C16:0 FA	3	39.3	0.8	200.2	0.4	186.9	0.1
Minimal	Batch (Stationary)	19.4	158.8	C16:0 FA	3	38.6	0.8	277.6	1.0	199.0	0.2
Minimal	Batch (Stationary)	19.4	158.8	C16:0 FA	3	39.0	0.7	279.0	0.5	199.2	0.1
Minimal	Batch (Stationary)	158.4	180.4	C16:0 FA	3	39.0	0.9	398.7	8.6	217.8	1.3
Minimal	Batch (Stationary)	158.4	180.4	C16:0 FA	3	39.6	0.9	400.7	2.0	218.1	0.3
Minimal	Batch (Stationary)	258.0	195.9	C16:0 FA	3	39.7	0.9	477.6	1.8	230.1	0.3
Minimal	Batch (Stationary)	258.0	195.9	C16:0 FA	3	39.2	0.6	486.0	12.8	231.4	2.0
Minimal	Batch (Stationary)	-87.6	142.1	C18:1 FA	3	42.6	1.0	199.2	1.0	186.8	0.2
Minimal	Batch (Stationary)	-87.6	142.1	C18:1 FA	3	42.9	1.0	201.2	4.3	187.1	0.7
Minimal	Batch (Stationary)	19.4	158.8	C18:1 FA	3	44.4	0.9	272.9	3.4	198.2	0.5
Minimal	Batch (Stationary)	19.4	158.8	C18:1 FA	3	44.5	0.9	273.8	2.4	198.4	0.4
Minimal	Batch (Stationary)	158.4	180.4	C18:1 FA	3	43.1	1.0	386.2	10.6	215.9	1.7
Minimal	Batch (Stationary)	158.4	180.4	C18:1 FA	3	43.8	1.1	384.3	8.0	215.6	1.2
Minimal	Batch (Stationary)	258.0	195.9	C18:1 FA	3	44.1	1.0	462.6	4.3	227.8	0.7
Minimal	Batch (Stationary)	258.0	195.9	C18:1 FA	3	44.1	0.9	467.5	7.4	228.5	1.2
Minimal	Batch (Stationary)	-87.6	142.1	cyclo-C19:0 FA	3	9.0	0.2	207.5	1.5	188.0	0.2
Minimal	Batch (Stationary)	-87.6	142.1	cyclo-C19:0 FA	3	8.4	0.0	209.7	1.2	188.4	0.2
Minimal	Batch (Stationary)	19.4	158.8	cyclo-C19:0 FA	3	7.1	0.1	272.7	2.9	198.2	0.5
Minimal	Batch (Stationary)	19.4	158.8	cyclo-C19:0 FA	3	6.7	0.1	276.9	5.6	198.9	0.9
Minimal	Batch (Stationary)	158.4	180.4	cyclo-C19:0 FA	3	8.4	0.1	394.0	4.4	217.1	0.7
Minimal	Batch (Stationary)	158.4	180.4	cyclo-C19:0 FA	3	7.6	0.1	380.0	2.9	214.9	0.4
Minimal	Batch (Stationary)	258.0	195.9	cyclo-C19:0 FA	3	7.3	0.2	459.3	9.4	227.3	1.5
Minimal	Batch (Stationary)	258.0	195.9	cyclo-C19:0 FA	3	6.7	0.1	468.9	14.0	228.8	2.2

Table D.7 – Isotopic composition of major (>5%) *P. aeruginosa* lipid components in water fraction factor experiments with Minimal medium. Data is corrected for the effects of derivatization on isotopic composition. Reported error is the standard deviation of the replicate analyses (n) for identical samples. Biological replicates are listed separately.

Medium	Condition	δD_{H_2O} [‰]	${}^2F_{H_2O}$ [ppm]	Compound	n	Peak [$\%_{total}$]	σ [%]	δD_{FA} [‰]	$\sigma_{\delta D}$ [‰]	${}^2F_{FA}$ [ppm]	$\sigma_{^2F}$ [ppm]
SCFM	Batch (Exponential)	-80.5	143.2	C16:1 FA	1	7.5		74.8		167.4	
SCFM	Batch (Exponential)	-80.5	143.2	C16:1 FA	1	7.9		65.8		166.0	
SCFM	Batch (Exponential)	-80.5	143.2	C16:1 FA	1	7.8		72.3		167.0	
SCFM	Batch (Exponential)	1.0	155.9	C16:1 FA	1	7.6		137.3		177.1	
SCFM	Batch (Exponential)	1.0	155.9	C16:1 FA	1	7.7		127.9		175.7	
SCFM	Batch (Exponential)	80.7	168.3	C16:1 FA	1	8.3		167.1		181.8	
SCFM	Batch (Exponential)	80.7	168.3	C16:1 FA	1	7.4		196.7		186.4	
SCFM	Batch (Exponential)	80.7	168.3	C16:1 FA	1	7.3		207.4		188.0	
SCFM	Batch (Exponential)	162.6	181.1	C16:1 FA	1	7.2		258.7		196.0	
SCFM	Batch (Exponential)	162.6	181.1	C16:1 FA	1	8.4		230.4		191.6	
SCFM	Batch (Exponential)	162.6	181.1	C16:1 FA	1	7.2		256.6		195.7	
SCFM	Batch (Exponential)	243.1	193.6	C16:1 FA	1	7.5		304.5		203.2	
SCFM	Batch (Exponential)	243.1	193.6	C16:1 FA	1	7.7		308.0		203.7	
SCFM	Batch (Exponential)	243.1	193.6	C16:1 FA	1	7.2		320.9		205.7	
SCFM	Batch (Exponential)	-80.5	143.2	C16:0 FA	1	37.2		54.8		164.3	
SCFM	Batch (Exponential)	-80.5	143.2	C16:0 FA	1	37.1		49.8		163.5	
SCFM	Batch (Exponential)	-80.5	143.2	C16:0 FA	1	37.0		50.7		163.6	
SCFM	Batch (Exponential)	1.0	155.9	C16:0 FA	1	37.4		120.3		174.5	
SCFM	Batch (Exponential)	1.0	155.9	C16:0 FA	1	36.9		114.5		173.6	
SCFM	Batch (Exponential)	80.7	168.3	C16:0 FA	1	37.5		163.2		181.1	
SCFM	Batch (Exponential)	80.7	168.3	C16:0 FA	1	37.6		192.8		185.8	
SCFM	Batch (Exponential)	80.7	168.3	C16:0 FA	1	37.7		186.8		184.8	
SCFM	Batch (Exponential)	162.6	181.1	C16:0 FA	1	37.7		251.0		194.8	
SCFM	Batch (Exponential)	162.6	181.1	C16:0 FA	1	37.7		235.1		192.3	
SCFM	Batch (Exponential)	162.6	181.1	C16:0 FA	1	38.0		248.6		194.5	
SCFM	Batch (Exponential)	243.1	193.6	C16:0 FA	1	37.3		307.2		203.6	
SCFM	Batch (Exponential)	243.1	193.6	C16:0 FA	1	37.0		305.0		203.2	
SCFM	Batch (Exponential)	243.1	193.6	C16:0 FA	1	37.9		317.5		205.2	
SCFM	Batch (Exponential)	-80.5	143.2	C18:1 FA	1	46.8		64.6		165.8	
SCFM	Batch (Exponential)	-80.5	143.2	C18:1 FA	1	48.5		60.4		165.1	
SCFM	Batch (Exponential)	-80.5	143.2	C18:1 FA	1	47.3		62.6		165.5	
SCFM	Batch (Exponential)	1.0	155.9	C18:1 FA	1	46.9		130.0		176.0	
SCFM	Batch (Exponential)	1.0	155.9	C18:1 FA	1	47.7		122.4		174.8	
SCFM	Batch (Exponential)	80.7	168.3	C18:1 FA	1	49.6		169.9		182.2	
SCFM	Batch (Exponential)	80.7	168.3	C18:1 FA	1	46.6		197.9		186.6	
SCFM	Batch (Exponential)	80.7	168.3	C18:1 FA	1	46.5		193.0		185.8	
SCFM	Batch (Exponential)	162.6	181.1	C18:1 FA	1	46.2		258.7		196.0	
SCFM	Batch (Exponential)	162.6	181.1	C18:1 FA	1	49.5		240.4		193.2	
SCFM	Batch (Exponential)	162.6	181.1	C18:1 FA	1	46.6		256.0		195.6	
SCFM	Batch (Exponential)	243.1	193.6	C18:1 FA	1	47.5		313.4		204.5	
SCFM	Batch (Exponential)	243.1	193.6	C18:1 FA	1	48.0		310.0		204.0	
SCFM	Batch (Exponential)	243.1	193.6	C18:1 FA	1	46.0		323.1		206.0	
SCFM	Batch (Stationary)	-80.5	143.2	C16:1 FA	1	12.0		126.1		175.4	
SCFM	Batch (Stationary)	-80.5	143.2	C16:1 FA	1	11.7		127.1		175.5	
SCFM	Batch (Stationary)	-80.5	143.2	C16:1 FA	1	11.9		125.4		175.3	
SCFM	Batch (Stationary)	1.0	155.9	C16:1 FA	1	12.2		183.8		184.4	
SCFM	Batch (Stationary)	1.0	155.9	C16:1 FA	1	11.6		182.6		184.2	
SCFM	Batch (Stationary)	80.7	168.3	C16:1 FA	1	11.9		229.2		191.4	
SCFM	Batch (Stationary)	80.7	168.3	C16:1 FA	1	12.2		235.1		192.4	
SCFM	Batch (Stationary)	162.6	181.1	C16:1 FA	1	12.5		241.9		193.4	
SCFM	Batch (Stationary)	162.6	181.1	C16:1 FA	1	11.8		296.3		201.9	
SCFM	Batch (Stationary)	162.6	181.1	C16:1 FA	1	11.6		282.7		199.8	
SCFM	Batch (Stationary)	243.1	193.6	C16:1 FA	1	12.4		341.2		208.9	
SCFM	Batch (Stationary)	243.1	193.6	C16:1 FA	1	12.5		347.5		209.9	
SCFM	Batch (Stationary)	243.1	193.6	C16:1 FA	1	12.0		339.7		208.6	
SCFM	Batch (Stationary)	-80.5	143.2	C16:0 FA	1	37.7		144.4		178.2	
SCFM	Batch (Stationary)	-80.5	143.2	C16:0 FA	1	37.1		140.4		177.6	
SCFM	Batch (Stationary)	-80.5	143.2	C16:0 FA	1	38.5		150.6		179.2	
SCFM	Batch (Stationary)	1.0	155.9	C16:0 FA	1	36.2		204.8		187.6	
SCFM	Batch (Stationary)	1.0	155.9	C16:0 FA	1	38.1		206.5		187.9	
SCFM	Batch (Stationary)	80.7	168.3	C16:0 FA	1	38.6		262.3		196.6	
SCFM	Batch (Stationary)	80.7	168.3	C16:0 FA	1	36.1		264.0		196.9	
SCFM	Batch (Stationary)	162.6	181.1	C16:0 FA	1	36.3		273.3		198.3	
SCFM	Batch (Stationary)	162.6	181.1	C16:0 FA	1	36.6		326.7		206.6	
SCFM	Batch (Stationary)	162.6	181.1	C16:0 FA	1	37.2		320.4		205.6	
SCFM	Batch (Stationary)	243.1	193.6	C16:0 FA	1	37.1		383.9		215.5	
SCFM	Batch (Stationary)	243.1	193.6	C16:0 FA	1	36.5		391.9		216.8	
SCFM	Batch (Stationary)	243.1	193.6	C16:0 FA	1	36.5		376.1		214.3	
SCFM	Batch (Stationary)	-80.5	143.2	C18:1 FA	1	48.4		155.1		179.9	
SCFM	Batch (Stationary)	-80.5	143.2	C18:1 FA	1	49.3		151.3		179.3	
SCFM	Batch (Stationary)	-80.5	143.2	C18:1 FA	1	47.5		165.2		181.5	
SCFM	Batch (Stationary)	1.0	155.9	C18:1 FA	1	49.6		210.2		188.5	
SCFM	Batch (Stationary)	1.0	155.9	C18:1 FA	1	48.3		214.9		189.2	
SCFM	Batch (Stationary)	80.7	168.3	C18:1 FA	1	47.6		266.9		197.3	

Medium	Condition	δD_{H_2O} [‰]	${}^2F_{H_2O}$ [ppm]	Compound	n	Peak [$\%_{total}$]	σ [%]	δD_{FA} [‰]	$\sigma_{\delta D}$ [‰]	${}^2F_{FA}$ [ppm]	$\sigma_{^2F}$ [ppm]
Minimal	Batch (Stationary)	-86.4	142.3	a-C15:0 FA	3	45.7	0.4	-151.2	3.2	132.2	0.5
Minimal	Batch (Stationary)	-86.4	142.3	a-C15:0 FA	3	43.1	0.5	-137.4	1.7	134.3	0.3
Minimal	Batch (Stationary)	23.7	159.4	a-C15:0 FA	3	45.8	0.3	-96.3	9.8	140.7	1.5
Minimal	Batch (Stationary)	23.7	159.4	a-C15:0 FA	3	43.9	0.4	-80.2	10.2	143.3	1.6
Minimal	Batch (Stationary)	128.9	175.8	a-C15:0 FA	3	46.8	0.4	-54.3	2.7	147.3	0.4
Minimal	Batch (Stationary)	128.9	175.8	a-C15:0 FA	3	48.9	0.2	-81.7	1.0	143.0	0.2
Minimal	Batch (Stationary)	249.4	194.6	a-C15:0 FA	3	47.6	0.5	8.7	2.2	157.1	0.3
Minimal	Batch (Stationary)	249.4	194.6	a-C15:0 FA	3	47.6	0.5	4.1	2.7	156.4	0.4
Minimal	Batch (Stationary)	-86.4	142.3	a-C17:0 FA	3	20.0	0.4	-116.9	4.4	137.5	0.7
Minimal	Batch (Stationary)	-86.4	142.3	a-C17:0 FA	3	16.1	0.6	-112.3	3.6	138.3	0.6
Minimal	Batch (Stationary)	23.7	159.4	a-C17:0 FA	3	17.9	0.3	-51.2	28.2	147.8	4.4
Minimal	Batch (Stationary)	23.7	159.4	a-C17:0 FA	3	16.7	0.4	-52.7	5.3	147.5	0.8
Minimal	Batch (Stationary)	128.9	175.8	a-C17:0 FA	3	22.0	0.5	-19.0	5.0	152.8	0.8
Minimal	Batch (Stationary)	128.9	175.8	a-C17:0 FA	3	27.3	0.3	-49.8	3.1	148.0	0.5
Minimal	Batch (Stationary)	249.4	194.6	a-C17:0 FA	3	18.9	0.4	44.4	1.8	162.7	0.3
Minimal	Batch (Stationary)	249.4	194.6	a-C17:0 FA	3	22.0	0.2	40.3	3.1	162.0	0.5
Minimal	Batch (Stationary)	-86.4	142.3	C18:0 FA	3	6.8	0.1	-36.1	6.8	150.1	1.1
Minimal	Batch (Stationary)	-86.4	142.3	C18:0 FA	3	11.6	0.1	-17.7	3.4	153.0	0.5
Minimal	Batch (Stationary)	23.7	159.4	C18:0 FA	3	7.2	0.0	32.8	3.9	160.8	0.6
Minimal	Batch (Stationary)	23.7	159.4	C18:0 FA	3	9.4	0.0	45.9	4.2	162.9	0.7
Minimal	Batch (Stationary)	128.9	175.8	C18:0 FA	3	5.8	0.0	63.8	3.7	165.7	0.6
Minimal	Batch (Stationary)	128.9	175.8	C18:0 FA	3	5.8	0.1	-11.4	3.5	154.0	0.5
Minimal	Batch (Stationary)	249.4	194.6	C18:0 FA	3	7.3	0.1	172.9	1.8	182.7	0.3
Minimal	Batch (Stationary)	249.4	194.6	C18:0 FA	3	6.3	0.1	113.5	4.2	173.4	0.7
Minimal	Batch (Stationary)	-86.4	142.3	i/a-C19:0 FA	3	10.7	0.1	-78.6	5.7	143.5	0.9
Minimal	Batch (Stationary)	-86.4	142.3	i/a-C19:0 FA	3	9.0	0.2	-61.2	7.0	146.2	1.1
Minimal	Batch (Stationary)	23.7	159.4	i/a-C19:0 FA	3	10.2	0.1	-18.9	5.4	152.8	0.8
Minimal	Batch (Stationary)	23.7	159.4	i/a-C19:0 FA	3	10.4	0.0	-8.6	2.1	154.4	0.3
Minimal	Batch (Stationary)	128.9	175.8	i/a-C19:0 FA	3	12.1	0.1	25.5	3.3	159.7	0.5
Minimal	Batch (Stationary)	128.9	175.8	i/a-C19:0 FA	3	9.3	0.2	-14.0	4.5	153.6	0.7
Minimal	Batch (Stationary)	249.4	194.6	i/a-C19:0 FA	3	9.7	0.1	90.5	2.6	169.8	0.4
Minimal	Batch (Stationary)	249.4	194.6	i/a-C19:0 FA	3	10.5	0.2	82.3	0.8	168.5	0.1
Minimal	Batch (Stationary)	-86.4	142.3	C20:0 FA	3	10.3	0.0	-23.4	3.2	152.1	0.5
Minimal	Batch (Stationary)	-86.4	142.3	C20:0 FA	3	14.8	0.2	-2.7	3.0	155.3	0.5
Minimal	Batch (Stationary)	23.7	159.4	C20:0 FA	3	13.2	0.6	38.1	2.9	161.7	0.5
Minimal	Batch (Stationary)	23.7	159.4	C20:0 FA	3	14.0	0.2	63.5	2.8	165.6	0.4
Minimal	Batch (Stationary)	128.9	175.8	C20:0 FA	3	8.8	0.1	95.0	2.6	170.5	0.4
Minimal	Batch (Stationary)	128.9	175.8	C20:0 FA	3	5.8	0.1	23.4	2.9	159.4	0.5
Minimal	Batch (Stationary)	249.4	194.6	C20:0 FA	3	10.6	0.2	192.1	3.1	185.7	0.5
Minimal	Batch (Stationary)	249.4	194.6	C20:0 FA	3	7.8	0.2	147.7	6.0	178.7	0.9

Table D.9 – Isotopic composition of major (>5%) *S. aureus* lipid components in water fraction factor experiments with Minimal medium. Data is corrected for the effects of derivatization on isotopic composition. Reported error is the standard deviation of the replicate analyses (n) for identical samples. Biological replicates are listed separately. The component i/a-C19:FA is the combined integration of i-C19:FA and a-C19:FA, which could not be fully resolved with the employed chromatographic program.

Medium	Condition	δD_{H_2O} [‰]	${}^2F_{H_2O}$ [ppm]	Compound	n	Peak [$\%_{total}$]	σ [%]	δD_{FA} [‰]	$\sigma_{\delta D}$ [‰]	${}^2F_{FA}$ [ppm]	$\sigma_{^2F}$ [ppm]
SCFM	Batch (Stationary)	-80.5	143.2	a-C15:0 FA	1	48.7		-97.5		140.6	
SCFM	Batch (Stationary)	-80.5	143.2	a-C15:0 FA	2	54.1	2.5	-53.4	3.4	147.4	0.5
SCFM	Batch (Stationary)	-80.5	143.2	a-C15:0 FA	1	51.7		-80.9		143.1	
SCFM	Batch (Stationary)	1.0	155.9	a-C15:0 FA	1	50.6		-56.7		146.9	
SCFM	Batch (Stationary)	1.0	155.9	a-C15:0 FA	1	50.4		-49.1		148.1	
SCFM	Batch (Stationary)	1.0	155.9	a-C15:0 FA	2	51.4	1.3	-30.9	2.6	150.9	0.4
SCFM	Batch (Stationary)	80.7	168.3	a-C15:0 FA	1	51.6		-19.7		152.7	
SCFM	Batch (Stationary)	80.7	168.3	a-C15:0 FA	1	51.5		-11.9		153.9	
SCFM	Batch (Stationary)	162.6	181.1	a-C15:0 FA	1	53.5		54.0		164.1	
SCFM	Batch (Stationary)	162.6	181.1	a-C15:0 FA	2	50.4	2.2	3.9	5.5	156.3	0.9
SCFM	Batch (Stationary)	162.6	181.1	a-C15:0 FA	1	54.3		53.0		164.0	
SCFM	Batch (Stationary)	243.1	193.6	a-C15:0 FA	2	52.2	1.6	67.3	5.9	166.2	0.9
SCFM	Batch (Stationary)	243.1	193.6	a-C15:0 FA	1	49.5		31.6		160.7	
SCFM	Batch (Stationary)	243.1	193.6	a-C15:0 FA	1	48.6		1.3		155.9	
SCFM	Batch (Stationary)	-80.5	143.2	a-C17:0 FA	1	26.5		-85.9		142.4	
SCFM	Batch (Stationary)	-80.5	143.2	a-C17:0 FA	2	30.8	0.4	-40.4	9.9	149.5	1.5
SCFM	Batch (Stationary)	-80.5	143.2	a-C17:0 FA	1	30.4		-65.6		145.5	
SCFM	Batch (Stationary)	1.0	155.9	a-C17:0 FA	1	28.6		-45.9		148.6	
SCFM	Batch (Stationary)	1.0	155.9	a-C17:0 FA	1	29.9		-32.5		150.7	
SCFM	Batch (Stationary)	1.0	155.9	a-C17:0 FA	2	30.6	0.1	-15.9	5.7	153.3	0.9
SCFM	Batch (Stationary)	80.7	168.3	a-C17:0 FA	1	29.5		-7.6		154.6	
SCFM	Batch (Stationary)	80.7	168.3	a-C17:0 FA	1	30.3		0.5		155.8	
SCFM	Batch (Stationary)	162.6	181.1	a-C17:0 FA	1	32.0		60.9		165.2	
SCFM	Batch (Stationary)	162.6	181.1	a-C17:0 FA	2	27.7	0.1	16.2	16.6	158.3	2.6
SCFM	Batch (Stationary)	162.6	181.1	a-C17:0 FA	1	31.5		59.0		164.9	
SCFM	Batch (Stationary)	243.1	193.6	a-C17:0 FA	2	29.9	0.3	77.8	15.6	167.9	2.4
SCFM	Batch (Stationary)	243.1	193.6	a-C17:0 FA	1	27.7		46.1		162.9	
SCFM	Batch (Stationary)	243.1	193.6	a-C17:0 FA	1	25.9		17.4		158.4	
SCFM	Batch (Stationary)	-80.5	143.2	i/a-C19:0 FA	1	11.4		-93.5		141.2	
SCFM	Batch (Stationary)	-80.5	143.2	i/a-C19:0 FA	2	7.1	0.5	-54.6	19.9	147.2	3.1
SCFM	Batch (Stationary)	-80.5	143.2	i/a-C19:0 FA	1	8.1		-72.3		144.5	
SCFM	Batch (Stationary)	1.0	155.9	i/a-C19:0 FA	1	8.7		-54.3		147.3	
SCFM	Batch (Stationary)	1.0	155.9	i/a-C19:0 FA	1	9.3		-39.2		149.6	
SCFM	Batch (Stationary)	1.0	155.9	i/a-C19:0 FA	2	8.0	0.4	-20.2	14.0	152.6	2.2
SCFM	Batch (Stationary)	80.7	168.3	i/a-C19:0 FA	1	8.5		-15.1		153.4	
SCFM	Batch (Stationary)	80.7	168.3	i/a-C19:0 FA	1	9.2		-4.5		155.0	
SCFM	Batch (Stationary)	162.6	181.1	i/a-C19:0 FA	1	7.0		40.7		162.1	
SCFM	Batch (Stationary)	162.6	181.1	i/a-C19:0 FA	2	8.6	0.6	1.3	10.6	155.9	1.7
SCFM	Batch (Stationary)	162.6	181.1	i/a-C19:0 FA	1	6.7		30.5		160.5	
SCFM	Batch (Stationary)	243.1	193.6	i/a-C19:0 FA	2	7.5	0.4	54.8	22.5	164.3	3.5
SCFM	Batch (Stationary)	243.1	193.6	i/a-C19:0 FA	1	8.7		33.5		161.0	
SCFM	Batch (Stationary)	243.1	193.6	i/a-C19:0 FA	1	9.6		10.2		157.3	

Table D.10 – Isotopic composition of major (>5%) *S. aureus* lipid components in water fraction factor experiments with SCFM medium. Data is corrected for the effects of derivatization on isotopic composition. Reported error is the standard deviation of the replicate analyses (n) for identical samples. Biological replicates are listed separately. The component i/a-C19:FA is the combined integration of i-C19:FA and a-C19:FA, which could not be fully resolved with the employed chromatographic program.

Medium	Condition	δD_{H_2O} [‰]	${}^2F_{H_2O}$ [ppm]	Compound	n	Peak [$\%_{total}$]	σ [%]	δD_{FA} [‰]	$\sigma_{\delta D}$ [‰]	${}^2F_{FA}$ [ppm]	$\sigma_{^2F}$ [ppm]
SCFM	Batch (Stationary)	-80.5	143.2	C14:0 FA	1	4.8		-12.4		153.8	
SCFM	Batch (Stationary)	-80.5	143.2	C14:0 FA	1	5.1		-20.9		152.5	
SCFM	Batch (Stationary)	-80.5	143.2	C14:0 FA	1	4.9		-17.8		153.0	
SCFM	Batch (Stationary)	1.0	155.9	C14:0 FA	1	4.9		38.4		161.7	
SCFM	Batch (Stationary)	1.0	155.9	C14:0 FA	1	4.9		35.4		161.3	
SCFM	Batch (Stationary)	1.0	155.9	C14:0 FA	1	4.9		33.5		161.0	
SCFM	Batch (Stationary)	80.7	168.3	C14:0 FA	1	5.2		91.0		169.9	
SCFM	Batch (Stationary)	162.6	181.1	C14:0 FA	1	5.1		143.2		178.0	
SCFM	Batch (Stationary)	162.6	181.1	C14:0 FA	1	4.8		143.3		178.1	
SCFM	Batch (Stationary)	162.6	181.1	C14:0 FA	1	4.8		138.7		177.3	
SCFM	Batch (Stationary)	243.1	193.6	C14:0 FA	1	4.8		190.1		185.3	
SCFM	Batch (Stationary)	243.1	193.6	C14:0 FA	1	5.0		191.2		185.5	
SCFM	Batch (Stationary)	243.1	193.6	C14:0 FA	1	4.9		193.6		185.9	
SCFM	Batch (Stationary)	-80.5	143.2	i-C15:0 FA	1	59.0		-35.5		150.2	
SCFM	Batch (Stationary)	-80.5	143.2	i-C15:0 FA	1	60.7		-38.8		149.7	
SCFM	Batch (Stationary)	-80.5	143.2	i-C15:0 FA	1	59.9		-38.6		149.7	
SCFM	Batch (Stationary)	1.0	155.9	i-C15:0 FA	1	58.8		2.7		156.2	
SCFM	Batch (Stationary)	1.0	155.9	i-C15:0 FA	1	59.9		1.8		156.0	
SCFM	Batch (Stationary)	1.0	155.9	i-C15:0 FA	1	59.3		-1.4		155.5	
SCFM	Batch (Stationary)	80.7	168.3	i-C15:0 FA	1	60.4		51.0		163.7	
SCFM	Batch (Stationary)	162.6	181.1	i-C15:0 FA	1	59.1		85.2		169.0	
SCFM	Batch (Stationary)	162.6	181.1	i-C15:0 FA	1	59.5		84.7		168.9	
SCFM	Batch (Stationary)	162.6	181.1	i-C15:0 FA	1	59.2		83.7		168.8	
SCFM	Batch (Stationary)	243.1	193.6	i-C15:0 FA	1	59.7		127.2		175.5	
SCFM	Batch (Stationary)	243.1	193.6	i-C15:0 FA	1	60.6		129.3		175.9	
SCFM	Batch (Stationary)	243.1	193.6	i-C15:0 FA	1	59.7		134.7		176.7	
SCFM	Batch (Stationary)	-80.5	143.2	a-C15:0 FA	1	17.0		-52.9		147.5	
SCFM	Batch (Stationary)	-80.5	143.2	a-C15:0 FA	1	16.0		-52.5		147.6	
SCFM	Batch (Stationary)	-80.5	143.2	a-C15:0 FA	1	16.6		-49.7		148.0	
SCFM	Batch (Stationary)	1.0	155.9	a-C15:0 FA	1	17.8		-4.9		155.0	
SCFM	Batch (Stationary)	1.0	155.9	a-C15:0 FA	1	17.0		-6.4		154.7	
SCFM	Batch (Stationary)	1.0	155.9	a-C15:0 FA	1	17.7		-8.5		154.4	
SCFM	Batch (Stationary)	80.7	168.3	a-C15:0 FA	1	16.4		36.1		161.4	
SCFM	Batch (Stationary)	162.6	181.1	a-C15:0 FA	1	17.4		80.5		168.3	
SCFM	Batch (Stationary)	162.6	181.1	a-C15:0 FA	1	17.4		79.5		168.1	
SCFM	Batch (Stationary)	162.6	181.1	a-C15:0 FA	1	17.7		76.0		167.6	
SCFM	Batch (Stationary)	243.1	193.6	a-C15:0 FA	1	17.6		118.9		174.3	
SCFM	Batch (Stationary)	243.1	193.6	a-C15:0 FA	1	16.6		117.2		174.0	
SCFM	Batch (Stationary)	243.1	193.6	a-C15:0 FA	1	17.4		124.9		175.2	
SCFM	Batch (Stationary)	-80.5	143.2	C16:0 FA	1	11.4		2.6		156.1	
SCFM	Batch (Stationary)	-80.5	143.2	C16:0 FA	1	11.3		-0.7		155.6	
SCFM	Batch (Stationary)	-80.5	143.2	C16:0 FA	1	11.0		-0.6		155.6	
SCFM	Batch (Stationary)	1.0	155.9	C16:0 FA	1	11.2		59.5		165.0	
SCFM	Batch (Stationary)	1.0	155.9	C16:0 FA	1	10.9		65.5		165.9	
SCFM	Batch (Stationary)	1.0	155.9	C16:0 FA	1	11.0		58.9		164.9	
SCFM	Batch (Stationary)	80.7	168.3	C16:0 FA	1	11.0		129.7		175.9	
SCFM	Batch (Stationary)	162.6	181.1	C16:0 FA	1	11.4		178.1		183.5	
SCFM	Batch (Stationary)	162.6	181.1	C16:0 FA	1	11.0		172.7		182.6	
SCFM	Batch (Stationary)	162.6	181.1	C16:0 FA	1	11.4		176.0		183.1	
SCFM	Batch (Stationary)	243.1	193.6	C16:0 FA	1	11.2		233.6		192.1	
SCFM	Batch (Stationary)	243.1	193.6	C16:0 FA	1	11.2		241.5		193.3	
SCFM	Batch (Stationary)	243.1	193.6	C16:0 FA	1	11.3		246.1		194.1	

Table D.11 – Isotopic composition of major (>5%) *S. maltophilia* lipid components in water fraction factor experiments with SCFM medium. Data is corrected for the effects of derivatization on isotopic composition. Reported error is the standard deviation of the replicate analyses (n) for identical samples. Biological replicates are listed separately.

Medium	Generation time	Time after spike	Compound	n	Peak $[\%_{total}]$	$\delta^2 H_{FA}$ [‰]	σ_δ [‰]	${}^2F_{FA}$ $[ppm]$	σ_{2_F} $[ppm]$
Minimal	2.16 hours	0 seconds	C16:1 FA	3	10.9	18.8	6.5	158.7	1.0
Minimal	2.16 hours	5 minutes	C16:1 FA	3	10.9	109.6	5.1	172.8	0.8
Minimal	2.16 hours	10 minutes	C16:1 FA	3	10.9	212.1	1.0	188.8	0.2
Minimal	2.16 hours	15 minutes	C16:1 FA	3	10.8	304.9	1.4	203.2	0.2
Minimal	2.16 hours	20 minutes	C16:1 FA	3	11.3	403.3	3.0	218.5	0.5
Minimal	2.16 hours	25 minutes	C16:1 FA	3	11.0	499.4	5.1	233.5	0.8
Minimal	2.16 hours	0 seconds	C16:0 FA	3	40.6	45.0	3.5	162.7	0.5
Minimal	2.16 hours	5 minutes	C16:0 FA	3	39.9	264.0	9.9	196.8	1.5
Minimal	2.16 hours	10 minutes	C16:0 FA	3	40.0	490.8	7.4	232.2	1.2
Minimal	2.16 hours	15 minutes	C16:0 FA	3	39.3	691.0	10.0	263.3	1.6
Minimal	2.16 hours	20 minutes	C16:0 FA	3	39.7	901.1	6.7	296.0	1.0
Minimal	2.16 hours	25 minutes	C16:0 FA	3	39.3	1064.4	5.7	321.4	0.9
Minimal	2.16 hours	0 seconds	C18:1 FA	3	45.3	44.5	4.4	162.7	0.7
Minimal	2.16 hours	5 minutes	C18:1 FA	3	45.0	223.7	3.1	190.6	0.5
Minimal	2.16 hours	10 minutes	C18:1 FA	3	45.8	402.7	2.9	218.5	0.5
Minimal	2.16 hours	15 minutes	C18:1 FA	3	45.8	572.3	3.9	244.8	0.6
Minimal	2.16 hours	20 minutes	C18:1 FA	3	45.7	731.5	3.7	269.6	0.6
Minimal	2.16 hours	25 minutes	C18:1 FA	3	45.9	878.6	4.4	292.5	0.7
Minimal	16.22 hours	0 seconds	C16:1 FA	6	8.5	61.5	11.9	165.3	1.8
Minimal	16.22 hours	30 minutes	C16:1 FA	6	8.1	222.5	11.4	190.4	1.8
Minimal	16.22 hours	1 hours	C16:1 FA	6	8.3	377.0	23.5	214.4	3.7
Minimal	16.22 hours	1.5 hours	C16:1 FA	5	8.0	502.3	37.6	233.9	5.9
Minimal	16.22 hours	2 hours	C16:1 FA	5	8.1	661.9	41.5	258.8	6.5
Minimal	16.22 hours	2.5 hours	C16:1 FA	6	8.4	824.0	44.3	284.0	6.9
Minimal	16.22 hours	0 seconds	C16:0 FA	6	42.4	97.8	4.0	171.0	0.6
Minimal	16.22 hours	30 minutes	C16:0 FA	6	41.4	389.5	10.3	216.4	1.6
Minimal	16.22 hours	1 hours	C16:0 FA	6	41.9	657.7	16.6	258.1	2.6
Minimal	16.22 hours	1.5 hours	C16:0 FA	5	43.3	890.6	24.1	294.4	3.8
Minimal	16.22 hours	2 hours	C16:0 FA	5	41.8	1137.7	25.8	332.9	4.0
Minimal	16.22 hours	2.5 hours	C16:0 FA	6	42.1	1355.2	36.7	366.7	5.7
Minimal	16.22 hours	0 seconds	C18:1 FA	6	37.6	98.2	3.7	171.0	0.6
Minimal	16.22 hours	30 minutes	C18:1 FA	6	37.9	325.7	7.0	206.4	1.1
Minimal	16.22 hours	1 hours	C18:1 FA	6	38.3	538.5	10.6	239.6	1.6
Minimal	16.22 hours	1.5 hours	C18:1 FA	5	39.3	724.9	17.5	268.6	2.7
Minimal	16.22 hours	2 hours	C18:1 FA	5	38.6	927.8	17.7	300.2	2.8
Minimal	16.22 hours	2.5 hours	C18:1 FA	6	38.0	1104.9	23.2	327.8	3.6
Minimal	16.22 hours	0 seconds	cyclo-C19:0 FA	3	8.4	115.1	3.6	173.7	0.6
Minimal	16.22 hours	30 minutes	cyclo-C19:0 FA	6	8.6	120.3	7.0	174.5	1.1
Minimal	16.22 hours	1 hours	cyclo-C19:0 FA	6	8.6	138.2	5.4	177.3	0.8
Minimal	16.22 hours	1.5 hours	cyclo-C19:0 FA	2	9.4	165.1	0.1	181.4	0.0
Minimal	16.22 hours	2 hours	cyclo-C19:0 FA	5	8.6	200.0	8.5	186.9	1.3
Minimal	16.22 hours	2.5 hours	cyclo-C19:0 FA	6	8.5	236.4	12.3	192.5	1.9
SCFM	5.35 days	0 seconds	C16:0 FA	2	48.7	-25.3	8.2	151.8	1.3
SCFM	5.35 days	2 hours	C16:0 FA	3	49.6	168.0	13.7	181.9	2.1
SCFM	5.35 days	4 hours	C16:0 FA	2	49.5	393.8	31.8	217.0	4.9
SCFM	5.35 days	6 hours	C16:0 FA	3	48.4	611.9	15.8	251.0	2.5
SCFM	5.35 days	8 hours	C16:0 FA	2	53.7	761.2	15.1	274.3	2.3
SCFM	5.35 days	10 hours	C16:0 FA	3	49.8	992.3	24.3	310.2	3.8
SCFM	5.35 days	0 seconds	C18:1 FA	2	14.5	-20.2	9.4	152.6	1.5
SCFM	5.35 days	2 hours	C18:1 FA	3	14.2	285.5	16.4	200.2	2.5
SCFM	5.35 days	4 hours	C18:1 FA	2	15.0	612.5	105.2	251.1	16.4
SCFM	5.35 days	6 hours	C18:1 FA	3	13.9	954.0	42.9	304.3	6.7
SCFM	5.35 days	8 hours	C18:1 FA	2	15.3	1194.5	59.7	341.7	9.3
SCFM	5.35 days	10 hours	C18:1 FA	3	14.4	1464.4	75.3	383.7	11.7
SCFM	5.35 days	0 seconds	cyclo-C19:0 FA	2	27.5	-11.1	14.6	154.0	2.3
SCFM	5.35 days	2 hours	cyclo-C19:0 FA	3	26.6	-3.2	11.8	155.2	1.8
SCFM	5.35 days	4 hours	cyclo-C19:0 FA	2	26.3	30.0	10.8	160.4	1.7
SCFM	5.35 days	6 hours	cyclo-C19:0 FA	3	28.4	71.5	9.3	166.9	1.5
SCFM	5.35 days	8 hours	cyclo-C19:0 FA	2	26.9	106.9	8.9	172.4	1.4
SCFM	5.35 days	10 hours	cyclo-C19:0 FA	3	26.3	180.3	12.2	183.8	1.9

Table D.12 – Isotopic composition of major (>5%) *P. aeruginosa* lipid components in isotope labeling experiments. Data is corrected for the effects of derivatization on isotopic composition. Reported error is the standard deviation of the replicate analyses (n) for identical samples.

Medium	Generation time	Time after spike	Compound	n	Peak $[\%_{total}]$	δ^2H_{FA} [‰]	σ_δ [‰]	${}^2F_{FA}$ $[ppm]$	$\sigma_{{}^2F}$ $[ppm]$
Minimal	6.38 hours	0 seconds	a-C15:0 FA	2	64.5	-149.3	6.4	132.5	1.0
Minimal	6.38 hours	10 minutes	a-C15:0 FA	3	65.3	-19.0	9.5	152.8	1.5
Minimal	6.38 hours	20 minutes	a-C15:0 FA	2	61.7	127.2	8.9	175.6	1.4
Minimal	6.38 hours	30 minutes	a-C15:0 FA	3	57.7	230.9	12.3	191.7	1.9
Minimal	6.38 hours	40 minutes	a-C15:0 FA	2	49.9	344.6	4.4	209.4	0.7
Minimal	6.38 hours	50 minutes	a-C15:0 FA	2	57.5	512.0	20.7	235.5	3.2
Minimal	6.38 hours	1 hours	a-C15:0 FA	2	63.9	622.5	35.7	252.7	5.6
Minimal	6.38 hours	0 seconds	a-C17:0 FA	1	35.5	-143.6		133.4	
Minimal	6.38 hours	10 minutes	a-C17:0 FA	2	34.7	-25.1	1.6	151.8	0.3
Minimal	6.38 hours	20 minutes	a-C17:0 FA	2	38.3	97.1	5.2	170.9	0.8
Minimal	6.38 hours	30 minutes	a-C17:0 FA	1	42.3	219.2		189.9	
Minimal	6.38 hours	40 minutes	a-C17:0 FA	2	50.1	317.7	7.0	205.2	1.1
Minimal	6.38 hours	50 minutes	a-C17:0 FA	2	42.5	437.2	7.3	223.8	1.1
Minimal	6.38 hours	1 hours	a-C17:0 FA	1	36.1	562.4		243.3	
Minimal	1.24 days	0 seconds	a-C15:0 FA	3	63.0	-95.3	5.0	140.9	0.8
Minimal	1.24 days	40 minutes	a-C15:0 FA	2	63.6	29.6	1.8	160.3	0.3
Minimal	1.24 days	1.37 hours	a-C15:0 FA	2	59.1	195.9	1.3	186.2	0.2
Minimal	1.24 days	2 hours	a-C15:0 FA	2	53.9	332.7	5.1	207.5	0.8
Minimal	1.24 days	2.67 hours	a-C15:0 FA	2	56.8	503.0	7.7	234.1	1.2
Minimal	1.24 days	3.33 hours	a-C15:0 FA	2	57.2	628.5	14.0	253.6	2.2
Minimal	1.24 days	0 seconds	a-C17:0 FA	3	37.0	-60.1	0.9	146.4	0.1
Minimal	1.24 days	40 minutes	a-C17:0 FA	2	36.4	19.1	4.3	158.7	0.7
Minimal	1.24 days	1.37 hours	a-C17:0 FA	2	40.9	130.4	4.5	176.0	0.7
Minimal	1.24 days	2 hours	a-C17:0 FA	2	46.1	219.7	2.2	189.9	0.3
Minimal	1.24 days	2.67 hours	a-C17:0 FA	2	43.2	330.9	5.4	207.3	0.8
Minimal	1.24 days	3.33 hours	a-C17:0 FA	2	42.8	415.0	4.1	220.4	0.6
SCFM	4.91 days	0 seconds	a-C15:0 FA	3	53.2	-70.7	18.4	144.7	2.9
SCFM	4.91 days	2 hours	a-C15:0 FA	3	53.9	-5.1	21.4	155.0	3.3
SCFM	4.91 days	4 hours	a-C15:0 FA	3	53.6	69.6	26.2	166.6	4.1
SCFM	4.91 days	6 hours	a-C15:0 FA	3	53.6	159.8	29.9	180.6	4.7
SCFM	4.91 days	8 hours	a-C15:0 FA	3	53.9	214.0	31.9	189.1	5.0
SCFM	4.91 days	10 hours	a-C15:0 FA	3	55.4	292.8	27.9	201.3	4.3
SCFM	4.91 days	0 seconds	a-C17:0 FA	3	31.7	-77.6	22.2	143.7	3.5
SCFM	4.91 days	2 hours	a-C17:0 FA	3	31.5	-44.7	22.7	148.8	3.5
SCFM	4.91 days	4 hours	a-C17:0 FA	3	31.8	-11.5	21.1	154.0	3.3
SCFM	4.91 days	6 hours	a-C17:0 FA	3	31.9	36.5	22.1	161.4	3.4
SCFM	4.91 days	8 hours	a-C17:0 FA	3	31.4	65.0	26.4	165.9	4.1
SCFM	4.91 days	10 hours	a-C17:0 FA	3	30.8	128.0	32.4	175.7	5.0
SCFM	4.91 days	0 seconds	i/a-C19:0 FA	3	9.8	-61.4	12.3	146.2	1.9
SCFM	4.91 days	2 hours	i/a-C19:0 FA	3	9.7	-32.6	13.8	150.7	2.1
SCFM	4.91 days	4 hours	i/a-C19:0 FA	3	9.5	-8.0	11.8	154.5	1.8
SCFM	4.91 days	6 hours	i/a-C19:0 FA	3	9.9	24.4	8.4	159.5	1.3
SCFM	4.91 days	8 hours	i/a-C19:0 FA	3	9.4	53.4	10.4	164.1	1.6
SCFM	4.91 days	10 hours	i/a-C19:0 FA	3	9.3	98.6	15.2	171.1	2.4
Minimal	13.34 days	0 seconds	a-C15:0 FA	5	50.4	-87.4	10.7	142.1	1.7
Minimal	13.34 days	5 hours	a-C15:0 FA	5	53.1	69.6	8.4	166.6	1.3
Minimal	13.34 days	10 hours	a-C15:0 FA	4	50.9	242.1	20.7	193.4	3.2
Minimal	13.34 days	15 hours	a-C15:0 FA	4	47.6	402.3	30.7	218.4	4.8
Minimal	13.34 days	20 hours	a-C15:0 FA	4	47.7	570.6	37.0	244.6	5.8
Minimal	13.34 days	1.04 days	a-C15:0 FA	4	54.8	762.0	39.9	274.4	6.2
Minimal	13.34 days	1.25 days	a-C15:0 FA	4	59.7	995.6	47.6	310.7	7.4
Minimal	13.34 days	0 seconds	a-C17:0 FA	4	49.6	-61.3	12.7	146.2	2.0
Minimal	13.34 days	5 hours	a-C17:0 FA	3	46.9	60.6	19.9	165.2	3.1
Minimal	13.34 days	10 hours	a-C17:0 FA	3	49.1	209.0	24.4	188.3	3.8
Minimal	13.34 days	15 hours	a-C17:0 FA	3	52.4	352.4	31.1	210.6	4.8
Minimal	13.34 days	20 hours	a-C17:0 FA	4	52.3	496.4	36.2	233.0	5.6
Minimal	13.34 days	1.04 days	a-C17:0 FA	4	45.2	666.0	44.0	259.4	6.9
Minimal	13.34 days	1.25 days	a-C17:0 FA	4	40.3	864.8	56.7	290.4	8.8

Table D.13 – Isotopic composition of major (>5%) *S. aureus* lipid components in isotope labeling experiments. Data is corrected for the effects of derivatization on isotopic composition. Reported error is the standard deviation of the replicate analyses (n) for identical samples.

Medium	Generation time	Time after spike	Compound	n	Peak $[\%_{total}]$	$\delta^2 H_{FA}$ [‰]	σ_δ [‰]	${}^2F_{FA}$ $[ppm]$	$\sigma_{{}^2F}$ $[ppm]$
Minimal	2.29 hours	0 seconds	C16:1 FA	3	27.5	-126.2	2.5	136.1	0.4
Minimal	2.29 hours	5 minutes	C16:1 FA	3	27.7	46.0	2.3	162.9	0.4
Minimal	2.29 hours	10 minutes	C16:1 FA	3	26.4	201.8	4.1	187.2	0.6
Minimal	2.29 hours	15 minutes	C16:1 FA	3	27.9	354.8	3.0	211.0	0.5
Minimal	2.29 hours	20 minutes	C16:1 FA	3	27.0	486.6	12.1	231.5	1.9
Minimal	2.29 hours	25 minutes	C16:1 FA	3	27.1	633.1	1.9	254.3	0.3
Minimal	2.29 hours	0 seconds	C16:0 FA	3	41.3	-113.3	0.7	138.1	0.1
Minimal	2.29 hours	5 minutes	C16:0 FA	3	41.6	12.6	3.9	157.7	0.6
Minimal	2.29 hours	10 minutes	C16:0 FA	3	41.3	140.7	1.5	177.6	0.2
Minimal	2.29 hours	15 minutes	C16:0 FA	3	41.5	267.2	8.9	197.3	1.4
Minimal	2.29 hours	20 minutes	C16:0 FA	3	41.5	376.2	6.2	214.3	1.0
Minimal	2.29 hours	25 minutes	C16:0 FA	3	41.6	497.9	2.0	233.3	0.3
Minimal	2.29 hours	0 seconds	cyclo-C17:0 FA	3	12.5	-100.0	5.3	140.2	0.8
Minimal	2.29 hours	5 minutes	cyclo-C17:0 FA	3	12.3	-89.2	9.6	141.8	1.5
Minimal	2.29 hours	10 minutes	cyclo-C17:0 FA	3	12.9	-65.0	4.4	145.6	0.7
Minimal	2.29 hours	15 minutes	cyclo-C17:0 FA	3	12.3	-34.2	8.2	150.4	1.3
Minimal	2.29 hours	20 minutes	cyclo-C17:0 FA	3	12.7	-17.2	7.7	153.1	1.2
Minimal	2.29 hours	25 minutes	cyclo-C17:0 FA	3	12.6	8.4	0.9	157.1	0.1
Minimal	2.29 hours	0 seconds	C18:1 FA	3	18.7	-122.5	8.9	136.7	1.4
Minimal	2.29 hours	5 minutes	C18:1 FA	3	18.3	-0.1	13.4	155.7	2.1
Minimal	2.29 hours	10 minutes	C18:1 FA	3	19.4	105.3	5.5	172.1	0.9
Minimal	2.29 hours	15 minutes	C18:1 FA	3	18.3	228.3	4.7	191.3	0.7
Minimal	2.29 hours	20 minutes	C18:1 FA	3	18.9	303.0	11.9	202.9	1.9
Minimal	2.29 hours	25 minutes	C18:1 FA	3	18.7	412.0	1.9	219.9	0.3

Table D.14 – Isotopic composition of major (>5%) *E. coli* lipid components in isotope labeling experiments. Data is corrected for the effects of derivatization on isotopic composition. Reported error is the standard deviation of the replicate analyses (n) for identical samples.

FAME	Label	Experiment	Peak $[\%_{total}]$	σ $[\%]$
i-C15	natural	Control	2.65	0.41
i-C15	natural	+ $^2H\,C_{15:0}$	0.73	0.17
i-C15	natural	+ $^2H\,C_{18:0}$	0.59	0.12
a-C15	natural	Control	39.59	1.56
a-C15	natural	+ $^2H\,C_{15:0}$	18.63	3.48
a-C15	natural	+ $^2H\,C_{18:0}$	17.64	2.99
C15	perdeuterated	Control	0.00	0.00
C15	perdeuterated	+ $^2H\,C_{15:0}$	4.92	0.83
C15	perdeuterated	+ $^2H\,C_{18:0}$	0.00	0.01
C16	natural	Control	1.07	0.22
C16	natural	+ $^2H\,C_{15:0}$	0.17	0.10
C16	natural	+ $^2H\,C_{18:0}$	0.17	0.12
C16	perdeuterated	Control	0.00	0.00
C16	perdeuterated	+ $^2H\,C_{15:0}$	0.00	0.00
C16	perdeuterated	+ $^2H\,C_{18:0}$	0.01	0.01
C17	natural	Control	0.10	0.07
C17	natural	+ $^2H\,C_{15:0}$	0.02	0.02
C17	natural	+ $^2H\,C_{18:0}$	0.02	0.01
i-C17	natural	Control	2.70	0.44
i-C17	natural	+ $^2H\,C_{15:0}$	0.02	0.03
i-C17	natural	+ $^2H\,C_{18:0}$	0.10	0.08
a-C17	natural	Control	41.01	1.44
a-C17	natural	+ $^2H\,C_{15:0}$	2.03	0.16
a-C17	natural	+ $^2H\,C_{18:0}$	5.69	0.23
C17	partly deuterated	Control	0.00	0.00
C17	partly deuterated	+ $^2H\,C_{15:0}$	21.53	0.98
C17	partly deuterated	+ $^2H\,C_{18:0}$	0.00	0.00
C18	natural	Control	7.14	0.46
C18	natural	+ $^2H\,C_{15:0}$	1.13	0.10
C18	natural	+ $^2H\,C_{18:0}$	1.06	0.07
C18	perdeuterated	Control	0.00	0.00
C18	perdeuterated	+ $^2H\,C_{15:0}$	0.00	0.00
C18	perdeuterated	+ $^2H\,C_{18:0}$	62.20	2.53
C19	partly deuterated	Control	0.00	0.00
C19	partly deuterated	+ $^2H\,C_{15:0}$	50.17	3.38
C19	partly deuterated	+ $^2H\,C_{18:0}$	0.00	0.00
C20	natural	Control	5.74	0.88
C20	natural	+ $^2H\,C_{15:0}$	0.65	0.10
C20	natural	+ $^2H\,C_{18:0}$	0.36	0.06
C20	partly deuterated	Control	0.00	0.00
C20	partly deuterated	+ $^2H\,C_{15:0}$	0.00	0.00
C20	partly deuterated	+ $^2H\,C_{18:0}$	12.26	0.76

Table D.15 – Recycling of exogenous fatty acids by *S. aureus*. Summary of the fatty acid profiles from recycling fatty acid experiments.

Appendix E

Supplementary material for Chapter 8

E.1 Error from shot noise

The number of ions N observed at a detector in a fixed time interval *t* follows a Poisson distribution. The corresponding probability mass function is $f(N) = P(X = N) = \frac{(at)^N e^{-at}}{N!}$. The expected value $E[N] = \bar{N}$ (mean) of a Poisson distribution is $\bar{N} = at$ (for a fixed time interval t). The variance $Var[N]$ of a Poisson distribution is identical to the expected value, and hence the standard deviation σ_N scales with the square root of $\bar{N}$ $\left(\sigma_N = \sqrt{Var[N]} = \sqrt{\bar{N}}\right)$. This has two important consequences for the quantification of ion currents:

- The relative error $\frac{\sigma_N}{N} = \frac{1}{\sqrt{N}}$ decreases with higher ion counts (i.e. longer counting at constant rates makes the measurement more precise)
- There are diminishing returns due to the $\sqrt{N}^{-1}$ dependence

As a concrete example, consider an ion current of 1000 ions/s. If you repeatedly observed this ion beam for exactly 1s, you would detect 1000 ions *on average*, but with $\sigma_N = 31.6$

(or 3.16% error). If you repeatedly observed this same ion beam for 2s instead, you would detect 2000 ions on average, but with $\sigma_N = 44.7$ (or 2.24% error, a $\sqrt{2}^{-1}$ improvement). This counting error ($\sigma_N = \sqrt{N}$) is propagated readily to the resulting isotope ratios $R = \frac{i_m}{i_M}$ (m=minor,M=major isotope), fractional abundances $F = \frac{i_m}{i_M + i_m}$ and δ-values $\delta = \frac{R_1}{R_2} - 1$ by standard error propagation. For details on σ_R and σ_δ, see Hayes (2001). σ_F is derived as follows.

$$\begin{aligned}
\sigma_F^2 &= \left(\frac{\partial F}{\partial N_m}\right)^2 \sigma_{N_m}^2 + \left(\frac{\partial F}{\partial N_M}\right)^2 \sigma_{N_M}^2 = \left(\frac{N_M}{(N_m + N_M)^2}\right)^2 \sigma_{N_m}^2 + \left(-\frac{N_m}{(N_m + N_M)^2}\right)^2 \sigma_{N_M}^2 \\
&= \frac{N_M^2 N_m^2}{(N_m + N_M)^4} \left[\left(\frac{\sigma_{N_m}}{N_m}\right)^2 + \left(\frac{\sigma_{N_M}}{N_M}\right)^2\right] = F^2 (1 - F)^2 \left[\left(\frac{\sigma_{N_m}}{N_m}\right)^2 + \left(\frac{\sigma_{N_M}}{N_M}\right)^2\right] \\
&\rightarrow \left(\frac{\sigma_F}{F}\right)^2 = (1 - F)^2 \left(\frac{1}{N_m} + \frac{1}{N_M}\right) = \frac{(1 - F)^2}{N_M F}
\end{aligned} \tag{E.1}$$

References

Hayes, J. M., 2001. Fractionation of carbon and hydrogen isotopes in biosynthetic processes. Geochemistry Of Non-Traditional Stable Isotopes 43, 225–277.

E.2 NanoSIMS analytical details

E.2.1 Quality control

As described in Section 8.2.4.3, single cell analyses of isotopic standards were processed with a quality-control algorithm to control for distortions by sample destruction. ROIs with isotopic value F_i in any frame deviating by more than $2 \cdot \sigma_F$ (eq. 8.1) and more than 1% from the frames' accumulated average F were discarded. This algorithm automatically discarded 35% of all data points from whole single cell analysis and 7% of all data points from embedded single cell analysis, consistent with the much stronger effects of sample

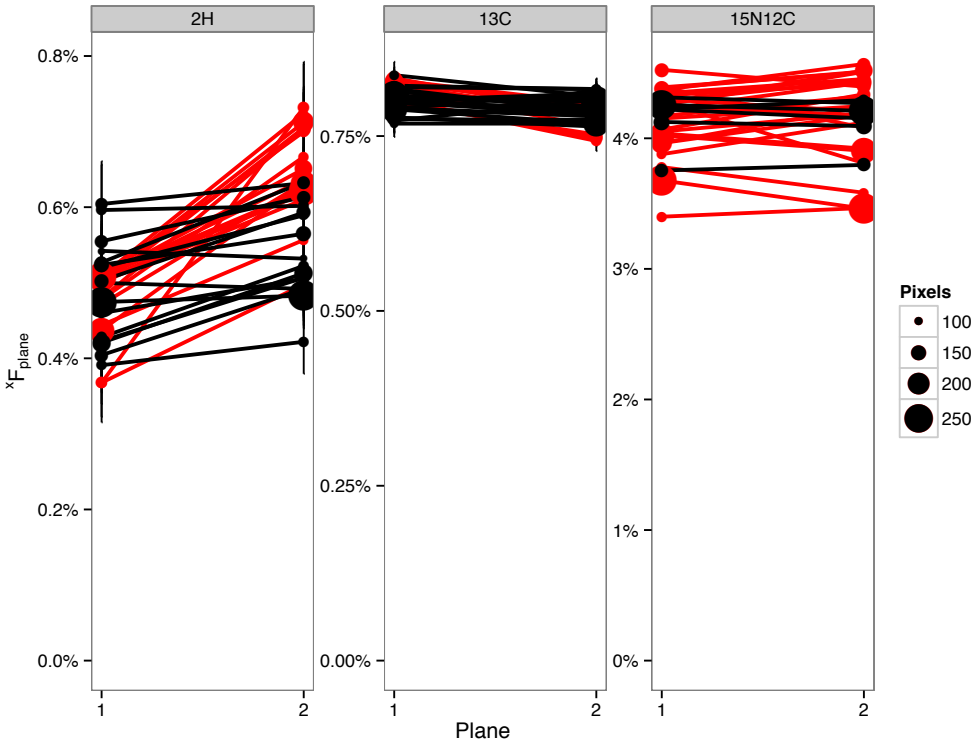

Figure E.1 – ROI quality control.

destruction on single whole cells than on embedded cells, as described in detail in Section 8.3.1.1. Figure E.1 shows data from one whole cell analysis (~20 cells) where rapid sample ablation destroyed part of the cells, and illustrates which data points were automatically discarded.

E.2.2 Single cell data

Organism	$^{2}H\,F_{fa}$ [%]	$^{15}N\,F_{bulk}$ [%]	$^{13}C\,F_{bulk}$ [%]
P. aeruginosa	0.017 ± 0.000	0.360 ± 0.003	1.084 ± 0.001
P. aeruginosa	0.030 ± 0.001	0.378 ± 0.002	1.198 ± 0.007
P. aeruginosa	0.177 ± 0.006	1.485 ± 0.007	1.646 ± 0.001
P. aeruginosa	0.237 ± 0.006	3.828 ± 0.044	2.152 ± 0.007
P. aeruginosa	0.599 ± 0.042	10.247 ± 0.120	10.657 ± 0.102
S. aureus	0.013 ± 0.000	0.364 ± 0.005	
S. aureus	0.026 ± 0.000	0.369 ± 0.004	
S. aureus	0.080 ± 0.002	0.860 ± 0.029	
S. aureus	0.276 ± 0.011	0.959 ± 0.001	
S. aureus	0.689 ± 0.056	4.496 ± 0.098	

Table E.1 – Bulk isotopic composition of microbial NanoSIMS standards. Standards are from single pure cultures harvested in mid-exponential phase; reported error is one standard deviation from replicate analyses.

Table E.1 lists the bulk hydrogen, carbon and nitrogen composition of the isotopic standards. Reported bulk hydrogen isotope compositions represent the mass balance weighted average isotopic composition of the whole membrane from all major fatty acid components for each organism (a-C15:0 and a-C17:0 fatty acid for *S. aureus* and C16:1, C16:0 and C18:1 fatty acid for *P. aeruginosa*).

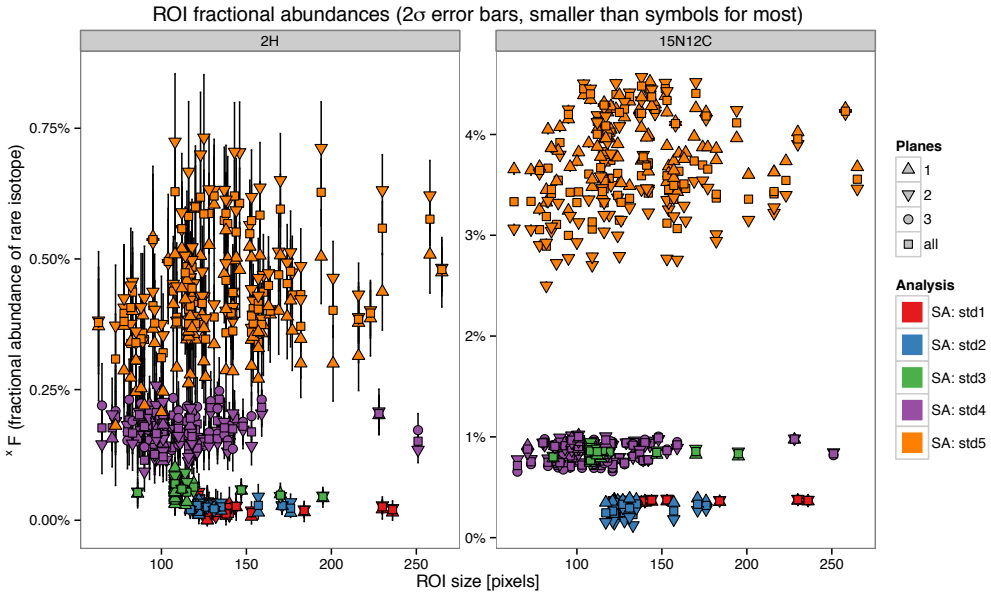

Figure E.2 – All ROIs from *S. aureus* standard whole single cells by analytical plane.

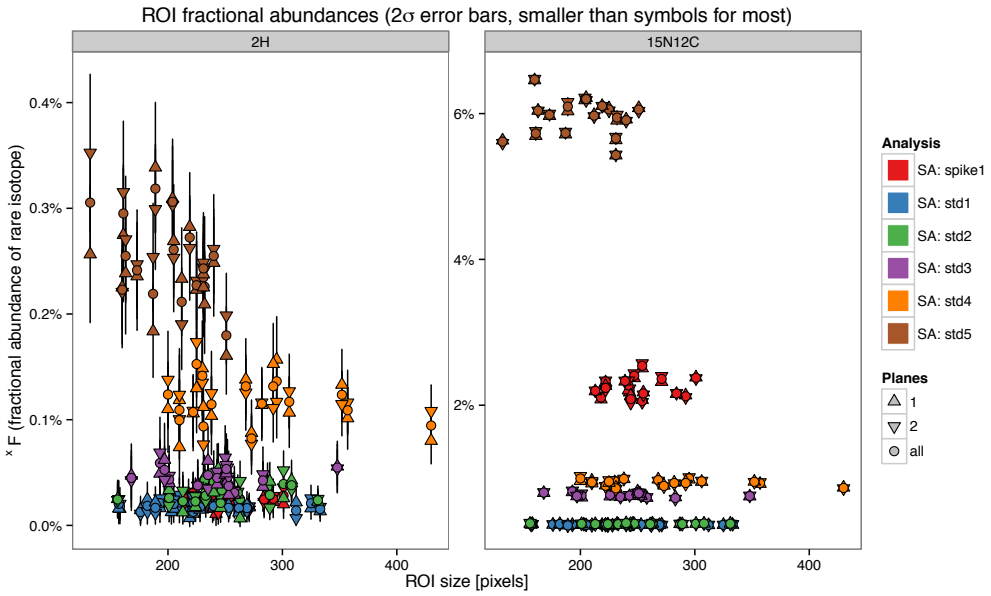

Figure E.3 – All ROIs from *S. aureus* standard embedded cells by analytical plane.

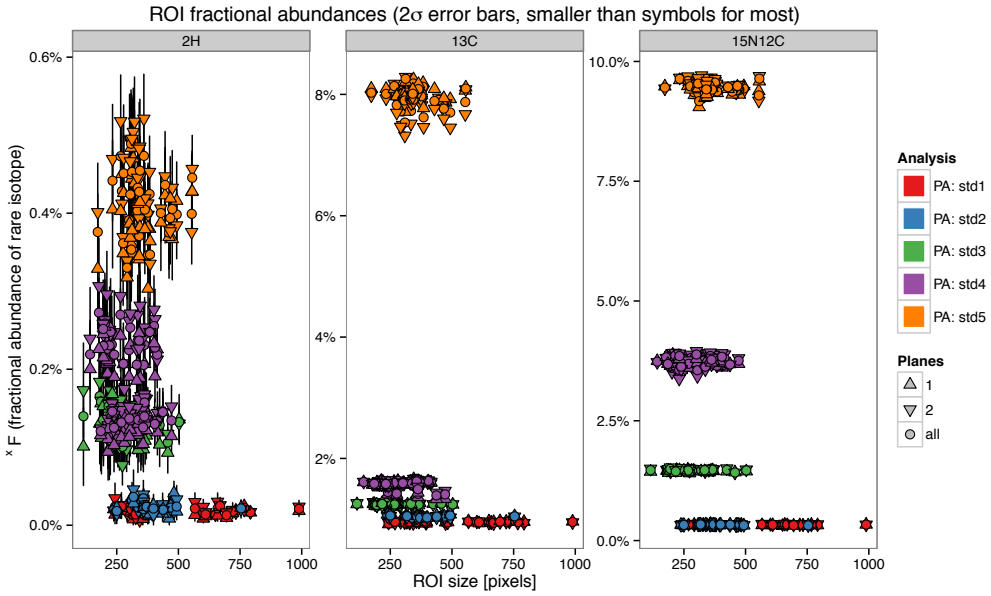

Figure E.4 – All ROIs from *P. aeruginosa* standard whole single cells by analytical plane.

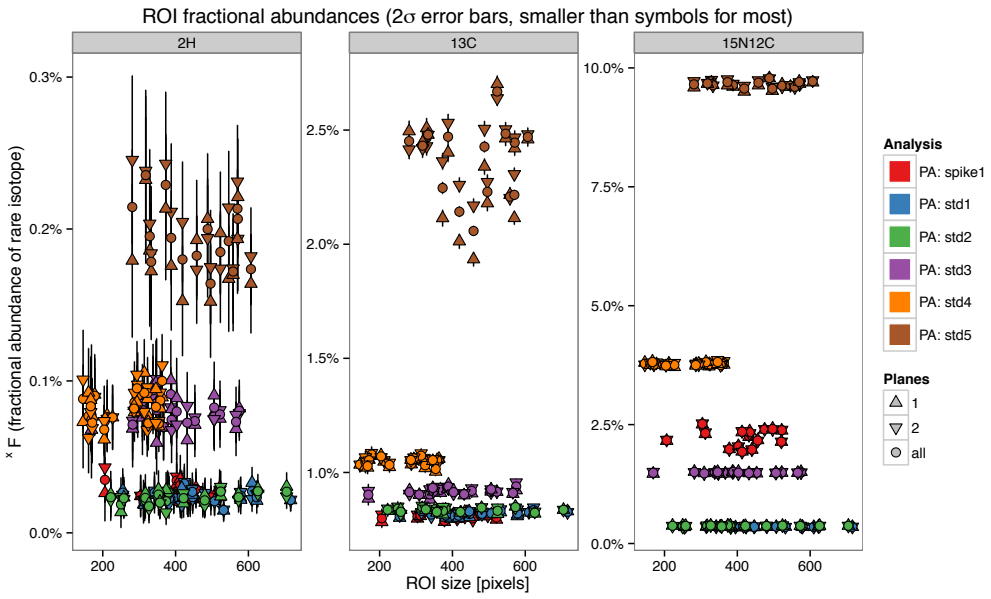

Figure E.5 – All ROIs from *P. aeruginosa* standard embedded cells by analytical plane.

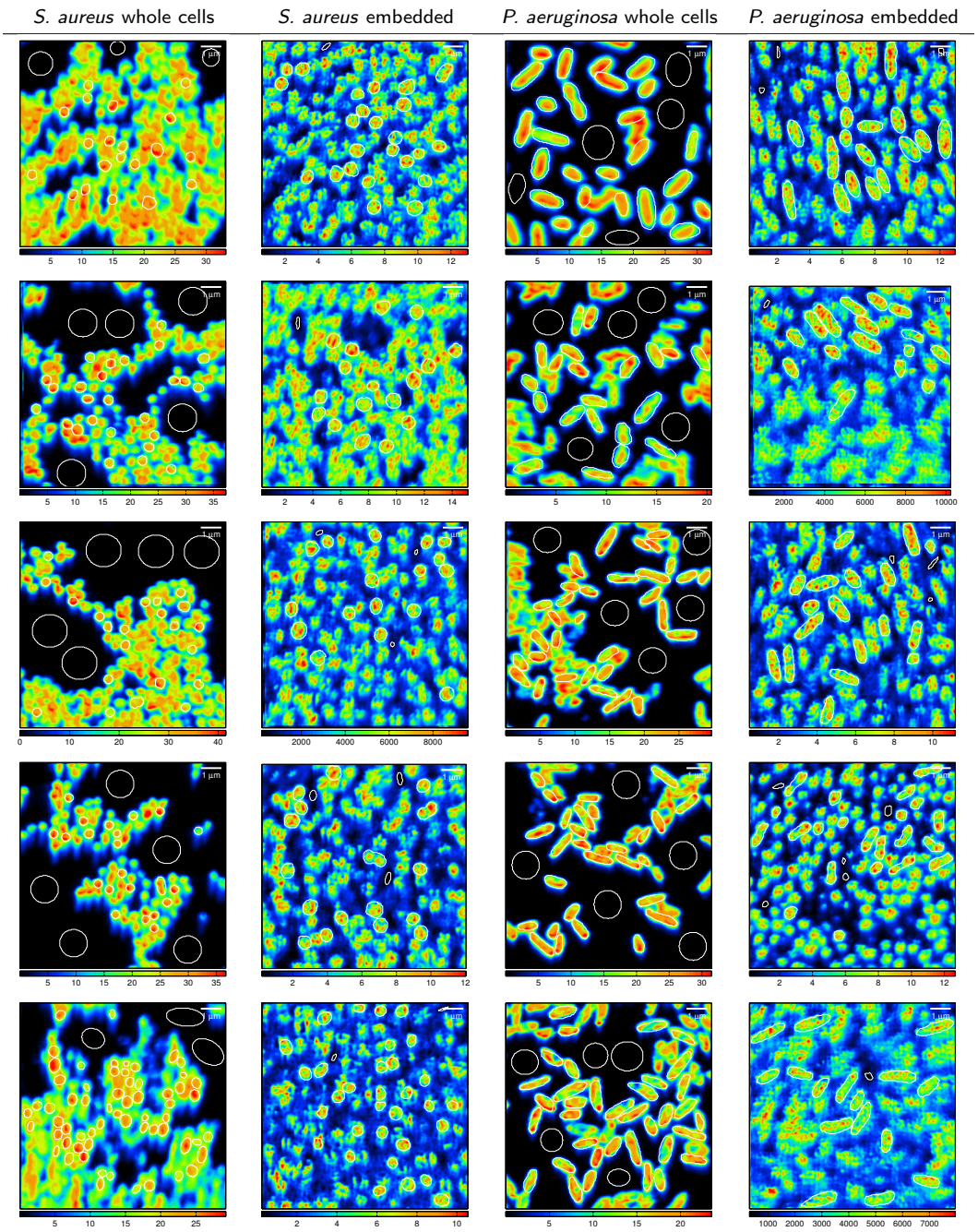

Figure E.6 – Examples of $^{14}N^{12}C$ ion maps of calibration standards. Ion maps of the calibration standards for *S. aureus* and *P. aeruginosa* with several ROI/cell outlines.

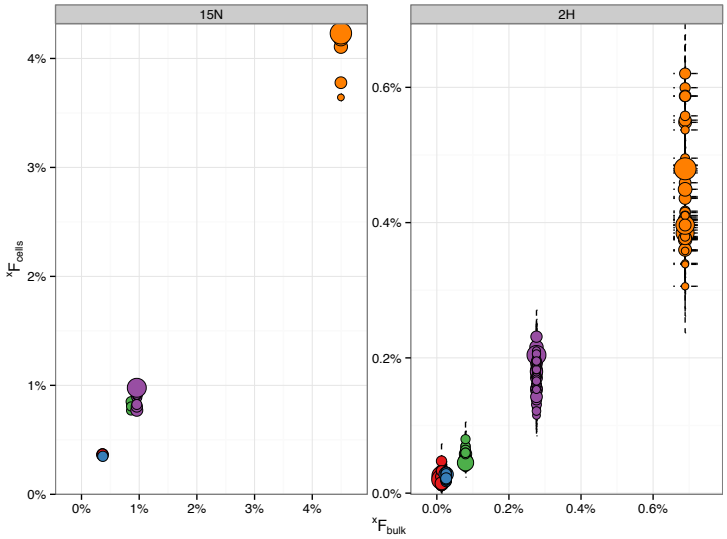

Figure E.7 – Calibration ROIs for whole single cells of *S. areus*. Individual data points represent individual cells (regions of interest or ROIs). The size of the data points reflects the relative size of the cells/ROIs. Horizontal error bars represent the maximum interval of the measured bulk isotopic composition (smaller than symbol sizes in most cases), dashed vertical error bars represent $2 \cdot \sigma_F$ of the error in the single cell isotopic composition from Poisson counting statistics.

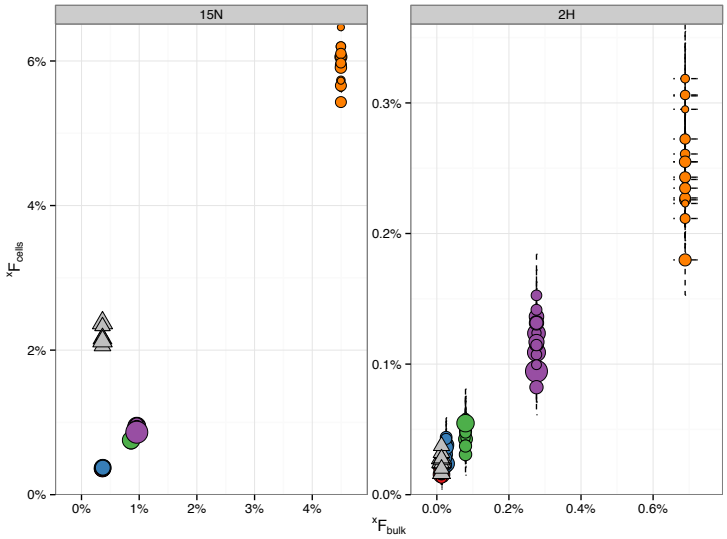

Figure E.8 – Calibration ROIs for embedded cells of *S. areus*. Gray triangles indicate cells that were fixed in the presence of an isotopic spike. They are pictured for ease of visual comparison, but were not included in the calibration.

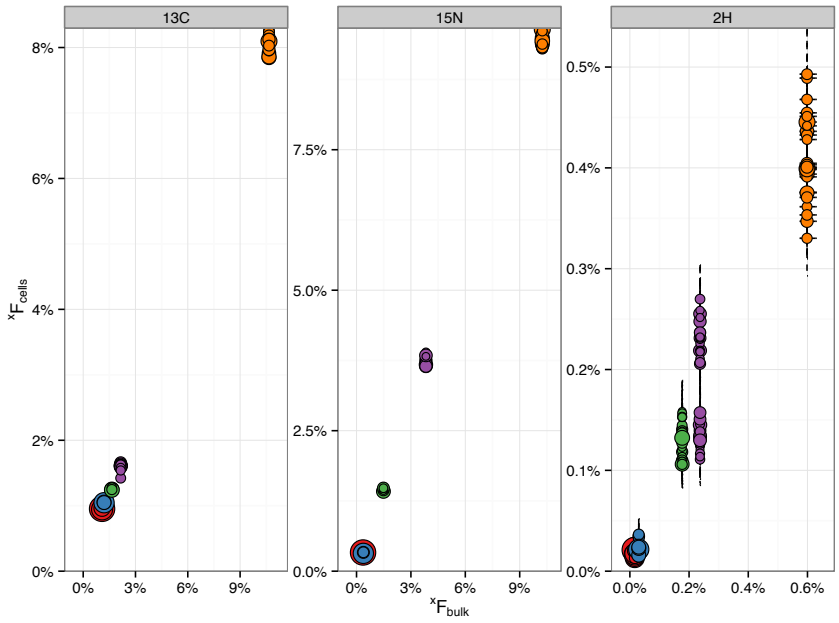

Figure E.9 – Calibration ROIs for whole single cells of *P. aeruginosa*.

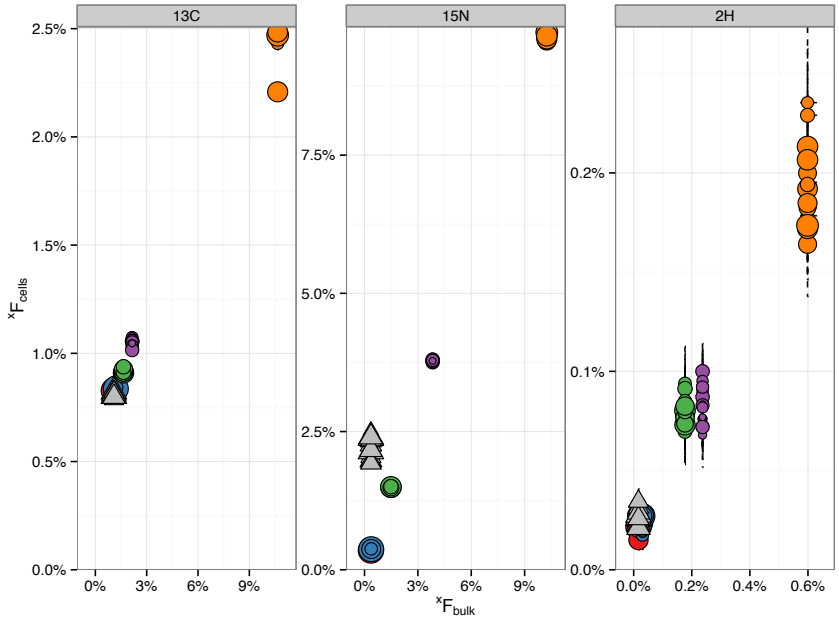

Figure E.10 – Calibration ROIs for embedded cells of *P. aeruginosa*. Gray triangles indicate cells that were fixed in the presence of an isotopic spike. They are pictured for ease of visual comparison but were not included in the calibration.

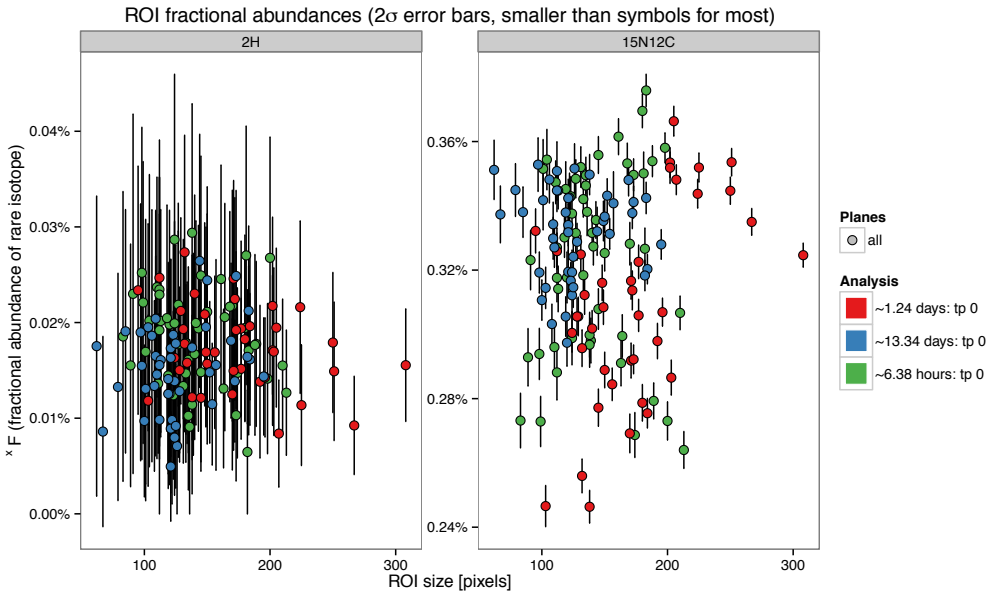

Figure E.11 – All ROIs from *S. aureus* continuous cultures, timepoint 0.

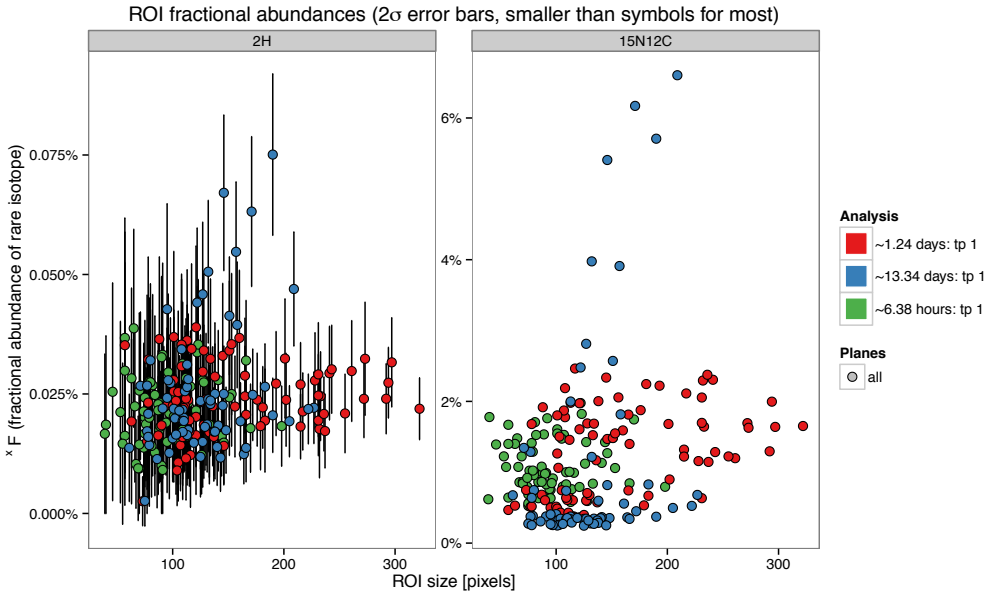

Figure E.12 – All ROIs from *S. aureus* continuous cultures, timepoint 1.

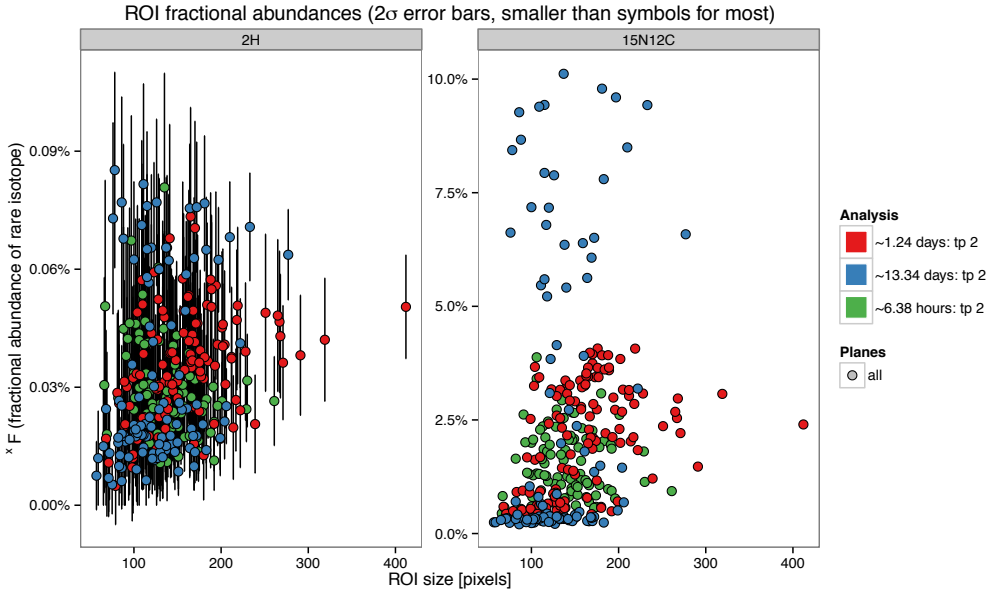

Figure E.13 – All ROIs from *S. aureus* continuous cultures, timepoint 2.

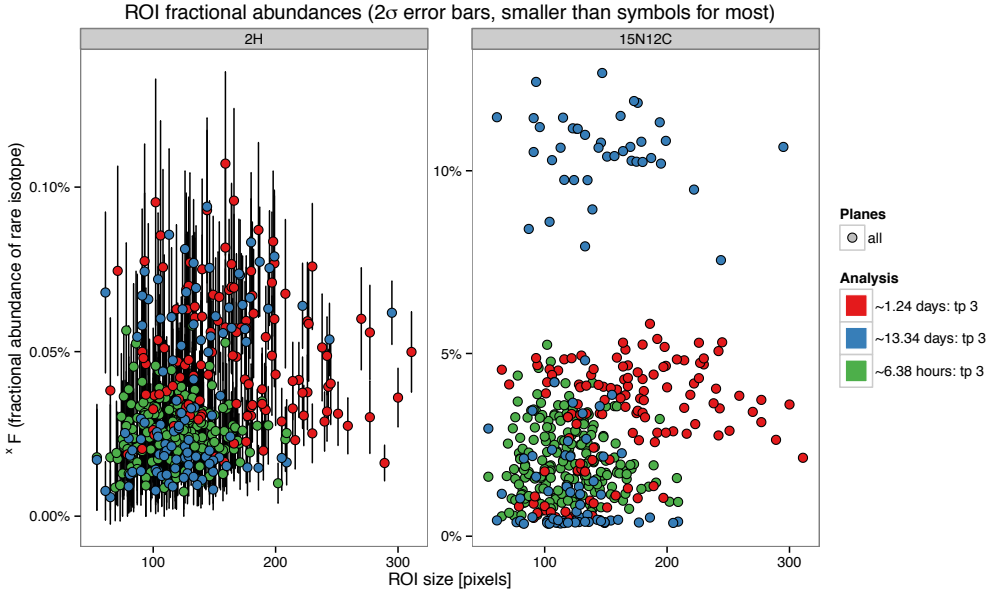

Figure E.14 – All ROIs from *S. aureus* continuous cultures, timepoint 3.

Appendix F

Supplementary material for Chapter 9

F.1 Supplementary figures

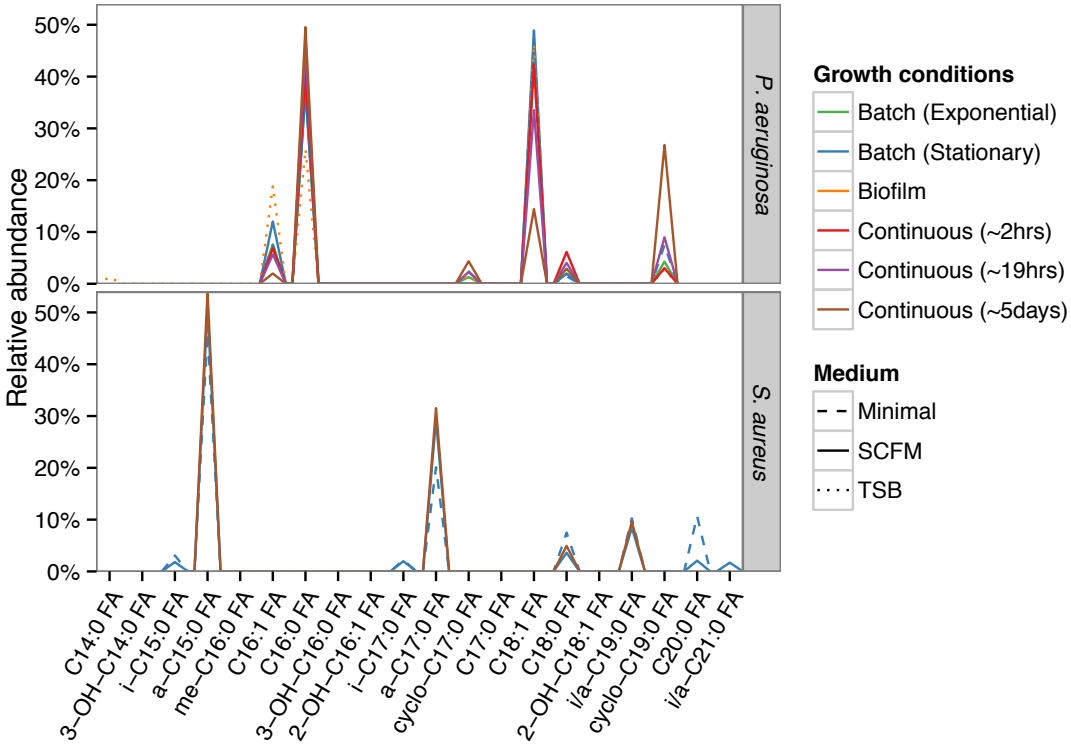

Figure F.1 – Growth condition dependent changes in fatty acids profiles.

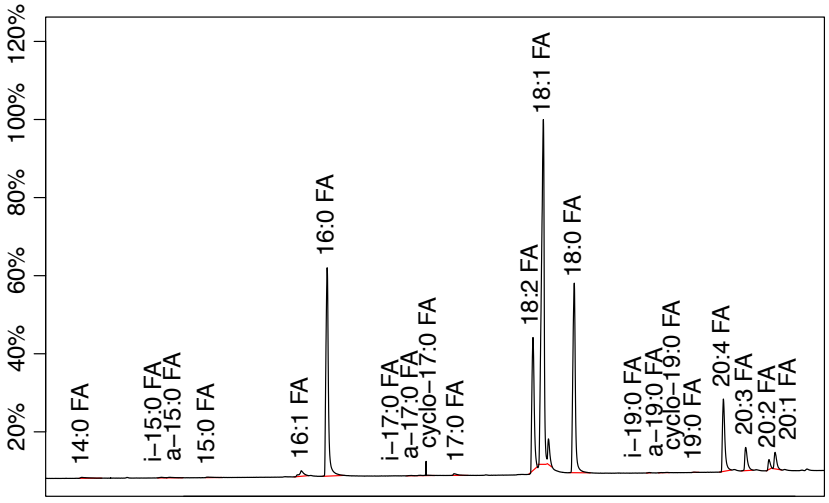

Figure F.2 – Clinical fatty acid profile. This figure illustrates the typical fatty acid profiles from a clinical lipid extracts, highlighting the predominance of many host-derived fatty acids and low abundance of the microbial targets (here, a-15:0 FA and a-17:0 for *S. aureus*).

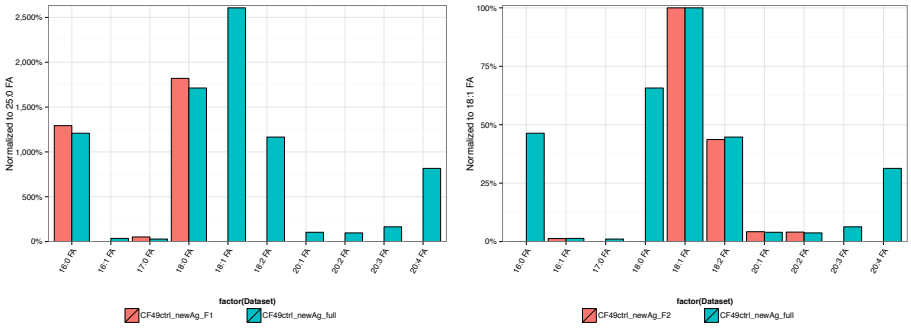

Figure F.3 – FAME separation by silver column chromatography. Separation of saturated from unsaturated fatty acids in a clinical sample. Left panel shows the saturated fraction F1 (red) vs. the whole sample (green), right panel shows the unsaturated fraction F2 (red) vs. the whole sample (green), illustrating quantitative separation of the different fatty acid types by their degree of saturation.

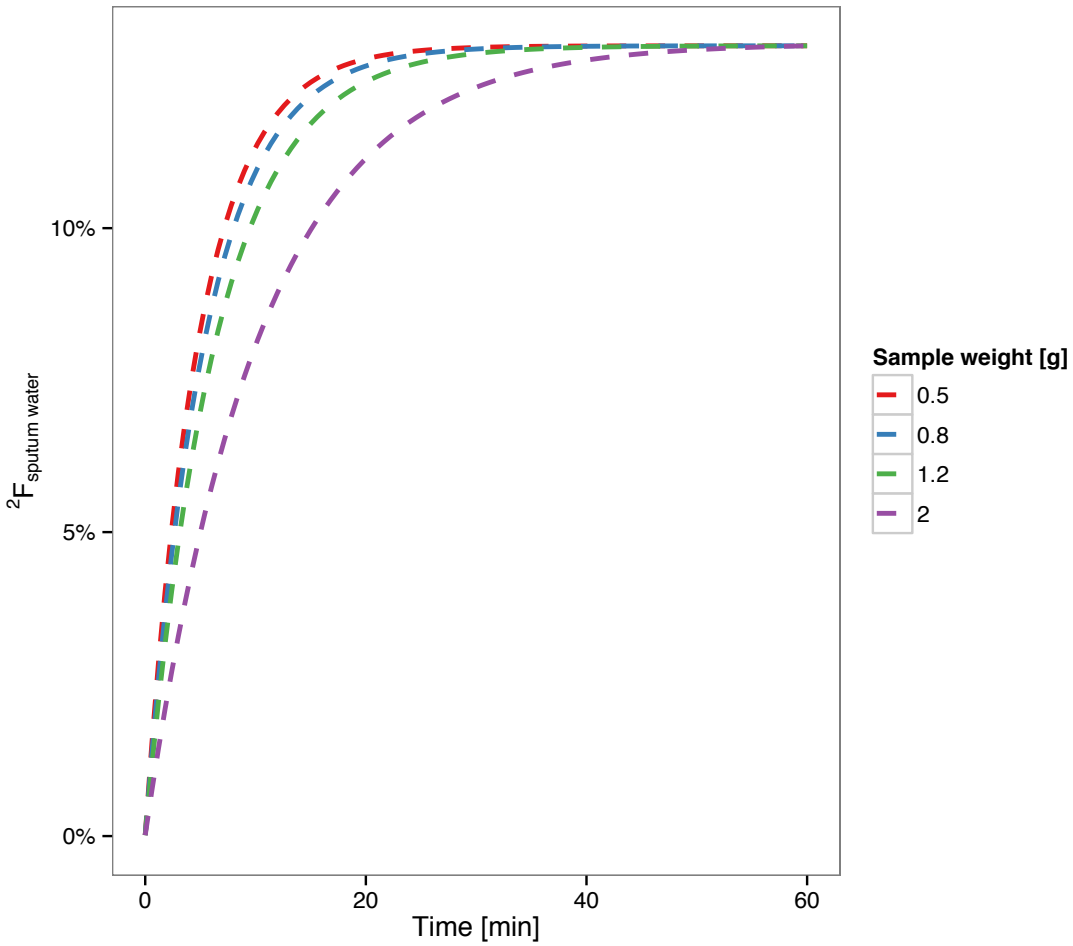

Figure F.4 – Example of weight-dependent water diffusion in sputum. This figure illustrates how the D_2O spike mixes with sputum water to increase the isotopic composition of the sputum water towards the equilibrium mix of both pools. The mixing rate constant depends on the weight of the sample, and is estimated from the relation shown in Figure 9.4, estimated here depending on the sample weight to illustrate the effect.

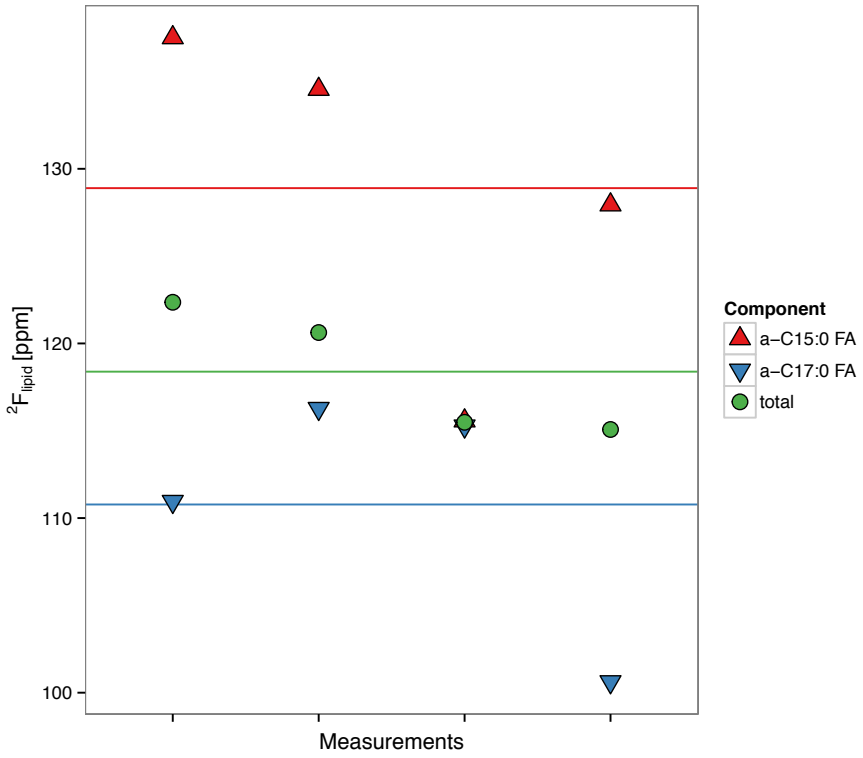

Figure F.5 – **Average natural isotopic composition of *S. aureus* fatty acids in clinical samples**. This figure illustrates the average values of naturally occurring a-C15:0 and a-C17:0 derived from clinical samples with sufficiently large volumes to split for control samples. The average is used for an estimate of natural abundance *S. aureus* fatty acids in growth-rate calculations for samples without enough volume to split the sample.

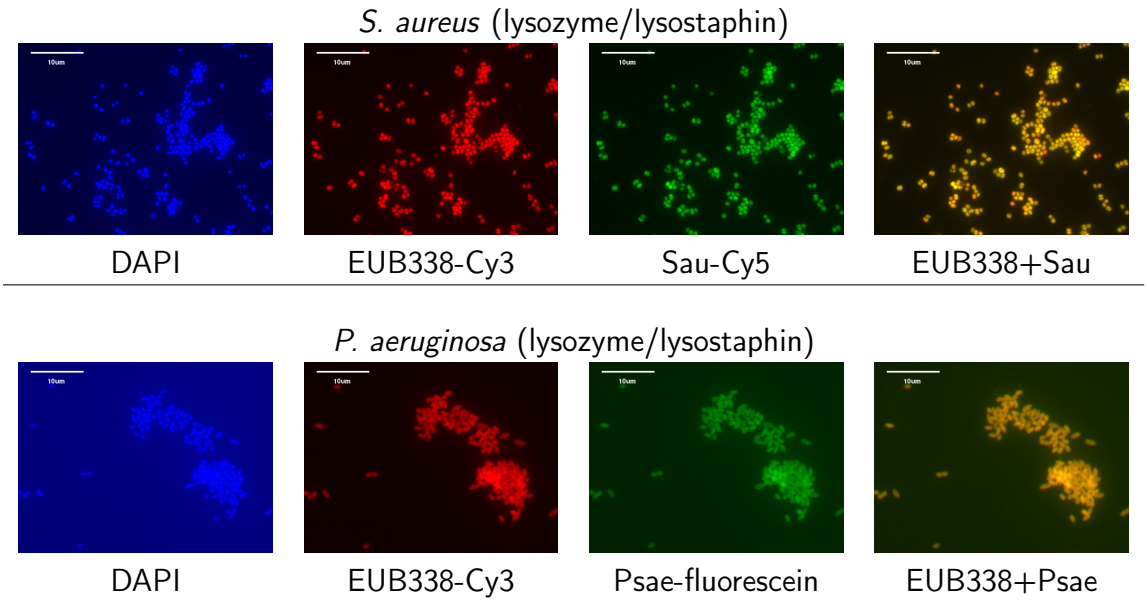

Figure F.6 – Fluorescent *in-situ* hybridization of whole *S. aureus* and *P. aeruginosa* cells. Single cell hybridization after on-slide cell wall digestion with lysozyme and lysostaphin.

S. aureus, lysozyme/lysostaphin **treated in thin-section**

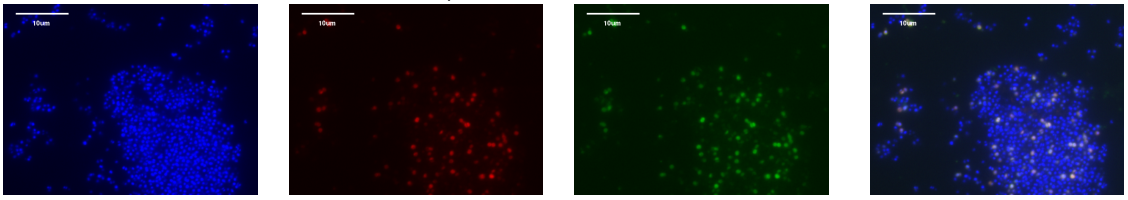

DAPI | EUB338-Cy3 | Sau-Cy5 | DAPI+EUB338+Sau

S. aureus, lysozyme/lysostaphin treated **before embedding**

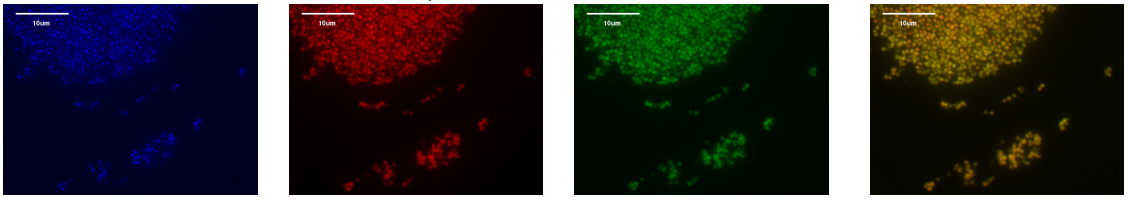

DAPI | EUB338-Cy3 | Sau-Cy5 | EUB338+Sau

P. aeruginosa, lysozyme/lysostaphin treated before embedding

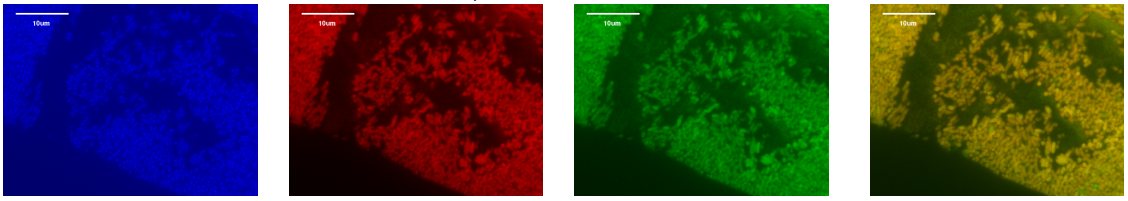

DAPI | EUB338-Cy3 | Psae-fluorescein | EUB338+Psae

Figure F.7 – Fluorescent *in-situ* hybridization of *S. aureus* and *P. aeruginosa* cells in plastic thin sections. Hybridization in plastic thin section with cell wall digestion on slide (top) vs. prior to embedding (bottom).

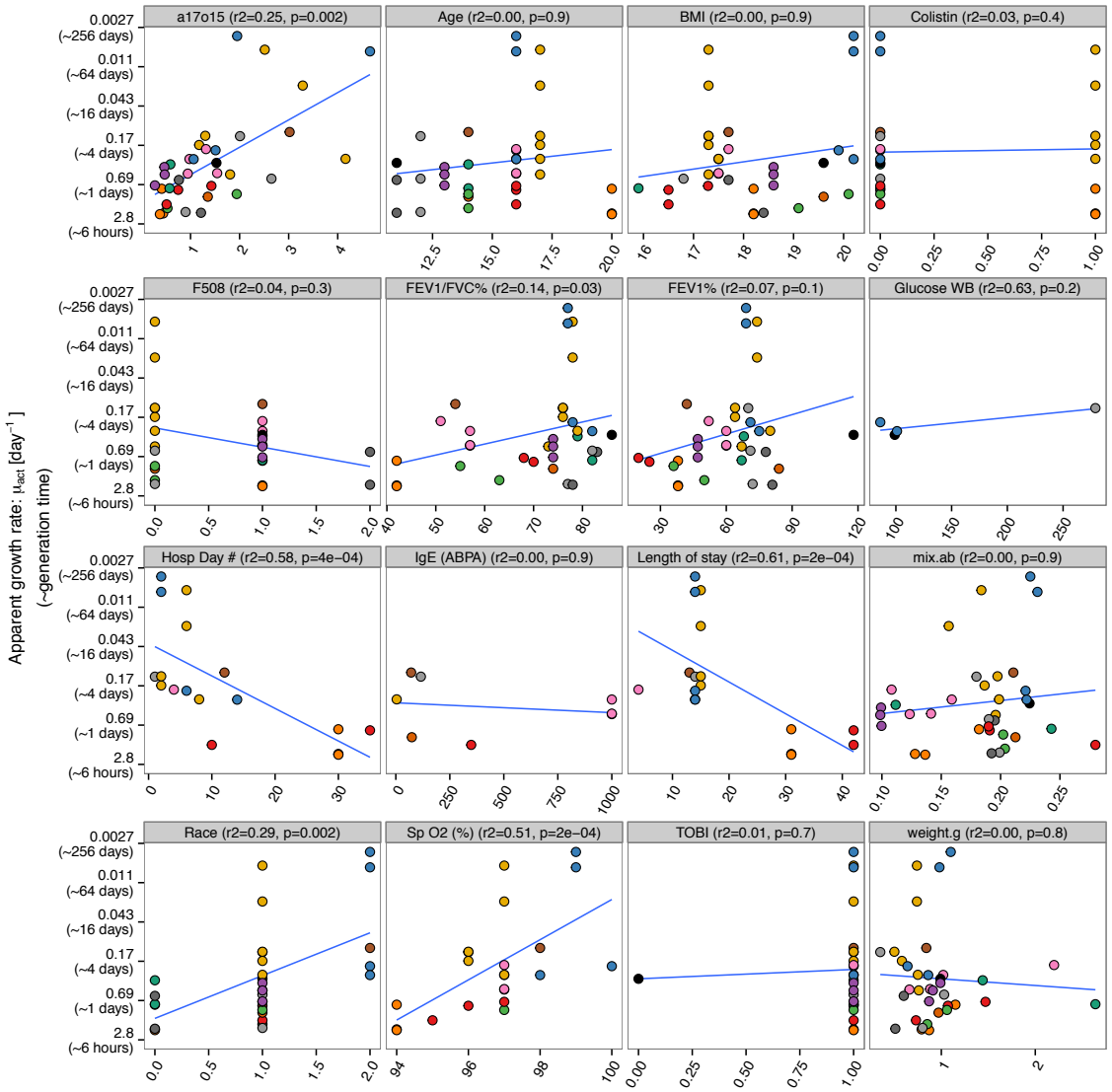

Figure F.8 – Correlation between microbial activity and all clinical parameters. This figure illustrates the correlation between a variety of recorded clinical parameters and the measured bulk growth rates for *S. aureus* in clinical samples. Each panel denotes a different parameter with the respective R^2, and p-value for the correlation with growth rate indicated in the header. The different colours indicate samples from different patients in the study. Not all clinical information was available for all data points.

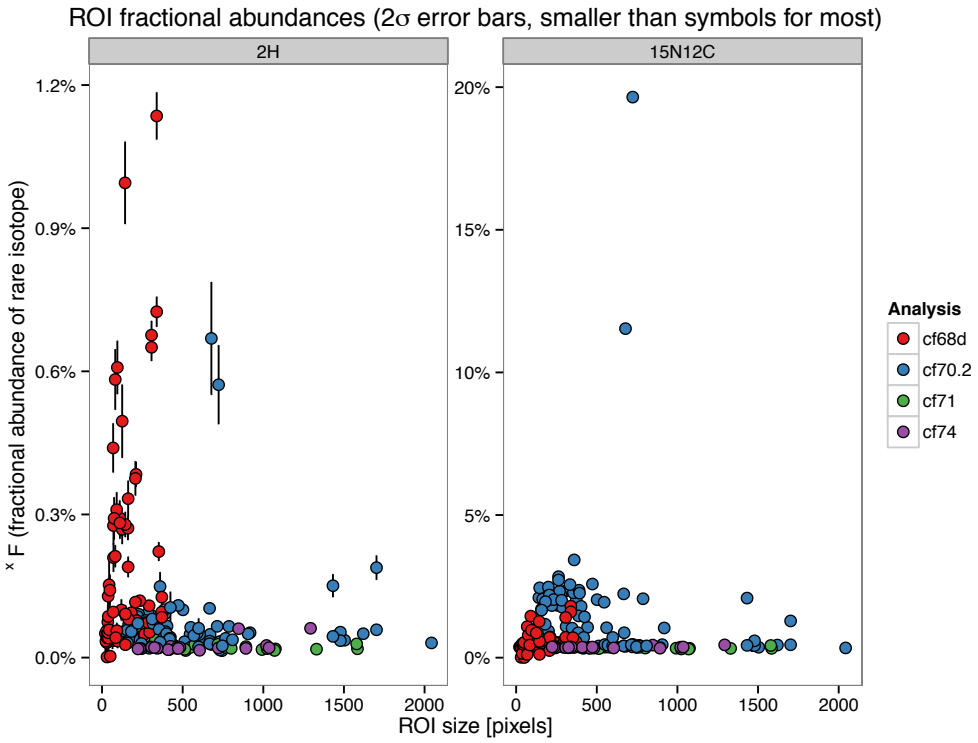

Figure F.9 – Isotopic composition of all ROIs from single-cell analyses.